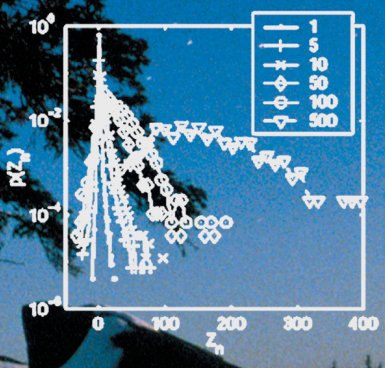
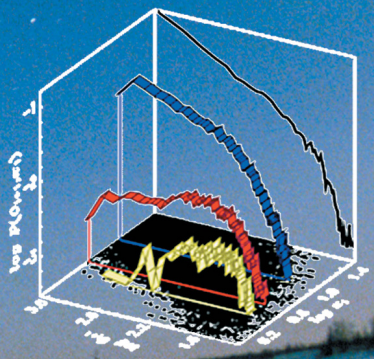
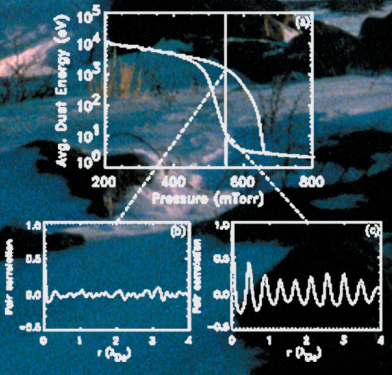
ASTROPHYSICS AND
SPACE SCIENCE LIBRARY

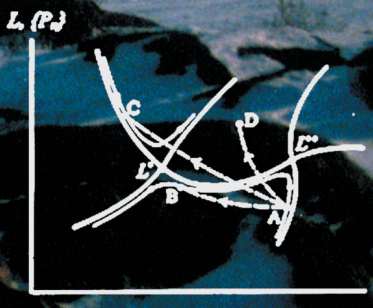
NONEQUILIBRIUM PHENOMENA IN PLASMAS

A. SURJALAL SHARMA
PREDHIMAN K. KAW
Editors









Springer

NONEQUILIBRIUM PHENOMENA IN PLASMAS

ASTROPHYSICS AND SPACE SCIENCE LIBRARY

VOLUME 321

EDITORIAL BOARD

Chairman

W.B. BURTON, National Radio Astronomy Observatory, Charlottesville, Virginia, U.S.A. (bburton@nrao.edu); University of Leiden, The Netherlands (burton@strw.leidenuniv.nl)

Executive Committee

J. M. E. KUIJPERS, *Faculty of Science, Nijmegen, The Netherlands*
E. P. J. VAN DEN HEUVEL, *Astronomical Institute, University of Amsterdam, The Netherlands*
H. VAN DER LAAN, *Astronomical Institute, University of Utrecht, The Netherlands*

MEMBERS

I. APPENZELLER, *Landessternwarte Heidelberg-Königstuhl, Germany*
J. N. BAHCALL, *The Institute for Advanced Study, Princeton, U.S.A.*
F. BERTOLA, *Universitá di Padova, Italy*
J. P. CASSINELLI, *University of Wisconsin, Madison, U.S.A.*
C. J. CESARSKY, *Centre d'Etudes de Saclay, Gif-sur-Yvette Cedex, France*
O. ENGVOLD, *Institute of Theoretical Astrophysics, University of Oslo, Norway*
R. McCRAY, *University of Colorado, JILA, Boulder, U.S.A.*
P. G. MURDIN, *Institute of Astronomy, Cambridge, U.K.*
F. PACINI, *Istituto Astronomia Arcetri, Firenze, Italy*
V. RADHAKRISHNAN, *Raman Research Institute, Bangalore, India*
K. SATO, *School of Science, The University of Tokyo, Japan*
F. H. SHU, *University of California, Berkeley, U.S.A.*
B. V. SOMOV, *Astronomical Institute, Moscow State University, Russia*
R. A. SUNYAEV, *Space Research Institute, Moscow, Russia*
Y. TANAKA, *Institute of Space & Astronautical Science, Kanagawa, Japan*
S. TREMAINE, *CITA, Princeton University, U.S.A.*
N. O. WEISS, *University of Cambridge, U.K.*

Nonequilibrium Phenomena in Plasmas

Edited by

A. SURJALAL SHARMA
University of Maryland,
College Park, MD, U.S.A.

and

PREDHIMAN K. KAW
Institute for Plasma Research,
Gandhinagar, India

Springer

A C.I.P. Catalogue record for this book is available from the Library of Congress.

ISBN-10 1-4020-3108-4 (HB) Springer Dordrecht, Berlin, Heidelberg, New York
ISBN-10 1-4020-3109-2 (e-book) Springer Dordrecht, Berlin, Heidelberg, New York
ISBN-13 978-1-4020-3108-3 (HB) Springer Dordrecht, Berlin, Heidelberg, New York
ISBN-13 978-1-4020-3109-0 (e-book) Springer Dordrecht, Berlin, Heidelberg, New York

---

Published by Springer
P.O. Box 17, 3300 AA Dordrecht, The Netherlands.

Cover Images
The background is an image of an aurora – one of the spectacular manifestations of substorms.
Photograph by Nori Sakamoto (http://www.auroraphoto.net/).

The four frames in the foreground represent cases of nonequilibrium phenomena.
Clockwise from the top right: the distribution of magnetospheric response for different solar wind conditions (Sharma et al., Chapter 6), the renormalization-group trajectories and fixed points (Chang et al., Chapter 3), the hysteresis loop from a simulation of dusty plasmas (Ganguli et al., Chapter 13), and the self-similarity of particle flux in the scrape-off layer of ADITYA tokamak (Jha et al., Chapter 9).

Printed on acid-free paper

springeronline.com

All Rights Reserved
© 2005 Springer
No part of this work may be reproduced, stored in a retrieval system, or transmitted in any form or by any means, electronic, mechanical, photocopying, microfilming, recording or otherwise, without written permission from the Publisher, with the exception of any material supplied specifically for the purpose of being entered and executed on a computer system, for exclusive use by the purchaser of the work.

Printed in the Netherlands.

Contents

Preface vii

Section 1: Space Plasmas

1. Nonequilibrium Phenomena in the Magnetosphere 3
A. S. Sharma, D. N. Baker and J. E. Borovsky

2. Complexity and Intermittent Turbulence in Space Plasmas 23
T. Chang, S. W. Y. Tam and C. C. Wu

3. Complexity and Topological Disorder in the Earth's Magnetotail Dynamics 51
G. Consolini T. Chang and A. T. Y. Lui

4. Simulation Study of SOC Dynamics in Driven Current-Sheet Models 71
Alex J. Klimas, Vadim M. Uritsky, Dimitris Vassiliadis and Daniel N. Baker

5. Two State Transition Model of the Magnetosphere 91
T. Tanaka

6. Global and Multiscale Phenomena of the Magnetosphere 117
A. S. Sharma, A. Y. Ukhorskiy and M. I. Sitnov

7. Low Frequency Magnetic Fluctuations in the Earth's Plasma Sheet 145
A. A. Petrukovich

8. Magnetospheric Multiscale Mission 179
A. S. Sharma and S. A. Curtis

Section 2: Laboratory Plasmas

9. Perspectives of Intermittency in the Edge Turbulence of Fusion Devices 199
R. Jha, P. K. Kaw and A. Das

10. Transition to Self-Organized High Confinement States in Tokamak Plasmas 219
P. N. Guzdar R. G. Kleva, R. J. Groebner and P. Gohil

11. Internal Transport Barriers in Magnetised Plasmas 239
X. Garbet, P. Ghendrih, Y. Sarazin, P. Beyer, C. Figarella and S. Benkadda

12. Characterization of Turbulence in Terms of Probability Density Function 257
C. Hidalgo, B. Gonçalves and M. A. Pedrosa

13. Phase Transition in Dusty Plasmas 273
Gurudas Ganguli, Glenn Joyce and Martin Lampe

Section 3: Cross-Disciplinary Studies

14. Precursors of Catastrophic Failures 293
Srutarshi Pradhan and Bikas K. Chakrabarti

15. Multi-Scale Interactions and Predictability of the Indian Summer Monsoon 311
B. N. Goswami and R. S. Ajaya Mohan

Preface

During the past few decades there has been increasing interest in the study of complexity with a view to better understand physical, biological, economic and social systems. The specific features of complexity dealing with nonequilibrium phenomena are intimately connected with statistical dynamics and form one of the growing research areas in modern nonlinear physics. These studies encompass the ideas of self-organization, phase transition, critical phenomena, self-organized criticality and turbulence. In this book we have tried to bring together into a coherent account the recent developments in the study of nonequilibrium phenomena in plasmas.

The complexity of plasmas is well recognized, arising mainly from its inherent nonlinearity and far from equilibrium nature, aspects that are actively being studied now. The nonequilibrium behavior of plasmas is evident in the natural setting, for example, in the Earth's magnetosphere. Similarly, laboratory plasmas like fusion bottles also have their fair share of complex behavior. The common issues of nonequilibrium phenomena in plasmas motivated us to convene a workshop in Ahmedabad, India during March 2001. This volume derives from the proceedings of the workshop, which brought together scientists from a broad spectrum of research areas. These articles present the studies of complexity in the context of nonequilibrium phenomena using theory, modeling, simulations and experiments, both in the laboratory and in nature.

The first group of articles in Section 1 represents a cross section of the recent developments in the study of complexity in space plasmas. The first chapter is an overview of the current developments and the different paradigms used to study complexity, mainly of geospace plasmas. The ubiquitous global and multiscale phenomena in the Earth's magnetosphere have been studied using the frameworks of phase transitions, self-organized criticality and turbulence. Chapter 2 presents a study of intermittency in multiscale fluctuations as seen in MHD simulations using dynamic renormalization techniques. The complexity of the magnetotail is studied in Chapter 3 using spacecraft data. The connection between the emergence of complexity and topological disorder is explored using the ideas of criticality. In Chapter 4, the avalanching behavior of magnetotail

dynamics is simulated using a resistive MHD model and compared with the characteristics of scale size distributions computed from the Polar spacecraft images of the auroral ionosphere. Chapter 5 is a study of the global transitions in the magnetosphere using an MHD code, highlighting its two state nature. Data-derived modeling in which long time series data is used to reconstruct the phase space to study the dynamical behavior is presented in Chapter 6. This approach has the advantage that no a priori assumptions of the physical processes are made and thus can represent the inherent characteristics of the system. The measurements of low frequency magnetic fluctuations in the magnetotail by Interball-1 mission and their study in terms of stochastic scale-invariant wave fields are presented in Chapter 7. The Magnetospheric Multiscale mission and the prospects of advancing the understanding of multiscale phenomena and the underlying fundamental processes with new measurements are discussed in Chapter 8.

The phenomena of self-organization, turbulence and intermittency, have been studied extensively in laboratory plasmas. In particular these studies have advanced our understanding of transport in tokamaks, laboratory fusion devices which have shown clear potential of operating in fusion reactor regimes. The second group of papers, Chapters 9 thru 12 are devoted to tokamak plasmas. Chapter 9 presents a summary of the present state of experimental research in the field of intermittency in edge turbulence of tokamaks and other toroidal fusion bottles. Chapters 10 and 11 discuss the interesting features of transition to good confinement regimes (such as the H-mode and the internal transport barrier mode) in tokamaks. Chapter 12 presents the probability distribution function approach for a study of turbulent transport in fusion plasmas. Chapter 13 presents the phase transition behavior in the nonequilibrium dusty plasmas modeled in terms of the inherent instabilities of such plasmas.

Many of the ideas, results and methods that are discussed in the context of plasmas have important implications for areas of physics well beyond plasma physics. The cross-disciplinary aspects of these are presented in the selected articles in the third and last section of the book. The nature of precursors of global transitions is studied using well-known models in Chapter 14 and show that they are well characterized. The role of multiscale interactions in the predictability of Indian monsoon is presented in Chapter 15. The co-existence and interaction between global and multiscale features is common to many systems.

During the preparation of this volume we have received co-operation and assistance from many persons. We would like to thank those who have participated in the review of the articles: Bikas Chakrabarti, Giuseppe Consolini, Yasha Dimant, Mervyn Freeman, Gurudas Ganguli, Parvez Guzdar, Carlos Hidalgo, Ratneswar Jha, Reinaldo Rosa, Abhijit Sen, and Xi Shao. We thank

Danny Pan for overcoming the multiple issues in the preparation of the articles for publication using electronic media.

A. Surjalal Sharma
University of Maryland
College Park, Maryland, U.S.A.

Predhiman K. Kaw
Institute for Plasma Research
Gandhinagar, Gujarat, India

Section 1

SPACE PLASMAS

Chapter 1

NONEQUILIBRIUM PHENOMENA IN THE MAGNETOSPHERE

Phase Transition, Self-organized Criticality and Turbulence

A. Surjalal Sharma[1], Daniel N. Baker[2] and Joseph E. Borovsky[3]
[1]*University of Maryland, College Park, Maryland, U.S.A.*
[2]*University of Colorado, Boulder, Colorado, U.S.A.*
[3]*Los Alamos National Laboratory, Los Alamos, New Mexico, U.S.A.*

Abstract: The magnetosphere is a large scale natural system powered by the solar wind that exhibits many nonequilibrium phenomena. A wide range of these phenomena are driven directly by the solar wind or arise from the storage-release processes internal to the magnetosphere. Under the influnce by the turbulent solar wind, the magnetosphere during geomagnetically active periods is far from equilibrium and storms and substorms are essentially non-equilibrium phenomena. In spite of the distributed nature of the physical processes and the apparent irregular behavior, there is a remarkable coherence in the magnetospheric response during substorms and the entire magnetosphere behaves as a global dynamical system. Alongwith the global features, the magnetosphere exhibits many multi-scale and intermittent characteristics. These features of the magnetosphere have been studied in terms of phase transitions, self-organized criticality and turbulence. In the phase transition scenario the global features are modeled as first-order transitions and the multi-scale behavior is interpreted as a manifestation of the scale-free nature of criticality in second order phase transitions. In the self-organized criticality framework substorms are considered as avalanches in the system when criticality is reached. Many features of the magnetosphere, in particular the power law dependence of scale sizes, can be viewed as a feature of a turbulent system. The common theme underlying these approaches is the recognition that the nonequilibrium phenomena in the magnetosphere could be understood in terms of processes generic to such systems. In many cases the power-law behavior of the magnetosphere seen in many observations is the starting point for these studies. This chapter is an overview of the recent understanding achieved using these different approaches, and identifies the common issues and differences.

A.S. Sharma and P.K. Kaw (eds.), Nonequilibrium Phenomena in Plasmas, 3–22.
© 2005 *Springer. Printed in the Netherlands.*

Key words: magnetosphere, solar wind, storms, substorms, complexity, phase transitions, self-organized criticality, turbulence, intermittency

1. Introduction

Earth's magnetosphere is a magnetic cavity formed by the interaction of the solar wind with the geoplasma in the dipole magnetic field. It is a large scale natural system which exhibits complex behavior originating from the turbulence in the solar wind as well as its internal processes. The time evolution of such systems is essentially determined by the interactions between its different components or subsystems, and by the characteristics of its driver, the solar wind. Underlying this behavior is the nonlinearity inherent in the magnetospheric plasma and fields.

The main dynamical features of the magnetosphere are storms and substorms, which are prevalent mainly when the solar wind is strongly coupled to the magnetosphere, e.g., due to enhanced magnetic reconnection at the magnetopause. Geospace storms and related processes have time scales of days and are associated with enhancements of the ring current in the inner magnetosphere. Substorms on the other hand have characteristic time scales of an hour or so and are associated mainly with the plasma processes in the magnetotail. While our understanding has advanced rapidly due to recent multi-spacecraft and ground-based measurements, and theory and modeling, many outstanding questions due to the complexity of the magnetosphere arising from the interactions among its components and the driving by the turbulent solar wind. Studies of the magnetosphere from the viewpoint of nonlinear dynamics and complexity provides a complementary framework for understanding the solar wind—magnetosphere coupling.

The dynamical behavior of the magnetosphere has been studied extensively using nonlinear dynamical techniques (see reviews: Sharma, 1995, 1997, 2003, 2004; Klimas et al., 1996). The evidence of large scale coherence in magnetospheric dynamics was first obtained in the form of low dimensional behavior using the time series data of auroral electrojet indices (Vassiliadis et al., 1990). This result is consistent with simplified dynamical models of the magnetosphere (Baker et al., 1990), its morphology derived from the observational data and theoretical understanding (Siscoe, 1991), and numerical simulations using global MHD codes (Lyon, 2000). The recognition of the effectively low dimensional dynamics of the magnetosphere has stimulated a new direction in the studies of the solar wind-magnetosphere coupling. Among the outcomes of this research is the capability of forecasting substorms (Vassiliadis et al., 1995; Ukhorskiy et al. 2004) and storms (Valdivia et al., 1996; Sharma et al., 2003) with high accuracy and reliability. Many models of the magnetosphere have

been developed based on the low-dimensionality of its dynamics (Baker et al., 1990; Klimas et al., 1992; Horton et al., 1996).

The multiscale behavior of the magnetosphere, on the other hand, has been recognized in many different ways. An earlier recognition of the multiscale behavior in the magnetosphere is, albeit indirectly, in the analogy between the dynamics of the magnetotail to the turbulence generated by a fluid flow past an obstacle (Rostoker, 1984). Subsequently, the power law dependences of the observed time series data, e.g., in the AE index (Tsurutani et al., 1990) provided quantitative measures of the multi-scale behavior. Studies of the auroral electrojet indices using more sophisticated techniques such as the structure function showed features that could be reconciled only with multi-scale behavior (Takalo et al., 1993). It should be noted that the concept of criticality in magnetospheric dynamics (Chang, 1992) implies multiscale behavior.

The coexistence of the global coherence with multiscale behavior is a key feature of the magnetosphere and has been modeled using many approaches. In the phase transition approach the global features are considered as phase transitions of the first order, while the multiscale properties originate from the scale-free properties of second order phase transitions (Sitnov et al., 2000, 2001; Sharma et al., 2001; Ukhorskiy et al., 2002, 2003, 2004; Shao et al., 2003). The framework of self-organized criticality have used model magnetospheric dynamics (Consolini, 1997; Chapman et al., 1998; Watkins et al., 1999; Klimas et al., 2002; Uritsky et al., 2002, 2003). The power law behavior of multiscale phenomena is akin to such characteristics of turbulent systems and these properties have been studied using spacecraft and ground based measurements (Borovsky et al., 1993; Ohtani et al., 1995, 1998; Freeman et al., 2000). These three approaches and the inter-relationship are discussed in the following sections in the context of magnetospheric complexity.

2. Phase Transition-Like Behavior

The phenomenon of phase transition is well known, e.g., the change of state or phase from liquid to gas at the boiling point. Such transitions in which there is an abrupt change in the density, e.g., water-steam transition at 100 deg. C under normal pressure, are the first order phase transitions. The boiling temperature however depends on the pressure and at higher pressures the transition takes place at higher temperatures. Also the changes in the density at higher pressures become smaller compared to those at normal pressure. This trend of higher pressure yielding higher boiling point and smaller change in the density continues until characteristic values of the pressure and temperature are reached and at these values there is no change in the density. This is the critical point of the liquid and the transition is the second order phase transition. For example, the critical point for water-steam transition is 374 deg C and 218 atmospheres.

The critical behavior is characterized by universality (being generic to a whole class of problems) and scale-invariance (the absence of a preferred scale length and the presence of all relevant scales). The study of the critical behavior (Stanley, 1971; Dixon et al., 1999) has been strongly motivated by these features and has led to new powerful theoretical techniques such as the renormalization group (Fisher, 1974; Wilson, 1983).

The correlated data of the coupled solar wind-magnetosphere compiled by Bargatze et al. (1985) has been used to study the phase transition-like behavior of substorms (Sitnov et al., 2000, 2001; Sharma et al., 2001, 2004). The data set consists of 34 intervals of correlated solar wind input and the magnetospheric response as an output. The solar wind input is the interplanetary electric field VB_s, where B_s is the southward component of the interplanetary magnetic field (IMF) and V is the component of the solar wind velocity along the Earth-Sun axis. The magnetospheric response to the solar wind is represented by the auroral electrojet index, AL.

The magnetospheric dynamics can be reconstructed from the time series data using time delay techniques (Abarbanel et al., 1993). Among these, the singular spectrum analysis is often used to reveal the main dynamical features inherent in the data. This techniques has been used earlier to reconstruct the autonomous dynamics of the magnetosphere from the auroral electrojet indices (Sharma, 1993; Sharma et al., 1993). The singular spectrum analysis is based on the singular value decomposition and uses the properties of the trajectory matrix constructed from the time series data by time delay embedding. The VBs-AL data can be used to construct the time delay vectors and consequently the trajectory matrix. Since the averaging time for this data set is 2.5 min the value of the embedding dimension m is chosen to be 32 to provide a time window of 80 min, appropriate for substorms. The singular value decomposition of this matrix provides orthogonal eigenfunctions corresponding to different eigenvalues. The original idea of the autonomous version of singular spectrum analysis (SSA) is that there should be a noise floor inherent in the data and the number of eigenvalues with magnitudes greater than the noise floor is an estimate of the effective dimension of the system. In many real systems the SSA spectrum has a clear power-law form, with no clear noise floor. In such cases, the projections of the data along the leading eigenvectors provide a good approximation of the system, similar to the so called mean-field or Landau approximation, often used in the phase transition theory as a zeroth-level approximation (Sitnov et al., 2000).

The first principal component obtained by singular spectrum analysis is a measure of the solar wind input averaged over the interval of about 80 min while the second principal component is of the similarly averaged AL index. The third component reflects the changes in the input with time (Sharma et al., 2001, Sitnov et al., 2000, 2001). The eigenvectors corresponding to these three

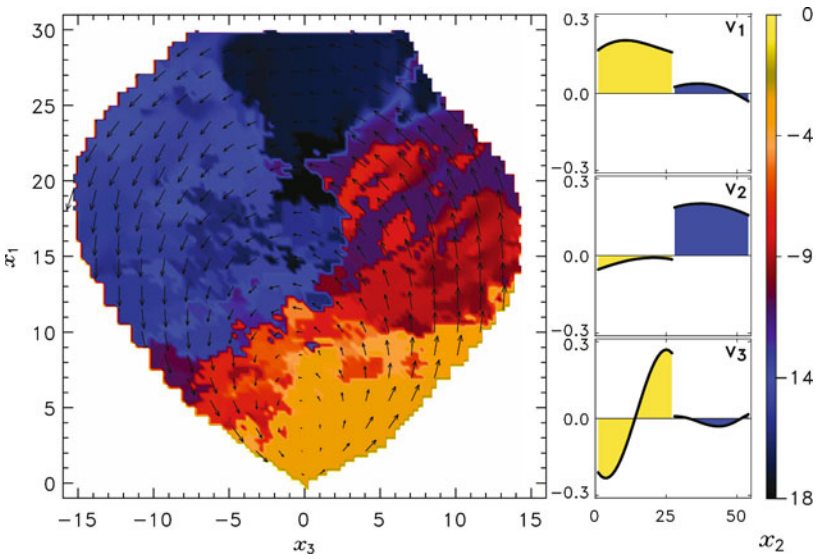


Figure 1. The global features of the magnetosphere obtained from the first three components of the dynamics computed from correlated solar wind-magnetosphere data (Bargatze et al., 1985). The eigenvectors corresponding to three largest eigenvalues are shown on the right panel. The first and second components are plotted along the y and x axes, respectively, and the color represents the third component (light color representing a higher elevation of the 3D surface). The circulation flows (arrows) represent the evolution of the solar wind parameters during the substorm cycle (Ukhorskiy et al., 2004).

components are shown in the right hand panel of Figure 1, whereas the structure of the three-dimensional space is shown in the left panel. The global dynamics of the magnetosphere derived from the Bargatze et al. (1985) data set are represented by the set of points representing the trajectory of the magnetospheric dynamics in this 3D space, and lie on a 2D surface (Sitnov et al., 2000; Ukhorskiy et al., 2004). Also shown in Figure 1 are the arrows indicating the circulation flows, which reflect the evolution of the system. The growth phase of substorms is reflected in Figure 1 by the lower right hand side of the surface, while the recovery phase corresponds to the left hand side. The substorm onset is located close to the middle.

The reconstructed surface shown in Figure 1 resembles the so-called temperature-pressure-density diagram typical for the well known first order phase transitions. The dynamical or nonequilibrium transitions exhibit hysteresis phenomenon in which different values of output parameter (AL index) may correspond to the same set of input parameters (VBs). Such features are important characteristics of the critical behavior or of the second order phase transition. However the surface shown in Figure 1 represent a mean-field feature

obtained by averaging over the data set and thus the features of hysteresis are absent.

The multi-scale behavior of the magnetosphere is evident from the singular spectra of the ground-based data (Sitnov et al., 2001) as well as global MHD simulations (Shao et al., 2003). The eigenvalue spectrum in these cases are close to the 1/f spectrum. In the reconstructed phase space the multi-scale portion of magnetospheric dynamics, averaged out in the mean-field model, is naturally coupled to the large-scale coherent component. It appears as fluctuations of data around the smooth manifold containing the trajectories of averaged system and thus it can be described in terms of conditional probability $P(O_{t+1} \mid \mathbf{x}_t)$ defined in the embedding space $\mathbf{x}_i$ for the predicted output O_{i+1} (Ukhorskiy et al., 2004). To investigate the role of the solar wind driver in the generation of the multi-scale dynamical features of substorms the evolution of conditional probability was considered as a function of input parameters. For this purpose $P(O_{t+1} \mid \mathbf{x}_t)$ was calculated in one and two-dimensional subspaces spanned by the first $\mathbf{v}_1$ and the third $\mathbf{v}_3$ principle components of vB_S-AL time series which characterize the input in the system. Distribution functions $P(O_t, x_1)$ calculated for different levels of solar wind activity are show in Figure 2 in blue, red and yellow colors. Their sum yields the cumulative distribution $P(O_t)$ shown in

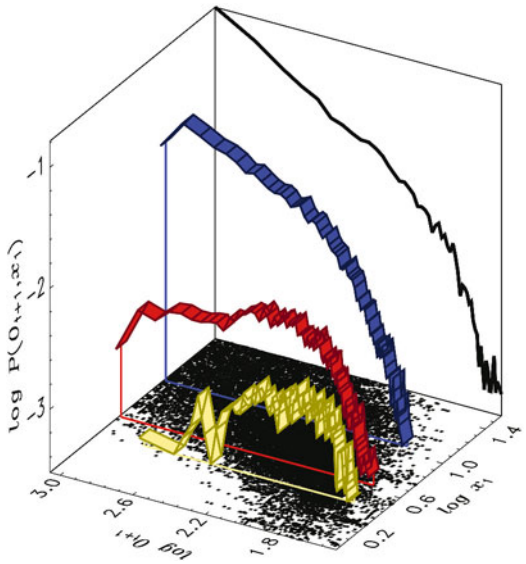


Figure 2. The conditional probabilities of AL as functions of solar wind conditions. The yellow, red and blue curves correspond to strong (vBs $>$ 9 mV), medium (0.6 $<$ vBs $<$ 9 mV) and low (vBs, 0.6 mV) solar wind activity levels, respectively. The floor shows all the points in the data base, corresponding to the marginal probability distribution function shown in the back panel (Ukhorskiy et al., 2004).

the back panel of the plot. It has a power-law shape with a break corresponding to $-AL \sim 500$ nT. The distribution functions corresponding to the medium and high activity have well distinguished maxima and do not exhibit scale-invariance. At the same time, the distribution function corresponding to the low solar wind activity has a broad-band structure similar to the scale-invariant cumulative distribution which is often interpreted as an indication of complexity in magnetospheric dynamics. However, if the input space is expanded from one to two dimensions, then this broad-band portion of $P(O_t|x_1)$ breaks into a number of distribution functions $P(O_t|x_1,\ x_3)$ with the pronounced peaks which width and position depend on both input parameters (Ukhorskiy et al., 2004). The conditional probability functions $P(O_{t+1}|\mathbf{x}_t)$ calculated in a space with dimension as low as two do not have a power-law shape. This indicates that a large portion of the scale-free distribution of *AL* is directly induced by the scale-invariance of the solar wind driver rather than been a result of the inherent complexity of magnetospheric dynamics. With increase in the phase space dimension the width of the corresponding distribution functions keeps decreasing until it saturates when the dimensionality of the mean-field model is reached.

3. Self-Organized Criticality

The multiscale characteristics of the magnetosphere have been studied in many ways. The power spectrum of the AE index was studied using 5-min averaged data from 1967 to 1980 (Tsurutani et al., 1990). The power spectrum is found to have a break at about 5 hrs, and at frequencies less than that corresponding to this time scale, the spectrum is close to 1/f and at higher frequencies the spectral index is -2.2, while that of the solar wind VBs is -1.42.

The power spectral nature of the magnetospheric response has been studied using the structure function, which characterizes the fractal nature, and the break in the spectrum was interpreted in terms of bicolored noise (Takalo et al., 1993). These results have shown that the fractal nature, and hence the self-similarity and scale in invariance, are indications that the dynamics may depart from that of a low-dimensional system. The multi-scale and intermittent behavior of the magnetosphere were investigated by Consolini (1996) using the multi-fractal approach. This result, based on the probability scale distribution computed from the AE index data, further emphasized the presence of the multi-scale behavior in the magnetospheric dynamics. This has motivated a view of the magnetosphere as a complex system and self-organized criticality (SOC) has been introduced as a new way to understand its complexity and multi-scale nature.

The framework of self-organized criticality was introduced as a way to describe the behavior of complex systems which exhibit 1/f spectrum (Bak et al., 1987). Such systems can naturally evolve into what is called a self-organized

critical state, which is far from equilibrium and barely stable. In this delicately balanced state the system is on the edge of collapse and yet responds resiliently to external driving by returning to a critical state. The simplest way to visualize such a dynamical behavior of systems made up of large number of interacting parts is the behavior of avalanches on sandpile surfaces. A sandpile can be built on a table by slowly adding grains of sand. From the initially flat state the sandpile gradually gets steeper and avalanches begin to occur, becoming bigger as the pile grows. The sandpile eventually reaches a critical state and the system regulates itself by balancing the accumulated amount of sand by that carried away by avalanches. This concept has been readily applied to so many diverse areas and a variety of computer models have been developed to study such systems (Creutz, 1997; Jensen, 1998).

The avalanche phenomenon exhibited by model sandpiles have motivated many models of the dynamics in the magnetosphere. These models are essentially cellular automaton models with the simplified rules chosen from considerations of the known properties of the system. They can be put into the categories of sandpile models (Chapman et al., 1998; Uritsky and Pudovkin, 2000), coupled-map lattice models (Takalo et al., 1999a, 1999b) and simulations based on simplified models (Klimas et al., 2000). Many studies have used observational data to identify the leading features of SOC, viz., power spectral distribution of scale sizes in satellite images of the aurora (Lui et al., 2002, Uritsky et al., 2001, 2002). The probability distributions computed from the Polar UVI images show a broad range of scale-free power law distributions, shown in Figure 3. The power distributions cover the entire range from the size of the bright auroral region to the smallest size determined by the pointing accuracy of the spacecraft (Uritsky et al., 2002).

The idea of self-organized criticality has been extended to include the forcing in the system and such a system may then exhibit forced and/or self-organized

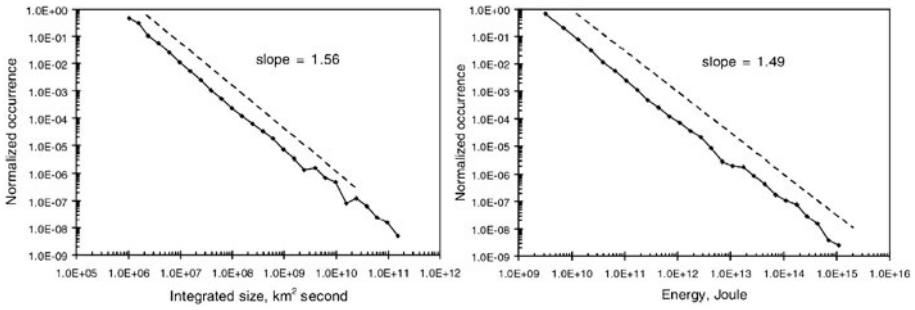


Figure 3. Normalized probability distributions for (left) size and (right) energy for the UVI measurements aboard Polar spacecraft (taken from Uritsky et al. (2002)).

criticality (FSOC). An application of the renormalization group approach to FSOC has given the power law index for the avalanches in the sandpile model of the magnetosphere (Tam et al., 2000). The renormalization group technique, developed in the study of critical phenomena (Fisher, 1974, 1998; Wilson, 1983), is based on searching for scale invariance by continued coarse-graining and rescaling of the system. The main purpose for the applications of this technique is to obtain the critical exponents characterizing the critical state, and thus this technique has the promise of yielding deeper insight into the criticality in the solar wind-magnetospheric coupling.

The recognition of the role of criticality in magnetospheric dynamics has motivated the development of models based on simplified physics considerations. While these models are not fully self-consistent they provide a means to study the relative roles of different physical processes known to be important in the magnetosphere. The WINDMI model (Horton et al., 1999) is based on the physical processes relevant to the coupled solar wind-magnetosphere-ionosphere system and describes many global and multi-scale features. This low dimemsional model naturally describes the global dynamics and the multiscale features arise due to the sequence of inverse bifurcations. A model of localized reconnection in the magnetotail based on resistive MHD considerations (Klimas et al., 2000, 2004) yields a power-law spectra and different features of internal and global dynamics. The model consists of simple equations of the type of a forced nonlinear diffusion equation, and the characteristics of the system under different forcing conditions are studied. The stregnth and nature of the forcing naturally plays an important role and the model yields avalanche phenomenon, which is consistent with SOC.

The SOC scenario has been used extensively to study the multiscale behavior of the magnetosphere. These models are inspired by the observational features such as the power law spectra of AE index and are based on simplified physics considerations. In this sense they are essentially like model sandpiles, and like most such cellular automaton models (Jensen, 1998) characterize the system in terms of the local slope, which is updated using a chosen rule, which to a large extent may be arbitrary. The distribution of the avalanches in such models and its comparison with the data of the physical systems usually yields a measure of the SOC model. The first such model (Chapman et al., 1998) showed two types of avalanches, corresponding to internal reorganization, with power distribution and SOC behavior, and to systemwide discharges which do not exhibit SOC.

The UVI images from Polar spacecraft was used to study the nature of the dynamics during global auroral energy deposition events (Lui et al., 2000). In this study using more than 9,000 frames of auroral images the internal scales of the magnetosphere were found to have the same power law in both quiet and active periods. The global energy dissipation during active periods however had a different scale. These features were interpreted as consistent with

an avalanching system that exhibts criticality. More detailed studies of these spacecraft images have shown a wide range of the power spectral distribution (Uritsky et al., 2001, 2002).

While the SOC models of substorms have given many interesting results, it should be noted that real sandpiles may behave in a manner more reminiscent of a first-order transition similar to the fold catastrophe than a second order one (Nagel, 1992). In the case of substorms similar deviations from the simplest SOC picture are evident in the form of the statistics of chorus events (Borovsky et al., 1993; Pritchard et al., 1996; Smith et al., 1996), which showed that the intensity and occurrence rate of substorms have a probability distribution with a well-defined mean. Independent studies of SOC models have shown that the critical points in some of them are not attractive. Also typical SOC models imply some specific tuning of either the state (Gil and Sornette, 1996) or control (Vespignani and Zapperi, 1998) parameters. An SOC model consistent with the above sandpile experiments has been proposed recently by Gil and Sornette (1996) within the framework of Landau-Gizburg theory of self-organized criticality.

The power law nature of auroral index AE however may not be due entirely to the internal magnetospheric dynamics. Studies of the solar wind induced electric field field VBs and the energy input into the magnetosphere have recently been found to have power law dependences (Freeman et al., 2000). This result has interesting implications for magnetospheric dynamics, especially the interpretation in terms of SOC phenomenon. The analysis of the probabilty density functions of the solar wind variables also show power law dependences. The power law form of the inter-burst intervals in the solar wind was found to be distinct from that of ideal SOC but not from SOC-like sandpile models. This result has a wider implication on the signatures of SOC.

4. Turbulence in the Magnetosphere

The turbulent aspects of the magnetosphere have been studied extensively. The statistics of chorus events seen in the groundbased data and spacecraft data of particle injections in the near-Earth magnetosphere (Borovsky et al., 1993; Pritchard et al., 1996; Smith et al., 1996) show that the intensity and occurrence rate of substorms have a probability distribution with a well-defined mean. While many studies have been based on the auroral indices data, many other studies have used the spacecraft data, notably from the fleet of ISTP spacecraft. Studies of the magnetic field fluctuations during the disruption of the magnetotail current have shown power spectrum dependence (Ohtani et al., 1995; 1998). The plasma flow in the inner plasma sheet measured by Geotail and Wind spacecraft have been used to study the nature of the intermittency in the magnetosphere (Angelopoulos et al., 1999). The probability density of the

magnitudes of the bursty bulk flows show power law dependence in time and their distribution is non-Gaussian.

Because the dissipation of vorticity is so weak in the collisionless, high-β plasma of the magnetotail, any flow there will have an extremely high Reynolds number and is expected to be MHD turbulent (Montgomery, 1989). Only recently have MHD computer simulations of the solar-wind-driven magnetosphere attained Reynolds numbers high enough see the turbulent flows of the magnetotail (White et al., 2001). For years there has been a theoretical analysis of MHD turbulent plasma-sheet flows by Antonova (e.g. Antonova 1985, 1987, 2000; Antonova and Ovchinnikov, 1998, 1999a,b, 2000, 2002).

The turbulent flow of the magnetotail plasma sheet has been studied with spacecraft measurements (Borovsky et al., 1997; Yermolaev et al., 2000; 2002; Ovchinnikov et al., 2000, 2002; Petrukovich, 2004; Petrukovich and Yermolaev, 2002; Borovsky and Funsten, 2003; Borovsky, 2004, Petrukovich, 2004). The data analysis of the turbulence has not been motivated by substorm dynamics, geomagnetic indices, or solar-wind driving of the magnetosphere; rather it has been motivated by questions about the physics of mass transport in the magnetosphere, the enabling of small-scale reconnection events in the magnetotail, and the magnetic-field structure of the magnetotail. Most of the data analysis examined the flow and field fluctuations to discern the dynamical nature of the MHD turbulence in the plasma sheet: i.e. whether it is an eddy turbulence of an Alfven-wave turbulence. The arguments favor a turbulence of eddies. Boundaries and time-dependent magnetosphere-ionosphere coupling (Borovsky and Bonnell, 2001) greatly complicate the analysis of the turbulence. The MHD turbulent fluctuations have $\delta v/v_o \gg 1$, $\delta B/B_o \sim 1$, and an Alfven ratio $R_A < 1$. The correlation times of the MHD fluctuations are a few minutes. The integral scale of the turbulence is $\sim$1.5 R_E, meaning large eddy scale sizes are about 1.5 R_E and magnetic-field domain sizes are about 1.5 R_E. Adding magnetic-field fluctuations with the statistical properties observed for fluctuations in the magnetotail plasma sheet to data-based models of the magnetospheric magnetic field (see Figure 4) results in a depiction of a "spaghetti plasma sheet" with a highly tangled magnetotail field. The MHD fluctuations of the turbulence show power-law frequency spectra. Statistics of the turbulent flows are non-Gaussian, but interpretation of those statistics are problematic. The range of MHD spatial scales in the plasma sheet available for the turbulence is very limited: $\sim$35,000 km is the thickness of the plasma sheet (largest scalesize) and $\sim$700 km is the ion gyroradius (smallest scalesize). With less than two decades of scalesizes available for the MHD turbulence, a "turbulence-in-a-box" picture has been put forth, with magnetosphere-ionosphere coupling having a major influence on the turbulence.

The multiscale turbulence in the magnetotail with external forcing is the motivation of another model based on percolation theory, which is intimately

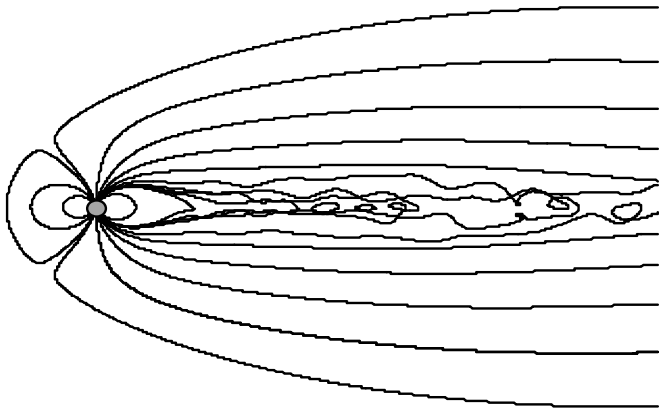


Figure 4. Magnetic-field fluctuations are added to the plasma-sheet region of T96 magnetic-field model (Tysaganenko, 1996) and magnetic-field lines are traced. The statistics of the added field fluctuations match the statistics of the MHD turbulence see by spacecraft in this region. See also Fig. 4 of Hruska (1973).

connected with the fractal structure and multiscale behavior. Substorms have been modeled in terms of a percolating network of cross-tail currents (Milovanov et al., 2001). In this scenario the network has different levels of fractal measures and at a critical level the structural stability breaks down and the onset corresponds to a topological phase transition. In a related approach, the plasma turbulence in the distant magnetotail has been found to have self-organizing properties and these have been described in terms of the fractal properties (Zelenyi et al., 1998).

5. Discussion

The main efforts in the study of the coupled solar wind -magnetosphere system has been to interpret and understand the extensive ground and spacecraft based data in terms of the interactions between plasmas and electric and magnetic fields. However the understanding of the complex magnetospheric dynamics apparent in the observational data of substorms continue to be a challenge. Recent advances to the study of complexity, in terms of low dimensional dynamics, phase transitions, self-organized criticality and turbulence, present new approaches to the modeling of the magnetospheric activity.

The substorms are consequences of the solar wind energy and momentum input into the magnetosphere and are essentially non-equilibrium processes. The main framework for understanding substorms is the formation of plasmoids in the magnetotail accompanied by the reconfiguration of the magnetosphere (Hones et al., 1983). The properties of the magnetosphere derived from the

observational data as well as models, show that magnetospheric behavior during substorms are more akin to a combination of such large scale features with the multiscale properties, such as due to a flow past an obstacle (Rostoker, 1984).

The SOC concept has stimulated a large number of applications in many areas (Jensen, 1999). Although its claims have been somewhat ambitious, it has made important contributions to the study of non-equilibrium phenomena. The current interest in granular matter (de Gennes, 1999) has been partly stimulated by SOC ideas. The transition between fluid and frozen phases of granular matter may in fact have features of phase transition and critical behavior. While the theory of SOC is not fully developed, a dynamic mean-field theory description in terms of transition probabilities (Vespignani and Zapperi, 1998) has been used to determine its relationship to other non-equilibrium phenomena. This approach describes SOC models as non-equilibrium systems which reach criticality by the fine tuning of the control parameters. The original SOC idea is based on the absence of fine tuning and the mean field theory of SOC brings it closer to conventional critical phenomena, rather than the non-equilibrium case. However it should be noted that there are subtle differences in the nature of tuning in the two cases.

Phase transitions as a framework for the solar wind-magnetosphere coupling is attractive because of its input-output nature. The phase transition picture provides a number of relationships between the control (input) and order (output) parameters in terms of critical exponents (Stanley, 1971; Dixon et al., 1999). These relationships provide a new way of understanding the solar wind-magnetosphere coupling. On the other hand the studies of SOC have emphasized the power spectral index as the main characteristics of the phenomenon. However, the phase transition picture of the global and multi-scale manifestations of the dynamics is not fully developed as yet. The next step in this direction would be to obtain analogues of the power-law spectra discussed above, where the state parameter of the system would be related not to scale or frequency but to some input (control) parameter of the system as it takes place in actual second order phase transitions or some advanced SOC models (Gil and Sornette, 1996), i.e., in terms of the critical exponents of the system. This is however a complicated task due to the non-equilibrium nature of the phase transition. One of the critical exponents for the solar wind-magnetosphere system has been computed from the VBs-AL data (Sitnov et al., 2001) and the conditional probabilities of the solar wind—magnetosphere system (Ukhorskiy et al., 2004) support such relationships. The global coherence of the magnetosphere during substorms can be viewed as a catastrophe (Lewis, 1991), akin to the phase transition behavior (Sitnov et al., 200). A minimal substorm model based on similar considerations (Freeman and Morley, 2004) yields good agreement with the probability distribution of substorm occurrence. Further, the peaked conditional probability distributions shown in Figure 2 are in agreement with

the correlation between the variabilities of the solar wind and the substoms (Freeman and Morley, 2004).

Acknowledgements

The research at the University of Maryland are supported by NSF grants ATM-0119196 and ATM-0318629.

References

Abarbanel, H. D., R. Brown, J. J. Sidorovich, and T. S. Tsimring, The analysis of observed chaotic data in physical systems, Rev. Mod. Phys., 65, 1331, 1993.

Angelopoulos, V., T. Mukai, S. Kokubun, Evidence for intermittency in Earth's plasma sheet and implications for self-organized criticality. Phys. Plasmas, 6, 4161, 1999.

Antonova, E. E., Nonadiabatic diffusion and equalization of concentration and temperature in the plasma layer of the magnetosphere of the Earth, Geomag. Aeron., 25, 517, 1985.

Antonova, E. E., On the problem of fundamental harmonics in the magnetospheric turbulence spectrum, Physica Scripta, 35, 880, 1987.

Antonova, E. E., Large scale magnetospheric turbulence and the topology of magnetospheric currents, Adv. Space Res., 25, 1567, 2000.

Antonova, E. E., and I. L. Ovchinnikov, Quasi-three-dimensional model of an equilibrium turbulent layer in the tail of the Earth magnetosphere and its substorm dynamics, Geomag. Aeron., 38, 14, 1998.

Antonova, E. E., and I. L. Ovchinnikov, Magnetostatically equilibrated plasma sheet with developed medium-scale turbulence: Structure and implications for substorm dynamics, J. Geophys. Res., 104, 17289, 1999a.

Antonova, E. E., and I. L. Ovchinnikov, Quasi-three dimensional modelling of the plasma sheet including turbulence on medium scales, Adv. Space Sci., 24, 121, 1999b.

Antonova, E. E., and I. L. Ovchinnikov, Medium scale magnetospheric turbulence and quasi three-dimensional plasma sheet modeling, Phys. Chem. Earth C, 25, 35, 2000.

Antonova, E. E., I. L. Ovchinnikov, and Y. I. Yermolaev, Plasma sheet coefficient of diffusion: Predictions and observations, Adv. Space Res., 30, 2689, 2002.

Bak, P., C. Tang, K. Wiesenfeld, Self-organized criticality: An explanation of 1/f noise. Phys. Rev. Lett., 50, 381–384, 1987.

Baker, D. N., A. J. Klimas, R. L. McPherron, and J. Buechner, The evolution from weak to strong geomagnetic activity: An interpretation in terms of deterministic chaos, Geophys. Res Lett., 17, 41, 1990.

Baker, D. N., T. I. Pulkkinen, V. Angelopoulos, W. Baumjohann, R. L. McPherron, Neutral line model of substorms: Past results and present view. J. Geophys. Res., 101, 12,975, 1996.

Bargatze, L. F., D. N. Baker, R. L. McPherron, E. W. Hones, Jr., Magnetospheric impulse response for many levels of geomagnetic activity. J. Geophys. Res., 90, 6387, 1985.

Borovsky, J. E., R. J. Nemzek, R. D. Belian, The occurrence rate of magnetospheric-substorm onsets: Random and periodic substorms. J. Geophys. Res., 98, 3807, 1993.

Borovsky, J. E., R. C. Elphic, H. O. Funsten, and M. F. Thomsen, The Earth's plasma sheet as a laboratory for flow turbulence in high-beta MHD, J. Plasma Phys., 57, 1, 1997.

Borovsky, J. E., Nemzek, R. J. Belian, R. D., The Earth's plasma sheet as a laboratory for flow turbulence in high beta MHD, J. Plasma Phys., 57, 1–34, 1997.

Borovsky, J. E., and J. Bonnell, The dc electrical coupling of flow vortices and flow channels in the magnetosphere to the resistive ionosphere, J. Geophys. Res., 106, 28967, 2001.

Borovsky, J. E., and H. O. Funsten, The MHD turbulence in the Earth's plasma sheet: Dynamics, dissipation, and driving, J. Geophys. Res., 108, 1284, 2003.

Borovsky, J. E., and H. O. Funsten, Role of solar wind turbulence in the coupling of the solar wind to the Earth's magnetosphere, J. Geophys. Res., 108(A6), 1246, doi:10.1029/2002JA009601, 2003.

Borovsky, J. E., and H. O. Funsten, MHD turbulence in the Earth's plasma sheet: Dynamics, dissipation, and driving, J. Geophys. Res., 108(A7), 3807, doi:10.1029/2002JA009625, 2003.

Borovsky, J. E., A Model for the Turbulence in the Earth's Plasma Sheet: Building Computer Simulation, to appear in Multiscale Processes in the Earth's Magnetosphere, edited by J. Safrankova and J. D. Richardson, NATO Science Series, 2004.

Chang, T., Low dimensional behaviour and symmetry breaking of stochastic systems near criticality—can these effects be observed in space and in the laboratory?. IEEE Trans. Plasma Sci., 20, 691–694, 1992.

Chapman, S. C., N. W. Watkins, R. O. Dendy, P. Helander, G. Rowlands, A simple avalanche model as an analogue for magnetospheric activity. Geophys. Res. Lett., 25, 2397, 1998.

Consolini, G., M. F. Marcucci and M. Candidi, Multifractal structure of auroral electrojet index data, Phys. Rev. Lett., 76, 4082, 1996.

Consolini, G., Sandpile cellular automata and magnetospheric dynamics. In Proc. "Cosmic Physics in the Year 2000", vol. 58, S. Aiello, N. Iucci, G. Sironi, A. Treves and U, Villante (eds.), SIF, Bologna, Italy, 1997.

Creutz, M., Self-organized criticality, in Multiscale Phenomena and Their Simulation, eds., F. Karsch, B. Monien and H. Satz, World Scientific, 1997.

de Gennes, P. G., Granular matter: a tentative view, Rev. Mod. Phys., 71, S374, 1999.

Dixon, J. M., J. A. Tuszynski, P. A. Clarkson, From Nonlinearity to Coherence: Universal Features of Nonlinear Behavior in Many-Body Physics, Oxford University Press, 1999.

Freeman, M. P., N. W. Watkins, and D. J. Riley, Evidence for a solar wind origin of the power law burst lifetime distribution of the AE index, Geophys. Res. Lett., 27, 1087, 2000.

Freeman, M. P., and S. K. Morley, A minimal substorm model that explains the observed statistical distribution of times between substorms, Geophys. Res. Lett., 31, L12807, doi:10.1029/2004GL019989, 2004.

Gil, L., and D. Sornette, Landau-Ginzburg theory of self-organized criticality. Phys. Rev. Lett., 76, 3991, 1996.

Horton, W., Doxas, I., A low-dimensional energy conserving model for substorm dynamics. J. Geophys. Res., 101, 27223, 1996.

Hruska, A., Structure of high-latitude irregular electron fluxes and acceleration of particles in the magnetotail, J. Geophys. Res., 78, 7509, 1973.

Huang, C.-S., G. D. Reeves, J. E. Borovsky, R. M. Skoug, Z. Y. Pu, and G. Le, Periodic magnetospheric substorms and their relationship to with solar wind variations, J. Geophys. Res., 108(A6), 3807, doi:10.1029/2002JA009704, 2003.

Jensen, H. J., Self-Organized Criticality: Emergent Complex Behavior in Physical and Biological Systems, Cambridge, University Press, 1998.

Klimas, A. J., J. A. Valdivia, D. Vassiliadis, D. N. Baker, M. Hesse, and J. Takalo, Self-organized criticality in the substorm phenomenon and its relation to localized reconnection in the magnetospheric plasma sheet, J. Geophys. Res., 105, 18,765, 2000.

Klimas, A. J., D. Vassiliadis, D. N. Baker and D. A. Roberts, The organized nonlinear dynamics of the magnetosphere, J. Geophys. Res., 101, 13,089, 1996.

Klimas, A. J., J. A. Valdivia, D. Vassiliadis, D. N. Baker, M. Hesse, and J. Takalo, Self-organized criticality in the substorm phenomenon and its relation to localized reconnection in the magnetospheric plasma sheet, J. Geophys. Res., 105, 18,765, 2000.

Klimas, A. J., V. M. Uritsky, D. Vassiliadis, and D. N. Baker, Simulation study of SOC dynamics in driven current-sheet models, this volume, 2004.

Lewis, Z. V., On the apparent randomness of substorm onset, Geophys. Res. Lett., 18, 1849, 1991.

Lui, A. T. Y., S. C. Chapman, K. Liou, P. T. Newell, C. I. Meng, M. Brittnacher, G. K. Parks, Is the dynamic magnetosphere an avalnching system?, Geophys. Res. Lett., 27, 911, 2000.

Lyon, J. G., The solar wind—magnetosphere—ionosphere system, Science, 288, 1987, 2000.

Malamud, B., Morein, G., Turcotte, D. L., Forest fires: An example of self-organized critical behavior. Science, 281, 1840, 1998.

Milovanov, A. V., L. M. Zelenyi, G. Zimbardo and P. Veltri, Self-organized branching of magnetotail current systems near the percolation threshold, J. Phys. Res. 106, 6291, 2001.

Montgomery, D., Magnetohydrodynamic turbulence, in Lecture Notes on Turbulence, pg. 75, World Scientific, Singapore, 1989.

Nagel, S. R., Instabilities in a sandpile, Rev. Mod. Phys., 64, 321, 1992.

Ohtani, S., Higuchi, T., Lui, A. T. Y., Takahashi, K., Magnetic fluctuations associated with tail current disruption: Fractal analysis. J. Geophys. Res., 100, 19,135, 1995.

Ohtani, S., Higuchi, T., Lui, A. T. Y., Takahashi, K., AMPTE/CCE-SCATHA simultaneous observations of substorm associated magnetic fluctuations. J. Geophys. Res., 103, 4671, 1998.

Ovchinnikov, I. L., E. E. Antonova, and Y. I. Yermolaev, Determination of the turbulent diffusion coefficient in the plasma sheet using the Project INTERBALL data, Comic Res., 38, 557, 2000.

Ovchinnikov, I. L., E. E. Antonova, and Y. I. Yermolaev, Turbulence in the plasma sheet during substorms: A case study for three events observed by the INTERBALL Tail Probe, Cosmic Res., 40, 521, 2002.

Petrukovich, A. A., Low frequency magnetic fluctuations in the olasma sheet, this volume, 2004.

Petrukovich, A. A., and Y. I. Yermolaev, Interball-Tail observations of vertical plasma motions in the magnetotail, Ann. Geophys., 20, 321, 2002.

Pritchard, D., Borovsky, J. E., Lemons, P. M., Price, C. P., Time dependence of substorm recurrence: An information theoretic analysis. J. Geophys. Res., 101, 15,359, 1996.

Rostoker, G., Implications of the hydrodynamic analogue for the solar terrestrial interaction and the mapping of high latitude convection pattern into the magnetotail, Geophys. Res. Lett., 11, 251, 1984.

Sergeev, V. A., Pulkkinen, T. I., Pellinen, R. J., Coupled mode scenario for the magnetospheric dynamics. J. Geophys. Res., 101, 13,047, 1996.

Shao, X., M. I. Sitnov, A. S. Sharma, K. Papadopoulos, C. C. Goodrich, P. N. Guzdar, G. M. Milikh, M. J. Wiltberger, and J. G. Lyon, Phase transition-like behavior of magnetospheric substroms: Global MHD simulation results, J. Geophys. Res., 108(A1), 1037, doi:10.1029/2001JA009237, 2003.

Sharma, A. S., Reconstruction of phase space from time series data by singular spectrum analysis, in: Physics of Space Plasmas—13, Eds. T. Chang and J. R. Jasperse, MIT Press, Cambridge, MA, p. 423, 1993.

Sharma, A. S., Vassiliadis, D. V., Papadopoulos, K., Reconstruction of low-dimensional magnetospheric dynamics by singular spectrum analysis. Geophys. Res. Lett., 20, 335, 1993.

Sharma, A. S., Assessing the magnetosphere's nonlinear behavior: its dimension is low, its predictability, high. Reviews of Geophysics (Suppl.), 35, 645–650, 1995.

Sharma, A. S., Nonlinear dynamical studies of global magnetospheric dynamics, in Nonlinear Waves and Chaos in Space Plasmas, eds. T. Hada and H. Matsumoto, pp. 359–389, Terra Scientific Pub., Tokyo, 1997.

Sharma, A. S., Sitnov, M. I., and Papadopoulos, K., Substorms as nonequilibrium phase transitions, J. Atmos. Sol. Terr. Phys., 63, 1399, 2001.

Sharma, A. S., M. I. Sitnov, A. Y. Ukhorskiy, and J. A. Valdivia, Modelling the magnetosphere from time series data, in Disturbances in Geospace: The Storm-substorm Relationship, Geophysical monograph series, vol. 142, edited by A. S. Sharma, Y. Kamide and G. S. Lakhina, Amer. Geophys. Union, pp. 231–241, 2003.

Sharma, A. S., A. Y. Ukhorskiy, and M. I. Sitnov, Global and multiscale dynamics of the magnetosphere, this volume, 2004.

Siscoe, G. L., The magnetosphere: A union of independent parts. EOS, Trans. AGU, 72, 494–497, 1991.

Sitnov, M. I., A. S. Sharma, K. Papadopoulos, D. Vassiliadis, J. A. Valdivia, A. J. Klimas, and D. N. Baker, Phase transition-like behavior of the magnetosphere during substorms. J. Geophys. Res., 105, 12,955, 2000.

Sitnov, M. I., A. S. Sharma, K. Papadopoulos, D. Vassiliadis, J. A. Valdivia, A. J. Klimas, and D. N. Baker, Modeling substorm dynamics of the magnetosphere: From self-organization and self-organized criticality tononequilibrium phase transitions, Phys.. Rev. E., 65, 016116, 2001.

Smith, A. J., M. P. Freeman, and G. D. Reeves, Postmidnight VLF chorus events, a substorm signature observed at ground near L = 4, J. Geophys. Res., 101, 24641, 1996.

Stanley, H. E., 1971. Introduction to Phase Transitions and Critical Phenomena. Oxford University Press, Oxford.

Takalo, J., J. Timonen, H. Koskinen, Correlation dimension and affinity of AE data and bicolored noise. Geophys. Res. Lett., 20, 1527, 1993.

Tam, S. W., T. Chang, S. Chapman, and N. W. Watkins, Analytical determination of power-law index for Chapman et al. sandpile (FSOC) analog for magnetospheric activity—a renormalization group analysis, Geophys. Res. Lett., 27, 1367, 2000.

Tsurutani, B., Sugiura, M., Iyemori, T., Goldstein, B. E., Gonzalez, W. D., Akasofu, S.-I., Smith, E. J., The nonlinear response of AE to the IMF Bs. Geophys. Res. Lett., 17, 279, 1990.

Tsyganenko, N. A., Effects of the solar wind conditions on the global magnetospheric configuration as deduced from data-based field models, in Proceedings of the Third International Conference on Substorms, Eur. Space Agency Spec. Publ., ESA SP-389, p. 181, 1996.

Ukhorskiy, A. Y., M. I. Sitnov, A. S. Sharma, and K. Papadopoulos, Global and multiscale aspects of magnetospheric dynamics in local-linear filters, J. Geophys. Res., 107(A11), 1369, 2002.

Ukhorskiy, A., M. I. Sitnov, A. S. Sharma, and K. Papadopoulos, Global and multiscale features in a description of the solar wind—magnetosphere coupling, Annales Geophysicae, 21(9), 1913, 2003.

Ukhorskiy, A. Y., M. I. Sitnov, A. S. Sharma and K. Papadopoulos 2004, Global and multiscale dynamics of the magnetosphere, Geophys Res. Lett., 31, L08802, doi:10.1029/2003GL018932, 2004.

Uritsky, V. M., and M. I. Pudovkin, Low frequency 1/f-like fluctuations of the AE-index as a possible manifestation of self-organized criticality in the magnetosphere, Ann. Geophys., 16(12), 1580, 1998.

Uritsky, V. M., A. J. Klimas, and D. Vassiliadis, Comparative study of dynamical critical scaling in the auroral electrojet index versus solar wind fluctuations, Geophys. Res. Lett., 28(19), 3809–3812, 2001.

Uritsky, V. M., A. J. Klimas, D. Vassiliadis, D. Chua, and G. D. Parks, Scale-free statistics of spatiotemporal auroral emissions as depicted by POLAR UVI images: The dynamic magnetosphere is an avalanching system, J. Geophys. Res., 107(A12), 1426, 2002.

Vassiliadis, D., Sharma, A. S., Eastman, T. E., Papadopoulos, K., 1990. Low-dimensional chaos in magnetospheric activity from AE time series. Geophys. Res. Lett., 17, 1841.

Vassiliadis, D., Klimas, A. J., Baker, D. N., Roberts, D. A., 1995. A description of solar wind-magnetosphere coupling based on nonlinear filters. J. Geophys. Res., 100, 3495.

Vespignani, A., and S. Zapperi, How self-organized criticality works: A unified mean-field picture, Phys. Rev. E, 57, 6345, 1998.

Watkins, N. W., S. C. Chapman, R. O. Dendy, G. Rowlands, Robustness of collective behaviour in strongly driven avalanche models: magnetospheric implications, Geophys. Res. Lett, 26, 2617, 1999.

White, W. W., J. A. Schoendorf, K. D. Siebert, N. C. Maynard, D. R. Weimer, G. L. Wilson, B. U. O. Sonnerup, G. L. Siscoe, and G. M. Erickson, MHD simulation of magnetospheric transport at the mesoscale, in Space Weather, P. Song, H. Singer, and G. Siscoe (eds.), American Geophysical Union, Washington, 2001.

Wilson, K., The renormalization group and critical phenomena, Rev. Mod. Phys., 55, 583, 1983.

Yermolaev, Y. I., A. A. Petrukovich, L. M. Lelenyi, E. E. Antonova, I. L. Ovchinnikov, and V. A. Sergeev, Investigation of the structure and dynamics of the plasma sheet: The CORALL experiment of the INTERBALL project, Cosmic Res., 38, 13, 2000.

Yermolaev, Y. I., A. A. Petrukovich, and L. M. Zelenyi, INTERBALL statistical study of ion flow fluctuations in the plasma sheet , Adv. Space Res., 30, 2695, 2002.

Zelenyi, L. M., A. V. Milovanov, and G. Zimbardo, Multiscale Magnetic Structure of the Distant Tail: Self-Consistent Fractal Approach, in New Perspectives on the Earth's Magnetotail, AGU monograph series, eds. A. Nishida, D. N. Baker, S. W. H. Cowley, 1998.

Chapter 2

COMPLEXITY AND INTERMITTENT TURBULENCE IN SPACE PLASMAS

Tom Chang and Sunny W.Y. Tam
Center for Space Research, Massachusetts Institute of Technology, Cambridge, MA 02139 USA

Cheng-chin Wu
Department of Physics and Astronomy, University of California, Los Angeles, CA 90095 USA

Abstract: Sporadic and localized interactions of coherent structures arising from plasma resonances can be the origin of "complexity" of the coexistence of non-propagating spatiotemporal fluctuations and propagating modes in space plasmas. Numerical simulation results are presented to demonstrate the intermittent character of the non-propagating fluctuations. The technique of the dynamic renormalization-group is introduced and applied to the study of scale invariance of such type of multiscale fluctuations. We also demonstrate that the particle interactions with the intermittent turbulence can lead to the efficient energization of the plasma populations. An example related to the ion acceleration processes in the auroral zone is provided.

Key words: Complexity, Space plasmas, Dynamic renormalization group, Forced and/or self-organized criticality, Topological phase transitions, Intermittency, Particle-Fluctuation interactions, Auroral ion acceleration

Introduction

In situ observations indicate that the dynamical processes in the space plasma environment generally entail anisotropic and localized intermittent fluctuations. It was suggested by Chang (1998a,b,c; 1999) that instead of considering this type of turbulence as an admixture of waves, such patchy intermittency could be more easily understood in terms of the development and interactions of coherent structures. Results of two-dimensional MHD simulations (Wu and

A.S. Sharma and P.K. Kaw (eds.), Nonequilibrium Phenomena in Plasmas, 23–50.
© 2005 *Springer. Printed in the Netherlands.*

Chang, 2000a,b; 2001) including the calculated fluctuation probability distribution functions and local intermittency measures (LIM) based on wavelet transforms seem to validate the suggested characteristics of the intermittent stochastic processes.

On the other hand, plasma waves are also generally observed in conjunction with the nonlinear, non-propagating fluctuations. It has been demonstrated that the coexistence of both propagating and non-propagating fluctuations in a plasma is a natural consequence of three-dimensional complexity for dynamical plasmas (Chang, 2003).

For nonlinear dynamical systems near criticality, the correlations among the fluctuations are extremely long-ranged. The dynamics of such systems are notoriously difficult to handle either analytically or numerically. It has been suggested that the technique of the dynamic renormalization-group (Chang et al., 1992) might be capable of addressing such difficulties. Illustrative examples will be provided to demonstrate the utility of this technique in handling dynamical complexity of space plasmas.

It has been suggested that the intermittent non-propagating and propagating plasma fluctuations can interact efficiently with the charged plasma particles (Chang, 2001; Chang et al., 2003; 2004). This idea will be applied to the energization of ionospheric ions to magnetospheric energies in the auroral zone.

1. Plasma Resonances and Coherent Structures

Most field theoretical discussions begin with the concept of propagation of waves. For example, in the MHD formulation, one can combine the basic equations and express them in the following propagation forms:

$$\rho d\mathbf{V}/dt = \mathbf{B}\cdot\nabla\mathbf{B} + \cdots, \quad d\mathbf{B}/dt = \mathbf{B}\cdot\nabla\mathbf{V} + \cdots \tag{1}$$

where the ellipses represent the effects of the anisotropic pressure tensor, the compressible and dissipative effects, and all notations are standard. Equation (1) admit the well-known Alfvén waves. For such waves to propagate, the propagation vector $\mathbf{k}$ must contain a field-aligned component, i.e., $\mathbf{B}\cdot\nabla \to i\mathbf{k}\cdot\mathbf{B} \neq 0$. However, at sites where the parallel component of the propagation vector vanishes (i.e., at the resonance sites), the fluctuations are localized. Around these resonance sites (usually in the form of curves), it may be shown that the fluctuations are held back by the background magnetic field, forming Alfvénic coherent structures (Waddell et al., 1979; Tetreault, 1992a; Chang, 1998a.b.c; 1999; 2001; 2003, Chang et al., 2003).

Coarse-grained helicity. Let us now consider the geometry of the Alfvénic coherent structures. For an ideal MHD system, it has been suggested

by Taylor (1974) that in a relaxed state such a structure would be approximately force-free (i.e., $\mathbf{J} \times \mathbf{B} = 0$) due to the approximate conservation of the coarse-grained helicity defined as $K = \int \mathbf{A} \cdot \mathbf{B} dV$ integrated over the coherent structure, where **J** and **B** are the current density and magnetic field and **A** is the vector potential.

To obtain some physical insight of these structures, let us consider the special situation for the auroral region and/or the solar wind and make the reasonable assumption that the perturbed magnetic field fluctuations are much smaller than and essentially transverse to the mean magnetic field B_0 (which will be temporarily assumed to be uniform for the current discussion). Thus, let us write $\mathbf{B} = (\delta B_x, \delta B_y, B_0)$, where z is in the direction of the mean magnetic field, and (x, y) are orthogonal coordinates normal to z. The force-free condition for constant B_0 and $\nabla \cdot \mathbf{J} = 0$ then leads approximately to the scalar condition $\mathbf{B} \cdot \nabla J_z = 0$, obtained by taking the z-component of the curl of $\mathbf{J} \times \mathbf{B} = 0$ (Rutherford, 1973; Tetreault, 1992b; Chang, 1998a,b,c). It can be shown that, with the inclusion of the kinetic effects through the anisotropic pressure terms and the generalized Ohm's law, the above results are still approximately valid. We have, then, approximately,

$$B_0 \partial J_z / \partial z = -(\delta B_x \partial / \partial x + \delta B_y \partial / \partial y) J_z + \cdots \tag{2}$$

where the ellipsis represents the other modifying effects. For convenience, let us introduce the flux function ψ by writing $(\partial \psi / \partial y, -\partial \psi / \partial x) = (\delta B_x, \delta B_y)$ for the perturbed transverse components of the magnetic field in the (x, y) directions such that $\nabla \cdot \mathbf{B} = 0$ is satisfied. Then, J_z and ψ are governed by Eq. (2) and the Ampere's law (neglecting the modifying effects represented by the ellipsis).

A simple example of the flux function and axial current density satisfying the above conditions would be the class of circularly cylindrical solutions of $\psi(r)$ and $J_z(r)$. Generally, the solutions would be more involved because of the variabilities of the local conditions of the plasma and the three-dimensional geometry. Moreover, the dynamic coherent structures with the inclusion of plasma pressure and other modifying effects (including electron-inertia terms) would be even more complicated. However, we expect these structures to be usually in the form of field-aligned flux tubes, Fig. 1.

Generally, there exist various types of propagation modes (whistler modes, lower hybrid waves, etc.) in a magnetized plasma. Thus, we envision a corresponding number of different types of plasma resonances and associated coherent structures that typically characterize the dynamics of the plasma medium under the influence of a background magnetic field.

Generally, such coherent structures may take on the shapes of convective forms, nonlinear solitary structures, pseudo-equilibrium configurations, as well as other types of spatiotemporal varieties. Some of them may be more stable

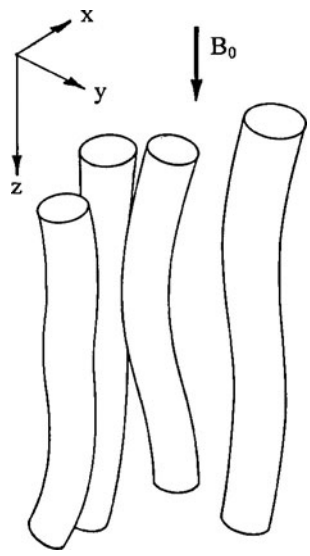


Figure 1. Field-aligned spatiotemporal coherent structures.

than the others. These spatiotemporal structures, however, generally are not purely laminar entities as they are composed of bundled fluctuations of all frequencies. Because of the nature of the physics of complexity, it will be futile to attempt to evaluate and/or study the details and stabilities of each of these infinite varieties of structures; although some basic understanding of each type of these structures will generally be helpful in the comprehension of the full complexity of the underlying nonlinear plasma dynamics.

These coherent structures will wiggle, migrate, deform and undergo different types of motions and interactions under the influence of the local plasma and magnetic topologies. In the next section, we will consider how the coherent structures can interact and produce the type of intermittency generally observed in a complex dynamical plasma.

2. Complex Interactions of The Coherent Structures

When coherent magnetic flux tubes of the same polarity migrate toward each other, strong local magnetic shears are created, Figs. 2. and 3. It has been demonstrated by Wu and Chang (2000a,b; 2001) that existing sporadic non-propagating fluctuations will generally migrate toward the strong local shear region. Eventually the mean local energies of the coherent structures will be dissipated into these concentrated fluctuations in the coarse-grained sense.

Such enhanced intermittency at the intersection regions has been observed by Bruno et al. (2001; 2002) in the solar wind using the tools of wavelet

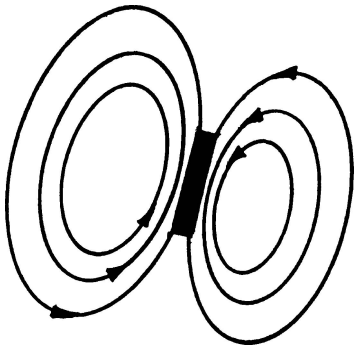


Figure 2. Cross-sectional view of coherent structures of the same polarity. Contours are $\psi =$ constants and arrows indicate directions of magnetic field in the (x, y)-plane. Blackened area is an intense current sheet.

analyses and local intermittency measure (LIM). The coarse-grained dissipation will then initiate "fluctuation-induced nonlinear instabilities" (Chang, 1999; Chang et al., 2002); and, thereby reconfigure the topologies of the coherent structures into a combined lower local energetic state, eventually allowing the coherent structures to merge locally. On the other hand, when coherent structures of opposite polarities approach each other due to the forcing of the surrounding plasma, they might repel each other, scatter, or induce magnetically quiescent localized regions. Under any of the conditions of the above interaction scenarios, new fluctuations will be generated. And, these new fluctuations can provide new resonance sites; thereby nucleating new coherent structures of varied sizes.

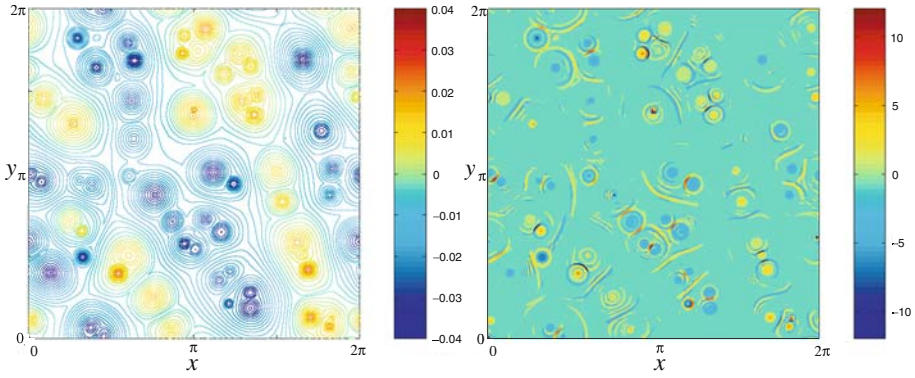


Figure 3. 2D MHD simulation of coherent structures (left panel) and current sheets (right panel) generated by initially randomly distributed current filaments after an elapsed time of $t = 300$ units. (For reference, the sound wave and Alfvén wave traveling times through a distance of 2π are approximately 4.4 and 60, respectively.)

All such interactions can occur at any location of a flux tube along its field-aligned direction, and the phenomenon is fully three-dimensional. In order to gain some insight of the physical picture of the overall dynamics of the interactions of the coherent structures, let us again consider the auroral zone or the solar wind as an illustrative example. We make the plausible assumption that some aspects of the plasma dynamics may be approximately understood in terms of the formulation of reduced magnetohydrodynamics (RMHD) (Seyler, 1988; Matthaeus et al., 1990). In this approximation, we assume that the mean magnetic field is much larger than the transverse fields, and the field-aligned fluctuations of the magnetic and velocity components are much smaller than their transverse counterparts. As a consequence, the density of the plasma is uniform. Writing the equations in SI units with $\rho = 1$ and $\mu_0 = 1$, we have (Strauss, 1976; Biskamp, 1993):

$$d\psi/dt = B_z \partial\phi/\partial z, \quad d\omega/dt = \mathbf{B} \cdot \nabla j \tag{3}$$

where $\psi(x, y)$ is the transverse flux function defined by $\mathbf{B} = \mathbf{e}_z \times \nabla\psi + B_z \mathbf{e}_z$, $\phi(x, y)$ is the transverse stream function defined by $\mathbf{v}_\perp = \mathbf{e}_z \times \nabla\phi$, and $\omega = \nabla_\perp^2 \phi$ is the vorticity, $j = \nabla_\perp^2 \psi$ is the field-aligned current density with $d/dt = \partial/\partial + \mathbf{v} \cdot \nabla$. The equations are written in the moving frame along the mean magnetic field direction z, and (x, y) are the transverse orthogonal directions.

From Equation (3), we note that the primary nonlinear interactions occur generally in the transverse direction to the mean magnetic field. And, the coupling in the field-aligned direction is essentially linear. Thus, fluctuations generated by the transverse nonlinear interactions will scatter and evolve nonlinearly primarily in the transverse direction. At this point, we realize that the RMHD formulation is too restrictive as some of the interactions of the flux tubes may become more oblique and thereby allowing the fluctuations to attain a broader range of values of $k_\parallel$ than otherwise would have been admitted by the RMHD approximation. Thus, a significant amount of the fluctuations generated by the interactions can become commensurate with the plasma dispersion relation and propagate in the field-aligned direction as Alfvén waves due to this three-dimensional complexity-induced enhanced transport. Eventually a dynamic topology of a complex state of coexisting propagating and non-propagating magnetic fluctuations is created. In the auroral region, the plasma may be electron-inertia dominated and the above discussion can be easily generalized to include such kinetic effects.

3. Invariant Scaling and Topological Phase Transitions

In the above sections, we provided some convincing arguments as well as numerical and observational evidences indicating that space plasma turbulence is generally in a state of topological complexity. By "complex" topological

states we mean magnetic topologies that are not immediately deducible from the elemental (e.g., MHD and/or Vlasov) equations (Consolini and Chang, 2001). Below, we shall briefly address the salient features of the analogy between topological and equilibrium phase transitions. A thorough discussion of these ideas may be found in Chang (1992, 1999; 2001, and references contained therein).

For nonlinear stochastic systems exhibiting complexity, the correlations among the fluctuations of the random dynamical fields are generally extremely long-ranged and there exist many correlation scales. The dynamics of such systems are notoriously difficult to handle either analytically or numerically. On the other hand, since the correlations are extremely long-ranged, it is reasonable to expect that the system will exhibit some sort of invariance under coarse-graining scale transformations. A powerful technique that utilizes this invariance property is the method of the dynamic renormalization group (Chang et al., 1978; 1992; and references contained therein). The technique is a generalization of the static renormalization group introduced by Wilson (Wilson and Kogut, 1974).

As it has been demonstrated by Chang et al. (1978), based on the path integral formalism, the behavior of a nonlinear stochastic system far from equilibrium may be described in terms of a "stochastic Lagrangian L", such that the probability density functional P of the stochastic system is expressible as:

$$P(\varphi(\mathrm{x}, t)) = \int D[\chi] \exp\left\{-i \int L(\dot{\varphi}, \varphi, \chi) d\mathrm{x} dt\right\} \tag{4}$$

where $\varphi(\mathbf{x}, t) = \phi_i (i = 1, 2, \ldots, N)$ are the stochastic variables such as the fluctuating magnetic, velocity and electric fields, and $\chi(\mathbf{x}, t) = \chi_i (i = 1, 2, \ldots, N)$ are the conjugate stochastic momentum variables that may be rigorously derived from the underlying stochastic equations governing φ (Chang et al., 1978; Chang, 1992; Chang et al., 1992).

Then, the renormalization-group (coarse-graining) transformation may be formally expressed as:

$$\partial L / \partial \ell = RL \tag{5}$$

where R is the renormalization-group (coarse-graining) transformation operator and ℓ *is* the coarse-graining parameter for the continuous group of transformations. It will be convenient to consider the state of the stochastic Lagrangian in terms of its parameters $\{P_n\}$. Equation (5), then, specifies how the Lagrangian, L, flows (changes) with ℓ in the affine space spanned by $\{P_n\}$, Fig. 4.

Forced and/or self-organized criticality. Generally, there exists a number of fixed points (singular points) in the flow field, at which $dL/d\ell = 0$. At

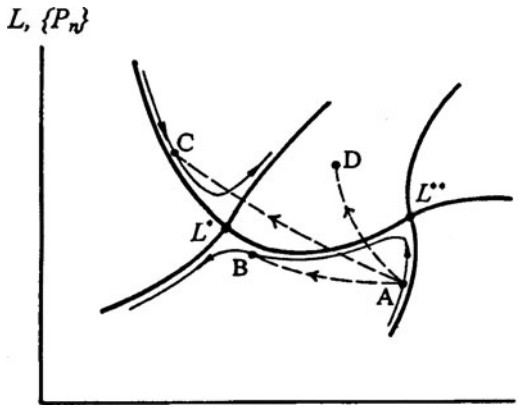


Figure 4. Renormalization-group trajectories and fixed points.

each such fixed point (L^* or L^{**} in Fig. 4), the correlation length should not be changing. However, the renormalization-group transformation requires that all length scales must change under the coarse-graining procedure. Therefore, to satisfy both requirements, the correlation length must be either infinite or zero. When it is at infinity, the dynamical system is then at a state of forced and/or self-organized criticality (FSOC) (Bak et al., 1987; Chang, 1992), analogous to the state of criticality in equilibrium phase transitions (Stanley, 1971). To study the stochastic behavior of a nonlinear dynamical system near such a dynamical critical state (e.g., the one characterized by the fixed point L^*), we linearize the renormalization-group operator R about L^*. The mathematical consequence of this approximation is that, close to dynamic criticality, certain linear combinations of the parameters that characterize the stochastic Lagrangian L will correlate with each other in the form of power laws. These include, in particular, the (k, ω), i.e. mode number and frequency, spectra of the correlations of the various fluctuations of the dynamic field variables.

Such power law behavior has been detected in the probability distributions of solar flare intensities (Lu, 1995), in the AE burst occurrences as a function of the AE burst strength (Consolini, 1997), in the global auroral UVI imagery of the statistics of size and energy dissipated by the magnetospheric system (Lui et al., 2000), in the probability distributions of spatiotemporal magnetospheric disturbances as seen in the UVI images of the nighttime ionosphere (Uritsky et al., 2002), and in the probability distributions of durations of Bursty Bulk Flows (Angelopoulos, 1999); although some of the above interpretations of observed data may, however, also be amenable to alternative explanations (Boffetta et al., 1999; Freeman et al., 2000; Watkins, 2002).

In addition, it can be demonstrated from such a linearized analysis of the dynamic renormalization group that generally only a small number of (relevant)

parameters are needed to characterize the stochastic state of the system near criticality (Chang, 1992) justifying the recent work suggesting that certain dynamic characteristics of the magnetotail could be modeled by the deterministic chaos of low-dimensional nonlinear systems (Baker et al., 1990; Klimas et al., 1992; Sharma et al., 1993).

Illustrative examples. The intermittency description for plasma turbulence of fluctuations may be modeled by the combination of a localized chaotic functional growth equation of a set of relevant order parameters and a functional transport equation of the control parameters (Chang and Wu, 2002; Chang et al., 2003). Below, we shall provide two simple phenomenological models, which may have some relevance to the auroral zone or the solar wind (Chang, 2003).

Model I. Assuming that the parallel mean magnetic field B_0 is sufficiently strong and the magnetic fluctuations dominate in the transverse directions, we introduce the flux function ψ for the transverse fluctuations as follows,

$$\mathbf{B} = \mathbf{e}_z \times \nabla\psi + B_0\mathbf{e}_z \tag{6}$$

The coherent structures for such a system are generally flux tubes approximately aligned in the mean parallel direction (Chang, 2001). Conservation of helicity (e.g., under the RMHD approximation) indicates that the integral of ψ over a flux tube is approximately constant. Instead of invoking the RMHD formalism, however, here we simply consider ψ as an order parameter. As the flux tubes merge and interact, they may correlate over long distances, which, in turn, will induce long relaxation times near FSOC (Chang, 1992). Let us assume that the transverse size of the system is sufficiently broad compared to the cross sections of the coherent structures (or flux tubes), such that we may invoke homogeneity and assume the dynamics to be independent of boundary effects. We may then model the dynamics of flux tube mergings and interactions, in the crudest approximation, in terms of the following order-disorder intermittency equation:

$$\partial\psi_k/\partial t = -\Gamma_k \partial F/\partial\psi_{-k} + f_k \tag{7}$$

where ψ_k are the Fourier components of the flux function, Γ_k an analytic function of k^2, $F(\psi_k, k)$ the state function, and f_k a random noise which includes all the other effects that are not included in the first two terms of this crude model.

Model II. In the above model, we have neglected both the effects of diffusion and convection. We next construct a phenomenological model that includes the transport of cross-field diffusion. We now assume the state function to depend on the flux function ψ and the local pseudo-energy measure ξ. Thus, in

addition to the dynamic equation (7), we now also include a diffusion equation for ξ. In Fourier space, we have

$$\partial \xi_k / \partial t = -Dk^2 \partial F / \partial \xi_{-k} + h_k \tag{8}$$

where ξ_k are the Fourier components of ξ, $D(k)$ is the diffusion coefficient, and the state function is now $F(\psi_k, \xi_k, k)$, and h_k is a random noise. By doing so, we separate the slow pseudo-energy transport due to diffusion of the local pseudo-energy measure ξ from the noise term of (7). We note that an approach similar to these ideas have been considered by Klimas et al. (2000).

Dynamic renormalization-group analysis. We have performed renormalization-group analyses as outlined above for the two kinetic models described above. We note that under the dynamic renormalization-group (DRG) transformation, the correlation function C of ψ_k should scale as:

$$e^{a_c \ell} C(k, \omega) = C(ke^{\ell}, \omega e^{a_\omega \ell}) \tag{9}$$

where ω is the Fourier transform of t, ℓ the renormalization parameter as defined in the previous section, and (a_c, a_ω) the correlation and dynamic exponents. Thus, $C/\omega^{a_c/a_\omega}$ is an absolute invariant under the DRG, or $C \sim \omega^{-\lambda}$, where $\lambda = -a_c/a_\omega$. DRG analysis of Model I with Gaussian noise yields the value of λ to be approximately equal to 2.0. DRG analyses performed for Model II for Gaussian noises for several approximations yield the value for λ to be approximately equal to 1.88 to 1.66.

Interestingly, for both models, DRG calculations give an approximate value of -1.0 for the ω-exponent for the trace of the transverse magnetic correlation tensor. Matthaeus and Goldstein (1986) had suggested that such an exponent might represent the superposition of discrete structures emerged from the solar convection zone; thereby giving some credence to the above modeling effort. Also, the corresponding k-exponent is found to be approximately equal to -2 for both models. These results compare rather favorably with the results of our 2D MHD numerical simulations, Fig. 5.

Symmetry breaking and topological phase transitions. As the dynamical system evolves in time (autonomously or under external forcing), the state of the system (i.e., the values of the set of the parameters characterizing the stochastic Lagrangian, L) changes accordingly. A number of dynamical scenarios are possible. For example, the system may evolve from a critical state A (characterized by L^{**}) to another critical state B (characterized by L^{*}) as shown in Fig. 4. In this case, the system may evolve continuously from one critical state to another. On the other hand, the evolution from the critical state A to critical state C as shown in Fig. 4 would probably involve a

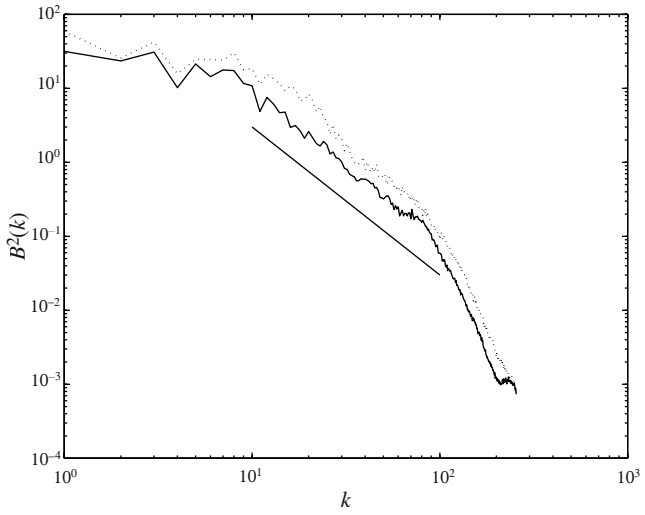


Figure 5. Fourier spectrum of $B^2(k)$ at $t = 300$ (dotted) and 600 (solid). Solid straight line indicates a slope of -2.

dynamical instability characterized by a first-order-like topological phase transition (fluctuation-induced nonlinear instability) because the dynamical path of evolution of the stochastic system would have to cross over a couple of topological (renormalization-group) separatrices. For such a situation the underlying magnetic topology and its related plasma state will generally undergo drastic changes. Similar ideas along these lines have been advanced by Sitnov et al. (2000) and simulated based on the cellular automata calculations of sandpile models (Chapman et al., 1998; Watkins et al., 1999).

Under either of these above scenarios, the spectra indices will generally change either continuously or abruptly. Such type of multifractal phenomena is commonly observed in the magnetotail, the auroral zone, and the solar wind (Lui, 1998; Hoshino et al., 1994; Milovanov et al., 1996; André and Chang, 1992; Chang, 2001; Bruno et al., 2001; 2002; Tu and Marsch, 1995; and references contained therein.)

Alternatively, a dynamical system may evolve from a critical state A to a state D (as shown in Fig. 4) which may not be situated in a regime dominated by any of the fixed points; in such a case, the final state of the system will no longer exhibit any of the characteristic properties that are associated with dynamic criticality. As another possibility, the dynamical system may deviate only moderately from the domain of a critical state characterized by a particular fixed point such that the system may still display low-dimensional scaling laws, but the scaling laws may now be deduced from straightforward dimensional arguments. The system

is then in a so-called mean-field state. (For general references of symmetry breaking and nonlinear crossover, see Chang and Stanley (1973); Chang et al. (1973a; 1973b); Nicoll et al. (1974; 1976).)

Experimental observations of plasma fluctuations in the Sun-Earth connection region generally yield broken power law spectra similar to those displayed in Fig. 5 of the 2D numerical simulation results. Such abrupt changes of scaling powers of the k-spectra are signatures of symmetry breaking. The broken symmetries may be due to the abrupt change of the degree of intermittency of fluctuations from large to small scales, or due to the change of the underlying physics (e.g., from MHD to kinetic processes), or variations of external forcing, or finite boundaries and other effects.

4. Intermittency

Nearly all fluctuations in space plasmas exhibit intermittency. For turbulent dynamical systems with intermittency, the transfer of energy (or other relevant scalars and tensors) due to fluctuations from one scale to another deviates significantly from uniformity. A technique of measuring the degree of intermittency is the study of the departure from Gaussianity the probability distribution functions of turbulent fluctuations at different scales. To demonstrate this point, let us refer to the 2D numerical simulation results described in Section 2. For example, we may generate the probability distribution function $P(\delta B^2, \delta)$ of $\delta B^2(x, \delta) \equiv B^2(x + \delta) - B^2(x)$ at a given time t for such simulations, where δ is the scale of separation in the x-direction. Figure 6 displays the calculated results of $P(\delta B^2, \delta)$ from a numerical simulation for several scales δ.

From this figure, we note that the deviation from Gaussianity becomes more and more pronounced at smaller and smaller scales. In an interesting paper by Hnat et al. (2002), they demonstrated that such probability distributions for solar wind fluctuations exhibit approximate mono-power scaling according to the following functional relation:

$$P(\delta B^2, \delta) = \delta^{-s} P_s(\delta B^2 \delta^{-s}, \delta) \tag{10}$$

where s is the mono-scaling power. We demonstrate that mono-power scaling also holds approximately for our simulated results with the value of s equal to approximately 0.335.

The reason for mono-power scaling for δB^2 may be understood in terms of the renormalization-group arguments presented in Section 3. If we assume that δB^2 is one of the relevant eigenoperators near a critical fixed point, then the probability distribution function for $P(\delta B^2, \delta)$, δB^2, as well as δ will scale linearly as follows:

$$P' = P \exp(a_p l), \quad \delta B^{2'} = \delta B^2 \exp(a_{B^2} l), \quad \delta' = \delta \exp(a_\delta l) \tag{11}$$

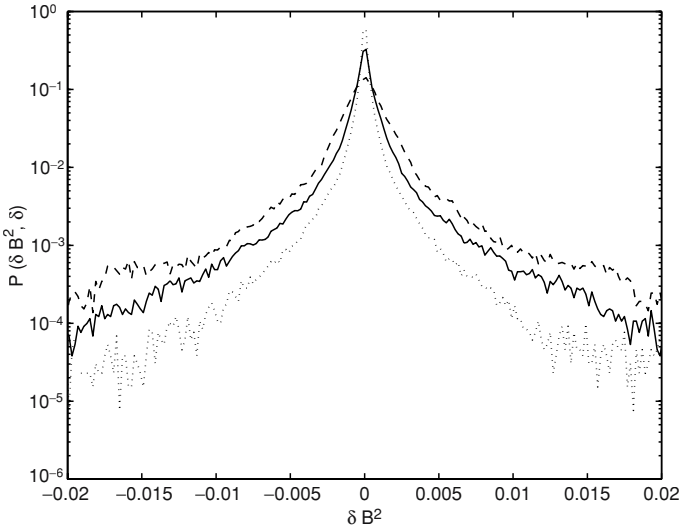


Figure 6. 2D MHD simulation result at $t = 300$ of PDF's of B^2 at scales of 2 (dotted), 8 (solid), and 32 (dashed) units of grid spacing ε.

where (a_p, a_{B^2}, a_δ) are scaling powers. Thus, we obtain two irreducible absolute invariants: $P/\delta^{a_P/a_\delta}$ and $\delta B^2/\delta^{a_{B^2}/a_\delta}$. Since $P = P(\delta B^2, \delta)$, there must be a functional relation between these two invariants (Chang et al., 1973a,b). Therefore, we obtain the following scaling relation among $(P, \delta B^2, \delta)$: $P/\delta^{ap/a_\delta} = F(\delta B^2/\delta^{a_{B^2}/a_\delta})$.

Without loss of generality, we may choose $a_\delta = 1$. With the additional constraint that the probability distribution functions are normalized, we immediately obtain the expression of Hnat et al. as shown in (6), Fig. 7.

Actually the scaling relation (6) is approximate in that the tails of the distributions in Fig. 7 do not exactly fall onto one curve. This is the intrinsic nature of the strong intermittency at small scales. Thus, representations of the probability density functions will involve multi-parameters in general and may sometimes, for example, be represented by the κ—or Castaing distributions (Sorriso-Valvo et al., 1999; Jurac, 2003; Forman and Burlaga, 2003; Weygand, 2003; Castaing et al., 1990). Their scaling properties are more subtle and will not be considered in this brief review.

Since the degree of intermittency generally increases inversely with scale, it will be interesting to study the degrees of intermittency locally at different scales. This can be accomplished by the method of Local Intermittency Measure (LIM) using the wavelet transforms. A wavelet transform generally is composed of modes which are square integrable localized functions that are capable of unfolding fluctuating fields into space and scale (Farge, 1992). Figure 8b is the

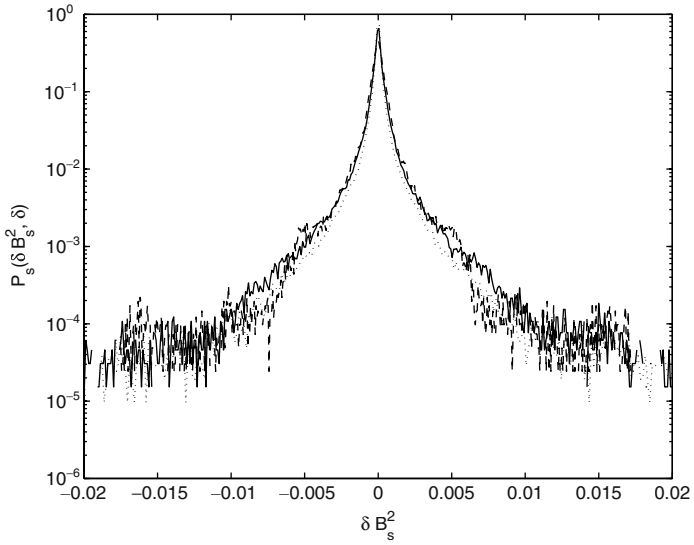


Figure 7. Scaled PDF's according to Eq. (10) with $s = 0.335$. Line styles are the same as in Figure 6.

power spectrum of a complex Morlet wavelet transform of the current density for one of the 2D MHD simulations mentioned in Section 2. We notice that the intensity of the current density is sporadic and varies nonuniformly with scale.

We now define LIM(1) as the ratio of the squared wavelet amplitude $|\psi(x, \delta)|^2$ and its space averaged value $< |\psi(x, \delta)|^2 >_x$. We note that LIM(1) = 1 for the Fourier spectrum. To emphasize the variation of intensity with scale, we also consider the logarithm of LIM(1). It has been suggested by Meneveau (1991) that the space average of the square of LIM(1), which is a scale dependent measure of the kurtosis or flatness, is a convenient gauge of the deviation of intermittency from Gaussianity. We denote this measure by LIM(2). It is equal to 3 if the probability distribution is Gaussian. Figures 8d,e and 9 are graphical displays of the calculated results of LIM(1), logLIM(1) and LIM(2) for our 2D numerical simulations using the complex Morlet transform. We notice that the fluctuations are indeed scale dependent, localized and strongly intermittent at small scales. Similar experimental results using the wavelet transforms have been found, for example, by Consolini et al. (2004) for the magnetotail and Bruno et al. (2001) for the solar wind.

In the above, we considered some simplified models and numerical examples that may have some relevance to intermittent turbulence in space plasmas. Realistic models for these phenomena will generally be much more complicated. For example, from the RMHD formulation of (3), we recognize that there should at least be two competing order parameters. These are the flux function ψ and the stream function ϕ (which is linearly proportional to the electrostatic potential).

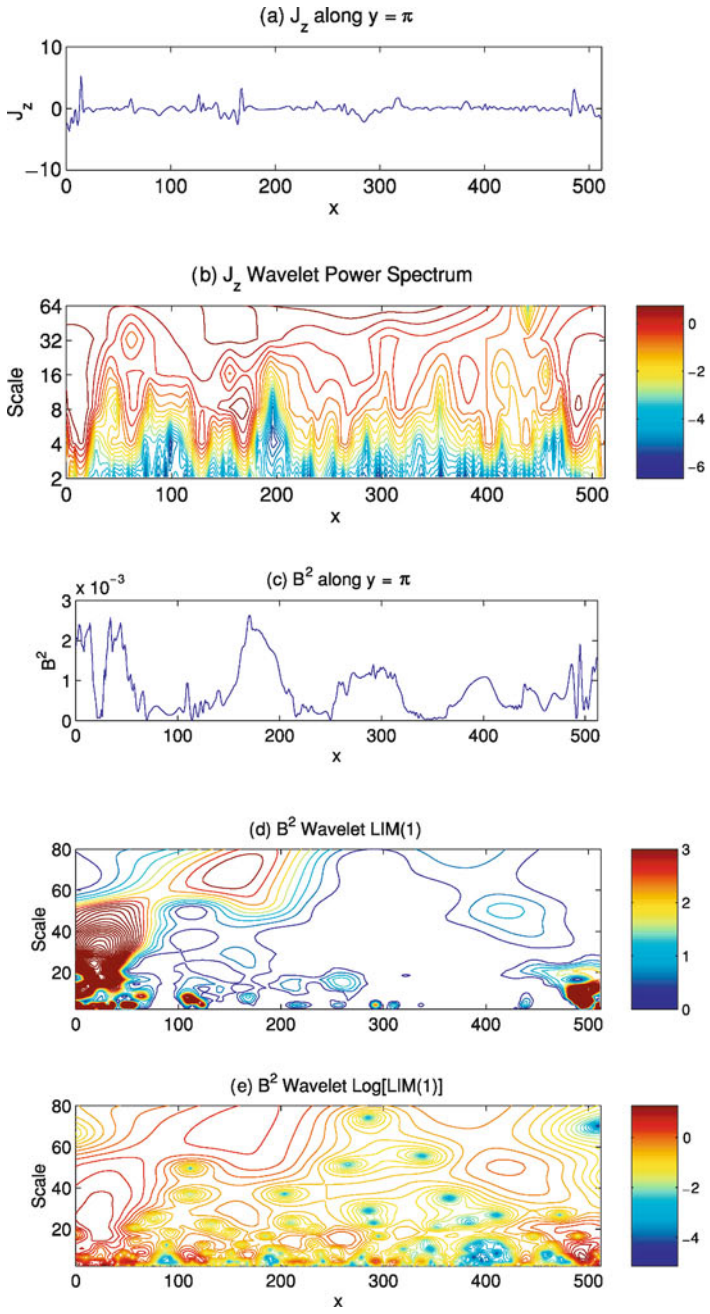


Figure 8. (a) 2D MHD simulation result of current density J_z along y-axis at $t = 300$. (b) Power spectrum of complex Morlet wavelet transform of J_z. (c) 2D MHD simulation result of B^2 distribution along the x-axis for $y = \pi$ at $t = 300$. (d and e) Contour plots of LIM(1) and LogLIM(1) of B^2. The x-axis and scale are in units of the grid spacing ε.

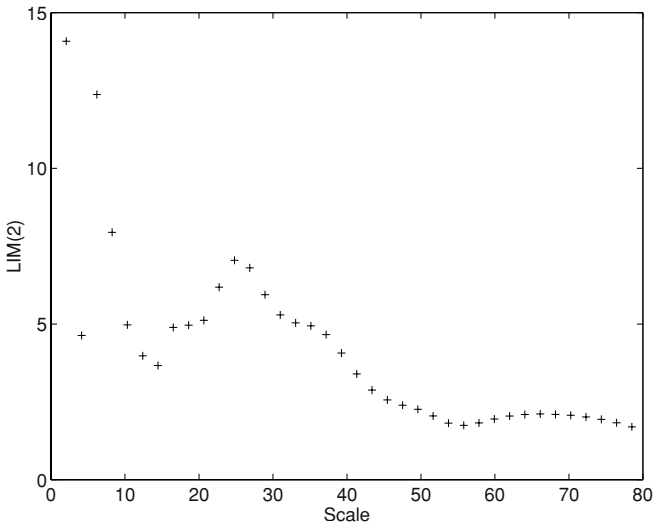


Figure 9. LIM(2) of B^2 for the same B^2 distribution of Figure 8c.

Thus, the intermittency equation (such as (7)) needs to be generalized to accommodate these coupled order parameters. Within the RMHD formulation, there exist useful Hamiltonian and operator-algebra structures (Morrison and Hazeltine, 1984), which should prove invaluable in developing the generalized state function F of the coupled order parameters and the state variables as well as the intermittency equation itself. Formulations of coupled order parameters and their related theoretical analyses for a variety of criticality problems in condensed matter physics have been considered by Chang et al. (1992; and references contained therein).

In addition, the transport equation such as (8) for the global system should generally also include convection and acceleration terms in addition to that of diffusion (Chang et al., 2003; 2004). Thus, at the minimum our model transport equation must take on the form of the RMHD (8) with the addition of "coarse-grained" dissipation terms, which generally will be functionals of the coupled order parameters. It should also contain terms representing the complexity-induced enhanced field-aligned transport. These generalizations will not be considered in this brief review.

5. Energization of Ions by Intermittent Fluctuations in The Auroral Zone

It has long been recognized that the commonly observed broadband, low frequency electric field fluctuations are responsible for the acceleration of oxygen ions in the auroral zone. In order for the fluctuating electric field to resonantly

accelerate the ions continuously as the ions evolve upward along the field lines, they must be in continuous resonance with the ions. There did not seem to exist a fully viable mechanism that can generate a spectrum of fluctuations broadband and incoherent enough to fulfill this stringent requirement.

Assuming that the RMHD formulation holds approximately in the auroral zone, the electrostatic fluctuations transverse to the field-aligned direction are given approximately by the velocity fluctuations:$\mathbf{v} \times B_z \mathbf{e}_z$. The ordering due to the stream function ϕ may be important in the auroral zone and therefore, the electrostatic fluctuations can be quite significant there. Because of the small scales involved, the dynamic intermittency produced by the merging and interactions of the coherent structures are probably generated by the whistler turbulence, electron-inertia related tearing modes, and/or other collisionless modes (Chang, 2001). Therefore, a significant portion of the fluctuations would be kinetic. Nevertheless, the electric field fluctuations would still be predominantly transverse and electrostatic. Thus, the low frequency fluctuations commonly observed in the auroral zone are probably contributed by these non-propagating intermittent fluctuations intermingled with a small fraction of propagating modes.

Below, we shall briefly discuss how such fluctuations can efficiently energize the oxygen ions from ionospheric to magnetospheric energies. Assuming the oxygen ions are test particles, they would respond to the transverse electric field fluctuations $\mathbf{E}_\perp$ near the oxygen gyrofrequency locally according to the Langevin equation:

$$d\mathbf{v}_\perp/dt = q_i \mathbf{E}_\perp / m_i \tag{12}$$

To understand the stochastic nature of the Langevin equation, we visualize an ensemble of ions $f(\mathbf{v}_\perp)$ and study its stochastic properties. Assuming that the interaction times among the particles and the local electric field fluctuations are small compared to the global evolution time, we may write within the interaction time scale:

$$f(\mathbf{v}_\perp, t + \Delta t) = \int f(\mathbf{v}_\perp - \Delta\mathbf{v}_\perp, t) P_t(\mathbf{v}_\perp - \Delta\mathbf{v}_\perp, \Delta\mathbf{v}_\perp) d\Delta\mathbf{v}_\perp \tag{13}$$

where $P_t(\mathbf{v}_\perp - \Delta\mathbf{v}_\perp, \Delta\mathbf{v}_\perp)$ is the normalized transition probability of a particle whose velocity changes from $\mathbf{v}_\perp - \Delta\mathbf{v}_\perp$ to $\mathbf{v}_\perp$ in Δt, and $\Delta\mathbf{v}_\perp$ ranges over all possible magnitudes and transverse directions. Standard procedure at this point is to expand both sides of (13) in Taylor series expansions:

$$\frac{\partial f}{\partial t}\Delta t + O((\Delta t)^2) = -\frac{\partial}{\partial \mathbf{v}_\perp} \cdot [\langle \Delta\mathbf{v}_\perp \rangle f] + \frac{1}{2}\frac{\partial^2}{\partial \mathbf{v}_\perp \partial \mathbf{v}_\perp} : [\langle \Delta\mathbf{v}_\perp \Delta\mathbf{v}_\perp \rangle f] + O((\Delta\mathbf{v}_\perp)^3) \tag{14}$$

where

$$\langle \Delta \mathbf{v}_\perp \rangle = \int P_t(\mathbf{v}_\perp, \Delta \mathbf{v}_\perp) \Delta \mathbf{v}_\perp d(\Delta \mathbf{v}_\perp), \text{ and}$$

$$\langle \Delta \mathbf{v}_\perp \Delta \mathbf{v}_\perp \rangle = \int P_t(\mathbf{v}_\perp, \Delta \mathbf{v}_\perp) \Delta \mathbf{v}_\perp \Delta \mathbf{v}_\perp d(\Delta \mathbf{v}_\perp).$$

If we assume the $O((\Delta \mathbf{v}_\perp)^3)$ terms are of order $(\Delta t)^2$ or higher, then in the limit of $\Delta t \to 0$, we obtain a Fokker-Planck equation (Einstein, 1905; Chandrasekhar 1943), where the drift and diffusion coefficients are defined as: $\mathbf{D}_1 = < \Delta \mathbf{v}_\perp > / \Delta t$ and $\mathbf{D}_2 = < \Delta \mathbf{v}_\perp \Delta \mathbf{v}_\perp > / 2\Delta t$ in the limit of $\Delta t \to 0$. These coefficients may be calculated straightforwardly using the Langevin equation. If the transition probability P_t is symmetric in $\Delta \mathbf{v}_\perp$, then $\mathbf{D}_1$ vanishes and (14) reduces to a diffusion equation in the transverse direction. We note that if the electric field fluctuations are Gaussian, then the higher order correlations of the fluctuations are automatically equal to zero.

We shall come back to the discussion of the effects of general intermittent fluctuations on particle energization processes. For the moment, let us assume the approach using the Fokker-Planck formulation is valid and proceed. Since we have assumed the time scale for the particle-fluctuation interactions is much smaller than the global evolution time of the ion populations, we may then write the steady-state global evolution equation along an auroral field line s under the guiding center approximation and neglecting the cross-field drift as (Chang et al., 1986; Retterer et al., 1987; Crew and Chang, 1988):

$$\frac{\partial}{\partial s}\left[\nu_\parallel \frac{f}{B_z}\right] + \frac{\partial}{\partial \nu_\parallel}\left[-\frac{\nu_\perp^2}{2B_z}\frac{dB_z}{ds}\frac{f}{B_z}\right] + \frac{1}{\nu_\perp}\frac{\partial}{\partial \nu_\perp}\left[\nu_\perp \frac{\nu_\perp \nu_\parallel}{2B_z}\frac{dB_z}{ds}\frac{f}{B_z}\right] = \frac{1}{\nu_\perp}\frac{\partial}{\partial \nu_\perp}\left[\nu_\perp D_\perp \frac{\partial}{\partial \nu_\perp}\frac{f}{B_z}\right] \quad (15)$$

where $\nu_\parallel$, $\nu_\perp$ are the parallel and perpendicular components of the particle velocity with respect to the field-aligned direction. This expression may be interpreted as a convective-diffusion equation for the density of the guiding center ions per unit length of flux tube f/B_z, in the coordinate space of $(s, \nu_\parallel, \nu_\perp)$.

To evaluate $D_\perp$, the gyrotropic perpendicular diffusion coefficient, from $\mathbf{D}_2$, we recognize that the fluctuations are broadband both in $k_\perp$ and ω. Therefore, at all times, some portion of the fluctuations will be in resonance with the ions. The resonance condition, however, is strongly dependent on the localization and scale dependency of the intermittent fluctuations (Chang, 2001). We demonstrate below, as a simple illustrative example, how such resonant interactions may be accomplished by neglecting the Doppler shifts due to $\mathbf{k}$ such that only the intermittent fluctuations clustering around the instantaneous gyrofrequency of the ions provide the main contributions to the diffusion process. Standard arguments then lead to the following expression for the perpendicular diffusion

coefficient:

$$D_{\perp} = \left(\pi q_i^2 / 2m_i^2\right) \left\langle \left| E^2 \right| (\Omega_i) \right\rangle_r \tag{16}$$

where $< \left|E^2\right|(\Omega_i) >_r$ is the resonant portion of the average of the square of the transverse electric field fluctuations evaluated at the instantaneous gyrofrequency of the ions, Ω_i.

Measurements by polar orbiting satellites indicate that the electric field spectral density Σ follows an approximate power law $\Sigma^{-\alpha}$ in the range of the local oxygen gyrofrequencies, where α is a constant. This is a natural consequence of the intermittent turbulence when the fluctuations are close to a state of forced and/or self-organized criticality. If we make the additional approximations by assuming that the spectrum observed at the satellite is applicable to all altitudes and choosing the geomagnetic field to scale with the altitude as s^{-3}, we would then expect $\Sigma(\Omega_i, s)$ to vary with altitude s as $s^{3\alpha}$. Because we have made some rather restrictive resonance requirements for the fluctuations to interact with the ions, we expect the resonant portion of the average of the square of the transverse electric field fluctuations to be only a fraction η of the total measured electric field spectral density. Therefore, we arrive at the following approximate expression for the diffusion coefficient:

$$D_{\perp} = \left(\eta \pi q_i^2 / 2m_i^2\right) \Sigma_0 (s/s_{\mathrm{o}})^{3\alpha} \tag{17}$$

We have performed global Monte Carlo simulations for Equations (15) and (17) for the conic event discussed by Retterer et al. (1987) with $\alpha = 1.7$ and $\Sigma_0 = 1.9 \times 10^{-7} (\mathrm{V/m})^2 \mathrm{sec/rad}$. Figure 10 shows the measured oxygen velocity distribution contours (top panel) along with the corresponding calculated contours for $\eta = 1/8$ (bottom panel) at the satellite altitude of $s_o = 2R_E$. Thus, with one eighth of the measured electric field spectral density contributing, the broadband fluctuations can adequately generate an oxygen distribution function with the energy and shape comparable to that obtained from observations. We have also calculated the oxygen ion distributions for a range of altitudes under the same conditions. Figure 11 is a plot of the average parallel energy versus the average perpendicular energy per oxygen ion as the ions evolve upward along the geomagnetic field line. We note that as the energies increase with altitudes, the ratio of the energies becomes nearly a constant.

These results are comparable to our previous calculated results based on the assumption that the relevant fluctuations were purely field-aligned propagating electromagnetic ion cyclotron waves (Chang et al., 1986; Retterer et al., 1987; Crew and Chang, 1988). As discussed in the previous sections, we generally expect the coexistence of non-propagating transverse electrostatic nonlinear fluctuations and a small fraction of field-aligned propagating waves in the auroral zone. Thus, the ion energization process in the auroral zone is probably due to a combination of both types of fluctuations. As it has been discussed

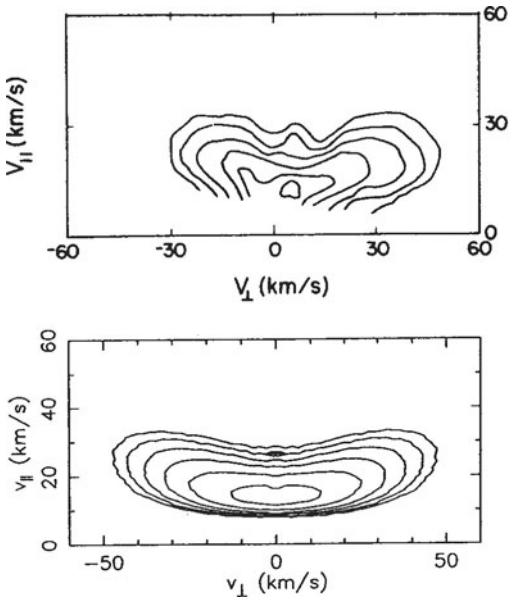


Figure 10. Observed and calculated velocity contour plots for conic event of Retterer et al. (1987).

in Chang et al. (1986), an asymptotic solution exhibiting such behavior may be obtained analytically in closed form. Therefore, in the asymptotic limit (i.e, at sufficiently high altitudes), it is expected that such an ion distribution will become entirely independent of its low altitude initial conditions. In fact, it has

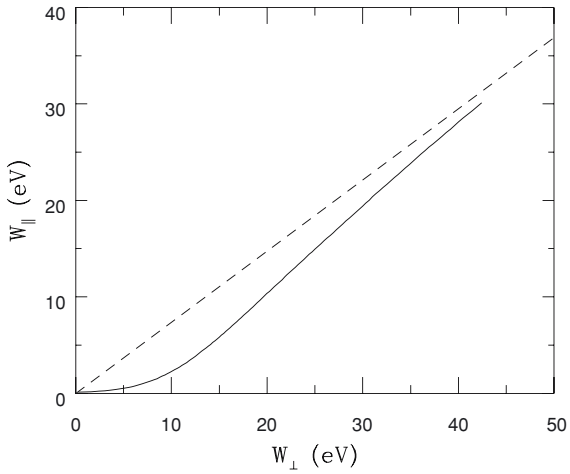


Figure 11. Solid line depicts $W_{||}$ versus $W_\perp$ for simulated conic events. Dashed line is the asymptote predicted by Chang et al. (1986).

been shown by Crew and Chang (1988) that the ion distributions will become self-similar at sufficiently high altitudes and everything will scale with the altitude.

The above sample calculations did not include the self-consistent electric field that must be determined in conjunction with the energization of the ions as well as the electrons. This is particularly relevant in the downward auroral current region where the electric field can provide a significant pressure cooker effect such as that suggested by Gorney et al. (1985) and demonstrated convincingly by Jasperse (1998) and Jasperse and Grossbard (2000) based on global evolutional calculations similar to those considered by Tam and Chang (1999a,b; 2001; 2002) for the solar wind and Tam et al. (1995, 1998) for the polar wind. These ideas will not be considered in this brief review.

We now return to the discussion of the effect of intermittency on ion heating. Measurements of the electric field spectral density are generally limited by the response capabilities of the measuring instruments. The faster the instruments can collect data, the more refined the scales of the measurements. As it has been seen in Section 4, we expect the measured spectrum density to exhibit small-scale intermittency behavior. In fact, it is known that fast response measurements generally exhibit strongly intermittent signatures of the fluctuations. In the diffusion approximation, the ion energization process is limited by the amplitude of the second moment of the probability distribution of the fluctuations. This amplitude may become smaller as the scale of measurements is reduced. Thus, in the limit of small scales, the amplitude of the measured spectrum may decrease and thereby requiring a larger value of η to accomplish the same level of energization.

But, the effects of the intermittency of the fluctuations on particle energization may be underestimated if we stay within the diffusion approximation. As it can be seen from the derivation of the diffusion approximation above, only the second order correlations of the fluctuations were included in the energization process. Since for intermittent turbulence, the probability distributions of the fluctuations are generally non-Gaussian, the effects of the intermittency can manifest in the higher order correlations beyond the second order diffusion coefficient. This implies that the higher order correlations of the velocity fluctuations may be of the order of Δt and therefore cannot be neglected in (14). Under such circumstances, the Fokker-Planck and diffusion approximations of the ion energization processes can become inadequate. A more appropriate approach to address such non-Gaussian stochastic processes is to refer directly to the functional equation (13) using the non-Gaussian transition probability or the Langevin equation (12) with the actual intermittent time series of the electric field fluctuations. Again, the details of these ideas will not be considered in this review.

6. Summary

We have provided a modern description of dynamical complexity relevant to the intermittent turbulence of coexisting non-propagating spatiotemporal fluctuations and propagating modes in space plasmas. The theory is based on the physical concepts of sporadic and localized interactions of coherent structures that emerge naturally from plasma resonances.

The technique of the dynamic renormalization-group is applied to the study of forced and/or self-organized criticality (FSOC) and scale invariance related to such type of multiscale fluctuations. We also demonstrated that the particle interactions with the intermittent turbulence could lead to the efficient energization of the plasma populations such as auroral ions. Numerical examples are presented to illustrate the concepts and methodology.

Acknowledgments

This review touches upon a broad range of research areas covering the physics of space plasmas and complexity. The authors wish to thank their past and present colleagues, M. André, V. Angelopoulos, R. Bruno, S. Chandrasekhar, S.C. Chapman, G. Consolini, B. Coppi, G.B. Crew, G. Ganguli, M. Goldstein, A. Hankey, J.R. Jasperse, S. Jurac, C.F. Kennel, P. Kintner, M. Kivelson, A. Klimas, A.T.Y. Lui, E. Marsch, W. Matthaeus, P. De Michelis, J.F. Nicoll, J.M. Retterer, C. Seyler, A.S. Sharma, M.I. Sitnov, H.E. Stanley, D. Tetreault, V. Uritsky, J. Valdivia, D. Vassiliadis, D. Vvedensky, N. Watkins, J. Weygand, F. Yasseen, and J.E. Young for very useful discussions. Our wavelet analysis employed some of the wavelet software provided by C. Torrence and G. Compo, which is available at URL: http://paos.colorado.edu/research/wavelets. This research was partially supported by AFOSR, NASA and NSF.

References

André, M., and T. Chang, Ion heating perpendicular to the magnetic field, *Physics of Space Plasmas*, Scientific Publishers, Inc., eds.: T. Chang and J.R. Jasperse, vol. 12, p. 35, 1992.

Angelopoulos, V., T. Mukai and S. Kokubun, Evidence for intermittency in Earth's plasma sheet and implications for self-organized criticality, *Physics of Plasmas*, 6, 4161, 1999.

Bak, P., C. Tang, and K. Wiesenfeld, Self-organized criticality: an explanation of 1/f noise, *Phys. Rev. Lett.*, 59, 381, 1987.

Baker, D., A.J. Klimas, R.L. McPherron and J. Büchner, The evolution from weak to strong geomagnetic activity: An interpretation in terms of deterministic chaos, *Geophys. Res. Lett.*, 17, 41, 1990.

Biskamp, D., *Nonlinear Magnetohydrodynamics*, Cambridge University Press, Cambridge, U.K., 1993.

Boffetta, G., V. Carbone, P. Giuliani, P. Veltri, and A. Vulpiani, Power laws in solar flares: Self-organized criticality or turbulence?, *Phys. Rev. Lett.*, 83, 4662, 1999.

Bruno, R., V. Carbone, P. Veltri, E. Pietropaolo, B. Bavassano, Identifying intermittency events in the solar wind, *Planetary and Space Science*, 49, 1201, 2001.

Bruno, R., V. Carbone, L. Sorriso-Valvo, B. Bavassano, Truncated Levy-flight statistics recovered from interplanetary solar wind velocity and magnetic field fluctuations, *EOS Trans.* AGU, 83(47), Fall Meet. Suppl., Abstract SH12A-0396, 2002.

Castaing, B., Y. Cagne, and E.J. Hopfinger, Velocity probability density functions of high Reynolds number turbulence, *Physica D*., 46, 177, 1990.

Chandrasekhar, S., Stochastic problems in physics and astronomy, *Rev. Mod. Phys.*, 15, 1, 1943.

Chang, T., and H.E. Stanley, Renormalization-group verification of crossover with respect to lattice anisotropy parameter, *Phys. Rev.*, B8, 1178, 1973.

Chang, T., A. Hankey, and H.E. Stanley, Double-power scaling functions near tricritical points, *Phys. Rev.*, B7, 4263, 1973a.

Chang, T., A. Hankey, and H.E. Stanley, Generalized scaling hypothesis in multi-component systems. I. Classification of critical points by order and scaling at tricritical points, *Phys. Rev.*, B8, 346, 1973b.

Chang, T., J.F. Nicoll and J.E. Young, A closed-form differential renormalization-group generator for critical dynamics, *Physics Letters*, 67A, 287, 1978.

Chang, T., G.B. Crew, N. Hershkowitz, J.R. Jasperse, J.M. Retterer, and J.D. Winningham, Transverse acceleration of oxygen ions by electromagnetic ion cyclotron resonance with broadband left-hand polarized waves, *Geophys. Res. Lett.*, 13, 636, 1986.

Chang, T., Low-dimensional behavior and symmetry breaking of stochastic systems near criticality—can these effects be observed in space and in the laboratory? *IEEE Trans. on Plasma Science*, 20, 691, 1992.

Chang, T., D.D. Vvedensky and J.F. Nicoll, Differential renormalization-group generators for static and dynamic critical phenomena, *Physics Reports*, 217, 279, 1992.

Chang, T., Sporadic, localized reconnections and multiscale intermittent turbulence in the magnetotail, *AGU Monograph on "Encounter between Global Observations and Models in the ISTP Era"*, vol. 104, p. 193, Horwitz, J.L., D.L. Gallagher, and W.K. Peterson, Am. Geophys. Union, Washington, D.C., 1998a.

Chang, T., Multiscale intermittent turbulence in the magnetotail, *Proc. 4th Intern. Conf. on Substorms*, ed. Kamide, Y. et al., Kluwer Academic Publishers, Dordrecht and Terra Scientific Publishing Company, Tokyo, p. 431, 1998b.

Chang, T., Self-organized criticality, multi-fractal spectra, and intermittent merging of coherent structures in the magnetotail, *Astrophysics and Space Science*, ed. Büchner, J. et al., Kluwer Academic Publishers, Dordrecht, Netherlands, vol. 264, p. 303, 1998c.

Chang, T., Self-organized criticality, multi-fractal spectra, sporadic localized reconnections and intermittent turbulence in the magnetotail, *Physics of Plasmas*, 6, 4137, 1999.

Chang, T., Colloid-like behavior and topological phase transitions in space plasmas: intermittent low frequency turbulence in the auroral zone, *Physica Scripta*, T89, 80, 2001.

Chang, T. and C.C. Wu, "Complexity" and anomalous transport in space plasmas, *Physics of Plasmas*, 9, 3679, 2002.

Chang, T., C.C. Wu, and V. Angelopoulos, Preferential acceleration of coherent magnetic structures and bursty bulk flows in Earth's magnetotail, *Physics Scripta*, T98, 48, 2002.

Chang, T., "Complexity" induced plasma turbulence in coronal holes and the solar wind, in *Solar Wind Ten*, ed. by M. Velli, R. Bruno, and F. Malara, AIP Conference Proceedings, vol. 679, Melville, NY, p. 481, 2003.

Chang, T., S.W.Y. Tam, C.C. Wu, and G. Consolini, Complexity, forced and/or self-organized criticality, and topological phase transitions in space plasmas, *Space Science Reviews*, 107, 425, 2003.

Chang, T., S.W.Y. Tam, and C.C. Wu, Complexity induced bimodal intermittent turbulence in space plasmas, *Physics of Plasmas*, 11, 1287, 2004.

Chapman, S.C., N.W. Watkins, R.O. Dendy, P. Helander and G. Rowlands, *Geophys. Res. Lett.*, 25, 2397, 1998.

Consolini, G., Sandpile cellular automata and magnetospheric dynamics, *Cosmic Physics in the Year 2000*, ed. S. Aiello, N. Lucci, G. Sironi, A. Treves and U. Villante, Soc. Ital. di Fis., Bologna, Italy, p. 123, 1997.

Consolini, G., and T. Chang, "Magnetic Field Topology and Criticality in Geotail Dynamics: Relevance to Substorm Phenomena", *Space Science Reviews*, 95, 309, 2001.

Consolini, G., T. Chang, and A.T.Y. Lui, Complexity and topological disorder in the Earth's magnetotail dynamics, Chapter 3, this volume, 2004.

Crew, G.B., and T. Chang, Path-integral formulation of ion heating, *Physics of Fluids*, 31, 3425, 1988.

Einstein, A.*, Ann. d. Physik*, 17, 549, 1905.

Farge, M., Wavelet transforms and their applications to turbulence, *Annual Reviews of Fluid Mechanics*, 24, 395, 1992.

Forman, M., and L.F. Burlaga, Exploring the Castaing distribution function to study intermittence in the solar wind at L1 in June 2000, in *Solar Wind Ten*, ed. M. Velli, R. Bruno, and F. Malara, AIP Conference Proceedings, vol. 679, Melville, NY, p. 554, 2003.

Freeman, M.P., N.W. Watkins and D.J. Riley, Evidence for a solar wind origin of the power law burst lifetime distribution of AE indices, *Geophys. Res. Lett.*, 27, 1087, 2000.

Gorney, D.J., Y.T. Chiu, and D.R. Croley, Trapping of ion conics by downward parallel electric fields, *J. Geophys. Res.*, 90, 4205, 1985.

Hnat, B., S.C. Chapman, G. Rowlands, N.W. Watkins, W.M. Farrel, *Geophys. Res. Lett.*, **29**(10), 10.1029/2001GL014587, 2002.

Hoshino, M., Nishida, A., Yamamoto, T., Kokubum, S., Turbulence magnetic field in the distant magnetotail: bottom-up process of plasmoid formation? *Geophys. Res. Lett.*, 21, 2935, 1994.

Jasperse, J.R., Ion heating, electron acceleration, and self-consistent *E* field in downward auroral current regions, *Geophys. Res. Lett.*, 25, 3485, 1998.

Jasperse, J.R., and N.J. Grossbard, The Alfvén-Fälthammar formula for the parallel *E*-field and its analogue in downward auroral-current region, *IEEE Trans. Plasma Science*, 28, 1874, 2000.

Jurac, S., private communication, 2003.

Klimas, A.J., D.N. Baker, D.A. Roberts, D.H. Fairfield and J. Büchner, A nonlinear dynamical analogue model of geomagnetic activity, *J. Geophys. Res.*, 97, 12253, 1992.

Klimas, A.J., J.A. Valdivia, D. Vassiliadis, D.N. Baker, M. Hesse, and J. Takalo, Self-organized criticality in the substorm phenomenon and its relation to localized reconnection in the magnetospheric plasma sheet, *J. Geophys. Res.*, 105, 18765, 2000.

Lu, E.T., Avalanches in continuum driven dissipative systems, *Phys. Rev. Lett.*, 74, 2511, 1995.

Lui, A.T.Y., Multiscale and intermittent nature of current disruption in the magnetotail, in *Physics of Space Plasmas*, MIT Geo/Cosmo Plasma Physics, eds.: T. Chang and J.R. Jasperse, vol. 15, p. 233, 1998.

Lui, A.T.Y., S.C. Chapman, K. Liou, P.T. Newell, C.I. Meng, M. Brittnacher, G.D. Parks, Is the dynamic magnetosphere an avalanching system?. *Geophys. Res. Lett*., 27, 911, 2000.

Matthaeus, W.H., and M.L. Goldstein, Low-frequency 1/f noise in the interplanetary magnetic field, *Phys. Rev. Lett.*, 57, 495, 1986.

Matthaeus, W.H., M.L. Goldstein and D.A. Roberts, Evidence for the presence of quasi-two-dimensional nearly incompressible fluctuations in the solar wind, *J. Geophys. Res.*, 95, 20673, 1990.

Meneveau, C., Analysis of turbulence in the orthogonal wavelet representation, *J. Fluid Mech.*, 232, 469, 1991.

Milovanov, A., Zelenyi, L., Zimbardo, G., Fractal structures and power law spectra in the distant magnetotail, *J. Geophys. Res.*, 101, 19903, 1996.

Morrison, P.J. and R.D. Hazeltine, Hamiltonian formulation of reduced magnetohydrodynamics, *Phys. Fluids*, 27, 886, 1984.

Nicoll, J.F., T. Chang, and H.E. Stanley, Nonlinear solutions of renormalization-group equations, *Phys. Rev. Lett.*, 32, 1446, 1974.

Nicoll, J.F., T. Chang, and H.E. Stanley, Nonlinear crossover between critical and tricritical behavior, *Phys. Rev. Lett.*, 36, 113, 1976.

Retterer, J.M., T. Chang, G.B. Crew, J.R. Jasperse and J.D. Winningham, Monte Carlo modeling of ionospheric oxygen acceleration by cyclotron resonance with broadband electromagnetic turbulence, *Phys. Rev. Lett.*, 59, 148, 1987.

Rutherford, P.H., Nonlinear growth of the tearing mode, *Phys. Fluids*, 16, 1903, 1973.

Sharma, A.S., D. Vassiliadis and K. Papadopoulos, Reconstruction of low-dimensional magnetospheric dynamics by singular spectrum analysis, *Geophys. Res. Lett.*, 20, 335, 1993.

Seyler, C.E., Jr., Nonlinear 3-D evolution of bounded kinetic Alfvén waves due to shear flow and collisionless tearing instability, *Geophys. Res. Lett.*, 15, 756, 1988.

Sitnov, M.I., A.S. Sharma, K. Papadopoulos, D. Vassiliadis, J.A. Valdivia, A.J. Klimas, and D.N. Baker, Phase transition-like behavior of the magnetosphere during substorms, *J. Geophys. Res.*, 105, 12955, 2000.

Sorriso-Valvo, L., V. Carbone, P. Veltri, G. Consolini, and R. Bruno, Intermittency in the solar wind turbulence through probability distribution functions of fluctuations, *Geophys. Res. Lett.* 26, 1801, 1999.

Stanley, H.E., *Introduction to Phase Transitions and Critical Phenomena*, Oxford University Press, New York, 1971.

Strauss, H.R., Nonlinear, three-dimensional magnetohydrodynamics of non-circular tokamaks, *Phys. Fluids*, 19, 134, 1976.

Tam, S.W.Y., F. Yasseen, T. Chang, and S.B. Ganguli, Self-consistent kinetic photoelectron effects on the polar wind, *Geophys. Res. Lett.*, 22, 2107, 1995.

Tam, S.W.Y., F. Yasseen, and T. Chang, Further development in theory/data closure of the photoelectron-driven polar wind and day-night transition of the outflow, *Ann. Geophys.*, 16, 948, 1998.

Tam, S.W.Y. and T. Chang, Kinetic evolution and acceleration of the solar wind, *Geophys. Res. Lett.*, 26, 3189, 1999a.

Tam, S.W.Y. and T. Chang, Solar wind acceleration, heating, and evolution with wave-particle interactions, *Comments on Modern Physics*, vol. 1, Part C, 141, 1999b.

Tam, S.W.Y. and T. Chang, Effect of electron resonant heating on the kinetic evolution of the solar wind, *Geophys. Res. Lett.*, 28, 11351, 2001.

Tam, S.W.Y. and T. Chang, Comparison of the effects of wave-particle interactions and the kinetic suprathermal electron population on the acceleration of the solar wind, *Astronomy & Astrophysics*, 395, 1001, 2002.

Tetreault, D., Turbulent relaxation of magnetic fields, 1. Coarse-grained dissipation and reconnection, *J. Geophys. Res.*, 97, 8531, 1992a; ibid, 2. self-organization and intermittency, 97, 8541, 1992b.

Taylor, J.B., Relaxation of toroidal plasma and generation of reversed magnetic fields, *Phys. Rev. Lett.*, 33, 1139, 1974.

Tu, C.Y. and E. Marsch, MHD structures, waves and turbulence in the solar wind: observations and theories, *Space Science Reviews*, 73, 1, 1995.

Uritsky, V.M., A.J. Klimas, D. Vassiliadis, D. Chua, and G.D. Parks, Scale-free statistics of spatiotemporal auroral emissions as depicted by POLAR UVI images: The dynamic magnetosphere is an avalanching system, *J. Geophys. Res.*, 107, 1426, 2002.

Waddell, B.V., B. Carreras, H.R. Hicks, and J.A. Holmes, Nonlinear interaction of tearing modes in highly resistive tokamaks, *Phys. Fluids*, 22, 896, 1979.

Watkins, N. W., Scaling in the space climatology of the auroral indices: Is SOC the only possible description?, *Nonlinear Processes in Geophysics*, 9, 389, 2002.

Watkins, N.W., S.C. Chapman, R.O. Dendy and G. Rowlands, Robustness of collective behavior in strongly driven avalanche models: magnetospheric implications, *Geophys. Res. Lett.*, 26, 2617, 1999.

Weygand, J., private communication, 2003.

Wilson, K.G. and J. Kogut, The renormalization group and the epsilon-expansion, *Physics Reports*, 12C, 76, 1974.

Wu, C.C., and T. Chang, 2D MHD Simulation of the Emergence and Merging of Coherent Structures*, Geophys. Res. Lett.*, 27, 863, 2000a.

Wu, C.C., and T. Chang, Dynamical evolution of coherent structures in intermittent two-dimensional MHD turbulence, *IEEE Trans. on Plasma Science*, 28, 1938, 2000b.

Wu, C.C., and T. Chang, Further study of the dynamics of two-dimensional MHD coherent structures—A large scale simulation, *Journal of Atmospheric Sciences and Terrestrial Physics*, 63, 1447, 2001.

Chapter 3

COMPLEXITY AND TOPOLOGICAL DISORDER IN THE EARTH'S MAGNETOTAIL DYNAMICS

Giuseppe Consolini
Istituto di Fisica dello Spazio Interplanetario, CNR
I-00133 Rome, Italy
consolini@ifsi.rm.cnr.it

Tom Chang
Center for Space Research, Massachusetts Institute of Space Technology,
Cambridge, MA 02139 USA
tsc@space.mit.edu

Anthony T. Y. Lui
The Johns Hopkins University Applied Physics Laboratory,
Laurel, 20723 MD, USA
Anthony.Lui@jhuapl.edu

Abstract: Recently, several observations suggested that the Earth's magnetospheric dynamics in response to solar wind changes may resemble the behavior of a complex system which operates out-of-equilibrium and near criticality. Here, we discuss the emergence of complexity and topological disorder in the magnetotail regions. In detail, we will show how several aspects regarding the multiscale nature of the magnetospheric response may be connected to the evolution of a complex topology of multiscale magnetic and plasma coherent structures.

Key words: Earth's magnetosphere, Magnetospheric dynamics, Complexity, Criticality

A.S. Sharma and P.K. Kaw (eds.), Nonequilibrium Phenomena in Plasmas, 51–70.
© 2005 *Springer. Printed in the Netherlands.*

Introduction

The near-Earth region where the geomagnetic field is confined by the solar wind, i.e. the so-called Earth's magnetosphere, is a highly structured dynamical region, which continuously interacts with the solar wind and the Earth's ionosphere by exchanging energy, mass and momentum. The effects of this continuous interaction with the solar wind are manifested in a wide variety of phenomena, which involve several regions of the magnetospheric cavity. As an example, the magnetospheric substorm is a comprise of phenomena involving several magnetospheric regions and during which the energy, previously stored in the magnetotail region, is suddenly released and dissipated.

In the framework of statistical mechanics, the dynamics of the Earth's magnetosphere may be considered to be equivalent to that of an open, extended stochastic system, usually in an out-of-equilibrium configuration which is a consequence of the continuous driving of the solar wind. Evidences of this out-of-equilibrium configuration and dynamics are in the non-symmetric shape and in the highly structured configuration of the magnetospheric cavity, as well as, in the existence of a complex system of currents, which continuously dissipates energy, and in the impulsive and avalanching character of the magnetospheric response to the solar wind changes.

Although significant advances in magnetospheric studies have been achieved from the early days to present, a complete understanding of the dynamical processes on the basis of the impulsive character of the magnetospheric dynamics has not yet been reached, leaving this topic one of the most relevant and puzzling problems in space physics. Our lack of understanding is essentially related to the highly irregular behavior of the magnetospheric dynamics during magnetic substorms and storms, particularly within the magnetotail regions, as well as, to the small-scale processes and the cross-coupling phenomena involving a wide range of scales. For instance, some substorm associated studies have shown that the magnetospheric activity extends from small-scale to large-scale processes, and often involves phenomena that are transient, localized and intermittent (Consolini et al., 1996; Lui and Najimi, 1997; Chang, 1998; Angelopoulos et al., 1999; Klimas et al., 2000; Lui et al., 2000).

Traditionally, the efforts to model magnetospheric dynamics were based on the magneto-hydrodynamic (MHD) concepts. Although the classical MHD approach to the magnetospheric dynamics has led to a significant understanding in the description of global and large-scale magnetospheric processes and phenomena, it has been suggested to be not always adequate to describe the highly irregular and structured behavior at smaller scales down to the kinetic scales (Chang, 1992; Lui and Najimi, 1997; Chang, 1999a; Chang et al., 2003). For example, this is particularly true in the case of the large magnetic fluctuations and rapid particle energizations observed

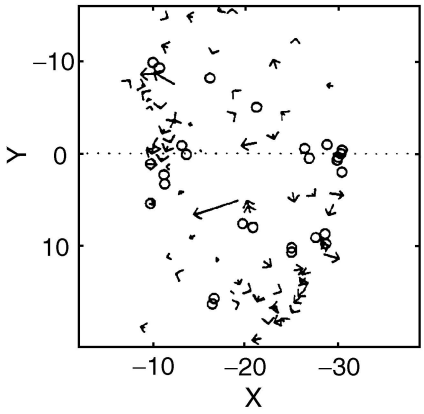


Figure 1. A synoptic plasma flow pattern at the substom onset as evaluated from superposed epoch analysis of 102 substorm events (adapted from Lui et al., 1998. Copyright [1998] American Geophysical Union. Reproduced/modified by permission of American Geophysical Union). The "○" denotes an event in which the plasma number density was too low for a reliable determination of plasma flow. This result is consistent with transient, localized and intermittent acceleration events.

at localized regions in the tail current sheet during the substorm expansion phase (Lui and Najimi, 1997; Consolini and Lui, 1999; Lui et al., 1999; Consolini and Lui, 2000; Lui, 2002). Furthermore, some inconsistencies, involving the occurrence of sporadic (time intermittency) and localized phenomena, were found with respect to the classical substorm scenario (see Figure 1). In this regard, recent in-situ satellite observations revealed the occurrence of spatiotemporally localized relaxation processes in the magnetotail regions (Lui et al., 1998; Angelopoulos et al., 1999). Thus, the above suggests that the small- and large-scale dynamics are closely connected, and that a global understanding of the magnetospheric and magnetotail dynamics requires one to investigate the underlying macro-, meso-, and micro-scale processes and the space-time cross-coupling among them. To stress this point we emphasize that the dynamic domain responsible for the solar-wind magnetosphere and magnetotail coupling involves temporal and spatial scales much larger than those that characterize the microscopic plasma parameters (e.g. the ion gyroradius, skin depth, the Debye length, and the ion cyclotron, lower hybrid or plasma parametres) in the magnetotail regions; i.e. the transport processes and the dynamics involve parameters differring by orders of magnitude. This is the reason why the magnetospheric studies have gradually moved in the last decade from the traditional classical MHD approach to the new modern techniques of analysis, based on the advancement in the study of nonlinear and complex systems, which offered new insights and different views of the magnetospheric dynamics.

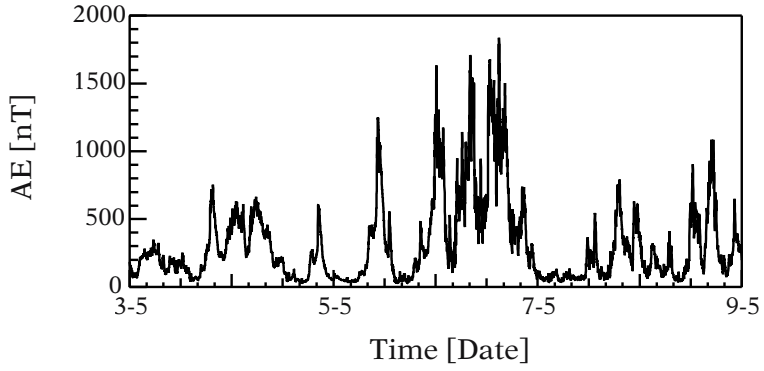


Figure 2. A sample of AE-index for the period from May, 03, 1988 to May, 09, 1988. Note the highly dynamical and bursty behavior of this index which is evidence of time intermittency in the magnetospheric dynamics. Data, available on Web, come from WDC-2, Kyoto, Japan.

In the aforementioned framework, at the beginning of the 90s it was suggested that the highly intermittent and irregular character of the magnetospheric dynamics, for instance as evidenced by the behaviour of the geomagnetic indices (see Figure 2), may be the result of low-dymensional chaos. In particular, some authors (Baker et al., 1990; Vassiliadis et al., 1990; Roberts et al., 1991; Sharma et al., 1991) suggested that certain features of the magnetic substorms may be modelled to some extent by such an approach. The evidence of a possible chaotic dynamics spurred new studies in the solar-wind magnetosphere-ionosphere coupling. However, there are some aspects of the magnetospheric dynamics that cannot be simply explained as due to a low-dimensional chaotic dynamics. This suggested that a more appropriate framework to discuss the magnetospheric dynamics is that of nonlinear input-output dynamical systems, instead of autonomous attractor dynamics (Sharma, 1995; Klimas et al., 1996).

A somewhat different framework for the magnetospheric dynamics was proposed by Chang (Chang, 1992). He pointed out that a nonlinear stochastic system, driven far-from-equilibrium near a "forced and/or self-organized critical point" (FSOC), could exhibit a low-dimensional dynamic behavior which is due to the limited number of relevant eigenoperators (i.e. the parameters characterizing the dynamics of the system) near the critical point. Furthermore, because near criticality the correlation length of the fluctuations of the random dynamical fields is long-ranged, the system itself should also display scale-invariance. When this scenario is applied to the Earth's magnetotail and geospace plasmas, it implies a strongly dynamical picture, where the geotail dynamics is essentially due to "the generation, dispersing and merging of multiscale localized coherent plasma structures" (Chang, 1998; Chang, 1999a; Chang, 2001). The emergence of a complex topology of coherent plasma and

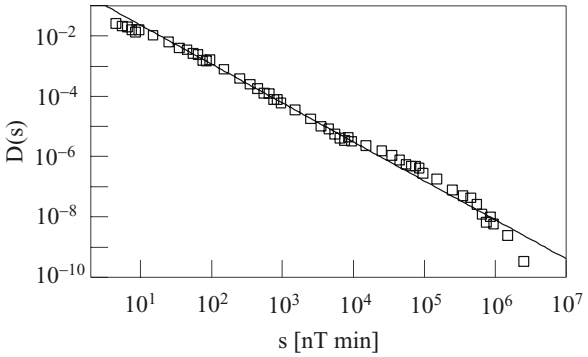


Figure 3. The burst size distribution function $D(s)$ for the AE-index behaviour (adapted from Figure 3 in Consolini, 2002, "Self-organized criticality: a new paradigm for the magnetotail dynamics", *Fractals*, 10 (2), 275. Copyright [2002] World Scientific Publishing Co. Reproduced/modified by permission of World Scientific Publishing Co.). The solid line is a power-law best fit with scaling exponent $\tau = [1.35 \pm 0.06]$. This result is consistent with a scale invariant dynamics near criticality (Consolini, 1997; Consolini and De Michelis, 2001; Consolini and Chang, 2002).

magnetic field structures was clearly demonstrated by recent 2D large-scale MHD numerical simulations (Wu and Chang, 2000; Wu and Chang, 2001).

Some of the first evidences of space-time intermittency and of a near-criticality dynamics were found by Consolini and his co-authors (Consolini et al., 1996; Consolini, 1997; Consolini and De Michelis, 1998) in investigating the scaling and bursty features of the auroral electrojet (AE) index, and by Lui et al. (Lui et al., 1998) in investigating plasma flow patterns in the geotail regions at the substorm onset. Further evidences of the above scenario were found in magnetotail "bursty bulk flows" (Angelopoulos et al., 1999), in the auroral displays (Lui et al., 2000; Uritsky et al., 2002), in numerical simulations by means of cellular automata and coupled-map lattices (Chapman et al., 1998; Uritsky and Pudovkin, 1998; Chapman et al., 1999; Takalo et al., 1999; Klimas et al., 2000; Consolini and De Michelis, 2001) and renormalization-group studies (Tam et al., 2000; Chang et al., 2003). Other authors suggested that the observed near-criticality features of the magnetospheric dynamics could be also due to a manifestation of the solar wind properties (Freeman et al., 2000; Takalo et al., 2000; Price and Newman, 2001). On the other hand, it has also been argued that the magnetospheric dynamics contain some features that cannot be adequately described by a near-criticality dynamics (SOC and/or FSOC). These evidences suggested that the global character of the magnetospheric dynamics could become reconciled with the evidence of a multiscale dynamics in terms of nonequilibrium phase transitions (Sitnov et al., 2000; Sitnov et al., 2001). Several workers

(Consolini and Lui, 1999; Consolini and Lui, 2000; Sitnov et al., 2000; Sitnov et al., 2001; Sharma et al., 2001), indeed, showed that the multiscale dynamics of the Earth's magnetosphere during magnetic substorms exhibits a number of features which are typical of phase transitions.

All the aforementioned points suggest that the understanding of the global and local magnetospheric dynamics, especially in the tail and auroral regions, requires the investigation of the role that complexity and topological disorder play.

Our aim here is to discuss the emergence, the meaning and the role of complexity and of topological disorder with respect to the local and global features of the magnetospheric and magnetotail dynamics.

1. Complexity and Topological Disorder: A Brief Introduction

In the last decade, a great deal of interest has been devoted to the study of complexity and complex systems in a wide variety of research fields from biology to physics, from economics to astronomy. Anyway, the word *complexity* seems to assume slightly different meanings in different research fields, mainly because of the intrinsic ambiguity of the term itself.

Although in common daily use, the term *complexity* is generally employed when we refer to something that seems to be hard to separate in elementary parts, in the framework of physical sciences complexity refers to a qualitative feature of a system consisting of several elementary parts, interacting together, and whose global features cannot be simply surmised from the ones of the elementary parts. Moreover, in contrast to what is commonly believed, the emergence of complexity does not require very complicated relations among the elementary parts that form the system. As a matter of fact, complexity may be observed for very simple systems with very simple evolution rules. To better demonstrate this point we show in Fig. 4 three patterns generated by simple cellular automata, defined according to the scheme of S. Wolfram (Wolfram, 2002). Each pattern starts with a black pixel at the center of the first lattice row (top), and evolves following a simple algorithmic and binary

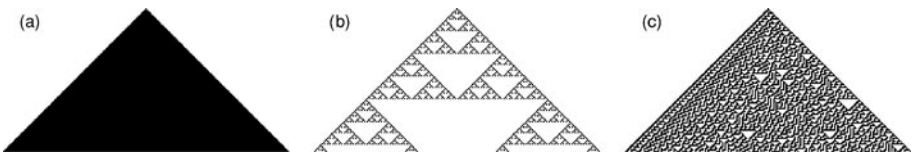


Figure 4. Three examples of patterns generated by simple cellular automata rules. From left to right the celluta automata rules to generate such patterns are Wolfram's rules # 254, 90 and 30, respectively.

rule:

- rule # 254

$$f_{i,j} = 1 - \bar{f}_{i-1,j-1}\bar{f}_{i,j-1}\bar{f}_{i+1,j-1}, \quad (1)$$

- rule # 90

$$f_{i,j} = \bar{f}_{i-1,j-1}f_{i+1,j-1} + f_{i-1,j-1}\bar{f}_{i+1,j-1}, \quad (2)$$

- rule # 30

$$f_{i,j} = \bar{f}_{i-1,j-1}f_{i,j-1} + \bar{f}_{i,j-1}(\bar{f}_{i-1,j-1}f_{i+1,j-1} + f_{i-1,j-1}\bar{f}_{i+1,j-1}), \quad (3)$$

where $f = 0, 1$ and $\bar{f}$ indicates the NOT operation (i.e. $\bar{f} = 1 - f$). Following these simple algorithmic rules, we may note how one can obtain different patterns ranging from trivial ones (rule # 254) to ordered fractal structured patterns (rule # 90) and/or to disordered patterns containing a huge number of structures at different scales (rule # 30). In particular, we may note how disorder and complexity can emerge by exact algorithmic rules. Thus, in spite of the simplicity of the aforementioned rules we can obtain very complex and structured patterns that cannot be directly envisioned on the basis of these elementary basic rules.

Although, in the above examples we have shown some examples dealing with the emergence of complex patterns (or structural complexity), in physical systems we can also observe dynamical complexity, i.e. the emergence of a non-trivial behavior due to the dynamics of the interacting subunits that form the system itself. Sometimes the complex dynamics, as well as, the structural complexity are the consequence of an out-of-equilibrium dynamics of the system. Quite often, systems forced out-of-equilibrium will self-organize in order to dissipate the excess of energy, and result in correlated and complex behavior (Nicolis and Prigogine, 1987).

The main aspect of systems exhibiting complexity is that we can provide their descriptions at different levels of understanding, where the higher levels generally require concepts and classifications which do not depend on the detailed microscopic elementary laws, i.e. which are universal. What differentiates the behavior of complex systems from classical systems is the emergence of long-range correlations, cooperativity, fractal topology, multiscale coherent structures, general scale-invariance, topological disorder, and criticality (see Figure 5 for an example of ordered and disordered topological patterns).

As already discussed in previous works (Consolini and Chang, 2001; Consolini and Chang, 2002) one of the most relevant features of complex systems is the emergence of criticality and the fundamental role that disorder plays in such systems. As a matter of fact, the scale invariance has been shown to be a fundamental property of breakdown processes in disordered systems, as well

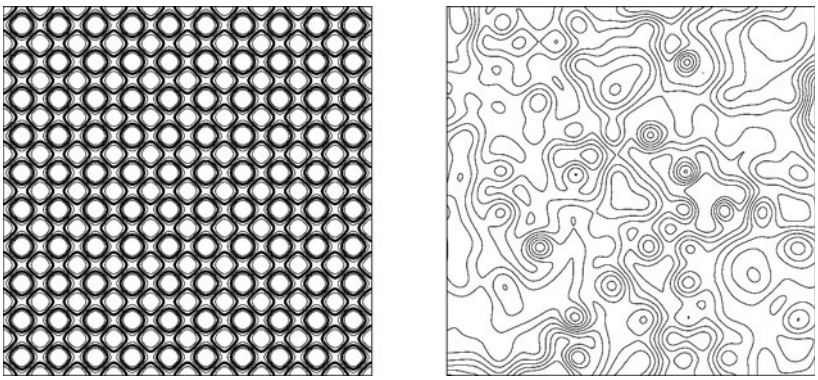


Figure 5. Two example of ordered (left panel) and disordered (right panel) topological patterns. The ordered pattern consists of a set of structures with the same characteristic scale located on the sites of a square lattice. The disordered pattern is generated as the ordered pattern but with a set of structures characterized by a gaussian distribution of the characteristic scales. Plots are contour-level plots.

as, of the dynamics of such systems in response to external parameter variations (Sethna et al., 2001). In analogy with what happens in the case of thermodynamic systems at criticality, the scale-invariance observed in the fluctuations of the aforementioned systems has been named "criticality". In this framework, it was shown that in some complex systems the amount of disorder plays an extremely relevant role like a relevant field, selecting between continuous and discontinuous phase transitions (Andersen, 1997; Berker, 1993). For example, in fracture processes, disorder has been shown to generate non-trivial fat distribution functions of the stress field, characterized by high kurtosis values (see Andersen, 1997 and references therein). In other words, the power-law distributions observed in several complex systems may arise from the *critical nature* of cracking processes in disordered and heterogeneous media.

The study of complex systems, as well as of cracking systems, may benefit from the *renormalization-group theory* which is able to describe the change of the evolution rules as a function of the scale of investigation (Chang et al., 1992; Sethna et al., 2001). As a matter of fact, although the renormalization-group theory was introduced in statistical mechanics to study second order phase-transitions, this theory represents the starting point to investigate and understand the emergence of fractal, scale-invariant and self-similarity features in complex systems.

2. Topological Disorder and Coherent Structures in Geotail Regions

As already mentoned in the introduction, in-situ observations of the Earth's magnetotail region revealed the local, intermittent, multiscale and turbulent

nature of the dynamics of this region. As suggested by Chang (Chang, 1998; Chang, 1999a), a better description of such type of patchy and intermittent dynamics would require the investigation of the development and the evolution of coherent magnetic and plasma structures instead of the interactions of plane waves.

The origin of such coherent structures may be understood in terms of resonance sites (Tetrault, 1992a; Tetrault, 1992b; Chang, 1999a; Chang, 1999b) for the propagation of magnetic fluctuations (Alfvén and lower hybrid waves, whistler mode etc.). Near these plasma resonance sites where the propagation conditions are not satisfied (e.g. $i\mathbf{k} \cdot \mathbf{B} = \mathbf{0}$ for Alfvénic fluctuations), the fluctuations are localized, forming coherent magnetic structures that in the case of the neutral sheet region in the Earth's magnetotail assume the shape of cross-tail current flux tubes. These coherent structures result from the self-organization of bundles of magnetic and plasma fluctuations covering a wide range of scales near the resonance sites, and thus these structures are themselves complex structures. We note that these coherent structures generally self-organize and coexist with an underlying stochastic and turbulent medium.

For example, when two of these structures of the same polarity (see Fig. 6) migrate toward each other, they can interact and generate an intense current sheet between them. As a result of this interaction the structures can merge while producing new fluctuations that propagate in the plasma medium and, successively, may eventually produce new coherent structures. Thus, the interaction of coherent structures can be viewed in terms of a local reconfiguration of the magnetic, current, and plasma structures, i.e. as a sort of local topological phase transition. If the interaction region of the coherent structures is smaller than that of the ion gyroradius, then the coarse-grained dissipation that will initiate the merging of these structures will probably involve the dynamic merging and mixing of the whistler coherent structures (Chang, 1999a; Chang et al., 2003).

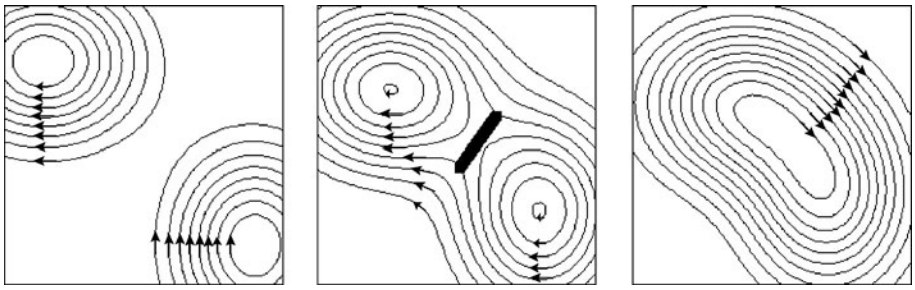


Figure 6. A schematic plot for the merging of two coherent structures of the same polarity. From left to right, prior, during and after merging. Contours are transverse magnetic field lines and arrows indicate sense of directions. The black solid segment indicates the site where an intense current sheet is generated and where the dissipation associated with the merging process occurs.

In other words, the local topological reconfiguration of the coherent structures could be driven and mediated by an intermittent whistler turbulence. Some evidences of the role played by whistlers in the topological changes occurring during the magnetic reconnection (here named *local reconfiguration*) has been recently found by Deng and Matsumoto (2001).

Thus, the emerging scenario consists of a complex disordered topology made of a multitude of multiscale coherent structures, that in the tail current sheet region might be the origin of a percolating fractal network of filamentary currents (Milovanov et al., 2001). Evidences of these coherent structures and of such a complex topology have been found through numerical simulations based on a compressible MHD model (Wu and Chang, 2000; Wu and Chang, 2001; Chang and Wu, 2002; Chang et al., 2002).

Near the neutral sheet region, i.e. in the region where it is most probable to observe the generation of such coherent structures, the evolution of such coherent current structures is responsible for the observed coarse-grained dissipation events, which have been observed by in-situ satellite measurements (Angelopoulos et al., 1999; Angelopoulos et al., 1999a) and in the auroral indices (Consolini, 1997) as crackling noise ($1/f$-noise).

On the basis of the aforementioned framework, the emerging picture is that of a highly dynamical system consisting of a disordered topology of multiscale coherent structures and fluctuations covering a wide range of cross-coupled scales from the large MHD scales down to the small kinetic scales. The evolution is mainly dominated by local coarse-grained dissipation processes, similar to the local breakdown and rupture phenomena that occur in disordered systems. As noted by Tetrault (Tetrault, 1992b), in analogy with what is typical of a phase-transition the local relaxation of the field topology is more efficient. In other words, the sporadic and intermittent dynamics is an efficient way to utilize the available free energy. This dynamical complexity is the cause of the observed critical behavior, i.e. of the observed scale-invariance of several quantities associated with the magnetotail and the magnetospheric dynamics. We underline that, although sometimes the global system may evolve toward a true dynamical critical point (FSOC) due to the external driving, the scale-invariance may be observed also out of this critical point in a limited range of scales as a consequence of the inherent topological disorder. A detailed description of the emergence of criticality (FSOC) out of the topological complexity may be found in Chang et al. (2003a, 2003b).

The main feature of such a dynamical model is the interplay among the coherent magnetic structures, emerging from the self-organization of bundles of fluctuations at the resonance sites, and the MHD turbulent medium. In this model, the intrinsic stochasticity of the topology of coherent structures regulates the dynamics of the overall system in terms of local and intermittent topological transitions. Thus, the dynamics of the system is mainly due to the stochastic

nucleation of the coherent structures, which involves a wide range of different scales (Chang et al., 2003b).

In such a framework the substorm onset would be associated with fluctuations of the complex and disordered topology of the coherent structures that could induce a sort of order-disorder topological phase transition (disorder → order), causing an apparent reduction of the topological disorder in the magnetotail region. A similar scenario for the magnetic substorm was proposed by Milovanov et al. (2001). As a matter of fact, they associate the magnetic substorm to "a structural catastrophe related to the gradual topological simplification of the percolating fractal network existing in the magnetotail current sheet".

3. An Example of a Local Topological Phase Transition: The Cross-Tail Current Disruption

One of the most important manifestations of the magnetospheric dynamics is magnetic substorm, a composition of phenomena involving a vast region of the near-Earth space (Lui, 1991). Among this set of phenomena, the most relevant one occurring at the substorm onset is the development of a current wedge, generally associated with the diversion or disruption of the near-Earth cross-tail current system and with dipolarization of the Earth's magnetic field in the tail region (Atkinson, 1967; Akasofu, 1972; Lui, 1996). During the last few years, this dipolarization phenomenon has been the subject of several studies, which underlined its multiscale and non-MHD nature (Lui et al., 1999).

In association with this phenomenon, briefly named *current disruption* (CD), large amplitude ($\Delta B/B > 1$) magnetic field fluctuations (see Fig.7) are

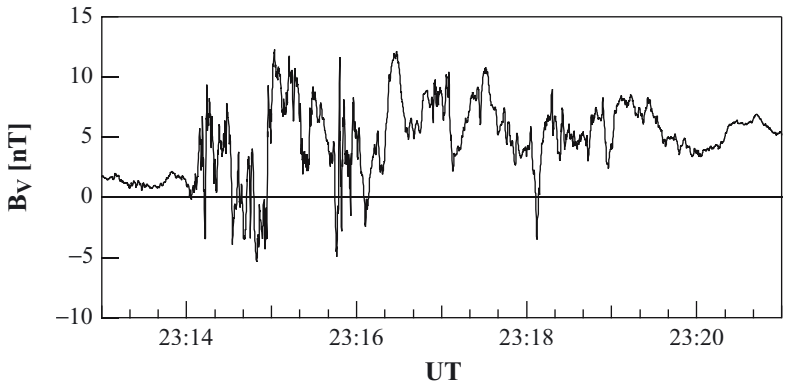


Figure 7. The B_V component of the magnetic field as measured by AMPTE/CCE spacecraft during the CD event of June 1, 1985 (85/152).

observed in the near-Earth magnetotail (Lui et al., 1988). Previous studies of these large-amplitude fluctuations demonstrated the nonlinear nature of the CD, and that during CD a broadband spectrum of fluctuations covering a wide range of timescales from below to above the ion cyclotron timescale is intermittently excited (Lui and Najimi, 1997; Ohtani et al., 1995). Furthermore, it has been shown that these fluctuations are characterized by intermittency at the smallest timescales, and nonlinear intermittent cross-coupling among them on different timescales (Consolini and Lui, 2000). On the other hand, it was shown that fast ion flows may be observed during the magnetic field dipolarization (Lui, 1999; Angelopoulos et al., 1999a). This fact seems to suggest that CDs and BBFs are similar phenomena (Angelopoulos et al., 1999a).

In analysing the features of the magnetic field fluctuations associated to CD, it was suggested that during CD a reorganization phenomenon takes place, and that this reorganization phenomenon can be viewed as a sort of topological phase-transition (Consolini and Lui, 1999). As a matter of fact, during this reorganization phenomenon, a change of the fractal features of the magnetic field fluctuations (see Fig. 8) was observed that seems to be in agreement with the occurrence of a topological rearrangement of the fractal percolating network of currents (Milovanov et al., 2001). This result seems also to be confirmed by the observations of Ohtani and co-authors (Ohtani et al., 1998) that described the CD as a system of chaotic filamentary electric currents.

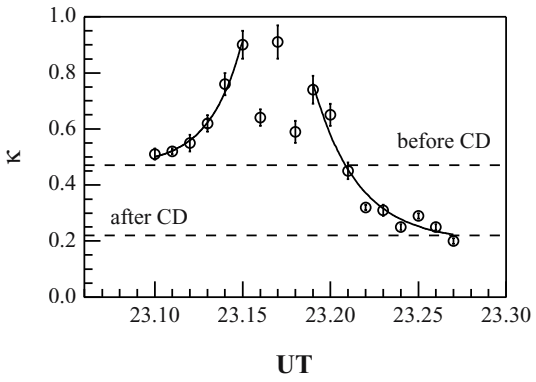


Figure 8. Change of the fractal features of the magnetic field fluctuations observed during CD event 85/152. The κ exponent is the so-called cancellation exponent and refers to the sign-singularity analysis of the fluctuations. The horizontal dashed lines represent the two values of the κ exponent before and after the CD. The observed change of the cancellation exponent suggests the ocurrence of a topological reorganization phenomenon. (Adapted from Consolini and Lui, 1999, "Sign-singularity analysis of current dsruption", *Geophys. Res. Lett.*, 26 (12), 1673. Copyright [1999] American Geophysical Union. Reproduced/modified by permission of American Geophysical Union).

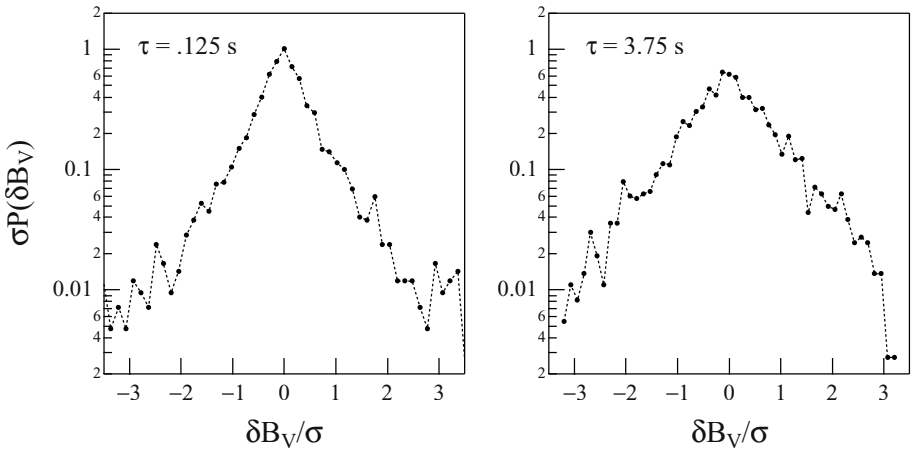


Figure 9. The normalized probability distribuzion functions of the magnetic field fluctuations δB_V at two different time scales below (left plot) and above (right) the ion gyroperiod, respectively, for the CD event of June 1, 1985 (85/152).

In Fig. 9 we show the rescaled normalized distribution functions $\sigma P(\delta B_V)$ of the magnetic field fluctuations δB_V during the CD (from 23:14 UT to 23:20 UT) at two different time scales (here σ is the variance of the fluctuations), respectively, below and above the prton gyroperiod. Data (in the VDH coordinate system) refer to the CD event occurred on June, 1, 1985 (85/152) and observed by the AMPTE/CCE spacecraft ($\sim$8.8 R_E, MLT $\sim$24, field latitude angle $\sim 90^\circ$). Since the magnetic field angle is very high during all the period under investigation, we may assume the spacecraft to be in the current sheet and the observed fluctuations to be mainly temporal. From this figure we note how the intermittent character of the magnetic field fluctuations during CD is more pronounced in the kinetic domain (i.e. below the proton gyroperiod) suggesting the occurrence of sporadic fast events in this regime. This fact is also confirmed by the values of the kurtosis λ for the fluctuations which are $\lambda \geq 20$ and $\lambda \approx 4$ in the kinetic and MHD domain, respectively.

In Fig. 10 we report the results of the local intermittency measure (LIM) analysis (Farge, 1992; Bruno et al., 1999; Bruno et al., 2001) on the event of June 1, 1985. The LIM analysis, based on wavelet decomposition, is able to extract and locate the coherent structures contained in the signal which are responsible for the observed intermittency. In detail, if $\psi(t, \tau)$ represents the set of the wavelet coefficients of a signal $f(t)$ evaluated at the scale τ, i.e.:

$$\psi(t, \tau) = \frac{1}{\sqrt{\tau}} \int_{-\infty}^{+\infty} f(t')\phi\left(\frac{t' - t}{\tau}\right) dt' \tag{4}$$

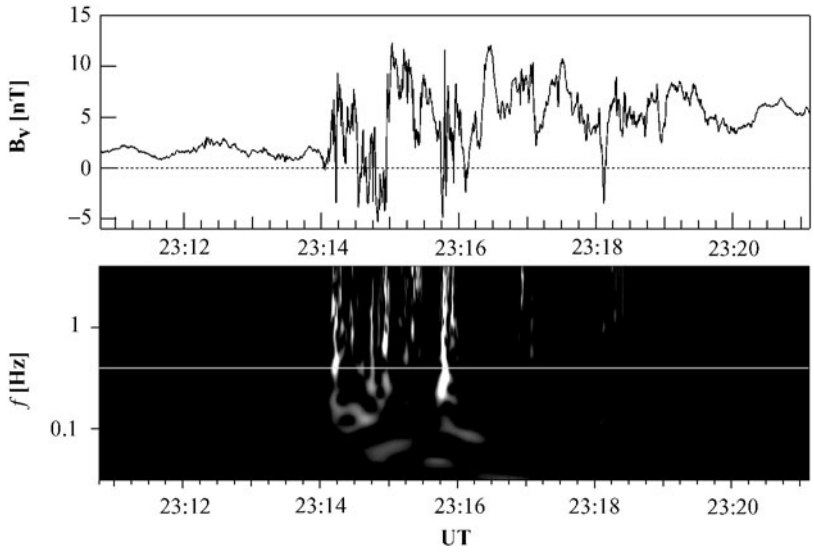


Figure 10. The LIM analysis of the magnetic field fluctuations during the CD of June 1, 1985. The horizontal line in the below panel refers to the mean proton gyrofrequency $f_\Omega \sim 0.4$ Hz.

where $\phi(\frac{t'-t}{\tau})$ is a delayed and rescaled wavelet, then the LIM is defined as the ratio of the wavelet squared amplitude $\mid \psi(t, \tau) \mid^2$ and its time averaged value $\langle \mid \psi(t, \tau) \mid^2 \rangle_t$, i.e.:

$$LIM \equiv \frac{\mid \psi(t, \tau) \mid^2}{\langle \mid \psi(t, \tau) \mid^2 \rangle_t}. \tag{5}$$

It follows that any value of $LIM > 1$, for any t and τ indicates that a certain scale or frequency (τ or f) at a certain time t contributes more than what is expected by the average spectrum. Here we used the well-known Morlet wavelet, and we evaluated the time average value of the wavelet squared amplitude in the time interval from 23:14 UT to 23:20 UT.

The most important results of the LIM analysis on the CD magnetic field fluctuations is that the intermittency involves scales below and above the proton gyrofrequency, suggesting an interplay and cross-coupling among MHD and kinetic scales.

This result suggests that the intermittency observed during CD in the kinetic domain might be due to the sporadic merging of whistler coherent structures, which could mediate the coalescence of the large scale current structures in order to reconfigure the current topology. In other words, this result seems to be well in agreement with the above-mentioned picture proposed by Chang (Chang, 2001; Chang et al., 2002) to explain the occurrence of localized reconnection events.

4. Summary

In this work, we have presented a review of some concepts dealing with the occurrence of dynamical complexity in the magnetotail phenomena. We have seen how it is possible to reconcile some observations with a model involving the generation, merging and dispersion of multiscale coherent magnetic and plasma structures. The role of these coherent structures and of their evolution has been discussed in connection with the observational results on local, sporadic and coarse-grained relaxation events. A special emphasis has been placed on the role that the topological disorder plays in the emergence of the observed near-critical behavior. An example is provided to illustrate how some of the aforementioned concepts may be used to interpret observational results.

Due to the fact that the physical concepts and the approach discussed in this work are nontraditional we suggest the readers to consult the original references.

Acknowledgments

The authors wish to thank their colleagues V. Angelopoulos, S. C. Chapman, P. De Michelis, C. F. Kennel, V. Uritsky, A. Klimas, D. Tetreault, S.W.Y. Tam, C.C. Wu, N. Watkins, D. Vassiliadis, A. S. Sharma, M. I. Sitnov for useful discussions. T. C. wishes to thank IFSI-CNR for the kind hospitality and AFOSR, NASA and NSF for partial research support. G. C. thanks the Italian National Programme for Antarctic Research (PNRA) for the partial funding of his studies.

References

Akasofu, S. -I."Magnetospheric substorm, a model", In Dryer, D., editor, *Solar Terrestrial Physics*, Part I. Pag. 131. D. Reidel, Norwell, Mass., 1972.

Aktinson, G. "An approximate flow equation for geomagnetic flux tubes and its application to polar substorms", *Jour. Geophys. Res.*, 72: 5373, 1967.

Andersen, J. V., D. Sornette and K. Leung. "Tricritical behavior in rupture induced by disorder", *Phys. Rev. Lett.*, 78: 2140, 1997.

Angelopoulos, V., T. Mukai and S. Kokubun. "Evidence for intermittency in Earth's plasma sheet and implications for self-organized criticality", *Phys. Plasmas*, 6: 4161, 1999.

Angelopoulos, V., F. S. Mozer, T. Mukai, K. Tsuruda, S. Kokubun and T.J. Hughes. "On the relationship between bursty flows, current disruption and substorms", *Geophys. Res. Lett.*, 26: 2841, 1999a.

Baker, D. N., A. J. Klimas, R. I. McPherron and J. Büchner. "The evolution from weak to strong geomagnetic activity: an interpretation in terms of deterministic chaos", *Geophys. Res. Lett.*, 17: 41, 1990.

Berker, A. N. "Critical behavior induced by quenched disorder", *Physica A*, 194: 72, 1993.

Bruno, R., B. Bavassano, E. Pietropaolo, V. Carbone and P. Veltri. "Effects of intermittency on interplanetary velocity and magnetic field fluctuations", *Geophys. Res. Lett.*, 26: 3185, 1999.

Bruno, R., V. Carbone, P. Veltri, E. Pietropaolo and B. Bavassano "Identifying intermittency events in the solar wind", *Planet. Space Sci.*, 49: 1201, 2001.

Chang, T. "Low-dimensional behavior and symmetry breaking of stochastic systems near criticality: can these effects be observed in space and in the laboratory", *IEEE Trans, Plasma Phys.*, 20: 691, 1992.

Chang, T., D. D. Vevedensky and J. F. Nicoll "Differential renormalization-group generators for static and dynamic critical phenomena", *Phys. Rep.*, 217: 279, 1992.

Chang, T. "Sporadic localized reconnections and multiscale intermittent turbulence in the magnetotail", In Horvitz, J. L et al., editors, *Geospace Mass and Energy Flow*. Geophysical Monograph, Vol. 104., pag. 193. AGU, Washington DC, 1998.

Chang, T. "Self-organized criticality, multifractal spectra, sporadic localized reconnections and intermittent turbulence in magnetotail", *Phys. Plasmas*, 6: 4137, 1999a.

Chang, T. "Self-organized criticality, multi-fractal spectra, and intermittent merging of coherent structures in the magnetotail", *Astr. and Space Sci.*, 264: 303, 1999b.

Chang, T. "Colloid-like behavior and topological phase transitions in space plasmas: intermittent low frequency turbulence in the auroral zone", *Physica Scripta*, T89: 80, 2001.

Chang, T., and C. C. Wu "Complexity and anomalous transport in space plasmas", *Phys. Plasmas*, 9: 3679, 2002.

Chang, T., C. C. Wu and V. Angelopoulos. "Preferential acceleration of coherent magnetic structures and bursty bulk flows in Earth's magnetotail", *Physica Scripta*, T98: 48, 2002.

Chang, T., S. W. Y. Tam, C. C. Wu and G. Consolini "Complexity, forced and/or self-organized criticality, and topological phase transitions in space plasmas", *Space Sci. Rev.*, 107: 425, 2003a.

Chang, T., S. W. Y. Tam, and C. C. Wu "Complexity induced anisotropic bimodal intermittent turbulence in space plasmas", submitted to *Phys. Plasmas*, 2003b.

Chapman, S. C., N. W. Watkins, R. O. Dendy, P. Helander and G. Rowlands "A simple avalanche model as an analogue for the magnetospheric activity", *Geophys. Res. Lett.*, 25: 2397, 1998.

Chapman, S. C., R. O. Dendy and G. Rowlands "A sandpile model with dual scaling regimes for laboratory, space, and astrophysical plasmas", *Phys. Plasmas*, 6: 4169, 1999.

Consolini, G., M. F. Marcucci and M. Candidi "Multifractal structure of auroral electrojet index data", *Phys. Rev. Lett.*, 76: 4082, 1996.

Consolini, G., "Sandpile cellular automata and the magnetospheric dynamics", In Aiello, S. et al., editors, *Cosmic Physics in the Year 2000, Proceedings of VIII GIFCO Conference*, pag. 123, SIF, Bologna, 1997.

Consolini, G. and P. De Michelis "Non-Gaussian distribution of AE-index fluctuations. Evidence for time intermittency", *Geophys. Res. Lett.*, 25: 4087, 1998.

Consolini, G. and A. T. Y. Lui "Sign-singularity analysis of current dsruption", *Geophys. Res. Lett.*, 26: 1673, 1999.

Consolini, G. and A. T. Y. Lui "Symmetry Breaking and Nonlinear Wave-Wave Interaction in Current disruption: Possible evidence for a phase Transition", In S. Ohtani et al., editors, *Magnetospheric Current Systems*. Geophysical Monograph, Vol. 118., pag. 395. AGU, Washington DC, 2000.

Consolini, G. and P. De Michelis "A revised forest-fire cellular automaton for the nonlinear dynamics of the Earth's magnetotail", *Jour. Atmos. Solar Terr. Phys.*, 63: 1371, 2001.

Consolini, G. and T. Chang "Magnetic field topology and criticality in geotail dynamics: relevance to substorm phenomena", *Space Sci. Rev.*, 95: 309, 2001.

Consolini, G. and T. Chang "Complexity, magnetic field topology, criticality, and metastability in magnetotail dynamics", *Jour. Atmos. Solar Terr. Phys.*, 64: 541, 2002.

Consolini, G. "Self-organized criticality: a new paradigm for the magnetotail dynamics", *Fractals*, 10: 275, 2002.

Deng, X. H. and H. Matsumoto "Rapid magnetic reconnection in the Earth's magnetosphere mediated by whistler waves", *Nature*, 410: 557, 2001.

Farge, M. "Wavelet transforms and their applications to turbulence", *Ann. Rev. Fluid Mech.*, 24: 395, 1992.

Freeman, M. P., N. W. Watkins and D. J. Riley "Evidence for a solar wind origin of the power law burst lifetime distribution of AE indices", *Geophys. Res. Lett.*, 27: 1087, 2000.

Klimas, A. J., D. V. Vassiliadis, D. N. Baker and D. A. Roberts. "The organized nonlinear dynamics of the magnetosphere", *Jour. Geophys. Res.*, 101: 13089, 1996.

Klimas, A. J., Valdivia J. A., D. V. Vassiliadis, D. N. Baker, M. Hesse and J. Takalo . "Self-organized criticality in the substorm phenomenon and its relation to localized reconnection in the magnetospheric plasma sheet", *Jour. Geophys. Res.*, 105: 18765, 2000.

Lui, A. T. Y., R. E. Lopez, S.M. Krimigis, R. W. McEntire, L. J. Zanetti and T. A. Potemra, "A case study of magnetotail current sheet disruption and diversion", *Geophys. Res. Lett.*, 15: 721, 1988.

Lui, A. T. Y. "A synthesis of magnetospheric substorm models", *Jour. Geophys. Res.*, 96: 1849, 1991.

Lui, A. T. Y. "Current disruption in the Earth's magnetosphere: observations and models", *Jour. Geophys. Res.*, 101: 13067, 1996.

Lui, A. T. Y. and A.-H. Najimi "Time-frequency decomposition of signals in a current disruption event", *Geophys. Res. Lett.*, 24: 3157, 1997.

Lui, A. T. Y., K. Liou, P. T. Newell, C. I. Meng, S.-I. Ohtani, T. Ogino, S. Kokubun, M. Brittnacher and G. K. Parks. "Plasma and magnetic flux transport associated with auroral breakups", *Geophys. Res. Lett.*, 25: 4059, 1998.

Lui, A. T. Y., K. Liou, M. Nosé, S.-I. Ohtani, D. J. Williams, T. Mukai, K. Tsuruda, and S. Kokubun. "Near-Earth Dipolarization: Evidence for a non-MHD Process", *Geophys. Res. Lett.*, 26: 2905, 1999.

Lui, A. T. Y. "Particle acceleration in disruption of the tail current sheet", *Phys. Chem. Earth*, 24C: 259, 1999.

Lui, A. T. Y., S. Chapman, K. Liou, P. T. Newell, C. I. Meng, M. Brittnacher and G. K. Parks. "Is the dynamic magnetosphere an avalanching system?", *Geophys. Res. Lett.*, 27: 911, 2000.

Lui, A. T. Y. "Multiscale phenomena in the near-Earth magnetosphere", *Jour. Atmos. Solar Terr. Phys.*, 64: 125, 2002.

Milovanov, A. V., L. M. Zelenyi, P. Veltri, G. Zimbardo and A. L. Taktakishvili. "Geometric description of the magnetic field and plasma coupling in the near-Earth stretched tail prior to a substorm", *Jour. Atmos. Solar Terr. Phys.*, 63: 705, 2001.

Nicolis, G. and I. Prigogine "Exploring Complexity. An Introduction", R. Piper GmbH & Co., Monaco, 1987.

Ohtani, S., T. Higuchi, A. T. Y. Lui, and K. Takahashi. "Magnetic fluctuations associated with tail current disruption: Fractal analysis", *Jour. Geophys. Res.*, 100: 19135, 1995.

Ohtani, S., K. Takahashi, T. Higuchi, A. T. Y. Lui, H. E. Spnce and J. F. Fennell. "AMPTE/CCE-SCATHA simultaneous observations of substorm-associated magnetic fluctuations", *Jour. Geophys. Res.*, 103: 4671, 1998.

Price, C. P. and D. E. Newman. "Using the R/S statistics to analyse AE data", *Jour. Atmos. Solar Terr. Phys.*, 63: 1387, 2001.

Roberts, D. A., D. N. Baker, A. J. Klimas and L. F. Bargatze. "Indications of low dimensionality in magnetospheric dynamics", *Geophys. Res. Lett.*, 18: 151, 1991.

Sethna, J. P., K. A. Dahmen and C. R. Myers. "Crackling noise", *Nature*, 410: 242, 2001.

Sharma, A. S., D. V. Vassiliadis, and K. Papadopoulos. *EOS, Trans. AGU*, 72: 402, 1991.

Sharma, A. S., "Assessing the magnetosphere's nonlinear behavior: its dimensional is low, its predictability is high", *Rev. Geophys.*, 33: 645, 1995.

Sharma, A. S., M. I. Sitnov and K. Papadopoulos. "Substorms as nonequilibrium transitions of the magnetosphere", *Jour. Atmos. Sol. Terr. Phys.*, 63: 1399, 2001.

Sitnov, M. I., A. S. Sharma, K. Papadopoulos, D. Vassiliadis, J. A. Valdivia, A. J. Klimas and D. N. Baker. "Phase transition-like behavior of the magnetosphere during substorms", *Jour. Geophys. Res.*, 105: 12955, 2000.

Sitnov, M. I., A. S. Sharma, K. Papadopoulos, and D. Vassiliadis. "Modeling substorm dynamics of the magnetosphere: from self-organization and self-organized criticality to non'equilibrium phase transitions", *Phys. Rev. E*, 65: 16116, 2001.

Takalo, J., J. Timonen, A. J. Klimas, J. Valdivia and D. V. Vassiliadis. "Nonlinear energy dissipation in a cellular automaton magnetotail field model", *Geophys. Res. Lett.*, 26: 1813, 1999.

Takalo, J., K. Mursula and J. Timonen "Role of the driver in the dynamics of a coupled-map model of the magnetotail: Does the magnetosphere act as a low-pass filter?", *Jour. Geophys. Res.*, 105: 27665, 2000.

Tam, S. W. Y., T. Chang, S. Chapman and N. W. Watkins. "Analytical determination of power-law index for the Chapman et al. sandpile (FSOC) analog for magnetospheric activity—a renormalization-group analysis", *Geophys. Res. Lett.*, 27: 1367, 2000.

Tetrault, D. "Turbulent relaxation of magnetic fields. 1. Coarse-grained dissipation and reconnection", *Jour. Geophys. Res.*, 97: 8631, 1992a.

Tetrault, D. "Turbulent relaxation of magnetic fields. 2. Self-organization and intermittency", *Jour. Geophys. Res.*, 97: 8541, 1992b.

Uritsky, V. M. and M. I. Pudovkin. "Low frequency $1/f$—like fluctuations of the AE-index as a possible manifestation of self-organized criticality in the magnetosphere", *Annals of Geophysics*, 16: 1580, 1998.

Uritsky, V. M. and A. J. Klimas, D. Vassiliadis, D. Chua and G. D. Parks. "Scale-free statistics of spatiotemporal auroral emissions as depicted by POLAR UVI images: The dynamic magnetosphere is an avalanching system", *Jour. Geophys. Res.*, 107: 1426, 2002.

Vassiliadis, D. V., A. S. Sharma, T. E. Eastman and K. Papadopoulos. "Low-dimensional chaos in magnetospheric activity from AE time series", *Geophys. Res. Lett.*, 17: 1841, 1990.

Wolfram, S. *A new kind of science*, Wolfram Media Inc., 2002.

Wu, C. C. and T. Chang. "2D MHD simulation of the emergence and merging of coherent structures", *Geophys. Res. Lett.*, 27: 863, 2000.

Wu, C. C. and T. Chang. "Further study of the dynamics of two-dimensional MHD coherent structures—a large scale simulation", *Jour. Atmos. Sol. Terr. Phys.*, 63: 1447, 2001.

Chapter 4

SIMULATION STUDY OF SOC DYNAMICS IN DRIVEN CURRENT-SHEET MODELS

Alex J. Klimas[1], Vadim M. Uritsky[2], Dimitris Vassiliadis[3] and Daniel N. Baker[4]

[1]*NASA Goddard Space Flight Center, Greenbelt, MD 20771 USA*

[2]*Institute of Physics, St. Petersburg State University, St. Petersburg 198504 Russia*

[3]*USRA, Goddard Space Flight Center, Greenbelt, MD 20771 USA*

[4]*LASP, University of Colorado, Boulder CO 80309 USA*

Abstract: Evidence is reviewed that suggests the presence self-organized critically dynamics in Earth's Magnetotail. It has been proposed that scale-free avalanching and spreading critical dynamics observed in auroral emissions are a reflection of these behaviors in the tail plasma sheet. Localized reconnection in the turbulent plasma sheet has been proposed as the local instability that collectively enables the avalanching process. A numerical simulation study of reconnection and magnetic field annihilation in driven current-sheet models is reviewed. Each of the models is composed of a resistive MHD component coupled to an idealized representation of an anomalous resistivity generating current-driven instability. Models in one- and two-dimensions are discussed. Behavior that indicates both models can evolve into self-organized criticality under steady driving is reviewed.

Key words: self-organized criticality, current-sheet, numerical simulation

1. Introduction

More than a decade ago, *Chang* [1992a; 1992b] suggested that the apparent low-dimensional dynamics of Earth's magnetosphere, a subject of considerable interest at the time (see [*Sharma*, 1995; *Klimas et al.*, 1996] and references therein), is possibly a manifestation of criticality in the magnetotail. Since then, numerous indications of critical dynamics in the magnetotail have been found [*Tsurutani et al.*, 1990; *Ohtani et al.*, 1995; *Consolini et al.*, 1996;

A.S. Sharma and P.K. Kaw (eds.), Nonequilibrium Phenomena in Plasmas, 71–90.
© 2005 *Springer. Printed in the Netherlands.*

Milovanov et al., 1996; *Borovsky et al.*, 1997; *Consolini and Marcucci*, 1997; *Consolini and De Michelis*, 1998; *Ohtani et al.*, 1998; *Uritsky and Pudovkin*, 1998; 1999a; *Angelopoulos et al.*, 1999b; *Consolini and Lui*, 1999; *Pavlos et al.*, 1999a; 1999b; *Lui et al.*, 2000; *Consolini and Chang*, 2001; *Uritsky et al.*, 2001b; 2002; 2003; *Vörös et al.*, 2003] and the concept of complexity in the tail plasma sheet [*Chang and Wu*, 2002; *Chang et al.*, 2002] has gradually grown in acceptance. At present, two theories of critical point dynamics in the magnetotail are being pursued, the first based on an assumption of first and second order phase transition-like behavior [*Sitnov et al.*, 2000; *Sitnov et al.*, 2002] and the second based on the assumption of forced (FSOC) [*Chang*, 1992a; *Chang*, 1999; *Chang et al.*, 2002] and/or self-organized criticality (SOC) [*Klimas et al.*, 2000a; 2000b; *Uritsky et al.*, 2001a; 2001c] in the tail. Both approaches have observational support but a reconciling relationship between them remains unknown. The theory of phase transition-like behavior is reviewed elsewhere in this volume, as is the work of Chang and coworkers. In this article, we review the recent work of *Uritsky et al.* [2002; 2003], which has provided perhaps the strongest evidence of SOC dynamics in the magnetotail, plus the attempts of *Klimas et al.* [2000b; 2003] and *Uritsky et al.* [2001a; 2001c] to model the magnetotail dynamics using numerical MHD+ (resistive MHD coupled to idealized resistivity-generating small-scale phenomena) simulations.

2. Evidence of SOC Dynamics in the Magnetotail

Uritsky et al. [2002], through a study of the evolution of bright nightside auroral emission regions in long sequences of Polar UVI images, have shown that the occurrence probabilities of several physical properties of the emission regions are governed by scale-free power-law distributions over remarkably large ranges of scales. More recently, *Uritsky et al.* [2003], using a superposed epoch analysis, have shown that the average spreading and decay rates of the emission regions exhibit signatures of critical dynamics. Taken together, these two results show that the UV auroral emission regions evolve statistically in exactly the same manner as avalanches in sand-pile models of self-organized criticality [*Bak et al.*, 1987; 1988; *Jensen*, 1998; *Sornette*, 2000]. The most straightforward and, at present, sole explanation for this result is SOC in the magnetotail plasma sheet. The well-established relationship of localized reconnection and associated fast flows in the plasma sheet to field-line mapped auroral emission supports this explanation [*Fairfield et al.*, 1999; *Lyons et al.*, 1999; *Zesta et al.*, 2000; *Ieda et al.*, 2001; *Nakamura et al.*, 2001a; 2001b]. It appears that the plasma sheet may contain a self-organized critical avalanching system with reconnection playing the role of the localized instability that collectively enables the avalanching process.

2.1 Polar UVI avalanche distributions

Extending a method introduced by *Lui et al.* [2000], *Uritsky et al.* [2002] have analyzed some statistical characteristics of the bright nightside auroral emissions observed by the UVI experiment on the Polar spacecraft during January and February of the years 1997 and 1998. A luminosity threshold was set well above the background noise level and each of the images was searched for contiguous emission regions that exceeded this threshold. Each of these bright spots was then tracked from its emergence to its demise and certain properties, such as lifetime, integrated luminosity, and integrated area, were tabulated. Only emission regions that were seen in two or more consecutive images were considered. In the cases of merging or splitting bright spots, rules that have been developed for the analysis of sandpile and cellular automaton models were applied. From these tabulated data, probability distributions were constructed.

Figure 1 shows the probability distributions that were found for integrated area and luminosity. These are typical results; probability distributions for other properties were constructed, sensitivity to the threshold level was ruled out, and the stability of these distributions under varying overall geomagnetic activity conditions was verified. In all cases, and for all emission region properties, no peaks or gaps that might be indicative of particular characteristic or dominant scales were found.

The broad range and stability of the scale-free power law distributions shown in Figure 1 are exceptional. It should be noted that the distributions are limited in range on the large event side by the dimensions and total brightness of the auroral region during substorm times and on the small event side by the pointing accuracy of the wobbling Polar spacecraft. There is no indication that these distributions would not continue to even smaller event sizes if the smaller emission regions could be resolved.

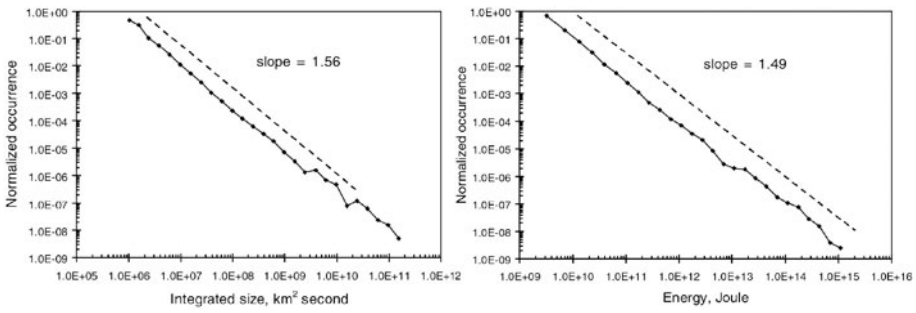


Figure 1. Normalized probability distributions for (left) size and (right) energy for combined data (taken from Uritsky et al. [2002]).

2.2 Polar UVI spreading dynamics analysis

Uritsky et al. [2003] have recently investigated the spreading dynamics of the bright nightside auroral emission regions defined in their earlier avalanche distribution analysis. A superposed epoch analysis was carried out to determine the averaged evolution of the emission regions following their emergence from the background. The average area of the superposed emission regions and the probability of an emission region to survive after any elapsed time were computed. For a broad class of spatially extended nonlinear systems these "spreading" and "survival" rates evolve as powers of time if the system is in the neighborhood of a critical point in its dynamics [*Munoz et al.*, 1999]. This superposed epoch method is considered a reliable method for finding such critical behavior. The exponents that define the power laws in time for the spreading and survival rates are called the spreading critical exponents.

Figure 2 shows the evolution with time of the spreading and survival of the UVI emission regions that *Uritsky et al.* [2003] found. Indeed, power-law evolution was found but the results were found to depend on the temporal resolution of the images and, in addition, the power-law evolution was found to fail for large times as evidenced by the breaks in the curves shown in Figure 2. Uritsky et al. were able to compute the dependence on temporal resolution and they were able, also, to show that the upper limits on the power-law evolution were due to a lack of events in the available data; the breaks in the curves of Figure 2 are at the one-count level in the data. In this way, Uritsky et al. were able to unify the results shown in Figure 2 and extrapolate them to the continuous time-resolution limit. They showed that, in this limit, the spreading critical exponents satisfy certain simple relationships to the avalanche distributions discussed in the preceding section, as expected for avalanching systems in SOC [*Munoz et al.*, 1999].

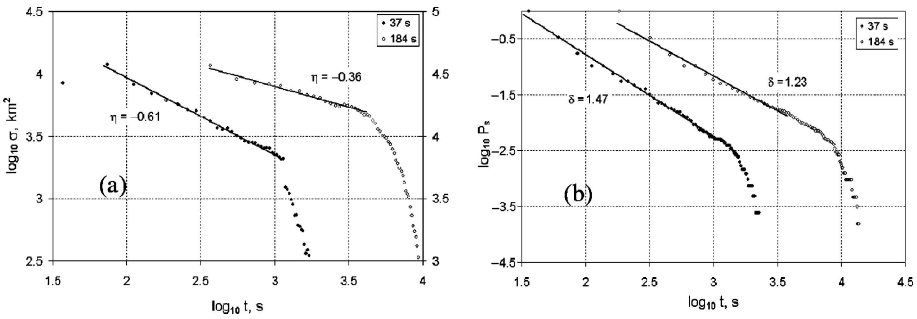


Figure 2. For 37 and 184 sec data, evolution of (a) average area and (b) survival probability for bright nightside UVI auroral emission regions. Taken from Uritsky et al. [2003].

2.3 Discussion

The avalanche distributions and the spreading dynamics results of *Uritsky et al*. [2002; 2003] show that the bright nightside auroral emission regions behave statistically as avalanches in numerical SOC models. A possible explanation for these results is that they are a reflection of a scale-free avalanching system in the plasma sheet. At present, we know of no other viable explanation. To confirm or refute this hypothesis, we feel that it will be necessary to examine the plasma sheet dynamics directly.

3. Driven Current-Sheet Models

A simulation study is in progress to guide a proposed *in situ* study of the plasma sheet dynamics. Driven 1-D and 2-D current-sheet models are under consideration at present. An important characteristic of these current-sheet models is strong coupling between resistive MHD phenomena at large scales and resistivity generating phenomena at small scales. This coupling is incorporated through the interaction of three components of the model: (1) a one- or two-dimensional resistive MHD component, (2) a simple equation for the growth and decay of anomalous resistivity, and (3) an idealized representation of a current-driven instability that, through its excitation and quenching, leads to the consequent growth or decay of the anomalous resistivity.

3.1 1-D driven current-sheet model

Lu [1995] has introduced a nonlinear diffusion model that he has shown exhibits some properties of numerical systems in SOC. The model is a continuum representation of a numerical sandpile model. In this section, we discuss a variant of this model, which is obtained through an extreme reduction of the resistive MHD system to one-dimension with resistivity that varies rapidly in space and time in accordance with the Lu model [*Klimas et al.*, 2000b]. This 1-D current-sheet model contains three components:

3.1.1 1-D resistive MHD. Assuming a magnetic field with only one vector component in the x direction, and with spatial dependence only in the orthogonal z direction, then

$$\frac{\partial B_x}{\partial t} = \frac{\partial}{\partial z}\left[D(z,t)\,\frac{\partial B_x}{\partial z}\right] + S(z,t) \tag{1}$$

in which $D(z, t)$ is the resistivity written as a diffusion coefficient and $S(z, t) = -\partial(V_z B_x)/\partial z$ governs the convection of the frozen-in magnetic field with the fluid velocity V_z.

3.1.2 Current-driven instability. Following *Lu* [1995], the anomalous resistivity in (1) is generated following the excitation of a current-driven instability. The current-driven instability is represented by

$$Q\,(|J|) = \begin{cases} D_{\min} & |J| < J_c \\ D_{\max} & |J| > \beta J_c \end{cases} \tag{2}$$

in which $J = \partial B_x/\partial z$. The instability is assumed excited and saturated instantaneously, and so enters the model as a simple switch that can take on two values, $D_{\min}$ and $D_{\max} \gg D_{\min}$. The notation on the right side of (2) indicates that Q takes on its high value when $|J|$ exceeds a critical value J_c, but it returns to its low value only when $|J|$ reduces to βJ_c with $\beta < 1$. This mechanism represents the known behavior of many plasma instabilities that are difficult to extinguish once excited [*Lu*, 1995]. In our numerical simulations, there is an independent Q switch at each grid site. The values of $D_{\min}$, $D_{\max}$, and J_c have not yet been related to the physics of the plasma sheet but studies of this relationship are in progress and will be reported in the future.

3.1.3 Anomalous resistivity. The evolution of the resistivity $D(z, t)$ is governed by

$$\frac{\partial D\,(z, t)}{\partial t} = \frac{Q\,(|J|) - D}{\tau} \tag{3}$$

This equation generates the growth of anomalous resistivity at any position where the current-driven instability has been excited, and the decay of the resistivity following the quenching of the instability. In effect, the growth or decay of the resistivity follows the excitation or quenching of the current driven instability, delayed by a time τ.

3.1.4 Closure. The system (1)–(3) is closed by assuming a form for $S(z, t)$ and treating it as a given source of magnetic flux, thereby decoupling (1) from the remainder of the MHD system. For this source, we have chosen $S(z, t) = S_0 \sin(\pi z/2L)$ on $-L \le z \le L$. Thus, we steadily load opposing flux with a reversal at $z = 0$. For boundary conditions, we choose $\partial B_x/\partial z = 0$ at $z = \pm L$ so that no magnetic flux can propagate out of the field reversal at the boundaries. The result is our 1-D current-sheet model. Under conditions of interest, its behavior consists of quiet loading intervals interspersed with intermittent unloading intervals during which the magnetic flux propagates in an extremely dynamic fashion toward the field reversal at $z = 0$ where it is annihilated.

It is important to note that, however idealized, this model includes cross-scale coupling between MHD and micro-turbulence and/or kinetic scales. In operation, this coupling is strong; it dominates the evolution of the model. It

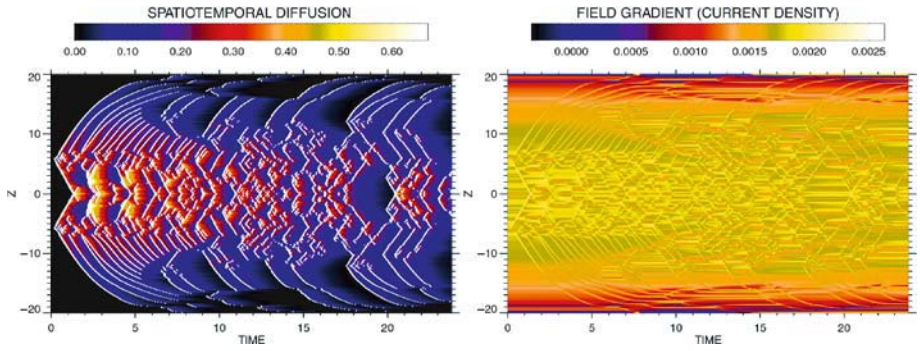


Figure 3. Details from the initial portion of an unloading event. Abscissa—time. Ordinate—position on simulation grid. (a) Color image shows evolution of resistivity with time. White dots show grid points on which current-driven instability is excited. (b) Current density in arbitrary units. Current-driven instability propagates via interacting waves leading to complex resistivity pattern. The instability propagates in association with an intense current layer that the instability generates. The current layer, in turn, maintains the instability. The wave is strongly nonlinear; most likely, no linear approximation to it exists.

is this strong coupling between disparate scales that leads to the multi-scale distributions demonstrated below. Those distributions are an essential element of the SOC dynamics of the model. Note also that this strong coupling is an important feature in the magnetotail dynamics. Reconnection at kinetic scales has a profound influence on the evolution of the tail on MHD and larger scales.

3.1.5 Selected results. Figure 3 illustrates our discovery of a new type of waveform that emerges as a result of the coupling between MHD and micro-scales. The current-driven instability propagates in waves generating resistivity in its wake. The mechanism for generating this waveform is explained in *Klimas et al.* [2000b]; very little else is known about its properties at this time.

We have been able to show that these waves lead to magnetic flux transport in a manner that produces scale-free avalanche distributions as in sandpile models when they are in self-organized criticality [*Uritsky et al.*, 2001c]. We analyzed the distributions of magnetic flux transport $-D(z, t)\partial B_x/\partial z$ in many unloading events such as that shown in Figure 3. A threshold was set for the magnitude of this quantity and contiguous regions in position and time where the threshold was exceeded were defined as avalanches. The size and duration of each of these avalanches was determined and the distributions of these quantities shown in Figure 4 were constructed. The distributions of avalanches, so defined, are scale free over the range of scales on which we have been

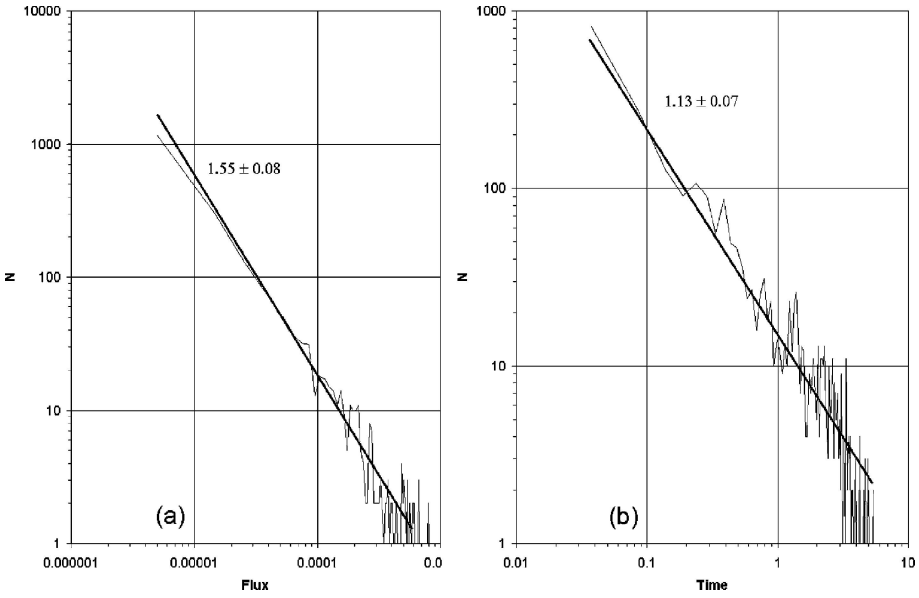


Figure 4. Scale-free size and duration distributions for "avalanches", as defined in the text.

able to construct them. This result provides an important contribution toward showing that the 1-D current-sheet model evolves into self-organized criticality and it provides a guiding principle for defining avalanches in the plasma sheet.

A sandpile model, as it approaches self-organized criticality, becomes extremely sensitive to small increments in its input; i.e., its "susceptibility" to the input grows large [Vespignani and Zapperi, 1998]. Through a numerical experiment consisting of a large number of long integrations of the 1-D current-sheet model we have been able to show that its susceptibility diverges in exactly the manner expected for a large class of sandpile models [Uritsky et al., 2001c]. This result is shown in Figure 5; it provides additional confirmation that the 1-D current-sheet model evolves into self-organized criticality. Further, this divergence is known to be a part of the process whereby the system becomes correlated over long spatial distances [Vespignani and Zapperi, 1998], a necessary behavior in the plasma sheet as the transition from isolated uncorrelated instability to global correlated instability takes place at substorm onset.

3.1.6 Summary. The 1-D current-sheet model is a large step away from sandpile models of the magnetospheric dynamics but, of course, it is only

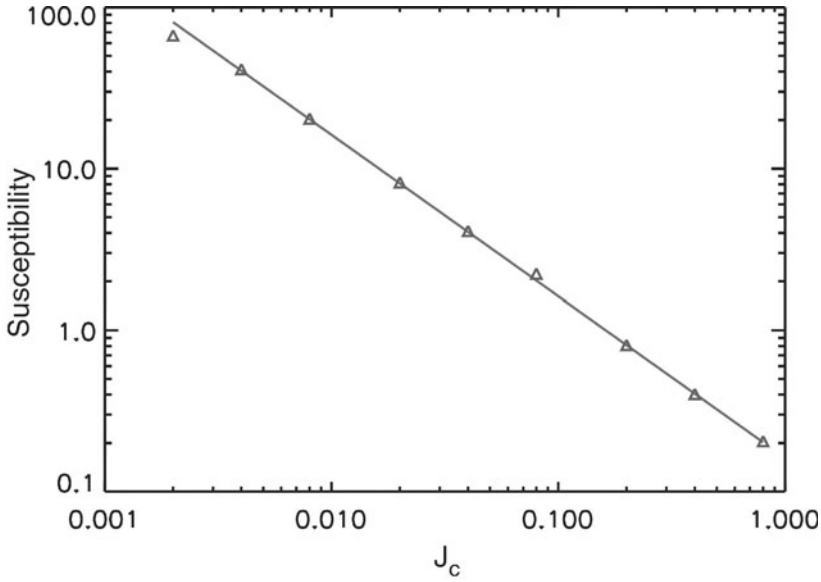


Figure 5. The divergence of the susceptibility of the 1-D current sheet model as the critical current is reduced. The divergence is given accurately as the inverse first power of the critical current, in agreement with theoretical expectations.

a small step toward a realistic model of the plasma sheet. Nevertheless, this simple model provides several important new concepts relevant to the plasma sheet: (1) A new waveform has been discovered that may be very important in the behavior of the plasma sheet at substorm onset; this point will be discussed further in the next section. (2) If the plasma sheet is in self-organized criticality, then there must be some feature in its behavior that plays the role of avalanches in sandpile models. Magnetic flux transport, following the excitation of the current-driven instability, plays this role in the 1-D current-sheet model. (3) The model susceptibility diverges as expected for systems in self-organized criticality. This divergence is related to the growth of correlated behavior over large spatial scales in sandpile models. The transition, in the plasma sheet, from isolated sporadic localized reconnection to global organized reconnection requires this growth of correlated behavior over large spatial scales.

3.2 2-D current-sheet model

The second model that we have constructed and studied is based on a 2-dimensional resistive MHD component.

3.2.1 2-D resistive MHD. The resistive MHD component of the 1-D model is replaced by the full MHD system

$$\frac{\partial \rho}{\partial t} + \nabla \cdot (\rho \mathbf{V}) = 0 \tag{4}$$

$$\frac{\partial \mathbf{V}}{\partial t} + (\mathbf{V} \cdot \nabla)\,\mathbf{V} = -\frac{1}{4\pi\rho}\nabla A\ (\Delta A) - \frac{\nabla P}{\rho} \tag{5}$$

$$\frac{\partial A}{\partial t} + (\mathbf{V} \cdot \nabla)\,A = D\Delta A \tag{6}$$

$$\left(\frac{1}{\gamma - 1}\right)\left[\frac{\partial P}{\partial t} + \mathbf{V} \cdot \nabla P\right] + \left(\frac{\gamma}{\gamma - 1}\right) P\,(\nabla \cdot \mathbf{V}) = \frac{1}{4\pi} D\,(\Delta A)^2 \tag{7}$$

in which $A(x, z, t)$ is the vector potential and $D(x, z, t)$ is the anomalous resistivity written as a diffusion coefficient. The second and third components of the 1-D model, the idealized current-driven instability and the resistivity component, remain unchanged except that they are defined on a 2-dimensional grid in this model and the current is given by $J = -\Delta A/\sqrt{8\pi}$.

3.2.2 Simulation configuration. To create a system that may evolve into self-organized criticality we must drive it through loading of a conserved quantity and it must be capable of unloading the conserved quantity. Further, we must drive the system long enough so that it can self-organize into a stationary state in response to the driver.

For both of our models, the conserved quantity is magnetic flux or energy. In the 1-D model unloading is due to magnetic field annihilation. Figure 6 illustrates the simulation configuration that we have chosen to extend that model to two dimensions. Plasma and reversed magnetic field are driven into the simulation region from above and below. The open boundary allows the plasma to exit the simulation region to the right. In this configuration, unloading is due to both annihilation and plasmoid release following reconnection.

3.2.3 Correlated localized reconnection. We have found that the instability waveform discovered in the 1-dimensional model survives the transition to the full MHD system in two dimensions. Further, we have found that this waveform provides a mechanism for localized reconnection sites to interact; a wave generated at one site may excite reconnection at another. This interaction is demonstrated briefly in this section.

Figure 7 shows the distributions of resistivity and current just after the excitation of an unloading event in the 2-D model. The behavior shown in this figure is analogous to that shown in Figure 1 at the very beginning of the unloading shown there. A pair of waves, in both the resistivity and the current, propagates

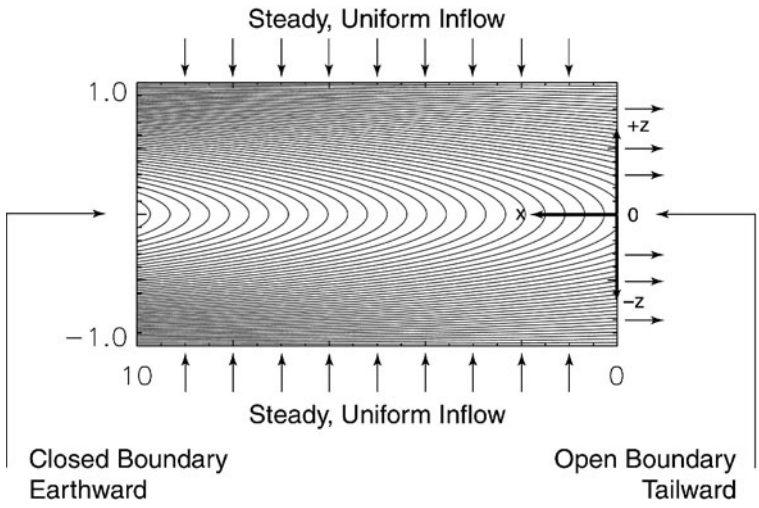


Figure 6. Simulation configuration for 2-D current sheet model.

away from a point at which the critical current has been exceeded. The high current had been supporting a bubble in the magnetic field surrounding an O-point. Consequently, localized reconnection splits the bubble into two bubbles, which move apart. In this case, localized reconnection at the position of the O-point produces a pair of instability waves that propagate away from the reconnection site. Later, these waves interact with the pre-existing irregular current distribution to produce more waves that also interact with the background current distribution, and with each other; the plasma evolution becomes complex, analogous to the behavior shown in the latter portion of Figure 3. To demonstrate an effect of these waves on the magnetic field topology, we have chosen to

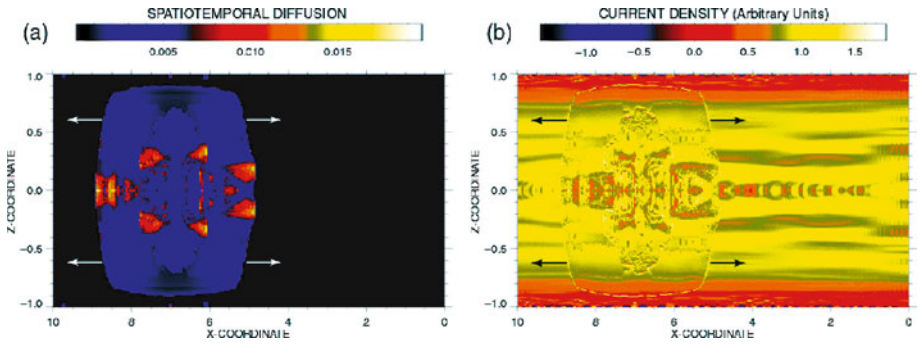


Figure 7. A pair of instability waves propagates away from a site of localized reconnection. (a) The resistivity distribution and (b) the current distribution that, otherwise, supports a reversal in the magnetic field.

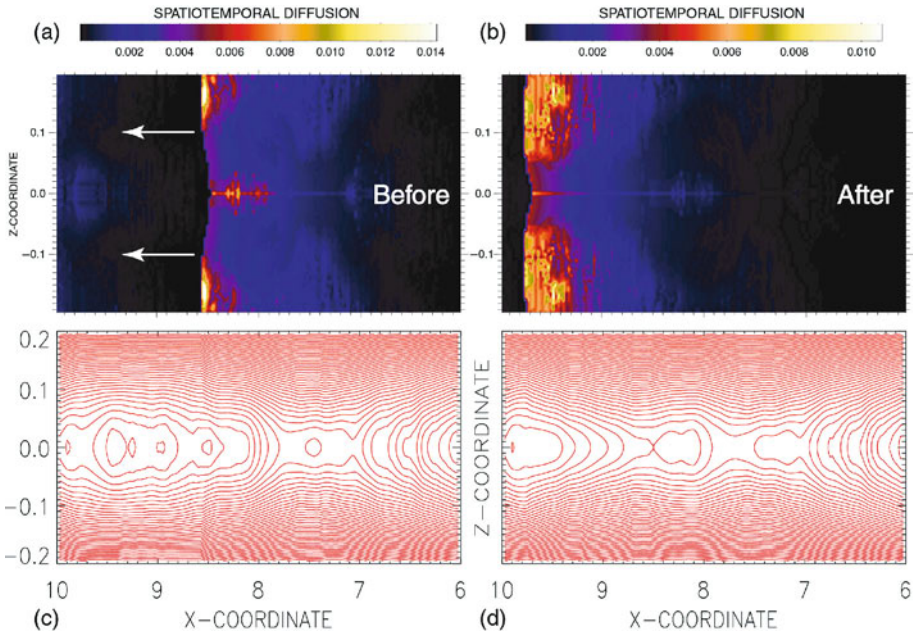


Figure 8. An instability wave (a) (b) propagates over a magnetic bubble (c) and splits it into two (d) through localized reconnection.

illustrate the very end of the unloading event when only a single decaying wave remains.

Figures 8a and 8b show the decaying wave in the resistivity at two instants very near the end of the unloading event. Figures 8c and 8d show the effects of this wave on the field topology. Notice that all of these figures have been zoomed in to a small portion of the full simulation grid shown in Figure 6. As the wave passes over a preexisting magnetic bubble, localized reconnection splits the bubble into two parts that then move apart. In this case, an instability wave produced earlier at a site of localized reconnection excites localized reconnection at a second site.

3.2.4 Avalanche distributions. Numerical SOC models exhibit scale-free distributions of certain avalanche measures. To construct these distributions, individual avalanches are followed from beginning to end and properties such as their duration, their total area, some measure of the size (for example, in a sandpile model, the number of grains involved in the avalanche), and others are tabulated. Occurrence distributions are constructed and usually normalized to produce probability distributions for the values of these tabulated properties. For models in SOC, all of these distributions have power-law forms containing no characteristic scales over a broad range of scales.

We have studied [*Klimas et al.*, 2003] the transport of the, predominantly magnetic, electromagnetic energy density via the Poynting flux (written here in terms of dimensional quantities for clarity)

$$\mathbf{S} = \frac{c}{4\pi}(\eta \mathbf{J} \times \mathbf{B}) + \frac{1}{4\pi} B^2 \mathbf{V}_\perp \tag{8}$$

in which η is the resistivity. We have restricted our attention to simulations containing a loading-unloading cycle in which reconnection and annihilation (unloading) occur in bursts that are distributed intermittently within otherwise quiet intervals during which the strengths of a magnetic field reversal and the current sheet supporting it are steadily driven upward (loading) by boundary conditions. In such simulations, we have found that the diffusive Poynting flux represented by the first term of (8) dominates over the convective Poynting flux represented by the second term during the unloading intervals and that both terms are negligibly small otherwise. We have examined the statistical properties of the diffusive transport of electromagnetic energy density during an unloading event. Our analysis followed exactly that of the POLAR UVI image data carried out by Uritsky et al. [2002].

We have constructed probability distributions for duration (not shown), size (integrated area), and energy (integrated Poynting flux magnitude) [*Klimas et al.*, 2003]. Figure 9 shows the probability distributions of sizes and energies, both for three threshold values. Except for the loss of larger events for the higher thresholds, the results are insensitive to threshold value over the range of values shown. The distributions are consistent with scale-free power-law distributions with slopes close to -1.5 over almost five decades in size or energy.

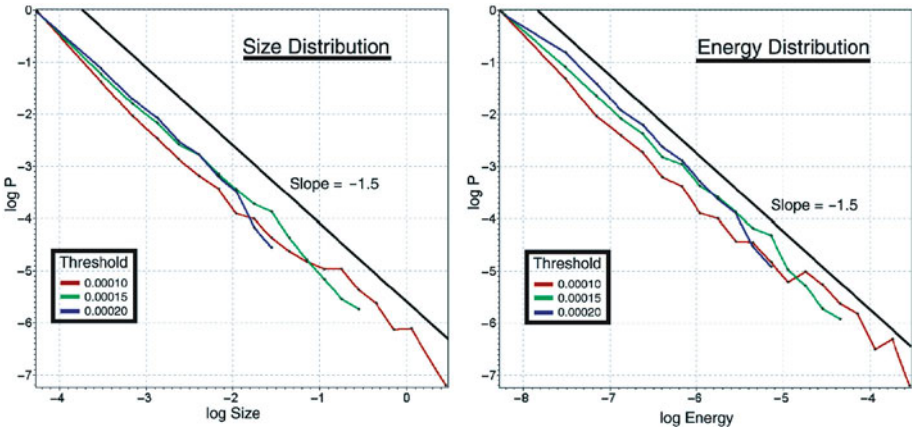


Figure 9. Size and energy probability distributions of regions in the evolving Poynting flux magnitude that exceed preset threshold values. The distributions have been constructed using three threshold values as indicated. (Taken from Klimas et al. [2003])

4. Discussion

At present, we feel that the only viable explanation of the POLAR UVI image analysis of *Uritsky et al.* [2002; 2003] is a scale-free avalanching system in Earth's magnetotail involving localized reconnection as the avalanche enabling local instability. We are convinced, however, that the true nature of this avalanching system will be revealed only through *in situ* observations of the tail. The intent of our simulation research is to provide preliminary guidance on which to base such observational studies. Our work is in a very early stage. We do not view our present models as valid representations of the magnetotail or its plasma sheet. The principal shortcomings of our most recent 2-D current-sheet model are (1) its two-dimensionality, and (2) its too general representation of some unspecified current-driven instability. Work is in progress to improve on these points; results will be reported later.

Systems in SOC govern the spatial transport of a conserved quantity (in the magnetotail, magnetic flux or energy) through the system to one or more boundaries where it is lost (field line merging in the current sheet, plasmoid release). At any position in the system, this transport is enabled through the excitation of a local threshold instability (localized reconnection); the transport must feed back to stabilize the local position and thus quench the instability. *Lu* [1995] has shown that is *impossible* to achieve scale-free avalanching in *any* continuum model of this process unless the transport in the model persists to below the local threshold of the enabling instability; i.e., the system must be "over stabilized" locally before the local transport is finally quenched. Lu suggested that the most natural way to produce this behavior would be to invoke, for the transport-enabling instability, the known property of many plasma instabilities that, having been excited, they persist until the state of the plasma is altered to somewhat below the threshold of the instability ($\beta < 1$ in (2)).

We recognize that the hysteretic instability ($\beta < 1$ in (2)) is not standard but we know of no concrete evidence against it. In addition, we reiterate, without this feature or some unknown equivalent, it would be impossible to produce scale-free avalanching in this, or any other continuum model of the plasma sheet [*Lu*, 1995]. It appears, however, that a scale-free avalanching process in the plasma sheet is the best explanation for the auroral emission scale-free distributions due to *Uritsky et al.* [2002] (see Figure 1). Thus, we have accepted the suggestion of Lu and have explored its consequences.

The hysteretic current-driven instability leads directly to the propagation of thin current sheets with intensities that fluctuate about the threshold level of the instability. Thus, these current sheets provide propagating locations for further excitation of the current-driven instability. Due to our assumption that the current-driven instability leads to the generation of anomalous resistivity when, and where, the instability is excited, these current sheets become a mechanism

for broadcasting resistivity away from an original locus of instability in the plasma. In our models, it is this mechanism that introduces the long-ranged correlated behavior that is normally associated with systems in SOC. The current sheets are most analogous to the avalanche fronts that are observed in discrete SOC models.

We have provided what we assert is conclusive evidence that the 1-D current-sheet model evolves into SOC when driven at an appropriate rate. Our assertion is based on the scale-free avalanching of magnetic flux that we have demonstrated plus the divergence of the susceptibility of the model as expected from the mean field theory of SOC due to *Vespignani and Zapperi* [1998]. An unusual property of this model, which we have not discussed in this article, is the reduced control parameter [*Uritsky et al.*, 2001c] that governs this divergence. An important consequence is that the scaling region of the model extends to large driving rates, in contrast to expectations for discrete SOC models.

The avalanche distributions shown in Figure 9 show that the transport of magnetic field energy into the central annihilation region of the 2-D current-sheet model is carried by an avalanching process that is scale-free over an exceptionally large range of scales. Further, these power-law distributions are quite similar to those found by *Uritsky et al.* [2002] in their analysis of the UVI auroral image data (see Figure 1). We have no explanation for this interesting result at present but, of course, we will investigate it in the future. Given (1) the insensitivity of the avalanche distributions to the threshold values used in their construction, (2) the large ranges of scales over which the distributions are scale-free, (3) the fact that at least three important quantities—duration (not shown), size, and energy—show these scale-free distributions, and (4) the appropriate setting within which the avalanching process operates, we conclude that the scale-free avalanche distributions provide strong evidence that the current-sheet model has evolved into SOC. An examination of the susceptibility of this model is in progress. Very early results are consistent with a divergence of the susceptibility as predicted by the mean field theory of SOC due to *Vespignani and Zapperi* [1998]. The results of this study will be presented in the future.

Acknowledgements

The authors wish to thank T. Chang, S. C. Chapman, D. Chua, G. Consolini, A. T. Y. Lui, G. Parks, A. S. Sharma, M. I. Sitnov, and N. Watkins for useful discussions. This research was supported in part by NASA grant 344-14-00-02.

References

Angelopoulos, V., F.S. Mozer, T. Mukai, K. Tsuruda, S. Kokubun, and T.J. Hughes, On the relationship between bursty flows, current disruption and substorms, Geophys. Res. Lett., 26 (18), 2841–2844, 1999a.

Angelopoulos, V., T. Mukai, and S. Kokubun, Evidence for intermittency in Earth's plasma sheet and implications for self-organized criticality, Phys. Plasmas, 6 (11), 4161–4168, 1999b.

Bak, P., C. Tang, and K. Wiesenfeld, Self-organized criticality: An explanation of 1/f noise, Phys. Rev. Lett., 59 (4), 381–384, 1987.

Bak, P., C. Tang, and K. Wiesenfeld, Self-organized criticality, Phys. Rev. A, 38 (1), 364–374, 1988.

Borovsky, J.E., R.C. Elphic, H.O. Funsten, and M.F. Thomsen, The Earth's plasma sheet as a laboratory for flow turbulence in high-beta MHD, J. Plasma Phys., 57, 1–34, 1997.

Chang, T., Low-Dimensional Behavior and Symmetry-Breaking of Stochastic-Systems Near Criticality—Can These Effects Be Observed in Space and in the Laboratory, Ieee Transactions On Plasma Science, 20 (6), 691–694, 1992a.

Chang, T., Path-Integrals, Differential Renormalization-Group, and Stochastic-Systems Near Criticality, International Journal of Engineering Science, 30 (10), 1401–1405, 1992b.

Chang, T., Self-organized criticality, multi-fractal spectra, sporadic localized reconnections and intermittent turbulence in the magnetotail, Phys. Plasmas, 6 (11), 4137–4145, 1999.

Chang, T., and C. Wu, "Complexity" and anomalous transport in space plasmas, Phys. Plasmas, 9 (9), 3679–3684, 2002.

Chang, T., C.C. Wu, and V. Angelopoulos, Preferential acceleration of coherent magnetic structures and bursty bulk flows in earth's magnetotail, Phys. Scr., T98, 48–51, 2002.

Consolini, G., M.F. Marcucci, and H. Candidi, Multifractal structure of auroral electrojet index data, Phys. Rev. Lett., 76 (21), 4082–4085, 1996.

Consolini, G., and M.F. Marcucci, Multifractal structure and intermittence in the AE index time series, Nuovo Cimento Della Societa Italiana Di Fisica C-Geophysics and Space Physics, 20 (6), 939–949, 1997.

Consolini, G., and P. De Michelis, Non-Gaussian distribution function of AE-index fluctuations: Evidence for time intermittency, Geophys. Res. Lett., 25 (21), 4087–4090, 1998.

Consolini, G., and A.T.Y. Lui, Sign-singularity analysis of current disruption, Geophys. Res. Lett., 26 (12), 1673–1676, 1999.

Consolini, G., and T.S. Chang, Magnetic field topology and criticality in geotail dynamics: Relevance to substorm phenomena, Space Sci. Rev., 95 (1–2), 309–321, 2001.

Fairfield, D.H., T. Mukai, M. Brittnacher, G.D. Reeves, S. Kokubun, G.K. Parks, T. Nagai, H. Matsumoto, K. Hashimoto, D.A. Gurnett, and T. Yamamoto, Earthward flow bursts in the inner magnetotail and their relation to auroral brightenings, AKR intensifications, geosynchronous

particle injections and magnetic activity, J. Geophys. Res., 104 (A1), 355–370, 1999.

Ieda, A., D.H. Fairfield, T. Mukai, Y. Saito, S. Kokubun, K. Liou, C.-I. Meng, G.K. Parks, and M.J. Brittnacher, Plasmoid ejection and auroral brightenings, Journal of Geophysical Research—Space Physics, 106 (A3), 3845–3857, 2001.

Jensen, H.J., Self-Organized Criticality: Emergent Complex Behaviour in Physical and Biological Systems, Cambridge University Press, Cambridge, UK, 1998.

Klimas, A.J., D. Vassiliadis, D.N. Baker, and D.A. Roberts, The organized nonlinear dynamics of the magnetosphere, J. Geophys. Res., 101 (A6), 13,089–13,113, 1996.

Klimas, A.J., V. Uritsky, J.A. Valdivia, D. Vassiliadis, and D.N. Baker, On the compatibility of the coherent substorm cycle with the complex plasma sheet, in International Conference on Substorms-5, edited by O. Troshichev, and V. Sergeev, pp. 165–168, ESA Publications Division, St. Petersburg, Russia, 2000a.

Klimas, A.J., J.A. Valdivia, D. Vassiliadis, D.N. Baker, M. Hesse, and J. Takalo, Self-organized criticality in the substorm phenomenon and its relation to localized reconnection in the magnetospheric plasma sheet, J. Geophys. Res., 105 (A8), 18,765–18,780, 2000b.

Klimas, A.J., V. Uritsky, D. Vassiliadis, and D.N. Baker, Reconnection and scale-free avalanching in a driven current-sheet model, J. Geophys. Res., in press, 2003.

Lu, E.T., Avalanches in continuum driven dissipative systems, Phys. Rev. Lett., 74 (13), 2511–2514, 1995.

Lui, A.T.Y., S.C. Chapman, K. Liou, P.T. Newell, C.I. Meng, M. Brittnacher, and G.D. Parks, Is the dynamic magnetosphere an avalanching system?, Geophys. Res. Lett., 27 (7), 911–914, 2000.

Lyons, L.R., T. Nagai, G.T. Blanchard, J.C. Samson, T. Yamamoto, T. Mukai, A. Nishida, and S. Kokubun, Association between Geotail plasma flows and auroral poleward boundary intensifications observed by CANOPUS photometers, J. Geophys. Res., 104 (A3), 4485–4500, 1999.

Milovanov, A.V., L.M. Zelenyi, and G. Zimbardo, Fractal structures and power law spectra in the distant Earth's magnetotail, J. Geophys. Res., 101 (A9), 19,903–19,910, 1996.

Munoz, M.A., R. Dickman, A. Vespignani, and S. Zapperi, Avalanche and spreading exponents in systems with absorbing states, Phys. Rev. E, 59 (5), 6175–6179, 1999.

Nakamura, R., W. Baumjohann, M. Brittnacher, V.A. Sergeev, M. Kubyshkina, T. Mukai, and K. Liou, Flow bursts and auroral activations: Onset timing and foot point location, J. Geophys. Res., 106 (A6), 10777–10789, 2001a.

Nakamura, R., W. Baumjohann, R. Schodel, M. Brittnacher, V.A. Sergeev, M. Kubyshkina, T. Mukai, and K. Liou, Earthward flow bursts, auroral streamers, and small expansions, J. Geophys. Res., 106 (A6), 10791–10802, 2001b.

Ohtani, S., T. Higuchi, A.T.Y. Lui, and K. Takahashi, Magnetic fluctuations associated with tail current disruption: Fractal analysis, J. Geophys. Res., 100 (A10), 19,135–19,145, 1995.

Ohtani, S., K. Takahashi, T. Higuchi, A.T.Y. Lui, H.E. Spence, and J.F. Fennell, AMPTE/CCE-SCATHA simultaneous observations of substorm-associated magnetic fluctuations, J. Geophys. Res., 103 (A3), 4671–4682, 1998.

Pavlos, G.P., M.A. Athanasiu, D. Kugiumtzis, N. Hatzigeorgiu, A.G. Rigas, and E.T. Sarris, Nonlinear analysis of magnetospheric data Part I. Geometric characteristics of the AE index time series and comparison with nonlinear surrogate data, Nonlinear Process Geophys., 6 (1), 51–65, 1999a.

Pavlos, G.P., D. Kugiumtzis, M.A. Athanasiu, N. Hatzigeorgiu, D. Diamantidis, and E.T. Sarris, Nonlinear analysis of magnetospheric data Part II. Dynamical characteristics of the AE index time series and comparison with nonlinear surrogate data, Nonlinear Process Geophys., 6 (2), 79–98, 1999b.

Sharma, A.S., Assessing the Magnetospheres Nonlinear Behavior—Its Dimension is Low, Its Predictability, Rev. Geophys., 33, 645–650, 1995.

Sitnov, M.I., A.S. Sharma, K. Papadopoulos, D. Vassiliadis, J.A. Valdivia, A.J. Klimas, and D.N. Baker, Phase transition-like behavior of the magnetosphere during substorms, J. Geophys. Res., 105 (A6), 12955–12974, 2000.

Sitnov, M.I., A.S. Sharma, K. Papadopoulis, and D. Vassiliadis, Modeling substorm dynamics of the magnetosphere: From self-organization and self-organized criticality to nonequilibrium phase transitions, Phys. Rev. E, 65 (1), 16116, 2002.

Sornette, D., Critical Phenomena in Natural Sciences. Chaos, Fractals, Self-Organization and Disorder: Concepts and Tools, Springer, Berlin, Germany, 2000.

Tsurutani, B.T., M. Sugiura, T. Iyemori, B.E. Goldstein, W.D. Gonzalez, S.I. Akasofu, and E.J. Smith, The nonlinear response of AE to the IMF Bs Driver: A spectral break at 5 hours, Geophys. Res. Lett., 17 (3), 279–282, 1990.

Uritsky, V., A.J. Klimas, and D. Vassiliadis, Evaluation of spreading critical exponents from the spatiotemporal evolution of emission regions in the nighttime aurora, Geophys. Res. Lett., 30 (15), art. no.-1813, 2003.

Uritsky, V.M., and M.I. Pudovkin, Low frequency 1/f-like fluctuations of the AE-index as a possible manifestation of self-organized criticality in the magnetosphere, Ann. Geophys., 16 (12), 1580–1588, 1998.

Uritsky, V.M., A.J. Klimas, J.A. Valdivia, D. Vassiliadis, and D.N. Baker, Stable critical behavior and fast field annihilation in a magnetic field reversal model, J. Atmos. Sol-Terr. Phy., 63 (13), 1425–1433, 2001a.

Uritsky, V.M., A.J. Klimas, and D. Vassiliadis, Comparative study of dynamical critical scaling in the auroral electrojet index versus solar wind fluctuations, Geophys. Res. Lett., 28 (19), 3809–3812, 2001b.

Uritsky, V.M., A.J. Klimas, and D. Vassiliadis, Multiscale dynamics and robust critical scaling in a continuum current sheet model, Physical Review E, 65 (4), 046113, 2001c.

Uritsky, V.M., A.J. Klimas, D. Vassiliadis, D. Chua, and G.D. Parks, Scale-free statistics of spatiotemporal auroral emissions as depicted by POLAR UVI images: The dynamic magnetosphere is an avalanching system, J. Geophys. Res., 107 (A12), 1426, 2002.

Vespignani, A., and S. Zapperi, How self-organized criticality works: A unified mean-field picture, Phys. Rev. E, 57 (6), 6345–6362, 1998.

Vörös, Z., W. Baumjohann, R. Nakamura, A. Runov, T.L. Zhang, M. Volwerk, H.U. Eichelberger, A. Balogh, T.S. Horbury, K.-H. Glaßmeier, B. Klecker, and H. Rème, Multi-scale magnetic field intermittence in the plasma sheet, Ann. Geophys., in press, 2003.

Zesta, E., L.R. Lyons, and E. Donovan, The auroral signature of Earthward flow bursts observed in the Magnetotail, Geophys. Res. Lett., 27 (20), 3241–3244, 2000.

Chapter 5

TWO STATE TRANSITION MODEL OF THE MAGNETOSPHERE

T. Tanaka

Faculty of earth and planetary sciences, Graduate school of sciences, Kyushu University, Fukuoka 812-8581, Japan

Abstract: The substorm onset as a state transition is investigated from a resistive magnetohydrodynamic (MHD) simulation. The simulation uses the finite volume total-variation diminishing (TVD) scheme on an unstructured grid system to evaluate the magnetosphere-ionosphere (M-I) coupling effect more precisely and to reduce the numerical viscosity in the near-earth plasma sheet. The calculation started from a stationary solution under a northward interplanetary magnetic field (IMF) condition with non-zero IMF B_y. After a southward turning of the IMF, the simulation results show the progress of plasma sheet thinning in the magnetosphere. This thinning is promoted by the drain of closed flux from the plasma sheet occurring under the enhanced convection. In this stage, the reclosure process of open field lines in the plasma sheet, which determines the flux piling up from the midtail to the near-earth plasma sheet, is not so effective, since it is still controlled by the remnant of northward IMF. The substorm onset occurs as an abrupt change of pressure distribution in the near-earth plasma sheet and an intrusion of convection flow into the inner magnetosphere. After the onset, the simulation results reproduce both the dipolarization in the near-earth tail and the near-earth neutral line (NENL) at the midtail, together with plasma injection into the inner magnetosphere and an enhancement of the nightside field-aligned current (FAC). During the dipolarization process, the magnetosphere changes from the force balance in the z direction to the configuration of force balance in the x direction. Thus, the dipolarization is not a mere pile up of the flux ejected from the NENL Associated with the establishment of force balance in the x direction, the pressure inside -10 Re peaks to self-adjust the restored magnetic tension. It is concluded that the direct cause of these onset processes is the state (phase-space) transition of the convection system from a thinned state to a dipolarized state associated with a self-organizing criticality.

Key words: substorm, state transition, convection

A.S. Sharma and P.K. Kaw (eds.), Nonequilibrium Phenomena in Plasmas, 91–116.
© 2005 *Springer. Printed in the Netherlands.*

1. Introduction

The confinement of the Earth's magnetic field by the dynamic pressure from the solar wind acting from one side is the primary reason for the formation of the comet-shaped magnetosphere. These foundations of the magnetospheric formation were established by Chapman and Ferraro (1931). In ideal magnetohydrodynamic (MHD) processes under the frozen-in principle, the solar wind plasma and magnetospheric plasma (if present) would not mix, resulting in a quiet magnetosphere. In the real situation, however, the solar wind plasma penetrates into the magnetosphere through non-ideal MHD processes such as reconnection and magnetopause instability, filling the magnetosphere with plasma. Associated with this plasma penetration, energy and momentum also flow into the magnetosphere to induce a large scale plasma motion involving the ionospheric plasma as well. This convection process becomes the most fundamental mechanism in transferring the free energy of disturbances in the magnetosphere-ionosphere (M-I) system.

One of the most important problems in the physics of the earth's magnetosphere concerns the cause-effect relationship which controls the substorm process. The concept of substorm was first introduced by Akasofu (1964). When the interplanetary magnetic field (IMF) is southward for about 1 hour, three phases of the substorm can be identified: the growth phase, the expansion phase, and the recovery phase. A northward-to-southward turning of the IMF enhances dayside reconnection due to its antiparallel-merging characteristic. Observations have revealed that the progress of magnetospheric convection accompanies a thinning of the plasma sheet and enhanced two-cell convection in the ionosphere with a gradual increase of current intensity in tail current, field-aligned currents (FACs), and ionospheric currents. This enhanced convection in the M-I system represents well-known features of the growth phase (Baker et al., 1996).

The expansion phase starts with a sudden brightening of the equatorward-most pre-onset arc, accompanied by an enhancement of electrojet activities. After the initial brightening, the region of intensified aurora moves poleward and westward (Akasofu, 1964; Elphinstone et al., 1996). In the near-earth plasma sheet where the ground onset position is mapped back, the expansion onset is signified by the dipolarization of the tail field (Lopez and Lui, 1990; Lui, 1996). The dipolarization accompanies the plasma injection into the inner magnetosphere, the current disruption (CD), and the formation of the current wedge. When a spacecraft is located in the near-earth tail during the dipolarization, a high level of magnetic-field fluctuation is observed that is associated with the CD events (Takahashi et al., 1987; Ohtani et al., 1998). In the middle tail, fast tailward plasma flows threaded by the southward magnetic field are often observed beyond 20–25 Re (Nagai et al., 1994). These observations suggest the

tail reconnection located at 20–25 Re. Flows in the near-earth region between 9 and 19 Re are observed as a form of bursty bulk flow (BBF) indicating that the tail reconnection is patchy-bursty (Baumjohann et al., 1990; Angelopoulos, et al., 1992).

This paper tries to seek the answer to the substorm mechanism by investigating the development of the magnetospheric convection that is inevitable during conditions of southward IMF. As shown in Tanaka (2003b), the magnetospheric convection is the basic process for the generation of disturbance phenomena in the earth's magnetosphere. It represents a process in which plasma and magnetic field in the magnetosphere and the ionosphere realize a quasi-circular motion without a considerable accumulation at all altitudes, by recognizing their relative motion through the exchange of the FAC. More basically, it is the fundamental process to generate almost all free energies for disturbance phenomena occurring in the M-I system. Analyzing the development of convection, this paper gives new interpretations for two key features of the substorm, namely the plasma sheet thinning during the growth phase and the dipolarization associated with the expansion phase. The most important question addressed in this paper is "What is responsible for the discontinuous behavior of the M-I system that characterizes the substorm onset". The magnetic disturbance is not called as substorm if it starts gradually (Yahnin et al., 1994; Sergeev et al., 1996).

2. MHD Model

The physics of convection depends on the topologies specific to the M-I system (Tanaka, 2003b). Almost all analytic models cannot be completed to treat the exact topology of the M-I system. A crucial method that can overcome this difficulty is the recent solar wind-magnetosphere-ionosphere (S-M-I) interaction model by the three-dimensional (3-D) MHD simulations coupled with a model ionosphere (Ogino et al., 1986; Tanaka, 1994, 1995, 1999, 2000a, 2000b, 2001, 2003a, 2003b; Crooker et al., 1998; Fedder et al., 1998; Siscoe et al., 2000). Recent MHD simulations have reproduced the ionospheric and magnetospheric closure processes of FAC simultaneously (Tanaka, 1995, 2003b), and revealed the relationship between convection and FAC, which has advanced our understanding of the interactions between plasma structure, current system, and convection. It is actually proved from MHD models that the magnetospheric and ionospheric convections construct a coupling system regulated by the exchange of FAC. In these studies, the clarification of 3-D structure of the FAC was the first step to investigate the mechanical structure of global convection in the M-I coupling regime (Tanaka, 1995). For the generation of FAC in a realistic magnetosphere and the projection of convection onto the ionosphere, MHD simulations provide a powerful tool.

However, application of MHD simulation had not been so straightforward because the magnetosphere and the ionosphere exhibit large differences in their characteristics. Three major difficulties arise in the numerical calculation of MHD when adapted to the S-M-I coupling simulation. The first difficulty comes from the situation that the respective sizes of the magnetosphere and the ionosphere are extremely different. To overcome this difficulty and to numerically project the convection onto the ionosphere, MHD simulations using unstructured grids are being studied (Tanaka, 1995; Fedder et al., 1998; Siscoe et al., 2000; Gombosi et al., 2000).

A wide range in the magnitude of magnetic field causes the second difficulty. The magnitude of the dipole magnetic field is about 30,000 nT in the ionosphere near the earth, while it diminishes rapidly in the magnetosphere to about 10 nT. Therefore, the ratio of variable to intrinsic components of the magnetic field becomes extremely small in the ionosphere. In order to avoid this difficulty, the MHD equations are reconstructed by dividing $\mathbf{B}$ as $\mathbf{B} = \mathbf{B}_0 + \mathbf{B}_1$, where $\mathbf{B}_0$ and $\mathbf{B}_1$ are known intrinsic and unknown variable components, respectively (Tanaka, 1994). In the S-M-I interaction problem, $\mathbf{B}_0$ adopts a dipole field.

The third difficulty concerns non-ideal MHD effects and numerical resistivity imbedded in the scheme (Gombosi et al., 2000). In the MHD regime, non-ideal MHD effects are considered through the transport coefficients. In almost all MHD models, however, the distribution of transport coefficients is left to the hand of the numerical dissipation. In this paper, high resolution schemes such as the total-variation diminishing (TVD) scheme are used to reduce background numerical resistivity. Then, actual resistivity is controlled by a given model (Tanaka, 2000b) so as to increase as it goes further downtail. It was shown by Tanaka (2000b) that this kind of resistivity model induces a reconnection that generates a realistic substorm solution.

The TVD scheme is also effective to resolve shocks and discontinuities which appear commonly in the space plasma (Tanaka, 1993, 1998b; Tanaka and Murawski, 1997; Tanaka and Washimi, 1999, 2002). It was shown by Tanaka (1994) that the TVD scheme can be organized even for the reconstructed equations treating $\mathbf{B}_1$. By adopting this method, Tanaka (1995) first reproduced the FAC numerically and reconstructed the 3-D structure of the FAC system. This success was the first step to discuss the self-consistent configuration of the M-I convection system. The following part of this paper will mainly focus on the self-consistent picture of convection system obtained from these MHD simulations employing unstructured grids and reconstructed equations. In the presentation of simulation results in this paper, the x axis is pointing toward the sun, the y axis is pointing toward the opposite direction of the earth's orbital motion, and the z axis is pointing toward the north.

In the MHD simulation, the Ohm's law acts as an inner boundary condition. Ionospheric conductance is determined as a sum of sunlight-induced part that

is calculated as a function of solar zenith angle and auroral-particle-induced part that is given as a function of pressure, temperature and FAC projected from the inner boundary along the magnetic field lines (Tanaka, 2000b). In the inner boundary, the number of fixed variables must coincide with the number of characteristic lines that are directed toward the calculation domain. The Ohm's law fixes two velocity components through the determination of potential. Up to three more variables are fixed in the inner boundary; radial component of the magnetic field, density, and pressure. However, this number depends on the flow direction in the inner boundary (depends on the polar wind case or precipitation case). If the flow at inner boundary is inward (precipitation case), density and pressure are determined by the projection of variables from the upper region. These processes must be constructed along the principle of characteristic line for hyperbolic equation.

3. Features of Numerically Reproduced Substorm

In reproducing the substorm by MHD simulations, careful considerations must be given for the choice of initial condition, since the initial state for the substorm simulation must be a stationary state for quiet magnetosphere. The most general configuration that satisfies these conditions may be the magnetospheric configuration shown by Tanaka (1999) (under northward IMF condition with nonzero IMF B_y). Starting from this solution and changing the IMF input from northward to southward, observed sequence of substorm presented above were numerically reproduced as shown in Figures 1 and 2. Figure 1 shows a sequence of simulated pressure distributions (normalized by the solar wind pressure P_{sw}) in the meridional plane of the magnetosphere. The temporal development of the tail configuration after a southward turning of the IMF can be observed from this figure. Figure 2 shows similar results for $-V_x$($-x$ velocity) distributions (normalized by the solar wind sound velocity C_s). Figure 3 shows ionospheric signatures (FAC and ionospheric conductivity) during the simulated substorm.

The first panel of Figure 1 at $t = 7.7$ minute illustrates the magnetospheric configuration soon after an IMF southward turning. At this time, a thick and low-pressure plasma sheet is still observed without a noticeable effect of the southward IMF. The flow structure in the first panel of Figure 2 indicates that the x line is situated beyond $x = -60$ Re shortly after the southward turning of the IMF. This structure, which is generally called the distant neutral line, is a continuation of the tail structure under the northward IMF condition shown in Tanaka (1999). At this time, sunward flow in the plasma sheet is still fairly slow. In the first panel of Figure 2, fast tailward flows seen on the magnetopause beyond $x = -32$ Re toward the tail are generated by the tension of disconnected field lines associated with the lobe-cell circulation.

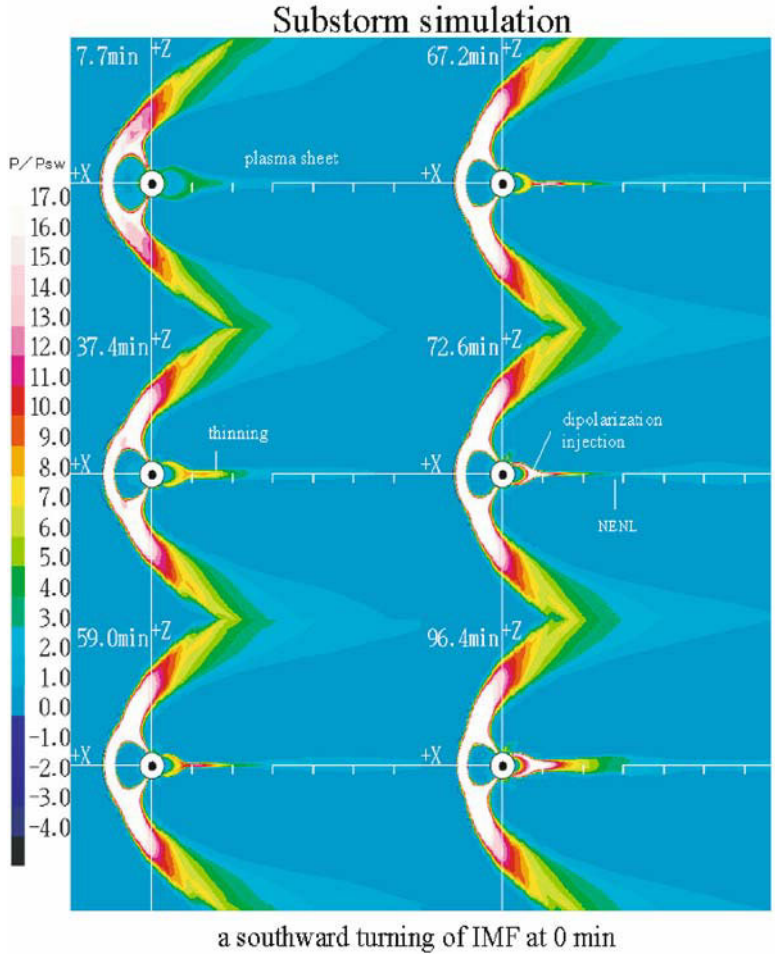


Figure 1. A sequence of simulated pressure (P) distribution in the meridian plane of the magnetosphere. The pressure values are normalized by the solar wind pressure (P_{sw}). The size of the earth is shown by black spheres. Marks on the $-x$ axis are 10 Re apart. Time is measured after the southward turning of the IMF. Thinning and dipolarization sequence is observable in this figure.

In Figures 1 and 2, the thinning of the near-earth plasma sheet (growth phase) develops continuously until the 3-rd panel at $t = 59.0$ minute. As thinning proceeds, earthward flow increases its speed in the near-earth tail. During this interval, the blue area in the dayside magnetosphere seen in Figure 1 tends to shrink slightly and the flaring angle of the tail lobe tends to increase considerably, due to an erosion effect. In the growth phase (the 2-nd and 3-rd panels of Figure 1), the pressure maximum in the plasma sheet exists around $x = -12$ Re.

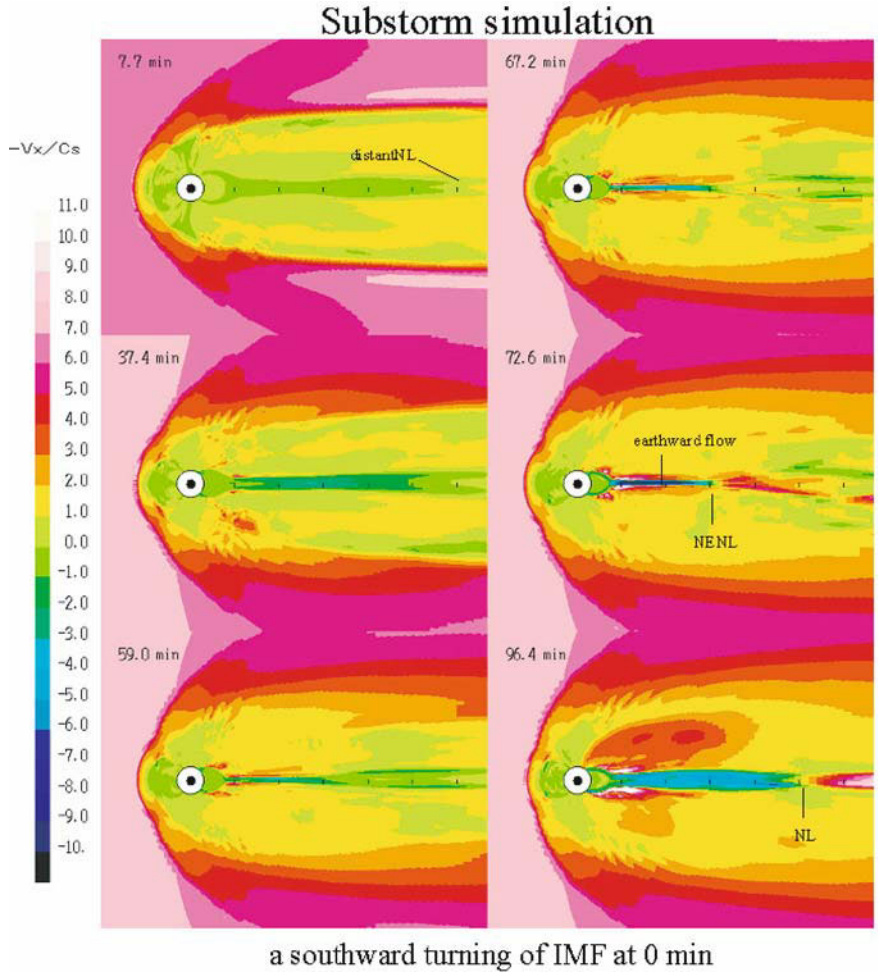


Figure 2. A sequence of simulated velocity ($-V_x$) distribution in the meridian plane of the magnetosphere. The velocity values are normalized by the solar wind sound velocity (C_s). The size of the earth is shown by black spheres. Marks on the $-x$ axis are 10 Re apart. Time is measured after the southward turning of the IMF. Neutral line position shifts from distant to near-earth tail.

The x dependence of the pressure profile in the plasma sheet inside $x = -20$ Re does not change severely between the 2-nd and 3-rd panels of Figure 1, even though the absolute value increases according to the development of thinning.

After the 3-rd panels of Figures 1 and 2, some qualitative changes occur in the tail configuration. At first, a remarkable tailward flow appears in the midtail at $t = 61.8$ minute. While the flow inside $x = -60$ Re is earthward throughout

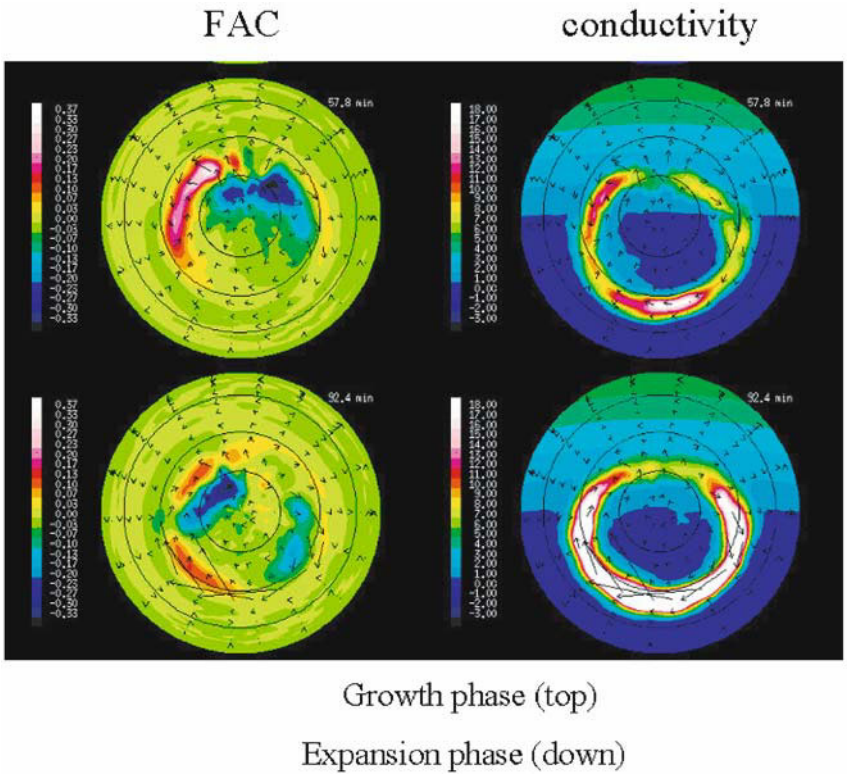


Figure 3. Distributions of FAC and ionospheric Pedersen conductivity during the growth phase (top) and expansion phase (bottom). Three circles show 60°, 70°, and 80° northern latitudes. Units for FAC and conductivity are $\mu A/m^{-2}$ and mho, respectively. For the FAC, plus sign corresponds to upward current and minus sign corresponds to downward current. After the onset, the peak position of region 1 FAC moves to nightside.

the growth phase as shown in Figure 2, flow around $x = -39$ Re changes tailward at this time ($t = 61.8$ minute). Associated with this tailward flow, negative B_z appears around $x = -34$ Re showing the reconnection in the plasma sheet. The next change is a start of the dipolarization. To show the thinning and dipolarization sequence, the solid curve in the lower panel of Figure 4 illustrates the development of the B_z component at $x = -6.6$ Re in the midnight equatorial plane (at the midnight geosynchronous orbit). A noticeable thinning starts after about 10 minutes from a southward turning of the IMF. As shown in Figure 4, the B_z component at the midnight geosynchronous orbit decreases continuously during the growth phase. This growth-phase signature continues for about 50 minutes until a dipolarization which starts at $t =$ 67.2 minute. After $t = 67.2$ minute, decreasing tendency of B_z at the midnight geosynchronous orbit changes to increasing. We define the onset by the start

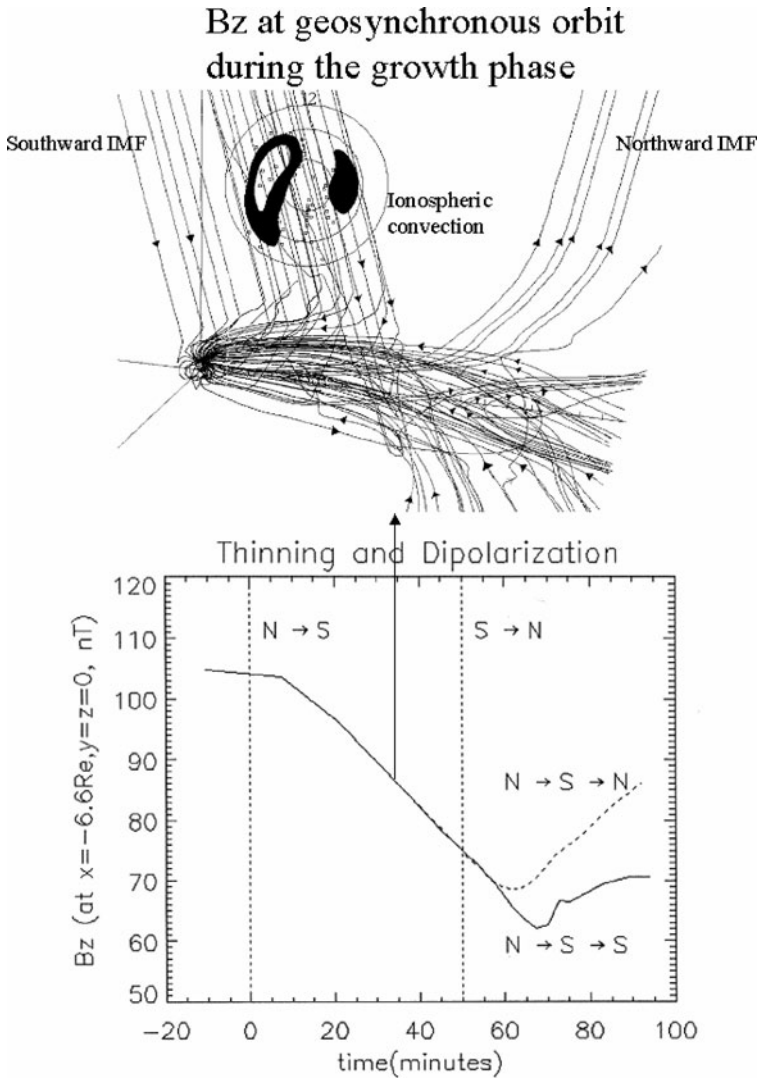


Figure 4. Magnetic configuration during the growth phase (upper) and development of B_z at the midnight geosynchronous orbit showing the thinning and dipolarization process (lower). The upper inset in the upper panel shows the ionospheric convection. It is seen in this inset that the two-cell convection is developed to a certain extent.

time of the B_z increase at the midnight geosynchronous orbit at $t = 67.2$ minute. Under a continuously southward IMF, dipolarization tends to saturate after 10 minutes. In the lower panel of Figure 4, dashed curve shows the case of northward re-turning of IMF at $t = 50.0$ minutes. In this case, dipolarization continues without saturation and, in addition, the onset time becomes earlier

indicating the substorm triggering by a northward turning of the IMF. The dipolarization is hastened 5 minutes compared with the steady southward IMF case. A northward re-turning of the IMF results in the deceleration of the ionospheric convection. The result in Figure 4 indicates that the ionosphere controls the substorm onset occurring in the M-I convection system under a dynamic balance (Tanaka, 2000b).

The 4-th panel of Figure 1 at $t = 67.2$ minute shows the pressure distribution at the onset. At this time, the pressure peek in the plasma sheet is shifting to the region inside $x = -10$ Re. In the next panel at $t = 72.6$ minute, the pressure peak appears at $x = -8$ Re and remains there afterward. In this way, the position of the peak plasma pressure shifts from $x = -12$ to $x = -8$ Re in less than 6 minutes. These variations show the signature of the dipolarization and injection occurring in the inner magnetosphere. From the development of the plasma sheet configuration in Figure 1, a plasmoid formation is observed after the onset, with the near-earth neutral line (NENL) formed around $x = -30$ Re. The 4-th panel of Figure 2 shows that before the onset the neutral line moves to the near-earth region around $x = -32$ Re. During the expansion phase, this NENL persists in the midtail, generating fast earthward flows inside (earthward of) $x = -32$ Re and tailward flows outside.

Figure 3 shows ionospheric distributions of FAC and Pedersen conductivity during the growth phase (top) and expansion phase (bottom). In the simulation of this paper Hall conductivity is set two times of the Pedersen conductivity. For the FAC, plus sign corresponds to upward current. During the growth phase region 1 FAC is mainly distributed in the dayside. After onset, on the contrary, the peak position of region 1 FAC moves to nightside. These features show that simulation results also reproduce the ionospheric signature of substorm to a certain extent.

4. Distant-Tail Neutral Line During the Growth Phase

The upper panel of Figure 4 at $t = 30$ minute shows a snapshot of the magnetospheric configuration during the growth-phase interval together with the ionospheric convection. While open field lines generated from the southward IMF through the dayside reconnection wrap the outer part of the lobe, the core part still consists of open field lines generated from the northward IMF. This situation is quite similar to the formation process of theta aurora and Z-shaped plasma sheet in the yz plane (cross tail Z) caused after a sign change of IMF B_y (Tanaka et al., 2003). In both cases, the outer part of tail is connected to new IMFs while the inner part is still controlled by old IMFs. In the thinning stage during the growth phase, therefore, the reclosure process in the plasma sheet (at $x = -60$ Re in Figure 2) is still slow, since it is controlled by the remnants of the northward IMF. From numerical results shown by Tanaka (1999),

it is well understood that the magnetic topology in the core part inhibits an effective reconnection in the plasma sheet because two bundles of lobe open field lines from the northern and southern hemispheres are twisted around the x axis limiting anti-parallelism.

The flaring angle theory is often proposed to explain plasma sheet thinning (Baker et al., 1996). Under this theory, the open magnetic field lines accumulate on the nightside due to the transport after reconnection on the dayside, producing a larger flaring angle. Therefore, the lobes are more strongly sailed by solar-wind pressure, which leads to increased lobe magnetic pressure. This increased lobe pressure compresses the plasma sheet and thins it. It is obvious that this theory relies upon an extension of the magnetospheric image based on localized MHD balance or single-particle description. Starting from the concept of convection, another growth-phase mechanism can be extracted from the magnetic topology during the growth phase shown in Figure 4, by reconsidering the principle controlling the convection as shown by Tanaka (2003b).

Before considering the growth-phase mechanism, the structure of distant neutral line must also be reconsidered. The M-I convection under the northward IMF condition consists of the lobe cell and merging cell. In the lobe cell, IMF reconnects with an open field line near the dayside cusp region. This cell is constructed only from open field lines classified as the type 1 by Tanaka (1999). On the contrary, the merging cell that is driven by the IMF reconnection with a closed field line includes both open and closed field lines. Figure 5 shows the structure of merging cell under the northward IMF condition with non-zero IMF B_y (Tanaka, 1999; Watanabe et al., 2003). This figure shows the structure of magnetic field lines constructing the merging cell. In addition to the magnetic configuration, cross points of magnetic field lines with the yz plane at $x = -70$ Re are shown in the upper right inset together with footpoints of field lines on the northern ionosphere in the upper left inset. In the upper right inset dashed line shows the inclined plasma sheet at $x = -70$ Re. After the IMF reconnection with a closed field line near the cusp, two different types of open field line must be generated. This fact was first recognized by Tanaka (1999) and two different types were classified as the type 2 and type 3. For the type 2, reconnection point and footpoint are in the same hemisphere, while they are in the opposite hemisphere for the type 3. After entering the lobe, the type 2 field line proceeds toward dawn in the midst of the lobe, and finally, type 2 field line approaches the plasma sheet near the dawn flank. The type 3 field proceeds toward the dawn for a while in the region nearest the plasma sheet, but it goes back toward the dusk and approaches the dusk plasma sheet. Corresponding to this motion, curvature of type 3 field is reversed in the deep tail region. As shown by Tanaka (1999), twist structure of type 2 and 3 field lines prevents the anti-parallelism. Results in Figure 5 indicate the occurrence of twist back process to resolve this prevention of

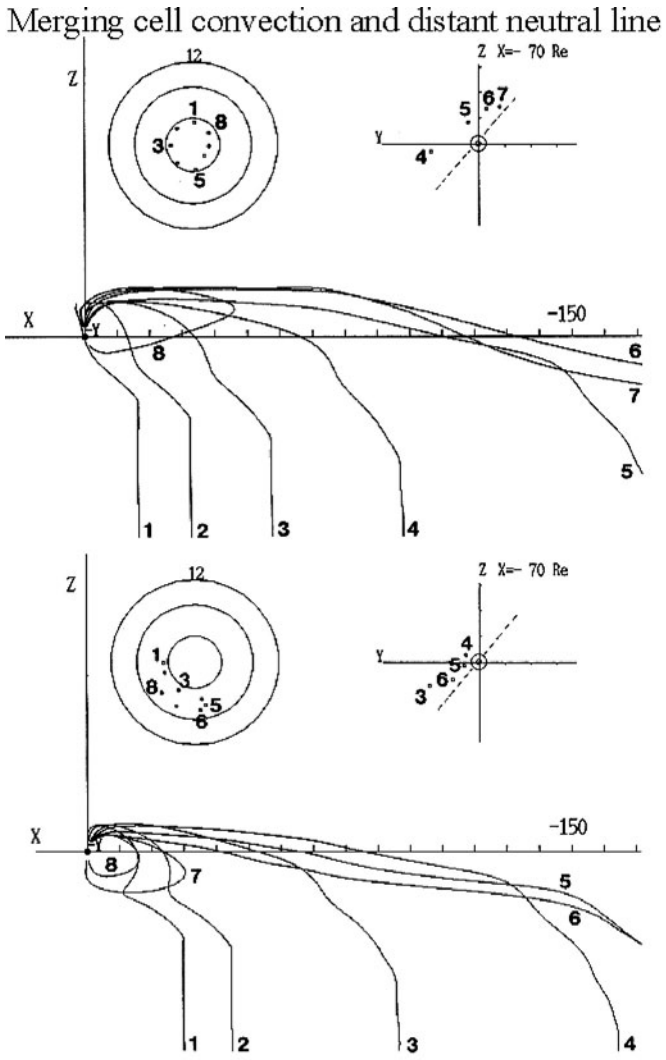


Figure 5. Structure of merging-cell convection generating the distant neutral line. This figure shows type 2 (upper) and type 3 (lower) field lines over a wide area as far as x = −150 Re. Upper left and right insets show footpoints on the ionosphere and cross points with yz plane at x = −70 Re. Dashed line shows the inclined plasma sheet at x = −70 Re. A peculiar feature is seen in the development of type 3 field line. Initially, it proceeds from dusk to dawn but it goes back to again toward dusk (skew back process).

anti-parallelism included in the merging cell. Obviously, the twist-back process makes the position of tail neutral line be at more distant region. This is the most natural understanding for the formation mechanism of the distant neutral line.

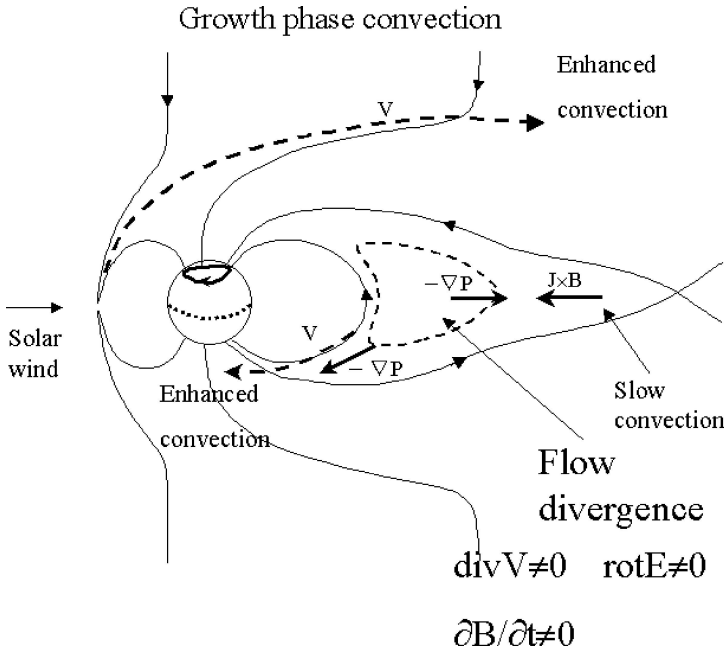


Figure 6. Schematic diagram showing the growth-phase convection. The bashed arrows show the regions of enhanced convection, while solid arrows show the force balance. The divergence thinning for the substorm growth phase is seen from this figure. Flow divergence is equal to inductive electric field, and consequently it generates a change in magnetic configuration.

The mechanism of the growth phase under such a distant-neutral-line structure is shown in Figure 6. With the development of the dayside reconnection, the magnetospheric convection from the dayside toward the nightside is enhanced. However, the distant-tail neutral line does not immediately disappear (Figure 4), and so the plasma-sheet backflow does not immediately increase in the magnetospheric convection. In the ionosphere, on the other hand, a large magnitude of B prevents the occurrence of a divergent flow (Kivelson and Southwood, 1991). This non-divergent nature of the ionospheric flow together with the fact that the magnetospheric dynamo driving the region 1 FAC is distributed in the near-earth cusp and mantle is responsible for a quick response of the ionospheric convection to a change in the IMF (Hashimoto et al., 2002). The convection in the inner magnetosphere is connected to the quickly responding two–cell convection in the ionosphere as shown in Figure 6, and consequently the flow from the inner edge of the plasma sheet must divert on both sides of the earth to the dayside.

Thus, magnetosphere and the ionosphere tend to have different timescales in their response to the change in IMF. It takes more than 30 minutes to propagate

the IMF change into the tail region, while the nightside ionosphere responses to the change in IMF within 5 minutes (Hashimoto et al., 2002). However, the ionosphere needs not to know the entire situation of the magnetosphere. In this case magnetospheric convection must be seen from the ionosphere as a non-divergent flow to match with the two-cell convection in the ionosphere that is expressed by a potential electric field. The magnetospheric convection can generate a non-divergent flow against the ionosphere by an expense of divergent flow in the plasma sheet that squeezes out the plasma already accumulated in the plasma sheet to dayside (Figure 6). This situation causes the outgoing sunward flux from the plasma sheet to exceed the supply flux to the plasma sheet from the distant tail. As schematically shown in Figure 6, the loss of closed magnetic flux from the near-earth tail prevails over the supply of closed magnetic flux to the near-earth tail. This net overloss of closed magnetic flux results in the plasma sheet thinning in the growth phase. The divergent flow corresponds to the condition $\partial \mathbf{B}/\partial t \neq 0$, and thinning is a natural consequence of this condition.

5. Signatures of Onset

No matter how large in magnitude the M-I disturbance may be, it would not be regarded as a substorm if it starts gradually. A major object of substorm study is to find an explanation for the appearance of discontinuity at onset. A dipolarization event that definitely corresponds to the condition $\partial \mathbf{B}/\partial t \neq 0$ characterizes onset, and must accompany the flow convergence in the magnetosphere. This convergent motion is not projected onto the ionosphere, because compressional motions generated at high altitude in the magnetosphere are almost perfectly reflected before reaching the ionosphere (Kivelson and Southwood, 1991). Conversely, the magnetosphere needs to generate such motion associated with the dipolarization as that confined to the magnetosphere.

The substorm onset occurs as an abrupt change of the magnetospheric configuration in the near-earth tail. The 5-th panels in Figures 1 and 2 show pressure and $-V_x$ distributions after the onset illustrating the appearance of the high-pressure region in the inner magnetosphere, fast earthward flow and the formation of the NENL in the midtail. From Figure 4, this change is identified as the dipolarization (onset).

Figure 7 shows pressure and V_x distributions along the $-x$ axis in the near-earth and midtail before and after the onset. Before the onset ($t < 70$ minute), the strongest $-\nabla P$ force acts in the region between $x = -10$ and -20 Re. As a result, earthward convection is obstructed at $x = -14$ Re. In addition, a gradual formation of NENL is seen at $x = -33$ Re before the onset. At $t = 70$ minute, a sudden change of pressure profile is seen to start just like a transition from one state to another. After the onset ($t > 70$ minute), the peak position in the pressure distribution shows a rapid inward movement. The pressure peek

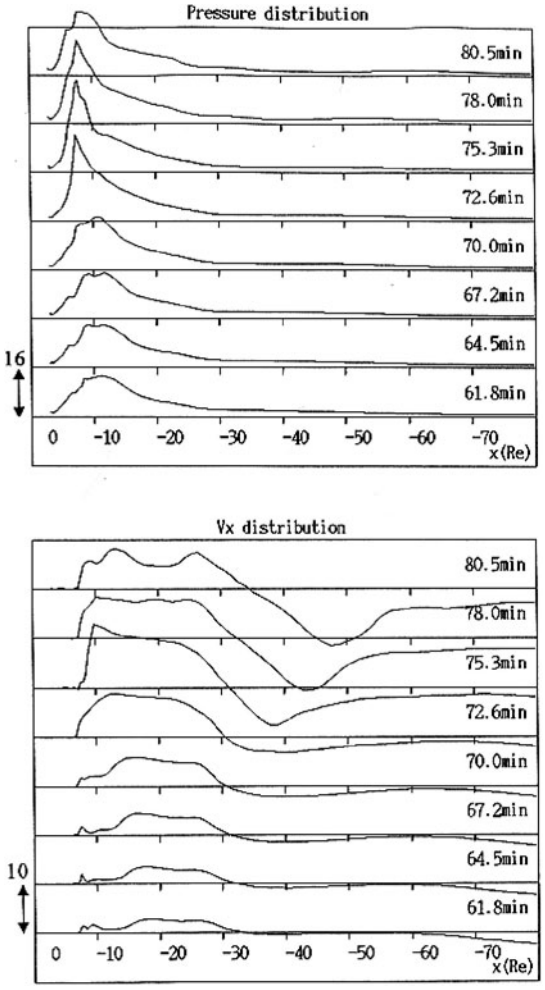


Figure 7. Time sequence of P and $-V_x$ distributions along the $-x$ axis around the onset. Pressure and velocity is normalized by solar-wind pressure and solar-wind sound velocity. Sudden transition is observable between $t = 70.0$ minute and 72.6 minute.

abruptly moves further inward to $x = -8$ Re. At the same time, the convection flow intrudes into the inner magnetosphere inside $x = -10$ Re increasing in magnitude. Through these transition processes, a new stress balance is achieved in the near-earth plasma sheet in which recovered magnetic tension is balanced by newly established pressure inside $x = -10$ Re. This pressure change is, in turn, a result of energy conversion from magnetic energy to internal energy caused by the pumping effect of convection associated with the recovery of magnetic tension. The fastest earthward flow in the plasma sheet appears after

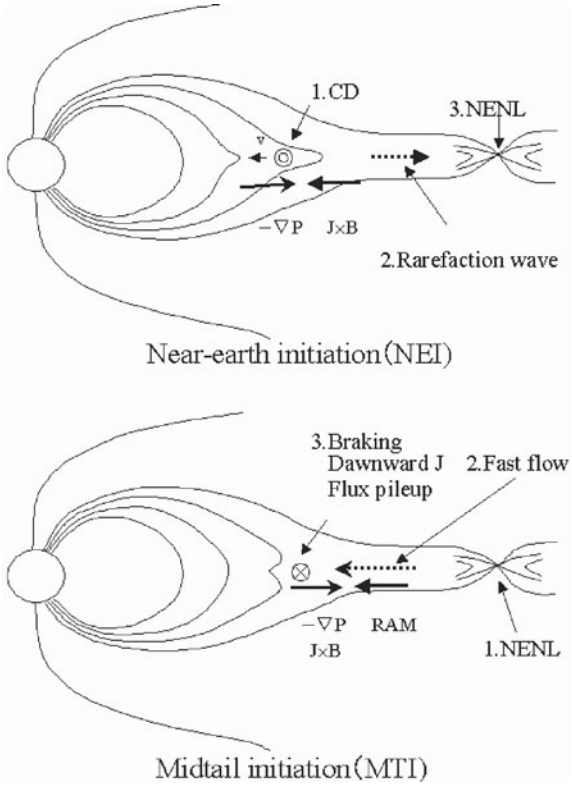


Figure 8. Schematic diagrams showing two different concepts for substorm initiation. Top and bottom panels represent near-earth-initiation and mid-tail-initiation models, respectively. If a primary cause for the onset is assumed, the resulting effects occur in sequence as show by numbers. Solid arrows show the force balance. In the lower panel (mid-tail initiation), dominance of kinetic energy is unavoidable in the near-earth region. On the contrary, onset is generated retaining $\mathbf{J} \times \mathbf{B} = -\nabla P$ in the near-earth-tail initiation.

about 5 minutes from the onset. Then, tailward flow increases its speed. After $t = 75.3$ minute, the NENL begins to gradually retreat downtail.

The NENL model in the lower panel of Figure 8 (Baker et al., 1996) explains flow convergence (dipolarization) as a pileup of fast flow from the NENL. Therefore, the motion is in a fast wave mode, in which both the magnetic field and fluid are similarly compressed. This produces tailward pressure force that is balanced by the earthward dynamic pressure. This mechanical structure is the same as that for the bow shock, and the negative $\mathbf{J} \cdot \mathbf{E}$ associated with the flow deceleration generates a dawnward current. This current is considered to correspond to the current wedge. The substorm discontinuity in this model results from the rapid development of NENL. The reconnection must develop

as an instability in this case, and is regarded as a result of kinetic processes. In this model, the onset proceeds from the tail to the inner magnetosphere (steps 1, 2, and 3 in Figure 8, bottom). The well known weakness of this model lies in the discordance in the brightening order of quiet arcs (which proceed from the equator to polar direction) that are already present before the onset. Furthermore, it fails to explain the fact that substorm onset is triggered by a northward turning of IMF (Lyons et al., 1997).

It was pointed out by Parker (1996, 2000) that fluid dynamic descriptions of plasma using **BV** as basic parameters can describe the evolution of global motion in a self-consistent manner. Performing a rotation operation on dipolarization results in the development of a CD, and under the **BV** paradigm, these two are different description of same physical process. In contrast to the NENL model, the CD model attributes the substorm discontinuity to the CD (= dipolarization). In the CD model, disturbance produced as a result of CD propagates downtail and triggers the NENL (Figure 8, top panel) (Lui, 1996). In this model, the onset proceeds from the inner magnetosphere to the tail (steps 1, 2, and 3 in Figure 8, top). The CD is a kinetic process and must also be an instability. Supporters of this model associate the severe magnetic oscillations accompanying dipolarization with non-MHD processes (Takahashi et al., 1987; Ohtani et al., 1998), and believe that there may even be a global-scale slip between the magnetic field and plasma (non-ideal MHD process). Therefore, this model is constructed under the **EJ** paradigm in which **E** is regarded as the cause of **V** and **J** is regarded as the cause of **B**. The CD model is consistent with the brightening glow order of the quiet arcs. Both of the NENL and CD models attribute the substorm onset to local plasma processes. In these models, global magnetospheric structure is controlled by local processes. On the contrary, the two-state transition model considers the change of global force balance associated with the convection motion as the main controlling factor for magnetospheric development.

6. Change of Mechanical Balance Associated with the Onset

In the near-earth region, plasma sheet is filled with plasma even during the growth phase. This plasma supports the $\mathbf{J} \times \mathbf{B}$ force in the x direction and constructs the convection system including the plasma population regimes (Tanaka, 2003b). In the region between –12 and –30 Re, the distribution of plasma pressure changes little even after the onset, whereas a drastic change of plasma pressure occurs in the near-earth region inside –12 Re (Figure 7). These results strictly coincide with observations given by Kistler et al. (1992). In the simulation result shown in Figure 1, therefore, the NENL is never a floating object in the space but an interaction system with the supporting plasma under the force

balance. In this situation with the force balance in the x direction, the convection in the plasma sheet is in the subsonic regime and nearly incompressible. Actually, flow surrounding the slant slow shock is almost incompressible (Lee, 1995). In the incompressible convection system, the flow configuration must change as a whole. Only a portion of the convection cannot become fast, since in such a case flow convergence is required at the front of the fast flow and flow divergence is required at the rear. Briefly speaking, a fluid element in the incompressible flow cannot move until a fluid element in the front position moves aside.

The concept of state transition in the substorm onset has been suggested by Atkinson (1991), followed by Sitonov et al. (2000), Shao et al. (2003) and Tanaka (2000b).The state transition model by Tanaka (2000b) regards the onset as a natural consequence of development process in convection. During the growth phase, the dominant element in the force balance is that between plasma pressure and magnetic pressure in the z direction, under a flat pressure distribution in the x direction. The dipolarization is considered to be an escape from this balance with a restoration of magnetic tension resulting from the shrinkage of the elongated magnetic field. In the dipolarization process, the restored tension balances with newly developed pressure which is, in turn, a result of the pumping effect associated with the plasma sheet convection that directs from low-pressure region to high-pressure region against $-\nabla P$ force (Tanaka, 2000b, 2003b). Thus, the energy conversion between the magnetic and internal energies acts as a kind of self-adjustment system. In other words, restored magnetic tension confines the plasma to enable a convergence of convection. At the onset, the magnetosphere and ionosphere are partially out of synchronization since a compressional motion cannot be mapped down onto the ionosphere. The change in force balance from the z direction to x direction enables the motion even under this condition (non-shear motion).

It is natural to observe earthward flow before the onset (Figure 7) because under the frozen-in condition the magnetic configuration cannot change without preceding flow which carries the magnetic field. The kinetic aspect of reconnection may be conspicuous in the pathway between the states. However, the discontinuous behavior at the onset is primarily attributed to a realization of initial and destination states in the MHD regime. The sudden dipolarization is interpreted as a self-organization phenomenon in a nonlinear system (Tanaka, 2000b). In this view, the onset is a bifurcation process from a tail-like state to a dipolar state through the change of force balance.

At the onset, magnetically driven motion due to the restored magnetic tension along the dipolarizing field lines accumulates plasma by transporting it along the magnetic field lines without a compression of magnetic field. This kind of motion corresponds to the slow mode variation. Recently such motion is confirmed from the satellite observations (Nakamizo and Iijima, 2003). The

development of pressure distribution within the plasma sheet shown in Figure 7 is similar to those observations by Kistler et al. (1992), and generates a maximum within 10 Re after onset. These variations are rapid, and within 1 minute, a transition of pressure distribution occurs from the growth phase to the expansion phase. In this process, the dipolarization is a restoration of tension and never a relaxation to the potential field.

In the NENL model of the substorm, on the contrary, the magnetic energy is converted to the kinetic energy through the NENL formation. The ground onset is attributed to the braking of this kinetic energy in the inner magnetosphere (Baker et al., 1996). Figure 9 shows distribution of internal and kinetic energy

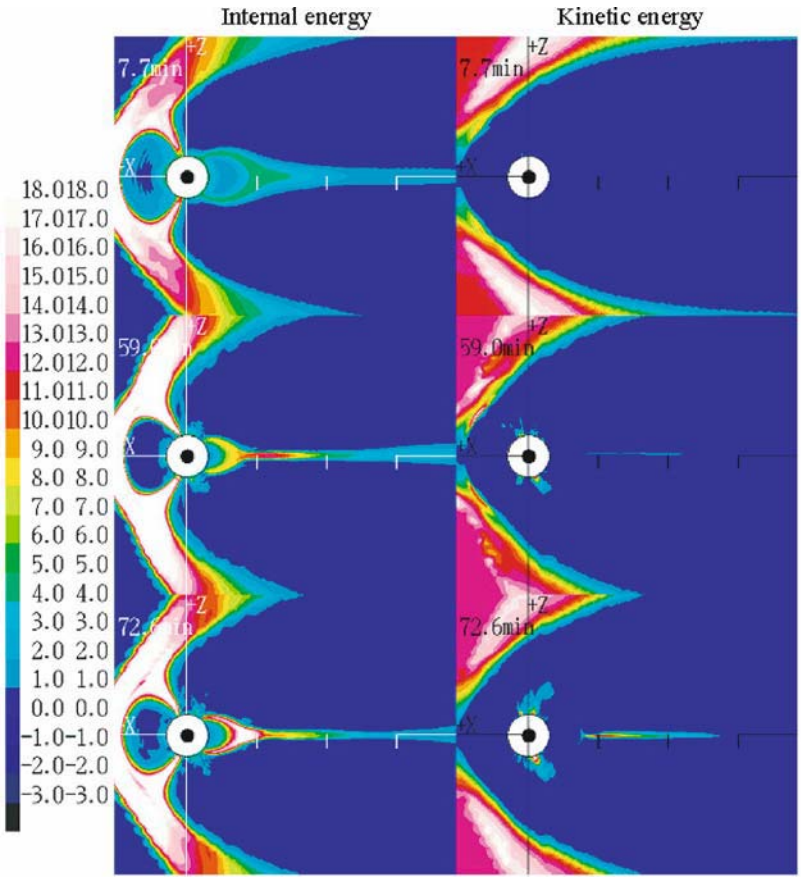


Figure 9. Distributions of internal energy (left) and kinetic energy (right) in the noon-midnight meridian plane. From top to bottom three panels show initial, growth, and expansion phases. In the magnetosphere, internal energy prevails over kinetic energy in all cases. In the solar wind, on the contrary, kinetic energy prevails over internal energy.

during the initial state, growth phase and expansion phase. Apparently the NENL model is inconsistent with the results shown in Figure 9. On the other hand, the state transition model can generate the substorm onset without the dominance of kinetic energy everywhere in the tail. It generates the onset along a natural extension of the incompressible convection in the M-I coupling system.

The NENL model and the CD model both assume that there must be a central player initiating the onset. In contrast, there is no central player in the state transition model. The state transition model resembles the economic model of major depressions, the Ising model for magnetization, or the avalanche model for substorms (Chapman et al., 1998). These models are all based on cooperative phenomena, and no central player exist. Instead, in these models, many similar elements coexist and interact with one another. The state transition of the interacting systems corresponds to the conditions of a major depression and of magnetization. The onset of substorm is the occurrence of state transition in the interacting system, as shown in Figure 7. The substorm does not involve as many elements as the economic model or the model for magnetic bodies. However, all elements in substorm have its characteristic topologies. Since the conditions differ significantly from those of typical complex systems found in economic models and models for magnetic bodies, we refer to the M-I system as a compound system.

The state transition in the near-earth region explains quite well why the onset starts from the equatorwardmost preonset arc. In general, the state transition requires the existence of multiple solutions for one boundary condition. As a consequence, it requires a nonlinearity of the system. On the other hand, the relation between the NENL solution and inflow and outflow boundary conditions is in one-to-one correspondence which generates no state transition (Lee, 1995).

The state transition model can also explain the triggering effect caused by the northward turning of IMF. The deceleration of the ionospheric convection reduces the flux exiting the plasma sheet to the dayside, creating a region of flow convergence. The triggering effect by northward turning of IMF is also explained by Lyons (1995). However, Lyons' theory attempts to explain the triggering effect as originating from the deceleration of convection caused by the penetration of the weakened solar wind electric field into the magnetosphere; this leads to the mistake of **EJ** paradigm pointed out by Parker (2000).

The difference between the state transition model and NENL model can be understood from the analogy of waterpower electric generation. The left panel of Figure 10 shows a water fall-like system. In this system, kinetic energy is the source for the generation of electric power. However, waterpower electric plants in practical use do not have such a configuration. They send water through water pipes as shown in the right panel of Figure 10. Here, even a slow flow can generate electric power. Under the incompressible condition, pressure inside

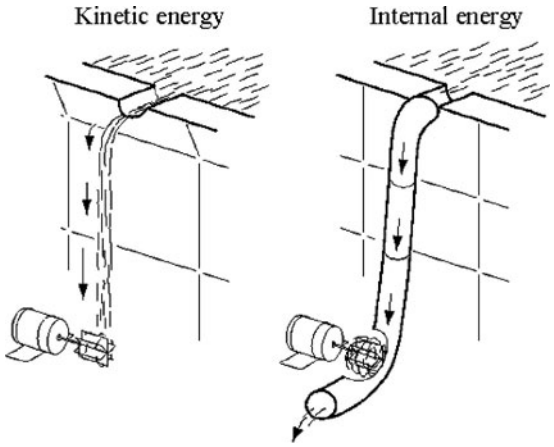


Figure 10. Water electric analogy for energy generation of substorm onset. Electromagnetic energy is generated from kinetic energy (left) or from internal energy (right).

the pipe at the bottom becomes very high and internal energy acts a major role for the generation of electric power. The energy conversion in the state transition model is in analogy with this system.

7. Pseudo Breakup and SMC

The pseudo breakup and steady magnetospheric convention (SMC, or convection bay) are phenomena resembling a substorm but which are grouped in a different category. The pseudo breakup displays a common morphology with substorms until the onset. However, it does not accompany poleward expansion or a westward traveling surge (WTS), and terminates before changes are propagated to the whole magnetosphere (Pulkkinen et al., 1998). The magnitude of disturbance in an SMC is comparable to that of the substorm, but an SMC progresses to the expansion phase without displaying a clear discontinuity, or onset (Yahnin et al., 1994; Sergeev et al., 1996). In an SMC, a strong stationary two-cell ionospheric convection is realized.

The pseudo breakup can be explained in terms of the NENL model as a mid-course termination of an initiated reconnection. In contrast, in the state transition model, it can be interpreted as follows. Normally, state transition is initiated in the inner magnetosphere with the extinction of the core part (distant-tail neutral line) shown in the upper panel of Figure 4, and the substorm proceeds to the expansion phase. However, if state transition occurs before the extinction of the core part (distant-tail neutral line) shown in Figure 4, the discontinuity at onset is realized, but the NENL cannot be formed at this stage due to the presence of the core structure. This results in a failure to proceed to the expansion phase,

and instead, the event ends as a pseudo breakup. If convection is promoted without state transition or after the state transition has been initiated, and the state of no distant-tail neutral line is maintained, then the event is an SMC. In this way, the state transition model provides simple explanations for the pseudo breakups and SMC.

References

Akasofu, S.-I., The development of the auroral substorm, *Planet. Space Sci., 12*, 273, 1964.

Angelopoulos, V., W. Baumjohann, C. F. Kenel, F. V. Coroniti, M. G. Kivelson, R. Pellat, R. J. Walker, H. Luhr, and G. Paschmann, Bursty bulk flows in the inner central plasma sheet, *J. Geophys. Res., 97*, 4027, 1992.

Atkinson, G., A magnetosphere WAGS the tail model of substorms, in *Magnetospheric substorms, Geophys. Monogr. Ser.*, vol. 64, edited by J. R. Kan, T. A. Potemra, S. Kokubun, and T. Iijima, p. 191, AGU, Washington, D.C., 1991.

Baker, D. N., T. I. Pulkkinen, V. Angelopoulos, W. Baumjohann, and R. L. McPherron, Neutral line model of substorms: Past results and present view, *J. Geophys. Res., 101*, 12,975, 1996.

Baumjohann, W., G. Paschmann, and H. Luhr, Characteristics of high-speed ion flows in the plasma sheet, *J. Geophys. Res., 95*, 3801, 1990.

Chapman, S., and V. C. A. Ferraro, A new theory of magnetospheric storms, Part 1, The initial phase, *J. Geophys. Res., 36*, 77, 1931.

Chapman, S. C., N. W. Watkins, R. O. Dendy, P. Helander, and G. Rowlands, A simple avalanshe model as an analogue for magnetospheric activity, *Geophys. Res. Lett., 25*, 2397, 1998.

Crooker, N. U., J. G. Lyon, and J. A. Fedder, MHD model merging with IMF B_y: Lobe cells, sunward polar cap convection, and overdraped lobes, *J. Geophys. Res., 103*, 9143, 1998.

Elphinstone, R. D., J. S. Murphree, and L. L. Cogger, What is a global auroral substorm, *Rev. Geophys., 34*, 169, 1996.

Fedder, J. A., S. P. Slinker, and J. G. Lyon, A comparison of global numerical simulation results to data for the January 27–28, geospace environment modeling challenge event, *J. Geophys. Res., 103*, 14,799, 1998.

Gombosi, T. I., K. G. Powell, and B. van Leer, Comment on "Modeling the magnetosphere for northward interplanetary magnetic field: Effects of electrical resistivity" by Joachim Raeder, *J. Geophys. Res., 105*, 13,141, 2000.

Hashimoto, K., T. Kikuchi, and Y. Ebihara, Response of the magnetospheric convection to sudden IMF change as deduced from the evolution of partial ring currents, *J. Geophys. Res.*, *107*(A11), 1337, doi:10.1029/2001JA009228, 2002.

Kistler, L. M., E. Mobius, W. Baumjohann, and G. Paschmann, Pressure changes in the plasma sheet during substorm injection, *J. Geophys. Res., 97*, 2973, 1992.

Kivelson, M. G., and D. J. Southwood, Ionospheric traveling vortex generated by solar wind buffering of the magnetosphere, *J. Geophys. Res*., *96*, 1661, 1991.

Lee, L. C., A review of magnetic reconnection: MHD models, in *Physics of magnetopause*, *Geophys. Monogr. Ser*., vol. 90, edited by P. Song et al., p. 139, AGU, Washington, D. C., 1995.

Lopez, R. E., and A. T. Y. Lui, A multi-satellite case study of the expansion phase of a substorm current wedge in the near-Earth magnetotail, *J. Geophys. Res., 95*, 8009, 1990.

Lui, A. T. Y., Current disruption in the earth's magnetosphere: Observations and models, *J. Geophys. Res., 101*, 13,067, 1996.

Lyons, L. R., A new theory for magnetospheric substorms, *J. Geophys. Res., 100*, 19,069, 1995.

Lyons, L. R., G. T. Blanchard, J. C. Samson, R. P. Lepping, T. Yamamoto, and T. Moretto, Coordinated observation demonstrating external substorm triggering, *J. Geophys. Res., 102*, 27,039, 1997.

Nakamizo, A., and T. Iijima, A new perspective on magnetotail disturbances in terms of inherent diamagnetic processes, *J. Geophys. Res. 108*(A7), 1286, doi:10.1029/2002JA009400, 2003.

Nagai, T., K. Takahashi, H. Kawano, T. Yamamoto, S. Kokubun, and A. Nishida, Initial geotail survey of magnetic substorm signatures in the magnetotail, *Geophys. Res. Lett.*, *25*, 2991, 1994.

Ogino, T., R. J. Walker, M. Ashour-Abdalla, and J. M. Dawson, An MHD simulation of the effects of interplanetary magnetic field B_y component on the interaction of the solar wind with the earth's magnetosphere during southward interplanetary magnetic field, *J. Geophys. Res., 91*, 10,029, 1986.

Ohtani, S., K. Takahashi, T. Higuchi, A. T. Y. Lui, H. E. Spence, and J. F. Fennell, AMPTE/CCE-SCATHA simultaneous observations of substorm-associated magnetic fluctuations, *J. Geophys. Res., 103*, 4671, 1998.

Parker, E. N., The alternative paradigm for magnetospheric physics, *J. Geophys. Res., 101*, 10,587, 1996.

Parker, E. N., Newton, Maxwell, and Magnetospheric Physics, in *Magnetospheric current systems, Geophys. Monogr. Ser*., vol. 118, edited by S. Ohtani et al., p. 1, AGU, Washington, D. C., 2000.

Pulkkinen, T. I., D. N. Baker, M. Wiltberger, C. Goodrich, R. E. Lopez, and J. G. Lyon, Pseudobreakup and substorm onset: Observations and MHD simulations compared, *J. Geophys. Res., 103*, 14,847, 1998.

Sergeev, V. A., R. J. Pellinen, and T. I. Pulkkinen, Steady magnetospheric convection: A review of recent results, *Space Sci. Rev., 75*, 551, 1996.

Shao, X, M. I. Sitnov, S. A. Sharma, K. Papadopoulos, C. C. Goodrich, P. N. Guzdar, G. M. Milikh, M. J. Wiltberger, J. G. Lyon, Phase transition-like behavior of magnetospheric substorms: Global MHD simulation results, *J. Geophys. Res., 108*(A1), doi:10.1029/2001JA009237, 2003.

Siscoe, G. L., N. U. Crooker, G. M. Erickson, B. U. O. Sonnerup, K. D. Siebert, D. R. Weimer, W. W. White, and N. C. Maynard, Global geometry of magnetospheric currents inferred from MHD simulations, in *Magnetospheric current systems, Geophys. Monogr. Ser.*, vol. 118, edited by S. Ohtani et al., p. 41, AGU, Washington, D. C., 2000.

Sitnov, M. I., A. S. Sharma, K. Papadopoulos, D. Vassiliadis, J. A. Valdivia, A. J. Klimas, and D. N. Baker, Phase transition-like behavior of the magnetosphere during substorms, *J. Geophys. Res.*, *105*, 12,955, 2000.

Takahashi, K., L. J. Zanetti, R. E. Lopez, R. W. McEntire, T. A. Potemra, and K. Yumoto, Disruption of the magnetotail current sheet observed by AMPTE/CCE, *Geophys. Res. Lett., 14*, 1019, 1987.

Tanaka, T., Configurations of the solar wind flow and magnetic field around the planets with no magnetic field: Calculation by a new MHD simulation scheme, *J. Geophys. Res., 98*, 17251, 1993.

Tanaka, T., Finite volume TVD scheme on an unstructured grid system for three-dimensional MHD simulation of inhomogeneous systems including strong background potential fields, *J. Comput. Phys.*, *111*, 381, 1994.

Tanaka, T., Generation mechanisms for magnetosphere-ionosphere current systems deduced from a three-dimensional MHD simulation of the solar wind-magnetosphere-ionosphere coupling processes, *J. Geophys. Res., 100*, 12,057, 1995.

Tanaka, T., Effects of decreasing ionospheric pressure on the solar wind interaction with non-magnetized planets, *Earth Planets Space, 50*, 259, 1998.

Tanaka, T., Configuration of the magnetosphere-ionosphere convection system under northward IMF condition with non-zero IMF B_y, *J. Geophys. Res., 104*, 14,683, 1999.

Tanaka, T., Field-aligned current systems in the numerically simulated magnetosphere, in *Magnetospheric current systems, Geophys. Monogr. Ser.*, vol. 118, edited by S. Ohtani et al., p. 53, AGU, Washington, D. C., 2000a.

Tanaka, T., The state transition model of the substorm onset, *J. Geophys. Res.*, *105*, 21,081, 2000b.

Tanaka, T., IMF B_y and auroral conductance effects on high-latitude ionospheric convection, *J. Geophys. Res., 106*, 24,505, 2001.

Tanaka, T., Finite volume TVD scheme for magnetohydrodynamics on unstructured grids, in *Space plasma simulation*, *Lecture notes in physics*, edited by J. Buchner et al., p. 275, Springer, 2003a.

Tanaka, T., Formation of magnetospheric plasma population regimes coupled with the dynamo process in the convection system, *J. Geophys. Res*., *108*(A8), 1315, doi:10.1029/2002JA009668, 2003b.

Tanaka, T., and K. Murawski, Three-dimensional MHD simulation of the solar wind interaction with the ionosphere of Venus: Results of two-component reacting plasma simulation, *J. Geophys. Res., 102*, 19,805, 1997.

Tanaka, T., and H. Washimi, Solar cycle dependence of the heliospheric shape deduced from a global MHD simulation of the interaction process between a nonuniform time-dependent solar wind and the local interstellar medium, *J. Geophys. Res., 104,* 12,605, 1999.

Tanaka, T., and H. Washimi, Formation of the three-ring structure around supernova 1987A, *Science, 296*, 321, 2002.

Tanaka, T., T. Obara, and M. Kunitake, Formation of the theta aurora by a transient convection during northward IMF, *J. Geophys. Res*., doi:10.1029/2003JA010271, in press, 2003.

Watanabe, M., G. J. Sofko, D. A. Andre, T. Tanaka, and M. R. Hairson, Polar cap bifurcation during steady-state northward interplanetary magnetic field with |By| $\sim$ Bz, *J. Geophys. Res.*, doi:10.1029/2003JA009944, in press, 2003.

Yahnin, A., M. V. Malkov, V. A. Sergeev, R. J. Pellinen, O. Aulamo, S. Vennerstrom, E. Friis-Christensen, K. Lassen, C. Danielsen, J. D. Craven, C. Deehr, and L. A. Frank, Features of steady magnetospheric convection, *J. Geophys. Res., 99*, 4039, 1994.

Chapter 6

GLOBAL AND MULTISCALE PHENOMENA OF THE MAGNETOSPHERE

A. S. Sharma[1], A. Y. Ukhorskiy[2] and M. I. Sitnov[3]
[1]*Department of Astronomy, University of Maryland, College Park, Maryland, U.S.A.*
[2]*Applied Physics Laboratory, Johns Hopkins University, Laurel, Maryland, U.S.A.*
[3]*Institute for Research in Electronics and Applied Physics, University of Maryland, College Park, Maryland, U.S.A.*

Abstract: The magnetosphere is a prototypical open system driven by the turbulent solar wind and exhibits complex behavior with global and multiscale characteristics. The multiscale behavior, characterized by the ubiquitous power law distributions of many variables, arises from the internal magnetospheric dynamics and the turbulence in the solar wind. On the other hand the overarching global dynamical behavior originates mainly from the internal dynamics and is evident in processes such as plasmoid formation and release. This combination of global and multiscale behavior is a nonequilibrium phenomenon typical of plasmas in Nature and in many laboratory settings. The global nature of the magnetosphere is characterized by low-dimensionality and is evident in the numerical simulations using global MHD models. The multiscale aspects have been studied using many approaches, such as multifractality, self-organized criticality, turbulence, intermittency, etc. Phase transitions, which exhibit global behavior (first order) and scale invariance (second order), provide a framework for a comprehensive model of the magnetosphere.

Key words: geospace storms and substorms, global and multiscale phenomena, power law, low dimensionality, phase transitions, forecasting, space weather

1. Introduction

The magnetosphere is an open system driven by the turbulent solar wind and extends from about 10 Earth radii upstream to several hundred radii downstream. The interaction of the solar wind magnetic field and plasma with the

A.S. Sharma and P.K. Kaw (eds.), Nonequilibrium Phenomena in Plasmas, 117–144.
© 2005 *Springer. Printed in the Netherlands.*

dipole field of the Earth at the dayside magnetopause leads to the penetration of solar wind mass, momentum and energy into the magnetosphere. The main mechanism of the interaction is magnetic reconnection and an imbalance between the reconnection rate on the dayside magnetopause and at the distant neutral line results in an accumulation of solar wind energy in the magnetotail, mainly in the form of magnetic energy. This accumulated energy is then suddenly released, giving rise to magnetospheric substorms and a variety of associated phenomena. Substorms are episodic in nature and have a many manifestations in the ionosphere (e.g., magnetic field perturbations at the polar regions, auroral brightening, particle precipitation, etc.) as well as in the mid and distant magnetotail (e.g., plasmoid formation and ejection, flux ropes, etc.). Magnetospheric activity during substorms extends from small-scale processes, such as pseudo-breakups, MHD turbulence and current disruption, to large-scale processes, such as global convection, field line dipolarization and plasmoid ejection. The geospace storms on the other hand are mainly inner magnetospheric phenomenon and results from a variety of processes, including substorms. Storms have characteristic times of tens of hours to days and produces dramatic changes in the radiation belt and strong perturbations to the Earth's dipole field. During storms and substorms the magnetosphere behaves as a nonlinear, open, spatially extended system, which on the one hand is well organized on the global scale and on the other hand exhibits activity over a wide range of spatial and temporal scales. The presence of global and multiscale features is common to many systems in Nature, e.g., earthquakes, atmospheric circulation, hydrological systems, etc.

The complexity of Earth's magnetosphere has two main origins, viz. its inherent nonlinearity and the driving by the turbulent solar wind. During geomagnetically active periods such as geospace storms and substorms the magnetosphere is far from equilibrium. The range of activities extends from a fraction to hundreds of the Earth radius R_E. The modeling of such a system is a difficult task as the processes range from the kinetic, with characteristic scales as short as electron Larmor radius, to the MHD processes with scale sizes up to the system size. Thus attempts to develop first principles models of the entire magnetosphere have to deal with processes from the kinetic to the magnetohydrodynamic. On the other hand the nonlinear dynamical approach based on observational data has the ability to yield the inherent dynamics, independent of modeling assumptions. The studies of magnetospheric dynamics using dynamical models derived from data has given a new framework for the understanding of the complex behavior of solar wind—magnetosphere interaction and complements the first principles approach.

Among the key achievements of the early nonlinear dynamical studies of the magnetosphere from the observational data is the elucidation of the global

features (Sharma, 1995; Klimas et al., 1996). The evidence of global coherence in magnetospheric dynamics was first obtained from the time series of AE index, derived from the magnetic field fluctuation measured on the ground, in the form of low dimensional behavior (Vassiliadis et al., 1990). These results are consistent with the morphology of the magnetosphere derived from data and theoretical understanding (Siscoe, 1991), and numerical simulations using global MHD codes (Lyon, 2000). The recognition of the global coherence in the magnetosphere has stimulated a new direction in the studies of the solar wind-magnetosphere coupling. Among the outcomes of this research is the capability of forecasting substorms (Vassiliadis et al., 1995; Ukhorskiy et al., 2003, 2004) and storms (Valdivia et al., 1996; Sharma, 1997) with high accuracy and reliability. This has resulted into efficient forecasting tools for space weather and near real time forecasts of geomagnetic activity are provided using the solar wind data from the ACE spacecraft.

The multi-scale phenomena of the magnetosphere, on the other hand, have been recognized mainly in the form of power law dependences of many observed variables (Tsurutani et al., 1990, Ohtani et al., 1995; 1998, Angelopoulos et al., 1999; Lui et al., 2000) and in the structure functions (Takalo et al., 1993). Recent studies using time series data have shown that the magnetosphere is inherently multiscale and the coherence on the global scale is obtained by averaging over chosen scales. However the scales over which the averaging is carried out may not be fixed uniquely and may need to be changed during its evolution (Ukhorskiy et al. 2002, 2003). This resembles the phenomenon of second order phase transition, which exhibits scale-invariance. Some aspects of this feature, away from the critical point, are described by a mean field model obtained by coarse-graining (Sitnov et al., 2000, 2001). The global features of the magnetosphere are modeled using a mean-field or low dimensional approach, but the remainder of its dynamics can not be treated as a purely random process. A new approach to model such systems is needed to combine the dynamical or mean field model with a statistical description based on Bayesian or conditional probabilities to capture the multiscale features (Ukhorskiy et al., 2003, 2004).

The main developments in the nonlinear dynamical modeling of the magnetosphere are reviewed in the following. The global dynamical features, modeled using the auroral electrojet indices and solar wind data, are described in the next section. The modeling and forecasting of the global magnetospheric dynamics have used local linear filters and the new concept of mean filed dimension is used to develop a new and more efficient forecasting tools. The multiscale behavior is modeled using an approach based on conditional probabilities of statistical physics. Thus the global and multiscale phenomena are modeled using a combination of nonlinear dynamics and statistical physics.

2. Nonlinear Dynamics of the Magnetosphere

2.1 Reconstruction of phase space: Delay embedding, center of mass and local-linear filters

In a nonlinear dynamical system the time series data of one of its observable variables contains the information necessary to describe its dynamics. A nonlinear and dissipative system essentially becomes low dimensional and a phase space large enough to unfold the dynamical attractor can be reconstructed from the time series data. The phase space reconstruction is based on the delay embedding method (Packard et al., 1980; Takens, 1981; Grassberger and Procaccia, 1983; Broomhead and King, 1986; Sauer et al., 1991). The embedding theorem (Takens, 1981) states that in the absence of noise, if $M \geq 2N + 1$, then M-dimensional delay vectors generically form an embedding of the underlying phase space of the N-dimensional dynamical system. These techniques have been applied to many systems (Kantz and Schriebber, 1997), mainly to autonomous systems. In the study of magnetospheric dynamics the time series data of auroral electrojet indices have been used to characterize the nature of its dynamics (Sharma, 1993, 1995; Sharma et al., 1993).

The coupled solar wind—magnetosphere system is essentially non-autonomous and is best modeled as an input-output system (Sauer, 1993; Abarbanel et al., 1993; Vassiliadis et al., 1995). Although Takens theorem is strictly valid for autonomous systems, numerous studies (e. g., Casdagli, 1992; Vassiliadis et al.,1995; Sitnov et al., 2000) have successfully used the delay embedding method for modeling non-autonomous dynamical systems. Given the scalar time series I(t) of the input and O(t) of response, the M-dimensional embedding space is formed by input-output delay vectors:

$$\vec{\mathbf{x}}_\mathbf{n} = \left(\vec{\mathbf{I}}_\mathbf{n}, \vec{\mathbf{O}}_\mathbf{n}\right)^\mathbf{T} = \left(\mathbf{I_n}, \mathbf{I_{n+1}}, \ldots, \mathbf{I_{n+(Mo-1)}}, \mathbf{O_n}, \mathbf{O_{n+1}}, \ldots, \mathbf{O_{n+(Mi-1)}}\right)^\mathbf{T} \tag{1}$$

where $\mathbf{I_n} = \mathbf{I}(t_0 + \mathbf{n}\cdot\boldsymbol{\tau})$, $\mathbf{O_n} = \mathbf{O}(t_0 + n\cdot\boldsymbol{\tau})$, $\boldsymbol{\tau}$ is the delay time, and $M = M_i + M_o$, the sum of the embedding dimensions M_i and M_o corresponding to the input and output, respectively. Defining a delay matrix $\mathbf{A}$ as

$$\mathbf{A} = \begin{pmatrix} \vec{\mathbf{x}}_0^\mathbf{T} \\ \vdots \\ \vec{\mathbf{x}}_\mathbf{Nt}^\mathbf{T} \end{pmatrix} \tag{2}$$

a covariance matrix $\mathbf{C}$ is defined as

$$\mathbf{C} = \mathbf{A}^\mathbf{T}\mathbf{A} = \sum_{\mathbf{k}=0}^{\mathbf{N}} \vec{\mathbf{x}}_\mathbf{k} \otimes \vec{\mathbf{x}}_\mathbf{k};$$
$$\mathbf{C}\vec{\mathbf{v}}_\mathbf{k} = \mathbf{w}_\mathbf{k}^2\vec{\mathbf{v}}_\mathbf{k}, \vec{\mathbf{v}}_\mathbf{k} \in \mathbf{R}^\mathbf{M}, k = 1, \ldots, M \tag{3}$$

Since **C** is Hermitian by definition, its eigenvectors $\{\vec{\mathbf{v}}_\mathbf{k}\}$ form an orthonormal basis in the embedding space. $\{\vec{\mathbf{v}}_\mathbf{k}\}$ are usually calculated by using the singular value decomposition (SVD) method, according to which any M × N matrix A can be decomposed as

$$\mathbf{A} = \mathbf{U} \cdot \mathbf{W} \cdot \mathbf{V}^\mathbf{T} = \sum_{\mathbf{k}=\mathbf{1}}^{\mathbf{M}} \mathbf{w}_\mathbf{k} \cdot \vec{\mathbf{u}}_\mathbf{k} \otimes \vec{\mathbf{v}}_\mathbf{k} \tag{4}$$

where

$$\mathbf{V} = (\vec{\mathbf{v}}_\mathbf{1}, \ldots, \vec{\mathbf{v}}_\mathbf{M}), \qquad \mathbf{U} = (\vec{\mathbf{u}}_\mathbf{1}, \ldots, \vec{\mathbf{u}}_\mathbf{M}), \qquad \mathbf{W} = \mathbf{diag}(\mathbf{w}_\mathbf{1}, \ldots, \mathbf{w}_\mathbf{M});$$
$$\mathbf{U} \cdot \mathbf{U}^\mathbf{T} = \mathbf{1}, \qquad \mathbf{V} \cdot \mathbf{V}^\mathbf{T} = \mathbf{1}$$

The effective dimension of the system is usually not known and consequently the value of the embedding dimension M need to be determined. In general the singular spectrum $\{\mathbf{w}_\mathbf{k}\}$ of the delay matrix decreases until it forms a plateau where the eigenvalues are roughly equal and usually associated with noise (Broomhead and King, 1980). This suggests that M should correspond to the dimension at which the dynamical information in the data may not be distinguished from the noise and the eigenvalue spectrum becomes flat. However, most open systems do not always behave this way. In the case of the magnetosphere, using the solar wind induced electric field VB_s as the input and the auroral electrojet index AL as the output, it was found that the singular spectrum has well defined power spectral shape over a wide range of scales with no sign of a distinct noise floor (Sitnov et al., 2000). Thus it is not always possible to find the appropriate value of M using the SVD technique alone. The local linear filters which relate the input to the output in a local region of the reconstructed phase space, can be used to determine the dimension of the embedding space (Ukhorskiy et al., 2003). This is achieved by considering M to be a free parameter of the model, and then minimize the prediction error with respect to this parameter, as discussed in detail in the following. The value of M which provides the minimum error is then the dimension required to yield a proper embedding.

The dynamical system becomes low dimensionality as its trajectories lie on an attractor, which is completely unfolded when the reconstructed states of the system have one-to-one correspondence with the states in the original phase space. The dynamics in the reconstructed space corresponds to the actual one and can be used to predict the future evolution of the system (Farmer and Sidorowich, 1987; Casdagli, 1989; Casdagli, 1992; Sauer, 1993). It is assumed here that the underlying dynamics can be described as a nonlinear scalar map $\mathbf{O}_{\mathbf{n}+\mathbf{1}} = \mathbf{F}(\vec{\mathbf{I}}_\mathbf{n}, \vec{\mathbf{O}}_\mathbf{n})$, which relates the current state to the next state—the output at the next time step. The nonlinear function **F** is unknown, and is approximated

localy for each step of the map by the linear filter:

$$\mathbf{O_{n+1}} \approx \mathbf{F}_0 + (\delta\vec{\mathbf{I}}_\mathbf{n}, \delta\vec{\mathbf{O}}_\mathbf{n})^\mathbf{T} \cdot \begin{pmatrix} \vec{\alpha} \\ \vec{\beta} \end{pmatrix} = \mathbf{F}(\vec{\mathbf{I}}^\mathbf{C}_\mathbf{n}, \vec{\mathbf{O}}^\mathbf{C}_\mathbf{n}) + \sum_{\mathbf{i=0}}^{\mathbf{Mi-1}} \alpha_\mathbf{i}(\mathbf{I_{n-i}} - \mathbf{I}^\mathbf{C}_\mathbf{n,i}) + \sum_{\mathbf{j=0}}^{\mathbf{Mo-1}} \beta_\mathbf{j}(\mathbf{O_{n-j}} - \mathbf{O}^\mathbf{C}_\mathbf{n,j}) \tag{5}$$

where $(\vec{\mathbf{I}}^\mathbf{C}_\mathbf{n}, \vec{\mathbf{O}}^\mathbf{C}_\mathbf{n})^\mathbf{T}$ is the point about which the expansion is made. The parameters of the filter ($\alpha_\mathbf{i}$, $\beta_\mathbf{j}$ and $\mathbf{F}_0$) are calculated using the known data, which is referred as the training set. The training set is searched for the states similar to the current state, that is the states closest to it, as measured by the distance in the embedding space. These states are referred to as nearest neighbors. Local-linear filters in the form of (5) are also known as local-linear ARMA filters, since the linear term on the right hand side of (5) is composed of moving average (MA) part, i.e. the weighted average of preceding inputs, and autoregressive (AR) part, i.e. the sum of previous outputs.

The zeroeth order term in (5) is a function of the point in reconstructed space about which the expansion is made and its choice is, strictly speaking, ambiguous and should be justified in each particular case. In the forecasts of substorms using AE index data (Price et al., 1994), and of storms using Dst time series (Valdivia et al., 1996), expansions about the origin were used. Another possible center of expansion can be the reference point—$(\vec{\mathbf{I}}_\mathbf{n}, \vec{\mathbf{O}}_\mathbf{n})^\mathbf{T}$. For forecasting using time series data of autonomous dynamical systems Sauer (1993) suggested that better predictability is achieved when the average state vector of NN nearest neighbors is taken as the center of expansion:

$$\left\langle (\vec{\mathbf{I}}_\mathbf{n}, \vec{\mathbf{O}}_\mathbf{n})^\mathbf{T} \right\rangle_\mathbf{NN} = \frac{\mathbf{1}}{\mathbf{NN}} \sum_{\mathbf{k=1}}^{\mathbf{NN}} (\vec{\mathbf{I}}^\mathbf{k}_\mathbf{n}, \vec{\mathbf{O}}^\mathbf{k}_\mathbf{n})^\mathbf{T} \tag{6}$$

which is also called the center of mass, since (6) is the formula for the center of mass of NN identical particles with coordinates $(\vec{\mathbf{I}}^\mathbf{k}_\mathbf{n}, \vec{\mathbf{O}}^\mathbf{k}_\mathbf{n})$. In this case, if the whole expression (5) is averaged over NN nearest neighbors, the leading term in the expansion $\mathbf{F_0}$ becomes $\langle \mathbf{O_{n+1}} \rangle_\mathbf{NN}$, i.e. the arithmetic average of the outputs corresponding to one step iterated nearest neighbors. Thus the resulting expression for the local-linear filters takes the form:

$$\mathbf{O_{n+1}} = \langle \mathbf{O_{n+1}} \rangle_\mathbf{NN} + \sum_{\mathbf{i=0}}^{\mathbf{Mi-1}} \alpha_\mathbf{i} \left(\mathbf{I_{n-i}} - \langle \vec{\mathbf{I}}_\mathbf{n} \rangle_\mathbf{NN} \right) + \sum_{\mathbf{j=0}}^{\mathbf{Mo-1}} \beta_\mathbf{j} \left(\mathbf{O_{n-j}} - \langle \vec{\mathbf{O}}_\mathbf{n} \rangle_\mathbf{NN} \right) \tag{7}$$

In the short and long-term predictions of auroral indices, Vassiliadis et al. (1995) have used local-linear ARMA filters with expansion around the center of mass and obtained better results than the model of Price et al. (1994). It may seem

that the center of mass is just a good choice as the expansion center for the filter function and thus is an auxiliary procedure that leads to some increase in the prediction accuracy. However, in the case of Earth's magnetosphere, and presumably for a large class of non-autonomous real systems, expansion about the center of mass may be the essential element of modeling the system's dynamics with the use of local-linear filters (Ukhorskiy et al., 2002). The center of mass concept and its implementation allows a separation of the regular component of the dynamics, stabilizes the prediction algorithm, and provides the basis for modeling the multi-scale portion of the dynamics. Moreover, it has been shown that if the filter function is expanded about the center of mass, the linear terms in equation (7) are irrelevant and can be omitted, as far as long-term predictions are concerned; and the best prediction results can be achieved using only the zero-order terms.

In the calculation of the center of mass, Eq. (7) is applied to each set of the nearest neighbors. This results in NN linear equations with M unknowns—filter coefficients $\alpha_{\mathbf{i}}$, $\beta_{\mathbf{j}}$:

$$\mathbf{A_{NN}}\vec{\mathbf{y}} = \vec{\mathbf{b}} \tag{8}$$

$$\vec{\mathbf{y}} = \begin{pmatrix} \vec{\alpha} \\ \vec{\beta} \end{pmatrix}; \quad \vec{\mathbf{b}} = \begin{pmatrix} \mathbf{O^1_{n+1}} - \langle \mathbf{O_{n+1}} \rangle_{\mathbf{NN}} \\ \vdots \\ \mathbf{O^{NN}_{n+1}} - \langle \mathbf{O_{n+1}} \rangle_{\mathbf{NN}} \end{pmatrix};$$

$$\mathbf{A_{NN}} = \begin{pmatrix} (\vec{\mathbf{I}}^{\mathbf{1}}_{\mathbf{n}}, \vec{\mathbf{O}}^{\mathbf{1}}_{\mathbf{n}})^{\mathbf{T}} - \langle (\vec{\mathbf{I}}_{\mathbf{n}}, \vec{\mathbf{O}}_{\mathbf{n}})^{\mathbf{T}} \rangle_{\mathbf{NN}} \\ \vdots \\ (\vec{\mathbf{I}}^{\mathbf{NN}}_{\mathbf{n}}, \vec{\mathbf{O}}^{\mathbf{NN}}_{\mathbf{n}})^{\mathbf{T}} - \langle (\vec{\mathbf{I}}_{\mathbf{n}}, \vec{\mathbf{O}}_{\mathbf{n}})^{\mathbf{T}} \rangle_{\mathbf{NN}} \end{pmatrix}$$

This system of equation is solved in the least square sense with use of SVD:

$$\vec{\mathbf{y}} = \mathbf{A^{-1}_{NN}}\vec{\mathbf{b}} = \sum_{\mathbf{k=1}}^{\mathbf{M'}} \frac{1}{\mathbf{w^{NN}_k}} \left(\vec{\mathbf{b}} \cdot \vec{\mathbf{u}}^{\mathbf{NN}}_{\mathbf{k}}\right) \vec{\mathbf{v}}^{\mathbf{NN}}_{\mathbf{k}} \tag{9}$$

where $M' \leq M$—number of singular values that lie above the prescribed noise floor (tolerance level). Finally, after the filter coefficients are found they are plugged into (7) and then $\mathbf{O_{n+1}}$ is calculated. Combining $\mathbf{O_{n+1}}$ with measured $\mathbf{I_{n+1}}$ and repeating the above steps of the algorithm the next value $\mathbf{O_{n+2}}$ can be evaluated. Thus, local-linear ARMA filters can be used to run the iterative predictions of the system's dynamics.

The local-linear filters were derived using the correlated database of solar wind and geomagnetic time series (Bargatze et al., 1985). The data are of solar wind parameters acquired by IMP 8 spacecraft and simultaneous measurements of auroral indices with resolution of 2.5 minutes. The database consists of 34

isolated intervals with 42216 points total. Each interval represents isolated auroral activity preceded and followed by at least two-hour-long quite periods ($VB_s \approx 0$, $AL < 50$ nT). Data intervals were arranged in the order of increasing geomagnetic activity. The solar wind convective electric field VB_s is a good choice as the input of the model. The magnetospheric response to the solar wind activity is represented by the AL index—the output of the model. As the VB_s and AL data are used together to construct the input-output phase space, their time series data are normalized by their respective standard deviations.

3. Prediction of Global Magnetospheric Dynamics

The modeling of the solar wind-magnetosphere coupling with the use of local-linear ARMA filters was studied by Vassiliadis et al. (1995). In this section we compare our findings with their results and isolate the features of local-linear filters that are important to the long-term forecasting of magnetospheric activity and analyze how its overall predictability can be reconciled with the multi-scale aspects of dynamics. For the forecasting of auroral indices Vassiliadis et al. (1995) have used ARMA filters with center of mass in the form of (7), taking VB_s as the model input. Applying them to various intervals of the Bargatze database they have shown that the filter response is stable, thus allowing long-term forecasting. The prediction error of their model is minimized at a low number of filter coefficients ($M = 3 - 6$) that was interpreted as a supporting argument for the low effective dimensionality of the magnetosphere.

Local-linear ARMA filters in the form of (7) are the starting point of the current work as well. The output of the model—AL index, was predicted on the basis on its driver, viz. VB_s. Filters were calculated for both high and low magnetospheric activity periods.

To define the optimal filter structure for long-term forecasting, the following sequence of steps was performed. First, the testing intervals, corresponding to different levels of magnetospheric activity, were selected from the database. As for the training set, both input and output data were available for the testing sets. Then, the AL index was predicted for each of the testing intervals using various values of filter parameters, and compared to real data, by calculating the forecasting error in terms of normalized mean square error (NMSE) (Gershenfeld and Weigand, 1993). The filter parameters that result in minimal value of NMSE were chosen as optimal. There are three parameters in the ARMA model that can be tuned to minimize NMSE. (1) The number of delays Mi and Mo. For simplicity all calculations were done for $Mi = Mo = M$. Conceivably, 2M also gives a linear hint as to the number of active degrees of freedom. (2) The number of nearest neighbors (NN), which is used in the calculation of filter coefficients. If NN is comparable to the total number of points in the training set, then the local-linear filter simply becomes a linear filter. (3) The tolerance level—the

signal-to-noise ratio, which controls the number of terms in the local singular value spectrum that should be included in the summation in (9).

After considering a wide range of these parameters and calculating filters for different activity intervals we discovered that for long-term predictions formula (7) can be further simplified. For the cases studied here the prediction error minimizes when only zeroeth-order terms are taken into account:

$$\mathbf{O_{n+1}} = \langle \mathbf{O_{n+1}} \rangle_{\mathbf{NN}} \tag{10}$$

That is, when the value of the output at the next time step is calculated as the arithmetic average of the outputs corresponding to the iterated nearest neighbors of the current state of the system. The forecasting algorithm in this form is very stable and allows iterative predictions of AL time series for several days in a row without adjusting the filter parameters or reloading the procedure.

Such filters have only two free parameters—NN and M, which should be adjusted to minimize the prediction error. The forecasting of the 31st interval of Bargatze et al. (1985) using the filters with the optimized parameters is shown in Figure (1) (Ukhorskiy et al., 2002). The difference between the real AL data and the model outcome is shown by grey shading. Iterative predictions of the high activity 31st interval were carried out for 2500 min, during which NMSE did not exceed 57%. This result is almost identical those of Vassiliadis et al (1995) model. However, by using a simplified and therefore a time-efficient algorithm we were able to achieve the same level of accuracy without reloading the procedure after the first 20.8 hours. The forecast of the low-activity interval is also very stable and follows the trend of real data with NMSE equal to 61%.

As can be seen from the plots, the model output closely reproduces the large-scale variations of AL, sometimes failing to capture the most abrupt changes and the sharp peaks. This is intuitively understandable, since the calculation of model outcome reduces to averaging the outputs corresponding to iterated nearest neighbors, the filter output comes inherently smoothed, which results in the observed discrepancy. The higher the number NN of nearest neighbors, the stronger the smoothing and less abrupt the variations of the data can be reproduced by the model. If NN is kept small, then the filter is capable of mimicking rather sharp peaks. However, since the nearest neighbors are identified as the states that have the smallest distance from the current state in the embedding space, an increase in M in this case may result in choosing false nearest neighbors, which leads to prediction error growth. The dependence of prediction error on filter parameters NN and M shows saturation as NN is increased for fixed M (Ukhorskiy et al., 2002).

If linear terms are included in local-linear filter expression, then the filter response can significantly change, depending on its parameters. If the tolerance level is high, that is a wide range of perturbation scales is taken into account in (9), and $2M \sim NN$ the algorithm becomes unstable and diverges after a few

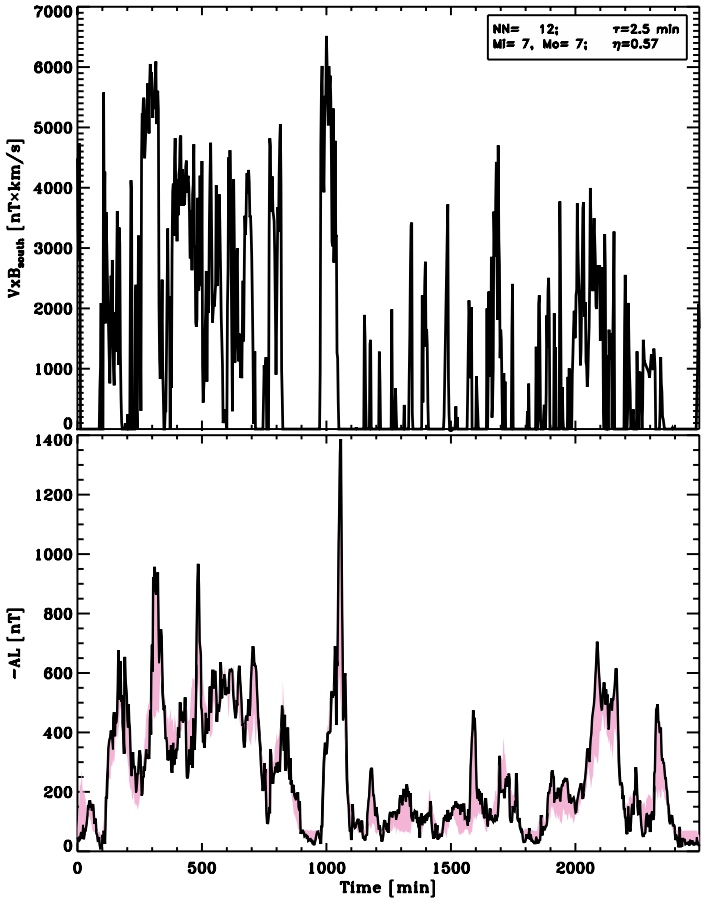


Figure 1. Long-term predictions of AL time series in the 31st interval of Bargatze et al. (1985). The solar wind VBz, used as the input is shown in the upper panel. The actual and predicted AL are shown in the bottom panel and the difference between them are shaded.

steps. This behavior of the filter outcome can be accounted for by the form of singular value spectrum obtained from the nearest neighbors matrix. Unlike the global singular spectrum, which has a power law shape, local singular spectrum has a steeper exponential form (Ukhorskiy et al., 2002). The spectra were calculated for the set of 80 nearest neighbors at each point of the interval are similar in form. The spectra consist of the main exponential part, which is preceded and followed by the shorter intervals of steeper drop. Moreover, singular values calculated for different points of the interval and therefore corresponding to different levels of substorm activity are very similar. This fact may be interpreted as an indication of self-similarity of the attractor that underlies the system dynamics.

In spite of its steepness, the form of the local singular spectra alone does not yield the number of delays M required to embed the underlying phase space. Indeed, the spectra retain their form over the wide range of scales ($10^{-3} < \mathbf{w}_k/\mathbf{w}_0 < 1$) without a noise plateau, and consequently the prescription of Broomhead and King (1989) cannot be used to obtain M. The conventional method used in such cases, i.e. choosing the number of singular values that minimizes the difference:

$$\left\| \mathbf{A}_{\mathbf{NN}} \left(\mathbf{A}_{\mathbf{NN}}^{-1} \vec{\mathbf{b}} \right) - \vec{\mathbf{b}} \right\| \tag{11}$$

at each step of the iterative predictions, is also not applicable. This follows from the fact that the variance in the estimate of the filter coefficients:

$$\sigma(\mathbf{y_j}) = \sqrt{\sum_{\mathbf{k=1}}^{\mathbf{M'}} \left(\frac{\mathbf{1}}{\mathbf{w_k^{NN}}} \left(\vec{\mathbf{v}}_{\mathbf{k}}^{\mathbf{NN}} \right)_{\mathbf{j}} \right)^{\mathbf{2}}} \tag{12}$$

grows exponentially, which results in the divergence of the prediction algorithm for $M' \sim NN$. If M is taken much greater or much less than NN, equation system (8) becomes either underdetermined or over determined. It has 2M gradually decreasing leading values, after which there is a sharp drop to the noise level (Ukhorskiy et al., 2002). Such singular spectra do not lead to the divergence of the prediction algorithm, however, since the equation system for the filter coefficients becomes strongly underdetermined, in most cases the prediction error increases. When the equation system (8) is over determined the forecasting algorithm also becomes stable, but in this case the filter becomes effectively linear, and prediction error increases. If the tolerance level is low, i.e. only a few leading singular values are included in the summation in (8), then the prediction algorithm becomes stable again. However the truncation of singular spectrum comes at the cost of information losses and therefore in this case including linear terms in the model does not improve the predictability. On the contrary in most cases this leads to an increase in forecasting error.

Consequently, for the long-term forecasting of AL time series the linear terms in the expression for conventional local-linear ARMA filters can be omitted. In this case the entire prediction procedure reduces to finding the mean-field response of the system, i.e. the average response of the similar states of the system in the reconstructed input-output phase space. The mean-field model output closely follows the trend of AL data during both high and low magnetospheric activity, reproducing best of all the large-scale variations. Thus, the mean-field model naturally represents the large-scale component of the AL dynamics. Being regular and predictable, it corresponds to the globally coherent features of the magnetospheric dynamics during substorms. Moreover, since the number of delays M is directly related to the effective dimension of the

system, the results indicate that the global component of the magnetospheric dynamics appears to be, if not low, at least of finite dimension.

3.1 Mean field dimension

An essential element in the data-derived modeling is the emphasis on the input-output nature by using the data of the solar wind as well as the magnetosphere. It is now clear that the magnetospheric dynamics can not be characterized as a simple low-dimensional chaotic system as such an approach leaves out a significant portion of the observed time series, due to the high-dimensional multi-scale dynamical constituents (Ukhorskiy et al., 2002). Recently Ukhorskiy et al. (2004) proposed a new method for modeling the global and multiscale properties based on the mean-field concept and the conditional probability computed from the solar wind and magnetosphere data. This approach is based on first obtaining the minimum dimension of the embedding space in which the averaged dynamics can be reconstructed with a given accuracy.

For low-dimensional dynamical systems the minimum embedding dimension can be inferred from data by a search for the space where all false crossings of the orbits due to the projection onto a lower dimensional space disappear (Kennel et al., 1992). This is achieved by examining whether for a given state its closest neighbor are true neighbors and not due to a projection onto space with a dimension lower than necessary. However, this method is not applicable to the time series data with significant randomness.

For a time series with irregular components the criterion for a good embedding can developed as follows. Given two states $\mathbf{x}_k$ and $\mathbf{x}_n$ which are close in the embedding space, the next states O_{k+1} and O_{n+1} predicted by a data-derived model (Ukhorskiy et al., 2002) should also be close together. In the presence of random features this is not necessarily true but an estimate of the proper embedding dimension can be obtained based on this recognition. Consider a state $\mathbf{x}_n$ in the space of dimension D together with its nearest neighbors $\{\mathbf{x}_n^{(i)} | i = 1, \ldots, NN\}$. This space is a suitable embedding if there is an NN such that the inclusion of $\mathbf{x}_n$ in $\{\mathbf{x}_n^{(i)} | i = 1, \ldots, NN\}$ does not change the average of the one step predictions $\langle O_{n+1} \rangle_{NN}$ for all states (Fig. 2):

$$\left\| \mathbf{x}_n^{cm_1} - \mathbf{x}_n^{cm_2} \right\| \to 0 \;\Rightarrow\; \left| \langle O_{n+1} \rangle_{NN_1} - \langle O_{n+1} \rangle_{NN_2} \right| \to 0, \tag{13}$$

where $\mathbf{x}_n^{cm_1} = (NN)^{-1} \sum_{k=1}^{NN} \mathbf{x}_n^{(k)}$, $\mathbf{x}_n^{cm_2} = (NN)^{-1} \left[\mathbf{x} +_n \sum_{k=1}^{NN-1} \mathbf{x}_n^{(k)} \right]$. Thus according to this definition the embedding procedure consists of finding two parameters D and NN such that the dynamics of the system is represented

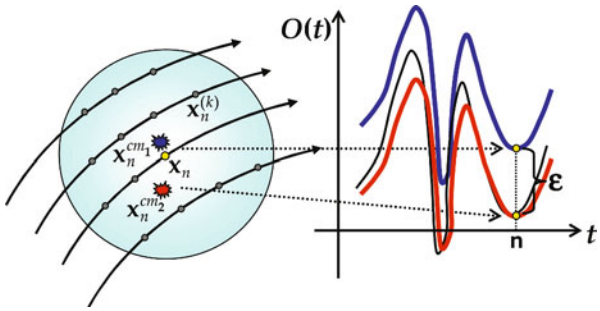


Figure 2. Computation of the embedding parameters using the states in a given neighborhood.

adequately. If such parameters are defined, then a dynamical model of the system can be introduced in the form of (2). The averaging over *NN* nearest neighbors defines the smooth manifold of dimensionality *D* or smaller that can be fit locally into the data and then used to predict its dynamics. For many random systems the choice of *D* and *NN* is not unique and *D* is usually a decreasing function of *NN*. A particular choice of the embedding parameters is usually dictated by the desired accuracy of the model.

The optimal choice of the embedding parameters *D* and *NN* is obtained by the following algorithm. For a fixed small value of *NN* the dimension of the embedding space is increased till the criterion (2.3) is satisfied for a value D_n:

$$\min\ D_n : \left\| \mathbf{x}_n^{cm_1} - \mathbf{x}_n^{cm_2} \right\| \to 0 \Rightarrow \left| \langle O_{n+1} \rangle_{NN_1} - \langle O_{n+1} \rangle_{NN_2} \right| < \varepsilon, \qquad (14)$$

where ε is a small parameter which sets the precision of the model. The probability distribution of the points in the embedding space can be used to determine if D_n is the appropriate dimension. If the system has a finite embedding dimension for chosen value of *NN*, then the distribution function will drop to a small value at this value. If there is no finite embedding dimension for this value of *NN* the distribution function has a power-law dependence. In this case *NN* is increased and the whole procedure is repeated until the finite dimension is found.

This approach is illustrated in Figure 3 for a synchronized Lorenz attractor in the presence of 1/f-noise. The distribution functions P(D) calculated for different values of *NN* show a convergent low-dimensionality at $NN = 50$. The minimum embedding dimension corresponds to the averaged dynamical systems, where the degree of averaging is set by *NN*. The small-scale component in the data is smoothed away due to the averaging and such a dimension represents a mean-field dimension.

4. Multiscale Phenomena of the Magnetosphere

The multi-scale behavior of the magnetosphere is ubiquitous, e.g., in power spectra (Tsurutani et al., 1990), structure functions (Takalo et al., 1993), multifractal characteristics (Consolini, 1996, 1997) and avalanches (Chapman et al., 1998; Chang, 1999; Freeman and Watkins, 2002). While many studies have been based on the auroral indices data, other studies have used spacecraft data. The magnetic field fluctuations during the disruption of the magnetotail current have shown power law dependence (Ohtani et al., 1995; 1998). The plasma flow in the inner plasma sheet measured by Geotail and Wind spacecraft has been used to study the nature of the intermittency in the magnetosphere (Angelopoulos et al., 1999). The probability density of the magnetotail bursty bulk flows shows power law dependence and their distribution is non-Gaussian. Studies of global auroral energy deposition events using satellite images show multiscale behavior in the form of power law dependences of the sizes of the events (Lui et al., 2000; Uritsky et al., 2002). The power law nature of the magnetosphere however may not be due entirely to the internal magnetospheric dynamics and the turbulence in the solar wind can play an important role (Freeman et al., 2000).

The magnetosphere exhibits global dynamical behavior over large scales in spite of its ubiquitous multiscale features. The universality of such characteristics in many physical systems, in nature and in laboratory, has motivated the research into new ways of understanding them, particularly in the study of critical phenomenon. The advances however are confined mainly to systems in thermodynamic equilibrium. In nature many systems that exhibit scale invariance, exhibited by the power law dependence of size distributions or the fractal structure, are neither at nor near equilibrium. Rather, they appear to be common to systems far form equilibrium in Nature and in the laboratory.

The global or mean-field approach to solar wind-magnetosphere coupling, described in the previous section, provides a framework for modeling the large-scale dynamics, for example as represented by AL time series, and for building a framework for space weather forecasting tools. However, this model does not capture the sporadic peaks and the most abrupt variations in the data, and thus it leaves out a significant portion of the dynamics.

The accuracy of the forecasts made by the model is limited by the variable number of singular values in the computation of the local-linear filters. The singular spectrum is analogous to a Fourier spectrum, and the singular values are nothing but the coefficients, that weigh the contribution of certain scale perturbations. Thus, the truncation of the singular spectrum, dictated by algorithm stability issues, limits the range of perturbation scales. Moreover, due to the algorithm divergence it is not clear what this range is, or whether it is finite or not. This issue is of great importance for understanding the dynamical properties

of the system as well as for developing more accurate forecasting tools. If the range of perturbation scales that are inherent in the observed time series is not finite, there is no finite dimensional space that provides a proper embedding for the system. This means that the dynamics of the system is not deterministic and the predictability of its evolution is limited to that of the mean-field model. On the other hand, if the range of perturbation scales is finite and can be somehow determined at each step of the iterative predictions, then including the higher order terms in filter expression can significantly increase the prediction accuracy.

This is an important issue for space weather forecasting and it can be addressed with use of local-linear ARMA filters in the form given by equation (7). For this purpose, instead of making the iterative predictions of AL for some testing interval and then minimizing the prediction error by adjusting the filter parameters, and the tolerance level for the whole prediction interval, filters can be used in an inverse problem manner. By comparing the filter prediction with real data at each step of iterative predictions, the number of terms M' of local singular spectrum that gives rise to the observed AL time series can be determined. This procedure, is referred as data reconstruction, and should return a different number M' at each time step. It is expected that in case of low dimensional system M' should oscillate around the mean value M*, which gives the linear estimate of the system dimensionality. However, in the case of a system with a significant multi-scale component, M' should be distributed between 1 and 2M, the total number of the embedding space dimension, irrespective of the value of M. This indicates that the observed time series consist of perturbations of all possible scales.

The multiscale behavior in a dynamical system has been studied using the case of a synchronized Lorenz system, whose dynamical properties are known in advance. If the X component of one Lorenz attractor is used as a driver for the second Lorenz attractor, then the attractors of both systems synchronize at the following values of parameters: $r = 60.0$, $b = 8/3$, $\sigma = 10$ (Pecora and Carroll, 1990), i.e. no matter what are the initial conditions of the second system after a few steps its trajectory converges to attractor of the driver. Thus, the Y component of the second Lorenz attractor can be considered as an output of the non-autonomous chaotic dynamical system driven by the input—the X component of the first Lorenz attractor. The reconstruction of the output by local-linear ARMA filter with $M = 20$ and $NN = 40$ is shown in Figure 4. As can be seen the reconstructed output literally coincides with the actual data—NMSE is only 0.03. The number of singular eigenvalues needed for the best reconstruction changes at it step and are shown on the third panel. As expected their distribution function has a narrow peak centered at $M^* = 6$, which indicates that we are dealing with a low-dimensional deterministic dynamical system (Ukhorskiy et al., 2002).

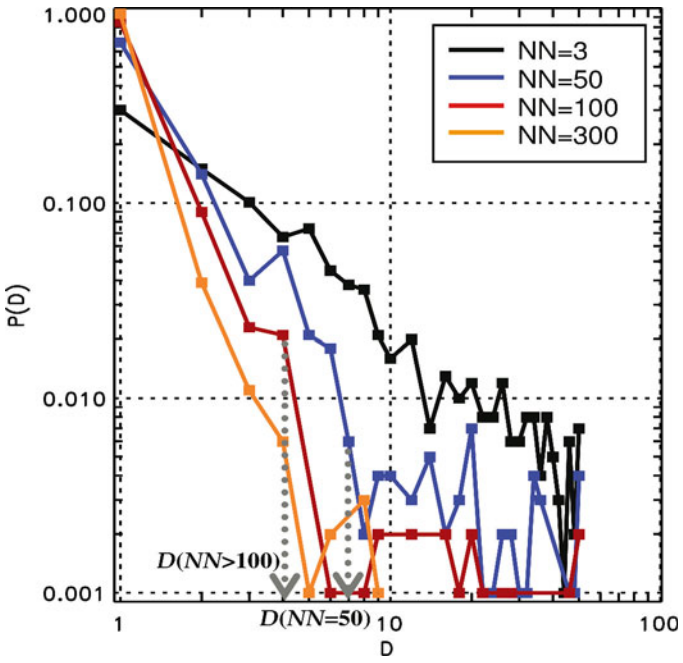


Figure 3. Distribution functions P(D) of D_n with $\epsilon = 0.5$ for a synchronized Lorenz attractor with 1/f-noise ($\sigma_{1/f} = 15$). For different *NN*, P(D) drops to a small value at different values of *D*. The mean-field dimension decreases with an increase in the averaging scale or NN. For NN = 50, D = 7 and for NN > 100, D = 4 (Ukhorskiy et al., 2003).

To investigate how the distribution of M′ changes when the dynamics of the system has two components, one—low dimensional and deterministic, and the other—high dimensional and multi-scale, a variation of a synchronized Lorenz system was considered. The second Lorenz attractor was now driven by the superposition of the first Lorenz attractor's X component and 1/f-noise time series. This input-output system can be reconstructed in the same manner as discussed earlier (Ukhorskiy et al., 2002). The filter parameters were chosen the same as in the previous example. The NMSE in this case is higher than in the case of the system without noise, but is still very small −0.21. The high-dimensional component in both input and output time series leads to dramatic changes in the distribution of the number of singular values at each step of the reconstruction. Variations in M′ now fills the whole range from 1 to 2M, moreover its distribution function does not have extrema in this range, which indicates that these variations are not low dimensional.

The results of AL time series reconstruction with the use of local-linear ARMA filter (M = 20, NN = 40) are shown in Figure 5. The reconstructed AL follows the real data much closer than the output of the simple mean-field

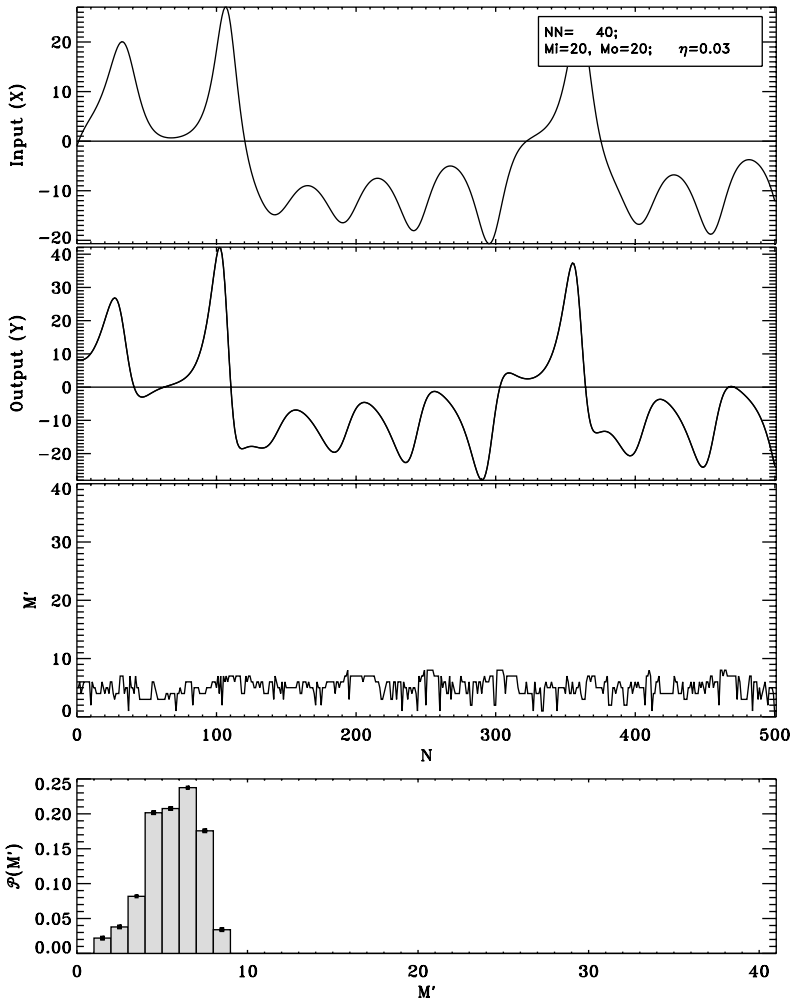


Figure 4. Reconstruction of Y component of synchronized Lorenz attractor from its driver, i.e., the X component. Reconstruction error is so small (NMSE = 0.03) that the difference between the reconstructed and original time series plotted on the second panel are indistinguishable. The distribution of singular values from the local singular spectrum that provide the best reconstruction is shown on the bottom panel (Ukhorskiy et al., 2002).

model. The NMSE has a very small of 0.18, which corresponds to a factor of four decrease compared to the long-term predictions. The singular values required for the best reconstruction at each step of the algorithm are shown in the bottom panels of Figure 5. As can be seen from the plot they are very analogous to M′ distribution function obtained for the contaminated Lorenz system, i.e. M′ values are distributed uniformly between 1 and 2M. Moreover, as in the case

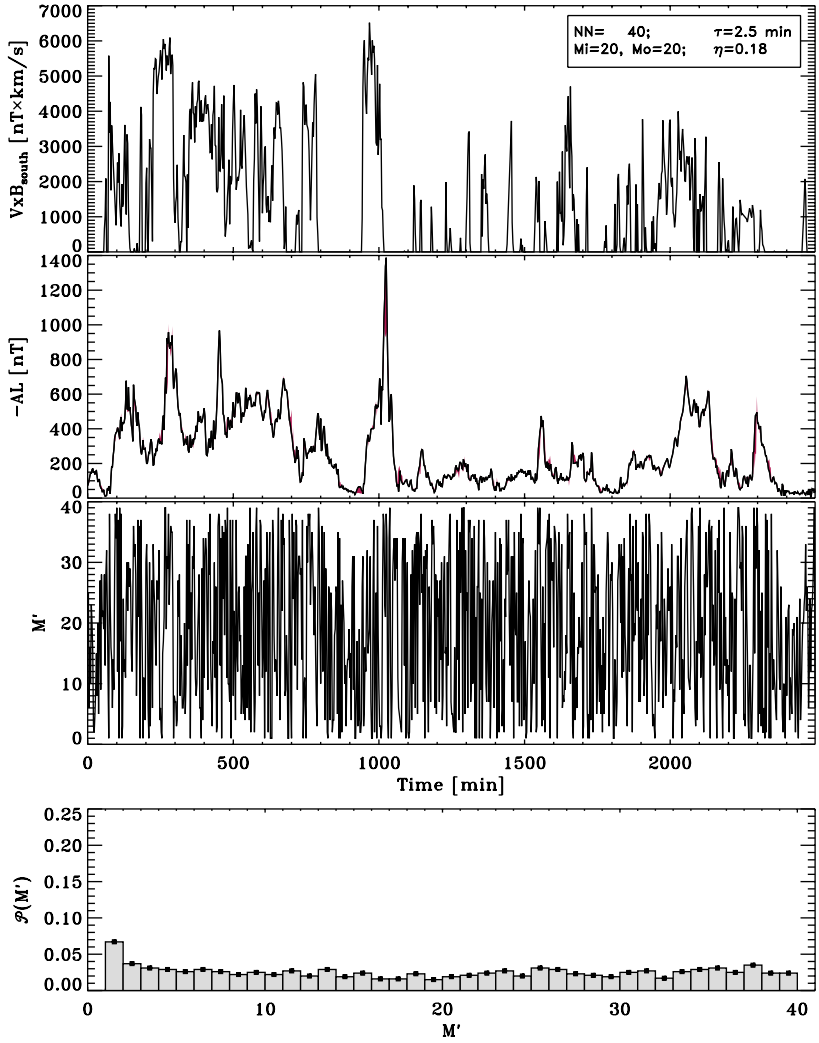


Figure 5. Reconstruction of AL time series in the 31st interval of Bargatze et al. (1985). The difference between the observed and predicted time series is shaded. The distribution of the singular values from the local singular spectrum that provide the best reconstruction is shown on the bottom panel (Ukhorskiy et al., 2002).

of Lorenz system this form of M′ distribution function holds the same even if the value of M is changed, no matter how big or small. This indicates that except for the low dimensional coherent component, which is well modeled by the mean-field approach, AL dynamics contains a substantial high dimensional portion, which is also multi-scale, i.e. it is build up by the perturbations of all possible scales. This also means that the reconstruction error should decrease when M is increased, since it extends the range of perturbation scales. These

results are very similar to those of the synchronized Lorenz system with 1/f noise (Ukhorskiy et al., 2002).

The distribution of singular eigenvalues, Figure 5, show that the linear terms of local-linear ARMA filters contain dynamical information that is not captured by the mean-field model. This component of magnetospheric dynamics is high dimensional and multi-scale in that it contains a wide range of perturbation scales, and its truncation leads to increase in prediction error. Inclusion of the proper number of singular values from the local spectrum can greatly improve the predictability of AL evolution. However, since the distribution of singular values required for the best predictions is uncertain and uniformly fills the whole input-output state space no matter what is its dimensionality, it is not clear yet what prescription will give the proper number of singular values at each prediction step.

4.1 Modeling the multiscale features with conditional probabilities

The embedding space constructed with the mean-field dimension provides the basis for data-derived models of the global dynamics. The solar wind-magnetosphere system as characterized by AL-VBs time series however does not correspond to a low dimensional dynamics on all interaction scales. As discussed above, the effective dimensionality of the system is a function of the interaction scale and on small scales the system is high dimensional. The multi-scale features not described by a low-dimensional model like local-linear filters require a statistical or probabilistic description. The probability distribution function (pdf) of AL, P(AL) computed for all solar wind conditions has a power-like shape (black curve in Figure 6), similar the power spectrum (Tsurutani et al., 1990). However, the magnetospheric dynamics is to a large extent driven by the solar wind and the probability of substorms (represented by AL) should be considered as functions of the solar wind, viz. should be described by a joint pdf, P(AL|SW). Such a Bayesian or conditional probability approach yields a decomposition of a power-law AL distribution function into a number of components with distinct maxima whose sum yields the power-law P(AL). The solar wind conditions determine the state of the system in the embedding space spanned by the principle components $\{I_1, I_2, \ldots, I_D\}$. Thus, the pdf of AL can be constructed in the form of $P = P(AL|\{I_1, I_2, \ldots, I_D\})$. The scatter plot of AL as a function of I_1, shown on the floor of Fig. 6, reveals a clear increase of the average magnitude of substorms with increase in the solar wind activity (Ukhorskiy et al., 2004). Consequently, the $P(AL|I_1)$ calculated for medium and strong solar wind activity have distinct maxima, as shown by the blue, red and yellow curves.

The conditional probability can be used to characterize the predictability of the magnetosphere. Using the embedding space constructed with the mean-field

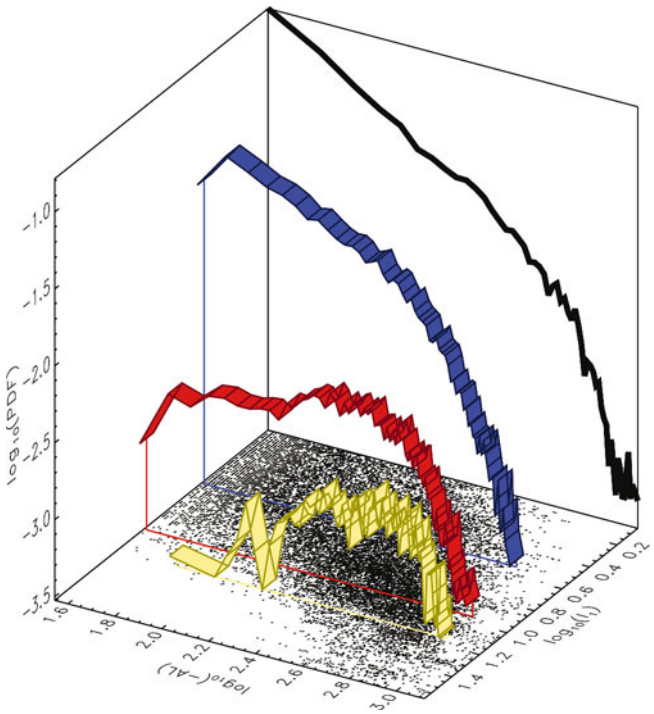


Figure 6. Power-law distribution of AL index and its constituents in the form of non-power-law conditional probabilities for chosen values of the solar wind input vBs (Ukhorskiy et al., 2004).

dimension, a predicted value AL_P of AL is obtained from an auto-regressive moving average (ARMA) filter and P(AL|AL_P)computed. These conditional probabilities provide a description of the statistical behavior not represented in the dynamical description, and has been used to construct a new model which combines the two aspects (Ukhorskiy et al., 2004). To predict the value of AL at the $(n+1)$ time step $AL_P(t_{n+1})$ is first computed using the standard deterministic model based on the local-linear filter and the known history of AL for $t < (t_{n+1} - T_p)$ and VB_S for $t \leq t_{n+1}$. T_p is the period for which the prediction is made. As discussed above $AL_P(t_{n+1})$ should be considered as an estimate of the average level of the substorm activity and the dynamical model often underestimates the AL peaks. This is where the statistical part of the model comes into play. Knowing $AL_P(t_{n+1})$ we can estimate the magnitude of AL deviation from the output of the deterministic model with the use of P(AL/$AL_P(t_{n+1})$). This function not only specifies the largest possible value of AL for a given AL_P, but also ranks it in terms of its probability. An example of AL predictions using the conditional probability approach is shown in Figure 7.

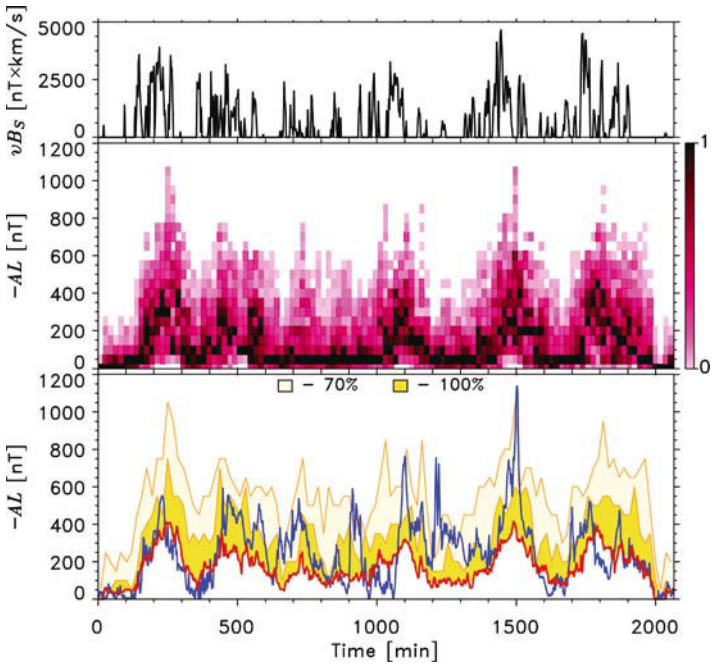


Figure 7. Predictions using the conditional probabilities. The solar wind input data (VB_S) is shown on the upper panel. The middle panel shows the distribution of the predicted AL for given solar wind conditions. In tis the solid black curve. The dynamical prediction (bold curve) yields the average trend. The curves with given percentages correspond to different values of $P(AL/AL_P)$ (Ukhorskiy et al., 2004).

4.2 Critical exponents of multiscale phenomena

The critical exponents reflecting scale-invariant properties of the magnetosphere has been computed using the analogy with phase transitions (Sharma et al., 2001; Sitnov et al., 2001). However, the non-equilibrium and non-stationary behavior of the system poses important challenges and it can be ameliorated by using the singular spectrum analysis which yields the principal components representing dynamics inherent in the data. Most of the classical critical exponents usually require for their evaluation, the coexistence curve (Stanley, 1971). However, a non-equilibrium and non-stationary system often evolves beyond the phase separation curve into a metastable state until it reaches the so called spinodal curve (Gunton et al., 1983). In the general case the transition from one state of the system to the other one takes place somewhere between these two curves mentioned above, and the classical definitions of the exponents may not be used. An exponent closely related to the classical critical exponent β has been computed from the data (Sitnov et al., 2001).

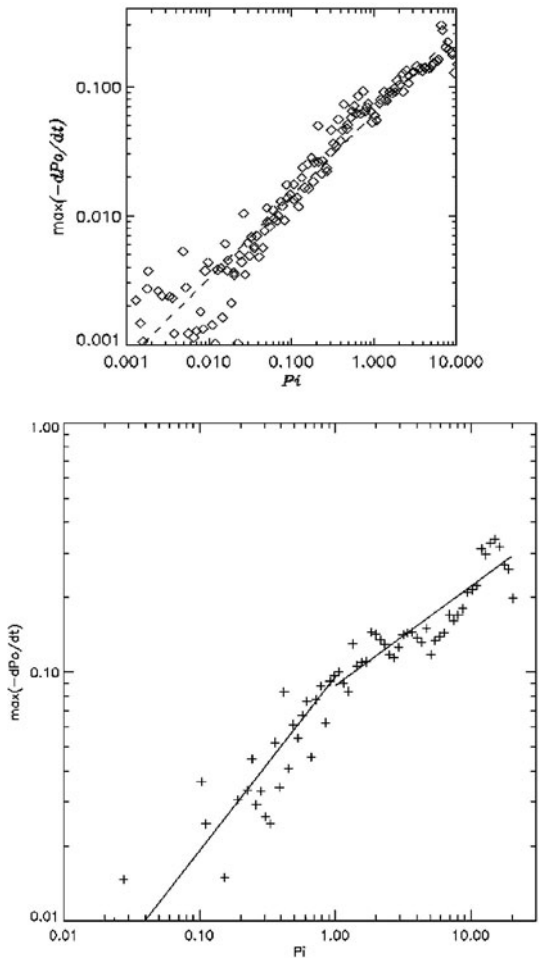


Figure 8. An analogue of the input-output critical exponent inferred from Bargatze et al. (1985) data set (top; Sitnov et al., 2001) and from the data of global MHD simulation (bottom; Shao et al., 2003).

Using the singular spectrum analysis the first three principal components (P_1, P_2, P_3) are obtained for the Bargatze et al. (1985) data set. The whole collection of data points in the plane (dP_2/dt, P_1) for the first 20 intervals of the set has two different envelopes, which are qualitatively different for positive and negative values of the parameter dP_2/dt, corresponding to expansion and recovery phases of substorms, respectively. While the envelope for the recovery phase is close to a straight line, that of the expansion phase resembles the typical non-analytical dependence, well known in the physics of phase transitions. Using a slight rotation of the eigenvectors corresponding to the principal components

P_1 and P_2, separating the axis P_1 into 136 bins on the logarithmical scale and finding the maximum of the dP_2/dt for each bin, we obtained the plot shown in the left panel of Figure 3.5. This plot implies the existence of a constant $\tilde{\beta}$ relating the P_1 and dP_2/dt for positive values of dP_2/dt and negative values of P_1:

$$\max\,(dP_2/dt) = C\,(-P_1)^{\tilde{\beta}\cdot} \tag{15}$$

with $\tilde{\beta} = 0.637 \pm 0.035$. Using the analogy with the mean field Ising model of phase transitions (Zeng and Zhang, 1998) one can show that this exponent is related to the classical β exponent relating P_1 and P_2 of the magnetosphere (Figure 8).

The multi-scale character of the substorm phenomenon is captured in the MHD simulations (Shao et al., 2003) as shown in Figure 8. One of its fundamental strengths of the MHD models is that it provides fully three-dimensional and temporal data of the plasma parameters and magnetic fields and flow velocities in a fully self-consistent manner. In view of the limited data based on satellite measurements along its trajectory, the MHD codes can provide a very complete set of surrogate data for the development of data-derived models. Since the code has detailed information about the nature of the turbulence, the more complete class of fluctuating quantities may be used as surrogate data for the study of multiscale phenomena. It should be emphasized here that similar to critical phenomena in phase transitions, the multiscale properties of the magnetosphere depend on the solar wind variables and the critical exponents characterize the relationship between input-output variables. The input-output critical exponent discussed above is distinct from the one derived from the magnetospheric data alone within the framework of self-organized criticality (Uritsky et al., 2003).

5. Conclusions

The magnetosphere exhibits both global and multi-scale features, and data-derived models have been used extensively to develop comprehensive models. The global scale phenomena have features of first-order phase transitions in the mean-field approximation, while the multi-scale phenomena are more akin to second-order transitions. The first-order transition picture of the magnetosphere has been studied using the principal components obtained from a singular spectrum analysis of the correlated VBs-AL data. The mean field picture of the magnetosphere obtained in terms of a center of mass of a set of nearest neighbors provide a good model of the global dynamics and can be used to make reliable predictions. The multiscale aspects on the other hand are modeled using conditional probability functions, analogous to the descriptions of such phenomena in statistical physics.

The new approach combining techniques of nonlinear dynamics and statistical physics is based on the recognition that such systems are neither clearly low dimensional nor completely random, but exhibit combinations of these two aspects. In the case of the solar wind—magnetosphere coupling such a combined approach yields an improved and effective tool for forecasting space weather. In a wider sense many complex systems exhibit large-scale organized behavior with scale-free properties over a wide range of spatial and temporal scales. This integrated approach presented here accounts for the dynamical and statistical properties and provides a new framework for modeling and prediction of such complex systems.

Acknowledgment

The research is supported by NSF grants ATM-0119196, ATM-0318629 and DMS-0417800.

References

Abarbanel, H. D., R. Brown, J. J. Sidorovich, T. S. Tsimring, The analysis of observed chaotic data in physical systems. *Rev. Mod. Phys., 65*, 1331, 1993.

Angelopoulos, V., T. Mukai, S. Kokubun, Evidence for intermittency in Earth's plasma sheet and implications for self-organized criticality, *Phys. Plasm.*, *6*, 4161, 1999.

Bargatze, L. F., D. N. Baker, R. L. McPherron and E. W. Hones, Magnetospheric impulse response for many levels of geomagnetic activity, *J. Geophys. Res., 90*, 6387, 1985.

Broomhead, D. S., and G. P. King, Extracting qualitative dynamics from experimental data, *Physica D, 20*, 217, 1986.

Casdagli, M., A dynamical approach to modeling inpt-output systems, in *Nonlinear Modeling and Forecasting*, Casdagli, M., and S. Eubank, editors, p. 265, Addison-Wesley, 1992.

Casdagli, M., Nonlinear prediction of chaotic time series, *Physica D*, *35*, 335, 1989.

Chang, T., Self-organized criticality, multi-fractal spectra, sporadic localized reconnections and intermittent turbulence in the magnetotail, *Phys. Plasm.*, *6*, 1999.

Chapman, S.C., N.W. Watkins, R.O. Dendy, P. Helander, G. Rowlands, A simple avalanche model as an analogue for magnetospheric activity, *Geophys. Res. Lett., 25*, 2397, 1998.

Consolini, G., M. F. Marcucci, and M. Candidi, Multifractal structure of auroral electrojet index data, *Phys. Rev. Lett., 76*, 4082, 1996.

Consolini, G., Sandpile cellular automata and magnetospheric dynamics, In: *Proceeding of the 8th GIFCO Conference, Cosmic Physics in the Year 2000:*

Scientific Perspectives and New Instrumentation, 8–10 April 1997, edited by S. Aiello et al., Soc. Ital. di Fis., Bologna, Italy, 1997.

Farmer, J. D., and J. J. Sidorowich, Predicting chaotic time series, *Phys. Rev. Lett*., 59, 845, 1987.

Freeman, M. P., N. W. Watkins, and D. J. Riley, Evidence for solar wind origin of the power law burst lifetime distribution of the AE indices, *Geophys. Res. Lett.*, *27*, 1087, 2000.

Gershenfeld, N. A., A. S. Weigend, The future of time series: Learning and understanding, in: *Time Series Prediction: Forecasting the Future and Understanding the Past*, Santa Fe Institute Studies in the Science of Complexity XV, A. S. Weigend and N. A. Gershenfeld, Eds. Addison-Wesley, Reading, MA, 1993.

Grassberger, P., and I. Procaccia, Measuring the strangeness of strange attractors, *Physica D*, 9, 189, 1983.

Gunton, J. D., M. S. Miguel, P. S. Sahni, The dynamics of first-order phase transitions, In: *Phase Transitions, Volume 8*, 267, Academic Press London, 1983.

Kantz, H., and T. Schrieber, *Nonlinear time series analysis,* Cambridge Univ. press., Cambridge, UK, 1997.

Kennel, M. B., and S. Isabell, Method to distinguish possible chaos from colored noise and to determine embedding parameters, *Phys. Rev. A*, *46*(6), 3111, 1992.

Klimas, A. J., D. Vassiliadis, D. A. Roberts, and D. N. Baker, The organized nonlinear dynamics of the magnetosphere, *J. Geophys. Res., 101*, 13089, 1996.

Lui, A. T. Y., A. C. Chapman, K. Liou, P. T. Newell, C. I. Meng, M. Brittnacher, and G. K. Parks, Is the dynamic of magnetosphere an avalanching system?, *Geophys. Res. Lett.*, *27*, 911, 2000.

Lyon, J. G., The Coupled solar wind—magnetosphere—ionosphere system, *Science* 288, 1987, 2000.

Ohtani, S., T. Higuchi, A. T. Lui, and K. Takahashi, Magnetic fluctuations associated with tail current disruption: Fractal analysis, *J. Geophys. Res.*, *100*, 19,135, 1995.

Ohtani, S., T. Higuchi, A. T. Lui, and K. Takahashi, AMPTE/CCE-SCATHA simultaneous observations of substorm associated magnetic fluctuations, *J. Geophys. Res.*, *103*, 4671, 1998.

Packard, N., J. Crutchfield, D. Farmer, R. Shaw, Geometry from a time series, *Phys. Rev. Lett.*, *45*, 712, 1980.

Pecora, L. M., T. L. Carroll, Synchronization in chaotic systems, *Phys. Rev. Lett.*, *64*, 821, 1990.

Price, C. P., and D. Prichard, The nonlinear response of the magnetosphere: 30 October 1978, *Geophys. Res. Lett.*, *20*, 771, 1993.

Sauer, T., J. A. Yorke, M. Casdagli, Embedology, *J. Stat. Phys.*, *65*, 579, 1991.

Sauer, T., Time series prediction by using delay coordinate embedding. in: *Time Series Prediction: Forecasting the Future and Understanding the Past*, Santa Fe Institute Studies in the Science of Complexity XV, A. S. Weigend and N. A. Gershenfeld, Eds. Addison-Wesley, Reading, MA, 1993.

Shao Xi, M. I. Sitnov, A. S. Sharma, P. N. Guzdar, K. Papadopoulos, C. C. Goodrich, G. M. Milikh, M. J. Wiltberger and J. G. Lyon, Phase transition-like behavior of substroms: Global MHD simulation results, *J. Geophys. Res*., *108(A1)*, 1037, doi:10.1029/2001JA009237, 2003.

Sharma, A. S., Reconstruction of phase space from time series data by singular spectrum analysis, in Physics of Space Plasmas, vol. 13, edited by T. Chang and J. R. Jasperse, p. 423, Mass. Inst. Technol. Cent. for Theor. Geo/Cosmo/Plasma Phys., Cambridge, 1993.

Sharma, A. S., Assessing the magnetosphere's nonlinear behavior: Its dimension is low, its predictability high (US National Report to IUGG, 1991–1994), *Rev. Geophys. Supple*., 33, pp. 645–650, 1995.

Sharma, A. S., Reconstruction of the global magnetospheric dynamics, in *Nonlinear Waves and Chaos in Plasmas,* T. Hada and H. Matsumoto, eds., Terra Scientific Pub., Tokyo, 1997.

Sharma, A. S., D. Vassiliadis, and K. Papadopoulos, Reconstruction of low dimensional magnetospheric dynamics by singular spectrum analysis, *Geophys. Res. Lett., 20*, 335, 1993.

Sharma, A. S., M. I. Sitnov, and K. Papadopoulos, Substorms as nonequilibrium transitions in the magnetosphere, *J. Atmos. Solar Terrest. Physics, 63*, 1399, 2001.

Siscoe, G. L., The magnetosphere: A union of independent parts. *EOS, Trans. AGU*, *72*, 494–497, 1991.

Sitnov, M. I., A. S. Sharma, K. Papadopoulos, D. Vassiliadis, J. A. Valdivia, A. J. Klimas, and D. N. Baker, Phase transition-like behaviour of the magnetosphere during substorms, *J. Geophys. Res.*, *105*, 12,955, 2000.

Sitnov, M. I., A. S. Sharma, K. Papadopoulos, D. Vassiliadis, Modeling substorm dynamics of the magnetosphere: From self-organization and self-criticality to nonequilibrium phase transitions, *Phys. Rev. E., 65*, 016116, 2001.

Stanley, H. E., *Introduction to Phase Transition and Critical Phenomena*, Oxford Univ. Press, New York, 1971.

Takalo, J., J. Timonen, H. Koskinen, Correlation dimension and affinity of AE data and bicolored noise, *Geophys. Res. Lett.*, *20*, 1527, 1993.

Takalo, J., J. Timonen, H. Koskinen, Properties of AE data and bicolored noise, *J. Geophys. Res.*, *99*, 13239, 1994.

Takalo, J., J. Timonen, A. J. Klimas, J. A. Valdivia, and D. Vassiliadis, Nonlinear energy dissipation in a cellular automation magnetotail model, *Geophys. Res. Lett, 26*, 1813, 1999.

Takens, F., Detecting strange attractors in fluid turbulence, *Dynamical Systems and Turbulence*, eds. D. Rand and L. S. Young, Springer, Berlin, 1981.

Tsurutani, B. T., M. Sugiura, T. Iyemori, B. E. Goldstein, W. D. Gonzalez, S. I. Akasofu, and E. J. Smith, The nonlinear response of AE to the IMF Bs driver: A spectral break at 5 hours, *Geophys. Res. Lett.*, *17*, 279, 1990.

Ukhorskiy, A. Y., M. I. Sitnov, A. S. Sharma, and K. Papadopoulos, Global and multiscale aspects of magnetospheric dynamics in local-linear filters, *J. Geophys. Res., 107(11),* 1369, doi:10.1029/2001JA009160, 2002.

Ukhorskiy, A. Y., M. I. Sitnov, A. S. Sharma, and K. Papadopoulos, Combining global and multiscale features in a description of the solar wind—magnetosphere coupling, *Ann. Geophys., 21,* 1913, 2003.

Ukhorskiy, A. Y., M. I. Sitnov, A. S. Sharma, and K. Papadopoulos, Global and multiscale features of solar wind—magnetosphere coupling: From modeling to forecasting, *Geophys. Res. Lett., 31*, L08802, 2004.

Uritsky V. M., A. J. Klimas, D. Vassiliadis, Evaluation of spreading critical exponents from the spatiotemporal evolution of emission regions in the nighttime aurora, Geophys. Res. Lett., 30 (15), 1813, doi:10.1029/2002GL016556, 2003.

Valdivia, J. A., A. S. Sharma and K. Papadopoulos, Prediction of magnetic storms with nonlinear dynamical models, *Geophys. Res. Lett., 23*, 2899, 1996.

Vassiliadis, D., A. S. Sharma, T. E. Eastman and K. Papadopoulos, Low dimensional chaos in magnetospheric activity from AE time series, *Geophys. Res. Lett., 17*, 1841, 1990.

Vassiliadis, D., A. J. Klimas, D. B. Baker, and D. A. Roberts, A description of the solar wind-magnetosphere coupling based on nonlinear filters, *J. Geophys. Res.*, *100*, 3495, 1995.

Vespignani, A., and S. Zapperi, How self-organized criticality works: A unified mean-field picture, *Phys. Rev. E*, *57*, 6345, 1998.

Zheng, B., M. Schulz, and S. Trimper, Deterministic equations of motion and dynamic critical phenomena, *Phys. Rev. Lett.*, *82*, 1891, 1999.

Chapter 7

LOW FREQUENCY MAGNETIC FLUCTUATIONS IN THE EARTH'S PLASMA SHEET

A. A. Petrukovich
Space Research Institute,
Russian Academy of Sciences,
Moscow, Russia
apetruko@iki.rssi.ru

Abstract: The paper reviews main observational features and suggested interpretations of magnetic field variations at frequencies below 10 Hz in the Earth's plasma sheet. Such wave activity is widely believed to be important for the magnetotail structure and substorm dynamics. This range contains tail flapping modes, MHD, ion cyclotron and lower hybrid range waves. As compared with the solar wind, the analysis is complicated by non-linearity of fluctuations, non-stationarity of the plasma sheet and relative shortness of data samples. The primary attention is devoted to discussion of the modern approach, considering fluctuations as the stochastic scale-invariant wave field. Basic analysis methods are illustrated with data examples from the Interball-1 mission.

1. Introduction

Ultimate goals of fluctuation studies in the Earth's plasma sheet might be formulated as: Do waves essentially contribute to the magnetotail structure or they are just unimportant "noise"? In particular, are substorm onsets triggered due to development of internal wave instabilities (Lui, 1996; Baker et al., 1996; Lyons, 1996)?

Favorably, the time scales of transient plasma sheet reconfigurations, MHD, ion cyclotron and lower hybrid range waves, that are of primary interest, are resolved by DC magnetic measurements, which are routinely and reliably taken with fluxgate magnetometers onboard almost every mission. Plasma measurements have much lower time resolution, while electric field data are less reliable and are not readily available.

A.S. Sharma and P.K. Kaw (eds.), Nonequilibrium Phenomena in Plasmas, 145–178.
© 2005 *Springer. Printed in the Netherlands.*

Therefore, despite the wide variety of plasma wave activity in the magnetotail (Treumann, 1999), this paper is concentrated on relatively low frequency (up to ∼10 Hz) magnetic fluctuations in the central nightside plasma sheet.

The main theoretical effort was initially directed to analysis of stability criteria of various wave modes in the plasma sheet environment. However, currently we are still far from any common viewpoint on the selection of the "responsible" instability and even on the general scenario of a substorm onset. Reliable identification of any candidate mode in the experimental data was not performed either. The state of debate can be assessed in the proceedings of the 4^{th} International Conference on Substorms (ICS-4, 1998).

In the recent years the alternative paradigm gained popularity. It is attempted to understand the magnetotail dynamics in the frame of the complex stochastic systems behavior, focusing on collective statistical properties of system parameters, rather than on specific physical properties of particular changes. The detailed description of the underlying theory and models can be found in the other papers of this volume and elsewhere (Klimas et al., 2000; Lui et al., 2000; Sitnov et al., 2001; Uritsky et al., 2002; Chang et al., 2003). Any model is finally justified, being compared with observable characteristics of the media, in our case, of local plasma sheet variations. The review concerns mainly this latter aspect, and describes the state of our experimental knowledge.

The similar approach received the wide attention in investigations of solar wind and interplanetary magnetic field (IMF) variations (Burlaga and Klein, 1986; Zelenyi and Milovanov, 1994), since they are probably the most convenient objects for in-situ turbulence studies in the space plasmas. Therefore we will also refer to some important results in this neighbor field of science.

It is convenient to consider magnetic fluctuations in three frequency ranges, selection of which is justified by a combination of theoretical considerations, data origin and results of the described research.

1. MHD range (<0.01 Hz). The proton cyclotron frequency is ∼0.15 Hz for 10 nT. The lowest frequency, accessible for the analysis, is mostly limited by the maximal length of a data sample, and is about ∼1 mHz. The main sources of activity in this range are magnetotail flapping motion (Sergeev et al., 1998) large-scale eddies, MHD wave modes such as kink or tearing (Daughton, 1999; Borovsky and Funsten, 2003).

2. Ion kinetic (IK) range (∼0.01–0.1 Hz) just below the proton cyclotron frequency. At these scales the non-adiabatic coupling of magnetic variations with the ion motion can not be neglected.

3. Lower hybrid frequency (LHF) range (∼0.1–10 Hz). LHF is ∼6.5 Hz for 10 nT. Waves in this range are believed to be the primary source of anomalous dissipation in the plasma sheet.

The paper is organized as follows. In the next section complications of fluctuation analysis in the plasma sheet are discussed. Section 3 reviews (mostly) experimental work. Section 4 is devoted to description of the analysis techniques and illustrations of the main results. Experimental findings are summarized in Section 5. Section 6 contains the review and discussion of the interpretation approaches.

The Interball-1 magnetic measurements were used for the data analysis. They were taken with the ASPI/MIF-M fluxgate magnetometer (Klimov et al., 1997). The primary sampling rate of the DC channel was 1 or 4 Hz, while the AC signal above >1 Hz was sampled with the 32 Hz rate. Thorough descriptions of this and other on-board instruments and presented events can be found in the relevant references.

2. Plasma Sheet Specifics and Complications

From the point of view of a data analyst, magnetic fluctuations in the plasma sheet is not the simplest object in the near-Earth plasma. We will briefly describe the plasma sheet structure, as far as it concerns the fluctuation activity, and discuss several complicating factors.

2.1 Magnetotail regions

The magnetic field in the magnetotail is a combination of the geomagnetic dipole and the cross-tail electric current contributions. In the neutral sheet, where the magnetic field reversal occurs, only weak vertical (normal to the sheet plane) component remains, and the plasma thermal pressure is higher than the magnetic pressure. With the increase of the downtail distance, the relative importance of the dipole component drops and the average normal component diminishes up to almost negligible values (less then 1 nT) in the distant tail.

In the near magnetotail (closer to Earth, than 10–15 R_E) the magnetic field normal component B_z is usually stable and large positive up to 10–15 nT. Hereafter the GSM frame of reference is used. Magnetic fluctuations are smaller, than the background field, besides relatively short substorm-associated activation periods, when strong Earthward plasma flows appear in the plasma sheet (Angelopoulos et al., 1992). Accompanying bursts of magnetic fluctuations and dipolarisation (B_z increase) are known as the current disruption phenomenon (Lui, 1996). It is not quite clear yet, whether a current disruption can occur in the absence of an Earthward flow. Figure 1 contains the example of magnetic field measurements in the near tail during the small substorm, recorded by the Interball-1 spacecraft (Petrukovich et al., 1998). Current disruption-related magnetic variations are one of the candidate processes on the role of the substorm onset driver.

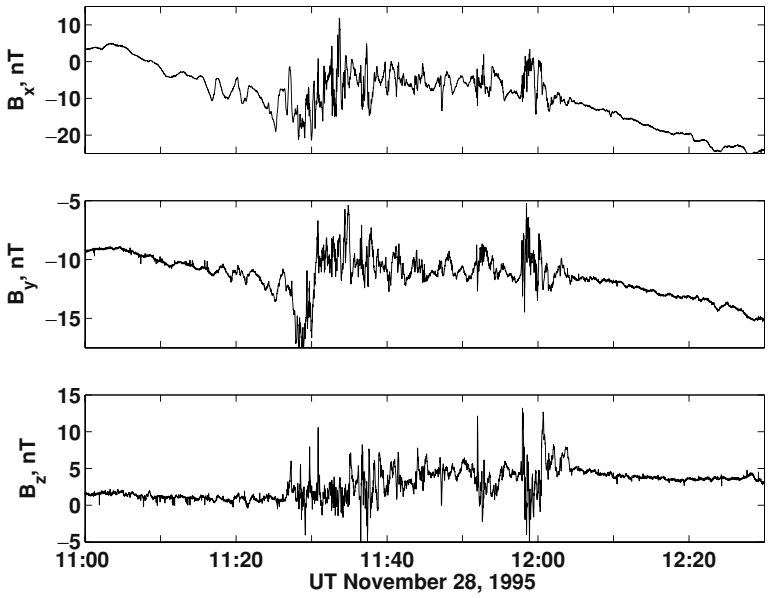


Figure 1. Example of the near-Earth tail fluctuations. Interball-1 observations, taken at (–11.5, –1.87, –2.48) R_E on November 28, 1995. Note the stretched (low B_z) quiet configuration before the substorm onset (at 11:26 UT) and the burst of fluctuations after it. Hereafter the GSM frame of reference is used.

In the distant tail (say, beyond 100 R_E) the average vertical magnetic component is smaller, than the permanently fluctuating component, and could be discerned only after averaging. The plasma is almost continuously convected tailward. Magnetotail flapping oscillations frequently move a spacecraft from the plasma sheet to the lobe and back. The example of the distant tail measurements by the Geotail spacecraft is in Figure 2 (Hoshino et al., 1994). The distant tail is supposed to have the passive role in substorms.

In the middle tail (lets limit ourselves with distances 15–30 R_E, where majority of the available data were taken), the plasma sheet dynamics is more complicated. The plasma sheet could be quiet with the quite large and close to dipolar B_z. Before a substorm the tail stretches, and the normal component B_z diminishes up to $\sim$1 nT (Baker et al., 1996). After a substorm onset or during intervals of the prolonged geomagnetic activity, magnetic fluctuation amplitudes are comparable with the background field, while plasma flows are sporadic and can be Earthward or tailward. Magnetic variations here are believed to be related (among other sources) to the reconnection process, which is another major candidate to act as the substorm driver. The Interball-1 example of the prolonged period of the inner plasma sheet observations, associated with southward IMF, is in Figure 3 (Yermolaev et al., 1999). Figure 4 presents

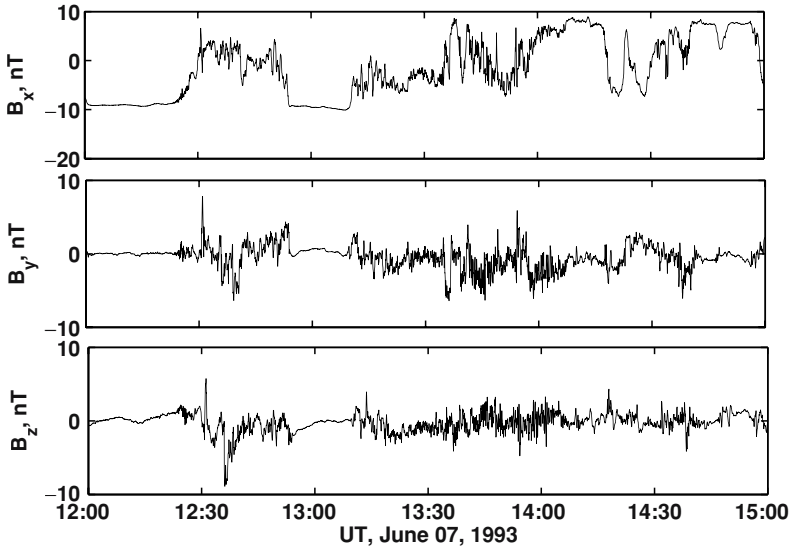


Figure 2. Example of magnetic variations in the distant tail. Geotail observations, taken at (−205, 15, 7) R_E (for 12 UT) on June 07, 1993.

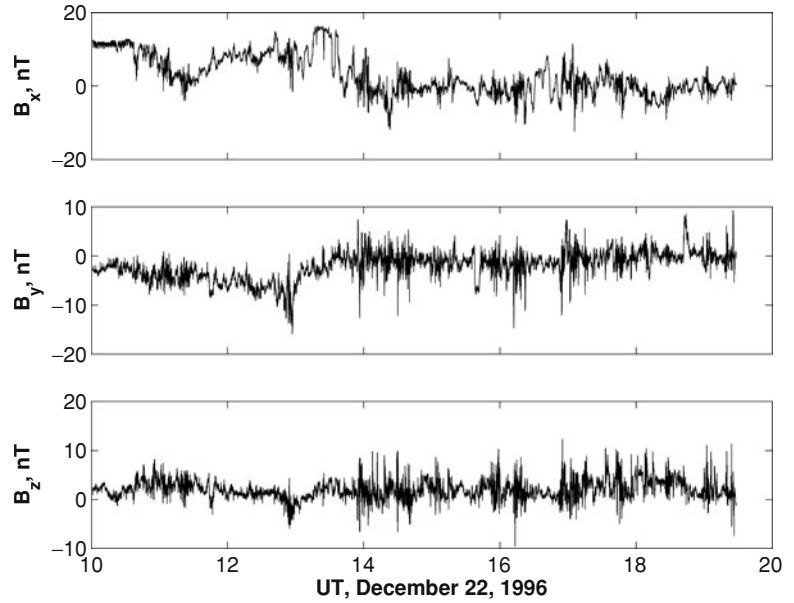


Figure 3. Example of the middle tail magnetic variations. Interball-Tail observations, taken at (–23.4, 12.2, –2.4) R_E (for 13 UT) on December 22, 1996.

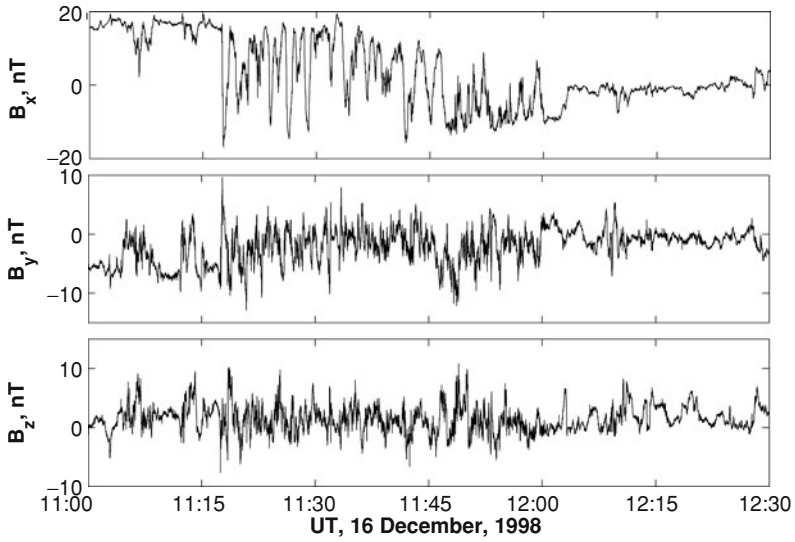


Figure 4. Example of the middle tail magnetic variations. Interball-Tail observations, taken at $(-24.12,\ 10.276\ -3.252\ )\ R_E$ (for 12 UT) on December 16, 1998.

another interesting and convenient for the fluctuations analysis interval, which was associated with the prolonged tailward plasma flowing.

2.2 Entanglement of spatial and temporal changes

Coupling between spatial and temporal changes, is the primary problem, common to all spacecraft observations in space plasmas. A spacecraft records the time sequence of measurements, while theories mostly operate with spatial characteristics, such as wavenumbers or boundary thicknesses. The magnetosphere is permanently "breathing" and its boundaries or plasma domains are entrained in a continuous motion, which is the order of magnitude faster, than typical spacecraft velocity (1–2 km/s) in the outer magnetosphere). Local variations or waves can have their own (phase) velocities. Therefore, changes, observed by a spacecraft, might be due to both a temporal evolution, and a spatial gradient, revealing itself via the relative motion.

The simplest and, probably, the only practically applicable approach is known as the Taylor hypothesis. It states, that the intrinsic time-dependence of (frozen-in) fluctuations can be neglected as they are convected past the spacecraft by the plasma bulk flow (Dudok de Wit and Krasnosel'skikh, 1996; Borovsky and Funsten, 2003). Equivalently, the frequency of a wave in the rest frame of reference should be much smaller, than the Doppler shift. For

sufficiently slow large-amplitude changes this approach seems to be quite reasonable. The multi-spacecraft observations could provide us with direct measurements of the relative velocity (in the approximation, that it is constant), or or one can use the measured plasma velocity, if it is high enough to be reliably detected. For frequencies above $\sim$0.01 Hz, characteristic for more local and faster variations, the degree of validity of this hypothesis in the plasma sheet remains largely unclear. Nevertheless, it is widely used and one has to hypothesize about convection velocity (see Sec. 6.1). At frequencies higher than 1 Hz, the Taylor hypothesis is most likely not applicable, since one can not neglect the wave's phase velocity.

2.3 Non-stationarity of the background and data selection

Geophysicists are not in the power to control conditions of their experiments, which rather depend on a combination of the solar wind input, unpredictable yet specifics of the magnetospheric dynamics, and satellite orbital motion. As a result, despite continuous data recording, number of events, suitable for the analysis, is usually quite limited.

Furthermore, when geomagnetic activity is high, the plasma sheet is quite variable: the characteristic time scale of a substorm is of the order of one hour (Aubry and McPherron, 1971), while more local bursty flows are typically several minutes long and can appear in sequences (Angelopoulos et al., 1992). After a rigorous selection of more or less stationary plasma sheet intervals (the formal prerequisite for any statistical data analysis), the remaining data segments might become considerably shorter than initial ones.

2.4 Non-linearity of variations

The next important aspect of magnetic fluctuations in the plasma sheet is their essential non-linearity: Effect of fluctuations on the background plasma can not be neglected. At very low frequencies, amplitudes of variations are often of the order of the lobe (maximal possible) magnetic field, so that the whole plasma sheet structure is distorted.

In the high-β plasma of the neutral sheet, where only the weak normal component of the background magnetic field remains, even energetically negligible magnetic fluctuations could be comparable with the ambient magnetic field. With a typical plasma sheet ion temperature of several keV, the proton cyclotron radius in 1-nT magnetic field is quite large ($\sim$1 R_E). Low-frequency fluctuations with the similar scale size distort trajectories of ions, carrying the cross-tail current. These topics will be discussed in more detail below.

3. Review of the Observations

3.1 General and frequency spectra studies

Low frequency magnetic fluctuations are in the focus of research in space plasma physics since the first spacecraft experiments. The early observations (Russell, 1972; Michalov et al., 1970) revealed a variety of magnetic wave phenomena in the magnetotail from ULF to ELF frequencies. In particular, were mentioned waves with periods of about 2 min, which cause the plasma sheet boundary and the neutral sheet to oscillate, waves from 0.1 to 1 Hz, detected in the plasma sheet during expansion, and sudden changes in the magnetic field magnitude and declination. The higher frequency was more intense 1–2 R_E away from the expected neutral sheet position and closer to Earth. The magnetic power spectral density (PSD) frequency spectra roughly followed the (negative) power law with respect to frequency: $P(f) \sim f^{-\alpha}$, with the power index $\alpha \sim 2$–2.5 (hereafter it will be called the PSD index) in the range 0.03–4 Hz, and were generally isotropic.

Later frequency power spectra of magnetic fluctuations, obtained by the AMPTE-IRM spacecraft were statistically surveyed in the ranges 0.1–25 mHz, 1–270 mHz, 0.03–8 Hz, and to determine their dependence on location, background magnetic field, plasma properties and geomagnetic indices (Bauer et al., 1995a; Bauer et al., 1995b).Average power spectra were increasing monotonically with decreasing frequency. PSD indices were equal to 2–2.5 between 0.03 and 2 Hz, and were below 1.5 for frequencies less than 1 mHz. Right-hand and left-hand polarization spectra were equal, while transverse fluctuations were much smaller than compressional fluctuations. The waves were enhanced during substorms and intervals with high-speed flows and strong changes in density and temperature. It was concluded, that magnetic variations in the range 0.15–1 mHz reflect substorm-related dynamics of the plasma sheet and flapping motions. In several occasions narrow-band oscillations with periods of 1–2 minutes and amplitudes comparable with the background field were observed in the vicinity of the neutral sheet several minutes before a substorm.

At the geostationary orbit (satellite GEOS-2) three types of field variations were detected during the substorm onset (Holter et al., 1995). Long period oscillations with periods of ∼300 s were interpreted as oscillations of entire field lines. Short period transient oscillations with periods 45–64 s were interpreted as wave modes, trapped in a current layer, and were observed only during the most active period of the breakup. The non-oscillatory sharp increase both of the parallel magnetic component and the energetic ion flux was attributed to the fast magnetosonic mode, transporting the breakup downtail.

The statistical investigation (Neagu et al., 2001; Neagu et al., 2002) of magnetic field and ion velocity fluctuations (quantified as the variance in 10-min

intervals) in the near Earth plasma sheet with the AMPTE-IRM measurements revealed no significant dependence on the down-tail distance or the distance from the neutral sheet. Amplitudes of field and velocity fluctuations were positively correlated with the geomagnetic activity (*AE* index). The strongest correlation was between velocity variations and velocity amplitudes. It was suggested finally, that geomagnetic activity is the global source of fluctuations and their possible local source is velocity shear instability.

In the distant magnetotail power laws in frequency spectra were investigated more quantitatively in terms of a turbulent magnetic reconnection process (Hoshino et al., 1994). The Geotail spacecraft magnetic measurements were used to compute spectra in the range 0.001–0.1 Hz. In spite of the differences among a wide variety of magnetic perturbations, the observed Fourier power spectral density of magnetic field could be approximated by a power law spectrum, which changed its slope around a turnover (kink) frequency ~0.04 Hz. The PSD indices were found to be between 2 and 3 for the higher frequency part and less than 2 for the lower frequency part. The kink frequency was close to the proton cyclotron frequency, but the data showed no preference to left or right polarization. The kink was less visible in the B_x component, but well in B_z. It was suggested, that the kink frequency corresponds to the most unstable tearing wavenumber. Higher frequencies are filled with the standard direct cascade process of the nonlinear wave coupling, while lower frequency waves are produced by the coalescence instability of magnetic islands (formed by tearing) and are finally evolving in the large scale plasmoids.

The complicated time history of different harmonics during the current disruption event was revealed with the help of the wavelet transform (Lui and Najmi, 1997). The low frequency signal appeared before the substorm onset, while in the course of the current disruption the burst of high-frequency oscillations and the subsequent cascade of power to lower frequencies were detected.

The wavelet technique was also used to analyze magnetic variations in the middle magnetotail during a particular substorm from 0.001 Hz to LHF range (Sigsbee et al., 2001). Large amplitude waves near the LHF were observed, when the large-scale gradients of density and magnetic field occurred. Fluctuations near the proton gyro-frequency and in the Pi-2 range were present throughout the event, but their amplitudes were small.

Magnetic noise bursts in the range around 1 Hz are generally suppressed near the neutral sheet, but are frequently observed during geomagnetically active times (Scarf et al., 1974; Gurnett et al., 1976; Coroniti et al., 1982). The properties of LHF range electromagnetic turbulence near the reconnection onset site were consistent with the numerical model of the lower hybrid drift instability

(Shinohara et al., 1998). Here the Geotail observations with the search-coil and the electric double probes were used.

Magnetic variations should generally be accompanied by electric field ones, but the latter are much harder to measure reliably. In the several rare observations the large amplitude waves up to 10–50 mV/m with periods from 0.1 s to tens of minutes were detected in the plasma sheet (Klimov et al., 1986; Cattell et al., 1986; Cattell and Moser, 1986; Cattell et al., 1994). When a perturbation electric field was added to the Tsyganenko magnetic field model with a convection electric field, significant modifications of the plasma convection pattern were found (Cattell et al., 1995).

The relatively low frequency MHD activity with periods above tens of seconds was analyzed in the bulk flow and magnetic field measurements of the ISEE-2 spacecraft (Borovsky et al., 1997). The plasma sheet was shown to be strongly turbulent, i.e., the flow was dominated by fluctuations, that are unpredictable, non-gaussian and larger, than mean velocities and fields. Flow velocities were typically subalfvenic. Autocorrelation times for velocities were of the order of 2 min, yielding the mixing length of about 2 R_E. Power frequency spectra of fluctuations had the power law form in the range from tens of minutes to minutes. The mean value of the velocity spectra slope was 1.5, and the magnetic field slope was 2.2. Significant non-gaussian tails of the plasma velocity probability distributions in the plasma sheet were revealed also in other investigations (Angelopoulos et al., 1999; Petrukovich and Yermolaev, 2002).

The new four-spacecraft Cluster mission provided the first possibility for a regular direct investigation of the spatial structure of variations below $\sim$0.01 Hz. It was found, that thickness of the plasma sheet at the downtail distance of about 20 R_E is typically 1–2 R_E, and might be even smaller than 1000 km during intervals of geomagnetic activity. Dominating B_x changes were interpreted in terms of sheet bifurcation, formation of vertical boundaries, kink and sausage-type sheet fluctuations, etc (Runov et al., 2003a; Runov et al., 2003b; Zhang et al., 2002; Sergeev et al., 2003; Volwerk et al., 2003; Nakamura et al., 2002).

3.2 Studies of scale-invariance

The power law form of frequency spectra is the characteristic signature of scale-invariant or fractal curves (Mandelbrot, 1977). The dependence of the curve length from the time step (time scale) τ will be hereafter called the length spectrum (LS). Initially this approach was used in the study of Voyager 2 solar wind magnetic measurements (Burlaga and Klein, 1986). The fractal dimension, determined as the index of the power law fit to the length spectrum, of the magnetic components in the range 10–100,000 s was $\sim 5/3$. See Sec. 4 for the method description.

A variation of the same method was used in the study of the Ampte-CCE magnetic field variations during the current disruption (Ohtani et al., 1995; Ohtani et al., 1998). Magnetic fluctuations were shown to have the characteristic timescale (kink in the spectra), of the order of several times the proton gyro-period. The detailed comparison between the length spectrum and the PSD spectrum was performed and the empirical relation between the kink values in frequency and time domains was established. The fractal dimension for the time scales smaller than several seconds was ∼1.3, while for the longer time scales it was ∼1.8 and very variable.

Scaling features of magnetic field during current disruption events were also investigated with the sign-singularity measure (Consolini and Lui, 1999; De Michelis et al., 1998). Different values of the scaling index (in the range 0.2–1) were obtained for the data before, during and after the disruption. In the course of disruption, the typical index was ∼0.7. These changes in scaling were interpreted as an indication of the reorganization phenomenon (symmetry breaking) and were discussed in the framework of the self-organized criticality and the 2^{nd} order phase transition. The similar approach of the first order structure function revealed indices ∼0.5–0.7 during the current disruption (Consolini and Lui, 2000). The complete review of the near-tail turbulence research, conducted in terms of current disruption and scale-invariance, was published by Lui, (2002).

The vast database of IMP-8 1.024 min averaged magnetic measurements in the solar wind and the magnetotail helped to determine, that the magnetic field increments are non-gaussian and self-affine (Kabin and Papitashvili, 1998). The fractal dimensions were 1.7 and 1.5, respectively. In the study of magnetic turbulence near the bow shock, observed by AMPTE/UKS spacecraft, it was discovered, that the PSD indices for both upstream and downstream regions were ∼4 above 1 Hz and ∼2.4 in the range 0.05–1 Hz (Dudok de Wit and Krasnosel'skikh, 1996).

3.3 Non-gaussianity and intermittency analysis

Variations in space plasmas are more complicated objects, than a simple scale-invariant (gaussian) model. More general turbulence models also account for sporadic appearance of small-scale non-gaussian irregularities in a signal, known as the intermittency phenomenon (sometimes the intermittence term is also used). The similar notion of the multifractality refers to objects, that are scale-invariant, but the scaling law varies locally. Infrequent events, forming the tails of distribution functions, might nevertheless carry a significant amount of energy. Intermittency analysis requires large data sets in order to collect reasonable statistics of rare events. The second-order moments (as Fourier power spectra) do not completely describe a non-gaussian signal and

the higher-order moments such that of structure functions must be investigated (Dudok de Wit and Krasnosel'skikh, 1996). For a non-intermittent signal, indices of the power law fits to structure functions of different order depend linearly on the order. Any deviation from the linearity is interpreted in terms of the non-zero intermittency.

In the first such investigation of interplanetary magnetic field and solar wind turbulence, significant intermittency on small scales was discovered (Burlaga, 1991). Comparison with the several theoretical models of intermittent media, have shown, that the P-model (the Cantor set) is the most adequate one. However, reliable distinction of the models is complicated, because insufficient statistics usually limits the analysis to structure functions below the 4*th*–6*th* orders, while significant differences between the models appear in scaling of structure functions only at orders $\sim$10 (Marsch and Tu, 1997). The interested reader can refer to several in-depth discussions of this issue in the studies of solar wind and geomagnetic variations (Dudok de Wit and Krasnosel'skikh, 1996; Horbury and Balogh, 1997; Marsch and Tu, 1997; Pagel and Balogh, 2003; Sorriso-Valvo et al., 1999; Carbone et al., 1996; Consolini and De Michelis, 1998 Consolini et al., 1996).

In the magnetotail the multifractal or intermittent nature of magnetic fluctuations was revealed during the three current disruption events (Lui, 2001). The expected difference (intermittency coefficient) between the measured fractal dimension of the intermittent signal and the real one was just 0.06–0.14, what is quite small in comparison with the typical variability of the observed spectral indices.

The alternative method of the local intermittence measure estimation (Vörös, 2000; Vörös et al., 2002) was used to analyze Cluster magnetic field observations in the plasma sheet (Vörös et al., 2003). As the Cluster spacecraft passed through different plasma regimes, physical processes exhibited non-stationary intermittence properties on MHD and small, possibly kinetic, scales. The observed transient nature of fluctuations (short data samples available) prevented the authors from selection of a model for the plasma sheet turbulence.

4. Analysis Methods and Examples

4.1 Frequency domain analysis

The main traditional method of time-series analysis is the frequency spectrum calculation, performed usually by means of the fast Fourier transform (Bendat and Piersol, 1986). Though this method is sometimes considered old-fashioned, it provides a lot of information about a signal and it's advantages and limitations are well understood.

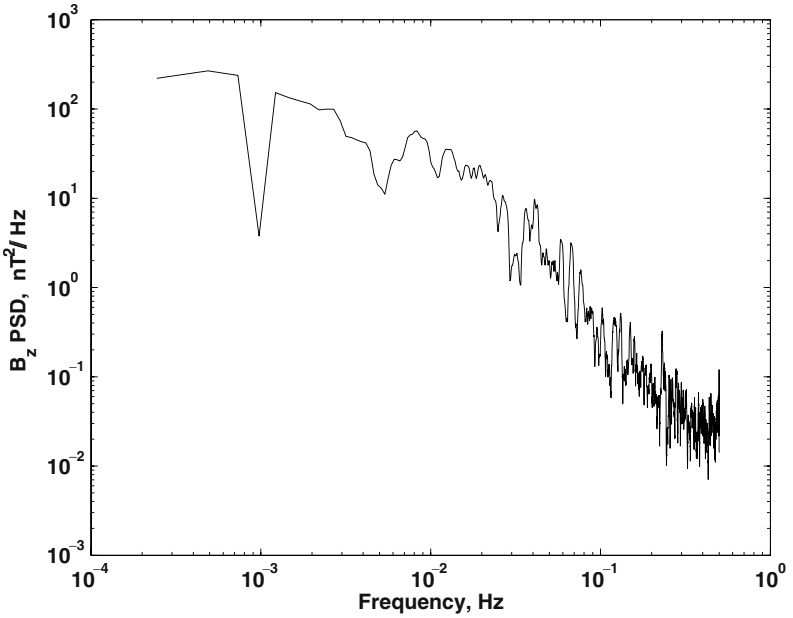


Figure 5. The sample PSD spectrum for B_z component, taken at ∼14 UT, December 22, 1996.

The typical PSD spectrum of the B_z plasma sheet variations is in Figure 5. Two dominating power law slopes are evident in the spectrum with the kink at ∼0.02 Hz. Several visible peaks are transient features and do not survive in the mean spectrum (Fig. 8, bottom). The flat part of the spectrum above 0.2–0.3 Hz (Fig.5) corresponds to the range, where the natural signal falls below the level of the measurement noise (Hoyng, 1976). B_z fluctuations are stronger, than the B_x ones, above ∼0.01 Hz, while the opposite is true at lower frequencies (Figure 6). Polarization features and level of coherency between components

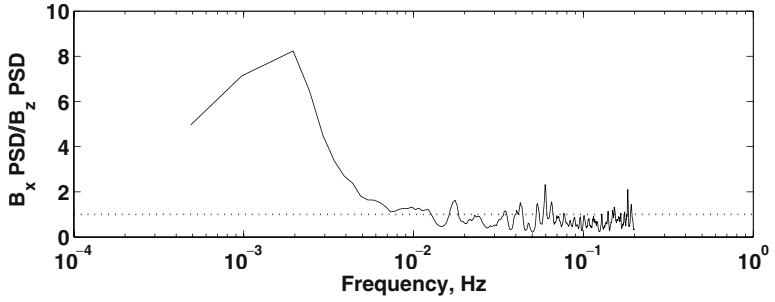


Figure 6. The ratio of fluctuation power in B_x and B_z components. Data as in Fig. 5.

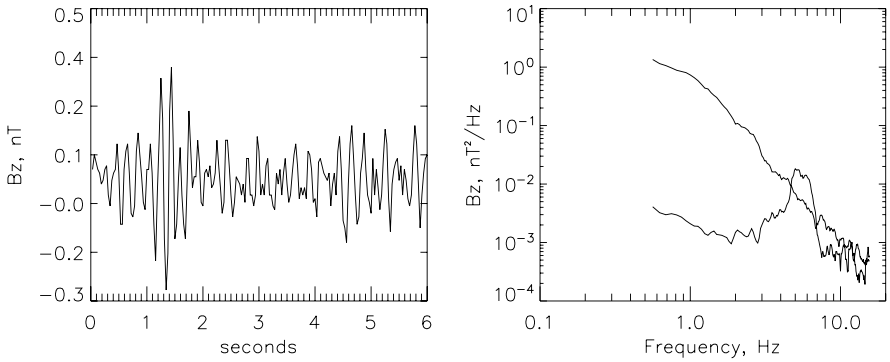


Figure 7. Example of the LHF range B_z wave packet (left) and its spectrum (right). The average spectrum is also shown (with the dominating power law slope). Data are from ∼14 UT, December 22, 1996.

at each frequency can be determined with a cross-spectral analysis. However, this method works best, when the studied signal contains more or less coherent waves, which is not the case with these data.

The kink frequency was found to be on average just higher than ∼0.01 Hz for all studied events in the Interball-1 data. In the upper frequency range 0.02–0.2 Hz, the PSD index was ∼1.7–2.6 with the average value of 2.23 (Fig. 8). At the lower frequencies, longer analysis intervals are necessary and the statistics is pourer. At 0.002–0.02 Hz indices were in the range 0.8–1.5 with the average value 0.88 (Fig. 8).

Sporadic bursts of higher frequency fluctuations above 1 Hz were spread over the studied intervals and were usually associated with strong magnetic field gradients and fast plasma flows. Maximal amplitudes of these waves were about a fraction of nT. The interesting example of a right hand polarized coherent wave packet is in the left panel of Figure 7. Its spectrum has the peak at 5–7 Hz, while the average spectrum has a clear power law slope with the index ∼3 (Figure 7, right panel).

4.2 Time domain analysis

The fractal dimension D of a planar curve (time sequence) is between 1 and 2. It is related with the PSD index α as $\alpha = 5 - 2D$ (Berry relation) (Mandelbrot, 1977). The length spectrum of a signal can be computed as $L(\tau) = \sum |B(t_k + \tau) - B(t_k)|$, where τ is the variable time step. For an ideal scale-invariant curve $L(\tau) = L_0 \tau^{1-D}$.

Ohtani et al. (1995) used the slightly different $L^*(\tau)$ expression with the additional τ in the denominator (so that $L^*(\tau) \sim \tau^{-D}$) and the special coefficient, adjusting for jumps in $L^*(\tau)$, when τ is comparable with the total length

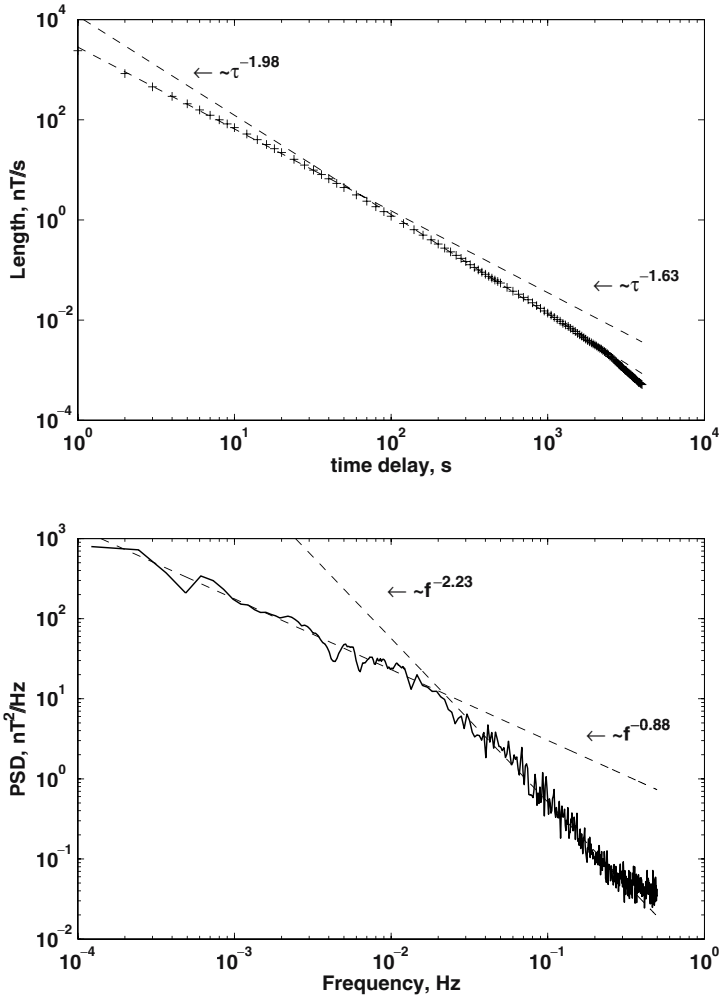


Figure 8. Comparison of the length spectrum and the average PSD spectrum of B_z for 11:00–19:30 UT, December 22, 1996. Fitted power law functions are shown by the dashed lines.

of the signal. When τ is larger, than the elementary time step (the sampling interval), there exist several subsets for the length computation (depending on the position of the first point) and it is advisable to average $L(\tau)$ over all such subsets. Hereafter for all examples $L^*(\tau)$ expression will be used.

In Figure 8 the average power spectrum is compared with the length spectrum. For the range 0.002–0.02 Hz and the corresponding range in the time scale, the PSD and LS indices were 0.88 and 1.98 respectively ($\alpha + 2D = 4.84$), while for the range 0.02–0.2 Hz they were 2.23 and 1.63 ($\alpha + 2D = 5.49$). The statistics of indices for the interval 0.02–0.2 Hz is in Figure 9. The scatter

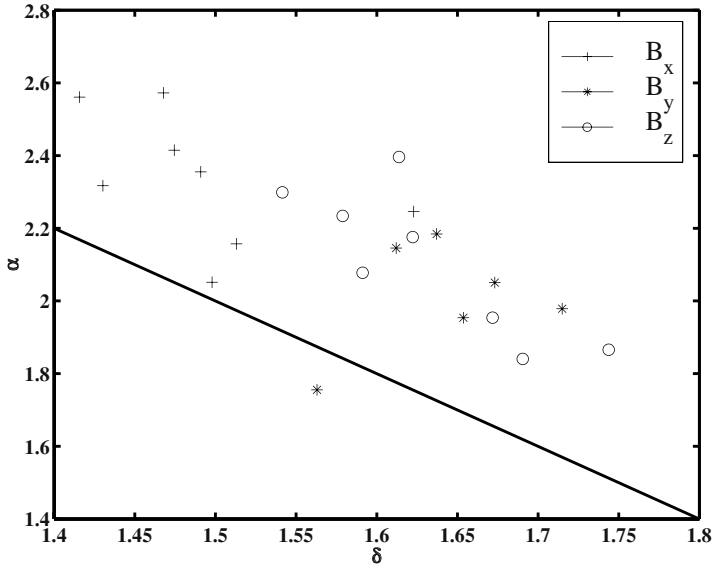


Figure 9. Statistics of PSD (α) and length spectra (δ) indices (0.02–0.2 Hz) of three magnetic components for December 16, 1998. The straight line is the expected Berry relation.

in D is comparable with the scatter in α, despite the fact, that the length spectra are visually less noisy, than the power spectra. Almost all points are displaced from the anticipated line $\alpha + 2D = 5$, but the dependence is similar. The statistical error of the $\alpha + 2D$ value is dominated by the error of the PSD index determination and is of the order of 0.4.

Such displacement in the $\alpha + 2D$ values in the frequency range 0.02–0.2 Hz is common for all studied plasma sheet intervals. In order to exclude possibility of the algorithm errors, the experimental data were substituted by the model fractional Brownian curve. In this test case, the error in D computation was less than 0.02 and $\alpha + 2D$ was equal to 5.02.

Ohtani et al. (1995) estimated the fractal dimension of magnetic field turbulence during the current disruption as >1.8 (their Fig. 4) at the time scales larger than several seconds, while our estimate is $\sim$1.6 (Fig. 8). This difference likely appeared due to the relatively short disruption activity duration in the former case, since estimates on the scales, close to the interval length, are less unreliable.

The several similar to $L(\tau)$ expressions are also in use. The structure function is defined as $S_q(\tau) = < |t_k + \tau) - B(t_k)|^q >$ (Dudok de Wit and Krasnosel'skikh, 1996). It is clear, that $S_1(\tau) \sim \tau \cdot L(\tau) \sim \tau^2 \cdot L^*(\tau)$. Unlike $L(\tau)$, $S_1(\tau)$ increases with τ (Fig. 11). The sign-singularity function (Ott et al., 1992; Consolini and Lui, 1999) was suggested as the alternative method

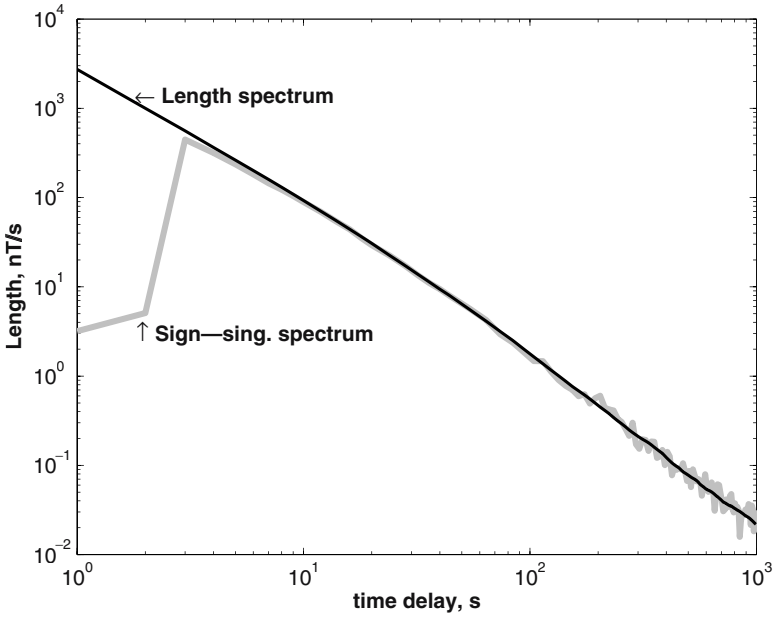


Figure 10. Comparison of the length spectrum and the sign-singularity spectrum (divided by the extra τ). Data are from ~14 UT, December 22, 1996.

of the scaling, but, in the particular numerical realization (Consolini and Lui, 1999), it is almost identical to the length spectrum. Indeed, the two curves, computed for the same interval (Fig. 10), nearly coincide without any adjusting factors after multiplying the sign-singularity expression by τ^{-1}. The scatter in the "sign-singularity" curve is due to the smaller number of differences, averaged at the each scale. The Holder exponent (Consolini and Lui, 2000) is more variant of essentially the same characteristic.

Taking into account the extra τ, the sign-singularity slope index ~0.7, determined for the current disruption interval (see Sec.3), is consistent with our estimate of the fractal dimension ~1.63. Low indices ~0.2–0.4, discovered before and after the disruption interval, are less easy to compare, but it appears, that, when magnetic field variations are small, most of the signal frequency range might be dominated by the instrument noise. The distinction between contributions of a natural signal and a noise in the time-domain length or sing-singularity spectra is not a trivial task, as compared with, e.g., the PSD spectra, for which the difference between noise and signals is almost obvious (see Sec 4.1).

4.3 Higher-order analysis

Distributions of magnetic field increments are often strongly non-gaussian on small scales (here 2 s) and almost gaussian on larger scales (1000 s)

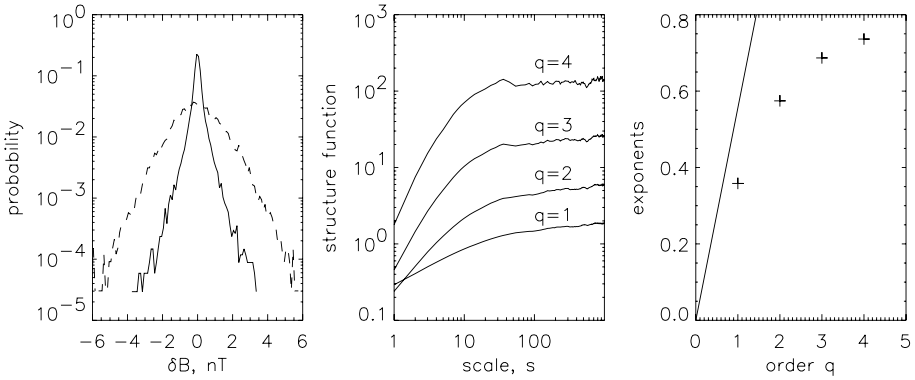


Figure 11. Left: Probability distributions of B_z magnetic field increments at scales 2 s (solid curve) and 1000 s (dashed curve). Note significant non-gaussian wings of the distribution for the smaller scale. Middle: A set of structure functions for the orders 1–4. Right: The scaling indices for time delay interval 1–20 s. The straight line is the expected dependence of indices for the gaussian signal. Data from 22 December, 1996, at 11:30–19 UT.

(Figure 11, left). One can quantify the degree of non-gaussianity (intermittency) via the scaling of higher-order structure functions (Figure 11, middle) (Dudok de Wit and Krasnosel'skikh, 1996; Dudok de Wit, 2003). For a gaussian signal, indices of the power law fits to structure functions are a linear function of the order and the fractal dimension. The sequence of slope indices (Figure 11, right), computed for $\tau = 1$–20 s, definitely departs from the linear dependence. The statistical reliability of higher-order structure functions might be estimated following Dudok de Wit and Krasnosel'skikh (1996). For this particular case it was found, that functions above the 4th order are not reliable.

Several models of intermittent signals are known from the literature (Marsch and Tu, 1997). However, it appears, that most of space plasma data sets (including the longest solar wind ones) are not long enough to perform a statistically significant selection between available models. Therefore we will refrain from the further analysis and just mention several alternative techniques.

Alternative method of intermittency (or multifractality) estimates, known as the large deviation multifractal spectrum (LDMS), was used to process a number of geophysical data sets (Vörös, 2000). The strength of local burstiness a, computed as the local coarse grain Holder exponent (in some range of spatial scales), has certain distribution of values $F(a)$ over the wave field in a case of an intermittent signal. The LDMS method estimates $F(a)$, basing on statistical kernels (Vehel and Vojak, 1998). Wider is $F(a)$, which has the concave shape, more intermittent is the signal. The local intermittence measure is introduced as the total area under the $F(a)$ graph. The MATLAB-based FRACLAB package is available via the INTERNET as the programming tool for this method.

Compatibility of this intermittency measure with the structure function approach remains unclear for the general reader. There exists no unified approach for estimation of the intermittency or multifractality measure $F(a)$ (Vehel and Vojak, 1998; Vörös, 2000). The scaling of structure functions allows us to characterize multifractality as $F_l(a)$ through the Legendre transform (Consolini et al., 1996). A geometrical description of the multifractal measure is based on the estimation of the Hausdorf dimensions $F_h(a)$ of subsets, having the same Holder exponents. The LDMS method provides $F_g(a)$. Generally, F_h, F_l, and F_g are not equivalent and not equal.

In the frequency domain, the higher-order technique implies calculations of bi- and tri-spectra. However, this method is computationally expensive and its results are usually interpreted in terms of wave-wave processes, rather than chaotic self-affine structures (Dudok de Wit and Krasnosel'skikh, 1995; Dudok de Wit, 2003).

4.4 Wavelet techniques

The wavelet technique (Wavelets in Geophysics, 1994) extends the researcher's capabilities in the frequency domain analysis. Dudok de Wit (2003) advocated the usage of the wavelet transform for the robust identification of power laws in frequency spectra, as the method, in his view, superior to the traditional Fourier transform.

Less evident are advantages of the wavelet technique in the time domain analysis. Veltri and Mangeney (1999) applied wavelets for the automation of structure function computation and further processing. Alternatively, it was suggested to filter the signal with the wavelets before calculation of a structure function in order to enhance poor spectral sensitivity of the time-domain analysis (Dudok de Wit and Krasnosel'skikh, 1996).

4.5 Summary for techniques

The Fourier transform proved to be the powerful and well-understood method. It can be recommended as the first step in almost any data analysis. The wavelet algorithms are useful to track dynamics of nonstationary signals.

The structure function is used in investigations of more chaotic signals for determination of their scaling properties (fractal dimension). Length spectrum or sign-singularity function are actually variations of the first order structure function.

The more general intermittency or multifractal analyses can be applied, when the signal is non-gaussian. There exists several approaches to quantification of intermittency, selection between which is not clear yet. Typical length of data samples in the plasma sheet (available statistics) is marginally sufficient for the higher-order analysis and obstructs comparisons with the intermittency models.

5. Summary of Experimental Findings

Major observational results, obtained with the data of ISEE-2, OGO-5, AMPTE-IRM, AMPTE-CCE, Geotail, Interball-1 missions, appear to be quite consistent.

1. Fluctuations are characteristic to all regions of the plasma sheet and enhance during periods of the geomagnetic activity and in association with the local intensifications such as plasma flows.

2. Thorough investigations didn't reveal any stable presence of coherent structures or peaks in the frequency spectra, certain polarization characteristics, or any other signatures, which allow to distinguish wave modes. Signals can be rather considered stochastic. Nevertheless, several occasional observations of quasi-periodic oscillations with frequencies around 0.01 Hz before substorm onsets were reported.

3. Sporadic bursts of the LHF range fluctuations appear to be related with larger scale activity (plasma flows and strong gradients) and have amplitudes typically below 1 nT.

4. Power spectral density spectra generally follow power laws with two kink frequencies. At frequencies below 0.01 Hz, the PSD index is $\sim$1; in the range $\sim$0.01–0.2 Hz, indices are typically around 2.2; above the second kink frequency $\sim$0.2 Hz, spectra are steeper (the index is $\sim$2.4–3). Indices vary significantly from spectrum to spectrum throughout an event. B_z variations are 30% higher, than that of B_x above 0.01 Hz. The opposite is true below 0.01 Hz. Power law in the spectrum is a signature of a scale-invariant (fractal) wave field. At time scales longer than $\sim$100 s, the fractal dimension is close to 2 (1.98), while at shorter scales it is $\sim$1.6.

5. Stable deviations from the Berry relation between PSD index and fractal dimension are discovered in the frequency range 0.02–0.2 Hz.

6. Magnetic field fluctuations are non-gaussian or intermittent on small scales. However, reliable quantitative estimation of intermittency proved to be not possible so far.

7. Scale invariance and intermittency features of plasma sheet variations are similar to properties of solar wind variations. The fractal dimension of interplanetary magnetic field was found to be 5/3 in the range 10–1000 s. Near-bow shock variations had the PSD index 2.4 below 0.5 Hz, and higher than 3 above 0.5 Hz.

Relatively few results and little attention to the LHF range magnetic variations are partially due to typical configuration of a magnetic experiment. In the

most of past missions, this frequency range falls between the ranges of DC fluxgate and AC search-coil magnetometers. Though instrument ranges formally overlap, the amplitude and/or phase of a signal are distorted at the edges of the passbands due to filtering or frequency aliasing, and data merging becomes a non-trivial task.

Finally, for the reliable recognition of scale-invariance, the same scaling law (and the same physics behind) should hold on a sufficiently wide range of scales. For example, the analysis of the solar wind variations reveals the same scaling for several orders of magnitude (Burlaga and Klein, 1986). The plasma sheet medium proved to be a much more complicated object, and the range of both temporal (measured) and relevant spatial scales, on which variations are scale-invariant, is usually limited to one order of magnitude or even less.

6. Approaches to Interpretation

6.1 Ion kinetic range

In the range 0.01–0.1 Hz, containing the ion cyclotron frequency, ion kinetic effects should play a role in formation of magnetic variations. Milovanov et al., (1996) suggested the self-consistent model of magnetic field structures in the distant tail, which is based on the concepts of fractal geometry. Ions, carrying the cross-tail electric current in the neutral sheet with weak normal magnetic field (typical to the distant tail), have large ion cyclotron radii and self-consistently interact with the background magnetic field to form the self-similar hierarchical structure of magnetic field clumps and voids, filled with current filaments. Through scaling of basic equations, the fractal dimension of such a wave field (dominated by B_z fluctuations) was estimated as $5/3$.

The spatial range of this network is supposed to be approximately between 8000 and 400 km. These scales were estimated as the minimum wavelength of the tearing, possible in the current sheet (at which MHD waves start to dominate) and the size of an elementary magnetic obstacle (minimal scale to which bulk of ions is sensitive) respectively. The main addition to the current is due to the particles with cyclotron radii between these two values (ion cyclotron radius for the typical plasma sheet temperature falls in this range). Colder particles are effectively trapped in small magnetic islands, while the hot ones do not sense the field geometry. Later this theory was extended to explain the near tail with the stretched magnetic field configuration (Milovanov et al., 2001a; Milovanov et al., 2001b). Correspondingly, two kinks in the power spectrum are predicted at $\sim$0.01 Hz and $\sim$0.1 Hz, using typical plasma bulk velocity of about 200 km/s for the distant tail. In the near tail bulk velocity could be of the order of 50 km/s, but typical scales are shorter, so that the kink frequencies are

approximately the same. (See Sec. 2.2 for the discussion of the time-to-space conversion problem.)

The PSD indices were predicted to be equal to 1 in the low frequency part, $7/3$—between the two kinks, and 3—above 0.1 Hz (Zelenyi et al., 1998). These values are consistent with the experimental findings. Most commonly mentioned as possible alternatives, the Kolmogorov and Kraichnan scaling laws (Dudok de Wit and Krasnosel'skikh, 1996) predict PSD indices $5/3$ and $3/2$ respectively.

The topological model of the magnetotail current sheet formation was extended to explain also the substorm phenomenon (Milovanov et al., 2001a; Milovanov et al., 2001b). It was suggested, that accumulation of free energy in the tail before a substorm leads to increase of the cross-tail current density and (self-consistently) of magnetic field fluctuations. The current system becomes more coarse and less brunched to allow for more current. Trying to find free corridors over the structures in the current sheet plane, some current filaments start to rise over the plane. If the escaping filaments cannot be brought back by "restoring" forces, inflationary stage (identified with the substorm onset) starts with a birth of the large-scale 3D current system. The substorm therefore might be treated as a structural catastrophe of topological origin, equivalent to a second-order phase transition between 2D and 3D current geometries.

The suggested picture of self-consistent magnetic field and electric current fluctuations is not an alternative to the standard approach, considering linear development of particular plasma wave modes. It should be rather understood as the common nonlinear stage of plasma wave activity, which depends not on initial conditions but rather on general properties of the system. The nonlinear regime should be quite close, since fluctuations promptly become comparable with the small normal magnetic component.

6.2 MHD range

At frequencies smaller than $\sim$0.01 Hz, well below the proton cyclotron frequency, most of variations can be considered in the frame of MHD approximation. The lower frequency boundary of the range under study is limited by the maximal possible time of an observation and is of the order of 1000 s or 0.001 Hz.

Some variations might be attributed to plasma sheet flapping (Sergeev et al., 1998), which is usually understood as vertical bulk motion of the plasma sheet. Tearing, kink or other large-scale plasma modes (Daughton, 1999; Borovsky and Funsten, 2003) are believed to develop in the upper part of this frequency range and are often considered as causes of a substorm onset. Almost monochromatic oscillations sometimes observed right prior some substorm onsets might be a signature of such instability development. Significant progress

in this problem could be achieved with the multi point Cluster measurements as soon as a case, suitable for the analysis, will be registered.

Borovsky et al., (1997) determined, that the scale lengths of variations below ~0.01 Hz are about 1–2 R_E, while the typical plasma sheet thickness was supposed to be about 6 R_E. In a later publication it was suggested, that this MHD turbulence appears to be the turbulence of eddies (frozen-in structures), rather than that of alfven or other MHD modes (Borovsky and Funsten, 2003). It was mentioned, that since one can not neglect the finite size of the magnetotail, the turbulence is best described as turbulence in a box or in a wake. Finally, unlike usual models of inertial turbulence, the dissipation is supposed to occur over all wavenumbers, and only the limited range of scales exists, where the scale-invariant dynamics occurs. Among most likely drivers of turbulence, velocity shear in bursty flows, LLBL flow, and flows in eddies were named.

According to Cluster observations at downtail distances of ~20 R_E, typical thickness of the plasma sheet is just 1–2 R_E and might even reach 1000 km before a substorm. The spatial structure of magnetic variations turned out to be quite complicated and was interpreted as the modification of the plasma sheet geometry. Therefore the low-frequency activity might be often best understood not as plasma variations in a box, but rather as variations of a plasma box. The suggested approach is consistent with results of our fluctuation analysis, showing, that B_x variations below ~0.01 Hz are on average stronger, than B_z ones. Indeed, B_x changes should be quite large, if in the course of a variation, spacecraft moves (in relative motion) are comparable with the plasma sheet scale size. Since the Cluster inter-spacecraft separation and time resolution of measurements are almost optimal for observations in this frequency range, the single-event studies are probably the most promising way to understand mechanisms of low frequency variations in the middle tail.

Approach of a wake turbulence in the thick plasma sheet (Borovsky and Funsten, 2003) seems to be more applicable in the near tail and at the tail flanks, where the tail thickness is larger on average, or during intervals of enhanced magnetospheric convection, when the the mid-tail plasma sheet is also quite variable and thick (Sergeev et al., 2001).

6.3 LHF range

Waves with frequencies above a fraction of Hz (in our case 0.1–10 Hz) are believed to be the main local source of anomalous resistivity in larger-scale activations such as reconnection (e.g., (Shinohara et al., 1998)) or current disruption (Lui, 1996). However, the general agreement among theorists on the role of different wave modes is still not reached (Sadovsky and Galeev 2001). Since with the single-point spacecraft magnetic measurements direct determination of a wavelength is impossible, the wave's contribution to resistivity can be only

estimated via indirect considerations. Unfortunately, relatively low amplitudes and sporadic appearance together with the "unlucky" frequency range, which happened to fall between typical measurement ranges of DC and AC magnetic field instruments, prevented from systematic investigations of such fluctuations in the magnetotail. In a rare quantitative study (Shinohara et al., 1998) associated fluctuations with the lower hybrid waves, but it was concluded, that their amplitudes are well below the level, necessary to provide sufficient resistivity.

6.4 Turbulence and the sheet thickness

Prolonged plasma sheet observations with sustained high level of fluctuations (such as in Fig. 2,3,4) are apparently instances of the relatively thick plasma sheet. Indeed, the 2000 km wide sheet will be crossed by a spacecraft (with a typical flapping speed of about 20 km/s) just in 100 s. Continuous observation of the order of one hour, therefore likely corresponds to a sheet with at least $\sim$20,000 km thickness. The distant magnetotail plasma sheet, which is always turbulent, might be several R_E thick (Hoshino et al., 1996). Near the Earth, turbulent sheet states are usually associated with continuous southward IMF and high geomagnetic activity.

The effect of fluctuations on the plasma sheet state was investigated numerically (Veltri et al., 1998; Greco et al., 2002). The model included the stretched background magnetic field and the power law-distributed magnetic fluctuations. Ions were introduced as test-particles. It was found, that turbulence is very effective in forming the stationary structure of the plasma sheet. The increase in the amplitude of fluctuation field widens the plasma sheet, while the increase of the normal magnetic component causes opposite effect.

The thick fluctuating sheet is not fully consistent with the 2D fractal sheet model (Milovanov et al., 1996). The later development of this model (Milovanov et al., 2001a) predicts formation of the 3D layer, when the current becomes too strong to pass through a wave field in 2D. Such a change in topology might be probably achieved, when amplitude and/or density of fluctuations are enhanced for some reason, for example, due to appearance of bursty plasma flows.

On the other hand, the thin stretched plasma sheet in the middle tail is usually rather quiet in terms of fluctuations. This could happen, because the spacecraft crosses the thin sheet too fast to detect enough variations, that usually fall into the 0.01 Hz range. Therefore, the existence of almost planar layer, filled with fluctuations (Milovanov et al., 1996), is not excluded even in the case of a thin quiet sheet, but this conclusion is hard to confirm observationally.

In the turbulent plasma sheet, the turbulent diffusion might be quite strong and comparable with the stationary convection. In such a case, the plasma

sheet thickness is determined by a balance of these two factors (Antonova and Ovchinnikov, 1999).

6.5 Scale-invariance, intermittency and criticality

Recently, the scale-invariant and intermittent nature of the magnetospheric response and, in particular, of the plasma sheet magnetic fluctuations was explained in terms of infinite-dimensional nonlinear systems near the state of forced or self-organized criticality: "... observed criticality can be due to the self-similarity of the accessible meta-stable configurations dealing with the topological complexity and that BBFs and sporadic behavior in the *AE* index may be connected to dynamical topological phase transitions among these meta-stable states." (Consolini and Chang, 2001; Chang, 1999). Similarly, Lui (2002) interpreted appearance of variations in the course of the current disruption, as the phase transition from an energy excess state to a new relaxed state, during which the system is in the self-critical state.

However, the leap from the immediate characteristics of turbulence (scale-invariance and intermittency) to more general system properties, such as criticality and phase transition, appears to be not obvious (Dudok de Wit, 2003; Consolini and Chang, 2001). The presence of the scale-invariance does not imply, that the system is necessarily in a critical (meta-stable) or transitional state.

The concrete mechanism of a phase transition in the magnetotail, suggested by Milovanov et al. (2001a), is fully applicable only to one class of fluctuation phenomena—"current disruption" (transient burst of variations in the otherwise quiet plasma sheet at the substorm onset). It is not quite clear, how the criticality paradigm could be used in the distant magnetotail or in the solar wind, where fluctuations are permanent. Indeed, spacecraft observations revealed similar scaling properties of plasma fluctuations in quite different regions (plasma sheet, solar wind etc), and one might even suggest, that scale-invariance and non-gaussianity (on certain scales) are permanent features of collisionless plasma. Statistically reliable estimates of intermittency properties were not obtained up to now. In the absence of the solid experimental basis, researchers have to stay with more qualitative arguments.

7. Conclusions

Low frequency magnetic field fluctuations in the plasma sheet received considerable attention, because reliable DC magnetic measurements were available, and the topic seemed to be quite important for the magnetospheric substorm studies. Interpretation of the observed wave field, however, turned out to be a challenging task due to a number of complications, such as entangling of spatial and temporal variations, non-adiabatic coupling of variations with

the cross-tail current, finite spatial size of the plasma sheet, non-stationarity of plasma background.

The linear approach, based on the paradigms of wave modes, anomalous resistivity, instabilities, seemed to be ineffective in describing structured and dynamical magnetotail processes. The interest during the recent years was focussed on the alternative hypotheses, addressing to properties of chaotic and complex systems. Analysis of observational data revealed the scale-invariance and non-gaussianity (intermittency) of fluctuations. Scaling indices of spectra could be successfully explained in the frame of the topological approach to formation of the cross-tail current. Quantitative assessment of more refined characteristics, such as intermittency, however, is complicated by high variability of the spectra and relative shortness of the available data samples.

One may point finally several promising directions of experimental studies. New Cluster multi-spacecraft data could provide the observational basis for a breakthrough in the understanding of low-frequency MHD variations and plasma sheet flapping modes. Waves in the lower hybrid frequency range are "responsible" for local dissipation at reconnection zones and definitely deserve more attention. The better theoretical and experimental insight in the nature of scale-invariance and intermittency in space plasmas appears to be essential.

Acknowledgments

The author is grateful to L. Zelenyi and A. Milovanov for useful discussions and initial motivation to this investigation, and to Z. Vörös for comments on multifractal characteristics. The Interball-1 magnetic experiment was designed and conducted by S. Klimov and S. Romanov. Geotail magnetic data were taken from the DARTS online archive (ISAS). The FRACLAB package was used for creation of test data (http://www-rocq.inria.fr/fractales/). The research was supported by the Russian Science Support Foundation grant (2001–2003).

References

Angelopoulos, V., W. Baumjohann, C.F. Kennel, F.V. Coroniti, M.G. Kivelson, R. Pellat, H. Lühr, G. Paschmann. (1992). Bursty bulk flow in the inner central plasma sheet, *J. Geophys. Res.*, 97, 4027.

Angelopoulos, V., T. Mukai, and S. Kokubun. (1999). Evidence for intermittence in the Earths plasma sheet and implications for self-organized criticality, *Phys. Plasmas*, 6, 4161–4168.

Antonova, E.E., and I.L. Ovchinnikov. (1999). Magnetostatically equilibrated plasma sheet with developed medium-scale turbulence: Structure and implications for substorm dynamics, *J. Geophys. Res.*, 104, 17,289–17,298.

Aubry, M.P., and R.L. McPherron. (1971). Magnetotail changes in relation to the solar wind magnetic field and magnetospheric substorms, *J. Geophys. Res.*, 76, 4381.

Baker, D.N., T.I. Pulkkinen, V. Angelopoulos, W. Baumjohann, and R.L. McPherron. (1996). Neutral line model of substorms: Past results and present view, *J. Geophys. Res.*, 101, 12,975–13,010.

Bauer, T.M., W. Baumjohann, R.A. Treumann, N. Sckopke, and H. Lühr. (1995a). Low-frequency waves in the near-Earth plasma sheet, *J. Geophys. Res.*, 100, 9605–9618.

Bauer, T.M., W. Baumjohann, and R.A. Treumann. (1995b). Neutral sheet oscillations at substorm onset, *J. Geophys. Res.*, 100, 23,737–23,742.

Bendat, J.S., and A.G. Piersol. 1986. *Random data. Analysis and measurement procedures*, Wiley.

Borovsky, J.E., R.C. Elphic, H.O. Funsten, and M.F. Thomsen. (1997). The Earths plasma sheet as a laboratory for flow turbulence in high-beta MHD, *J. Plasma Phys.*, 57, 1–34.

Borovsky, J.E., and H.O. Funsten. (2003). MHD turbulence in the Earths plasma sheet: Dynamics, dissipation, and driving, *J. Geophys. Res.*, 108(A7), 1284, doi:10.1029/2002JA009625.

Burlaga, L.F., L.W. Klein. (1986). Fractal structure of the interplanetary magnetic field, *J. Geophys. Res.*, 91, 347–350.

Burlaga, L.F. (1991). Multi-fractal structure of the interplanetary magnetic field, *Geophys. Res. Lett.*, 18, 69–72.

Carbone, V., P. Veltri, R. Bruno. (1996). Solar wind low-frequency magnetohydrodynamic turbulence: extended self-similarity and scaling laws, *Nonlin. Proc. Geophys.*, 3, 247–261.

Cattell, C.A., F.S. Mozer, E.W. Hones, Jr., R.R. Anderson, and R.D. Sharp. (1986a). ISEE observations of the plasma sheet boundary, plasma sheet and neutral sheet: 2. Waves, *J. Geophys. Res.*, 91, 5681.

Cattell, C.A., and F.S. Mozer. (1986b). Experimental determination of the dominant wave mode in the active near-Earth magnetotail. *Geophys. Res. Lett.*, 13, 221.

Cattell, C.A., F.S. Moser, K. Tsuruda, H. Hayakawa, N. Nakamura, T. Okada, S. Kokubun, and T. Yamamoto. (1994). Geotail observations of spiky electric fields and low frequency waves in the plasma sheet and plasma sheet boundary, *Geophys. Res. Lett.*, 21, 2987.

Cattell, C., I. Roth, and M. Linton. (1995). The effects of low frequency waves on ion trajectories in the Earth's magnetotail. *Geophys. Res. Lett.*, 22, 3445–3448.

Chang, T. (1999). Self-organized criticality, multi-fractal spectra, sporadic localized reconnections and intermittent turbulence in the magnetotail., *Physics of Plasmas*, 6, 4137.

Chang, T., S.W.Y. Tam, C.-C. Wu, G. Consolini. (2003). Complexity, forced and/or self-organized criticality, and topological phase transitions in space plasmas, *Space Sci. Rev.*, 107, 425.

Consolini, G., M.F. Marcucci, and M. Candidi. (1996). Multifractal Structure of Auroral Electrojet Index data. *Phys. Rev. Lett.*, 76, 4082–4085.

Consolini, G., and P. De Michelis. (1998). Non-Gaussian Distribution Function of AE-Index Fluctuations Evidence for time Intermittency, *Geophys. Res. Lett.*, 25, 4087–4090.

Consolini, G., and A.T.Y. Lui. (1999). Sign-singularity analysis of current disruption, *Geophys. Res. Lett.*, 26, 1673.

Consolini, G., and A.T.Y. Lui. (2000). Symmetry breaking and nonlinear waveñwave interaction in current disruption: possible evidence for a dynamical phase transition. In: Ohtani, S.-I., Fujii, R., Hesse, M., Lysak, R.L. (Eds.), *Magnetospheric Current Systems*, AGU Monograph 118. AGU, Washington, DC, 395.

Consolini, G., and T.S. Chang. (2001). Magnetic field topology and criticality in geotail dynamics: relevance to substorm phenomena, *Space Sci. Rev.*, 95, 309–321.

Coroniti, F.V., F.L. Scarf, L.A. Frank, and R.P. Lepping. (1982). Microstructure of a magnetotail fireball, *Geophys. Res. Lett.*, 5, 539–542.

Daughton, W. (1999). The unstable eigenmodes of a neutral sheet, *Phys. Plasmas*, 6, 1329–1343.

Dudok de Wit, T., and V.V. Krasnosel'skikh. (1995). Wavelet bicoherence analysis of strong plasma turbulence at the Earth's quasiparallel bow shock, *Phys. Plasmas*, 24307–4311.

Dudok de Wit, T., and V.V. Krasnosel'skikh. (1996). Non-gaussian statistics in space plasma turbulence: fractal properties and pitfalls, *Nonlin. Proc. Geophys.*, 3, 262–273.

Dudok de Wit, T. (2003). Numerical schemes for the analysis of turbulence—a tutorial, In: *Space Plasma Simulation*, J. Büchner, C. Dum, M. Scholer (Eds.), Lecture Notes in Physics, 615, Springer, 315–343.

Greco, A., A.L. Taktakishvili, G. Zimbardo, P. Veltri, and L.M. Zelenyi. (2002). Ion dynamics in the near-Earth magnetotail: Magnetic turbulence versus normal component of the average magnetic field, *J. Geophys. Res.*, 107(A10), 1267, doi:10.1029/2002JA009270.

Gurnett, D.A., L.A. Frank, and R.P. Lepping. (1976). Plasma waves in the distant magnetotail, *J. Geophys. Res.*, 81, 6059–6071.

Holter, O., C. Altman, A. Roux, S. Perraut, A. Pedersen, H. Pecseli, B. Lybekk, J. Trulsen, A. Korth, and G. Kremser. (1995). Characterization of low frequency oscillations at substorm breakup, *J. Geophys. Res.*, 100, 19,109.

Horbury, T.S., and A. Balogh. (1997). Structure function measurements of the intermittent MHD turbulent cascade, *Nonlin. Proc. Geophys.*, 4, 185–199.

Hoshino, M., A. Nishida, T. Yamamoto, and S. Kokubun. (1994). Turbulent Magnetic Field in the Distant Magnetotail: Bottom-Up Process of Plasmoid Formation?, *Geophys. Res. Lett.*, 21, 2935.

Hoshino, M., A. Nishida, T. Mukai, Y. Saito, and T. Yamamoto. (1996). Structure of plasma sheet in magnetotail: Double-peaked electric current sheet, *J. Geophys. Res.*, 101, 24,775–24,786.

Hoyng, P. (1976). An error analysis of power spectra, *Astron. and Astrophys.*, 47, 449–452.

Kabin, K., and V.O. Papitashvili. (1998). Fractal properties of the IMF and the Earth's magnetotail field, *Earth Planets Space*, 50, 87–90.

Klimas, A.J., J.A. Valdivia, D. Vassiliadis, D.N. Baker, M. Hesse, and J. Takalo. (2000). Self-organized criticality in the substorm phenomenon and its relation to localized reconnection in the magnetospheric plasma sheet, *J. Geophys. Res.*, 105, 18765.

Klimov, S.I., S.A. Romanov, M.N. Nozdrachev, S.P. Savin, A.Yu. Sokolov, L.M. Zeleny, J. Blencki, K. Kossacki, P. Oberc, B. Popielawska, J. Buchner, and B. Nikutowski. (1986). Comparative study of plasma wave activity in the plasma sheet boundary and near Earth plasma sheet, *Adv. Space. Res.*, 6, 153–158.

Klimov, S., S. Romanov, E. Amata, J. Blecki, J. Büchner, J. Juchniewicz, J. Rustenbach, P. Triska, L.J.C. Woolliscroft, S. Savin, Yu. Afanas'yev, U. de Angelis, U. Auster, G. Bellucci, A. Best, F. Farnik, V. Formisano, P. Gough, R. Grard, V. Grushin, G. Haerendel, V. Ivchenko, V. Korepanov, H. Lehmann, B. Nikutowski, M. Nozdrachev, S. Orsini, M. Parrot, A. Petrukovich, J.L. Rauch, K. Sauer, A. Skalsky, J. Slominski, J.G. Trotignon, J. Vojta, and R. Wronowski. (1997). ASPI experiment: measurements of fields and waves on board the INTERBALL-1 spacecraft, *Ann. Geophysicae*, 514–527.

Lui, A.T.Y. (1996). Current disruption in the Earth's magnetosphere: Observations and models, *J. Geophys. Res.*, 101, 13,067.

Lui, A.T.Y., and A.-H. Najmi. (1997). Time-frequency decomposition of signals in a current disruption event, *Geophys. Res. Lett.*, 24, 3157.

Lui, A.T.Y., S.C. Chapman, K. Liou, P.T. Newell, C.I. Meng, M. Brittnacher, and G.K. Parks. (2000). Is the dynamic magnetosphere an avalanching system? *Geophys. Res. Lett.*, 27, 911.

Lui, A.T.Y. (2001). Multifractal and intermittent nature of substorm associated magnetic turbulence in the magnetotail, *J. Atmosph. Sol.-Terr. Phys.*, 63, 1379–1385.

Lui, A.T.Y. (2002). Multiscale phenomena in the near-Earth magnetosphere, *J. Atmosph. Sol. Terr. Phys.*, 64, 125–143.

Lyons, L.R. (1996). Substorms: Fundamental observational features, distinction from other disturbances, and external triggering, *J. Geophys. Res.*, 101, 13011.

Mandelbrot, B. (1977). *Fractals: Form, Chance and Dimension.* Freeman, New York.

Marsch, E., and C.-Y. Tu. (1997). Intermittency, non-gaussian statistics and fractal scaling of MHD fluctuations in the solar wind, *Nonlin. Proc. Geophys.*, 4, 101–124.

Mihalov, J.D., C.P. Sonett, and D.S. Colburn. (1970). Reconnection and noise in the geomagnetic tail, *Cosmic Electrodynamics*, 1, 178–204.

De Michelis, P., G. Consolini, and A. Meloni. (1998). Sign-singularity in the secular acceleration of the Geomagnetic Field, *Phys. Rev. Lett.*, 81, 5023–5026.

Milovanov, A.V., L.M. Zelenyi, and G. Zimbardo. (1996). Fractal structures and power law spectra in the distant Earth's magnetotail, *J. Geophys. Res.*, 101, 19,903–19,910.

Milovanov, A.V., L.M. Zelenyi, G. Zimbardo, and P. Veltri. (2001a). Self-organized branching of magnetotail current systems near the percolation threshold, *J. Geophys. Res.*, 106, 6291–6308.

Milovanov, A.V., L.M. Zelenyi, P. Veltri, G. Zimbardo, and A.L. Taktakishvili. (2001b). Geometric description of the magnetic field and plasma coupling in the near-Earth stretched tal prior to a substorm, *J. Atmosph. Solar-Terr. Phys.*, 63, 705–721, 2001.

Nakamura, R., W. Baumjohann, A. Runov, M. Volwerk, T.L. Zhang, B. Klecker, Y. Bogdanova, A. Roux, A. Balogh, H. Reme, J.-A. Sauvaud, and H.U. Frey. (2002). Fast flow during current sheet thinning, *Geophys. Res. Lett.*, 29(23), 2140, doi:10.1029/2002GL016200.

Neagu, E., S.P. Gary, J.E. Borovsky, W. Baumjohann, and R.A. Treumann. (2001). Constraints on magnetic fluctuation energies in the plasma sheet, *Geophys. Res. Lett.*, 28, 919–922.

Neagu, E., J.E. Borovsky, M.F. Thomsen, S.P. Gary, W. Baumjohann, and R.A. Treumann. (2002). Statistical survey of magnetic field and ion velocity fluctuations in the near-Earth plasma sheet: Active Magnetospheric Particle Trace Explorers/Ion Release Module (AMPTE-IRM) measurements, *J. Geophys. Res.*, 107, A7, 10.1029/2001JA000318.

Ohtani, S., T. Higuchi, A.T.Y. Lui, and K. Takahashi. (1995). Magnetic fluctuations associated with tail current disruption: fractal analysis, *J. Geophys. Res.*, 100, 19, 135.

Ohtani, S., K. Takahashi, T. Higuchi, A.T.Y. Lui, H.E. Spence, and J.F. Fennell. (1998). AMPTE/CCE-SCATHA simultaneous observations of

substorm-associated magnetic fluctuations, *J. Geophys. Res.*, 103, 4671–4682.

Ott, E., et al. (1992). Sign-singular measures: Fast magnetic dynamos, and high- Reynolds-number fluid turbulence, *Phys. Rev. Lett.*, 69, 2654.

Pagel, C., and A. Balogh. (2003). Radial dependence of intermittency in the fast polar solar wind magnetic field using Ulysses, *J. Geophys. Res.*, 108(A1), 1012, doi:10.1029/2002JA009498.

Petrukovich, A.A., V.A. Sergeev, L.M. Zelenyi, T. Mukai, T. Yamamoto, S. Kokubun, K. Shiokawa, C.S. Deehr, E.Y. Budnick, J. Buchner, A.O. Fedorov, V.P. Grigorieva, T.J. Hughes, N.F. Pissarenko, S.A. Romanov, and I. Sandahl. (1998). Two spacecraft observations of a reconnection pulse during an auroral breakup, *J. Geophys. Res.*, 103, 47–59.

Petrukovich, A.A., and Yu.I. Yermolaev. (2002). Vertical Ion flows in the plasma sheet: INTERBALL-Tail observations, *Ann. Geophys.*, 20, 321–327.

Runov, A., R. Nakamura, W. Baumjohann, T.L. Zhang, M. Volwerk, H.-U. Eichelberger, and A. Balogh. (2003a). Cluster observation of a bifurcated current sheet, *Geophys. Res. Lett.*, 30(2), 1036, doi:10.1029/-2002GL016136.

Runov, A., R. Nakamura, W. Baumjohann, R.A. Treumann, T.L. Zhang, M. Volwerk, Z. Voŕös, A. Balogh, K.-H. Glassmeier, B. Klecker, H. Reme, and L. Kistler. (2003b). Current sheet structure near magnetic X-line observed by Cluster, *Geophys. Res. Lett.*, 30(11), 1579, doi:10.1029/2002GL016730.

Russell, C.T. (1972). Noise in the geomagnetic tail, *Planet. Space Sci.*, 20, 1541–1553.

Sadovsky, A.M. and A.A. Galeev. (2001). Quasilinear Theory of the Ion Weibel Instability in the Earths Magnetospheric Tail, *Plasma Physics Reports*, 27, 490–496, 2001. Translated from Fizika Plazmy, 27, 519–525.

Scarf, F.L., L.A. Frank, L.A. Ackerson, and R.P. Lepping. (1974). Plasma wave turbulence at distant crossings of the plasma sheet boundaries and the neutral sheet. *Geophys. Res. Lett.*, 1, 189–192.

Sergeev, V.A., V. Angelopoulos, C. Carlson, and P. Sutcliffe. (1998). Current sheet measurements within a flapping plasma sheet, *J. Geophys. Res.*, 103, 9177–9187.

Sergeev, V.A., M.V. Kubyshkina, K. Liou, P.T. Newell, G. Parks, R. Nakamura, and T. Mukai. (2001). Substorm and convection bay compared: Auroral and magnetotail dynamics during convection bay, *J. Geophys. Res.*, 106, 18,843.

Sergeev, V., A. Runov, W. Baumjohann, R. Nakamura, T.L. Zhang, M. Volwerk, A. Balogh, H. Reme, J.-A. Sauvaud, M. Andre, and B. Klecker. (2003). Current sheet flapping motion and structure observed by Cluster, *Geophys. Res. Lett.*, 30(6), 1327, doi:10.1029/2002GL016500.

Shinohara, I., T. Nagai, M. Fujimoto, T. Terasawa, T. Mukai, K. Tsuruda, and T. Yamamoto. (1998). Low-frequency electromagnetic turbulence observed near the substorm onset site, *J. Geophys. Res.*, 103, 20,365–20,388.

Sigsbee, K., C.A. Cattell, F.S. Moser, K. Tsuruda, and S. Kokubun. (2001). Geotail observations of low frequency waves from 0.001 to 16 Hz during the November 24, 1996 Geospace Environment Modelling substorm challenge event, *J. Geophys. Res.*, 106, 435–445.

Sitnov, et al. (2001). Modelling substorm dynamics of the magnetosphere: from self-organization and self-organized criticality to non equilibrium phase transitions, *Phys. Rev. E*, 65, 16116.

Sorriso-Valvo, L., V. Carbone, P. Veltri, G. Consolini, and R. Bruno. (1999). Intermittency in the solar wind turbulence through probability distribution functions of fluctuations, *Geophys. Res. Lett.*, 26, 1801–1804.

Substorms-4. (1998). Eds. S. Kokubun, and Y. Kamide, Kluwer.

Treumann, R.A. (1999). Wave turbulence in the plasma sheet and low latitude boundary layers, *Adv. Space. Res.*, 24, 3–12.

Uritsky, V.M., A.J. Klimas, D. Vassiliadis, D. Chua, and G. Parks. (2002). Scale-free statistics of spatiotemporal auroral emissions as depicted by POLAR UVI images: The dynamic magnetosphere is an avalanching system, *J. Geophys. Res.*, 107, 1426.

Vehel, J.L. and R. Vojak. (1998). Multifractal analysis of Choquet capacities: preliminary results, *Adv. Appl. Math.*, 20(1), 1.

Veltri, P., G. Zimbardo, A.L. Taktakishvili, and L.M. Zelenyi. (1998). Effect of magnetic turbulence on the ion dynamics in the distant magnetotail, *J. Geophys. Res.*, 103, 14,897–14,916.

Veltri, P., and A. Mangeney. (1999). Scaling laws and intermittent structures in solar wind MHD turbulence, in *Solar Wind IX*, edited by S.A. Habbal and R. Esser, AIP Conf. Proc. 471, 543–546.

Volwerk, M., K.-H. Glassmeier, A. Runov, W. Baumjohann, R. Nakamura, T.L. Zhang, B. Klecker, A. Balogh, and H. Reme. (2003). Kink mode oscillation of the current sheet, *Geophys. Res. Lett.*, 30, 1320, doi:10.1029/2002GL016467.

Vörös, Z. (2000). On multifractality of high-latitude geomagnetic fluctuations, *Ann. Geophys.*, 18, 1273–1282.

Vörös, Z., D. Jankovicova, and P. Kovacs. (2002). Scaling and singularity characteristics of solar wind and magnetospheric fluctuations, *Nonlin. Proc. Geophys.*, 9, 149–162.

Vörös, Z., W. Baumjohann, R. Nakamura, A. Runov, T.L. Zhang, M. Volwerk, H.U. Eichelberger, A. Balogh, T.S. Horbury, K.-H. Glasslmeier, B. Klecker, and H. Reme. (2003). Multi-scale magnetic field intermittence in the plasma sheet, *Ann. Geophys.*, 21, 1955–1964.

Wavelets in Geophysics. (1994). edited by E. Foufoula-Georgiou and P. Kumar. Academic, San Diego, Calif.

Yermolaev, Yu.I., V.A. Sergeev, L.M. Zelenyi, A.A. Petrukovich, J.-A. Sauvaud, T. Mukai, and S. Kokubun. (1999). Two spacecraft observation of plasma sheet convection jet during continuous external driving, *Geophys. Res. Lett.*, 26, 177–180.

Zelenyi, L.M., and A.V. Milovanov. (1994). Fractal and multifractal structures in the solar wind, *Geomagn. Aeron.*, 33, 425–432.

Zelenyi, L.M., A.V. Milovanov, and G. Zimbardo. (1998). Multiscale magnetic structure of the distant Tail: self-consistent fractal approach In: *New Perspectives on the Earth's magnetotail*, Edited by A. Nishida, D.N. Baker, S.W.H. Cowley, Geophysical Monograph 105, AGU, Washington, DC., 321–339.

Zhang, T.L., W. Baumjohann, R. Nakamura, A. Balogh, and K.-H. Glassmeier. (2002). A wavy twisted neutral sheet observed by CLUSTER, *Geophys. Res. Lett.*, 29(19), 1899, doi:10.1029/2002GL015544.

Chapter 8

MAGNETOSPHERIC MULTISCALE MISSION

Cross-scale Exploration of Complexity in the Magnetosphere

A. Surjalal Sharma
University of Maryland, College Park, Maryland, U.S.A.

Steven A. Curtis
NASA Goddard Space Flight Center, Greenbelt, Maryland, U.S.A.

Abstract: The physical processes in the magnetosphere span a wide range of space and time scales and due to the strong cross-scale coupling among them the fundamental processes at the smallest scales are critical to the large scale processes. For example, many key features of magnetic reconnection and particle acceleration are initiated at the smallest scales, typically the ion gyro-radii, and then couples to meso-scale and macro-scale processes, such as plasmoid formation. The Magnetospheric Muliscale (MMS) mission is a multi spacecraft mission dedicated to the study of plasma physics at the smallest scales and their cross-scale coupling to global processes. Driven by the turbulent solar wind, the magnetosphere is far from equilibrium and exhibits complex behavior over many scales. The processes underlying the multi-scale and intermittent features in the magnetosphere are fundamental to sun-earth connection. Recent results from the four spacecraft Cluster and earlier missions have provided new insights into magnetospheric physics and will form the basis for comprehensive studies of the multi-dimensional properties of the plasma processes and their inter-relationships. MMS mission will focus on the boundary layers connecting the magnetospheric regions and provide detailed spatio-temporal data of processes such as magnetic reconnection, thin current sheets, turbulence and particle acceleration. The cross-scale exploration by MMS mission will target the microphysics that will enable the discovery of the chain of processes underlying sun-earth connection.

Key words: magnetosphere, multiscale phenomena, cross-scale coupling, multi-spacecraft mission, reconnection, particle acceleration, thin current sheets

A.S. Sharma and P.K. Kaw (eds.), Nonequilibrium Phenomena in Plasmas, 179–196.
© 2005 *Springer. Printed in the Netherlands.*

1. Introduction

The magnetosphere is driven by the turbulent solar wind and exhibits multiscale features over a wide range of spatio-temporal scales, ranging from the smallest scale of kinetic processes to the global scale of magnetohodrodynamic phenomena. There is strong cross-scale coupling among the different phenomena in the five main regions of geospace, viz. magnetosheath, tail lobes, plasma sheet, ring current and ionosphere. These regions are interconnected through boundaries, viz. the magnetopause, cusp, plasma sheet boundary layer and magnetotail current sheet, and the dominant dynamical processes are initiated at these boundaries. The magnetopause is a thin current sheet and magnetic reconnection there leads to the transfer of mass, momentum and energy from the solar wind into the magnetosphere. The magnetotail plasma sheet has a thin current sheet embedded in it and is the site of processes responsible for the onset of explosive release of energy during substorms. The processes at the boundaries and sheets are kinetic in nature and their coupling to the meso- and macro-scales are essential elements in unraveling the multiscale physics of geospace. The cross-scale coupling in the magnetosphere due arises due to the nonlinearity of its plasma and fields and consequently the multiscale behavior is an inherent feature.

The main dynamical features of the magnetosphere are storms and substorms, which are prevalent mainly when the solar wind is strongly coupled to the magnetosphere, e.g., due to enhanced magnetic reconnection at the magnetopause. The geospace storms and related processes have time scales of days and are associated with enhancements of the ring current in the inner magnetosphere. The substorms on the other hand have characteristic time scales of an hour or so and are associated mainly with the plasma processes in the magnetotail. While our understanding has advanced rapidly due to the recent multi-spacecraft and ground-based measurements, and theory and modeling, many outstanding questions remain due to the complexity of the magnetosphere arising from the plethora of processes with overlapping space and time scales.

The dynamics of magnetospheric boundaries during storms and substorms are essential elements in the chain of multiscale phenomena in geospace. The main reasons for the complexity of geospace are: the inherent nonlinearity of the plasma and fields, and its nonequilibrium nature. The complicated fields and plasma with very short scale lengths make in-situ measurements as well as theoretical analysis difficult. Also the nonequilibrium nature of the magnetosphere introduces time variations that challenge the current capabilities of measuring short time scale processes in sufficient detail. The Magnetospheric Multiscale Mission (MMS) is designed to carry out such measurements with four spacecraft in strategically configured formations in the key regions (Curtis, 1999).

The dynamical behavior of the magnetosphere embodied in observational data has been studied extensively using nonlinear dynamical techniques (see reviews: Sharma, 1995, 2003; Klimas et al., 1996). The evidence of large scale coherence in magnetospheric dynamics, first obtained in the form of low dimensional behavior (Vassiliadis et al. al., 1990), is consistent with its morphology (Siscoe, 1991), and MHD simulations (Lyon, 2000). The multiscale behavior of the magnetosphere, on the other hand, has been recognized mainly through the power law dependences, e.g., in the AE index (Tsurutani et al., 1990), spacecraft images of the auroral region (Uritsky et al., 2002), bursty bulk flows (Angelopoulos et al., 1999), turbulence (Borovsky and Funsten, 2003), etc. These studies make extensive use of observational data to develop data-derived models of the complexity in the magnetosphere. The key advantage of these approach is its ability to model the inherent dynamical features without a priori assumptions, and complements the first principle models. The study of multiscale phenomena using these two approaches is expected to yield a more comprehensive understanding of the magnetosphere.

2. Magnetosperic Complexity: from Microscale to Macroscale

The most ubiquitous features of the magnetosphere during geomagnetically active periods are the global scale processes such as plasmoid formation and release. However these large scale phenomena originate from the microscale physical processes occurring at the boundary layers of the magnetosphere such as the magnetopause and magnetotail. A canonical example of such cross-scale coupling is a substorm in which the onset of reconnection occurs in the magnetotail thin current sheet, with thickness as small as an ion gyro radius ($\sim$400 km), and may involve processes at the electron gyro radius scale ($\sim$80 km). The reconnection onset, most likely due to the tearing instability (Sitnov et al., 1998, 2002), is followed by flows and turbulence on many scales, including those associated with Alfven waves, and leads to possibly flux ropes and a large scale plasmoid with a size of $\sim$100 R_E. A simulation of the magnetosphere during a substorm (March 9, 1995) using an MHD code and its connection to the magnetic reconnection simulated using a particle code is shown in Figure 1 (Lyon, 2000). The small inset shows magnetotail current sheet where magnetic reconnection is initiated at the x-line in the magnetotail. The large inset is a particle code simulation of reconnection (Shay et al., 1999). The phenomena on the global as well as the micro-scales are strongly coupled through the multiscale processes.

The multi-scale behavior of the magnetosphere is evident in many studies of the distribution of scale sizes, typically in the form of power spectra. Most of these studies use the magnetospheric data such as the magnetic field and

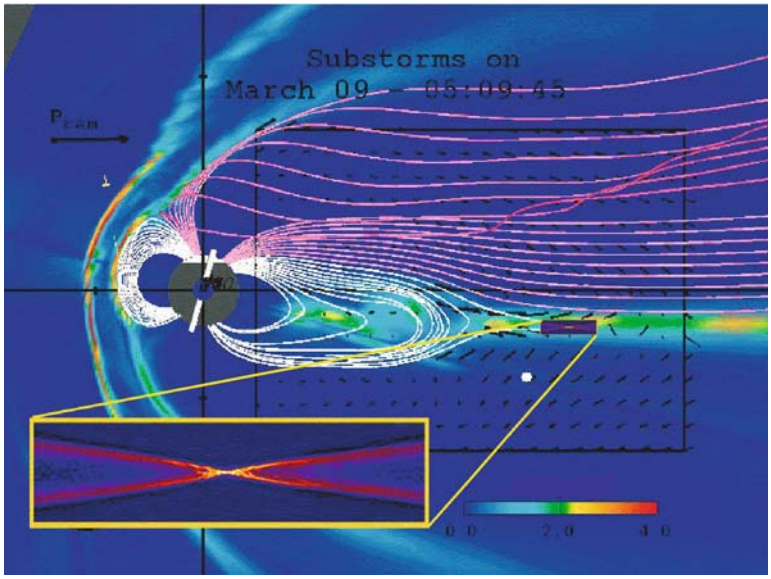


Figure 1. The magnetosphere as simulated using a global MHD code for the substorm of March 9, 1995 (Lyon et al., 2000) showing the global magnetospheric configuration. The background indicates the magnitude of the perpendicular current with a set of field lines showing the magnetic field geometry in the tail. The large inset shows a particle code simulation of magnetic reconnection (Shay et al., 2000) in a region indicated by the small inset. The plasma processes initiated at such narrow regions lead to large scale dynamics such as plasmoid formation.

plasma flows, or geomagnetic indices (Tsurutani et al., 1990; Borovsky et al., 1997; Angelopoulos et al., 1999; Uritsky et al., 2002).

Considering the driven nature of the magnetosphere and the variability of the solar wind, it is however important to use the correlated data of the solar wind and the magnetospheric response. A widely used data set of the coupled solar wind-magnetosphere is the Bargatze et al. (1985) data set consisting of the solar wind induced electric field VB_s (B_s is the southward component of the interplanetary magnetic field and V is the component of the solar wind velocity along the Earth-Sun axis) and the magnetospheric response is the auroral electrojet index AL. This data set has been used to study the multi-scale behavior (Sitnov et al., 2000, 2001; Sharma et al., 2001).

A common technique for studying multiscale phenomena is the power spectrum analysis using Fourier transforms. For nonlinear systems such as the magnetosphere it is essential to use techniques with retain the nonlinear effects, such as phase space reconstruction from observational data. The singular spectrum analysis, based on the singular value decomposition, is often used to reconstruct the phase space of the coupled solar wind- magnetosphere system from the time series data by time delay embedding (Sitnov et al., 2000, 2001). The singular

value decomposition of the VBs-AL data yields the orthonormal components in the reconstructed phase space with different strengths, expressed in terms of an eigenvalue spectrum, and exhibits multiscale behavior, with a spectrum close to 1/f (Sitnov et al., 2001). Similar distribution of scales is found in the global MHD simulations (Shao et al., 2003).

The magnetospheric response strongly depends on the solar wind conditions, with a wide variability in the nature of the response. Thus it is essential to study the magnetospheric response for specific types of solar wind conditions. Such a study can be readily carried out in the phase space reconstructed from the correlated solar wind—magnetosphere data. The global features of the magnetosphere are represented by the first few leading coordinates in this phase space. The multi-scale parts are naturally coupled among themselves and to the large-scale or global component, and appear as fluctuations of the data around an average state. The distribution of these fluctuations can be described in terms of conditional probabilities $P(O_{t+1} \mid \mathbf{x}_t)$ defined in the embedding space $\mathbf{x_t}$ for given solar wind conditions and the magnetospheric output O_{i+1} (Ukhorskiy et al., 2004).

The probability density distributions of the magnetospheric response are shown in Figure 2 and depend strongly on the solar wind conditions. The

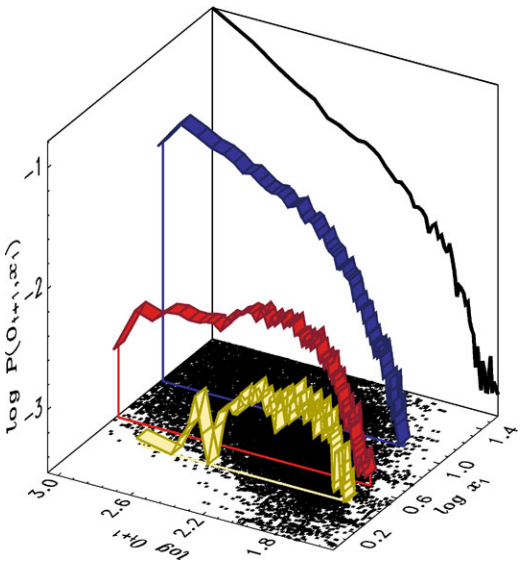


Figure 2. The conditional probabilities $P(O_{t+1} \mid \mathbf{x}_t)$ of the magnetosperic state O_{i+1} as a function of solar wind conditions, represented by $\mathbf{x}_t$. The yellow, red and blue curves correspond to strong (vBs > 9 mV), medium ($0.6 < vB_s < 9$ mV) and low (vBs < 0.6 mV) solar wind activity levels, represented by $\mathbf{x}_t$. The floor shows all the points in the data base, corresponding to the marginal probability distribution function shown in the back panel (Ukhorskiy et al., 2004).

response has a nearly power law distribution when the solar wind driving is weak (blue curve, $vB_s < 0.6$ mV), deviates from power law and has a broad response for medium driving (red curve, $0.6 < vB_s < 9$ mV) and has a more peaked response for stronger driving (yellow curve, $vB_s > 9$ mV) (Ukhorskiy et al., 2004).

3. Magnetospheric Multiscale Mission

The objective of Magnetospheric Multiscale mission is two-fold: exploration and understanding. It will study the microscale phenomena—the basic plasma processes that transport, accelerate, and energize plasmas in thin boundary and current layers. These are the processes that control the structure and dynamics of the Earth's magnetosphere and have been inaccessible so far. For example, the whole range of processes associated with magnetic reconnection will be studied. Magnetospheric Multiscale will measure 3D fields and particle distributions and their temporal variations and 3D spatial gradients, with high resolution, while dwelling in the key magnetospheric boundary regions, from the subsolar magnetopause to the distant tail. It will uniquely separate spatial and temporal variations over scale lengths appropriate to the processes being studied—from the electron gyro radius up to structures with sizes >1000 km. From the measured gradients and curls of the fields and particle distributions, spatial variations in currents, density, velocities, pressures, and heat fluxes can be calculated. Magnetic reconnection will be directly observed in each of the regimes where it is thought to occur around the Earth. This process, initiated at thin current sheets, is vital for transferring energy from magnetic fields to plasmas, and for coupling different regimes. It is central to many astrophysical theories, yet its operation in collisionless space plasmas is very poorly understood. The goals of Magnetospheric Multiscale are different from those of the ESA Cluster mission, which will explore selected regions (bow shock, cusp, midtail) to spatial scales down to >100 km from a single polar orbit. Magnetospheric Multiscale is designed to study boundary processes throughout the magnetosphere over scales down to <100 km, commensurate with the scales of microphysical processes acting within many of the critical boundaries of interest.

The four identical spacecraft of Magnetospheric Multiscale will fly in a tetrahedral configuration with spacing variable from 10 km to more than 1000 km. Each spacecraft will contain an identical set of 3D instruments with high spectral and temporal resolution (plasma electron and ion composition, energetic electron and ion composition, magnetometer, electric fields and waves). Inter spacecraft ranging and communication will determine spacing and allow simultaneous high rate data recording on all spacecraft for maximum resolution of boundaries or events.

The thrust of the science objectives of MMS mission is to explore and understand fundamental processes on microscale that control the flow of energy, momentum, and mass within and across plasma boundaries.

The key science question that will be addressed by MMS mission is what physical processes contribute to magnetic reconnection? The broader questions it will address are: 1) How do microscale processes near plasma boundaries couple to larger scale dynamics and structures? 2) What controls the transport of magnetic fields, and thus energy, across plasma boundaries? 3) How are electric currents generated at boundaries to influence distant magnetospheric regions? 4) How do processes at plasma boundaries accelerate charged particles?

The MMS mission will consist of four spacecraft fly in close proximity to form a single probe that can uniquely separate space time and will use of interspacecraft ranging and communication to explore wide range of scales down to <100 km. Four different orbital phases will be used to cover the entire magnetosphere.

The strategies for measurements in geospace dynamics is broadly divided into five mission types, viz. global configuration, microscope, networks, inner and outer boundaries, and solar plasma variations (Vondrak et al., 2003). The microscope type missions are MMS and Cluster, designed to carry out detailed measurements of plasma dynamics using tetrahedronal clusters of spacecraft. The strategic targets are unprecedented determination of values, gradients, curls, and divergences at all scale of interest in magnetic and electric fields, plasma, including composition; energetic particles; and plasma and radio waves.

4. Key Microscale Physics Problems

4.1 Reconnection

Magnetic reconnection is one of the most widely studied phenomenon in the laboratory and natural plasmas. The laboratory plasmas are usually collisional and reconnection in this context is relatively well understood. However in the nearly collisionless plasmas in space, understanding reconnection remain a challenge. The main issues in the theory of collisionless reconnection are the mechanism of onset, rate of reconnection and saturation. Recent advances in simulations using particle-in-cell, hybrid, Hall MHD and MHD codes have shown that the reconnection rate is governed mainly by ion dynamics and the outflow region is crucial to the reconnection process (Birn et al., 2001). However these studies assume the existence of an X-line and thus avoid the issue of reconnection onset or X-line formation. The tearing mode is a natural candidate for the onset of reconnection and has been studied extensively since

it was first proposed soon for the magnetotail current sheet (Coppi et al., 1966) soon after the discovery of the magnetotail. The complicated kinetic theory of tearing instability in the thin current sheet with very short scale lengths or sharp gradients and consequently complex particle orbits has a checkered history. Recent studies using kinetic stability codes capable of resolving these issues have shown that the tearing instability can be destabilized due to the presence of transient electrons along with those trapped in the current sheet (Sitnov et al., 2002). This implies that the tearing instability is a viable mechanism for reconnection onset. In order to understand the formation of X-line in more detail the nonlinear development of the instability and its saturation need to be studied. The development of analytic theory of kinetic instabilities and their nonlinear development in such a complicated situation is difficult and particle simulation codes may yield new advances. However such codes have not succeeded in showing the tearing instability in realistic geometry of the magnetotail current sheet. It should however be noted that although a system is linearly unstable it may be nonlinearly stable and the role of the instability is then limited. This implies that these phenomena are nonequilibrium in nature (Sitnov and Sharma, 1998) and this recognition has lead to new perspective for solar flares (Priest, 2000; Somov, 2000).

The crucial next advance in the understanding of reconnection can be expected from the detailed in-situ measurements of the plasma and field variables. Such measurements are expected from multispacecraft Cluster and MMS missions. Recent studies using multi-spacecraft observations have given direct confirmation of reconnection and associated processes at the magnetopause (Phan et al., 2000). Also single spacecraft passes such as by Geotail through the magnetopause (Deng and Matsumoto, 2001) and the magnetotail current sheet by Wind (Oieroset et al., 2001, 2002) gave detailed in-situ measurements.

The bi-directional jets resulting from reconnection at the magnetopause were measured by Geotail and Equator-S satellites, separated by $\sim 4\ R_E$ in the north-south, and $\sim 3\ R_E$ in the east-west, direction. The X-line with a length of $> 3\ R_E$ in the north-south direction and extending to the sub-solar point and over to the dusk flank, was $\sim 40\ R_E$ (Figure 3). These provide key measurements of the reconnection phenomena and more detailed measurements will require shorter spatial resolution as well as longer residence time of the spacecraft in the region. The MMS mission will have capabilities to measure many physical variables on space scales at least an order of magnitude smaller and with the strategically preplanned trajectories, much more encounters of the reconnection region are expected. The onset and saturation are two outstanding problems of reconnection, and multi-dimensional and short scale measurements are crucial for new advances in their understanding.

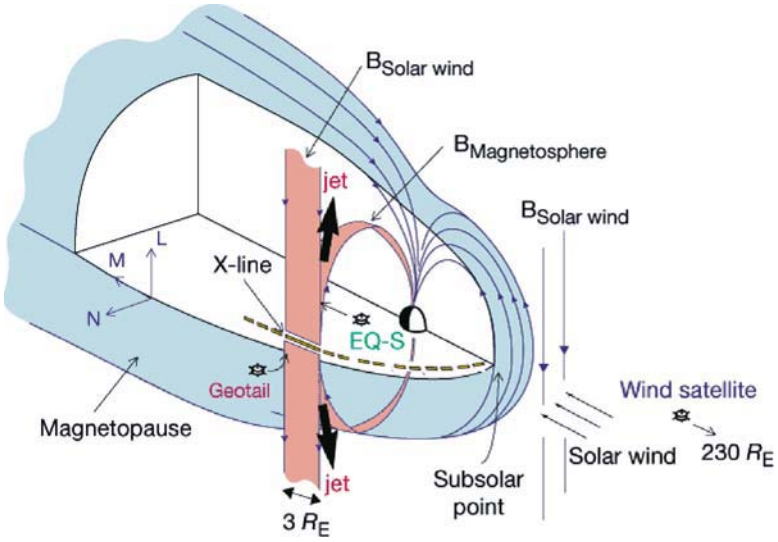


Figure 3. Cutaway view of the magnetosphere showing the spacecraft positions and the presence of an extended reconnection line. Geotail and Equator-S (EQ-S) satellites were separated by ∼4 R_E in the north–south, and ∼3 R_E in the east–west, direction. Bi-directional reconnection jets detected at both spacecraft locations indicate a reconnection X-line (yellow solid line) along the dawn flank magnetopause and slightly north of the equatorial plane. The inferred X-line (yellow dashed line) extends to the subsolar point and over to the dusk flank. The boundary normal (LMN) coordinate system is defined such that the N axis points outward along the magnetopause normal and the (L, M) plane is tangential to the magnetopause with L orientated due north and M due west (Phan et al., *Nature, 404*, 848, 2000).

4.2 Thin current sheets

Thin current sheets in many astrophysical, solar, planetary, magnetospheric and laboratory plasmas are the key regions where the release of stored magnetic energy is triggered. They are ubiquitous in the interfaces or boundaries between plasma and magnetic fields. The X-ray luminosity of the Sun and stellar bodies arise from processes in the thin current sheet sheets (Parker, 1994). The structure and dynamics of the current sheets play an important role in the understanding of the microscale processes and their cross-scale coupling to the meso- and macro-scale processes. Spacecraft experiments provide the only possibility of in-situ study of current sheets in collisionless plasmas. Before Cluster, most of our understanding of the current sheets have come from the measurements by single spacecraft, which has strong limitations in separating spatial and temporal changes, and thus of structure and dynamics. The closely spaced MMS spacecraft will present a unique opportunity to study the

spatio-temporal changes of the plasma variables, e.g., in the magnetotail current sheet.

The current sheets can be as thin as the ion gyro radius, possibly the electron gyro radius, and as such needs a kinetic description of the microscale processes. Given the complexity of the magnetotail and the magnetopause, the theory of such regions pose significant challenges. For example, most studies are for the simplified one-dimensional structure of thin current sheets. Recent studies of such sheets have given a new understanding of their stability against many plasma instabilities, in particular the tearing instability. New theories and techniques of kinetic plasma equilibria in multi-dimensions are needed to develop multi-dimensional models to compare with MMS in a meaningful manner. Due to the complexity of such plasma configurations reliable results are expected to emerge mainly from studies that use judiciously the capabilities of analytic theory and numerical simulations. For example, the stability of these equilibria has been studied using the finite element techniques (Sharma, 1983; Sitnov et al., 2002), which can account for the strongly inhomogeneous magnetic field geometry and the consequently complicated particle orbits. A combination of such studies with simulations has the potential of yielding new results on reconnection onset and related processes.

The internal structure of current sheets and the details of particle populations are important to the understanding of their evolution. The possibility of the studies of such microphysical properties using single spacecraft measurements are rather limited and multi-spacecraft MMS mission can provide the relevant data to the required detail. In the case of the magnetotail, the particle distributions of the trapped or transient particles evolve and lead to changes in the self-consistent structure. Recent studies have found that the change of the particles from being transient to trapped lead to changes in the cross-tail current and eventually flattens the profile of the magnetic field near the midplane (Zelenyi et al., 2002). As a result the current profile attains a double humped profile (Figure 4), which in turn can play a major role in its evolution. This result is in agreement with the Geotail (Hoshino et al., 1996) and Cluster (Sergeev et al., 2003) observations of double-humped (also referred to as bifurcated) current sheets in the Earth's magnetotail. The understanding of the double humped current profiles and their role in the evolution of the current sheet will require measurements of the particle distributions, and the plasma and magnetic filed profiles, and such measurements are expected from MMS.

4.3 Particle acceleration

The magnetic energy released during reconnection leads to fast flows, heating and acceleration. While the fast flows and heating involve a large fraction of the particles, only a small fraction is accelerated to high energies. The acceleration

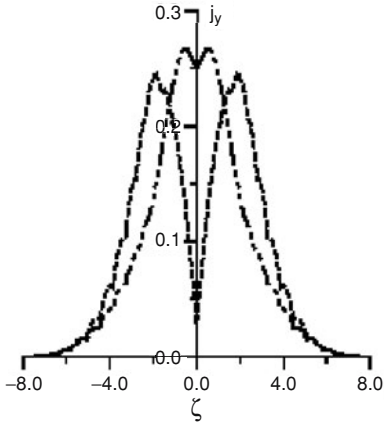


Figure 4. The normalized current density j_y as a function of the distance (normalized) across the sheet evolves from a peaked initial value to the double-humped or bifurcated profiles (Zelenyi et al., 2002).

is often associated with sharp gradients in the plasma variables and occurs in the electric and magnetic fields. The thin current sheets or the reconnection regions are characterized by plasmas with short scale lengths and thus are potential sites for particle acceleration. The energization processes need to be studied in detail as they can lead to an understanding of the microphysical processes at such boundaries and layers.

The accelearion of particles by localized electric fields is usually limited by the strength of the field, and higher energies are achieved by multiple steps mediated by either stochastic processes or coherent mechanisms. The processes of stochastic acceleration through scattering by waves and turbulence are well known (Terasawa and Scholer, 1989). On the other hand coherent mechanisms such as surfatron (Ragdeev and Shapiro, 1973) can produce very high energies.

In general particles are accelerated to high energies by a combination of mechanisms such as Fermi acceleration, betatron acceleration, wave-particle interactions, inductive electric fields, parallel electric fields. The manner in which these mechanisms work together to yield highenergy particles will depend on the nature of the fields and plasma. MMS is targeted to make measurements of the distributions of the electrons and ions, and the electric and magnetic fields to enable an understanding of the different acceleration mechanisms operating at the magnetospheric boundaries and layers.

One of the unsolved puzzles of the geospace storms and substorms is the origin of energetic oxygens in the storm-time ring current. During many storms the ratio of the oxygen ion to proton densities are enhanced during substorms (Korth et al., 2003). While these oxygen ions may have come from the ionosphere

(Daglis and Axford, 1996), the processes responsible for their acceleration from energies of ∼eV in the ionosphere to hundreds of keV in the ring current are not well understood. The ions are accelerated to by the field aligned electric fields as they flow out of the ionosphere and then by the reconnection related processes in the magnetotail. The dipolarization of the magnetic field, which transports them to the inner magnetosphere will further energize these ions. The understanding of the acceleration processes in the magnetotail, e.g., the required initial energy, different energization processes and the final energy, will need detailed measurements at the micro-scale.

4.4 Turbulence

At the microscopic level the physics of reconection, thin current sheets, particle acceleration are intimately inter-connected. The presence of turbulent fields will affect the nature of reconnection, making it more like collisional reconnection through anomalous collisions that depend on the strength of the turbulence. Turbulence can affect the structure and dynamics of current sheets because of the altered particle trajectories and consequently the currents and fields. Also the stochastic acceleration can be due to the turbulent waves. The measurement strategies of MMS (Curtis, 1999) target these issues to advance the understanding of the micro-scale physics.

The multiscale aspect of turbulence is important in the understanding of how processes at micro-scale level affect those at the global scale. The micro-scale component forms one end of the multiscale features and the scaling of turbulent fluctuations in the range of measurements by MMS will provide details of the micro- to meso-scale coupling.

Turbulence in the magnetosphere has been studied using many data sets and techniques. The statistics of chorus events seen in the groundbased and spacecraft data of particle injections in the near-Earth magnetosphere (Borovsky et al., 1993; Pritchard et al., 1996) show the intensity and occurrence rate of substorms to have a probability distribution with a well-defined mean. While many studies have been based on the auroral indices data, many other studies have used the spacecraft data. Studies of the magnetic field fluctuations during the disruption of the magnetotail current have shown power spectrum dependence (Ohtani et al., 1995; 1998). The plasma flow in the inner plasma sheet measured by Geotail and Wind spacecraft have been used to study the nature of the intermittency in the magnetosphere (Angelopoulos et al., 1999). The probability density of the magnitudes of the bursty bulk flows show power law dependence in time and their distribution is found to be non-Gaussian.

Turbulence in the distant tail has been modeled using percolation theory, which intimately connected with the fractal structure and multiscale behavior (Zelenyi et al., 1998). In this study the plasma turbulence in the distant

magnetotail has been found to have self-organizing properties and these have been described in terms of the fractal properties (Zelenyi et al., 1998).

5. Discussion

Geospace is a local cosmos that provides a uniquely accessible laboratory in which plasmas can be studied in a wide range of environments at scales not possible in the laboratory and in detailsnot accessible compared to astrophysical situations (National Research Council Report, 2004). The understanding of the fundamental processes at the boundary layers is the prime target of MMS and in the same time it will yield unprecedented data for studying the complexity of the magnetosphere. The scaling of the physical phenomena that will be studied by varying the separation among the spacecraft will provide a new understaning of the multiscale phehenomena. The understanding achieved from MMS, a microscope type of geospace mission (Vondrak et al., 2003), is crucial to success of missions exploring phenomena at larger scales, such as Magnetospheric Constellation.

Acknowledgments

The research at the University of Maryland are supported by NASA and NSF grants.

References

Angelopoulos, V., T. Mukai, and S. Kokubun, Evidence for intermittency in Earth's plasma sheet and implications for self-oganized criticality, *Phys. Plasmas, 6*, 4161, 1999.

Asano, Y., T. Mukai, M. Hoshino, Y. Saito, H. Hayakawa, and T. Nagai. (2003). Evolution of the thin current sheet in a substorm observed by Geotail, J. Geophys. Res., 108, doi:10.1019/2002JA009785, 2003.

Baker, D. N., A. J. Klimas, R. L. McPherron, and J. Buechner, The evolution from weak to strong geomagnetic activity: An interpretation in terms of deterministic chaos, *Geophys. Res Lett., 17*, 41, 1990.

Baker, D. N., Pulkkinen, T. I., Angelopoulos, V., Baumjohann, W., McPherron, R. L., Neutral line model of substorms: Past results and present view. *J. Geophys. Res., 101*, 12,975, 1990.

Bargatze, L. F., Baker, D. N., McPherron, R. L., Hones, Jr., E. W., Magnetospheric impulse response for many levels of geomagnetic activity. *J. Geophys. Res., 90*, 6387, 1985.

Borovsky, J. E., Nemzek, R. J. Belian, R. D., The occurrence rate of magnetospheric-substorm onsets: Random and periodic substorms. *J. Geophys. Res., 98*, 3807, 1993.

Borovsky, J. E., Nemzek, R. J. Belian, R. D., The Earth's plasma sheet as a laboratory for flow turbulence in high beta MHD, *J. Plasma Phys., 57*, 1–34, 1997.

Borovsky, J. E., and H. O. Funsten, MHD turbulence in the Earth's plasma sheet: Dynamics, dissipation, and driving, *J. Geophys. Res., 108(A7)*, 3807, doi:10.1029/2002JA009625, 2003.

Curtis, S. A., *The Magnetospheric Multiscale Mission: Resolving Fundamental Processes in Space Plasmas*, NASA/TM-2000–209883, National Aeronautics and Space Administration, 1999.

Daglis, I. A., and W. I. Axford, Fast ionospheric response to enhanced activity in geospace: Ion feeding of the inner magnetotail, *J. Geophys. Res.*, 101, 5047, 1996.

Deng, X. H., and H. Matsumoto, Rapid magnetic reconnection in the Earth's magnetosphere mediated by whistler waves, *Nature*, 410, 557, 2001.

Drake, J. M. . ,

Freeman, M. P., Watkins, N. W., D. J. Riley, Evidence for a solar wind origin of the power law burst lifetime distribution of the AE index, *Geophys. Res. Lett.*, *27*, 1087, 2000.

Hoshino, M, R. L. Stenzel and K. Shibata (eds.), *Magnetic Reconnection in Space and Laboratory Plasmas*, Terra Sci. Pub., Tokyo, 2001.

Huang, C.-S., G. D. Reeves, J. E. Borovsky, R. M. Skoug, Z. Y. Pu, and G. Le, Periodic magnetospheric substorms and their relationship to with solar wind variations, *J. Geophys. Res., 108(A6)*, 3807, doi:10.1029/2002JA009704, 2003.

Jensen, H. J., *Self-Organized Criticality: Emergent Complex Behavior in Physical and Biological Systems*, Cambridge, University Press, 1998.

Klimas, A. J., J. A. Valdivia, D. Vassiliadis, D. N. Baker, M. Hesse, and J. Takalo, Self-organized criticality in the substorm phenomenon and its relation to localized reconnection in the magnetospheric plasma sheet, *J. Geophys. Res., 105*, 18,765, 2000.

Korth, A., Friedel, R. H. W., M. G. Henderson, F. Frutos-Alfaro, and C. G. Moukis, O+ transport into the ring current: Storm versus substorm, in *Disturbances in Geospace: The Storm-Substorm Relationship, Geophysical Monograph series, Vol. 142*, eds., A. S. Sharma, Y. Kamide and G. S. Lakhina, Amer. Geophys. Union, 2003.

Lyon, J. G., The solar wind—magnetosphere—ionosphere system, *Science, 288*, 1987, 2000.

National Research Council, *Plasma Physics of the Local Cosmos*, The National Academies Press, Washington, DC, 2004.

Ohtani, S., Higuchi, T., Lui, A. T. Y., Takahashi, K., Magnetic fluctuations associated with tail current disruption: Fractal analysis. *J. Geophys. Res., 100*, 19,135, 1995.

Ohtani, S., Higuchi, T., Lui, A. T. Y., Takahashi, K., AMPTE/CCE-SCATHA simultaneous observations of substorm associated magnetic fluctuations. *J. Geophys. Res., 103*, 4671, 1998.

Oieroset, M., T. D. Phan, M. Fujimoto, R. P. Lin, and R. P. Lepping, In situ detection of collisioless reconnection in the Earth's magnetotail, *Nature, 412*, 414, 2001.

Oieroset, M., R. P. Lin, T. D. Phan, D. E. Larson and S. D. Bale, Evidence for elctron acceleration up to ∼300 keV in the magnetic reconnection diffusion region of Earth's magnetotail, *Phys. Rev. Lett., 89*, 195001, 2002.

Parker, E. N., Magnetic reconnection and the lowest energy state, in *Magnetic Reconnection in Space and Laboratory Plasmas*, pp. 411–416, Terra Sci. Pub., Tokyo, 2001.

Parker, E. N., *Spontaneous Current sheets in Magnetic Fields*, Oxford Univ. Press., Oxford, 1994.

Phan, T. D., L. M. Kistler, B. Klecker, G. Haerendel, G. Paschmann, B. U. O. Sonnerup, W. Baumjohann, M. B. Bavassano-Cattano, C. W. Carlson, A. M. DiLellis, K. H. Fornacon, L. A. Frank, M. fujimoto, E. Geogescu, S. Kokubun, E. Moebius, T. Mukai, M. Oieroset, W. R. Paterson, and H. Reme, Extended magnetic reconnection at the Earth's magnetopause from detection of bi-directional jets, *Nature, 404*, 848, 2000.

Priest, E. R., Solar flare theory and the status of flare understanding, in *High Energy Solar Astrophysics—Anticipating HESSI*, eds. R. Ramaty and N. Mandzhavidze, ASP Conf. Ser. 206, pp. 13–26, Astron. Soc. Pacific, 2000.

Pritchard, D., Borovsky, J. E., Lemons, P. M., Price, C. P., Time dependence of substorm recurrence: An information theoretic analysis. *J. Geophys. Res., 101*, 15,359, 1996.

Rostoker, G., Implications of the hydrodynamic analogue for the solar-terrestrial interaction and the mapping of high latitude convection pattern into the magnetotail, *Geophys. Res. Lett., 11*, 251, 1984,

Sergeev, V. A., Pulkkinen, T. I., Pellinen, R. J., Coupled mode scenario for the magnetospheric dynamics. *J. Geophys. Res., 101*, 13,047, 1996.

Sergeev, V. A., A. Runov, W. Baumjohann, R. Nakamura, T. L. Zhang, M. Volwerk, A. balogh, H. reme, J. A. Sauvaud, M. Andre, and B. Klecker, Current sheet flapping motion and structure observed by Cluster, *Geophys. Res. Lett., 30*, 1327, doi:10.1029/2002GL016500, 2003.

Shao, X., M. I. Sitnov, A. S. Sharma, K. Papadopoulos, C. C. Goodrich, P. N. Guzdar, G. M. Milikh, M. J. Wiltberger, and J. G. Lyon, Phase transition-like behavior of magnetospheric substroms: Global MHD simulation results, *J. Geophys. Res., 108(A1)*, 1037, doi:10.1029/2001JA009237, 2003.

Sharma, A. S., Assessing the magnetosphere's nonlinear behavior: its dimension is low, its predictability, high. *Reviews of Geophysics (Suppl.), 35*, 645–650, 1995.

Sharma, A. S., Sitnov, M. I., and Papadopoulos, K., Substorms as nonequilibrium phase transitions, *J. Atmos. Sol. Terr. Phys., 63*, 1399, 2001.

Sharma, A. S., Vassiliadis, D. V., Papadopoulos, K., Reconstruction of low-dimensional magnetospheric dynamics by singular spectrum analysis. *Geophys. Res. Lett., 20*, 335, 1993.

Sharma, A. S., Papadopoulos, K., Vassiliadis, D., Valdivia, J. A., Klimas, A. J., and Baker, D. N., Phase transition-like behavior of the magnetosphere during substorms. *J. Geophys. Res., 105*, 12,955, 2000b.

Sharma, A.S., Sitnov, M. I., Ukhorskiy, A. Y., and J. A. Valdivia, Modelling the magnetosphere from time series data, in *Disturbances in Geospace: The Storm-substorm Relationship, Geophysical monograph series, vol. 142*, edited by A. S. Sharma, Y. Kamide and G. S. Lakhina, Amer. Geophys. Union, pp. 231–241, 2003.

Shay., M. A., J. F. drake, B. N. Rogers and R. R. E., The scaling of magnetic reconnection for large systems, *Geophys. Res. Lett., 26*, 2163, 1999.

Siscoe, G. L., The magnetosphere: A union of independent parts. *EOS, Trans. AGU, 72*, 494–497, 1991.

Sitnov, M. I., and A. S. Sharma, Role of Transient Electrons and Microinstabilities in the Tearing Instability of the Geomagnetic Current Sheet and the General Scenario of the Substorm as a Catastrophe, in *Substorms-4: Proc. 4th Internl. Conf. on Substorms*, edited by S. Kokubun and Y. Kamide, Terra Sci., Tokyo, pp. 539–542, 1998.

Sitnov, M. I., Sharma, A. S., Papadopoulos, K., Vassiliadis, D., Valdivia, J. A., Klimas, A. J., and Baker, D. N., Phase transition-like behavior of the magnetosphere during substorms. *J. Geophys. Res., 105*, 12,955, 2000.

Sitnov, M. I., L. M. Zelenyi, H. V. Malova, and A. S. Sharma, Thin current sheetembedded within a thicker plasma sheet: Self-consistent kinetic theory, *J. Geophys. Res., 105*, 13,029, 200b.

Sitnov, M. I., Sharma, A. S., Papadopoulos, K., Vassiliadis, D., Valdivia, J. A., Klimas, A. J., and Baker, D. N., Modeling substorm dynamics of the magnetosphere: From self-organization and self-organized criticality tononequilibrium phase transitions, *Phys.. Rev. E.*, 65, 016116, 2001.

Somov, B. V., *Cosmic Plasma Physics*, Kluwer Academic Pub., 2000.

Terasawa, T., and M. Scholer, The heliosphere as an astrophysical laboratory for particle acceleration, *Science, 244*, 1050, 1989.

Ukhorskiy, A. Y., M. I. Sitnov, A. S. Sharma and K. Papadopoulos 2004, Global and multiscale dynamics of the magnetosphere, *Geophys Res. Lett., 31*, L08802, doi:10.1029/2003GL018932, 2004.

Uritsky, V. M., A. J. Klimas, D. Vassiliadis, D. Chua, and G. D. Parks, Scale-free statistics of spatiotemporal auroral emissions as depicted by POLAR UVI images: The dynamic magnetosphere is an avalanching system, *J. Geophys. Res., 107*(A12), 1426, 2002.

Vassiliadis, D., Sharma, A. S., Eastman, T. E., Papadopoulos, K., 1990. Low-dimensional chaos in magnetospheric activity from AE time series. *Geophys. Res. Lett., 17*, 1841.

Vondrak, R., J. Slavin, L. Zelenyi, M. Guhathakurta, S. Curtis and B. Tsurutani, Measurement strategies for future missions to understand geospace dynamics, in *Disturbances in Geospace: The Storm-substorm Relationship, Geophysical monograph series, vol. 142*, Eds. A. S. Sharma, Y. Kamide and G. S. Lakhina, Amer. Geophys. Union, pp. 255–268, 2003.

Zelenyi, L. M., D. C. delcourt, H. V. Malova, and A. S. Sharma, "Aging" of the magnetotail thin current sheet, *Geophys. Res. Lett., 29, (12)*, 49–1, doi:10.1029/2001GL013789, 2002.

Section 2

LABORATORY PLASMAS

Chapter 9

PERSPECTIVES OF INTERMITTENCY IN THE EDGE TURBULENCE OF FUSION DEVICES

R. Jha, P. K. Kaw and A. Das
Institute for Plasma Research
Bhat, Gandhinagar-382 428, INDIA

Abstract: Experimental observations of intermittency phenomena in the edge plasma turbulence of fusion devices are summarized. New results from ADITYA tokamak are presented which show that the intermittent particle flux obeys a stable Lévy distribution. The distribution function is self-similar over a range of time-scales extending upto 50 decorrelation times. The distribution of waiting time between successive bursts of particle flux follows an asymptotic power-law. These observations indicate that the intermittent particle flux is caused by a mechanism involving "storage and release". An attempt is made to present a perspective for the intermittency in edge turbulence in comparision to similar phenomena observed in fluid turbulence.

Key words: Fusion devices, edge turbulence, intermittency, particle flux

1. Introduction

The magnetically confined plasma in toroidal devices (e.g., tokamaks and stellarators) necessarily has a boundary layer which separates the hot main plasma from the cold material wall. This boundary layer is characterized by open magnetic field lines which terminate on the limiter or the diveror plates [1]. The width of the boundary layer (also known as the scrape-off layer) is typically a few centimeters. In contrast, the main plasma is confined by nested magnetic flux surfaces formed by endless field lines. Although the boundary layer plasma constitutes an insignificant part of the plasma in the device in terms of geometrical dimensions and heat content, it influences the global confinement in a significant way. The boundary layer plasma is characterized by sharp change in the gradients of plasma parameters, namely temperature,

A.S. Sharma and P.K. Kaw (eds.), Nonequilibrium Phenomena in Plasmas, 199–218.
© 2005 *Springer. Printed in the Netherlands.*

density and electric field. The free energy available in these gradients, together with that associated with the curvature of field lines, drives the boundary layer plasma turbulent. The boundary layer and a couple of centimeters part of the nearby main plasma are intimately related and together form the so-called edge plasma. The diffusion and convection by the turbulent edge plasma influences the loss rates of heat and particles even from the core through the boundary conditions they create at the edge; this has led to an extensive study of these effects over the last two decades.

Early studies concentrated on characterizing the stationary state of edge turbulence [2,3]. Main results are summarized as follows: (i) the turbulence consists of low frequency ($\omega < \omega_{ci}$, where ω_{ci} is the ion cyclotron frequency) and small wave length ($k_\perp \rho_s \leq 0.1$, where $k_\perp$ is the perpendicular wave number and ρ_s is the ion gyroradius at electron temperature) electrostatic fluctuation, (ii) the parallel wave number, $k_\parallel \ll k_\perp$, (iii) the wave number and frequency spectrum, $S(k, \omega)$ is broad and statistical dispersion relation, $k(\overline{\omega})$ is linear [see for example, Fig. (1)], (iv) typical correlation time is 10–100 μs and perpendicular correlation length is 2–5 cm, (v) a significant amount of three-wave coupling as measured by bispectrum is present, (vi) the fluctuation levels ($\delta n_e/n_e$ and $e\delta\phi_f/T_e$, where n_e and T_e are the mean values of plasma density

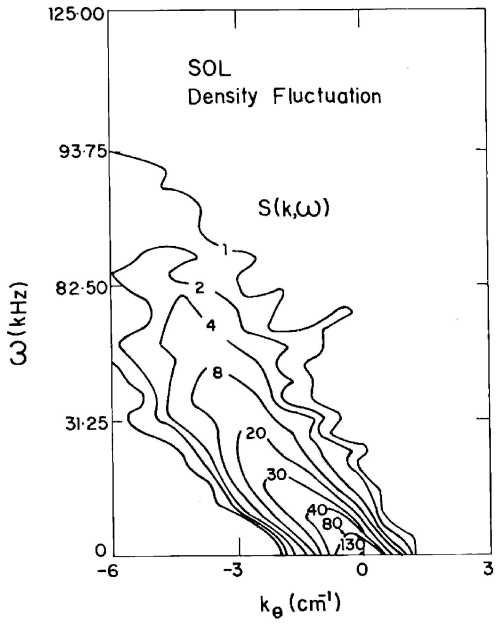


Figure 1. $S(k, \omega)$ spectrum for ion saturation current fluctuations in the scrape-off layer plasma of ADITYA tokamak. The details are in Sen and Saxena [8].

and electron temperature, ϕ_f is the floating potential, e the electronic charge and δ indicates fluctuation) increase with the minor radius, r, and may become as large as 25–50%, (vii) the saturation level of density fluctuation scales linearly with ρ_s/L_n in several devices, where L_n is the gradient scale length [$L_n = (\frac{1}{n_e}\frac{dn_e}{dr})^{-1}$]. This is consistent with the saturation at the mixing length level, $1/k_\perp L_n$, (viii) the fluctuation propagates in the electron diamagnetic direction inside the last closed flux surface and in the ion diamagnetic direction inside the scrape-off layer (SOL). (ix) in addition, there is an $\mathbf{E} \times \mathbf{B}$ poloidal flow. A sharp gradient in the $\mathbf{E} \times \mathbf{B}$ velocity gives rise to a velocity shear layer (about 5 mm in width) near the last closed flux surface (LCFS) which can suppress turbulence.

During the past decade the focus of study has shifted towards non- stationary and intermittent features of edge turbulence. Although the results are still limited in scope, some aspects of intermittency of the edge turbulence are now widely accepted. For example, probability distribution functions (PDFs) of fluctuations in plasma density are reported to be non-Gaussian in all fusion devices; similarly, the floating potential is also non-Gaussian in many devices. When these signals are bandpass filtered, the non-Gaussianity increases with band pass frequency, thus indicating that the intermittency becomes stronger at shorter scales like in conventional hydrodynamic turbulence. Similarly, it is believed that these non-Gaussian PDFs may be related to coherent structures embedded in the turbulence. Several measurements support this point of view. An aspect of intermittency which has received some attention is the nature of nonlinear interactions among the various modes. It has been reported that interactions involve a wide range of frequencies and wave numbers. The important issue of self-similarity in the edge turbulence has also been experimentally investigated during the last few years. Analysis of edge fluctuation data from a number of fusion devices shows that fluctuation amplitudes exhibit self-similarity of different kinds over different ranges of time scales extending from a few multiples of the decorrelation time to the confinement time of the device. Finally, among derived quantities, the maximum amount of work has been done on intermittency studies of fluctuation induced particle flux across the confining magnetic field. This is a topic of great practical interest to the fusion scientists. The time series of the turbulent particle flux show all characteristic features of intermittency, viz. non-Gaussian PDFs, relationship with coherent structures, self-similarity of various kinds etc.

These somewhat preliminary results on intermittency in plasma turbulence may be contrasted with the more detailed and significant studies on the subject of intermittency in fluid turbulence [4]. In fluids , the existence of intermittency has been related to non-Gaussianity of PDFs for velocity gradients, patchiness of the "dissipation rate" in space and time, the existence of transient coherent entities like "vortex ropes, filaments, patches etc.", deviation of the observed

scaling exponent in the spectral energy density from the Kolmogorov value of $-5/3$ etc. All of this work has culminated in the quantitative description of fluid intermittency in terms of deviation of the scaling exponent of the p^{th} order structure function, $S_p(\ell) \equiv \langle [\delta v_\parallel(\ell)]^p \rangle \sim \ell^{\zeta_p}$ from the Kolmogorov prediction, namely $\zeta_p = p/3$. Here $\delta v_\parallel(\ell)$ is the longitudinal velocity increment of length scale ℓ and p is the order of the moment. These measurements of the p^{th} order structure function are then modeled using simple multifractal cascade models of dissipation which try to abstract the dynamics of the nonlinear terms in simple physical terms. At the moment, there are no first principles models of intermittency in hydrodynamic turbulence which are based on the Navier-Stokes equations and are also simple to understand and/or calculate. In the case of plasma edge turbulence in fusion devices, the situation is more primitive for several reasons: the edge plasma problem is conceptually more difficult because the excitation scales of instabilities (i.e., energy containing range of turbulence) are not widely separated from the dissipation scales and so the existence of an "inertial range" is questionable; the typical scale lengths of variation in the boundary layer are also very short making the turbulence highly inhomogeneous and anisotropic; the measurements are harder because the Taylor hypothesis may not be appropriate, the plasma supporting several natural modes of oscillation which propagate as linear and nonlinear wave-like entities in the plasma through dispersive effects etc. Given these qualifications, we realize that the study of intermittency in plasma turbulence is still at a relatively primitive stage ; however, we feel that it is worthwhile to summarise what has happened in this field of research during the past decade or so. Our purpose, therefore is to present a summary of experimental results on intermittency and try to correlate them. We use results from ADITYA tokamak as examples. Some recent results on self-similarity of particle flux are also presented which illustrate a new trend in our understanding of intermittency phenomena.

2. Probability Distribution Function

It is well known that a Gaussian PDF naturally arises when modes with completely random phases are superposed. The Gaussian PDF has zero odd order moments and all even order moments can be expressed in terms of the second order moment. In theoretical descriptions of fluid turbulence, an assumption of near- Gaussian PDF is usually made to facilitate closure of moments. Under this assumption, the turbulent fluctuation has a finite but small third order moment and all higher moments are Gaussian. Such a fundamental assumption has far reaching consequences. The turbulence is thus seen as an ensemble of space filling (and stationary) plane waves with random phases. In the framework of Kolmogorov's theory, such an assumption is valid in the inertial range of scales [4]. However, measurements showed a deviation from the theoretical

prediction. Although, the velocity fluctuations had a Gaussian PDF, velocity increments and higher derivatives were non-Gaussian [5–7]. These measurements indicated the existence of short scale transient coherent structures, like concentrated vortex filaments, patches etc. which could lead to patchiness of turbulence dissipation parameters in space and time.

The subject of intermittency has attracted the attention of the fusion community with the report of non-Gaussian PDFs of plasma fluctuations and fluctuation induced flux in the edge plasma of ADITYA tokamak [8,9]. These results have now been confirmed in a large number of fusion devices [10–17]. The measured PDFs of fluctuations in plasma density, floating potential and particle flux are leptokurtic with peaked central region and fatter wings. An example is shown in Fig. (2). The non-Gaussianity is quantified in terms of skewness (the third order moment) and kurtosis (the fourth order moment) of the PDF.

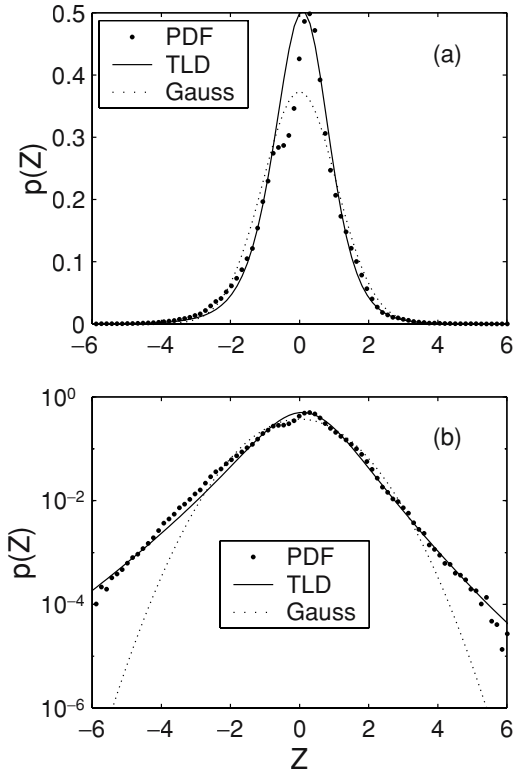


Figure 2. The PDF of floating potential fluctuation in ADITYA which shows clear deviation from a Gaussian distribution. The linear plot (a) shows the deviation near the origin, while the semilog plot (b) shows the deviation at the wings. A truncated Lévy distribution (TLD) has been fitted [42].

While most of these measurements are obtained with Langmuir probes, results from CT-6B [12] and Alcator C-Mod [15] uses H_α and D_α light intensity for the measurements of plasma density (or plasma pressure). Typical results indicate skewness (S) and kurtosis (K) of density fluctuation as 0.1–1 and 1–3 respectively above their Gaussian levels (S = 0, K = 3). The values of skewness and kurtosis for the particle flux are 1–2 and 5–30 respectively. The electric potential and plasma density are the relevant turbulence quantities in the edge plasma just like the fluid velocity and its gradient are the relevant quantities in fluid turbulence. However, it is not yet clear how the non-Gaussianity of fluctuations in plasma turbulence may be related to intermittency of vorticity and dissipation rate, as in the case of fluid turbulence.

The shear layer, near the last closed flux surface can influence the statistical properties of fluctuations. Results from TJ-I tokamak indicate that PDFs of floating potential and density fluctuations in the main plasma near the shear layer (r_{sh}) are Gaussian, but in the SOL region ($r/r_{sh} > 1$), the PDFs become clearly non-Gaussian [11]. However, particle flux is non-Gaussian through out the edge region ($r/r_{sh} = 0.9 - 1.1$). Similar observations have been reported from Tore Supra [13,14], Alcator C-Mod [15] and D-IIID [18] tokamaks. Sanchez *et al*. [19] have presented results for boundary regions of Advanced Toroidal Facility (ATF) and Wendelstein 7-Advanced Stellarator (W7-AS) and Joint European Torus (JET). In all the three machines, fluctuations in ion saturation current and floating potential have a near-Gaussian character in the proximity of the shear layer. However, fluctuations deviate from a Gaussian distribution when moving inside of the plasma edge ($r < r_{sh}$) and into the SOL region ($r > r_{sh}$). It is now understood that velocity shear can decorrelate fluctuations and destroy localized coherent structures which are primarily responsible for the non-Gaussian PDFs.

An important feature of intermittency in fluid turbulence is that the non-Gaussianity (measured in terms of kurtosis of velocity difference) increases as order of the difference (or derivative) is increased [5–7]. Since higher order derivatives selectively pick up higher wave numbers, this observation indicates that the non-Gaussianity increases with wave numbers. Thus, small scale fluctuations are more intermittent than large scale ones. Similar studies have been carried out in edge turbulence of ADITYA tokamak using band pass wavelet filter and it is concluded that low frequency components are nearly Gaussian [20]. Figure 3 shows an example of intermittency in the high frequency components of the fluctuation data. The non-Gaussianity appears at frequencies above 20 kHz indicating that the intermittency is basically a small time scale (<50μs) phenomenon. Since fluctuation propagate with phase velocity of $\sim 2 \times 10^5$ cm/s), the intermittent time scales correspond to structures of size <10 cm. The floating potential fluctuation in the Reverse Field Pinch device RFX [21] and the stellarator L-2M [16] have also been analysed using

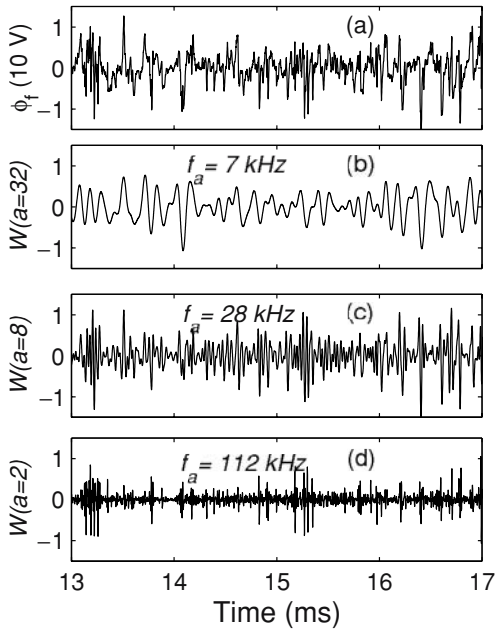


Figure 3. (a) The floating potential data from ADITYA discharge no. 2009 is filtered using wavelet [20] and shown here for three wavelet components: (b) $W(a = 32)$, (c) $W(a = 8)$ and (d) $W(a = 2)$, where a is the scale parameter. The wavelet components are shown after normalization with $1/\sqrt{a}$. The frequency, f_a at which the bandpass filter has peak response is also shown in figures (b–d). The results show that fluctuation data are more intermittent at higher frequencies.

similar technique and the same conclusion has been arrived at. Magnetic fluctuation, δb, has been analysed in the RFX device using digital filtering and it has been concluded that intermittency increases at small scales and on moving towards the wall [22]. Measurement of scaling exponent of the structure function, $S_p(\tau) = \langle[\delta b(\tau)]^p\rangle \sim \tau^{\zeta_p}$, has also been attempted and it is found that deviation of ζ_p from $p/3$ increases on moving towards the wall [22].

3. Localized Coherent Structures

The non-Gaussian PDF is related to granular features in the time series of plasma fluctuations. Measurements of two-dimensional structures of plasma fluctuations in the radial-poloidal $(r - \theta)$ plane have been reported from the Caltech tokamak using Langmuir probes [23]. The structures in the edge plasma $(r/a = 0.85–0.95)$ appear to be localized and have a short life time (a few tens of μs). A detailed measurement of two-dimensional structures have been reported from ADITYA tokamak using conditional averaging technique [24].

This technique allows to build up a statistically averaged picture of coherent structures. For this purpose, a suitable condition is applied on the fluctuation time series at a fixed reference probe and conditional structures (e.g., potential blobs) are picked up by a number of probes. These probes form a linear array (in poloidal direction) and can be moved to predetermined radial locations in different discharges. An ensemble averaging of potential blobs at each probe location (a 10×10 matrix) help to retain coherent part and incoherent components are eliminated. The experiment on ADITYA has shown that coherent structures are found on both sides of the LCFS (i.e., $r/a = 1$) and they are generally isolated [see Fig. (4)]. The poloidal span of the structure is generally larger than the

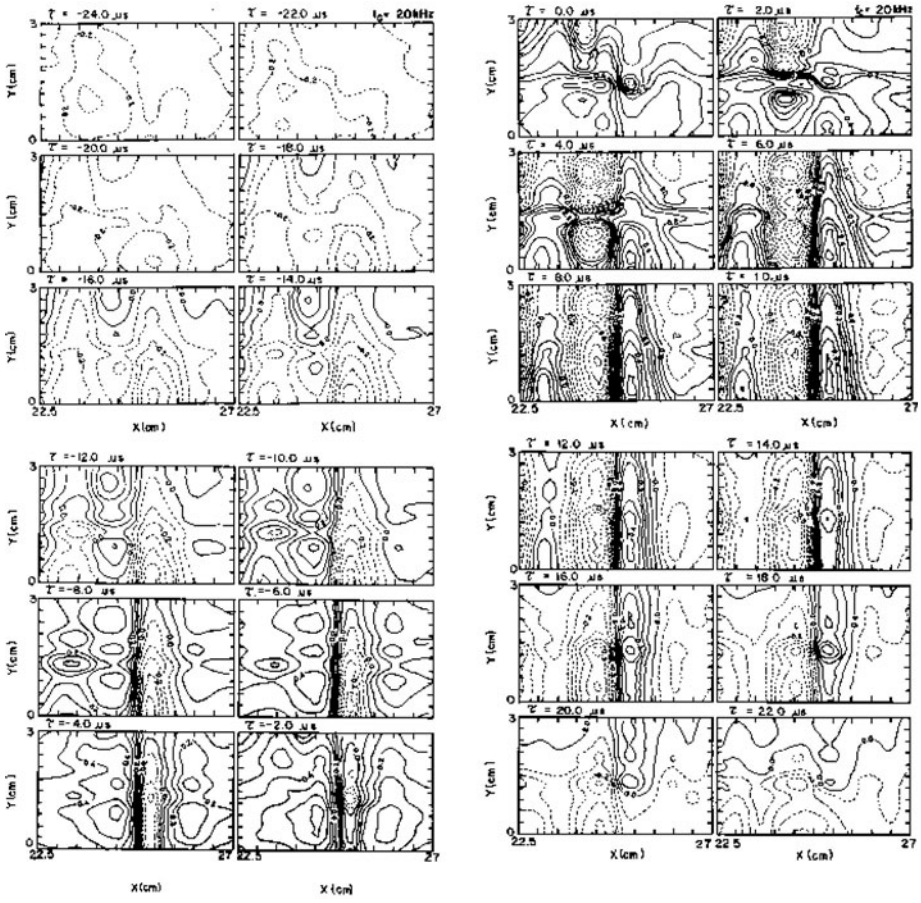


Figure 4. Iso-amplitude contours of conditional averages of floating potentials at 10×10 grid points covering an area is 4.5×3.0 cm^2 in the radial (X) and vertical (Y) plane. The limiter position is X = 25 cm. The conditional structures are found on both sides of the limiter. The details are in Ref. [24].

radial span except when the isolation is broken. This happens at large amplitude. When the isolation breaks, the potential contour gets aligned in the radial direction indicating that the coherent structure has crossed the LCFS. The structure crosses the LCFS with an estimated radial velocity (E_θ/B_ϕ) in the range (0.5–1) km/s. This convection velocity is about an order of magnitude larger than the diffusion velocity ($v_{diff} = D_\perp/L_n$, where $D_\perp$ is the perpendicular diffusivity). Such fast transport events can be recognized as streamers in the framework of low frequency magnetized plasma turbulence such as turbulence due to drift waves, resistive ballooning modes etc. [25]. Normally the coherent structures are poloidally elongated and radially localized which can be recognized as the well known low frequency modes saturated by the self-consistently generated velocity shear due to associated zonal flows. The streamer events can break and propagate through a transport barrier that is generated by this velocity shear.

Sometimes, the streamer events can be seen in the form of dense, radially convecting blobs of plasma moving across the magnetic field in the low density background plasma. The convection of density blobs in the edge plasma has directly been observed in D-IIID tokamak using beam emission spectroscopy [26]. The density blobs move in poloidal as well as radial direction. The poloidal velocity is typically twice the radial velocity (0.5–2 km/s). Similar observation has also been reported using gas puff imaging (GPI) diagnostics on NSTX and Alcator C-Mod tokamaks [27–29]. The GPI diagnostics allow observation in the $r - \theta$ plane when a gas puff is released in the limiter shadow. The observation plane is defined by the leading ionization front and the rear emission front. The observation shows blobs of H_α (or D_α) light moving in radial and poloidal directions. The typical size of the blob is 1–2 cm and the life time is few tens of micro-seconds. The blobs actually represent localized regions of plasma pressure. In most C-Mod and NSTX discharges, the blobs are seen outside the LCFS while DIII-D measurements show that they are formed near the LCFS. It appears that separatrix and/or open field lines are involved in their generation and/or transport. Detailed experiment has further shown that as the mean density ($\overline{n_e}$) is raised towards the Greenwald limit ($\overline{n_e}/n_{GW} \sim 0.7$), the blobs can also be seen inside the LCFS. Thus, GPI observations complement the measurements with Langmuir probes and demonstrate that intermittently occuring blobs are responsible for the large amplitude non-Gaussian distributed events on the probes.

In addition to the direct observation in the $r - \theta$ plane, the coherent structures being the cause of intermittency has also been inferred from advanced analysis of time series data. Langmuir probe data from ADITYA and ASDEX have been analysed using biorthogonal decomposition technique to characterize coherent structures [30]. They have shown that such structures effectively contribute to radial transport and intermittency. Similarly, coherent structures of density fluctuations have been observed in CT-6B tokamak

plasma by analysing the measured H_α intensity using wavelet correlation technique [12]. The structures exhibit strong temporal and spatial intermittency with a life time of 20–100 μs and radial size of 1–4 cm.

4. Broadband Nonlinear Interactions

Evidence of three wave nonlinear coupling in the edge plasma of fusion devices has been reported [31–33]. The nonlinear coupling is measured in terms of bicoherence between three frequency components, ω_1, ω_2 and ω_3 such that $\omega_3 = \omega_1 \pm \omega_2$. A finite bicoherence in the fluctuation time series indicates that ω_3 is produced by frequency mixing of ω_1 and ω_2. The bispectral analysis of fluctuation time series at two probe points can give bicoherence among wave numbers $k_3 = k_1 \pm k_2$ as well as power transfer due to linear and nonlinear wave coupling. Such studies have shown that both forward (i.e., $\omega_3 = \omega_1 + \omega_2$) and inverse (i.e., $\omega_3 = \omega_1 - \omega_2$) cascade of energy do take place in the turbulent edge plasma [32]. A new bispectral analysis technique has been introduced by Milligen *et al.* [34] in which wavelet transform is used in place of Fourier transform. Since a wavelet is a localized basis function (as against nonlocal sinusoid), this technique allows studies of intermittency phenomena. The presence of nonlinear coupling among wavelet components is measured in terms of wavelet bicoherence. The analyses of probe and reflectometry data in ATF stellarator [32] and probe data in ADITYA tokamak [20] show that fluctuation time series have episodes of strong nonlinear coupling among wavelet components punctuated by quiescent periods when the coupling is absent. Analysis of ADITYA discharges has further shown that wavelet bicoherence is strong in presence of well separated (sparse) structures [36]. When the structures are closely packed, the wavelet bicoherence is negligible. The wavelet bicoherence measurements of plasma fluctuations in D-IIID tokamak have shown that total bicoherence temporally varies in both L- and H-mode discharges but L-mode displays much weaker intermittency than H-mode discharges [37].

5. Self-Similarity of Time Scales

The experimental results summarized in previous sections indicate that the edge turbulence contains localized coherent structures embedded in random fluctuations. Detailed three- or two-dimensional imaging of such structures has not been possible because of the limitation of diagnostics. Images of structures in fluid turbulence have been analysed to provide geometric description of turbulence in terms of fractals [38,39]. In the edge turbulence of fusion devices, however, most measurements consist of time series of plasma density, floating potential and particle flux as recorded by Langmuir probes. Therefore, self-similarity studies using fluctuation time series give information about the self-similar time scales. The studies based on rescaled (R/S) range analysis

essentially implies a power law dependence of auto-correlation function over a long range of delay times. This approach has attracted considerable attention in recent times [40]. The time series of turbulent fluctuations in several fusion devices have been shown to exhibit self-similarity [41]. The self-similarity time scales lie between the decorrelation time and the confinement time of the device, which is the so called mesoscale range. Recently we have reported on the studies of self-similarity in the scrape-off layer plasma of ADITYA tokamak, using the probability distribution function (PDF) approach [42]. We have shown that fluctuations in floating potential and its spatial derivative exhibit two self-similar scaling ranges: (i) a short time scale which extends up to three times the decorrelation time (τ_d), and (ii) a long time scale ($>3\tau_d$). The first scaling range is the fluctuation scale range and the second one is the mesoscale range. The PDFs in the fluctuation range follow a truncated Lévy distribution whereas those in the mesoscale range follow a Gaussian distribution. Recent results from Uragan-3M stellarator [17] also show that plasma fluctuations exhibit stable Lévy distribution.

Since the time series of particle flux is derived from the time series of density and radial velocity, the statistical properties of the flux should depend on the relative phases of the two quantities. It is not yet clear how the relative phases of density and radial velocity would influence the self-similarity property of the particle flux. The time series of fluctuation induced particle flux in the scrape-off layer plasma of W7-AS stellarator has been analysed for self-similarity and a self-similar mesoscale range has been reported [43].

We now present some of our recent analysis showing self-similarity of particle flux in the scrape-off layer plasma of ADITYA tokamak. The particle flux is measured using an array of ten Langmuir probes. The probe array is located in the scrape-off-layer (SOL) region, at 10 mm behind the limiter which is outside the shear layer. The particle flux is determined from simultaneous measurements of ion saturation current (I_s) and floating potential (ϕ) in alternate pins of the probe array. The data are digitally sampled at a rate of 1 MHz. The time series of particle flux is obtained from the product, $\Gamma_j \equiv I_s \Delta\phi$, where $\Delta\phi$ is the potential difference at adjacent probes. The ion saturation current is assumed to be proportional to the plasma density and $-\Delta\phi$ is proportional to the radial velocity (E_θ / B_ϕ). The burst in particle flux arises when the plasma density and radial velocity are in the same phase (Fig. 5). A time series consisting of about 200,000 data points are generated by combining data from about five discharges. The PDF of the elementary data is strongly peaked at the centre and the positive wing is longer than the negative wing [see Fig. 6, $n = 1$]. The measured skewness and kurtosis are 3.8 and 40 respectively. The positive skewness indicates longer positive wing of the PDF and a net outward flux. This measurement is similar to measurements reported in other tokamaks (e.g., ASDEX [10], TJ-1 [11], Alcator C-mod [15]).

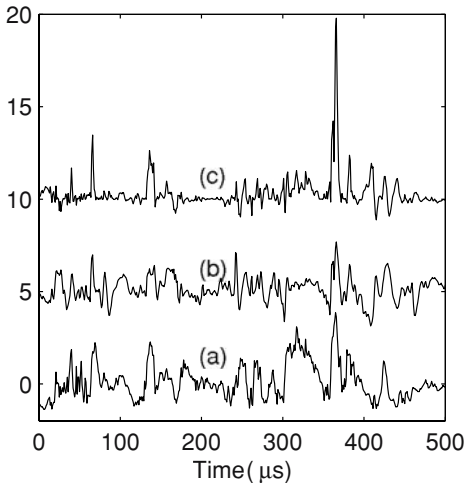


Figure 5. Time series of (a) plasma density (i.e., ion saturation current), (b) poloidal electric field E_θ and (c) particle flux. The amplitude of a flux event is large only when plasma density and poloidal electric field are in the same phase.

The PDF approach of studying self-similarity involves the following steps:

(i) subdivide the experimental time series $\{\Gamma\}$ into non-overlapping blocks of n data points and generate a reformed time series $\{Z_n\}$ such that $Z_n = \sum_{i=1}^{n} \Gamma_i$ in each block,

(ii) determine the PDF, $p(Z_n)$,

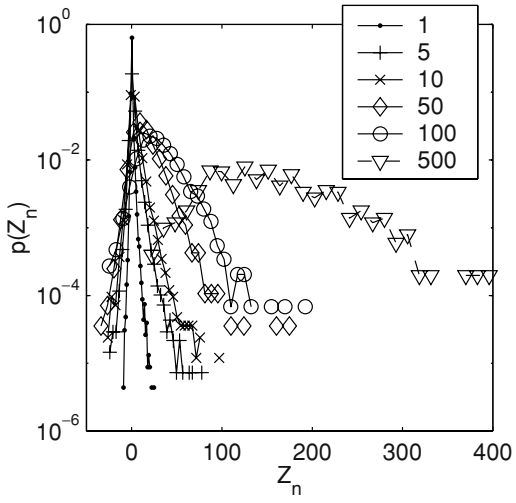


Figure 6. The PDF, $p(Z_n)$ for different values on n (see the legend box). The PDFs are determined for 16 values of n and only 5 such PDFs are shown for clarity. The values of n are shown in the inset. The experimental points (symbols) are joined for easy identification.

(iii) plot the peak value of $p(Z_n)$ vs. n on a log-log scale,

(iv) determine Lévy scale index, α from the power law dependence $\hat{p}(Z_n) \sim n^{-1/\alpha}$, where $\hat{p}(Z_n)$ is the peak value of $p(Z_n)$ and

(v) determine the rescaled PDFs by the following transformations: $DZ_s = (Z_n - D_n)n^{-1/\alpha}$ and $p_s(DZ_s) = p(Z_n)n^{1/\alpha}$, where D_n is the shift of $\hat{p}(Z_n)$ from the origin (i.e., $Z_n = 0$).

The details of the procedure are described in [42] and references therein. Only the transformation rule (v) is modified here by including the shift D_n because the flux PDFs are shifted from the origin unlike the PDFs for the floating potential reported in [40]. It should be noted that the power law dependence of peak of PDF, $\hat{p}(Z_n) \sim n^{-1/\alpha}$ is the basis of self-similarity of PDFs. The collapse of rescaled PDFs on top of one another is an evidence that the self-similarity exists for the entire PDF and not just the peak value.

Figure 6 shows the PDFs, $p(Z_n)$ of the reformed time series for different values of n. It is observed that as n increases, the $\hat{p}(Z_n)$ shifts toward the positive value of Z_n. This is because of high positive skewness (3.8) of the elementary data ($n = 1$). The mean value of the elementary data is 0.26 which translates to an outward flux of 9.5×10^{15} cm^{-2} s^{-1}. We have determined PDFs for $n = 1$, 2, 3, 5, 7, 10, 20, ... 1000. The PDFs up to $n = 500$ are well defined, whereas those for $n = 700$ and 1000 are not so well defined.

Figure 7 shows the plot of $\hat{p}(Z_n)$ vs. n on a log-log graph. The Lévy scale index α as determined from the slope of the graph is 1.43. We observe that

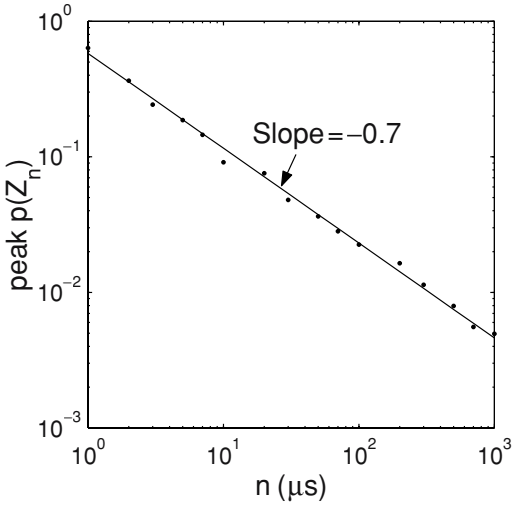


Figure 7. The peak of $p(Z_n)$ as a function of n (shown by bullets). The Lévy index α (= 1.43) is determined from the slope. Since the sampling time is 1 μs, the convolution number, n is expressed in the unit of μs.

although the similar analysis of ion saturation current and floating potential show two scaling ranges [42], the flux data exhibit a single scaling range.

The Lévy scale index α is used to rescale the PDFs as explained earlier. The rescaled PDFs are shown in Fig. (8). It should be noted that without accounting for the shift D_n in the rescaling, all PDFs do not collapse together [44]. Since the shift is caused because of the skewness present in the elementary PDF, it is necessary to include it in the rescaling. The self-similarity range is 1-500 μs. Because of the limited number of data points, the PDFs for higher convolution are not well defined. Figure (8) also shows that the rescaled distribution can be fitted with a truncated Lévy distribution [42].

6. Waiting Time Distribution

The time series of particle flux appears bursty. The burst can be defined when the amplitude of the flux exceeds a certain magnitude. For uncorrelated random bursts, the waiting time distribution, $p(t_w)$, is given by Poisson law: $p(t_w) = e^{-t_w/\tau_w}/\tau_w$, where τ_w is the average waiting time between successive bursts. Thus, the waiting time distribution of experimental flux data would indicate whether the bursts are random or correlated. Figure 9 shows the definition of waiting time. The discrimination level which defines the waiting time is set at $4\sigma_\Gamma$ above the mean flux $< \Gamma >$, where σ_Γ is the standard deviation of the flux time series. The discrimination level is deliberately set high so that only large flux events are used in the analysis and the burst time is small compared to the

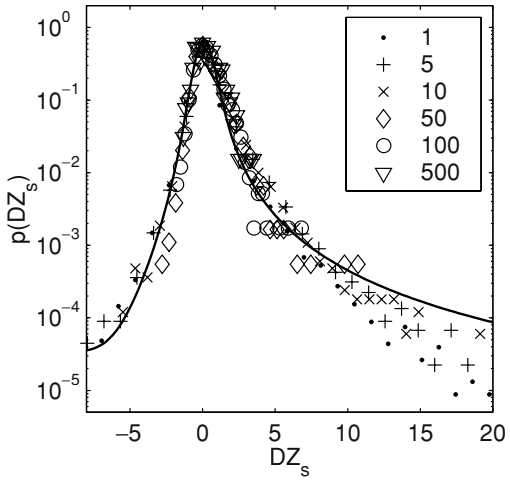


Figure 8. The rescaled PDFs $p_s(DZ_s)$ as a function of DZ_s for different values of n shown in the inset. The solid line shows a truncated Lévy distribution function with following fit parameters: $A_+ = A_- = 1$, $t = 1.5$, $\lambda_+ = 0$, $\lambda_- = 0.1$ and $\alpha = 1.43$. The fitted function is given in Ref. [42].

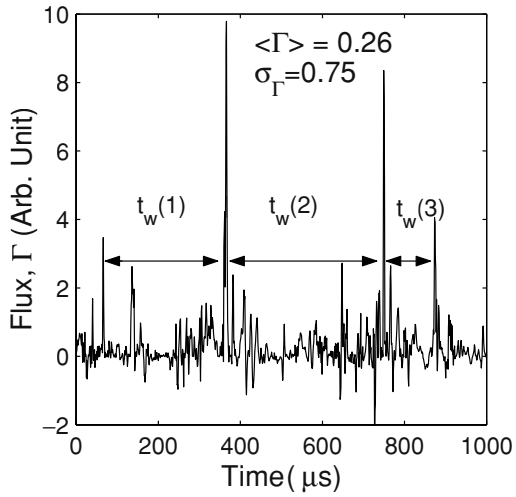


Figure 9. The time series of particle flux. The flux events whose amplitude exceeds $4\sigma_\Gamma$ above the mean flux $< \Gamma >$ are used for determining the waiting time distribution. Here σ_Γ is the standard deviation of the flux. The waiting times, $t_w(1)$, $t_w(2)$, ..., are much larger than the duration of flux events.

waiting time. Recently, there has been considerable debate about the influence of burst time on the waiting time distribution when the two are comparable [45]. Figure 10 shows the experimental results. It is observed that $p(t_w)$ is an asymptotic power law of the form: $p(t_w) = A(1 + t_w/\tau_w)^{-\alpha-1}$ where $A = 0.45$

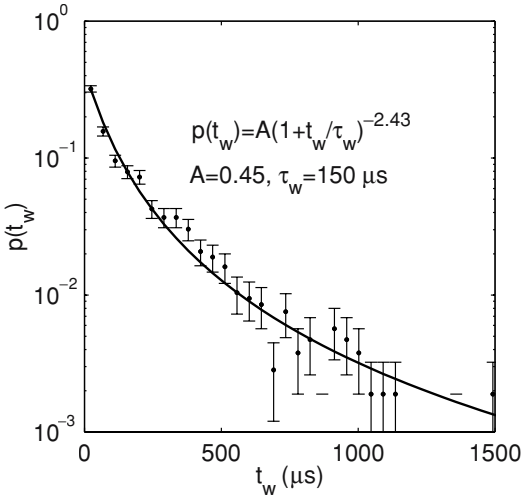


Figure 10. The PDF of waiting time between successive bursts identified when their amplitudes exceed 4 times the standard deviation. The solid line shows a fit to the experimental data (shown by bullets with error bars). The fitting function is an asymptotic power-law.

and $\tau_w = 150$ μs. In the fit, we have used $\alpha = 1.43$ as obtained from the Lévy analysis presented in Fig. (7). The asymptotic power law of waiting time distribution indicates correlated bursts. Similar conclusion has been derived from the analysis of time series of plasma density on RFX reverse field pinch [46,47]. These results question the validity of self-organized criticality model of turbulent transport in fusion devices. The self-similar truncated Lévy distribution and the asymptotic power-law of waiting time distribution indicate a "storage and release" mechanism may be involved in the generation of intermittent particle flux [48].

7. Concluding Remarks

The experimental results summarized in previous sections help us to take a perspective view of intermittency in the edge plasma of fusion devices. The non-Gaussian PDFs of plasma fluctuations and short decorrelation time indicate that localized coherent structures are embedded in random fluctuations. Such inference is validated by direct measurement of coherent structures using conditional sampling as well as observation of blobs using imaging techniques. These structures are typically 2–6 cm and they last for 20–100 μs indicating that there are characteristic length and time scales. However, such conclusion may have been influenced by measurement techniques employed. For example, conditional sampling picks up those structures which satisfy the condition on the fluctuation amplitude and its time derivative. The averaging over an ensemble washes out the small structures. Similar constraint on the spatial resolution apply on the blobs observed using the imaging techniques. If self-similar structures without any characteristic scale are present in the plasma, their measurement would have to await development of better diagnostic techniques. Such an expectation is consistent with the fact that wavelet filtering of fluctuation data shows that the non-Gaussianity increases at small scales.

The small scales in the edge plasma can be produced by two means. First, the velocity shear induced decorrelation gives rise to a Gaussian ensemble for small scales. Such randomization has indeed been observed close to the shear layer in the edge plasma. Second, small scales can also be generated by nonlinear interactions among larger scales. Such nonlinearity induced small scales would be non-Gaussian and intermittent as observed in the edge plasma. The bicoherence measurements also indicate that significant nonlinear interactions exist among a wide range of scales (i.e., frequencies and wave numbers). The interaction producing sum frequencies leads to energy transfer to small scales and the interaction producing difference frequencies leads to energy transfer to large scales. The simultaneous presence of both direct and inverse cascade of energy is an important feature of intermittency in the edge plasma. Measurements of wavelet bicoherence in some machines have revealed that nonlinear

interactions are also intermittent. Since the wavelet bicoherence studies have been carried out on fluctuation measurements in a flowing plasma, it is indicated that there are regions of edge plasma with strong and weak nonlinear interactions.

We finally compare and contrast the respective perspectives of plasma physicists and fluid physicists as regards as the problem of intermittency is concerned. In incompressible hydrodynamics, there are no natural modes of oscillation or waves; this is because when we discuss effects due to flows much slower than the sound speed (where incompressibility assumption is good), sound waves cannot be excited. Thus the turbulent flow can generate nonlinear eddies which do not propagate but interact with other eddies all over space. This leads to eddy viscosity, eddy birth and eddy decay, intermittency and a host of other turbulence effects. Plasma, in contrast, supports many different kinds of waves and oscillations. Even at the low frequencies that we are concerned with, there are drift waves, Alfven waves, ion acoustic waves etc. which can be excited by the free energy sources. These waves have dispersion and group propagation. The first attempt of plasma physicists was to develop nonlinear theories of the weak turbulence type, where the nonlinearity is small and one essentially has an interaction of propagating, weakly dispersive wave packets. It was however noted that saturation amplitudes of drift-like waves are such that the nonlinearity cannot be treated as a small parameter; specifically, the width (in frequency) acquired by the wavepacket because of nonlinear effects was found to be comparable or bigger than the frequency itself. Under these conditions, the linear dispersive modes lost their meaning and new nonlinear coherent effects drivng the system into coherent structures was assumed to be important. This was first demonstrated by Zakharov [49] who described the strong turbulence of plasma waves and ion acoustic waves in an unmagnetized plasma in terms of a collection of collapsing cavitons which were created by a modulational instability mechanism from the plasma wave turbulence. For the low frequency modes of interest to us in the edge turbulence, this has led to the concepts of generation of zonal flows and streamers by modulational instability of the low frequency magnetized plasma turbulence. Thus, new coherent structures form and interact to describe the turbulent state. These coherent structures are created transiently at random locations and do not propagate much before they decay away because of turbulent viscosity effects. In this sense they again resemble eddies, which can then lead to eddy viscosity, transport, creation and destruction of other eddies, intermittency etc. Under these strong turbulence conditions the edge plasma turbulence seems to have a lot in common with the hydrodynamic turbulence problem. It is only much further detailed work which will elucidate the similarities and differences between these two paradigms of observed nonlinear systems.

References

[1] John Wesson, *Tokamaks*, Clarendon Press, Oxford, UK (1997).
[2] P. C. Liewer, Nucl. Fusion **25**, 543 (1985).
[3] A. J. Wootton, B. A. Carreras, H. Matsumoto, K. McGuire, W. A. Peebles, Ch. P. Ritz, P. W. Terry and S. Zweben, Phys. Fluids B **2**, 2879 (1990).
[4] U. Frisch, *Turbulence: The Legacy of A. N. Kolmogorov,* Cambridge University Press, New Delhi, (1999), p. 120.
[5] G. K. Batchelor and A. A. Townsend, Proc. R. Soc. London Ser. A **199**, 238 (1949).
[6] A. A. Townsend, Proc. R. Soc. London Ser. A **208**, 534 (1951).
[7] D. A. Kennedy and S. Corrsin, J. Fluid Mech. **10**, 366 (1961).
[8] R. Jha, P. K. Kaw, S. K. Mattoo, C. V. S. Rao, Y. C. Saxena and the ADITYA Team, Phys. Rev. Lett. **69**, 1375 (1992); A. Sen and Y. C. Saxena, Current Science **65**, 25 (1993).
[9] R. Jha, B. K. Joseph, R. Kalra, P. K. Kaw, S. K. Mattoo, D. Raju, C. V. S. Rao, Y. C. Saxena, A. Sen and the ADITYA team, Proc. 15$^{\text{th}}$ International Conf. Plasma Phys. and Control. Nucl. Fusion, Seville, 26 September-1 October, 1994 (IAEA 1995), Vol. 1, p. 583.
[10] M. Endler, H. Niedermeyer, L. Giannone, E. Holzhauer, A. Rudyj, G. Theimer, N. Tsois, S. Zoletnik, the ASDEX team and the W7-AS team, Nucl. Fusion **35**, 1307 (1995).
[11] B. A. Carreras, C. Hidalgo, E. Sanchez, M. A. Pedrosa, R. Balbin, I. Garcia-Cortes, B. van Milligen, D. Newman and V. E. Lynch, Phys. Plasmas **3**, 2664 (1996).
[12] L. Dong, L. Wang, C. Feng, Z. Li, Q. Zhao and G. Wang, Phys. Rev. E **57**, 5929 (1998).
[13] G. Y. Antar, S. I. Krasheninnikov, P. Devynck, R. P. Doerner, E. M. Hallmann, J. A. Boedo, S. C. Luckhardt and R. W. Conn, Phys. Rev. Lett. **87**, 65001 (2001).
[14] G. Y. Antar, P. Devynck, X. Garbet and S. C. Luckhardt, Phys. Plasmas **8**, 1612 (2001).
[15] B. LaBombard, M. Greenwald, R. L. Boivin, B. A. Carreras, J. W. Hughes, B. Lipschultz, D. Mossessian, C. S. Pitcher, J. L. Terry, S. J. Zweben and the Alcator C-Mod team, Proc. 19th International Conf. Plasma Phys. and Control. Nucl. Fusion, Lyon, October 14–19, 2002, IAEA-CN-94/ EX/D2-1.
[16] W. K. Kharchev, N. N. Skvortsova and K. A. Sarksyan, J. Math. Sci. **106**, 2691 (2001).
[17] V. Yu Gonchar, A. V. Chechkin, E. L. Sorokovoi, V. V. Chechkin, L. I. Grigoreva and E. D. Volkov, Plasma Physics Reports **29**, 380 (2003).

[18] J. A. Boedo, D. Rudakov, R. Moyer, S. Krasheninnikov, D. Whyte, G. McKee, G. Tynan, M. Schaffer, P. Stangeby, P. West, S. Allen, T. Evans, R. Fonck, E. Hallmann, A. Leonard, A. Mahdavi, G. Porter, M. Tillack and G. Antar, Phys. Plasmas **8**, 4826 (2001).
[19] E. Sánchez, C. Hidalgo, D. Lopez-Bruna, I. garcia-Cortes, R. Balbin, M. Pedrosa, B. van Milligen, C. Riccardi and G. Chiodini, J. Bleuel, M. Endler, B. A. Carreras and D. E. Newman, Phys. Plasmas **7**, 1408 (2000).
[20] R. Jha and Y. C. Saxena, Phys. Plasmas **3**, 2979 (1996).
[21] V. Carbone, G. Regnoli, E. Martines and V. Antoni, Phys. Plasmas **7**, 445 (2000).
[22] V. Carbone, L. Sorriso-Valvo, E. Martines, V. Antoni and P. Veltri, Phys. Rev. E **62**, R49 (2000).
[23] S. J. Zweben and R. W. Gould, Nucl. Fusion **25**, 171 (1985).
[24] B. K. Joseph, R. Jha, P. K. Kaw, S. K. Mattoo, C. V. S. Rao, Y. C. Saxena, and the ADITYA team, Phys. Plasmas **4**, 4292 (1997).
[25] P. Beyer, S. Benkadda, X. Garbet and P. H. Diamond Phys. Rev. Lett. **85**, 4892 (2000).
[26] J. A. Boedo, D. L. Rudakov, R. A. Moyer, G. R. McKee, R. J. Colchin, M. J. Schaffer, P. G. Stangeby, W. P. West, S. L. Allen, T. E. Evans, R. J. Fonck, E. M. Hollmann, S. Krasheninnikov, A. W. Leonard, W. Nevins, M. A. Mahdavi, G. D. Porter, G. R. Tynan, D. G. Whyte and X. Xu, Phys. Plasmas **10**, 1670 (2003).
[27] R. J. Maqueda, G. A. Wurden, S. Zweben, L. Roquemore, H. Kugel, D. Johnson, S. Kaye, S. Sabbagh and R. Maingi, Rev. Sci. Instrum. **72**, 931 (2001).
[28] S. J. Zweben, D. P. Stotler, J. L. Terry, B. Labombard, M. Greenwald, M. Muterspaugh, C. S. Pitcher, the Alcator C-Mod group, K. Hallatschek, R. J. Maqueda, B. Rogers, J. L. Lowrance, V. J. Mastrocola and G. F. Renda, Phys. Plasmas **9**, 1981 (2002).
[29] J. L. Terry, S. J. Zweben, K. Hallatschek, B. LaBombard, R. J. Maqueda, B. Bai, C. J. Boswell, M. Greenwald, D. Kopon, W. M. Nevins, C. S. Pitcher, B. N. Rogers, D. P. Stotler and X. Q. Xu, Phys. Plasmas **10**, 1739 (2003).
[30] S. Benkada, T. D. de Wit, A. Verga, A. Sen, the ASDEX team and X. Garbet, Phys. Rev. Lett. **73**, 3403 (1994).
[31] Ch. P. Ritz and E. J. Powers, Physica **20D**, 320 (1986).
[32] Ch. P. Ritz, E. J. Powers and R. D. Bengtson, Phys. Fluids B **1**, 153 (1989).
[33] H. Y. W. Tsui, K. Rypdal, Ch. P. Ritz and A. J. Wootton, Phys. Rev. Lett. **70**, 2565 (1993).
[34] B. Ph. van Milligen, C. Hidalgo and E. Sánchez, Phys. Rev. Lett. **74**, 395 (1995).

[35] B. Ph. van Milligen, E. Sanchez, T. Estrada, C. Hidalgo, B. Branas, B. Carreras, and L. Garcia, Phys. Plasmas **2**, 3017 (1995).
[36] R. Jha, S. K. Mattoo and Y. C. Saxena, Phys. Plasmas **4**, 2982 (1997).
[37] R. A. Moyer, R. D. Lehmer, T. E. Evans, R. W. Conn, L. Schmitz, Plasma Phys. Control. Fusion **38**, 1273 (1996).
[38] K. R. Sreenivasan and C. Meneveau, J. Fluid Mech. **173**, 357 (1986).
[39] P. Constantin, I. Procaccia and K. R. Sreenivasan, Phys. Rev. Lett. **67**, 1739 (1991).
[40] B. A. Carreras, B. van Milligen, M. A. Pedrosa, R. Balbin, C. Hidalgo, D. E. Newman, E. Sanchez, M. Frances, I. Garcia-Cortes, J. Bleuel, M. Endler, S. Davies and G. F. Matthews, Phys. Rev. Lett. **80**, 4438 (1998).
[41] B. A. Carreras, B. van Milligen, M. A. Pedrosa, R. Balbin, C. Hidalgo, D. E. Newman, E. Sanchez, M. Frances, I. Garcia-Cortes, J. Bleuel, M. Endler, C. Ricardi, S. Davies and G. F. Matthews, Phys. Plasmas **5**, 3632 (1998).
[42] R. Jha, P. K. Kaw, D. R. Kulkarni, J. C. Parikh and the ADITYA team, Phys. Plasmas **10**, 699 (2003).
[43] B. A. Carreras, B. van Milligen, C. Hidalgo, R. Balbin, E. Sanchez, I. Garcia-Cortes, M. A. Pedrosa, J. Bleuel and M. Endler, Phys. Rev. Lett. **83**, 3653 (1999).
[44] R. Jha, P. K. Kaw, D. R. Kulkarni and J. C. Parikh, *PLASMA 2002*, Proc. 17^{th} National Symposium on Plasma Science and Technology, Allied Publishers, Chennai (India), December 2002, pp. 45–54.
[45] R. Sánchez, D. E. Newman and B. A. Carreras, Phys. Rev. Lett. **88**, 68302 (2002).
[46] E. Spada, V. Carbone, R. Cavazzana, L. Fattorini, G. Regnoli, N. Vianello, V. Antoni, E. Martines, G. Serianni, M. Spolaore, L. Tramontin, Phys. Rev. Lett. **86**, 3032 (2001).
[47] V. Antoni, V. Carbone, R. Cavazzana, G. Regnoli, N. Vianello, E. Spada, L. Fattorini, E. Martines, G. Serianni, M. Spolaore, L. Tramontin and P. Veltri, Phys. Rev. Lett. **87**, 45001 (2001).
[48] I. M. Sokolov, J. Klafter and A. Blumen, Physics Today, November 2002, pp. 48–54.
[49] V. E. Zakharov, Sov. Phys. JETP **35**, 908 (1972).

Chapter 10

TRANSITION TO SELF-ORGANIZED HIGH CONFINEMENT STATES IN TOKAMAK PLASMAS

Transition to H-mode in Tokamak Plasmas

P. N. Guzdar
Institute for Research in Electronics and Applied Physics
University of Maryland, College Park, MD 20742
guzdar@umd.edu

R. G. Kleva
Institute for Research in Electronics and Applied Physics
University of Maryland, College Park, MD 20742
kleva@umd.edu

R. J. Groebner
General Atomics
P.O. Box 85608, San Diego, CA 92186
groebner@fusion.gat.com

P. Gohil
General Atomics
P.O. Box 85608, San Diego, CA 92186
gohil@fusion.gat.com

Abstract: Shear flow stabilization of edge turbulence leads to self-organized high (H) confinement modes in tokamak plasmas. Thus understanding the mechanisms for generation of shear/zonal flow and fields in finite β plasmas is an important area of research. A brief review of various mechanisms for shear flow generation and discussion of our recent theory which yields a criterion for bifurcation from low

A.S. Sharma and P.K. Kaw (eds.), Nonequilibrium Phenomena in Plasmas, 219–238.
© 2005 *Springer. Printed in the Netherlands.*

to high (L-H) confinement mode is presented. The predicted threshold based on this parameter shows good agreement with edge measurements on discharges undergoing L-H transitions in DIII-D with ∇B both towards and away from the X-point, as well as for pellet induced H-modes.

Key words: L-H transition, tokamaks, theory and data comparison

Introduction

Since the first observations on low to high confinement (L-H) transitions in the AxiSymmetric Divertor Experiment (ASDEX) tokamak over two decades ago, significant experimental, theoretical and computational modeling effort has been undertaken to provide an understanding of this self-organizing transition (Wagner et al., 1982; Burrell, 1992; Groebner, 1993). The currently accepted paradigm for this improved confinement regime is the generation of localized zonal flow, which is believed to be responsible for suppressing fluctuations, creating a transport barrier and consequently steepened pedestals for the density and the electron and ion temperatures. Connor and Wilson (Connor and Wilson, 2000) have provided a comprehensive review of the experimental and theoretical studies devoted to L-H transitions in tokamaks in the last two decades. Although many theories for L-H transitions have been developed, the basic "trigger" mechanism for this transition has remained elusive. This is perhaps because of various intriguing results which complicate the issues. For instance, for single null divertor plasmas, the heating power threshold for discharges with the ion ∇B drift away from the X-point is about a factor of two higher than that for those discharges with ∇B drift towards the X-point (Carlstrom et al., 2000), indicating the importance of X-point geometry. Yet, on the other hand H-mode transitions also occur in limiter discharges. Another bewildering observation is that the injection of a pellet into the plasma induces an H-mode transition at heating power significantly below that of the conventional threshold (Gohil et al., 2001). This observation seemed to imply that theories which predict a critical edge temperature for the L-H transitions are doomed to fail, since the injection of the pellet cools the plasma edge and yet the transition occurs. Thus finding a critical parameter which provides an explanation of all these features has been a formidable task.

Since the fundamental indication is that a shear flow layer develops in the edge region of the tokamak and therefore improves confinement by suppressing the turbulence, to understand the spontaneous transition to this self-organized state it is necessary to understand the mechanism for the generation of the shear flow layer. One particular direction of research involves investigating the generation of shear flow by mode-coupling processes. The shear flow generated by

this mechanism have been referred to as zonal flows. This mechanism in general can lead to multiple shear layers or "zones" of such flows from which it derives its name. However if the zonal flow profile is localized to the region of steep density gradient, only one shear layer can occur. Thus the shear flow set up by the zonal flow drive and localized by the overall profile variation is responsible for the suppression of turbulence and subsequent improved confinement. Basically the various studies involving mode-coupling can be classified into two categories. The first one uses the classical coherent parametric instability approach to study the mechanism associated with the generation of shear flow (Chen et al., 2000; Drake et al., 1992; Finn et al., 1992; Guzdar, 1995, Guzdar et al., 2001a; Hermiz et al., 1995; Howard and Krishnamurti, 1986; Jenko et al., 2000; Rogers et al., 2000) generated by a large amplitude pump wave which, for instance can be a drift wave, or an ion temperature gradient mode. This approach will be discussed later. In the second approach (Kaw et al., 1999; Lebedev et al., 1995; Sagdeev et al., 1978; Shapiro et al., 1993; Smolyakov et al., 2000a; Smolyakov et al., 2000b) the drift waves are represented by a wave-kinetic equation whose dynamics is affected by the zonal flow. The zonal flow equation in turn is driven by a broadband spectrum of drift waves. In this analysis there is an intrinsic separation of the scale lengths between the "short" scale drift wave and the long scale zonal flows. Both these studies obtain conditions for the growth for the "modulational" instability analysis for the generation of shear flow, though their scalings and regimes of validity are different.

Besides these type of studies in which the dominant mechanism for the generation of the flow is related to the nonlinear mode-coupling, other mechanisms for producing the flow have been investigated. The first such study was an ion-orbit loss mechanism (Itoh and Itoh, 1988; Shaing and Crume, 1989) creating a radial electric field and subsequently a localized poloidal flow. The anomalous Stringer-Winsor (Hassam et al., 1991) and anomalous viscosity due to toroidal geometry which can lead to multiple equilibria with flow (Rozhansky and Tendler, 1992) are alternate mechanisms. Direct finite β stabilization of drift waves transition models (Kerner et al, 1998) offer yet another theory for the transition. The stability criterion for peeling (edge current gradient driven) modes (Connor et al., 1998) has been advanced as a possible onset condition for the transition and more recently a two-fluid self-organized singular layer model (Mahajan and Yoshida, 2000) has also been investigated. The interested reader can find details in the review by Connor and Wilson where the authors have carefully documented criteria and conditions for the L-H transition for each theory and its variants, developed in the last two decades.

Nonlinear computational modeling of L-H transitions in tokamak plasmas has also been an active area of research. Starting with the work of Guzdar et al., (1993), Rogers et al. (1998), with inclusion of finite β effects, and

Xu et al., (2001) for realistic geometry, three-dimensional fluid codes have been systematically developed for studying the cause of anomalous transport in the L phase and the subsequent improvement in confinement in the H phase by solving the reduced set of Braginskii equations. Rogers et al., in their finite-beta simulations of drift-resistive ballooning modes, have identified a two-dimensional parameter-space involving α_{MHD} and α_D in which the edge plasma displays dramatic changes in transport. The parameter $\alpha_{MHD} = \beta q^2 R/L_n$, with q the safety factor, R the major radius, L_n the density gradient scale-length, and β the ratio of the plasma pressure to the magnetic pressure, is the standard MHD parameter identified for the onset of ideal ballooning modes. The parameter α_D is the ratio of the diamagnetic drift frequency $\rho_s c_s/L_0 L_n$ to the ideal growth-rate $c_s/\sqrt{RL_n/2}$. Here ρ_s is the ion Larmor radius with the electron temperature and c_s is the ion acoustic velocity. In the dimensionless reduced Braginskii equations, a characteristic scale-length L_0 is obtained by an optimal ordering which renders the inertial term, the curvature interchange term, and the parallel electron dynamics term in the vorticity equation comparable (Guzdar et al., 1993; Rogers et al., 1998)

$$L_0 = 2\pi q R(\nu_{ei}\rho_s/2\Omega_e R)^{1/2}(2R/L_n)^{1/4}. \tag{1}$$

Here ν_{ei} is the electron ion collision frequency, Ω_e is the electron cyclotron frequency, and the other parameters have been defined earlier.

Rogers et al. showed that for finite α_D, as α_{MHD} was increased, a transition from a poorly confined state (L-mode) to a well confined state (H mode) occurred. Also as the diamagnetic parameter was increased, the turbulence changed from resistive ballooning in character to drift-wave like characterized by more of an adiabatic electron response. The spontaneous transition was clearly seen in their simulations which allowed the equilibrium density to evolve. For $\alpha_D \sim 1$, as α_{MHD} was ramped up beyond a critical value, the density gradient spontaneously steepened. The suppression of turbulence which caused the steepening was a consequence of the build-up of zonal flow, which led to further steepening and subsequent increase in the strength of the zonal flow. This important prediction was compared with data from ASDEX (Suttrop et al., 1999), C-Mod (Hubbard et al., 1998) and D-IIID (Carlstrom et al., 1999) and the numerically computed boundary for the L-H transition was in found to be in reasonable agreement with observations. These simulation results indicate that it is necessary to study the generation of shear flow in finite β plasmas. Most of the earlier works discussed above were limited to the investigation of shear flow generation in low β plasma. Thus guided by the simulation results of Rogers et al., (1998), Guzdar et al. (2001a) developed a simple theory for the generation of shear/zonal flow (with ϕ_s, the scalar zonal potential) and field ($A_{||s}$, the zonal vector potential) by finite β drift waves. These investigations indicated that the important dimensionless parameter that determines the growth

rate of the zonal flow and field is $\hat{\beta} = \beta(qR/L_n)^2/2$. As a function of $\hat{\beta}$ the growth rate for zonal flows has a minimum at $\hat{\beta}_c$ which is identified as the threshold point for the onset of L-H transition. For $\hat{\beta} > \hat{\beta}_c$ the shear/zonal flow stabilization and suppression of fluctuations leads to steepening of the density profile. This increases $\hat{\beta}$ which in turn increases the growth rate of shear/zonal flow. The runaway situation for shear flow generation, suppression of turbulence and subsequent steepening of the density would trigger the transition to H-mode. A simple threshold condition could be derived for L-H transitions in tokamaks. Results of the comparison of this threshold criterion with observations on DIII-D were presented in Guzdar et al. (2002, 2003). Here in section one, a brief summary of the analysis, followed by a derivation of the threshold is presented. In section two a detailed comparison of the criterion with twenty one discharges in DIII-D is given, followed by a summary and conclusion in section three.

1. Theoretical Model

The basic equations used for studying zonal flow/field generation by drift waves and drift-Alfven waves in a finite β plasma, were derived by Zeiler et al., (1997). They are

$$\frac{dn}{dt} + \frac{{c_s}^2}{\Omega_i}\frac{1}{L_n}\frac{\partial \phi}{\partial y} - \nabla_\parallel J = 0 \tag{2}$$

$$\frac{{c_s}^2}{{\Omega_i}^2}\nabla_\perp \frac{d}{dt}\nabla_\perp \phi - \nabla_\parallel J = 0 \tag{3}$$

$$\frac{\partial \psi}{\partial t} + \frac{{c_s}^2}{\Omega_i}\frac{1}{L_n}\frac{\partial \psi}{\partial y} - v_A \nabla_\parallel (\phi - n) = 0 \tag{4}$$

with

$$J = v_A \frac{{c_s}^2}{{\Omega_i}^2}\nabla_\perp{}^2 \psi \tag{5}$$

$$\nabla_\parallel = \nabla_{\parallel 0} + \frac{{c_s}^2 R_0}{\Omega_i v_A}\nabla\zeta \times \nabla\psi \cdot \nabla \tag{6}$$

and

$$\frac{d}{dt} = \frac{\partial}{\partial t} + \frac{{c_s}^2 R_0}{\Omega_i}\nabla\zeta \times \nabla\phi \cdot \nabla \tag{7}$$

Here $n = \tilde{n}/n_0, \phi = e\tilde{\phi}/T_e, \psi = (\Omega_i v_A/c_s^2 B_0)\tilde{\psi}$ are the normalized perturbed density, electrostatic potential and parallel vector potential respectively. In these equations R_0 is the major radius, Ω_i is the ion gyro-frequency, c_s is the ion acoustic speed computed with only the electron temperature, L_n is the density

gradient scale length, v_A is the Alfven velocity and ζ is the toroidal angle. It is assumed that the initial pump wave is a drift wave for which all three quantities n, ϕ and ψ can be written as can

$$\xi = \xi_0 \exp(ik_y y + ik_\parallel z - i\omega_0 t) \tag{8}$$

where ξ represents any one of the three quantities n, ϕ and ψ.

For a linear theory of the zonal flow generation, the perturbed quantities which couple the pump wave with zonal and field flows, the two potentials ϕ and ψ can be represented as

$$\begin{aligned}\xi = {} & \xi_s \exp(ik_x x - i\omega t) + \xi_+ \exp(+ik_x x + ik_y y + ik_\parallel z - i\omega_+ t) \\ & + \xi_- \exp(ik_x x - ik_y y - ik_\parallel z - i\omega_- t)\end{aligned} \tag{8}$$

where $\omega_\pm = \omega \pm \omega_0$. The zonal flow does not have any density perturbation associated with it, but the two sidebands do namely, n_+ and n_-. This representation is the local version of the decomposition used by Chen et al., (2000), and the complex representation of that used by Guzdar (Guzdar, 1995; Guzdar et al., 2001a). Inserting Eq. (8) into Eqs. (2)–(7), the four coupled equations for the scalar potentials side-bands $\phi_\pm$ and the zonal flow ϕ_s and zonal field ψ_s are:

$$(\omega + \Delta)\phi_+ = i\Gamma\left[M_A \phi_0 \phi_s + M_B \phi_0 \psi_s\right] \tag{9}$$

$$(\omega - \Delta)\phi_- = -i\Gamma\left[M_A \phi_0^* \phi_s + M_B \phi_0^* \psi_s\right] \tag{10}$$

$$\omega\phi_s = i\Gamma\left[1 - \left(\frac{\omega_0}{k_\parallel v_A}\right)^2\right]\left[\phi_0^* \phi_+ - \phi_0 \phi_-\right] \tag{11}$$

$$\omega\psi_s = i\Gamma\left(\frac{\omega_0}{k_\parallel v_A}\right)^2\left[\phi_0^* \phi_+ - \phi_0 \phi_-\right] \tag{12}$$

Here

$$M_A = \left[1 - 2\frac{\omega_0}{k_\parallel^2 v_A^2}\left(\omega_0 - \frac{\omega_*}{2}\right) + \frac{k_x^2 - k_y^2}{k_\perp^2}\left(1 - \frac{\omega_*}{\omega_0} - k_x^2\rho_s^2\right)\right] \Big/ A \tag{13}$$

$$M_B = -\left[\frac{2k_y^2}{k_\perp^2}\left(1 - \frac{\omega_*}{\omega_0} + k_y^2\rho_s^2\right)\right] \Big/ A \tag{14}$$

$$A = 1 + k_\perp^2\rho_s^2 - \frac{3\omega_0\left(\omega_0 - 2\omega_*/3\right)}{k_\parallel^2 v_A^2} \tag{15}$$

The parameter $\Delta = k_x^2\rho_s^2\omega_0/A$ is the frequency shift between the pump wave and the sidebands. This frequency shift arises due to the dispersive nature of the drift and kinetic drift-Alfven waves. Here $k_\perp^2 = k_x^2 + k_y^2$, $\omega_* = k_y\rho_s c_s/L_n$

is the electron diamagnetic frequency and $\gamma_s = \Gamma |\ \phi_0\ | = (k_x k_y c_s^2/\Omega_i)|\ \phi_0\ |$ is the maximum growth rate for the shear flow instability for the electrostatic case.

In the absence of the coupling terms, the linearized Eqs. (2)–(7) yield the dispersion relation for the drift and drift-Alfven pump waves, namely

$$1 + k_y^2 \rho_s^2 - \frac{\omega_*}{\omega_0} - \frac{\omega_0 (\omega_0 - \omega_*)}{k_\parallel^2 v_A^2} = 0 \tag{16}$$

The general dispersion relation obtained from this system of equations is

$$\omega^2 - \Delta^2 = \gamma_s^2 \left\{ M_A \left[1 - \left(\frac{\omega_0}{k_\parallel v_A} \right)^2 \right] + M_B \left(\frac{\omega_0}{k_\parallel v_A} \right)^2 \right\} \tag{17}$$

This dispersion relation is the finite-beta slab version of Eq. (10) in the work of Chen et al., (2000) and the dissipationless version of Eq. (17) of Guzdar et al., (2001c). In the limit of $v_A \to \infty$, the dispersion relation reduces to that for the electrostatic case derived in Guzdar et al., (2001a).

$$\omega^2 - \Delta^2 + \gamma_s^2 \left(1 + k_y^2 \rho_s^2 - k_x^2 \rho_s^2\right) = 0 \tag{18}$$

Including the density perturbation for the zonal mode would have yielded an incorrect result. The density perturbation is absent because, for the zonal mode, the adiabatic response is not the correct electron dynamics. The dynamics for this mode is given by the perpendicular motion very much like the two-dimensional incompressible Navier-Stokes fluid. Normalizing the frequency ω_0 to the drift frequency ω_*, there are four dimensionless parameters in the dispersion relation Eq. (17): (1) $k_y \rho_s$, (2) $k_x \rho_s$, (3) $\hat{\beta} = \beta (q R/L_n)^2/2$, and (4) $|\phi_0| L_n/\rho_s$. In these studies only the drift wave (including its finite beta effects)will be considered as the pump wave. Fig. 1, shows the contours of growth which amplifies the zonal flow, zonal field and the side-bands as a function of $k_x \rho_s$ and $\hat{\beta}$ for $k_y \rho_s = 0.4$ and $|\phi_0| L_n/\rho_s = 1.0$. At a given value of $\hat{\beta}$, the growth rate increases as a function of $k_x \rho_s$, reaches a maximum, and then becomes zero beyond a critical mode number.

This stabilizing influence arises from the mismatch frequency Δ. As $\hat{\beta}$ is increased the instability growth rate first decreases and then increases. In the 2D parameter space the most unstable mode shifts to lower wavenumber $k_x \rho_s$ as $\hat{\beta}$ is first increased above zero, reaching a minimum in growth rate. Also at this value of $\hat{\beta}$, the width of the unstable spectrum is the narrowest. However as $\hat{\beta}$ is increased beyond that value, both the wavenumber of the most unstable mode and the width of the unstable spectrum in $k_x \rho_s$ increases. In our earlier work Guzdar01a this minimum $\hat{\beta}_c$ was identified as the onset condition for L-H transitions in tokamaks, since the increase in the maximum growth-rate as a function $\hat{\beta}$ leads to a runaway situation in which the steepening of the density profile, (hence larger $\hat{\beta}$) makes the growth of zonal flow faster and

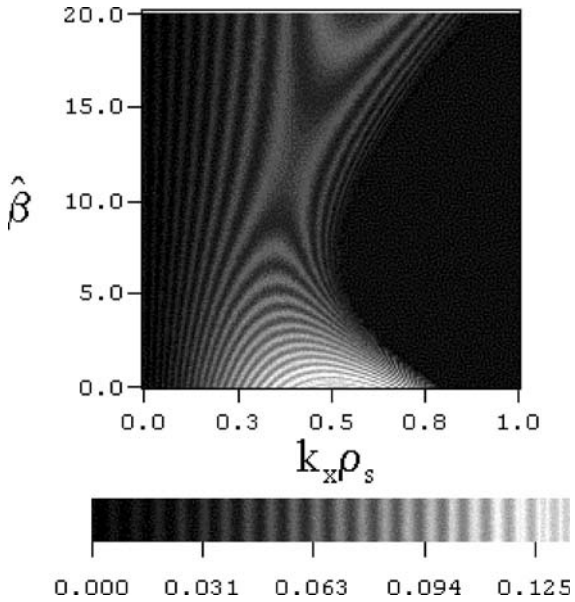


Figure 1. Contours of growth rate as function of $k_x\rho_s$ and $\hat{\beta}$ for $k_y\rho_s = 0.45$ and $|\phi_0|L_n/\rho_s = 1.0$.

thereby facilitates more steepening of the density profile. The maximization of $(k_y\rho_s)^2\hat{\beta}_c$ as a function of $k_y\rho_s$ and $|\phi_0|L_n/\rho_s$ yields the following criterion for the threshold for L-H transitions

$$(k_y\rho_s)^2\hat{\beta}_c \simeq 2.0 \tag{19}$$

where $k_y = 2\pi/L_0$. This condition can be recast in terms of α_D and α_{MHD} to compare with the curve obtained in the simulations of Rogers et al., (1998). However here it is expressed it in terms of measurable plasma parameters and the predictions of the threshold are compared with various discharges in the DIII-D tokamak. By using the definitions of the quantities in Eq. (19), the onset criterion for L-H transitions can be written as $\Lambda/\Lambda_c = 2.0\pi^2\hat{\beta}_c/{L_0}^2 > 1$,where

$$\Lambda = \frac{T_e(keV)(R(m)A_i)^{1/6}}{L_n(m)^{1/2}B_T(T)^{2/3}Z_{eff}^{1/3}} \tag{20}$$

with the critical value $\Lambda_c = 0.45$. Here A_i is the ion mass relative to hydrogen and Z_{eff} is the effective ion charge. The local parameters T_e and L_n are their values at the location of the steepest part of the density gradient in the edge region of tokamaks inside the last closed flux surface. Thus for a given discharge, the parameter $\Theta = T_e/\sqrt{L_n}$, which varies in time, has to reach a critical value

Θ_c to trigger the transition. The critical value is defined as

$$\Theta_c = 0.45 \frac{B_T(T)^{2/3} Z_{eff}^{1/3}}{(R(m)A_i)^{1/6}}. \tag{21}$$

It is expressed in terms of known and measurable quantities for the discharge. Since the temperature scales as the cube root of the constant in Eqn. (19), the uncertainty in the coefficient due to the simplicity of the model is significantly reduced.

2. Comparison with DIII-D Data

The theoretical predictions are now compared with edge plasma data from twenty-one shots on the DIII-D tokamak. Over the years the DIID-D group has improved the resolution of the data in the edge region. This allows for a reliable quantitative estimate of very steep density gradients in this region. This is important for comparison with theoretically derived scalings which depend on plasma scale-lengths. The edge electron parameters were obtained from the DIII-D multi-point, multi-time Thomson scattering system (Carlstrom et al., 1992). The local parameters used in the expressions above were derived from fits of a hyperbolic tangent function the electron temperature and density profilew, which were evaluated at the location of the steepest density gradient (Groebner et al., 2001). Half this value of the computed density scale-length was used. This is because in DIII-D the density and temperature determined by Thompson scattering are measured along a vertical chord of the laser. This would map into a steeper density on the outboard side of the discharge, where our local theory with the strong ballooning approximation is valid. Each data set provides a time history of the required plasma parameters, namely, the electron temperature, density, magnetic field, density gradient as the discharge makes a transition from an L-Mode to an H-Mode. Most of the discharges are normal in the sense that the ∇B drift is towards the X-point. But there are a few with ∇B away from the X-point. Some of these discharges have a time resolution as low as 5 ms while others have a resolution of 12 ms. A three-point central average of the density gradient scale lengths and the electron temperatures, to remove the large fluctuations associated with the high level of turbulence in the edge without compromising temporal changes occuring on the transition time, have been used.

In Fig. 2 the unaveraged data from 21 discharges were utilized, since the results are to be viewed as a statistical comparison. Fourteen of these discharges were used to parameterize low mode and high mode plasma states using a pattern recognition algorithm (Deranian et al., 2002). The full set of discharges had plasma current scans from 1 to 2 MA, line average density scans from 10^{19} to 4×10^{19} m^{-3} and toroidal field variation from 1.1 to 2.18 T. Each point

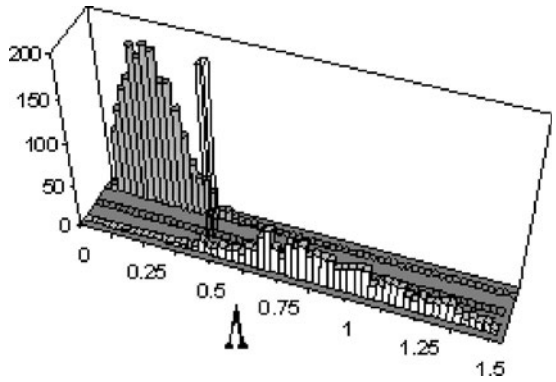


Figure 2. Histogram of L mode points (in grey) in the back array, the H modes points (in white) in the front array and the single vertical column in the central array at $\Lambda = \Lambda_c$ for 21 DIII-D discharges versus Λ.

in the data set was identified as an L-mode or an H-mode. There are 1193 data points in the H-mode and 1913 in the L mode.

An instructive way of comparing the data to the model is by computing the value of Λ defined by Eq. (20). In Fig. 2 is shown the three-dimensional histogram of the parameter Λ for the L mode points (grey rods) and the H mode points (white rods) for the above-mentioned dataset. The histogram has 61 uniform bins between 0 and 1.5. In the vicinity of the critical point $\Lambda_c = 0.45$ (represented by the single transparent rod centered around the critical value) the number of data points are a minimum. This behavior at the critical point occurs because the L mode discharge becomes unstable and subsequently evolves to the new stable H mode. For this dataset the present theory provides a reliable onset condition.

A few individual discharges and their time history are now examined. This is to compare the observed L-H transition time with the theoretical transition time, which is when the parameter Θ crosses the critical value Θ_c for each discharge. In Figs. 3(a-d) the temporal evolution of the measured onset parameter Θ is plotted (solid) as a function of time for four different discharges: shot #084026 with $B_T = -2.12$ T and $I_P = 1.33$ MA, shot #078155 with $B_T = -2.13$ T and $I_P = 1.98$ MA, shot #102025 with $B_T = -2.07$ T and $I_P = 1.57$ MA and finally shot #102015 with $B_T = -2.12$ T and $I_P = 1.08$ MA. The horizontal solid line is the critical value Θ_c given by Eq. (21). The vertical solid line is the location of the last data point in the time-history identified as an L-mode and the vertical dashed line is the first data point identified unambiguously as an H mode as indicated by the D-alpha signal. The first two discharges have the ∇B drifts towards the X-point. Since the magnetic field for these two cases are the same (but the plasma current is 1.5 time larger for the second discharge),

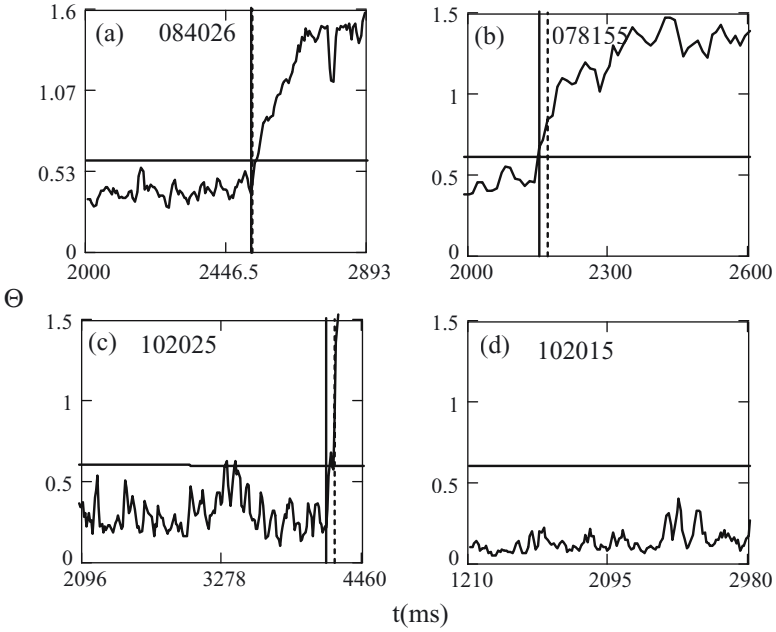


Figure 3. Θ (solid), the critical value Θ_c (horizontal) versus time for DIII-D discharges (a) 84026, (b) 78155, (c) 102025 and (d) 102015. The vertical solid line is the last L-mode point prior to transition and the vertical dashed line is the first H-mode point after transition.

the threshold for the transition are the same. The transition occurs a little earlier (approximately 6 ms, the resolution time for this dataset) than expected from the theory for #084026 and at around the time when the experimental data for Θ crosses the threshold values Θ_c for #078155. Fig. 3(c) for shot #102025 is an interesting case study. In the early phase of the discharge, ∇B drift was towards the X-point. Also the neutral beam power was ramped up so as to get the discharge to make a transition. However at t = 3450 ms, the X-point was moved from the bottom of the plasma to the top of the plasma. Thus the ∇B drift was now away from the X-point. As seen from the plot for Θ, the discharge almost became an H mode; however due to reversal of the drift, somehow the discharge retreated from going into the H-mode indicating that either the temperature was reduced or the density gradient scale-length was increased by this reversal. The parameter Θ decreased and finally at t = 4400 ms, when the neutral beam power was ramped up to 10 MW, the discharge made a transition into the H-mode. Finally, the shot #102015 shown in Fig. 3(d) is a discharge with ∇B away from the X-point. For this case the transition did not occur even when a pellet was injected at t = 2645 ms. Θ stays well below the critical value Θ_c during the displayed time-history of the discharge.

From discharge # 102025 shown in Fig. 3c, this is the first indication that for ∇B away from the X-point, the same Θ parameter determines the transition, even though the power threshold for L-H transitions is a factor of two larger than that for a similar discharges with ∇B towards the X-point. The role of ∇B is addressed in some detail for the two discharges studied by Carlstrom et al. (2000). For shot #96338 the ∇B drift was towards the X-point. For shot #96348 the direction of the toroidal field was reversed while all other plasma parameters were the same. In Fig. 4a is plotted (solid) the parameter Θ versus time for shot

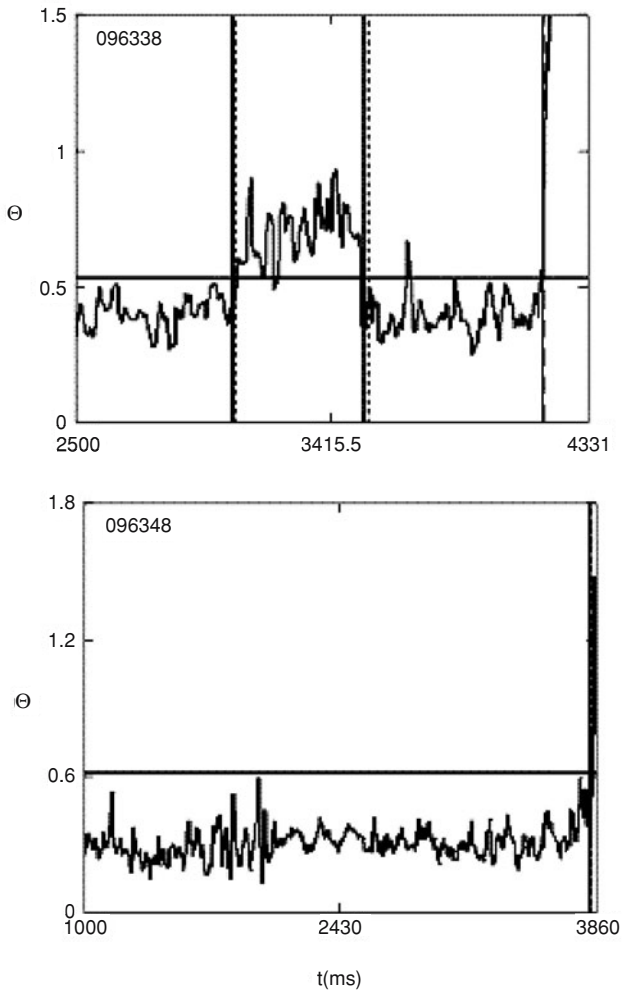


Figure 4. Θ (solid) for shots (a) #96338 (∇B towards X-point) and (b) #96348 (∇B away from X-point) versus time. Solid horizontal line is Θ_c, vertical solid line for last point of L(H)-mode before transition and vertical dashed line for first H(L)-mode point after transition for L-H (H-L) transitions for this discharge.

96338. Also shown in the plot is the critical value Θ_c (solid horizontal) of this parameter for both these discharges. There were three transitions triggered in this discharge by changing the beam power. The first one is an L-H transition around $t = 3.062$ s (solid vertical line for last L-mode and dashed vertical at first H-mode points).

After that an H-L transition occurs. Since the neutral beam power was reduced below threshold, the discharge slipped back into an L mode at t = 3.55 s (solid vertical line for last H and dashed vertical for first L for the second transition). Θ decreases below the critical value just prior to the indicated back transition. What is interesting to note is that the H-L transition occurs at the same value of the parameter Θ_c. Unlike the power, there is no hysteresis in this onset parameter for the L-H and H-L transitions. Finally the beam power was increased and at t = 4.16 s, the discharge made a second transition to the H mode. In Fig. 4b is displayed the time trace of Θ for shot #96348 with plasma parameters same as the previous shot but with the ∇B field away from the X-point. The transition to the H mode (at much higher power), as indicated by the D-alpha signal, occurs at t = 3.831 s. This trace shows that the transition occurs when the onset parameter exceeds the same critical value Θ_c though it does so for a much higher input power. One thing to note is that the predicted transition times and the observed times do not match up for these shots. Again the descrepancy is within one or two resolution times of the data.

This surprising result indicated that one of the plasma parameters either T_e or L_n is affected by the change in the direction of ∇B which in turn leads to the different power thresholds. In Fig. 5a the time history of the electron temperature for shot #96338 (solid) and for shot #96348 (dashed) is plotted and in Fig. 5b is shown the density gradient scale-length for the two shots. For this plot a eleven point central-averaging of the relevant data was performed. What is evident is that the temperature for the two discharges are very similar in the L-mode phase but the density scale-lengths are indeed different. The density scale-length for shot #96348 with ∇B away from the X-point is approximately twice as large as that for shot #96338 with ∇B towards the X-point. Recent simulation by Xu et al. 43 indicates that the fluctuation levels and anomalous transport are indeed larger for the case with ∇B away from the X-point. The ∇B motion of the ions towards the X-point stabilizes the fluctuations since the local shear increases rapidly near the X-point. For a given outward particle flux the density gradient would be steeper (since the anomalous transport would be lower due to the stabilized fluctuations) for the case with ∇B towards the X-point than away from the X-point. This perhaps is not the only explanation since the edge recycling and fueling plays a significant role in determining the scale-length in the edge region (Boedo et al., 2000) and these parameters might be different for the two plasma configurations. This is actually seen in the elegant calculation by Connor and Pogutse, (2001), which shows that the

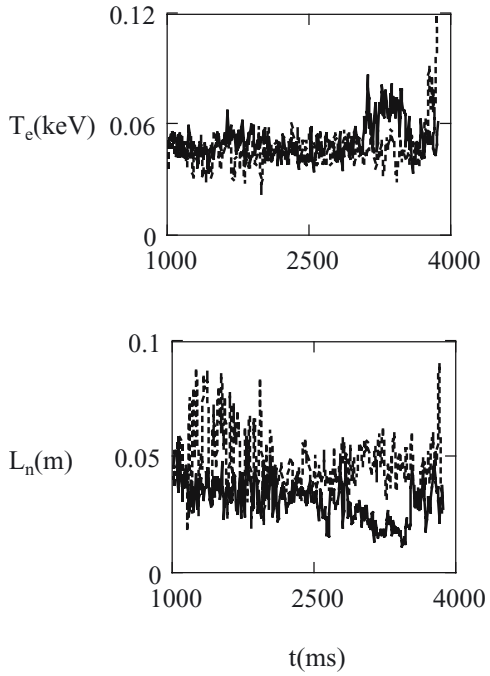


Figure 5. (a) T_e and (b) L_n for shot #96338 (∇B towards X-point) (solid) and shot #9638 (∇B away from X-point) (dashed) versus time.

plasma β gradient in the edge is steeper in an X-point geometry when the ∇B is towards the X-point than when it is away from the X-point. They used this to explain the asymmetry in the L-H transition threshold for the theory of L-H transition based on the stabilization of drift-Alfven turbulence by finite β effects (Kerner et al., 1998). Thus, although the neutral beam power threshold is different for the transition for these two discharges, the transition occurs when the Θ parameter exceeds the same critical value. This indicates that the underlying physics for the onset is the same for both these cases. The difference in the transport, edge recycling and edge fueling for the two cases will need to be examined more critically both experimentally and with transport codes with detailed edge physics.

Two shots in which H-modes were induced by pellet injection are discussed next. One of these shots (shot #99559) was reported in detail by Gohil et al., (2001). Both these discharges had ∇B drift away from the X-point. In shot #100162 the pellet (inside launch, high field side) was injected at t = 3624.7 ms, while for shot #99559 the third pellet (all outside launches, on the low field side) was injected at t = 4257.9 ms which triggered the transition. The time evolution of Θ for these two shots are the solid black lines in Figs. 6(a) and 6(b)

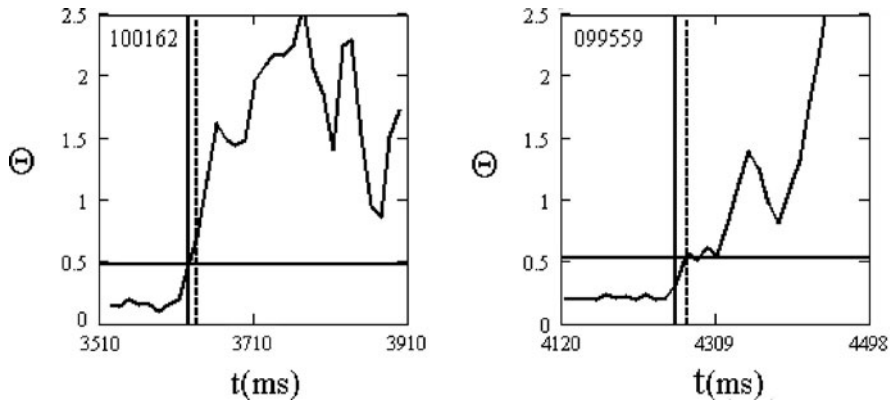


Figure 6. Θ (solid black), Θ_c (solid horizontal) versus time for DIII-D discharge (a) 100162 (inside launch), (b) 99559 (outside launch). Solid vertical line is last instant of time for L mode; dotted vertical line is the first instant of time for H mode.

respectively. The critical value Θ_c are the solid horizontal lines in each of these plots. The vertical solid lines are the last points in the time-series identified as an L mode and the vertical dashed lines are the first points in the time-history indicated as an H mode. Once again there is clear evidence of the occurrence of the transition when the onset parameter Θ crosses the critical value Θ_c and this occurs in the time interval between the indicated last L and first H mode points. On examining the density and temperature profiles for shot #99559 (Gohil et al., 2001), 2 ms after the pellet injection which triggered the H-mode, even though the density gradient at the edge was the steepest, the discharge did not transition in to the H mode. This was because there was significant cooling of the edge and a drastic reduction in the electron temperature. Sometime later once the edge temperature recovered and the edge temperature and density gradient scalelength, yielded the value of Θ that exceeded the critical value to trigger the transition.

3. Conclusion

A brief review of shear flow generation studies and L-H transition models, followed by our theoretical model for shear flow and field generation by finite beta drift waves in tokamak edge plasmas has been presented. A critical trigger parameter Λ_c or Θ_c defined by Eqs. (20) and (21), respectively, which predicts the onset of L-H and H-L transitions in tokamak plasmas has been identified. The transition occurs at the same critical value of the parameter for discharges with oppositely directed ∇B drifts. The difference in anomalous turbulent transport, particle fueling and recycling or a combination of these effects could be the cause for the difference in the local density scale-lengths in the two

cases and therefore responsible for the different power thresholds. Finally the pellet-induced H modes which occur for power levels thirty percent below the conventional values also occur for the same value of the onset parameter. Thus seemingly different transition mechanisms are unified by the identification of the relevant trigger parameter for all such transitions. These preliminary encouraging conclusions need to be validated by using data on other tokamaks.

Since the present study seems to indicate that the fundamental difference in the discharges with oppositely directed ∇B drifts is the density gradient scale-length, it is necessary to investigate the cause of this difference more carefully. Calculations by Connor and Pogutse, (2001) for a simple X-point geometry does indicate that profiles in the vicinity of the last closed flux surface are affected by the direction of the ∇B drift. However most of the changes occur near the X-point. This theory needs to be implemented in a more realistic geometry for each of the devices to get a more quantitative understanding. Based on the present studies it would appear that changes, like shaping (elongation and triangularization) of discharges can affect the edge gradient and therefore influence the threshold for the transition. Such issues need to be addressed. Differences observed in the power threshold in single and double null discharges in MAST have been attributed to the change in local gradients by Meyer et al., (2002). Finally, from a practical point of view one has to recast this condition in terms of the true control parameters in the plasma, namely heating power, plasma current, plasma density, aspect ratio and toroidal magnetic field. To relate this local onset condition to a power threshold requires knowledge of the turbulent particle and energy transport, edge fueling and recycling, and global power-balance to determine reliably the density scale-length and the electron temperature at the desired location. The turbulent transport scaling and parameterization can be accomplished by using the three-dimensional simulation codes of Rogers et al., (1998), and Xu et al., (2000). The anomalous transport coefficients can then be used in 1D and 2D transport codes like TRANSP, BALDUR or CalTrans and UEDGE, which contain the detailed physics of edge recycling and particle sources. The heating power at which the modeled discharge attains the critical value Θ_c given by Eq. (20) will determine the power threshold for L-H transitions. By varying the plasma parameters like the current, line-averaged density, and tokamak characteristics like aspect-ratio, toroidal field strength and plasma shaping (elongation and triangularity) the power threshold can be mapped out as a function of the operational control parameters.

Acknowledgments

This work was supported by the US Department of Energy under Grant DE-FG02-93ER54197 at UMD, Contract DE-AC03-99ER54463 and Grant DE-F602-89ER53296 at GA.

References

Boedo, J. A., M. J. Schaffer, R. Maingi, and C. J. Lasnier, Electric field-induced plasma convection in tokamak divertors, *Phys. Plasmas*, 7, 1075, 2000.

Burrell, K. H., and DIII-D Team, Physics of the L-mode to H-mode transition in tokamaks, *Plasma Phys. Controlled Fusion* 34, 1859, 1992.

Carlstrom, T. N., G. L. Campbell, J. C. DeBoo *et al.*, Design and operation of the multipulse Thomson scattering diagnostic on DIII-D, *Rev. Sci. Instrum.*, 63, 4901, 1992.

Carlstrom, T. N., K. H. Burrell, R. J. Groebner, A. W. Leonard, T. H. Osborne, and D. M. Thomas, Comparison of L-H transition measurements with physics models, *Nucl. Fusion*, 39, 1941, 1999.

Carlstrom, T. N., J. A. Boedo, and K. H. Burrell, *et al.*, Edge E_r structure and the ∇B effect on the L-H transition, *2000 Proc. 27th Eur. Phys. Soc. Conf. on Controlled Fusion and Plasma Physics* (Budapest, Hungary), vol. 24B (Budapest: European Physical Society), p. 756, (2000).

Chen, Liu, Zhihong Lin, and Roscoe White, Excitation of zonal flow by drift waves in toroidal plasmas, *Phys. Plasmas*, 7, 3129, 2000.

Connor, J. W., R. J. Hastie, H. R. Wilson, and R. L. Miller, Magnetohydrodynamic stability of tokamak edge plasmas, *Phys. Plasmas*, 5, 2687, 1998.

Connor, J. W., and H. R. Wilson, A review of theories of the L-H transition, *Plasma Phys. Controlled Fusion*, 42, R1, 2000.

Connor, J. W., and O. P. Pogutse, Influence of an X-point on the L-H transition power threshold, *Phys. Plasmas Controlled Fusion*, 43, 281, 2001.

Deranian, R. D., R. G. Groebner, and D. T. Pham, Use of a pattern recognition algorithm to obtain a parametrization of low-mode and high-mode plasma states, *Phys. Plasmas*, 9, 2667, 2002.

Drake, J., J. Finn, P. Guzdar, V. Shapiro, V. Shevchenko, F. Waelbroeck, A. Hassam, C. S. Liu, and R. Sagdeev, Peeling of convection cells and the generation of sheared flow, *Phys. Fluids B*, 4, 488, 1992.

Finn, J. M., J. F. Drake, and P. N. Guzdar, Instability of fluid vortices and generation of sheared flow, *Phys. Fluids B*, 4, 2758, 1992.

Gohil, P., R. Baylor, T. C. Jernigan, K. H. Burrell, and T. N. Carlstrom, Investigations of H-mode plasmas triggered directly by pellet injection in the DIII-D tokamak, *Phys. Rev. Lett.*, 86, 644, 2001.

Groebner, R. J., An emerging understanding of H-mode discharges in tokamaks, *Phys. Fluids B*, 5, 2343, 1993.

Groebner, R. J., D. M. Thomas, and R. D. Deranian, Evidence for edge gradients as control parameters of the spontaneous high-mode transition, *Phys. Plasmas*, 8, 2722, 2001.

Guzdar, P. N., J. F. Drake, A. B. Hassam, D. McCarthy, and C. S. Liu, Three-dimensional fluid simulations of the nonlinear drift-resistive ballooning modes in tokamak edge plasmas, *Phys. Fluids B*, 5, 3712, 1993.

Guzdar, P. N., Shear-flow generation by drift/Rossby waves, *Phys. Plasmas*, 2, 4174, 1995.

Guzdar, P. N., R. G. Kleva, and L. Chen, Shear flow generation by drift waves revisited, *Phys. Plasmas*, **8**, 459 2001a.

Guzdar, P. N., R. G. Kleva, A. Das, and P. K. Kaw, Zonal flow and zonal magnetic field generation by finite beta drift waves: A theory for L-H transitions in tokamaks, *Phys. Rev. Lett.* 86, 15001, 2001b.

Guzdar, P. N., R. G. Kleva, A. Das, and P. K. Kaw, Zonal flow and field generation by finite beta drift waves and kinetic drift-Alfven waves, *Phys. Plasmas*, 8, 3907, 2001c.

Guzdar, P. N., R. G. Kleva, R. J. Groebner, and P. Gohil, Comparison of a low to high confinement transition theory with experimental data from DIII-D, *Phys. Rev. Lett.* 89, 24001, 2002.

Guzdar, P. N., R. G. Kleva, A. Das, P. K. Kaw, R. J. Groebner, and P. Gohil, Low to high confinement transition theory of finite-beta drift-wave driven shear flow and its comparison with data from DIII-D, to appear in *Phys. Plasmas*, 2003.

Hassam, A. B., T. M. Antonsen, Jr., J. F. Drake, and C. S. Liu, Spontaneous poloidal spin-up of tokamaks and the transition to the H mode, *Phys. Rev. Lett.*, 66, 309, 1991.

Hermiz, K. B., P. N. Guzdar, and J. M. Finn, Improved low-order model for shear flow driven by Rayleigh-BÈnard convection, *Phys. Rev. E*, 51, 325, 1995.

Howard, L. N., and R. Krishnamurti, Large-scale flow in turbulent convection: a mathematical model, *J. Fluid Mech.*, 170, 385, 1986.

Hubbard, A. E., R. L. Boivin, J. F. Drake, M. Greenwald, Y. In, J, H, Irby, B. N. Rogers, and J. A. Snipes, Local variables affecting H-mode threshold on Alcator C-Mod, *Plasma Phys. Controlled Fusion*, 40, 689, 1998.

Itoh, S.-I., and K. Itoh, Model of L to H-mode transition in tokamak, *Phys. Rev. Lett.*, 60, 2276, 1988.

Jenko, F., W. Dorland, M. Kotschenreuther and B. N. Rogers, Electron temperature gradient driven turbulence, *Phys. Plasmas*, 7, 1904, 2000.

Kaw, P. K., and R. Singh, Coherent nonlinear states of drift wave turbulence modulated by self consistent zonal flow, *Bull. Am. Phys. Soc.* 44, No1. Part II, RP01(109), 1262, 1999.

Kerner, W., Yu. Igitkhanov, G. Janeschitz, and O. Pogutse, The scaling of the edge temperature in tokamaks based on the Alfven drift-wave turbulence, *Contrib. Plasma Phys.*, 38, 118, 1998.

Lebedev, V. B., P. H. Diamond, V. D. Shapiro, and G. I. Soloviev, Modulational interaction between drift waves and trapped ion convective cells: A paradigm for the self-consistent interaction of large-scale sheared flows with small-scale fluctuations, *Phys. Plasmas*, 2, 4420, 1995.

Mahajan, S. M., and Z. Yoshida, A collisionless self-organizing model for the high-confinement (H-mode) boundary layer, *Phys. Plasmas*, 7, 635, 2000.

Meyer, H., A. Kirk, L. C. Appel *et al.*, The effect of magnetic configurations on H-mode in MAST, *2002 Proc. 29th Eur. Phys. Soc. Conf. on Controlled Fusion and Plasma Physics* (Montreux, Switzerland), vol. 26B (ECA), P-1.056 2002.

Rogers, B., J. F. Drake, and A. Zeiler, Phase space of tokamak edge turbulence, the L-H transition, and the formation of the edge pedestal, *Phys. Rev. Lett.*, 81, 4396, 1998.

Rogers, B. N., W. Dorland, and M. Kotschenreuther, Generation and stability of zonal flows in ion-temperature-gradient mode turbulence, *Phys. Rev. Lett.*, 85, 5336, 2000.

Rozhansky, V., and M. Tendler, The effect of the radial electric field on the L-H transitions in tokamaks, *Phys. Fluids B*, 4, 1877, 1992.

Sagdeev, R. Z., V. D. Shapiro, and V. I. Shevchenko, Convective clees and anomalous plasma diffusion, *Sov. J. Plasma Phys.*, 4, 306, 1979.

Shaing, K. C., and E. C. Crume, Bifurcation theory of poloidal rotation in tokamaks: A model for L-H transition, *Phys. Rev. Lett.*, 63, 2369, 1989.

Shapiro, V. D., P. H. Diamond, V. B. Lebedev, G. I. Soloviev, and V. I. Shevchenko, Generation of dipolar structures in drift wave turbulence, *Plasma Phys. Controlled Fusion*, 35, 1033, 1993.

Smolyakov, A. I., P. H. Diamond, and M. Malkov, Coherent structure phenomena in drift wavezonal flow turbulence, *Phys. Rev. Lett.*, 84, 491, 2000a.

Smolyakov, A. I., P. H. Diamond, and V. I. Shevchenko, Zonal flow generation by parametric instability in magnetized plasmas and geostrophic fluids, *Phys. Plasmas*, 7, 1349, 2000b.

Suttrop, W., V. Mertens, H. Murmann, J. Neuhauser, J. Schweinzer, and ASDEX-Upgrade Team, Operational limits for high edge density H-mode tokamak operation, *J. Nucl. Mater.*, 266–269(O), 118, 1999.

Wagner, F., and ASDEX Team. Regime of improved confinement and high beta in neutral-beam-heated divertor discharges of the ASDEX tokamak, *Phys. Rev. Lett.*, 49, 1408, 1982.

Xu, X. Q., R. H. Cohen, T. D. Rognlien, and J. R. Myra, Low-to-high confinement transition simulations in divertor geometry, *Phys. Plasma*, 7, 1951, 2000.

Zeiler, A., J. F. Drake, and B. Rogers, Nonlinear reduced Braginskii equations with ion thermal dynamics in toroidal plasma, *Phys. Plasmas*, 4, 2134, 1997.

Chapter 11

INTERNAL TRANSPORT BARRIERS IN MAGNETISED PLASMAS

X. Garbet, P. Ghendrih, Y. Sarazin
Association Euratom-CEA sur la Fusion, CEA Cadarache, 13108
St Paul-Lez-Durance. France.

P. Beyer, C. Figarella, S. Benkadda
LPIIM, Centre Universitaire de Saint-Jerôme, 13397 Marseille cedex 20, France.

Abstract: The mechanisms leading to the onset and sustainment of an Internal Transport Barrier are overviewed. It is shown that both magnetic shear and shear flow are important at different stages of a barrier evolution. The role of turbulent structures is also assessed. Large scale transport events are found to be impeded by the shear flow that takes place within a transport barrier. Zonal Flows appear to be quenched in most cases due to the cancellation of the Reynolds stress.

Key words: plasma turbulence, transport barriers

1. Introduction

Since their discovery in the 90's, Internal Transport Barriers (ITB) have been extensively studied in fusion devices (Hugon et al 1992, Moreau et al 1992, Koide et al 1994, Levinton et al 1994, Strait et al 1995, Gormezano 1996, Wolf et al 2001) (see (Wolf 2003) for an overview of experimental results). In spite of a wealth of experimental and theoretical results, the physics underlying the onset and sustainment of a barrier is still debated. The definition itself of an ITB has long been a subject of discussion. It will be defined here as layer where the turbulent transport is lower then in the surrounding plasma. Since fluxes are fixed in a fusion device, such a layer is also the location of strong gradients. Plasmas with an ITB provide a promising operation regime that combines

A.S. Sharma and P.K. Kaw (eds.), Nonequilibrium Phenomena in Plasmas, 239–256.
© 2005 *Springer. Printed in the Netherlands.*

good confinement and a large fraction of self-generated ("bootstrap") current. Therefore it opens the route towards steady-state, high quality fusion plasmas. On the other hand, ITB's are prone to MHD instabilities and to impurity accumulation when the density profile is peaked. As a consequence, the control of transport barriers has become a priority. Obviously a good control requires a deep understanding of the mechanisms leading to the appearance and survival of a barrier. This is therefore a very active domain of research. Two key ingredients are believed to play a central role: the magnetic shear (defined here as the logarithmic gradient of the rotational transform in a tokamak) and the shear of the velocity perpendicular to the equilibrium magnetic field. The profile of safety factor seems to be crucial in the early phase of the barrier development. Once a barrier is established in the ion channel, the barrier enters a self-amplifying loop where the enhanced gradients increase the flow shear, which in turn further improves the confinement. Other parameters such as the density gradient, plasma β or impurity content may play some role when a barrier appears.

This picture relies essentially on linear stability considerations. A legitimate question is whether it is affected by non linear effects. During the recent years, structures such as Zonal Flows and Streamers have been found to play an important role in turbulent transport. Zonal Flows are fluctuations of the poloidal velocity, which tend to lower the turbulent transport, whereas Streamers are convective cells elongated in the radial direction, which tend to boost the transport. Whether these structures affect the onset or self-sustainment of ITB's is clearly an issue, which has not been studied in detail up to now. The aim of this paper is twofold. The first objective is to give an overview of the mechanisms that are believed to be important for the onset and sustainment of an internal transport barrier. The second goal is to assess the role of structures in the barrier dynamics. This complex physics will be illustrated with a simplified model of fluid turbulence in tokamaks.

The paper is organised as follows. The section 2 presents the fluid models that have been used to produce most of the results presented in this overview. The chapter 3 describes the main ingredients involved in the physics of transport barriers. Some comparison with experimental results will be done when available. The chapter 4 describes the behaviour of the structures in presence of a barrier. A conclusion follows.

2. Models of Fluid Turbulence in Tokamaks

As an illustration, we will use here two fluid models of turbulence in tokamak plasmas. The first one is based on a set of 5 fluid equations to describe a collisionless Ion Temperature Gradient (ITG) and Trapped Electron Mode

(TEM) turbulence in the hot core of a tokamak plasma

$$d_t n_e = i\omega_{dte}\left(n_{e,eq}\phi - p_e\right) + S_n \tag{1a}$$

$$d_t p_e = i\omega_{dte}\Gamma\left(n_{e,eq}\phi + T^2_{e,eq}n_e - 2T_{e,eq}p_e\right) + S_{pe} \tag{1b}$$

$$d_t \Omega = -n_{e,eq}\nabla_{//}v_{//i} - i\omega_{di}\left(n_{e,eq}\phi + p_i\right) \tag{1c}$$

$$-i\omega_{dte}f_t\left(n_{e,eq}\phi - p_e\right) + \left[p_{i,eq}, \nabla^2_\perp\phi\right] + f_c\left[n_{e,eq}, \phi\right]$$

$$d_t v_{//i} = -\nabla_{//}\left(\phi + p_i/n_{e,eq}\right) + S_v \tag{1d}$$

$$d_t p_i = -i\omega_{di}\Gamma\left[p_{i,eq}\left(1 - f_c T_{i,eq}/T_{e,eq}\right)\phi - T^2_{i,eq}n_e + 2T_{i,eq}p_i\right] \tag{1e}$$

$$-\Gamma p_{i,eq}\nabla_{//}v_{//i} + S_{pi}$$

where n_s, T_s, p_s, $v_{//s}$, ϕ are the normalised density, temperature, pressure, parallel velocity and electric potential (the labels 'e' and 'i' are for electrons and ions, no impurity is included). The generalised vorticity Ω is defined as

$$\Omega = n_{e,eq}[f_c(\phi - \phi_{eq})/T_{e,eq} - \nabla^2_\perp\phi] \tag{2}$$

The normalisation is of the gyroBohm type,

$$n_e \to a/\rho_{s0}n_e/n_0,\ p_{e,i} \to a/\rho_{s0}p_{e,i}/p_0,\ \phi \to a/\rho_{s0}e\phi/T_0,\ v_{//i} \to a/\rho_{s0}v_{//i}/c_{s0} \tag{3}$$

where ρ_{s0} is the ion gyroradius ($\rho_{s0} = m_i c_{s0}/e_i B_0$, c_{s0} is the sound speed $(T_0/m_i)^{1/2}$), a and R are the minor and major radius, n_0, T_0, $p_0 = n_0 T_0$ are reference values. Time and spatial co-ordinates are normalised to a/c_{s0} and ρ_{s0}. The geometry of flux surfaces corresponds to a set of circular concentric tori, (r,θ,φ) being the labels of the minor radius, poloidal and toroidal angles ($\rho = r/a$ is the normalised minor radius). The fraction of trapped (resp. passing) electrons is $f_t = 2/\pi(2r/R)^{1/2}$ (resp. $f_c = 1 - f_t$). The electron precession drift and the ion curvature drift operators are respectively

$$\omega_{dte} = i2\varepsilon_a\lambda_t\rho_{s0}qr^{-1}\partial_\varphi; \quad \lambda_t = 1/4 + 2s/3 \tag{4}$$

and

$$\omega_{di} = i2\varepsilon_a\rho_{s0}(\cos(\theta)r^1\partial_\theta + \sin(\theta)\partial_r) \tag{5}$$

The function $\lambda_t = 1/4 + 2s/3$ characterises the dependence of the precession frequency on the magnetic shear $s = rdq/qdr$ and the inverse aspect ratio $\varepsilon_a = a/R$ parameterises the curvature. The Lagrangian time derivative is defined as $d_t = \partial_t + [\phi s] - D$, where D is a "collisional" diffusion operator and $[f,g] = r^1(\partial_r f\partial_\theta g\partial_\theta f\partial_r g)$. The functions S_n, S_v, S_{pe}, S_{pi} are particle, momentum, ion and electron heat sources. A label 'eq' indicates a flux average. Note that the

perturbed part of $f_t n_e$ is the fluctuating density of trapped electrons, whereas $n_{e,eq}$ is the total equilibrium electron density. The adiabatic compression index is $\Gamma = 5/3$.

The vorticity equation (1c) expresses an ambipolarity condition. The vorticity is coupled via the curvature drifts to electron and ion pressure, which are governed by Eqs.(1b) and (1e). This coupling is responsible for TEM and toroidal ITG instabilities, while the coupling with the parallel momentum equation (1d) is responsible for the slab ITG instability. A highly simplified (but useful) estimate of the growth rate can be obtained by assuming low wave numbers ($k_\perp \rho_i \ll 1$), strongly ballooned ($\theta \ll 1$), large pressure gradient and no density gradient, and pure convection of the electron and ion pressure $d_t p = 0$, namely

$$\gamma_0^2 = f_t \omega_{dte} \omega_{pe}^* + \omega_{di} \omega_{pi}^* \tag{6}$$

where

$$\omega_{pe}^* = -\frac{nq}{r} \rho_{s0} \frac{a \partial_r p_{e,eq}}{n_{e,eq}} \; ; \; \omega_{pi}^* = \frac{nq}{r} \rho_{s0} \frac{a \partial_r p_{i,eq}}{n_{e,eq}} \tag{7}$$

and n is the toroidal wave number. A subset of equations describing ITG modes is obtained by setting $f_t = 0$ (no trapped electrons).

The second model describes a Resistive ballooning mode (RBM) turbulence at the collisional edge of a tokamak plasma. It is based on reduced resistive MHD equations for the normalised electrostatic potential ϕ and pressure p,

$$d_t \nabla_\perp^2 \phi = -\nabla_{//}^2 \phi - G \cdot p \tag{8}$$

$$d_t p = \delta_c G \cdot \phi + \chi_{//} \nabla_{//}^2 p + S_p \tag{9}$$

Eq.(8) corresponds to the charge balance in the drift approximation involving the divergences of the polarization current, the parallel current, and the diamagnetic current, respectively. Eq.(9) represents the energy balance, where $\chi_{//}$ is an effective parallel collisional heat diffusivity and $S_p(r)$ is an energy source. The curvature terms $G \cdot p$ and $G \cdot \phi$ arise from the compressibility of diamagnetic current and $E \times B$ drift, respectively. In this MHD model, the diamagnetic velocity is neglected with respect to the $E \times B$ velocity and the parallel current is evaluated using a simplified electrostatic Ohm's law, $\eta_{//0} j_{//} = -\nabla_{//} \phi$ (in dimensional units), where $\eta_{//0}$ is a reference value of the parallel resistivity. The system (8-9) has been normalised using the resistive interchange time τ_{int} and the resistive ballooning length ξ_{bal} with $\tau_{int}^2 = R_0 L_p / (2 c_{s0}^2)$ and $\xi_{bal}^2 = n_0 m_i \eta_{//0} L_s^2 / (\tau_{int} B_0^2)$. Here, R_0, L_p, and L_s are characteristic values of the major radius, the pressure gradient length, and the magnetic shear length, respectively. Time is normalised to τ_{int} and the perpendicular and parallel length scales are given by ξ_{bal}, and L_s respectively. Electrostatic potential and pressure are normalised to $B_0 \xi_{bal}^2 / \tau_{int}$

and $\xi_{bal}B_0/L_p$, respectively. The curvature operator is $G = i/(\varepsilon_a\rho_{s0})\omega_{di}$ and $\delta_c = (5/3)2L_p/R_0$. The Lagrangian time derivative d_t as well as the gradient along field lines $\nabla_{//}$ are identical to those in the ITG/TEM model. RBM turbulence is expected to be relevant in collisional edge plasmas. Assuming a monotonically increasing safety factor q(r), the domain chosen for the study of RBM turbulence typically covers a region between $q = 2$ and $q = 3$ at the plasma edge.

The spatial structure of the linear modes is beyond the scope of this overview. However, the special role of resonant surfaces must be emphasised here in order to introduce the next section. The gradient along the equilibrium field lines is given by $\nabla_{//} = 1/R(\partial_\varphi + q^{-1}\partial_\theta)$. The parallel gradients of various fields play a stabilising role (the typical damping rate is a parallel wave number times a sound speed). For an harmonic oscillation exp[i(nφ-mθ)], the parallel wave number is $k_{//} = 1/R(n - m/q)$ and vanishes on the "resonant" surface $r = r_{mn}$ such that $q(r_{mn}) = m/n$. A perturbation oscillating as exp[i(nφ-mθ)] will tend to be spatially localised on such a resonant surface in order to minimise the damping.

3. Onset and Self-Sustainment of a Transport Barrier

3.1 Shear flow

Shear flow is a very efficient way to produce an improved confinement. Stabilisation via vortex shearing has been extensively studied in the literature and will not be detailed here (see (Terry 2000) for an overview). There exist 3 criteria at least to quantify a quench of turbulence by a shear flow. The first one is the Biglari-Diamond-Terry (BDT) criterion [1990]

$$\left(Dk_\theta^2 V_E^{'2}\right)^{1/3} > \tau_c^{-1} \tag{10}$$

where D is the turbulent diffusion coefficient, k_θ a typical poloidal wave number, $\tau_c$ga turbulence auto-correlation time, and V'_E is the shear rate of the poloidal velocity. This criterion expresses the distortion of a convective cell, ultimately dissipated by some diffusion process (Fig.1).

The second one, proposed Waltz et al., comes from simulations of ITG turbulence and reads [1994]

$$\left|V_E^{'}\right| > \gamma_{lin} \tag{11}$$

where γ_{lin} is the maximum linear growth rate (calculated without shear flow). The third one, proposed by Hamaguchi and Horton, is based on the linear theory of ITG modes [1992]

$$\frac{\left|V_E^{'}\right|}{s} > \gamma_{lin} \tag{12}$$

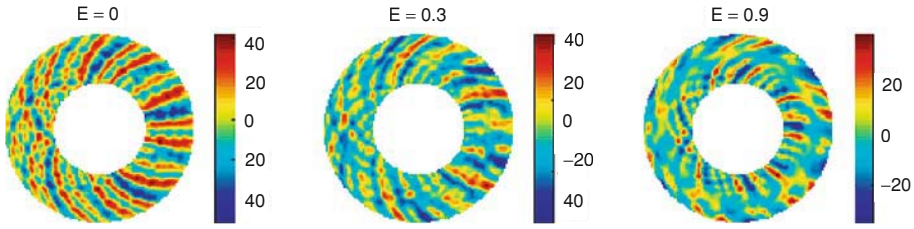


Figure 1. Effect of a shear flow on the electrostatic potential in a resistive ballooning turbulence (from [13]).

where s = rdq/qdr is the magnetic shear. The BDT criterion is the one that corresponds the most closely to the physics of vortex distortion. For practical reasons however, the criterion (11) is more often used. The reason is that the linear growth rate is easier to estimate from measurements than a correlation time that is rarely measured.

There exist many numerical simulations analysing the effect of a shear flow on a developed turbulence. One way to proceed is to impose a profile of velocity via an appropriate source in the vorticity equation. A transport barrier usually appears as can be seen in figure 2 for an ion turbulence ($f_t = 0$).

One important question is whether the reduction of the turbulent flux $3/2 < pv_{Er} >$ is due to a decrease of pressure fluctuations, velocity fluctuations or to a change of the cross-phase between pressure and velocity. Fig.2 indicates that the decrease in the level of potential fluctuations (and therefore of the level of velocity fluctuations) is substantial whereas the level of pressure fluctuations is moderate. Pressure fluctuations do not change significantly for weak and moderate barriers because the decrease in velocity fluctuations is balanced by the increase of the equilibrium pressure gradient in the layer. For very strong

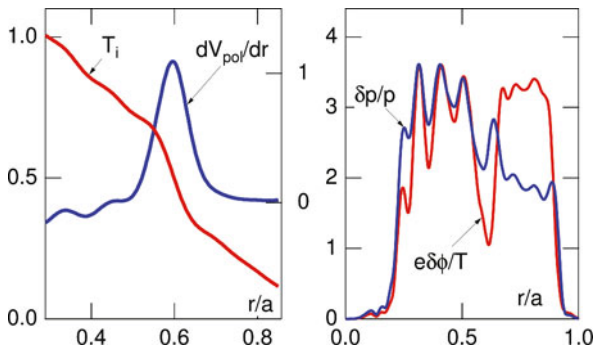


Figure 2. Left panel: Ion temperature profile (red) and externally imposed shear flow (blue). The ion temperature is a normalised one, and the shear flow unit is a/c_{s0}. Right panel: level of potential fluctuations (red) and pressure fluctuations (blue), in units of ρ_{s0}/a.

barriers however, the level of pressure fluctuations ultimately decrease with increasing shear flow rate. The cross-phase also decreases in the barrier, but less than the amplitude of the velocity, as showed by Figarella et al. [2003].

A very important feature of tokamak plasmas is the reinforcement of the shear flow with the gradients. This comes from the radial projection of the force balance equation,

$$E_r = \frac{T_i}{e_i}\frac{dn_i}{n_i dr} + (1 - k_{neo})\frac{dT_i}{e_i dr} + V_{Ti}B_p \tag{13}$$

where V_{Ti} is the toroidal velocity and B_p the poloidal magnetic field. The coefficient k_{neo} depends on the collisonality regime ($k_{neo} = 1.17$ in the collisionless regime). This link allows a positive loop where enhanced gradients lead to a larger shear rate, which in turn further improves the confinement. The various bifurcation schemes associated to this loop have been reviewed by Terry [2000]. The possibility of a tangent bifurcation played historically an important role and was first emphasised by Staebler and Hinton [1993].

A simple example is given here by analysing the case of a barrier in toroidal momentum. Assuming that the toroidal velocity contribution is dominant in Eq.(13), the shear rate is then approximated by

$$\gamma_E = \frac{r}{qR}\frac{dV_{Ti}}{dr} \tag{14}$$

To account for the stabilising effect of a shear flow, we use a diffusion coefficient of the form (see [Figarella])

$$D = \frac{D_0}{1 + (\gamma_E \tau_c)^2} \tag{15}$$

where D_0 is a the turbulent viscosity without shear flow. The resulting flux of toroidal momentum is

$$\phi_V = -\frac{D_0}{1 + C\left(\frac{dV_{Ti}}{dr}\right)^2}\frac{dV_{Ti}}{dr} - D_{coll}\frac{dV_{Ti}}{dr} \tag{16}$$

where D_{coll} is the collisional viscosity and C is a constant. Drawing the momentum flux versus the gradient of velocity exhibits an S-curve (see figure 3, left panel). A bifurcation is therefore expected above a critical momentum flux. It is sometimes called 1st order transition, by reference to the terminology of phase transition. The criterion for the transition onset is still debated. M.A. Malkov and P.H. Diamond found that the critical flux should satisfy the Maxwell construction of equal area [2004] (see Fig. 3), whereas S-I. Itoh et al. proposes a modified Maxwell construction to account for the effect of noise [2002] (in the latter case, the S-curve appears for the radial electric field versus the gradients). Similar calculations can be done for the other transport channels. These

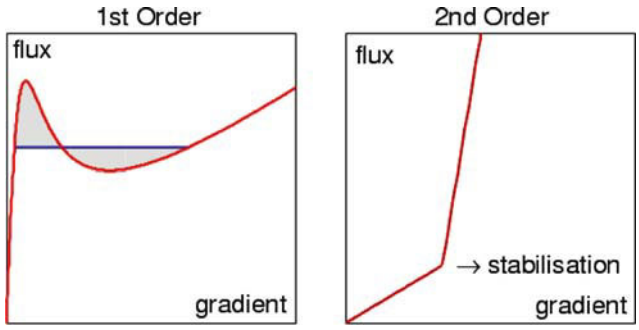


Figure 3. Left panel : schematic curve of a flux versus gradient in presence of a shear flow. The horizontal line indicates the flux that satisfies the Maxwell construction. Right panel: flux vs gradient in presence of an instability threshold. A barrier may be produced by a local increase of the threshold.

calculations are less straightforward since the derivative of the radial electric field given by Eq.(13) involves second derivatives of the density and temperature, thus introducing non-local effects. Second order transitions are also possible. There exist several mechanisms for this type of a transition where there is no discontinuity in the gradient. One way is a strong increase of the instability threshold within a layer (because of the magnetic shear for instance), in other words a linear stabilisation of modes (see Fig.3, right panel). All these schemes usually lead to a critical value of the heat flux, which has to be exceeded for a transition to take place. the heat flux in recent simulations of ITG turbulence with low magnetic shear (Voitsekhovitch et al 2003), consistently with a 1st order transition. This jump is not observed with negative magnetic shear, which would then be consistent with a 2nd order transition. Also numerical simulations have definitely shown that a self-amplifying process Although turbulence simulations indicate a dependence of the diffusion coefficient on shear flow rate that is consistent with Eq.(15) (Figarella et al 2003), the existence of an S-curve has not been demonstrated numerically up to now. A "jump" in the gradient was observed when increasing does take place when a shear layer appears, consistently with Eq.(13).

3.2 Magnetic shear

For most instabilities, the linear growth rate exhibits a parabolic shape with the magnetic shear, so that both negative and positive high shear improves the stability. An example is shown on Fig. 4 for ITG/TEM modes. At large absolute values of the magnetic shear, the stabilisation comes from the large values of the parallel wave numbers. Moreover, at negative shear, the interchange drive decreases (Brunner et al 1998). For trapped particles, this appears trough a

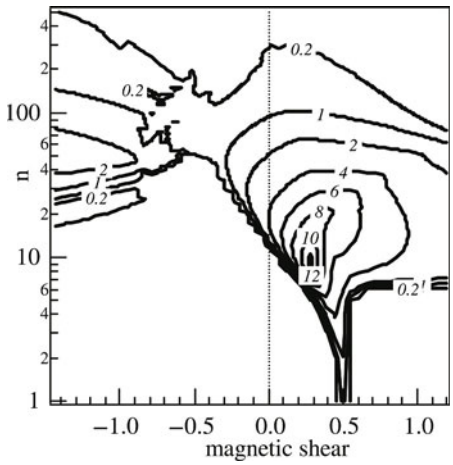


Figure 4. Mixing length diffusion coefficient for ITG/TEM modes versus the local magnetic shear and toroidal wave number n (from (Maget et al 1999)).

reversal of the precession drift, as it can be seen from Eq.(4), which predicts a reversal for $s < -3/8$.

In addition, the surface where the magnetic shear vanishes plays a special role. This is indeed a place where the density of rational numbers (and thus of resonant surfaces) decreases provided that the poloidal wave numbers are upper bounded (e.g. $k_\theta \rho_i < 1$). This behaviour is amplified when the position $r = r_{min}$ where safety factor is minimum $q = q_{min}$ is a simple rational number. The width of the gap in resonant surfaces near $q_{min} = m_0/n_0$ is given by the relation

$$d_{gap} = \left[\frac{2 q_{min} \rho_i}{n_0 r_{min} q''_{min}} \right]^{1/2} \tag{17}$$

For a low curvature of the q profile and low values of n_0 (low order rational number), this gap width is larger than the width of an individual m,n mode. In this case, the interchange drive vanishes due to a lack of overlapping between adjacent m,n modes. An alternative explanation based on the distribution of "noble" numbers, whose associated resonant surfaces are the most resilient to chaos according to the KAM theorem, also emphasises the role of a low order rational q_{min} (Misguich 2000). These effects are not taken into account in linear model such as the one used to provide the result shown on Fig.4. Flux tube simulations seem to favour an explanation based on a decrease of the interchange drive (Waltz et al 1995, Beer et al 1997, Jenko et al 2000, Dimits et al 2000). The best confinement is usually obtained for negative shear. The effect is amplified with increasing Shafranov shift ("α stabilisation", see (Beer

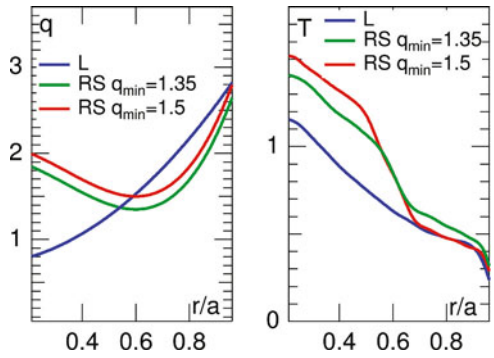


Figure 5. 3 different types of q profiles (left) and corresponding temperature profiles (right) (from [26]).

et al 1997) and next section). Full torus simulations are more sensitive to the density of rational surfaces. An example is given in Fig.5. The best confinement is then usually found at $s = 0$ (Kishimoto et al 1998, Thyagaraja 2000, Garbet et al 2001).

3.3 Density gradient, impurity and α effect

Although less often quoted than the velocity and magnetic shears, impurity, density gradient and the Shafranov shift may play a role in the formation and self-sustainment of a barrier.

The stabilisation by a density gradient comes from the diamagnetic drift that comes in the vorticity equation (last term of Eq.(1c)). A linear stability analysis of the system (1a–1e) shows that for a strongly unstable ITG mode ($f_t = 0$), the growth rate is of the form

$$\omega = \frac{1}{2}\left(\omega^*_{ni} - \omega^*_{di}\right) + i\left[\gamma_0^2 - \frac{1}{4}\left(\omega^*_{ni} - \omega^*_{di}\right)^2\right]^{1/2} \tag{18}$$

where

$$\omega^*_{ni} = -\omega^*_{ne} = \frac{nq}{r}\rho_{s0}\frac{a\partial_r n_{e,eq}}{n_{e,eq}} \tag{19}$$

This simple expression shows that a peaked density profile is stabilising. Unfortunately, this expression does not apply close to the threshold. The density gradient turns out to be destabilising in this case. It is only when the plasma is sufficiently collisional that a stabilisation is recovered. This mechanism could therefore explain why the confinement is usually improved when a pellet is injected since this corresponds usually to a collisional situation.

The stabilisation due to impurity is a dilution effect. This leads to a growth rate for ITG modes that behaves as $1/Z^{0.5}$, where Z is the charge number. This effect is actually not covered by the Eqs (1a–1e), which are written with $Z = 1$. This mechanism is of little interest for fusion since a dilution means also a reduced reactivity. However, it is possible that this effect is involved transiently to trigger an ITB with a lower amount of additional power.

Pressure gradient, parameterised by the $A = q^2 R d\beta/dr$ parameter (β is the plasma toroidal beta $2\mu_0 p/B^2$), destabilises ideal MHD ballooning modes. However, a further increase of α is ultimately stabilising via magnetic surface compression (Shafranov shift). This domain of stable and large values of α is known as the "2nd stability region" (Mercier 1978, Sykes et al 1978, Zakharov 1978). In principle, the 1st and 2nd regions of stability are disconnected, but a continuous transition is possible if the magnetic shear is low enough or negative. This is why the effects of α and magnetic shear are linked. This stabilising process has been shown to be effective for most instabilities driven by an interchange effect, in particular TE modes (Beer 1997). It is not explicitly included in the Eqs(1a–1e), but can be easily added by changing $\lambda_t = 1/4 + 2s/3$ into $\lambda_t = 1/4 + 2s/3 - 2\alpha/5$ (Maget et al 1999). This mechanism is effective when A is of order 1. Clearly this corresponds to high values of the pressure. On the other hand, this process offers another positive loop where the pressure increases when the barrier is set on. The corresponding increase in α further decreases the turbulent diffusivity, thus reinforcing the barrier (Bourdelle et al 2004). The most successful barriers obtained up to now reach a range of α values that are in the right range for this effect to be operative.

3.4 Comparison to experimental results

The comparison between theory and experiment would deserve an overview by itself. Results from the JET tokamak can be briefly summarised as follows. Once a barrier is established, a stability analysis indicates that the shear flow rate is large enough to overcome the largest growth rate calculated without shear flow (Budny et al 2002). Therefore the picture of a self-amplifying positive loop seems to be correct. On the other hand, shear flow cannot be the only explanation for the onset of a barrier. For instance there exists electron barriers without neither toroidal torque nor fuelling. Eq.(13) then indicates that the radial electric field is small.

In fact in many cases, negative or zero magnetic shear seems to be the key ingredient for producing the barrier (see for instance (Litaudon et al 2002, Esposito et al 2003)). Also resonant surfaces seem to play an important role in the formation of the barrier. Indeed many barriers appear when the minimum of the safety factor reaches a simple rational number (Challis et al 2001, Joffrin et al 2004). Two main explanations have been proposed. The first one rely on

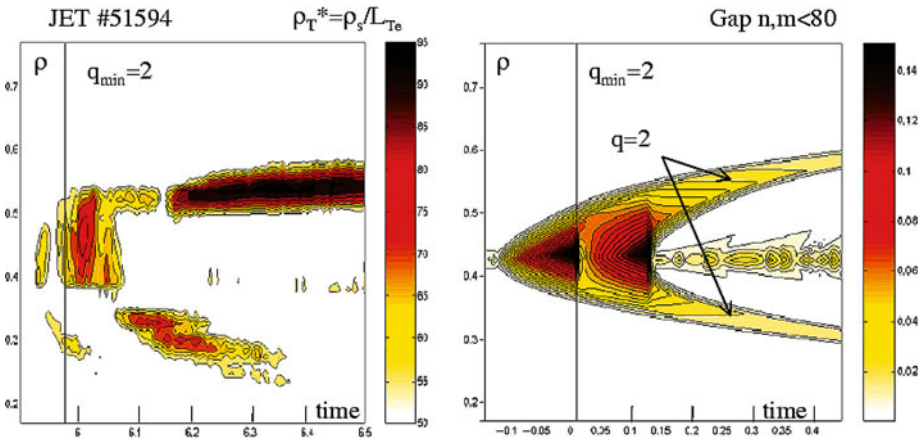


Figure 6. Contour lines of $\rho_T^* = \rho_s/L_{Te}$ (left panel) and of the distance (in meters) between adjacent resonant surfaces such that n,m < 80 (right panel) (from [37]).

a localised shear flow produced by an island located at $q = q_{min}$ (Garbet et al 2003). The second explanation is based on a rarefaction of rational surfaces close to a low order rational surface, as explained above (see (Garbet et al 2003) and references therein for details). The latter mechanism is illustrated by Fig.6, which compares the inverse of the temperature gradient length to the width of the gaps in resonant surfaces. This case is an interesting one where a barrier appears when $q_{min} = 2$, then splits into two barriers that follow the position of the $q = 2$ surfaces (in these pulses the q profile relaxes slowly so that q_{min} decreases continuously).

A pending question is whether the onset of a barrier corresponds to a 1st or 2nd order transition. The answer is not clear at the moment. For an established barrier, an element of response comes from transient experiments. A perturbation (cold pulse) usually erodes the barrier, whereas an S curve (Fig.3) would predict a strengthening of the barrier (Mantica et al 2002). This question is under investigation.

4. Structure Dynamics and Interaction with Transport Barriers

4.1 Large scale transport events

The possibility of profile relaxation over large scales was first proposed by Diamond and Hahm [1995] in the context of turbulence in fusion plasmas. Several turbulence simulations have then demonstrated the existence of large scale transport events, which enhance the anomalous transport (Drake et al

1988, Jenko et al 2000, Carreras et al 1996, Sarazin et al 1998, Garbet et al 1999, Beyer et al 2000). Two mechanisms, avalanches and streamers, have been identified.

Avalanches appear via a domino effect: if a gradient of temperature (or density) locally exceeds an instability threshold, it generates a burst of transport that expels some heat or matter, thus increasing the gradient on a neighbouring radial position, where the same process may occur again (Carreras et al 1996). There is some similarity between this process and sand pile automatons proposed as a paradigm for Self-Organised Critical systems (Bak et al 1987). Streamers are convective cells that are elongated in the radial direction. They have been observed in particular in simulations of ETG modes (Drake et al 1988, Jenko et al 2000), Resistive Ballooning Modes (Beyer et al 2000), and interchange turbulence in the Scrape-Off Layer of a tokamak (Garbet et al 1999). A bi-stable model has been recently proposed to describe this type of behaviour (Tangri et al 2003).

It is expected that both avalanches and streamers are sensitive to a shear layer. Indeed, simulations show that avalanches do not cross a transport barrier, except the strongest events. Figures 7, 8 and 9 illustrate this property. Fig.7 show the contour lines in a poloidal plane of the perturbed electric potential in the L mode (left panel) and in an internal transport barrier produced with a magnetic shear reversal and a strong velocity shear (right panel). The time slice in the L-mode corresponds to the development of a large scale transport event, which corresponds to the transient establishment of an elongated convective cell. The ITB case illustrates the effect of a strong shear flow, which tears apart the vortices. Fig.8 shows the map of the turbulent heat flux in a RBM turbulence.

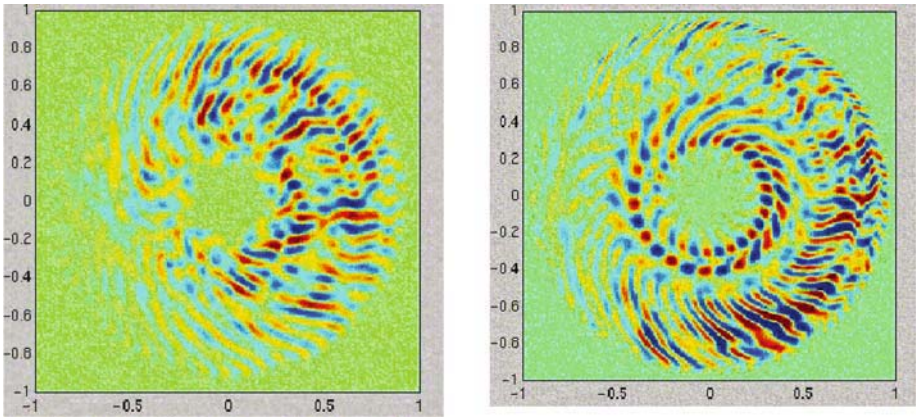


Figure 7. Contour lines of the perturbed electric potential in the L mode (left panel) and in an internal transport barrier (right panel).

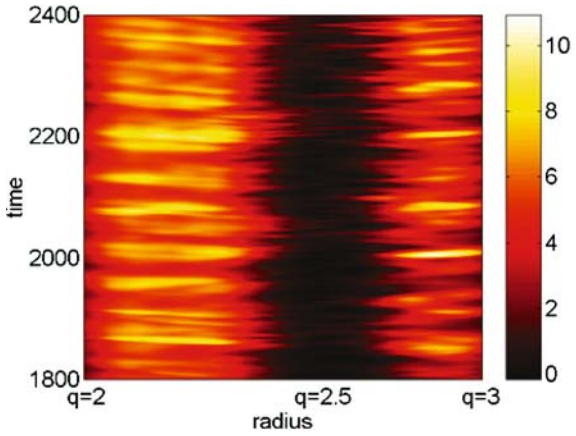


Figure 8. Map of turbulent flux for a RBM turbulence with an imposed velocity shear.

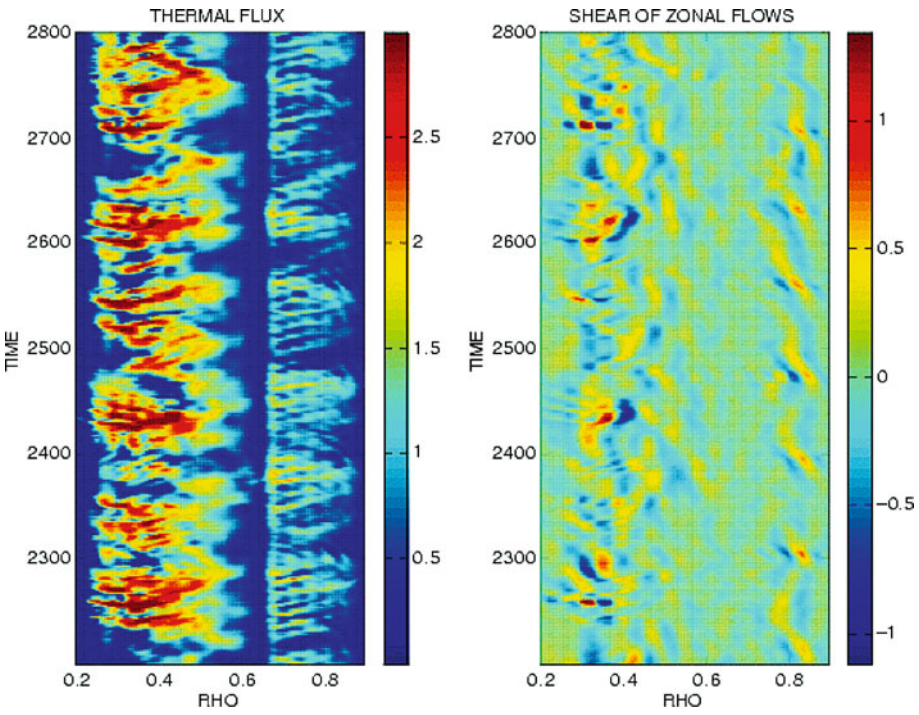


Figure 9. Contour lines of the heat flux (left panel) and shearing rate associated to Zonal Flows (right panel) in an ITB produced with a magnetic shear reversal for an ITG turbulence.

In this case, the transport barrier was produced by an externally imposed shear flow. Again large scale transport events do not cross the barrier, except for the strongest events.

4.2 Zonal flows

Zonal flows play an important role in turbulence simulations. This statement can be verified by comparing a computation with radial modes (m = 0,n = 0) of the electric potential with a simulation where there are artificially suppressed (Beer 1995, Lin et al 1998). The generation and disappearance of Zonal Flows has motivated a large number of works. The mechanism which is often advocated for the generation of Zonal Flows is the turbulent Reynolds stress $<\mathbf{v}_E\mathbf{v}_E>$, whose non zero divergence drives the plasma velocity in poloidal and toroidal directions (Diamond et al 1998). The resulting sheared poloidal velocity back reacts on fluctuations. The stabilisation occurs through a shearing process similar to the effect of a mean shear flow, although this process is more diffusive like in the wave number space (Diamond et al 1998). Other mechanisms have been proposed, which rely on the Kelvin-Helmholtz instability (Rogers et al 2000) or on Geodesic Acoustic Modes (Hallatschek et al 2001).

The dynamics of Zonal Flows in transport barriers seems to depend on the strength of turbulence. For a strong barrier, the level of fluctuations is very low, and no Zonal Flows develop within the barrier, as shown on Fig.9. A simple explanation for this behaviour is the suppression of the Reynolds stress inside the barrier. This behaviour brings some support to the models Zonal Flows generation via the Reynolds stress. However it is stressed that GAM modes are not implemented in the codes presented here. For weaker barriers, Zonal Flows are found to be more active within the barrier. Quite interestingly, the level of activity seems to be connected to the type of turbulence that is considered. Zonal Flows are usually more active in a TEM/ITG turbulence than in a pure ITG one (no trapped electrons). When Zonal Flows are active, the amplitude of avalanches is weaker. This confirms the interplay between Zonal Flows and large scale transport events already observed in Resistive Ballooning Mode turbulence.

Again a difference must be made between a self-sustained barrier, for which Zonal Flows do not seem to play a crucial role, and the formation of a barrier. It was recently proposed that Zonal Flow may help in establishing a barrier (Kim et al 2003). This question has not been investigated numerically up to now.

5. Conclusion

The picture for the onset and sustainment of a barrier is now well established. The profile of safety factor seems to play a crucial role in the onset of the barrier. Several reasons have been proposed for this key role. Negative magnetic shear

is known to play a linear stabilising effect on most interchange instabilities. Also zero magnetic shear is a region of rarefaction of resonant surfaces, in particular close to a low order rational value of the safety factor. Finally, an island may appear when the minimum of safety factor is a rational number, thus inducing a localised shear flow. Once a barrier is established in the ion channel, the barrier enters a self-amplifying loop where the enhanced gradients increase the flow shear, which in turn further improves the confinement. The behaviour of structures is not completely clarified in this picture. It seems that large scale transport events (streamers or avalanches) are prevented by the strong shear flow that takes place within a barrier. However the strongest events are able to cross it. Zonal Flows are usually quenched within the strongest barriers. A simple explanation for this behaviour is the cancellation of the Reynolds stress tensor due to the low level of electric potential fluctuations. Whether Zonal Flows help in forming the barrier remain to be investigated numerically.

References

Bak, P., Tang, C., Wiesenfield, K., Phys. Rev. Lett. 59, 381 (1987).

Beer, M., Hammett, G.W., Rewoldt, G., Synakowski, E.J., Zarnstoff, M.C., and Dorland, W., Phys. Plasmas 4, 1792 (1997).

Beer, M.A., thesis, D., Princeton University 1995.

Beyer, P., Benkadda, S., Garbet, X., Diamond, P.H., Phys. Rev. Lett. 85, 4892 (2000).

Biglari, H., Terry, W., Phys. Fluids B 2, 1 (1990).

Bourdelle, C. et al., submitted to Phys. Plasmas.

Brunner, S., Fivaz, M., Tran, T.M., Vaclavik, J., Phys. Plasmas 5, 3929 (1998).

Budny, R.V., Andre, R., A. Bécoulet, et al., Plasma Phys. Control. Fusion 44, 1215 (2002) .

Carreras, B.A., Newman, D., Lynch, V.E., Diamond, P.H., Phys. Plasmas 3, 2903 (1996).

Challis, C. et al., Plasma Phys. Control. Fusion 43, 861(2001).

Diamond, P.H. et al., in Proceedings of the 17th IAEA Fusion Energy Conference, IAEA-CN-69/TH3/1 1998.

Diamond, P.H., Phys. Rev. Letters 90, 185006 (2003).

Diamond, P.H., Hahm, T.S., Phys. Plasmas 2, 3640 (1995).

Dimits, A.M., Cohen, B.I., Nevins, W.M., Shumaker, D.E., "Progress in Gyrokinetic Simulations of Toroidal ITG Turbulence", to appear in Proceedings of the 18th Fusion Energy Conference, Sorento, 2000, (IAEA, Vienna).

Drake, J.F., Guzdar, P.N., Hassam, A.B., Phys. Rev. Lett. 61, 2205 (1988).

Esposito, B. et al., "JET internal transport barriers: experiment vs theory", accepted for publication in Plasma Physics and Control. Fusion (2003).

Figarella, C., Benkadda, S., Beyer, P., Garbet, X., Voitsekhovitch, I., Phys. Rev. Lett. 90, 015002 (2003).
Garbet, X., Sarazin, Y., Beyer, P., Ghendrih, P., Waltz, R.E., Ottaviani, M., Benkadda, S., Nucl. Fusion 39, 2063 (1999).
Garbet, X., Bourdelle, C., Hoang, G.T., et al., Phys. Plasmas 8, 2793 (2001).
Garbet, X. et al., Nuclear Fusion 43, 975 (2003).
Hahm, T.S., Phys. Plasmas 2, 3640 (1995).
Hallatschek, K., D. Biskamp, Phys. Rev. Lett. 86, 1223 (2001).
Hamaguchi, S., Horton, W., Phys. Fluids B4, 319 (1992).
Hinton, F.L., Staebler, G.M., Phys. Fluids B5, 1291 (1993).
Hugon, M., Smeulders, P., et al., Nuclear Fusion 32, 33 (1992).
Itoh, S-I., Itoh, K., Toda, S., Phys. Rev. Lett. 89, 215001 (2002).
Jenko, F., Dorland, W., Kotschenreuther, M., Rogers, B.N., Phys. Plasmas 7, 1904 (2000).
JET Team, Gormezano, C., in Plasma Physics and Controlled Nuclear Fusion Research (Proc. 16th Int. Conf., Montreal, 1996), Vol. 1, IAEA, Vienna (1997), p. 487.
Joffrin, E. et al., submitted to Nucl. Fusion.
Kim, E.J., Diamond, P.H., Phys. Rev. Letters 90, 185006 (2003).
Kishimoto, Y., Horton, W., et al., Plasma Phys. Cont. Fusion 40, A663 (1998).
Koide, Y., Kikuchi, M., Mori, M., et al., Phys. Rev. Lett. 72, 3662 (1994).
Levinton, F., Zarnstorff, M., Batha, S., Phys. Rev. Lett. 75, 4417 (1995).
Lin, Z. et al., Science 281, 1835 (1998).
Litaudon, X., Crisanti, F., Alper, B., Plasma Phys. Control. Fusion 44, 1057 (2002).
Maget, P., Garbet, X., Géraud, A., Joffrin, E., Nucl. Fusion 39, 949 (1999).
Malkov, M.A., Diamond, P.H., submitted.
Mantica, P. et al., "Transient Heat Transport Studies in JET Conventional and Advanced Tokamak Plasmas", in Plasma Physics and Controlled Nuclear Fusion Research 2002, 19th International Conference, Lyon, 2002 (IAEA, Vienna, 2002) , IAEA-CN-94/EX/P1-04)
Mercier, R., in Plasma Physics and Controlled Nuclear Fusion Research (Proc. 7th Int. Conf. Innsbruck, 1978), Vol. 1, IAEA, Vienna(1979) 701.
Misguich, J., Bull. Am. Phys. Soc. 45, 257 (2000).
Moreau, D., and the Tore Supra Team, in Proceedings of the 14th International Conference on Plasma Physics and Controlled Nuclear Fusion Research, Würtzburg, 1992, (IAEA,Vienna, 1994), vol. I, p. 649.
Rogers, B.N., Dorland, W., Kotschenreuther, M., Phys. Rev. Letters 85, 5336 (2000).
Sarazin, Y., Ghendrih, P., Phys. Plasmas 5, 4214 (1998).
Strait, E., Lao, L., Mauel, M., et al., Phys. Rev. Lett. 75, 4421 (1995).

Sykes, A., Turner, M.F., Fielding, P.J., Haas, F.A., in Plasma Physics and Controlled Nuclear Fusion Research (Proc. 7th Int. Conf. Innsbruck, 1978), Vol. 1, IAEA, Vienna(1979) 625.
Tangri, V., Das, A., Kaw, P., Singh, R., Phys. Rev. Lett. 91, 025001 (2003).
Terry, P.W., Rev. Mod. Phys. 72, 109 (2000).
Thyagaraja, A., Plasma Phys. Contr. Fusion 42 B 255 (2000).
Voitsekhovitch, I. et al., Comm. Non Linear Science and Numerical Simulation 8, 519 (2003).
Waltz, R.E., Kerbel, G.D., Milovitch, J., Phys. Plasmas 1, 2229 (1994).
Waltz, R.E., Kerbel, G.D., Milovitch, J., Hammett, G.W., Phys. Plasmas 2, 2408 (1995).
Wolf, R.C., Hobirk, J., Conway, G.D., et al., Nucl. Fusion 41, 1259 (2001).
Wolf, R.C., Plasma Phys. Control. Fusion 45, R1-R91 (2003).
Zakharov, L.E., in Plasma Physics and Controlled Nuclear Fusion Research (Proc. 7th Int. Conf. Innsbruck, 1978), Vol. 1, IAEA, Vienna(1979) 689.

Chapter 12

CHARACTERIZATION OF TURBULENCE IN TERMS OF PROBABILITY DENSITY FUNCTION

A New Approach to Describe Transport in Fusion Plasmas

C. Hidalgo, B. Gonçalves*, and M. A. Pedrosa
Laboratorio Nacional de Fusión por Confinamiento Magnético, Asociación Euratom-Ciemat, 28040 Madrid, Spain

**Associação Euratom-IST, Av. Rovisco Pais, 1049-001 Lisbon, Portugal*

Abstract: A new approach, based on multi-field probability density function statistical analysis, is proposed to describe transport in non-equilibrium systems and to unravel the overall picture connecting transport, gradients and flows in fusion plasmas. Based on this approach, significant improvement in our understanding of the statistical properties of fluctuations, the non-linear link between transport and gradients and the physics of flows have been recently achieved in fusion plasmas. An empirical similarity in the scaling properties of the probability distribution function (PDF) of turbulent transport has been observed in the plasma edge region in fusion plasmas. The investigation of the dynamical interplay between fluctuation in gradients, turbulent transport and radial electric fields has shown that these parameters are strongly coupled. The bursty behavior of turbulent transport is linked with a departure from the most probable radial gradient. The dynamical relation between fluctuations in gradients and transport is strongly affected by the presence of sheared poloidal flows which organized themselves near marginal stability. Experimental results show that there is a dynamical relationship between transport and parallel flows, showing that turbulent transport can drive parallel flows in the plasma boundary of fusion plasmas. These results emphasize the importance of the statistical description of transport processes in fusion plasmas as an alternative approach to the traditional way to characterize transport based on the computation of effective transport coefficients.

Key words: Fusion, Turbulent transport, E × B shear

A.S. Sharma and P.K. Kaw (eds.), Nonequilibrium Phenomena in Plasmas, 257–272.
© 2005 *Springer. Printed in the Netherlands.*

1. Introduction

Nuclear fusion energy is released when the nuclei of light elements join together to form a heavier ones. The easiest reaction to achieve is between the two isotopes of hydrogen (deuterium and tritium). By heating the deuterium-tritium fuel to very high temperatures, sufficient energy can be given to the nuclei that the repulsive (coulomb) force can be overcome and they fuse together. The fusion brought about in this way is called thermonuclear fusion (Wesson 1997).

Because of being a mixture of charged (positive and negative) particles the plasma is influenced by magnetic fields. With a suitable magnetic field configuration ("magnetic bottle"), it should be possible to confine the plasma in the required density and temperature range and a sufficiently long time (confinement time) to obtain a net energy gain. So far, the magnetic configuration that has advanced furthest to achieve fusion reactor conditions is the tokamak. Besides the tokamak, the most mature line is the stellarator which offers attractive properties (inherent steady state operation). In the stellarator concept the magnetic field configuration is fully produced by a set of coils (toroidal, poloidal, helical). In the deuterium-tritium reaction temperatures in excess 100 million degrees (i.e. 10 KeV) are required. At such temperatures the fuel is fully ionized and is given a special name (plasma). In a fusion reactor it would be necessary to confine the energy of sufficiently dense plasmas for a (confinement) time which allows an adequate fraction of the fuel to react. In a fusion reactor the values of ion temperature (T_i), density (n_i) and energy confinement time must be such that their product is higher than 5×10^{21} s keV m^{-3}. For density around 10^{20} m^{-3} and ion temperatures in the range 10–20 keV, the confinement time is of the order of one second.

Magnetically confined plasmas are necessarily out of equilibrium. A possible relaxation mechanism is by Coulomb collisions; in toroidal magnetic devices (e.g. tokamaks, stellarators) the resulting particle and energy flows are termed neoclassical transport. In addition, the plasma can relax toward equilibrium through different types of instabilities. Transport caused by microinstabilities (turbulent induced transport) is in general larger than neoclassical transport (Carreras 1997).

Although the dominant free energy source driving microinstabilities has not been identified, one of the important achievements of the fusion community has been the development of techniques to control plasma fluctuations based in the $E \times B$ stabilizing mechanism (Terry 2000). Sheared $E \times B$ flows can influence the turbulence by shear decorrelation mechanisms and, as a consequence, modify the induced transport. A strong radial gradient in the radial electric field (E_r) produces strong shear in the particle ($E_r \times B$) drift velocity (B being the toroidal magnetic field). This tears apart the coherent cellular pattern of the unstable modes, as shown in figure 1. When the $E \times B$ shearing rate ($\omega_{E\times B}$)

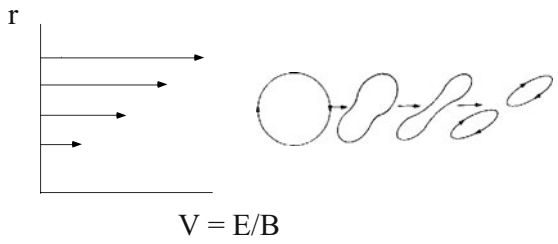


Figure 1. Sheared E × B flows can influence the turbulence by shear decorrelation mechanisms and, as a consequence, modify the turbulent induced transport.

approaches the frequency characteristic of the turbulence ($\Delta\omega_T$), $\omega_{E\times B} \approx \Delta\omega_T$, a reduction in the turbulence amplitude is predicted. This control allows the transition to improved confinement regimes and the generation of transport barriers in fusion plasmas. The generality of the E × B mechanism is based on the fact that the drift of charged particles in the presence of an electric (E) and magnetic field (B) does not depend on the mass or charge of the particles. Recently the theory of E × B shear suppression of turbulence has been extended to include time dependent E × B flows (Hahm et al. 1999). The best performance of existing fusion plasma devices has been obtained in plasma conditions where E × B shear stabilization mechanisms are likely playing a key role: both edge and core transport barriers are related to a large increase in the E × B sheared flows. These results emphasize the importance of clarifying the driven mechanisms of sheared flows in fusion plasmas.

Several distinct mechanisms have been invoked to explain the connection between turbulent fluxes and gradients (which provide a free energy source to drive instabilities in magnetically confined plasmas) (Carreras 1997, Terry 2000, Itoh et al. 1999) (Fig. 2). Non-linear relations between heat fluxes and gradients, in which heat fluxes increase non-linearly as gradient becomes steeper, can explain the confinement degradation with the heating power reported in magnetically

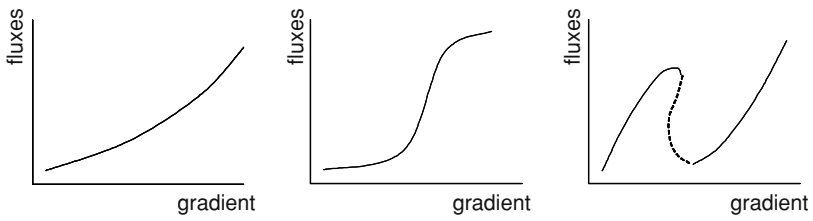


Figure 2. a) Non-linear relation between fluxes and gradients can explain the degradation of confinement with heating power. b) Expected relation between transport and gradient in the framework of the marginal stability approach. c) Non linear relation (bifurcation) between gradient and flux.

confined fusion plasmas. Instabilities governed by a threshold may lead to a self-organized critical (SOC) system by producing transport events at all scales, called avalanches. In the context of these models, the functional dependence between heat and particle transport is expected to show sharp jumps as the system crosses instability thresholds. The transition to improved regimes implies non-monotonic relations (bifurcations) between gradients and transport. First and second order critical transition models have been invoked to explain bifurcations and transport barrier dynamics in fusion plasmas (Terry 2000, Itoh et al. 1999). From this perspective, it is important to understand the dynamical relation between turbulent transport, gradients and radial electric fields.

This paper reports recent results, based on multi-field probability density function statistical analysis, to unravel the overall picture connecting transport, gradients and flows in fusion plasmas (Hidalgo et al. 2003a, Gonçalves et al. 2002, Hidalgo et al. 2003b, Gonçalves et al. 2003a, Hidalgo et al. 2002, Gonçalves et al. 2003b). The statistical properties of turbulent transport in the plasma boundary are discussed in section 2. The investigation of transport in terms of multi-field probability density functions is presented in section 3. The physics of sheared flows is discussed in section 4. Finally conclusions are presented in section 5.

2. Statistical Properties of Turbulent Transport

Characterization of fluctuations and fluctuation driven particle and energy fluxes requires experimental techniques for measuring the variations in parameters such as density, temperature and magnetic and electric fields with good temporal and spatial resolution. With the present state of the art in plasma diagnostics this kind of measurements is mostly limited to the plasma edge where material probes can be used (Hidalgo 1995, Ritz et al. 1988). In order to assess the role of both turbulence and E $\times$ B sheared flows on transport in the core of the plasma there is a need for improved diagnostics and analysis tools for fluctuating quantities.

Broadband electrostatic and magnetic fluctuations have been observed in the boundary region of magnetically confined devices. The electrostatic fluctuations produce a fluctuating radial velocity given by, $\tilde{v}_r = \tilde{E}_\theta / B$, where $\tilde{E}_\theta$ is the fluctuating poloidal electric field and B is the toroidal magnetic field. The electrostatic fluctuation driven radial particle flux is given by $\Gamma_{\mathrm{E\times B}} = \langle \tilde{n}\, \tilde{v}_r \rangle$. An effective radial velocity can be defined as the normalized E $\times$ B turbulent particle transport to the local density: $v_{eff} = \Gamma_{\mathrm{E\times B}} / \langle n \rangle$. Ignoring poloidal and toroidal asymmetries the total electrostatic fluctuation driven particle fluxes can be computed. It has been experimentally shown that in some cases the fluctuating flux can account for an important part of the total particle flux in the edge region (Martines et al. 1999). However, it should be noted that in some

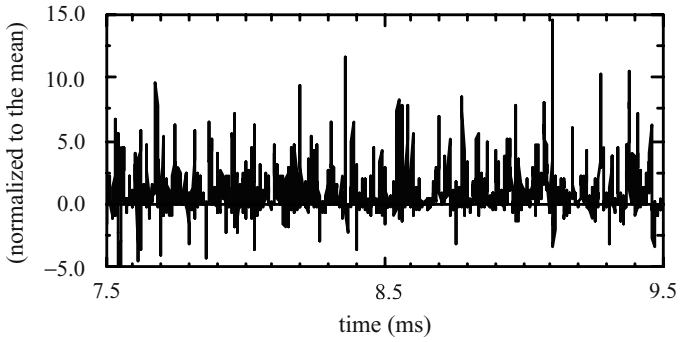


Figure 3. Time evolution of E × B turbulent transport in the plasma boundary of fusion devices. A significant fraction of transport is due to the presence of large and sporadic events.

cases fluctuation fluxes appear too high to be consistent with global particle balance (García-Cortés et al. 2001). Poloidal asymmetries, large scale convective cells or the possible role of temperature fluctuations may account for these apparent inconsistencies. At present, this disagreement still remains as an open question (Labombard 2002).

It is well known that local E × B turbulent driven transport is bursty: that is to say, a significant fraction can be attributed to the presence of large and sporadic transport events (Fig. 3). As a consequence, in order to go deeper into the mechanisms underlying turbulent transport it is important not only to compute the average value of the fluctuation induced transport, but also the statistical properties of the time resolved turbulent flux.

A systematic investigation of the statistical properties of turbulence has been investigated in the plasma edge of the stellarator (TJ-II) and tokamak (JET) plasmas (Hidalgo 2002). The flexibility of the TJ-II configurations makes TJ-II an ideal device to study the onset of fluctuations and related phenomena in a controlled way. In the TJ-II stellarator, as in other devices (Endler et al. 1995, Huld et al. 1991), the probability density function (PDF) of the turbulent transport shows significant non-gaussian features. The Probability Density Functions (PDFs) of the local E × B turbulent flux are modified when decreasing magnetic well (Castellano et al. 2002) which is the main stabilizing term in the TJ-II device (Figure 4): these changes are mainly an increase on the probability of large amplitude flux transport events. The PDF of E × B turbulent fluxes can be rescaled using a finite-size scaling law (Frette et al. 1996),

$$\mathrm{PDF}(\Gamma_{\mathrm{E}\times\mathrm{B}}) = \mathrm{L}^{-1}\mathrm{g}(\Gamma_{\mathrm{E}\times\mathrm{B}}/\mathrm{L}) \tag{1}$$

where $\Gamma_{\mathrm{E}\times\mathrm{B}}$ is the turbulent E × B flux and L is an scaling factor. In order to identify the relation of the scaling parameter with plasma parameters it is important to keep plasmas with similar properties (magnetic topology, collisionality,

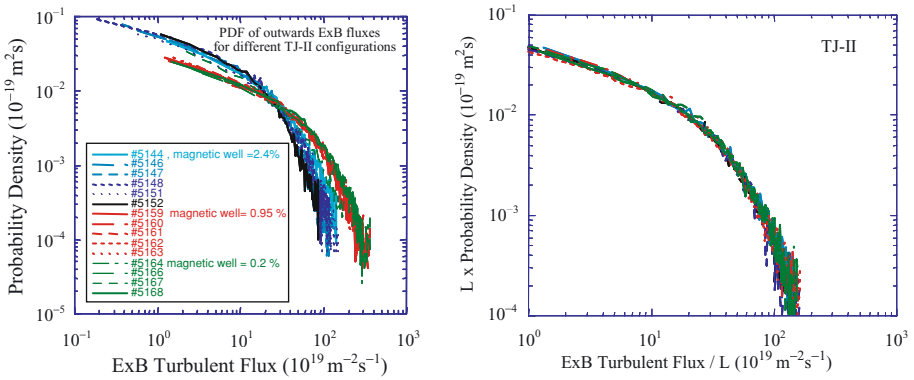


Figure 4. PDFs of turbulent transport measured in plasmas with different magnetic wells (a), rescaled PDFs (b) in the TJ-II stellarator (Hidalgo et al. 2002).

etc.) but with different level of fluctuations. This study has shown that the scaling parameter L is directly related with the level of fluctuations. Similar dependence has been recently observed in the JET tokamak. These results are consistent with previous findings that have shown an empirical similarity of frequency spectra of edge plasma fluctuations in different toroidal magnetic confinement devices (Pedrosa et al. 1999). Frequency spectra can be re-scaled using the expression, $P(\omega) = P_0\ g(\lambda, \omega)$, where λ and P_0 are parameters to be determined for each device. The empirical similarity in turbulent fluxes suggests that edge plasma turbulent transport evolves into a state in which the PDFs of transport exhibit the same behaviour over the entire amplitude range of transport events. This result supports the view that turbulent transport in fusion plasmas, as many other dynamical systems, displays universality.

The functional form for the PDF given by expression (1) might be partially explained considering that the flux is a quadratic function of two fluctuating and correlated density and radial velocity fields. On the other hand, this kind of rescaling might also be a consequence of self-similar properties of the PDF of turbulent transport. A more systematic analysis of the PDF of transport from other confinement devices is needed to clarify the interpretation of the present findings. In particular, it would be very interesting to look the properties of PDFs in non-fusion plasmas (like linear devices and toroidal plasmas without rotational transform) where it is not expected to have self-similarity on the structure of fluctuations.

3. Multi-field Probability Distribution Functions

Fluxes of particle, momentum and energy contain all the dynamical information on transport processes. The traditional way to characterize transport in

fusion plasmas is based on the computation of effective transport coefficients (i.e. particle, energy and momentum diffusion coefficients) and on average quantities (i.e., gradients and fluxes). Under the assumption of diffusive-like fluxes (i.e. fluxes depends on the profile gradients), it follows,

$$
\begin{aligned}
Q_i &\equiv -\chi_i^{eff} n \nabla T_i \\
Q_e &\equiv -\chi_e^{eff} \nabla T_e \\
\gamma_\phi &\equiv -\chi_\Phi^{eff} nm \nabla v_\Phi \\
\gamma_\theta &\equiv -\chi_\theta^{eff} nm \nabla v_\theta \\
\Gamma &\equiv -D \nabla n
\end{aligned}
$$

where $Q_{i,e}$ represent the energy fluxes (ions and electrons), $\Gamma$is the particle flux, $\gamma_{\Phi,\theta}$ are the fluxes of momentum (toroidal and poloidal) and D and χ are the effective diffusivities (Carreras 1997, Scott et al. 1990).

Many experiments have been carried out to understand the link between gradients and fluxes (Carreras 1997, Itoh 1999). It has been recently argued that in order to go deeper into the underlying physics of those mechanisms a multi-field statistical approach is needed to characterize transport (Hidalgo et al. 2003a, Gonçalves et al. 2002, Hidalgo et al. 2003b). This *new way of thinking* emphasizes the importance of the statistical description of transport processes (in terms of in Probability Distribution Functions) in fusion plasmas as an alternative approach to the traditional way to characterize transport based on the computation of effective transport coefficients.

The joint probability P_{ij} of the two variables X and Y, meaning the probability that at a given instant X and Y occur simultaneously, is given by $P_{ij} = P(X_i, Y_j) = N_{ij}/N$ where N_{ij} the number of events that occur in the interval $(X_i, X_i + \Delta X)$ and $(Y_i, Y_i + \Delta Y)$ and N the time series dimension. ΔX and ΔY are the bin dimension of X and Y time series, respectively, where the indices stands for i-th (or j-th) bin average value. The expected value of X at a given value of Y_j is defined as

$$
E[X \mid Y_j] = \frac{\sum_i P_{ij} X_i}{\sum_i P_{ij}}
$$

and represents the average value of the probability distribution of X at a given value of Y.

Recent improvement in edge plasma diagnostics has allowed to compute the joint probability function of transport and gradient fluctuations (Hidalgo et al. 2003a, Gonçalves et al. 2002, Hidalgo et al. 2003b). The experimental set up consists of arrays of Langmuir probes, allowing the simultaneous

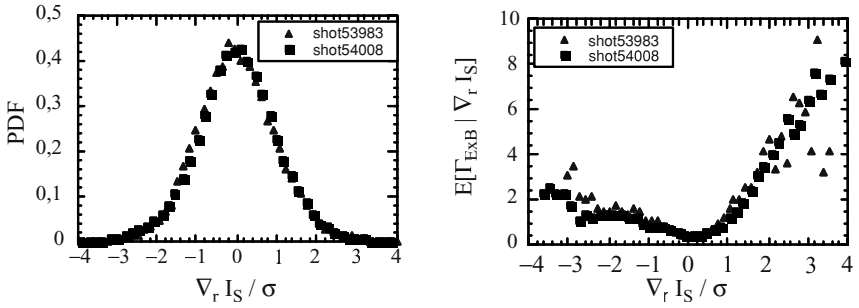


Figure 5. Radial transport versus fluctuations in gradients in the JET boundary region (Hidalgo et al. 2003a, Gonçalves et al. 2002).

investigation of the radial structure of fluctuations and electrostatic driven turbulent transport. Turbulent particle transport ($\Gamma_{E\times B}$) has been calculated from the correlation between poloidal electric fields and density fluctuations. Fluctuations in the radial gradients have been computed from the ion saturation current fluctuations (∇_r I_s) simultaneously measured at two different plasma locations radially separated 0.5 cm. Parallel flows have been investigated by means of Mach probes (Hidalgo et al. 2003b).

Figure 5 shows the probability density function (PDF) for fluctuations in gradients, and the expected value of the E × B flux for a given density gradient ($E[\Gamma_{E\times B} \mid \nabla_r I_S]$) in the plasma boundary region of the Joint European Torus (JET) tokamak. The results show that most of the time the plasma is at its average gradient and the size of transport events has minimum amplitude ($\Gamma_{E\times B}/\langle\Gamma_{E\times B}\rangle \approx 0.5$). Large amplitude transport events ($\Gamma_{E\times B}/\langle\Gamma_{E\times B}\rangle \approx 3-8$) take place when the plasma displaces from the most probable gradient average value. The expected value of E × B turbulent transport events increases strongly as the gradient increases above its most probable value.

The present experimental results show that the bursty and strongly non-gaussian behavior of turbulent transport is strongly coupled with fluctuations in gradients (Hidalgo et al. 2003a, Gonçalves et al. 2002). As the density gradient increases above the most probable gradient the E × B turbulent driven transport increases and the system perform a relaxation which tends to drive the plasma back to the marginal stable situation which minimized the size of transport events.

Figure 6 shows the expected value of the effective radial velocity of fluctuations for a given density gradient ($E[v_{eff} \mid \nabla_r I_S]$). The radial velocity is close to 20 m/s for small deviations from the averaged gradient but increases up to 500 m/s for large transport events implying a strong deviation from the most probable radial gradient. Experimental evidence of intermittent events

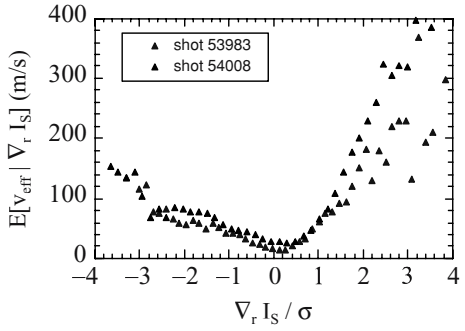


Figure 6. Radial velocity versus fluctuations in gradients.

propagating radially with velocities in the range of 1000 m/s has been previously reported (Boedo et al. 2001, Antar et al. 2001, Heller et al. 1999).

Edge localized modes (ELMs) are repetitive fluctuation activity which appears, in addition to residual small-scale turbulence, near the edge plasma in improved confinement regimes in magnetically confined plasmas (see Figure 7).

This instabilities affect both energy and particle confinement decreasing the plasma energy and particle content. Therefore, they can provide particle control in improved confinement regimes. In determining the ELM energy and particle losses it is important to clarify the possible link between the amplitude and the radial propagation of ELMs. This effect might have an important consequence in the extrapolation of the impact of ELM in the divertor plates on future devices. The investigation of the radial propagation of Edge Localized Modes (ELMs) in tokamaks also suggest a link between the radial velocity and the size of transport events (Figure 8) (Gonçalves et al. 2003a).

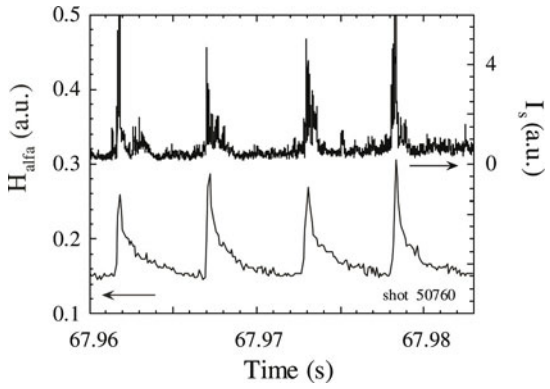


Figure 7. Edge localized instabilities (ELMs) in the plasma boundary of the JET tokamak.

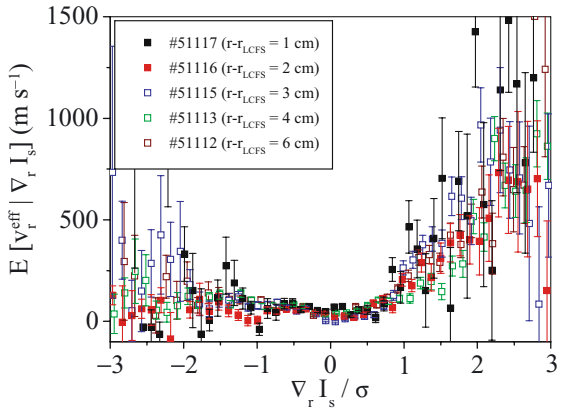


Figure 8. Expected value of the radial effective velocity for a given density gradient at different radial locations in the plasma boundary region region in the JET tokamak. The maximum effective velocity seems to be independent of the distance to the LCFS, suggesting a ballistic rather than diffusive propagation mechanism in the SOL region (Gonçalves et al. 2003a).

Recent experiments have shown that the dynamical relation between fluctuations in gradients and transport is strongly affected by the presence of sheared flows, heating power and the proximity to instability thresholds: the size of large transport events decreases in the proximity of sheared flows and increases with heating power and in the proximity of instability thresholds (Figure 9) (Gonçalves et al. 2003b).

The mechanisms underlying the generation of parallel plasma flows play a crucial role to understand transport in magnetically confined plasmas. In the plasma boundary region flows along the field line are a key element to understand impurity transport and plasma recycling (Stangeby 2000). Furthermore, plasma flows are an important ingredient to access to improved confinement regimes, both in edge and core plasma transport barriers. Simulations of plasma flows have been previously investigated including the effects of different drifts. In general, calculated parallel flow profiles can qualitatively reproduce the radial shape of the experimentally measured radial profile of parallel flows. However, the amplitude of measured parallel flow (Erents et al. 2000) is significantly larger than those resulting from simulations (Rozhansky et al. 2001).

These findings might suggest that there is a missing ingredient (e.g. turbulent driven flows) in previous simulations to explain the generation of parallel flows in the plasma boundary region.

The study of the dynamical coupling between turbulent transport and parallel flows has shown that there is a dynamical relationship between radial transport and parallel flows (Fig. 10) (Hidalgo et al. 2003b). As the size of transport

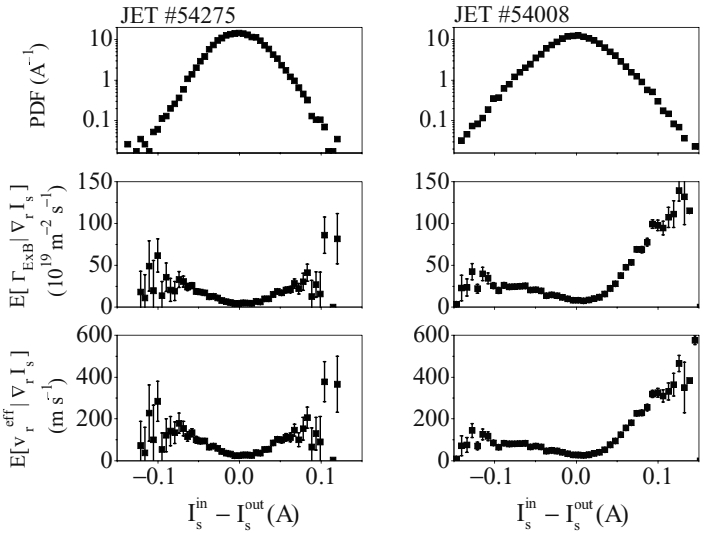


Figure 9. Probability density function of gradients, transport and radial effective velocity in ohmic (shot 54275) and L-mode plasmas (shot 54008) in the plasma boundary region. As heating power increases (L mode) the size of transport events and radial velocities increases (Gonçalves et al. 2003b).

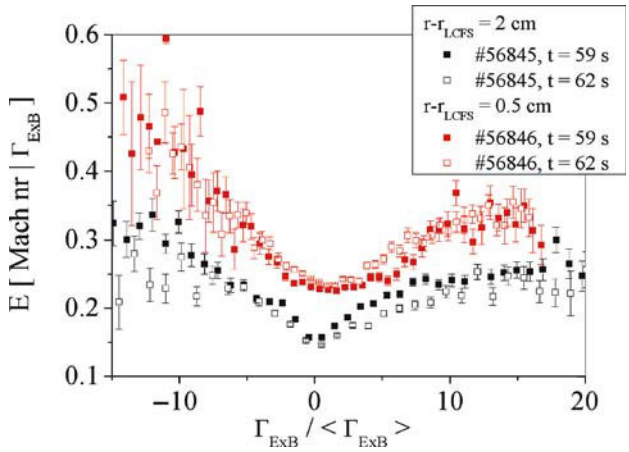


Figure 10. Expected value of the parallel flow versus the local turbulent transport in the plasma boundary region of the Joint European Torus (JET) (Hidalgo et al. 2003b).

events increases parallel flows also increase. These results show that turbulent transport can drive parallel flows in the plasma boundary of fusion plasmas. This new type of measurement is an important element to unravel the overall picture connecting radial transport and flows in fusion plasmas. However, it

remains as an open question to identify the mechanisms providing the coupling between radial transport and parallel flows. In this context it must be noted that the observed connection between turbulent transport and parallel flows does not necessarily imply a causal and direct link between them. Actually, parallel flows can be directly coupled to transport via Reynolds stresses, which provide a (non-local) energy transfer between high and low wave-numbers (Hidalgo et al. 2003b).

4. On the Physics of Flows and Turbulence

The structure of plasma profiles in the proximity of the last closed flux surface (LCFS) has been investigated in tokamak, stellarators and reversed-field pinches by using Langmuir probes (Hidalgo et al. 1991, Ritz et al. 1990, Antoni et al. 1998, Tynan et al. 1994). Typically, the ion saturation current increases and the floating potential becomes more negative when the probe is inserted into the plasma edge. From the wave number and frequency spectra S(k,ω), computed from the two points correlation technique (Ritz et al. 1984), we define the poloidal phase velocity of fluctuations as,

$$V_{\text{phase}} = \Sigma S(k, \omega)(w/k)/\Sigma S(k, \omega)$$

A reversal in the phase poloidal velocity of fluctuations (shear layer) and parallel flows has been observed in the proximity of the last closed flux surface (usually $\pm$ 1–2 cm) in magnetic fusion devices (Figure 11). The shear layer location provides a convenient reference point for the characterization of the structure of fluctuations. The maximum in the fluctuation flux appears to be linked to the location of the velocity shear layer (which acts as an effective confinement radius).

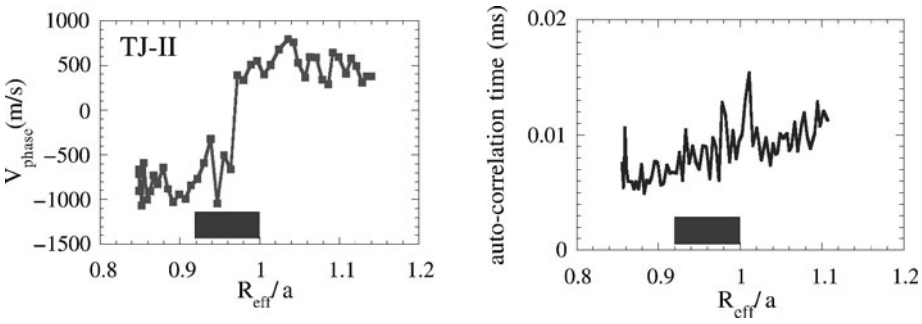


Figure 11. Radial gradient of the phase velocity of fluctuations and auto-correlation times in the plasma edge of the TJ-II stellarator. The shaded area indicates the location of the velocity shear layer.

Experiments carried out in magnetically confined plasmas show that the resulting radial gradient dv_{phase}/dr is in the range of 10^5 s^{-1}, that turns out to be comparable to the inverse of the correlation time of fluctuations, in the range of 10 μs (Fig. 11). This result suggests that E × B flows and fluctuations organized themselves closed to marginal stability (i.e. the shearing rate is close to the critical value to modify plasma turbulence). This result implies that there is not a continuous increase of the E × B flow shear when approaching the critical power threshold for the transition from low confinement to improved confinement regimes. On the contrary, sheared flows with decorrelation rates close to the critical value to reduce turbulence are already developed well below the transition to improved confinement regimes.

Understanding the mechanisms which drive E × B sheared flows is a key issue to control turbulent transport in fusion plasmas. From the radial force balance it follows that the radial electric field can be generated via poloidal and toroidal flows and by pressure gradients. Concerning the physics of poloidal flows several driving mechanisms have been proposed (Carreras 1997): ion temperature gradients, Stringer spin-up, ion orbit losses and Reynolds stress. From this perspective, an open question is the following: which mechanism allows fluctuations and poloidal flows organize themselves to be close to marginal stability? Recent numerical simulations have shown that turbulent driven fluctuating radial electric field (via Reynolds stress) has the property to get $\omega_{E\times B}$ critical (García et al. 2001) (i.e. $\omega_{E\times B} \approx \Delta\omega_T$) and experiments indicate that this mechanism can play an important role to create sheared poloidal flow in the edge region of tokamak plasmas (Xu et al. 2000). It is easy to understand why Reynolds stress driven flows allows poloidal flows and fluctuations to reach the condition $\omega_{E\times B} \approx \Delta\omega_T$. The Reynolds stress measures the degree of anisotropy in the radial-poloidal structure of fluctuations (e.g. $\langle \tilde{v}_\theta \, \tilde{v}_r \rangle$) allowing turbulence to rearrange the profile of poloidal momentum, generating sheared poloidal flows. In the plasma boundary region, strong gradients in the level of fluctuations can provide a modification in the degree of anisotropy in the radial-poloidal structure of fluctuations. Once turbulent driven sheared flows reach the critical value to modify fluctuations a negative feedback mechanism will be established which will keep the plasma near the condition $\omega_{E\times B}$ critical.

From this perspective it is crucial to investigate the energy transfer between flows and turbulence in fusion plasmas (Pope 2000). This is directly related with the momentum flux (e.g. $\langle \tilde{v}_\theta \, \tilde{v}_r \rangle$) and the radial gradient in the DC flow (dv_θ/dr) and it is given by,

$$\textit{Energy transfer}_{\text{DC flows} - \text{turbulence}} = -\langle \tilde{v}_\theta \tilde{v}_r \rangle \frac{dV_\theta}{dr}$$

The energy transfer can be either positive or negative (i.e. energy can be transferred from the mean flow to the turbulence, implying a damping of mean

flows, or energy can be transferred from turbulence to the mean flow, implying an acceleration driven by turbulence). It remains as a challenge for experimentalists to quantify the Probability Density function of the energy transfer between flows and turbulence.

The stabilizing effect of sheared flows on plasma turbulence has opened a new era on nuclear fusion research. The best fusion performance in the existing fusion devices has been obtained in plasma conditions where turbulent transport reduction by shear decorrelation is taking place. For the first time, it has been possible to reduce the rate of ion thermal transport to the minimum level set by particle collisions (neoclassical transport) over the whole plasma. These results represent a revolutionary step forward in the control of plasma turbulence and transport.

5. Conclusions

A new approach, based on multi-field statistical approach to describe transport in non-equilibrium systems, has been proposed to unravel the overall picture connecting transport, gradients and flows in fusion plasmas. It emphasizes the importance of the statistical description of transport processes in fusion plasmas as an alternative approach to the traditional way to characterize transport based on the computation of effective transport coefficients.

Based on this approach, significant improvement in our understanding of the statistical properties of fluctuations, the physics of $E \times B$ sheared flows, have been recently achieved in fusion plasmas. The main conclusions can be summarized as follows:

a) An empirical similarity in the non-gaussian probability distribution function (PDFs) of turbulent transport has been observed in the plasma edge region in fusion plasmas.

b) The investigation of the dynamical interplay between fluctuations in gradients and turbulent transport has shown that their PDFs are strongly coupled. The bursty behavior of turbulent transport is linked with a departure from the most probable radial gradient. Furthermore the radial velocity of transport events is liked with their amplitude.

c) Sheared poloidal flows and fluctuations organize themselves near marginal stability, having a direct impact on the dynamical coupling between gradients and transport. A characterization of the energy transfer between turbulence and DC flows in terms of probability distribution functions is clearly needed.

d) The bursty and strongly non-gaussian behavior of turbulent transport is coupled with fluctuations in parallel flows. This dynamical coupling

reflects that parallel flows are, at least partially, driven by turbulence mechanisms. Then, turbulent transport is an important ingredient to explain the generation of parallel flows in the plasma boundary region in fusion plasmas.

Looking into future developments a systematic comparison of multi-field joint probability functions of radial transport, flows and free energy sources from non-linear simulations and experimental results is needed. The understanding and development of methods for controlling plasma turbulence have opened a new path in plasma physics research and contributed to design of a nuclear fusion plant.

References

Antar, G.Y. et al., Phys. Rev. Lett. 87 (2001) 065001.
Antoni, V. et al., Phys. Rev. Lett. 80 (1998) 4185.
Boedo, J.A., et al., Phys. of Plasmas 8 (2001) 4826.
Carreras, B.A., IEEE Transactions on Plasma Science 25 (1997) 1281.
Castellano, J., Jiménez, J.A., Hidalgo, C., et al., Phys. of Plasmas 9 (2002) 1300.
Endler, M., Niedermeyer, H., Giannone, L., et al., Nuclear Fusion 35 (1995) 1307.
Erents, S.K., Chankin, A.V., Matthews, G.F., Stangeby, P.C., Plasma Phys. Control. Fusion 42 (2000) 905.
Frette, V., Christensen, K., Malthe-Sorensen, A., Feder, J., et al., Nature 379 (1996) 49.
García, L., Carreras, B.A., Lynch, V.E., et al., Phys. Plasmas 8 (2001) 4111.
García-Cortés, I., et al., J. Nuclear Materials 290 (2001) 604.
Gonçalves, B., Hidalgo, C., Pedrosa, M.A., et al., Nuclear Fusion 42 (2002) 1205.
Gonçalves, B., Hidalgo, C., et al., Plasma Phys. Control. Fusion, 45 (2003a) 1627.
Gonçalves, B., Hidalgo, C., et al., Czech. J. Phys. (2003b) (in press).
Hahm, T.S., Beer, M.A., Lin, Z., et al., Phys. of Plasmas 6 (1999) 922.
Heller, M.V.A. et al., Phys. of Plasmas 6 (1999) 846.
Hidalgo, C., Plasma Phys. Control Fusion 37 (1995) A53.
Hidalgo, C., Harris, J.H., Uckan, T., et al., Nuclear Fusion 8 (1991) 1471.
Hidalgo, C., Gonçalves, B., Pedrosa, M.A., et al., Plasma Phys. and Control. Fusion 44, 1557 (2002).
Hidalgo, C., Gonçalves, B., Pedrosa, M.A., et al., J. Nuclear Materials 313 (2003a) 863.
Hidalgo, C., Gonçalves, B., Silva, C., et al., Phys. Review Letters 91 (2003b) 065001.

Huld, T., Nielsen, A.H., Pécseli, H.L., Rasmussen, J.J., Phys. Fluids B 3 (1991) 1609.
Itoh, K., Itoh, S.I., Fukuyama, A., "Transport and Structural Formation in Plasmas", Plasma Physics Series, Institute of Physics Publishing (Bristol, 1999).
Labombard, B., Phys. of Plasmas 9 (2002) 1300.
Martines, E. et al., Nuclear Fusion 39 (1999) 581.
Pedrosa, M.A., Hidalgo, C., Carreras, B.A., et al., Phys. Rev. Letters 82 (1999) 3621.
Pope, S.B., "Turbulent flows", Cambridge University press (2000).
Ritz, P., Bengtson, R.D., Levinson, S.J., et al., Phys. Fluids 27 (1984) 2956.
Ritz, P., Powers, E.J., Rhodes, T.L., et al., Rev. Sci. Instrum 59 (1988) 1739.
Ritz, P., Lin, H., Rhodes, T.L., Wootton, A., Phys. Rev. Lett 65 (1990) 2543.
Rozhansky, V.A., Voskoboynikov, S.P., Kaveeva, E.G., Coster, D.P., Schneider, R., Nuclear Fusion 41 (2001) 387.
Scott, S.D., Diamond, P.H., Fonck, R.J., et al., Phys. Rev. Letters 64 (1990) 531.
Stangeby, P., "The plasma Bounadry of Magnetic Fusion Devices", IOP, Bristol (2000).
Terry, P.W., Review of Modern Physics, 72 (2000) 109.
Tynan, G.R., Schmitz, L., Blush, L., et al., Phys. Plasmas 1 (1994) 3301.
Wesson, J., "Tokamaks", Oxford University Press, Oxford 1997.
Xu, Y.H., Yu, X., Luo, J.R., et al., Phys. Rev. Lett. 84 (2000) 3867.

Chapter 13

PHASE TRANSITION IN DUSTY PLASMAS

Gurudas Ganguli, Glenn Joyce, and Martin Lampe
Plasma Physics Division, Naval Research Laboratory, Washington, DC 20375-5346

Abstract: We discuss the microphysical processes that trigger phase transitions in a dusty plasma not in thermodynamic equilibrium and subject to ion streaming. For pressures below the critical pressure P_c for condensation, the grains acquire a large random kinetic energy and form a weakly coupled fluid. If pressure is increased to greater than P_c, the grains lose their kinetic energy and reach a strongly coupled crystalline state. The dust heating in the fluid phase is due to an ion-dust two-stream instability, which is stabilized at $P > P_c$ by the combined effect of ion-neutral and dust-neutral collisions. When the pressure is decreased from the crystalline state to below the critical pressure P_m for melting, transverse phonons are destabilized by ion streaming, which destroys the short range ordering of the dust grains and triggers melting. It is found that $P_m < P_c$. For $P_m < P < P_c$ mixed phase states can exist. Although the system is not in thermodynamic equilibrium, the process resembles closely to a first order phase transition.

Key words: Dusty plasma, phase transition

1. Introduction

Solid particulates or "dust grains" immersed in plasma discharges acquire a large negative charge and settle into a dust cloud at the edge of the sheath, where they are levitated by the sheath electric field. In this region, the plasma ions stream toward the electrode at a velocity u_i of order of the ion sound speed $c_s = (T_e/m_i)^{1/2}$, where T_e is the electron temperature and m_i is the ion mass. For any fixed set of plasma parameters, the dust reaches a steady state that may resemble a solid, liquid or gas. However, it must be kept in mind that the state is not a thermodynamic equilibrium, since the dust is not an isolated system: energy and momentum are exchanged with the streaming ions, via collective modes as well as individual-particle interactions. Early on, experimentalists noticed that the background neutral gas pressure P is a key control parameter.

A.S. Sharma and P.K. Kaw (eds.), Nonequilibrium Phenomena in Plasmas, 273–290.
© 2005 *Springer. Printed in the Netherlands.*

If P is sufficiently high, the random kinetic energy of the grains is damped by gas friction, and their kinetic temperature T_d settles down to a low value that is probably comparable to the neutral gas temperature. In this regime, the interaction potential energy between grains typically far exceeds T_d, i.e. the dust is strongly coupled and self-organizes into a crystalline configuration (Melzer et al., 1996a; 1996b, 1994; Thomas et al., 1994, 1996, Chu and Lin, 1994). For lower P a very different behavior is seen: despite the dissipation of grain kinetic energy to gas friction, the dust grains reach a steady-state value of T_d which far exceeds the temperature of any other component in the plasma. The physical mechanism responsible for dust heating has only recently been understood (Joyce et al. 2001). In this low-pressure regime, T_d is so large that the dust acts like a fluid (Melzer et al., 1996a; 1996b, 1994; Thomas et al., 1994, 1996, Chu and Lin, 1994). As P is slowly varied, the dust undergoes melting/freezing transitions that display characteristics of a first order phase transition. However, in this non-equilibrium system it is the unique features of plasma instabilities that govern all of the "thermodynamics" of the dust. In this article we provide an *ab initio* model for this behavior and discuss the microphysical processes underlying the observed characteristics.

2. Dynamically Shielded Interaction and the DSD Simulation Model

A dusty plasma consists of electrons, positive ions and negatively-charged dust grains, all interacting with each other electrically and mechanically. However, it is possible to faithfully represent the system as consisting of only one type of particle, dust grains, with the ions and electrons appearing only as a dielectric medium which mediates the interaction between grains. This representation simplifies the theory enormously, and in a simulation code it completely eliminates the electron and ion time scales, which are many orders of magnitude faster than the dust time scales of interest.

The basis for this reduction is the realization that the dust grains may be strongly coupled to each other, but the electrons and ions are only weakly coupled to the grains. The typical kinetic energy of an electron is of course of order T_e. In a discharge, usually T_e is much larger than the ion temperature T_i, but nonetheless the typical ion kinetic energy is also of order T_e, since the ions are streaming at velocity of order c_s. The potential at a grain surface is of the order of $-T_e$, and falls off faster than r^{-1}. Since the grain radius a is normally much smaller than the mean spatial separation between ions or electrons, at any given time very few ions and electrons are close to a grain. Except for these few, the interaction potential energy between ions and grains, or electrons and grains, is small compared to the typical kinetic energy of an ion or electron. Thus it is quite accurate to treat the plasma by linear response theory

(Rostoker and Rosenbluth 1960, Krall and Trivelpiece 1973). Accordingly, the interaction between grain j located at $\mathbf{r}_\mathrm{j}$ and another grain located at $\mathbf{r}$ is given by the *dynamically-shielded* Coulomb potential

$$\phi(\mathrm{r}) = \int \mathrm{d}^3\mathbf{k} \sum_\mathrm{j} \mathrm{e}^{\mathrm{i}\mathbf{k}\cdot(\mathbf{r}-\mathbf{r}_\mathrm{j})}\phi_\mathrm{j}(\mathrm{k}), \tag{1a}$$

where

$$\phi_\mathrm{j}(\mathrm{k}) = \frac{-\mathrm{Z_j e}}{2\pi^2 \mathrm{k}^2 \mathrm{D}(\mathrm{k}, -\mathbf{k}\cdot\mathbf{u} + \mathrm{i}\nu_\mathrm{i})}, \tag{1b}$$

and D(k, ω) is the plasma dielectric given by

$$\mathrm{D}(\mathrm{k},\omega) = 1 + \frac{1}{\mathrm{k}^2\lambda_\mathrm{De}^2} + \frac{\omega_\mathrm{i}^2}{\mathrm{k}^2} \frac{\int \mathrm{d}^3\mathbf{v} \dfrac{\mathbf{k}\cdot\partial \mathrm{f_{i0}}(\mathbf{v})/\mathrm{d}\mathbf{v}}{\omega - \mathbf{k}\cdot\mathbf{v} + \mathrm{i}\nu_\mathrm{i}}}{1 - \mathrm{i}\nu_\mathrm{i}\int \mathrm{d}^3\mathbf{v} \dfrac{\mathrm{f_{i0}}(\mathbf{v})}{\omega - \mathbf{k}\cdot\mathbf{v} + \mathrm{i}\nu_\mathrm{i}}}. \tag{1c}$$

Here $-\mathrm{Z_j e}$ is the charge on the $\mathrm{j^{th}}$ dust grain, λ_De is the electron Debye length, $\mathrm{f_{i0}}$ is the ambient ion distribution function, ω_i is the ion plasma frequency, and ν_i is the ion-neutral collision frequency. Equations (1) represent the *complete* linear response of the plasma ions and the warm electrons, including wakefields, ion-neutral collisions, and Landau damping. Note that the electron thermal speed is invariably much higher than their streaming speed, and hence the electron contribution to the dielectric (1c) reduces to Debye shielding, as represented by the second term on the right hand side. Since the plasma response is linear, the force exerted on any particular grains by all of the other grains is given just by the linear superposition of dynamically shielded potentials of the form (1a). The representation (1) is thus a very great simplification in the theory, which is soundly based on the physics. If it is further assumed that the ion distribution function is a drifted Maxwellian,

$$f_{i0}(\mathbf{v}) = \left(\frac{m_i}{2\pi T_i}\right) \exp\left[-\frac{m_i(\mathbf{v}-\mathbf{u}_i)^2}{2T_i}\right], \tag{2a}$$

then Eq. (1c) becomes

$$D(\omega, k) = 1 + \sum_\alpha \frac{\omega_\alpha^2}{k^2 \mathrm{v}_\alpha^2} \frac{1 + \varsigma_\alpha Z(\varsigma_\alpha)}{1 + \left(\dfrac{i\nu_\alpha}{|k|\,\nu_\alpha}\right) Z(\varsigma_\alpha)}, \tag{2b}$$

where α denotes the species (electrons, ions or dust), v_α is the thermal velocity, $\mathbf{u}_\alpha$ is the streaming velocity for species α, $\varsigma_\alpha = (\omega - \mathrm{k}\cdot\mathrm{u}_\alpha + i\nu_\alpha)/|k|\nu_\alpha$, and

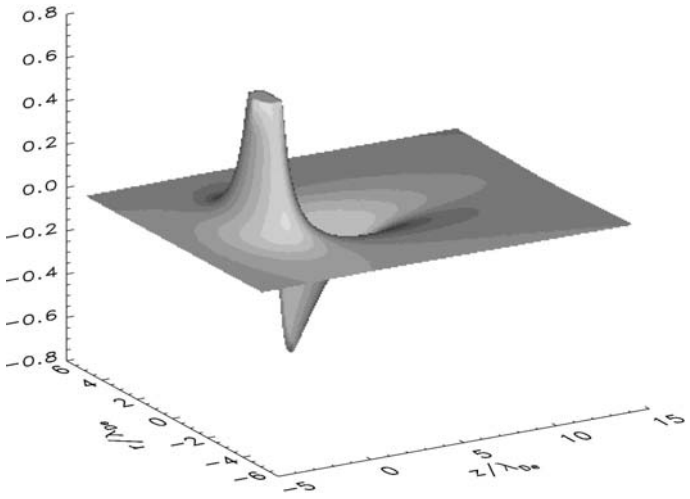


Figure 1. A three dimensional plot for the wake field potential. The dust grain is centered at the point where the potential is large and positive. The ions stream from left to right in the z direction. In the downstream direction there is a region of attractive potential.

$Z(\zeta)$ is the plasma dispersion function,

$$Z(\zeta) = \exp(-\zeta^2)\left(i\pi^{1/2} - 2\int_0^{\zeta} dt\,\exp(t^2)\right). \tag{2c}$$

The three-dimensional profile of the potential $-\phi(\mathbf{r})$ is shown in Fig. 1, where the ion streaming is along the z direction. The potential structure is seen to be rather simple and repulsive (Debye-like) upstream and sideways. But downstream of each grain the ion flow results in an elaborately structured electrostatic wakefield, which includes positively charged regions that attract other grains. This is understood to be the reason dust typically crystallizes in a simple hexagonal dust crystal structure, with the grains lined up directly behind each other along the streaming direction, but with a hexagonal lattice in the plane transverse to the streaming (Melzer et al., 1996a; 1996b, 1994; Thomas et al., 1994, 1996, Chu and Lin, 1994). Figure 2 is a plot of ϕ on axis (y = 0) as a function of z, showing the effects of ion-neutral collisions. We see that at low pressure, where ion-neutral collisions are infrequent, there are several nodes of the wakefield potential in the downstream region. As the pressure increases, ion-neutral collisions smear out these nodes, and for high pressure (typically the case in experiments) only the primary node survives. The potential structures resulting from the solutions of Eq. (1) are very similar to full

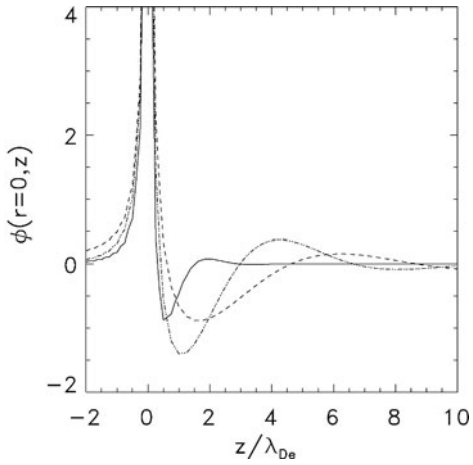


Figure 2. A y = 0 cut of the plot in Fig. 1. The dotted and dashed lines are the same plot for increasing ion-neutral collision frequency.

nonlinear solutions obtained from particle simulations (Winske and Daughton, 2000, Winske, 2001).

The theoretical picture described above has been embodied in a particle simulation code that we call the DSD (Dynamically Shielded Dust) model. The details of the simulation model were described earlier (Lampe et al., 2001, Joyce et al., 2003) and will not be repeated here. Briefly, only the dust grains appear as simulation particles. Electrons and ions are included via the dynamically-shielded Coulomb interaction Eq. (1), which represents the interaction between grains. In various versions of the code, we have used particle-in-cell (PIC) or molecular dynamics (MD) techniques, or some combination of the two, to compute the interaction force. We find that the known experimental features are generally well reproduced in the simulations, additional features are revealed, and the simulations are particularly suitable for critically examining the phenomena and developing physics-based models. The rest of this paper will be concerned with the use of simulation and theory to elucidate the physics underlying the phases and phase transitions of dust in the presence of streaming ions.

3. Fluid/Crystal Phase Transitions

In typical experiments, the dust is confined within in a disk-shaped layer above the lower electrode. The disk is very wide radially, and can reasonably be regarded as infinite in lateral extent, but in most cases it is only a few grains thick vertically. The finite thickness of the dust layer, and therefore the presence of free surfaces above and below the dust layer, significantly

complicate the determination of the dust configuration and dynamics. These effects will be discussed briefly later in the paper. However, in the present work, we simplify the situation by considering a dust cloud that is uniform and essentially unbounded in all directions. In the DSD simulation code, this situation is represented by performing the simulation within a finite rectangular volume, but using periodic boundary conditions in all directions (so that the boundaries of the simulation box have no significance), and making sure that the box is large enough so that all wavelengths of interest are resolved.

To illustrate the principal phenomena, we first show in Fig. 3 the results of a DSD simulation in a rectangular volume $9\lambda_D \times 9\lambda_D \times 9\lambda_D$ in extent, filled with 6859 dust grains, each with charge -1.65×10^4e, radius 4.5×10^{-4} cm, and mass 5.6×10^{-10} gm. The average spacing between grains is thus $0.47\lambda_D$, chosen to approximate the spacing in many typical experiments. The plasma parameters for this particular simulation are taken to be $T_e = 1.3$ eV, $T_i = 0.052$ eV, plasma density $n = 5 \times 10^8$ cm^{-3}, ion streaming velocity $u_i = c_s$ in the z-direction, and the neutral gas is taken to have zero temperature. The

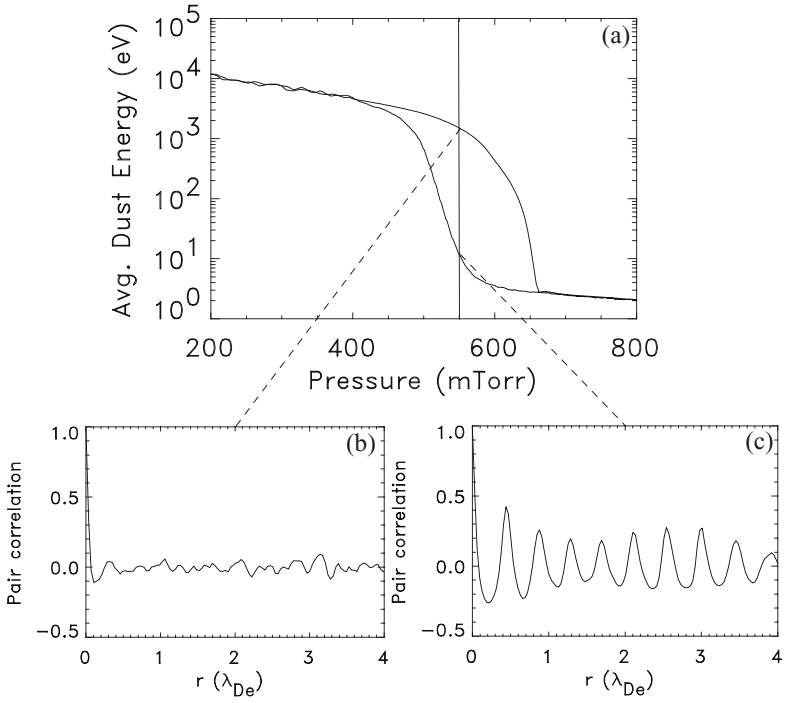


Figure 3. (a) Hystersis loop for $T_d(P)$, as seen in a DSD simulation. (b) Dust grain pair correlation function for $P = 550$ on the upper branch of the hystersis loop. (c) Pair correlation function for $P = 550$ on the lower branch of the hystersis loop.

simulation was begun with pressure P = 100 mTorr. The pressure was then slowly varied during the simulation, from 100 mTorr up to 800 mTorr, and then back down to 200 mTorr. We notice that at low pressure T_d is of order 10^4 eV, i.e. four orders of magnitude greater than T_e. T_d is also a factor of ten greater than the average grain-grain interaction potential energy, and the dust therefore acts like a gas. T_d decreases only slightly as P is increased up to 550 mTorr, but then abruptly falls three orders of magnitude as P increases from 550 mTorr to 700 mTorr. This transition coincides with the freezing of the dust into a crystalline configuration, with essentially no zero-point motion. As P is then decreased, the dust remains cold for P down to 550 mTorr. Between 550 and 500 mTorr, the temperature increases three orders of magnitude, the dust crystal melts, and the dust returns to the original gaseous state. Notice that the melting transition, as the pressure decreases, occurs at a lower pressure than the crystallization transition as the pressure increases. There is in fact an intermediate range of P where both phases are stable. Figures 3b and 3c show the grain pair correlation function, at P = 550 mTorr, as seen for the parts of the hysteresis loop corresponding to increasing and decreasing pressure. Clearly the latter corresponds to a solid phase which exhibits long range order, while the former is a disordered fluid phase. As we shall see, this hysteresis occurs because the instability which triggers melting is different from the instability which heats the dust in the fluid phase, and thereby inhibits freezing.

We shall now discuss these transition processes in more detail, as well as the underlying physical processes that are responsible for this remarkable behavior.

4. Dust Fluid State and Fluid-to-Crystal Transition (Condensation)

At low pressure the dust grains have a very high level of random kinetic energy and are not strongly correlated to each other. In other words, they behave like just another charged species within the plasma. (The reason for the high dust temperature will become apparent shortly.) Since the ions stream past the dust grains at velocity $\mathbf{u}_i$ on their way toward the electrode, a two-stream instability can occur between the ions and the dust. Treating the plasma as a three-component system, the dispersion relation for this situation is given by (Rosenberg, 1996)

$$D(\omega, k) = 0, \tag{3}$$

where D is defined in Eq. (2b). However, in situations of interest, the streaming speed u_i is of order c_s, which is much less than the electron thermal speed but much larger than the ion or dust thermal speed. Thus the ions and dust may be treated as cold species, and the electrons as a very hot species. The dispersion

relation thus simplifies (Joyce et al., 2002) to

$$1 + \frac{1}{(k\lambda_{De})^2} - \frac{\omega_d^2}{\omega(\omega + iv_d)} - \frac{\omega_i^2}{(\omega - \mathbf{k}\cdot\mathbf{u})(\omega - \mathbf{k}\cdot\mathbf{u} + iv_i)} = 0, \qquad (4)$$

where ω_d is the dust plasma frequency and v_d is the dust-neutral collision frequency. The last two terms are familiar from the classical theory of the two-stream instability in collisionless plasmas. However, we also include ion-neutral and dust-neutral collisions, which appear not to have been investigated in the earlier plasma literature. (Although, Kaw and Sen (1998) used the generalized hydrodynamic framework to derive a dispersion relation and an analytical expression of the growth rate which included collisions, in the more general case where one of the components may be strongly coupled.) These collision terms are stabilizing. In addition, the electron Debye shielding term is stabilizing.

Both collision frequencies are proportional to the neutral pressure, and may be written in the form

$$v_{i,d} = K_{i,d}P. \qquad (5)$$

Usually, it is assumed that the dust collison coefficient K_d is given by the Epstein formula (Epstein 1924). For Ar, we use the ion collision coefficient $K_i = 0.21 u_i s^{-1}$ mTorr^{-1}. If k is scaled to λ_D, and ω to ω_i, it is apparent that Eq. (4) depends on three dimensionless parameters, u_i/c_s, $K_i\omega_d/K_d\omega_i$, and T_e/T_i, as well as the pressure P. For the particular case shown in Fig. 3, with $u_i/c_s = 1$ and $K_i\omega_d/K_d\omega_i = 13.2$, the instability growth rates Im $\omega(k,\theta)$ are shown in Fig. 4 for three different pressures. Here θ is the angle between $\mathbf{k}$ and $\mathbf{u}_i$. We see that at low pressure (P = 200 mTorr) the instability is strongly growing, with a broad spectrum of unstable modes. As the pressure is increased, the growth rates are reduced, as a result of the combined effects of ion-neutral and dust-neutral collisions. In addition, the unstable part of the spectrum shrinks down to a narrow band of modes that are nearly perpendicular to $\mathbf{u}_i$. This occurs because the Debye shielding term in Eq. (4) is strongly stabilizing

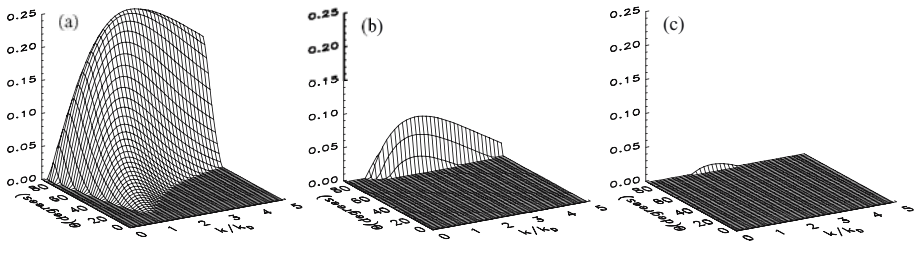


Figure 4. Normalized linear growth rates for the ion-dust two-stream instability in a fluid (Eq. (4)) plotted against normalized wave vectors for different pressures: (a) P = 200 mTorr, (b) P = 600 mTorr, and (c) P = 800 mTorr.

for modes propagating at small or moderate angle θ to $\mathbf{u}_i$. As $\theta \to \pi/2$, ion thermal effects eventually become important, and the instability becomes a dust acoustic instability, which is much weaker than a true two-stream instability. For pressures above 850 mTorr all waves are damped.

To investigate the evolution of this instability, we have performed DSD code runs at a series of fixed pressures. It may seem surprising that the instability is even present in the code, since only dust grains are represented as simulation particles. However, we (Joyce et al., 2002) have shown that the physics of the instability is fully and faithfully represented by the plasma dielectric that appears within the dynamically shielded potential Eq. (1). An interesting aspect relates to the convective nature of the instability. It is well known that the collisionless two-stream instability is an absolute instability. However, it can be shown that, with the inclusion of collisions, the instability becomes convective in the dust frame. Therefore, in thin dust layers the instability saturates due to linear wave convection. In accord with this, the extent of dust heating is found to increase with the dust cloud thickness. In an earlier paper (Joyce et al. 2002), we studied a case in which the dust layer was approximately 3 grains thick. Even in this case, there was sufficient dust heating to maintain the dust in a fluid state. However, T_d was of the order of 100 eV, as compared to 10^4 eV in the present case of an infinite homogeneous dust cloud.

To summarize, theory predicts that an ion-dust two-stream instability will occur for pressures below a critical pressure P_c, but that for pressures above P_c the instability is stabilized by the combined effects of ion-neutral and dust-neutral collisions. For the parameters used in these simulations, $P_c = 800$ mTorr. Within a transition regime at pressures slightly below P_c, (530 mTorr $<$ P $<$ 800 mTorr) instability is present but with an increasingly narrow spectrum of nearly transverse unstable modes. DSD simulations confirm that for pressures below 530 mTorr, a broad spectrum of waves is excited to large amplitude, and the dust is heated to a true temperature which far exceeds the potential energy of grain interactions. In this regime, the dust shows virtually no order and behaves like a gas. As P increases beyond 530 mTorr, the spectrum of excited waves narrows down to nearly transverse waves and T_d falls rapidly. At about 600 mTorr, the dust grains condense into strings aligned along the streaming direction. Each string is held together by the wakefield forces. However, the strings show substantial transverse motion, as well as a substantial level of transverse oscillation within each string, and there is little or no long range order governing the transverse arrangement of the strings. As P increases to about 700 mTorr, the transverse kinetic energy steadily decreases and increasingly consists of transverse sloshing motion. The strings of grains arrange themselves into a hexagonal lattice in the transverse plane. For $P > P_c$, there are no unstable modes present, the grain kinetic energy is damped by collisions with neutrals, and (with the neutral temperature taken to be zero in the sim-

ulations) T_d drops to essentially zero. Since the ion-dust streaming instability is the heat source that keeps the dust in the weakly-coupled fluid phase, its elimination is the trigger for condensation into the dust-crystal phase.

This behavior is also in at least qualitative agreement with experimental observations. However, it should be recognized that we have considered here an infinite homogeneous dust cloud, with no confining forces. In laboratory experiments, the dust is confined by weak horizontal forces, as well as much stronger vertical confining forces, and in many cases the dust cloud is only a few grains thick in the vertical direction. One feature that is almost invariably observed is that the dust crystallizes into a lattice with well-defined horizontal planes, and with the grains in adjacent planes arranged directly above each other in vertical strings. The strings are very clearly evident in the simulations, but the horizontal planes are not. However, in an earlier paper (Joyce et al., 2002) we showed simulations of vertically thin dust clouds confined by vertical forces, and these simulations did show ordering into simple hexagonal crystals with horizontal planes. The ordering into horizontal planes is in fact entirely due to the vertical confining force, which is absent in these infinite homogeneous simulations. The repulsive horizontal forces between grains actually opposes the arrangement of adjacent grains into horizontal planes, and favors a more nearly isotropic crystal structure such as close-packed hexagonal.

5. Solid-to-Fluid Transition (Melting)

5.1 Instability mechanism and analytic theory

Melzer, Piel, V. and A. Schweigert, and collaborators (Melzer et al., 1996a; 1996b, 1994, Schweigert et al., 1998), and Melandso (1997) have shown that the asymmetry of the dynamically screened Coulomb potential in the presence of flowing ions, the very same feature that is responsible for the anisotropic structure of dust crystals, also renders the resulting crystal susceptible to instabilities, and that melting of the crystal is associated with growth of the unstable modes to large amplitude. These authors construct a heuristic model in which the ion wake is represented as a single fictitious positively-charged point particle, rigidly attached behind each negative grain. The charge on the fictitious particle, and its separation from the grain, are fit to simulations of ion flow. Although this two-parameter model captures the essence of the physics, it cannot accurately represent the inter-grain potential at all vector grain separations (e.g. at large deviations from crystalline order), nor does it provide analytic scaling for the dependence of the forces on physical parameters. The correct representation of the inter-grain potential is the dynamically shielded Coulomb interaction given by Eq. (1) (Lampe et al., 2001a,b, Joyce et al., 2002, 2003, Ganguli et al., 2003, Nambu et al., 1995, Vladimirov and Ishihara, 1996). Since this formulation shows how the upstream/downstream

asymmetry of the wakefields originates in the ion streaming (as manifested within the plasma dielectric), it is clear that the instabilities of the dust crystal are in fact a form of ion-grain two-stream instability specific to the dust crystal phase.

Both longitudinal and shear modes of the crystal can be driven unstable, as well as obliquely propagating mixed modes, and indeed we believe that several types of modes are involved in the later stages of the melting process. However, both experiments and DSD simulations suggest that the mode that initiates the melting process is a shear mode with propagation vector **k** parallel to the ion streaming, i.e. a mode in which the grains oscillate horizontally, so that each horizontal plane of grains is undistorted, but each plane of grains is misaligned with respect to the adjoining planes. This particular mode suggests a simple linearized model that is easily amenable to analysis. To construct the model, we first neglect all grain-grain interactions other than nearest-neighbor interactions. Secondly, we note that for the shear mode, there is no net restoring force due to horizontal nearest neighbor interactions, since all of the grains in any horizontal plane oscillate together. Thus, we include only the force on any given grain due to the displacement of its upstream or downstream nearest neighbors. In essence this reduces the problem to the calculation of the transverse normal modes of a string of grains aligned along the streaming direction. In this simplest representation, the ideal crystal can be considered to be an ensemble of such 1D strings. Third, we consider here only an infinite, uniformly spaced string of grains, although we shall comment later on the effect of finite string length and end effects, which are actually of considerable significance.

With these assumptions, the equation of motion of a grain in the j^{th} layer is

$$m\ddot{x}_j = C^+(x_{j+1} - x_j) + C^-(x_{j-1} - x_j) - m\nu_d\dot{x} \tag{6}$$

where x_j is the displacement of the grain from its equilibrium position in the x direction (transverse to the streaming direction z),

$$C^{\pm} \equiv \left[\frac{\partial^2 Ze\phi(x, z = \mp d)}{\partial x^2}\right]_{x=0}, \tag{7}$$

$\phi(x, z)$ is the dynamically-shielded potential given by Eq. (1), and d is the separation between grain layers. For a normal mode with $x_j \sim \exp[i(jkd\text{-}\omega t)]$, Eq. (6) leads to a dispersion relation

$$\omega = -\frac{i\nu_d}{2}\left\{1 \mp \sqrt{1 - \frac{4}{m\nu_d^2}\left[(C^+ + C^-)(1 - \cos kd) - i(C^+ - C^-)\sin kd\right]}\right\}. \tag{8}$$

Equation (8) is the familiar dispersion relation for normal modes of a vibrating string of discrete grains, or transverse phonons in a crystal. However, the key

point is that in ordinary matter, $C^+ = C^-$, whereas $C^+ \neq C^-$ in the dust crystal, because of the asymmetry resulting from ion streaming. In fact, normally C^- is attractive while C^+ is repulsive. Instability occurs because $C^+ \neq C^-$. However the instability can be stabilized at high pressure due to the dust collisionality ν_d, which is visible explicitly in Eq. (8), and/or the ion collisionality ν_i, which appears as damping of the attractive wake force C^- through the dielectric D in Eq. (1c).

It should be noted that (unlike the forces between atoms in an ordinary crystal), the wakefield force downstream from a grain is quite long range compared to typical vertical spacings in dust crystals. The non-nearest-neighbor interactions have a stabilizing effect on the shear mode, and for quantitative accuracy it is usually necessary to include several vertical neighbors. The analysis can be done without the vertical nearest neighbor assumption, but it becomes rather unwieldy and will not be pursued here.

As in the gaseous-dust phase, the dispersion relation Eq. (8) can be put into a dimensionless form that depends on the neutral pressure P, in addition to three dimensionless parameters u_i/c_s, $K_i\omega_d/K_d\omega_i$, and T_e/T_i that characterize the dust size, mass, charge and mean separation; the ion species, density, temperature and streaming velocity; and the electron temperature. In Fig. 5 we plot the instability growth rate Im ω(k) from Eq. (8), for the same parameters considered in Figs. 3 and 4, and three different values of P. The vertical separation d between grains is set to $1.3\lambda_D$. The dispersion relation Eq. (8) should be accurate for this case, since the value of d is large enough to justify our neglect of next-nearest-neighbor interactions. In laboratory dust crystals that are stably confined by external confining fields d is generally smaller, typically $\sim 0.5\lambda_D$. For such cases the effects of the next nearest neighbors become important and

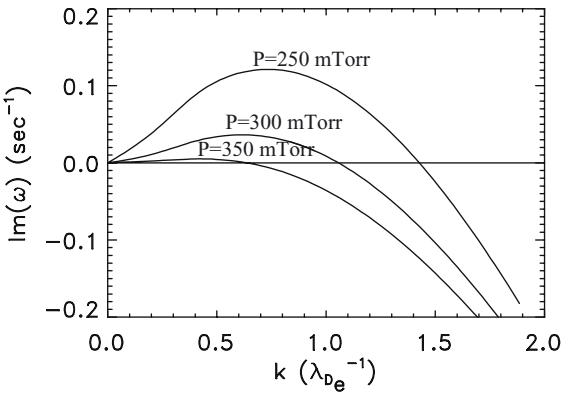


Figure 5. The growth rate of phonon instability (from Eq. (8)) due to ion streaming for different neutral pressures.

Eq. (8) must be modified for higher accuracy. Note that in both cases, the growth rate falls with increasing pressure. Similarly to the two-stream instabilities of the gaseous-dust phase shown in Fig. 4, all modes are damped when the pressure exceeds a critical pressure P_m. However, P_m is approximately 350 mTorr, which is substantially smaller than the pressure P_c for stabilization of the gaseous-dust modes. This is typical; it seems always to be true that the stabilization pressure for the crystal instabilities is less than the gas phase two-stream instabilities.

5.2 Simulations of string instabilities

We have performed DSD simulations to study the nonlinear evolution of the unstable modes, for a single infinite string of identical dust grains with no external confining forces. The simulations include the shielded interactions between all grains (not just nearest neighbors). The grains in the string are started in equilibrium with $d = 1.3\lambda_D$, vertically aligned, with no external forces. A small perturbation is then introduced, and the evolution is followed until a new steady state is reached. In Fig. 6 we plot T_d as a function of time for pressures 250, 300 and 360 mTorr. The evolution seen in Fig. 6 is in good agreement with the predictions of the linear dispersion relation shown in Fig. 5. For pressures lower than the critical pressure $P_m = 350$, T_d increases with time, indicative of the growth of unstable modes. For pressures above P_m the waves are stable and the grains freeze into their spatial locations in the stable string (shown in Fig. 7c), as the grain kinetic energy decreases steadily due to friction on the neutrals. The value of P_m qualitatively agrees with the value predicted by linear theory as shown in Fig. 5. In Fig. 7 we show the string configuration

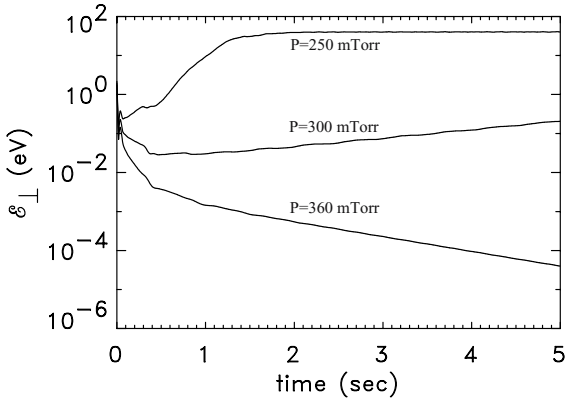


Figure 6. The mean kinetic energy of the dust grains is plotted as a function of time for three different pressure values. For pressures lower than 325 mTorr, the grains gain kinetic energy and above this pressure they loose kinetic energy due to neutral friction.

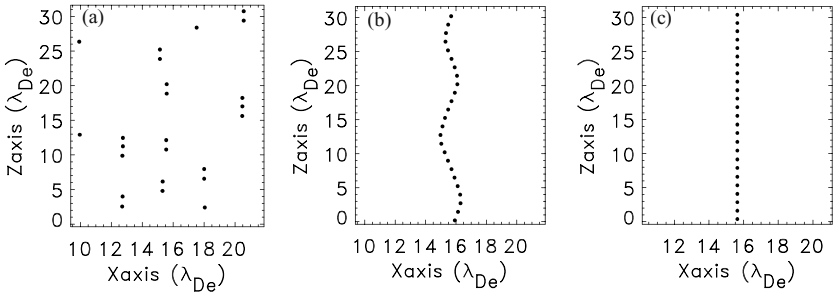


Figure 7. String configuration at saturation for (a) P = 50, (b) P = 250 and (b) 350 mTorr. The simulations show temporally growing transverse modes at all pressures below the predicted critical melting pressure, P_m.

at the end of the run, for the case shown in Fig. 6, at pressures 50, 250 and 350 mTorr. The simulations show clearly defined, temporally growing transverse modes at all pressures below the critical pressure P_m. However, the modes reach saturation without breaking up the string, if P is greater than another critical pressure P_s, whose value is 50 mTorr in this case. The saturated amplitude increases as P decreases. The saturation mechanism has not been determined definitively, but it is probably due to the anharmonic weakening of the spring constants at large perturbation amplitudes. At pressures below P_s, the wave amplitude grows to the point of destroying the string, as shown in Fig. 7a. Once an isolated string breaks up into small fragments, it cannot reassemble into a long string.

5.3 Melting of dust crystals

We now return to consideration of the infinite homogeneous dust crystal simulation, shown in Fig. 3. The parameters for this case are identical to those of the dust string simulated in Figs. 6 and 7 but the interparticle spacing is $0.47\lambda_D$. And indeed, as the pressure is decreased from 800 mTorr, the behavior of the crystal is closely related to that of the string. Above a pressure $P_m = 600$ mTorr the crystal is stable, and each grain sits in its equilibrium position with virtually no zero-point motion. As P falls below 600 mTorr, instability occurs, and the grains begin to oscillate, primarily in the horizontal plane, about their equilibrium locations. T_d increases steadily as the pressure falls. However, the dust kinetic energy at this point is mainly ordered vibrational energy, rather than true temperature. The crystal remains intact, with long-range order, until the pressure falls to $P = 500$ mTorr, at which point melting occurs, and the dust kinetic energy is truly randomized. Once the ordered crystal structure is broken up, the dust-ion system is subject to the ordinary two-stream instability, which further increases T_d. As P is decreased further, the curve of T_d vs. P retraces

the curve generated by increasing P from the gas phase. The similarities of the crystal and string melting indicate that the transverse instability in its non-linear phase leads to the break-up or melting of both the string and the crystal. However, the crystal is the more complex system, and other instability modes become increasingly important as the crystalline order is disrupted.

5.4 Vertically-confined dust crystals of finite thickness

Similarly to the two-stream instabilities of the dust gas phase, the instabilities of a dust string or a dust crystal are convective, beginning at the upper (upstream) surface of the dust region and growing to increasing amplitude with increasing distance from the edge of the dust region. This is of course of no significance for the infinite homogeneous dust crystals considered above, but it is important for crystals with only a few layers. Figure 8 shows results from a DSD simulation of an isolated, vertically-confined seven layer string, with parameters similar to those of Fig. 7, and pressure 240 mTorr, in the unstable regime. Snapshots of the grains are shown, at two times late in the evolution. Transverse oscillations are seen, with an amplitude which increases from top to bottom. The oscillations have reached a saturated state, due simply to the convective nature of the instability, and the topmost grain is nearly undisturbed. At a still lower pressure, the string is seen to break up into smaller fragments. Similarly, simulations of a full 3-D crystal of finite vertical thickness show that it is only when the instability of the lowest crystal layer reaches critical amplitude that the crystal breaks up. As a result, bounded confined crystals melt at lower pressure than infinite homogeneous crystals. In 3-D crystals, the break-up of the lower layers liberate high energy grains that also disrupt the upper layers. A quantitative treatment of the instabilities of a finite crystal is beyond the scope of the present paper, but will be considered in future work.

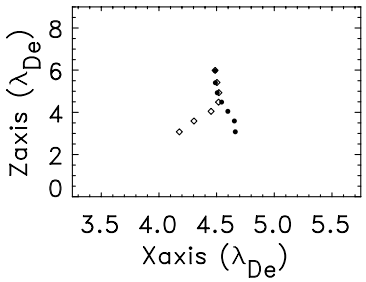


Figure 8. Transverse oscillation of an isolated vertically confined string at two times denoted by solid circles and hollow diamonds with P = 240 mTorr.

6. Discussion

We have discussed the microphysical processes underlying the non-equilibrium phase transitions between the dust-crystal and dust-fluid phases in a dusty plasma. The discussion was based on a realistic representation of the plasma-mediated interaction between grains, rather than the simple two-parameter model fit to earlier models. The fluid-to-crystal transition was modeled from first principles, without any simplifying assumptions, and was shown to be associated with the stabilization of the ion-dust two-stream instability, which maintains the fluid phase by keeping the dust heated. Since the stabilization resulted from ion and grain collisions with neutrals, stability (and therefore freezing) was shown to occur for pressures above a critical pressure P_c. In considering the crystal-to-fluid transition, we focused on the transverse shear instability of the crystal, which initiates the melting, and to simplify the analytic theory we considered only vertical nearest-neighbor interactions. These simplifications reduce the crystal instability problem to the one-dimensional problem of unstable transverse modes of a vertical string of grains, which we solved analytically within the context of linear theory, and also studied nonlinearly with DSD code simulations. The instabilities of a string were shown also to be stabilized by collisions with neutrals, and therefore to be stable above a critical pressure P_m. The onset of melting was associated with pressures below P_m. One key result is that $P_m < P_c$, and therefore the melting/freezing processes are not reversible. In the pressure range $P_m < P < P_c$, both the dust-crystal and dust-fluid phases are viable, and mixed-phase states are possible. Such states have in fact been seen in experiments, and the picture presented here is in good general agreement with the experimental evidence. However, there are many features of the dusty-plasma crystal, and the transition to and from the fluid phase, which remain to be explored. First, it should be noted that the equilibrium structure of real dust crystals is more complicated than has usually been discussed. Dust crystals have a first and a last layer, and both of these introduce free-surface effects that propagate well into the interior of the crystal. As a result, the spacing of layers in a dusty plasma crystal will not be uniform as assumed in the simple representations. It is also true that the layering of the dust grains into simple hexagonal planes results from the vertical confining forces on the dust layer, rather than from intrinsic features of the grain-grain interaction. As a result, it is to be expected that there will be many interstitial grains, and in certain situations the crystal structure will be more like the usual fcc, bcc and hcp structures seen in ordinary solids. Another area that remains to be explored is the nonlinear saturation of the ion-dust two-stream instability in the fluid-dust phase, and the consequent thermalization of the dust kinetic energy. In connection with the melting transition, much more work is needed on the chain of instabilities that complete the melting process,

and again on the nonlinear saturation and thermalization processes. We are currently exploring a number of these areas and the results will be discussed elsewhere.

Acknowledgements

The authors are happy to acknowledge stimulating discussions with A. Melzer, H. Thomas, A. Piel, G. Morfill, and G. Kalman. This work was supported by NASA and ONR.

References

Chu, J. H. and Lin I: 1994, 'Direct observation of Coulomb crystals and liquids in strongly coupled rf dusty plasmas', *Phys. Rev. Lett.* **72**, 4009.

Epstein, P.: 1924, "On the resistance experienced by spheres in their motion through gases", *Phys. Rev.* **23**, 710.

Joyce, G, Lampe, M. and Ganguli, G.: 2003, 'Particle simulation of dusty plasmas', in J. Buchner, C. T. Dum, and M. Scholer, (eds.), *Lecture Notes in Physics, #615*, Springer, pp. 125.

Ganguli, G., Joyce, G. and Lampe, M.: 2002, 'Phase transition in a dusty plasma: A microphysical description', in R. Bharuthram, M.A. Hellberg, P.K. Shukla, and F. Verheest (eds.), *Dusty Plasmas in the New Millennium*, American Institute of Physics Conference Proceedings 649, New York, pp. 157–161.

Joyce, G., Lampe, M. and Ganguli, G.: 2002, 'Instability triggered phase transition to a dusty plasma condensate', *Phys. Rev. Lett.*, **88**, 095006.

Kaw, P. and Sen, A.: 1998, 'Low frequency modes in strongly coupled dusty plasmas', *Phys. Plasmas*, **10**, 3552.

Krall, N.A. and Trivelpiece, A.W.: 1973, *Principles of Plasma Physics*, McGraw-Hill, New York, Chap. 11.

Lampe, M., Joyce, G. and Ganguli, G.: 2001, 'Particle simulation of dust structures in plasmas', *IEEE Trans. Plasma Sci.*, **29**, 238.

Lampe, M., Joyce, G. and Ganguli, G.: 2001, 'Analytical and simulation studies of dust grain interaction and structuring', *Phys. Scripta* **T89**, 106.

Melandso, F.: 1997, 'Heating and phase transitions of dust-plasma crystals in a flowing plasma', *Phys. Rev. E* 55, 7495.

Melzer, A., Schweigert, V.A., Schweigert, I.V., Homnann, A., Peters, S. and Piel, A.: 1996a, 'Structure and stability of the plasma crystal', *Phys. Rev. E* **54**, R46.

Melzer, A., Homnann, and Piel, A.: 1996b, 'Experimental investigation of the melting transition of the plasma crystal', *Phys. Rev. E* **53**, 2757.

Melzer, A., Trottenberg, T. and Piel, A.: 1994, 'Experimental determination of the charge on dust particles forming Coulomb lattice', *Phys. Lett. A* **191**, 301.

Nambu, M., Vladimirov, S.V. and Shukla, P.K.: 1995, 'Attractive forces between charged particulates in plasmas', Phys. Lett. A, **203**, 40.

Rosenberg, M, J.: 1996, 'Ion-dust streaming instability in processing plasmas', *Vac. Sci. Technol. A*, **14**, 631.

Rostoker, N. and Rosenbluth, M.N.: 1960, 'Test particles in a completely ionized plasma', *Phys. Fluids* **3**, 1.

Schweigert, V.A., Schweigert, I.V., Melzer, A., Homnann, A. and Piel, A.: 1996, 'Alignment and instability of dust crystals in plasmas', *Phys. Rev. E* 54, 4155.

Schweigert, V.A., Schweigert, I.V., Melzer, A., Homnann, A. and Piel, A.: 1998, 'Plasma crystal melting: a nonequilibrium phase transition', *Phys. Rev. Lett.* **80**, 5345.

Thomas, H., Morfill, G.E. and Demmel, V.: 1994, 'Plasma Crystal: Coulomb Crystallization in a Dusty Plasma' *Phys. Rev. Lett*. **73**, 652.

Thomas, H., and Morfill, G.E.: 1996, 'Melting dynamics of a plasma crystal', *Nature*, London, **379**, 806.

Thomas, H. and Morfill, G.E.: 1996, 'Solid/liquid/gaseous phase transitions in plasma crystals', *J. Vac. Sci. Technol. A* **14**, 501.

Vladimirov, S.V. and Ishihara, O.: 1996, 'On plasma crystal formation', *Phys Plasmas*, **3**, 444.

Winske, D, Daughton, W., Lemons, D.S. and Murillo, M.S.: 2000, 'Ion kinetic effects on the wake potential behind a dusty grain in a flowing plasma', *Phys. Plasmas,* **7**, 2320.

Winske, D.: 2001, 'Nonlinear wake potentials in a dusty plasma', *IEEE Trans. Plasma Sci. 29*,191.

Section 3

CROSS-DISCIPLINARY STUDIES

Chapter 14

PRECURSORS OF CATASTROPHIC FAILURES

Srutarshi Pradhan[1] and Bikas K. Chakrabarti[2]
Saha Institute of Nuclear Physics, 1/AF Bidhan Nagar, Kolkata 700064, India
[1]e-mail: spradhan@cmp.saha.ernet.in
[2]e-mail: bikas@cmp.saha.ernet.in

Abstract: We review here briefly the nature of precursors of global failures in three different kinds of many-body dynamical systems. First, we consider the lattice models of self-organised criticality in sandpiles and investigate numerically the effect of pulsed perturbations to the systems prior to reaching their respective critical points. We consider next, the random strength fiber bundle models, under global load sharing approximation, and derive analytically the partial failure response behavior at loading level less than its global failure or critical point. Finally, we consider the two-fractal overlap model of earthquake and analyse numerically the overlap time series data as one fractal moves over the other with uniform velocity. The precursors of global or major failure in all three cases are shown to be very well characterized and prominent.

Key words: Fracture, earthquake, avalanches in sandpile, self-organised criticallity, fiber bundle, fractals, Cantor sets

1. Introduction

A major failure of a solid or a dynamic catastrophe can often be viewed as a phase transition from an unbroken or non-chaotic phase to a broken or chaotic phase. Some obvious correlations existing in the system before the failure, are lost in the failure process. However, the equivalence can be made precise and in fact the critical behavior goes to the bone of any failure or catastrophic phenomena.

Several dynamical models of cooperative failure dynamics [1] are now well-studied and their criticality at the global failure point are well established. Here, we have reviewed some of the numerical studies of precursor behavior in

A.S. Sharma and P.K. Kaw (eds.), Nonequilibrium Phenomena in Plasmas, 293–310.
© 2005 *Springer. Printed in the Netherlands.*

two self-organising dynamical [1] models as one approaches the self-organised critical (SOC) point of the avalanches in the lattice sandpile models. The critical behavior of a random fiber bundle model [2] of failure or fracture of a solid under global load sharing is now very precisely demonstrated. The dynamics of failure also become critically slow there and all these have been demonstrated analytically. The precursors of the global failure in the fiber bundle models can therefore be discussed analytically. The resulting universality of the surface roughness in any such fracture process has also been well documented and analysed. The two-fractal overlap model [3] is a very recent modeling approach of earthquake dynamics. The time series of overlap magnitudes obtained, when one fractal slides over the other with uniform velocity, represents the model seismic activity variations. This time series analysis suggests some precursors of large events in this model.

2. Precursors in SOC Models of Sandpile

A 'pile' of dry sand is a unique example SOC system in nature. A growing sandpile gradually comes to a 'quasi-stable' state through its self-organising dynamics. This 'quasi-stable' state is called the critical state of the system as the system exhibits power law behavior there. Because of avalanches of all sizes, this critical point in the pile is also a catastrophic one. The dynamics of growing sandpiles are successfully modeled by the lattice model [4] of Bak, Tang and Wisenfeld (BTW) in 1987. A stochastic version of sand pile model has been introduced by Manna [5] which also shows SOC, although it belongs to a different universality class. Both the models have been studied extensively at their criticality. Here, we study the sub-critical behavior of both the models and look for the precursors of the critical state.

BTW model. Let us consider a square lattice of size $L \times L$. At each lattice site (i, j), there is an integer variable $h_{i,j}$ which represents the height of the sand column at that site. A unit of height (one sand grain) is added at a randomly chosen site at each time step and the system evolves in discrete time. The dynamics starts as soon as any site (i, j) has got a height equal to the threshold value ($h_{th} = 4$): the site topples, i.e., $h_{i,j}$ becomes zero there, and the heights of the four neighboring sites increase by one unit

$$h_{i,j} \to h_{i,j} - 4, h_{i\pm1,j} \to h_{i\pm1,j} + 1, h_{i,j\pm1} \to h_{i,j\pm1} + 1. \qquad (1)$$

If, due to this toppling at site (i, j), any neighboring site become unstable (its height reaches the threshold value), they in turn follow the same dynamics. The process continues till all sites become stable ($h_{i,j} < h_{th}$ for all (i, j)). When toppling occurs at the boundary of the lattice (four nearest neighbors are not available), extra heights get off the lattice and are removed from the system.

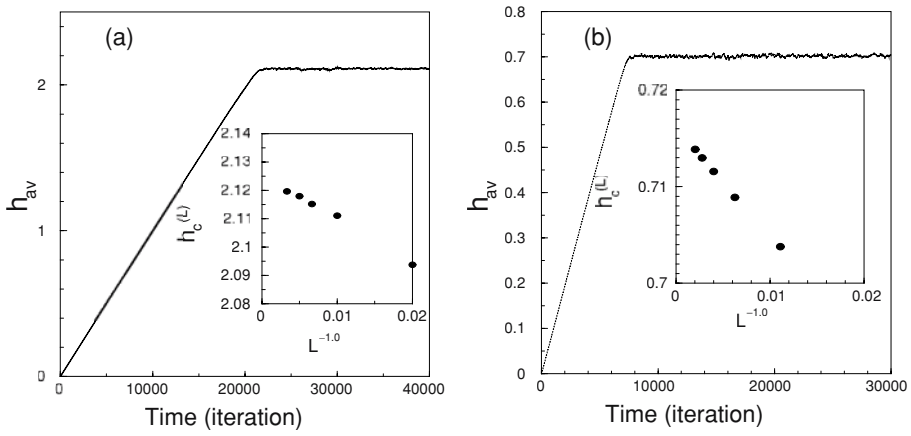


Figure 1. The growth of average height h_{av} against the number of iterations of adding unit heights (L = 100). Eventually h_{av} settles at $h_c(L)$. In the inset, we show the finite size behavior of the critical height $h_c(L)$, obtained from simulation results for different L. (a) For the BTW model; (b) for the Manna model.

With a very slow but steady rate of addition of unit height (sand grain) at random sites of the lattice, the avalanches get correlated over longer and longer ranges and the average height (h_{av}) of the system grows with time. Gradually the correlation length (ξ) becomes of the order the system size L. Here, on average, the additional height units start leaving the system as the system approaches toward a critical average height $h_c(L)$ and the average height h_{av} remains stable there (see Fig. 1(a)). Also the system becomes critical here (for $L \to \infty$) as the distributions of the avalanche sizes and the corresponding life times follow robust power laws [4].

Here, a finite size scaling fit $h_c(L) = h_c(\infty) + \mathrm{C}L^{-1/\nu}$ (obtained by setting $\xi \sim \mid h_c(L) - h_c(\infty) \mid^{-\nu} = L$), where C is a constant, with $\nu \simeq 1.0$ gives $h_c \equiv h_c(\infty) \simeq 2.124$ (see inset of Fig. 1(a)). Similar finite size scaling fit with $\nu = 1.0$ gave $h_c(\infty) \simeq 2.124$ in earlier large scale simulations [7].

Manna model. BTW model is a deterministic one. Manna proposed the stochastic sand-pile model [5] by introducing randomness in the dynamics of sandpile growth. Here, the critical height is 2. Therefore at each toppling the rejected two grains choose their host among the four available neighbors randomly with equal probability. After constant adding of sand grains, the system ultimately settles at a critical state.

We consider now the Manna model on a square lattice of size $L \times L$, where the sites can be either empty or occupied with unit height i.e., the height variables can have binary states $h_{i,j} = 1$ or $h_{i,j} = 0$. A site is chosen randomly and

one height is added at that site. If the site is initially empty, it gets occupied:

$$h_{i,j} \rightarrow h_{i,j} + 1, \tag{2}$$

If the chosen site is previously occupied then a toppling or 'hard core interaction' rejects both the heights from that site:

$$h_{i,j} \rightarrow h_{i,j} - 2, \tag{3}$$

and each of these two rejected heights stochastically chooses its host among the 4 neighbors of the toppled site. The toppling can happen in chains if any chosen neighbor was previously occupied and thus cascades are created. After the system attains stable state (dynamics stopped), a new site is chosen randomly and unit height is added to it. Thus the system evolves in discrete time steps. Here again the boundary is assumed to be completely absorbing so that heights can leave the system due to the toppling at the boundary.

With a slow rate of addition of heights (sand grains) at random sites, initially the average height of the system grows with time and soon the system approaches toward a critical average height h_c (see Fig. 1(b)). Here also the critical average height h_c has a finite size dependence and a similar finite size scaling fit $h_c(L) = h_c(\infty) + CL^{-1/\nu}$ gives $\nu \simeq 1.0$ and $h_c \equiv h_c(\infty) \simeq 0.716$ (see inset of Fig. 1(b)). This is close to an earlier estimate $h_c \simeq 0.71695$ [7], made in a somewhat different version of the model. The avalanche size distribution has got power laws similar to the BTW model, at this self-organised critical state at $h_{av} = h_c$. However the exponents seem to be different [5] for this stochastic model, compared to those of BTW model.

Precursors of the SOC point

In the BTW model. At an average height h_{av} ($<h_c(L)$), when all sites of the system have become stable (dynamics have stopped), a fixed number of height units $h_p = 4$ (pulse of sand grains) is added at any central point of the system. Just after this addition, the local dynamics starts and it takes a finite time or iterations (τ) to return back to the stable state ($h_{i,j} < 4$ for all (i, j)) after several toppling events Δ; and the disturbance spreads over a length ξ, the correlation length of the system [6,7]. All these three parameters are seen [7] to diverge as h_{av} approaches the critical height h_c from below following power laws $\tau \sim (h_c - h_{av})^{-\gamma}$, where $\gamma \cong 1.2$; $\Delta \sim (h_c - h_{av})^{-\delta}$, where $\delta \cong 2.0$; $\xi \sim (h_c - h_{av})^{-\nu}$, where $\nu \cong 1.0$ (see Fig. 2).

In the Manna model. The precursor parameters in Manna model have been measured using similar method as in BTW model. Here the pulse of height is $h_p = 2$ and is added to any arbitrary central site. We get [7] exactly similar

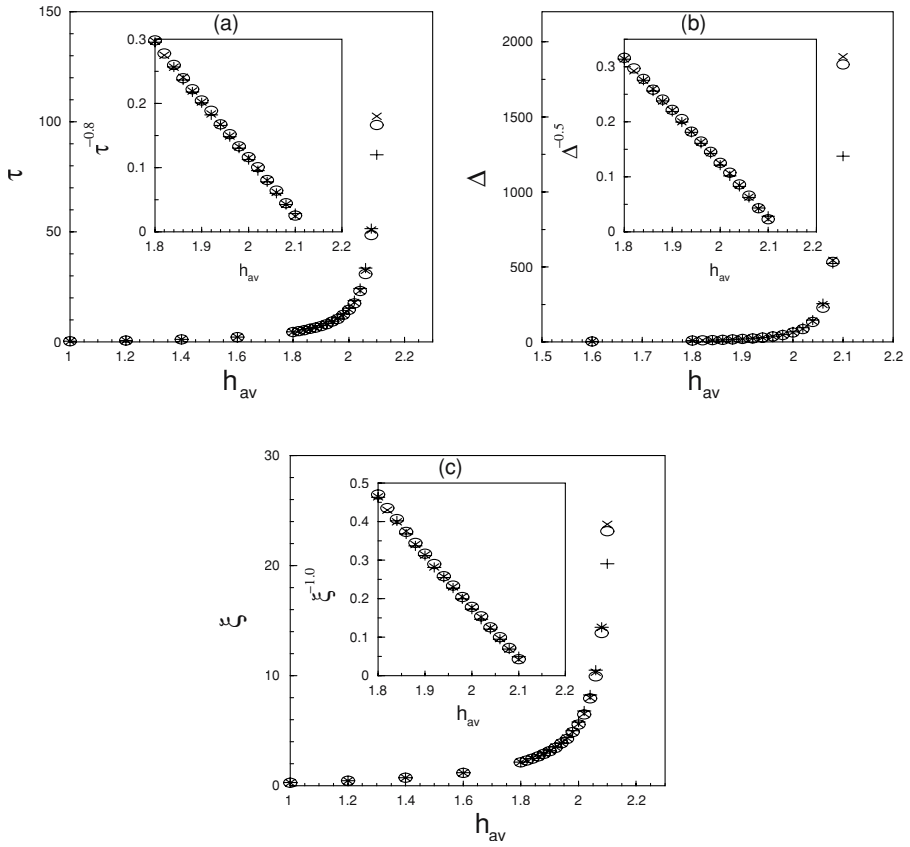


Figure 2. The variations of the precursors with h_{av} ($<h_c(L)$) in the BTW model for different system sizes: $L = 100$ (plus) $L = 200$ (cross) and $L = 300$ (open circle). (a) For relaxation time τ; in the inset $\tau^{-0.8}$ is plotted against h_{av}. (b) For the total number of topplings Δ; inset shows $\Delta^{-0.5}$ versus h_{av} plot. (c) For the correlation length ξ; in the inset, $\xi^{-1.0}$ is plotted against h_{av}.

power law behaviors for all the parameters as the critical point is approached from below: $\tau \sim (h_c - h_{av})^{-\gamma}$, where $\gamma \cong 1.2$; $\Delta \sim (h_c - h_{av})^{-\delta}$, where $\delta \cong 2.0$; $\xi \sim (h_c - h_{av})^{-\nu}$, where $\nu \cong 1.0$ (see Fig. 3).

The Monte Carlo studies showed that these response parameters like the relaxation time τ, size of the damage Δ and its radial size ξ, all tend to diverge, following the above mentioned robust power laws, in both the models. Precise knowledge of these power laws can therefore help estimating the critical or catastrophic point (h_c) by extrapolating the inverse power of these quantities for informations at h_{av} ($<h_c$) (see insets of Figs. 2 and 3). Similar critical slowing down phenomena should be of interest in the context of magnetohydrodynamics of plasma [8].

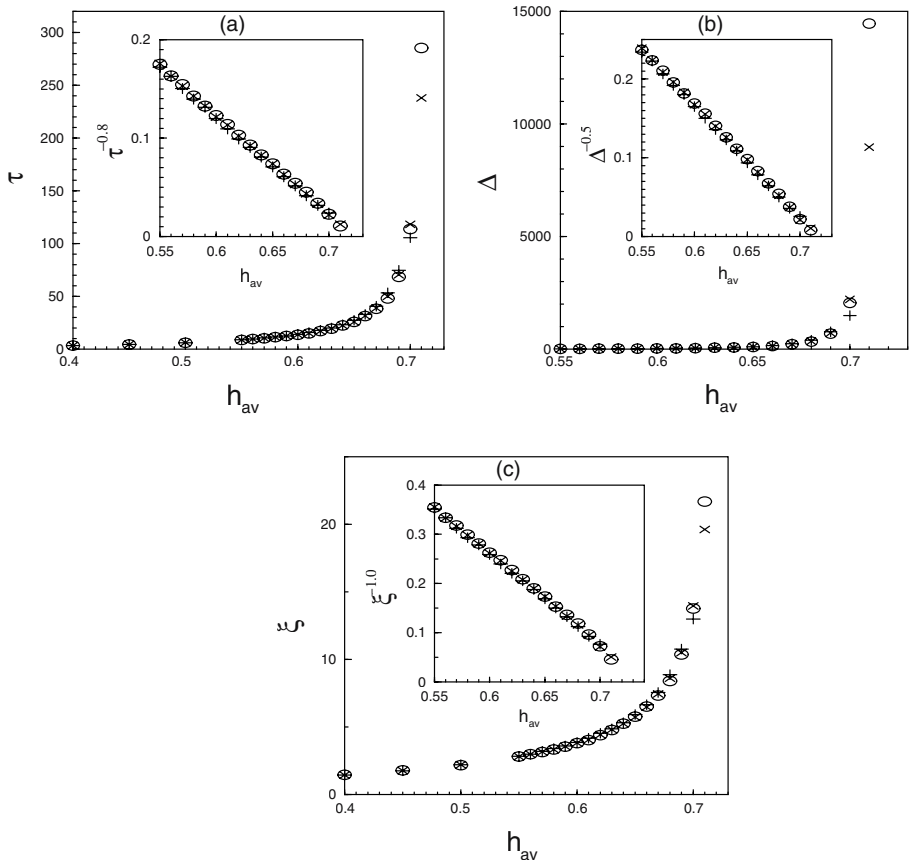


Figure 3. The variations of the precursors with h_{av} ($<h_c(L)$) in the Manna model for different system sizes: $L = 100$ (plus) $L = 200$ (cross) and $L = 300$ (open circle). (a) For relaxation time τ; in the inset $\tau^{-0.8}$ is plotted against h_{av}. (b) For the total number of topplings Δ; inset shows $\Delta^{-0.5}$ versus h_{av} plot. (c) For the correlation length ξ; in the inset, $\xi^{-1.0}$ is plotted against h_{av}.

3. Precursors of Fracture-Failure in Fiber Bundles

The fiber bundle model was introduced by Peirce [2] in the context of testing the strength of cotton yarns. Fiber bundles are of two classes with respect to the time dependence of fiber strength: The 'static' bundles contain fibers whose strengths are independent of time, where as the 'dynamic' bundles are assumed to have time dependent elements to capture the creep rupture and fatigue behaviors. According to the load sharing rule, fiber bundles are being classified into two groups: Global load-sharing (democratic) bundles and local load-sharing bundles. In democratic bundles intact fibers bear the applied load

equally and in local load-sharing bundles the terminal load of the failed fiber is given equally to all the intact neighbors. With steadily increasing load, the fiber bundles approach their respective failure point obeying a dynamics determined by the load sharing rule. The phase transition [9] and dynamic critical behavior of the fracture process in such democratic bundles has been established through recursive formulation [2, 9] of the failure dynamics. The exact solutions of the recursion relations in the global load-sharing case suggest universal values of the exponents involved.

We discuss here the failure of a static fiber bundles under global load sharing (democratic bundles) with steadily increasing load on the bundles. We show analytically the variation of associated precursor parameters with the applied stress which help to estimate the failure point accurately.

The model assumes equal load sharing, i.e., the intact fibers share the applied load equally. The strength of each of the fibers in the bundle is determined by the stress value (σ_{th}) it can bear, and beyond which it fails. The strength of the fibers are taken from a randomly distributed normalised density $\rho(\sigma_{th})$ within the interval 0 and 1 such that

$$\int_0^1 \rho(\sigma_{th}) d\sigma_{th} = 1. \tag{4}$$

The global load sharing assumption neglects 'local' fluctuations in stress (and its redistribution) and renders the model as a mean-field one.

Breaking dynamics of the democratic bundles. The breaking dynamics starts when an initial stress σ (load per fiber) is applied on the bundle. The fibers having strength less than σ fail instantly. Due to this rupture, total number of intact fibers decreases and now these intact fibers have to bear the applied load on the bundle. Hence effective stress on the fibers increases and this compels some more fibers to break. These two sequential operations, the stress redistribution and further breaking of fibers continue till an equilibrium is reached, where either the surviving fibers are strong enough to bear the applied load on the bundle or all fibers fail.

This breaking dynamics can be represented by recursion relations in discrete time steps. Let U_t be the fraction of fibers in the initial bundle that survive after time step t, where time step indicates the number of (elemental) stress redistributions. Then the redistributed load per fiber after t time step becomes

$$\sigma_t = \frac{\sigma}{U_t}; \tag{5}$$

and after $t + 1$ time steps the surviving fraction of fiber is

$$U_{t+1} = 1 - P(\sigma_t); \tag{6}$$

where $P(\sigma_t)$ is the cumulative probability of corresponding density distribution $\rho(\sigma_{th})$:

$$P(\sigma_t) = \int_0^{\sigma_t} \rho(\sigma_{th}) d\sigma_{th}. \tag{7}$$

Using now Eqns. (1.5) and (1.6) we can write the recursion relations which show how σ_t and U_t evolve in discrete time:

$$\sigma_{t+1} = \frac{\sigma}{1 - P(\sigma_t)}; \sigma_0 = \sigma \tag{8}$$

and

$$U_{t+1} = 1 - P(\sigma/U_t); U_0 = 1. \tag{9}$$

The recursion relations (1.5) and (1.6) represent the basic dynamics of failure in global load sharing models. At the equilibrium or steady state $U_{t+1} = U_t \equiv U^*$ and $\sigma_{t+1} = \sigma_t \equiv \sigma^*$. This corresponds to a fixed point of the recursive dynamics. Eqn. (1.6) can be solved at the fixed point for some particular distribution of $\rho(\sigma_{th})$ and these solutions near U^* (or σ^*) give the detail features of the failure dynamics of the bundle.

Precursors of global failure

For uniform distribution of fiber strength. We choose first the uniform density of fiber strength distribution to solve the recursive failure dynamics of democratic bundle. Here, the cumulative probability becomes

$$P(\sigma_t) = \int_0^{\sigma_t} \rho(\sigma_{th}) d\sigma_{th} = \int_0^{\sigma_t} d\sigma_{th} = \sigma_t. \tag{10}$$

Therefore U_t follows a simple recursion relation (following Eqn. (1.6))

$$U_{t+1} = 1 - \frac{\sigma}{U_t}. \tag{11}$$

At the equilibrium state ($U_{t+1} = U_t = U^*$), the above relation takes a quadratic form of U^*:

$$U^{*^2} - U^* + \sigma = 0. \tag{12}$$

The solution is

$$U^*(\sigma) = \frac{1}{2} \pm (\sigma_c - \sigma)^{1/2}; \sigma_c = \frac{1}{4}. \tag{13}$$

Here σ_c is the critical value of the initial applied stress beyond which the bundle fails completely. The solution with (+) sign is the stable one, whereas the one with (−) sign gives unstable solution. The quantity $U^*(\sigma)$ must be real valued

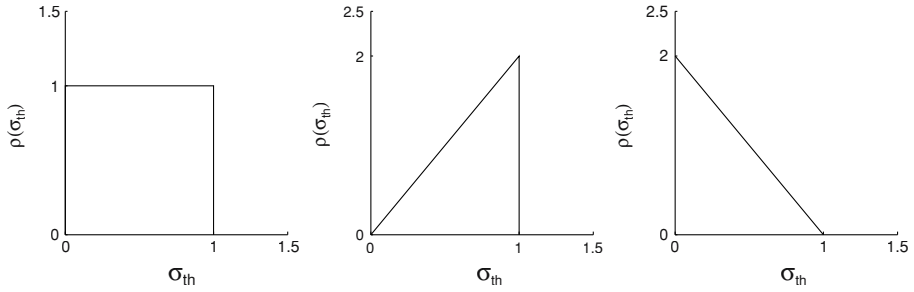


Figure 4. Three simple models considered here assume (a) uniform, (b) linearly increasing and (c) linearly decreasing density $\rho(\sigma_{th})$ of the fiber strength distribution up to a cutoff strength.

as it has a physical meaning: it is the fraction of the original bundle that remains intact under a fixed applied stress σ when the applied stress lies in the range $0 \leq \sigma \leq \sigma_c$. Clearly, $U^*(\sigma_c) = 1/2$ (putting $\sigma = \sigma_c$ in Eqn. (1.13)). Therefore the stable solution can be written as

$$U^*(\sigma) = U^*(\sigma_c) + (\sigma_c - \sigma)^{1/2}; \sigma_c = \frac{1}{4}. \tag{14}$$

For $\sigma > \sigma_c$ we can not get a real-valued fixed point as the dynamics never stops until $U_t = 0$, when the bundle breaks completely. It may be noted that the quantity $U^*(\sigma) - U^*(\sigma_c)$ behaves like an order parameter that determines a transition from a state of partial failure ($\sigma \leq \sigma_c$) to a state of total failure ($\sigma > \sigma_c$) [9]:

$$O \equiv U^*(\sigma) - U^*(\sigma_c) = (\sigma_c - \sigma)^{\beta}; \beta = \frac{1}{2}. \tag{15}$$

To study the dynamics away from criticality ($\sigma \to \sigma_c$ from below), we replace the recursion relation (1.11) by a differential equation

$$-\frac{dU}{dt} = \frac{U^2 - U + \sigma}{U}. \tag{16}$$

Close to the fixed point we write $U_t(\sigma) = U^*(\sigma) + \epsilon$ (where $\epsilon \to 0$). This, following Eq. (1.13), gives [9]

$$\epsilon = U_t(\sigma) - U^*(\sigma) \approx \exp(-t/\tau), \tag{17}$$

where $\tau = \frac{1}{2}\left[\frac{1}{2}(\sigma_c - \sigma)^{-1/2} + 1\right]$. Near the critical point we can write

$$\tau \propto (\sigma_c - \sigma)^{-\alpha}; \alpha = \frac{1}{2}. \tag{18}$$

Therefore the relaxation time diverges following a power-law as $\sigma \to \sigma_c$ from below [9].

One can also consider the breakdown susceptibility χ, defined as the change of $U^*(\sigma)$ due to an infinitesimal increment of the applied stress σ [7,9]

$$\chi = \left| \frac{dU^*(\sigma)}{d\sigma} \right| = \frac{1}{2}(\sigma_c - \sigma)^{-\eta}; \eta = \frac{1}{2} \tag{19}$$

from Eqn. (1.13). Hence the susceptibility diverges as the applied stress σ approaches the critical value $\sigma_c = \frac{1}{4}$. Such a divergence in χ had already been observed in the numerical studies [7].

For linearly increasing distribution of fiber strength Here, the cumulative probability becomes

$$P(\sigma_t) = \int_0^{\sigma_t} \rho(\sigma_{th}) d\sigma_{th} = 2 \int_0^{\sigma_t} \sigma_{th} d\sigma_{th} = \sigma_t^2. \tag{20}$$

Therefore U_t follows a recursion relation (following Eq. (1.6))

$$U_{t+1} = 1 - \left(\frac{\sigma}{U_t} \right)^2. \tag{21}$$

At the fixed point ($U_{t+1} = U_t = U^*$), the above recursion relation can be represented by a cubic equation of U^*

$$(U^*)^3 - (U^*)^2 + \sigma^2 = 0. \tag{22}$$

Solving the above equation we get [9] the value of critical stress $\sigma_c = \sqrt{4/27}$ which is the strength of the bundle for the above fiber strength distribution. Here, the order parameter, susceptibility, relaxation time all follow the same power laws (Eqns. (1.15), (1.18) and (1.19)) observed for uniform strength distribution.

For linearly decreasing distribution of fiber strength. In this case, the cumulative probability becomes

$$P(\sigma_t) = \int_0^{\sigma_t} \rho(\sigma_{th}) d\sigma_{th} = 2 \int_0^{\sigma_t} (1 - \sigma_{th}) d\sigma_{th} = 2\sigma_t - \sigma_t^2 \tag{23}$$

and U_t follows a recursion relation (following Eqn. (1.6))

$$U_{t+1} = 1 - 2\frac{\sigma}{U_t} + \left(\frac{\sigma}{U_t} \right)^2. \tag{24}$$

At the fixed point ($U_{t+1} = U_t = U^*$), the above recursion relation can be represented by a cubic equation of U^*

$$(U^*)^3 - (U^*)^2 + 2\sigma U^* - \sigma^2 = 0. \tag{25}$$

Solution of the above equation gives [9] the value of critical stress $\sigma_c = 4/27$ which is the strength of the bundle. Here also, the precursor parameters, the order parameter, susceptibility and relaxation time, all follow the same power laws (Eqns. (1.15), (1.18) and (1.19)) observed for uniform strength distribution.

Thus the democratic fiber bundles (for different fiber strength distributions) show phase transition from a state of partial failure to total failure with a well defined precursors (order parameter, susceptibility and relaxation time) which show similar power law variation on the way as the critical point is approached; characterized by the universal values of the associated exponents (α, β and η). All the above scaling behaviors represented by Eqns. (1.15), (1.18) and (1.19) for stress (σ) below the global failure stress (σ_c) of the bundle suggests that a prior knowledge of the responses like the fraction of failed fibers, relaxation time etc. can be extrapolated following the above power laws to estimate the global failure point σ_c.

4. Two-Fractal Overlap Model of Earthquake and the Prediction Possibility of Large Events

The two-fractal overlap model of earthquake [3] is a very recent modeling attempt. Such models are all based on the observed 'plate tectonics' and the fractal nature of the interface between tectonic plates and earth's solid crust. The statistics of overlaps between two fractals is not studied much yet, though their knowledge is often required in various physical contexts. For example, it has been established recently that since the fractured surfaces have got well-characterized self-affine properties [10], the distribution of the elastic energies released during the slips between two fractal surfaces (earthquake events) may follow the overlap distribution of two self-similar fractal surfaces [3, 11]. Chakrabarti and Stinchcombe [3] had shown analytically that for regular fractal overlap (Cantor sets and carpets) the contact area distribution follows a simple power law decay. The two fractal overlap magnitude changes in time as one fractal moves over the other. The overlap (magnitude) time series can therefore be studied as a model time series of earthquake avalanche dynamics [12].

Here, we study the time (t) variation of contact area (overlap) $m(t)$ between two well-characterized fractals having the same fractal dimension as one fractal moves over the other with constant velocity. We have chosen only very simple fractals: regular and random Cantor sets, gaskets and percolating cluster. We analyse the time series data of Cantor set overlaps only to find the prediction possibility of large events (occurrence of large overlaps). We show that the time series $m(t)$ obtained by moving one fractal uniformly over the other (with periodic boundary condition) has some features which can be utilized to predict the 'large events'. This is shown utilizing the discrete or a 'quantum' nature of the integrated (cumulative) overlap over time.

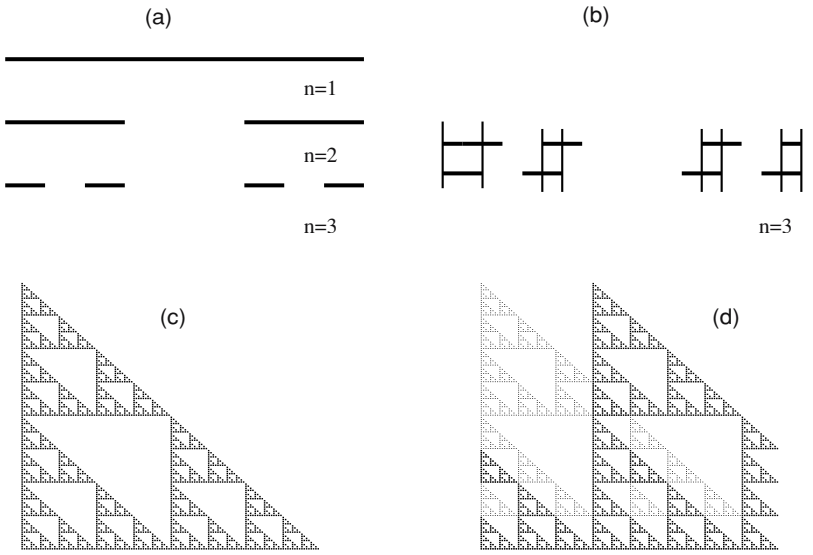


Figure 5. (a) A regular Cantor set of dimension $\ln 2/\ln 3$; only three finite generations are shown. (b) The overlap of two identical (regular) Cantor sets, at $n = 3$, when one slips over other; the overlap sets are indicated within the vertical lines, where periodic boundary condition has been used. (c) A regular gasket of dimension $\ln 3/\ln 2$ at the 7th generation. (d) The overlap of two identical regular gaskets at same generations ($n = 7$) is shown as one is translated over the other; periodic boundary condition has been used for the translated gasket.

Two-fractal overlaps

We now discuss the two-fractal overlap sizes. Let us take two identical Cantor sets at finite generation and slide one over the other, assuming periodic boundary condition. Two such cases for a regular Cantor sets as well as a gasket are shown in Fig. 5. Similar cases for random fractals are shown in Fig. 6.
Next, we study the overlap distribution of two well-characterised random fractals; namely the percolating fractals [13]. It seems, although many detailed features of the clusters will change with the changes in (parent) fractals, the subtle features of the overlap distribution function remains unchanged.

Our earlier study [9] on the overlap statistics for regular and random Cantor sets, gaskets and percolating clusters indicated a universal scaling behavior of the overlap or contact area (m) distributions $P(m)$ for all types of fractal set overlaps mentioned: $P'(m') = L^{\alpha} P(m, L); m' = mL^{-\alpha}$, where L denotes the finite size of the fractal and the exponent $\alpha = 2(d_f - d)$; d_f being the mass dimension of the fractal and d is the embedding dimension. Also the overlap distribution $P(m)$, and hence the scaled distribution $P'(m')$, are seen to decay with m or m' following a power law (with exponent value equal to the embedding dimension of the fractals) for both regular and random Cantor sets

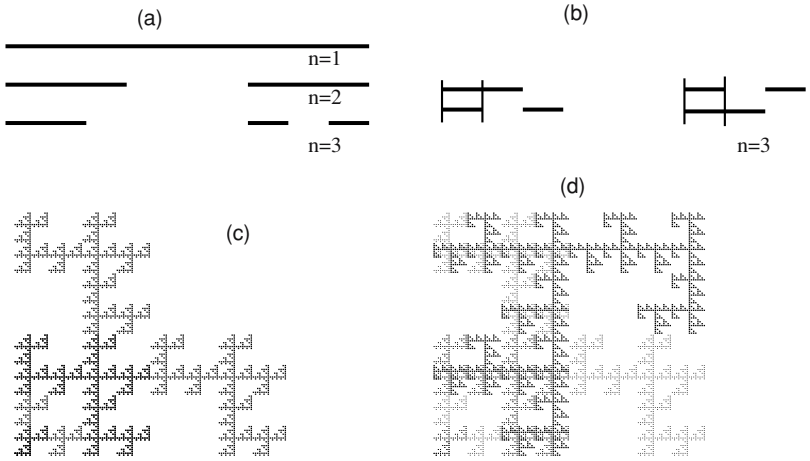


Figure 6. (a) A random Cantor set of dimension $\ln 2/\ln 3$; only three finite generations are shown. (b) Overlap of two random Cantor sets (at $n = 3$; having the same fractal dimension) in two different realisations. The overlap sets are indicated within the vertical bars. (c) A random realisation of a gasket of dimension $\ln 3/\ln 2$ at 7th generation. (d) The overlap of two random gaskets of same dimension and of same generation but generated in different realisations.

and gaskets: $P(m) \sim m^{-\beta}; \beta = d$. However, for the percolating clusters [13], the overlap size distribution takes a Gaussian form.

We consider now the time series obtained by counting the overlaps $m(t)$ as a function of time as one Cantor set moves over the other (periodic boundary condition is assumed) with uniform velocity. The analysis presented here follows our previous study [14].

Overlap time series data. The time series are shown in Fig. 8, for finite generations of Cantor sets of dimensions $\ln 2/\ln 3$ and $\ln 4/\ln 5$ respectively.

Cumulative overlap sizes. Now we calculate the cumulative overlap size $Q(t) = \int_o^t m dt$ and plot that against time in Fig. 9. Note, that 'on average' $Q(t)$ is seen to grow linearly with time t for regular as well as random Cantor sets. This gives a clue that instead of looking at the individual overlaps $m(t)$ series one may look for the cumulative quantity. We observe $Q(t) \simeq ct$, where c is dependent on the fractal. This result is even more prominent in the case of Cantor sets with $d_f = \ln 4/\ln 5$.

Cumulative overlap quantization. We first identify the 'large events' occurring at time t_i in the $m(t)$ series, where $m(t_i) \geq M$, a pre-assigned magnitude. We then look for the cumulative overlap size $Q_i(t) = \int_{t_{i-1}}^t m dt$, $t \leq t_i$, where the successive large events occur at times t_{i-1} and t_i. The behavior of Q_i

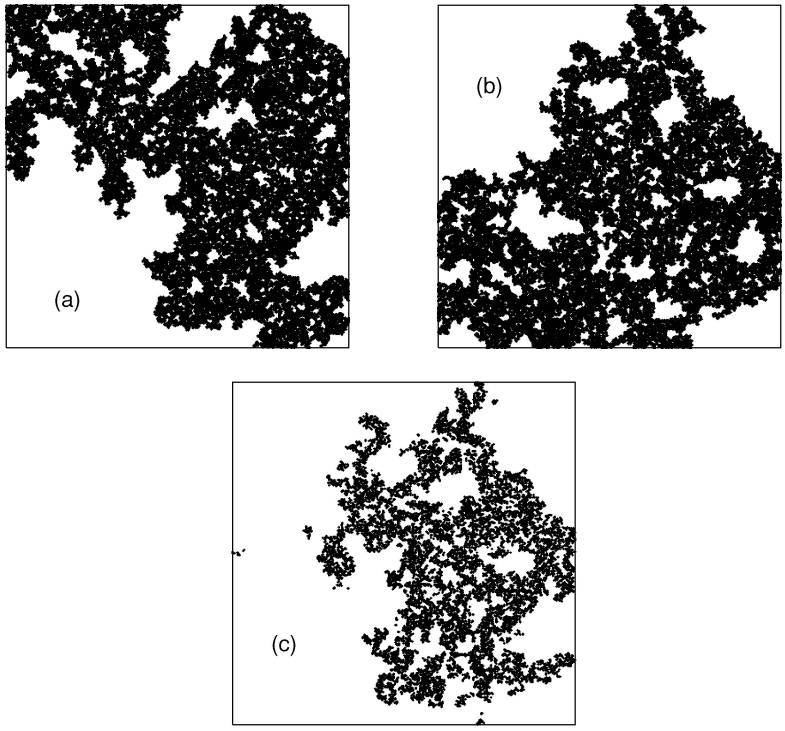


Figure 7. The overlap between two percolating clusters; (a) and (b) are two typical realisations of the same percolating fractal on square lattice ($d_f \simeq 1.89$) and (c) their overlap set. Note, the overlap set need not be a connected one.

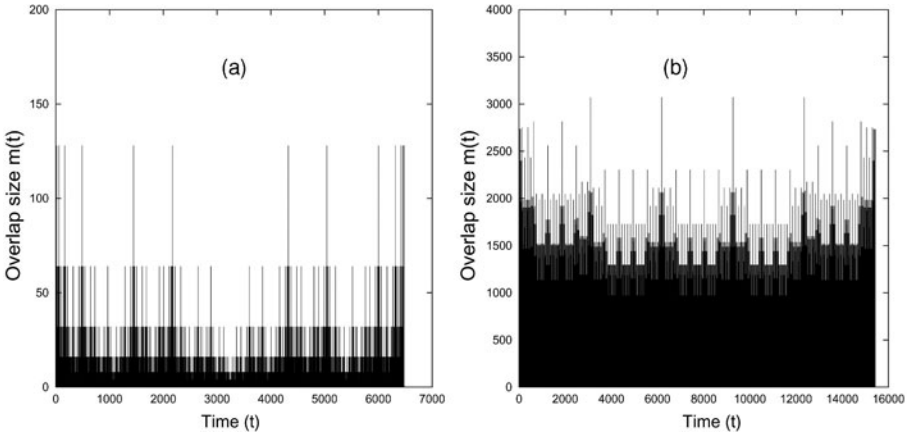


Figure 8. The time (t) series data of overlap size (m) for regular Cantor sets: (a) of dimension $\ln 2/\ln 3$, at 8th generation: (b) of dimension $\ln 4/\ln 5$, at 6th generation. The obvious periodic repeat of the time series comes from the assumed periodic boundary condition of one of the sets (over which the other one slides).

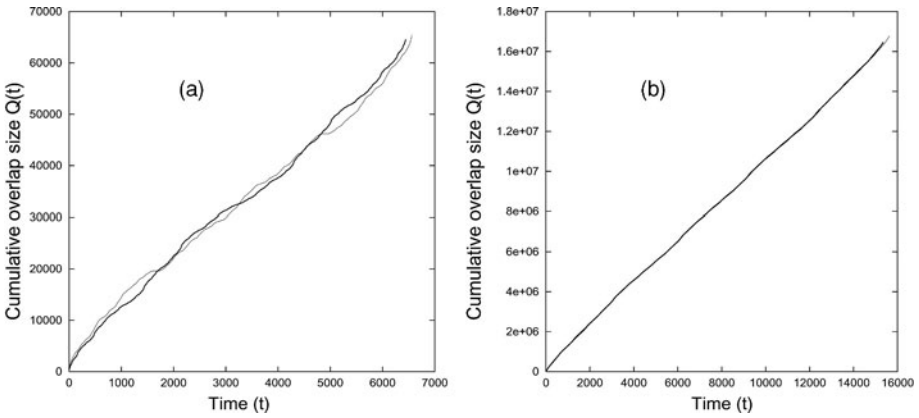


Figure 9. The cumulative overlap Q versus time; for pure cantor sets: (a) of dimension $\ln 2/\ln 3$ (at 8th generation) and (b) of dimension $\ln 4/\ln 5$ (at 6th generation). The dotted line corresponds to those for two identical but random Cantor sets. In (b) the two lines fall on each other.

with time is shown in Fig. 10 for regular cantor sets with $d_f = \ln 2/\ln 3$ at generation $n = 8$. Similar results are also given for Cantor sets with $d_f = \ln 4/\ln 5$ at generation $n = 6$ in Fig. 11. $Q_i(t)$ is seen to grow almost linearly in time up to $Q_i(t_i)$ after which it drops down to zero. It appears that there are discrete (quantum) values of $Q_i(t_i)$. One can therefore anticipate large events when the cumulative seismic overlap $Q_i(t)$, since the last major event at t_{i-1}, grows linearly with time t to the discrete levels lQ_0, specific to the series of events.

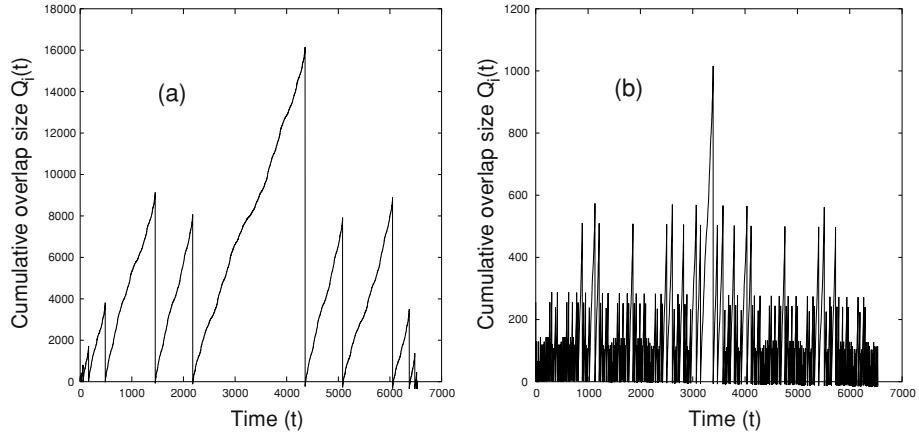


Figure 10. The cumulative overlap size variation with time (for regular Cantor sets of dimension $\ln 2/\ln 3$, at 8th generation), where the cumulative overlap has been reset to 0 value after every big event (of overlap size $\geq M$ where $M = 128$ (a) and 32 (b) respectively).

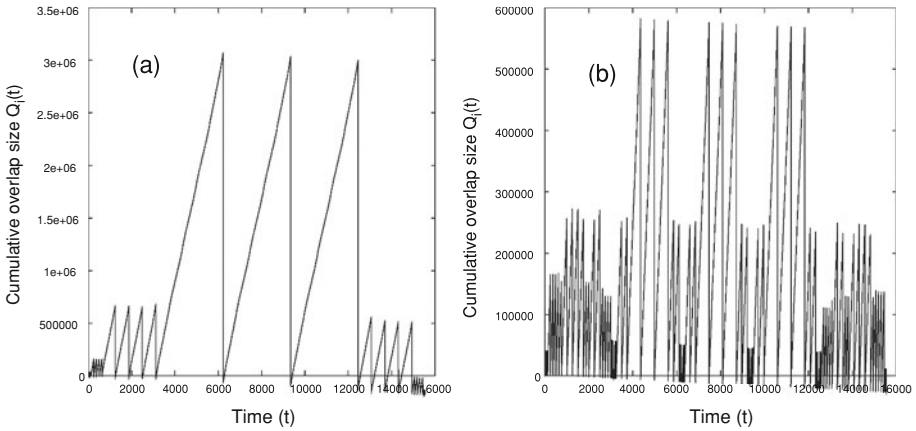


Figure 11. The cumulative overlap size variation with time (for regular Cantor sets of dimension $\ln 4/\ln 5$, at 6th generation), where the cumulative overlap has been reset to 0 value after every big event (of overlap size $\geq M$ where $M = 2400$ (a) and 2048 (b) respectively).

No major event occurs during the growth period of $Q_i(t)$ for the intermediate values.

5. Summary and Discussions

In all the dynamical models of sandpile avalanches (discussed in section 2), we find that the growing correlations in the dynamics of constituent elements manifest themselves as various precursors. The number of topplings Δ, relaxation time τ and the correlation length ξ, in both BTW and Manna model, grow and diverge following power laws as the systems approach their respective critical points h_c from below (see Figs. 2 and 3): $\Delta \sim (h_c - h_{av})^{-\delta}$, $\tau \sim (h_c - h_{av})^{-\gamma}$ and $\xi \sim (h_c - h_{av})^{-\nu}$. For two dimensional systems, we find numerically here $\delta \simeq 2.0$, $\gamma \simeq 1.2$ and $\nu \simeq 1.0$ for both BTW and Manna model. Basically, we studied the behavior for $h_{av} < h_c$, the precursor behavior, where ξ is necessarily finite. As we add here the tiny pulse at some central site of a relatively large system, the boundary effect can not be really felt because of the smallness of ξ compared to L for most values of h_{av}. This explains the lack of finite size effect in our precursor studies.

For the global failure or fracture in fiber bundle models (discussed in section 3), we find that the breakdown susceptibility χ (giving the increment in the number of broken fibers for an infinitesimal increment of load on the bundle) and the corresponding relaxation time τ (required for the bundle to stabilise, after successive failures of the fibers), both diverge as the external load or stress approaches its global failure point σ_c from below: $\tau \sim (\sigma_c - \sigma_{av})^{-\alpha}$ and $\chi \sim (\sigma_c - \sigma_{av})^{-\eta}$; $\alpha = \eta = 1/2$. These results are of course analytically derived for

different fiber strength distributions and the universality class of the model has been confirmed.

If one Cantor set moves uniformly over another, the overlap between the two fractals change quasi-randomly with time (see eg., Fig. 8). These time series are taken as model seismic activity variations in such two-fractal overlap model of earthquake. The overlap size distribution was argued [3] and shown [9] to follow power law decay. We showed numerically (see section 4) that if one fixes a magnitude M of the overlap sizes m, so that overlaps with $m \geq M$ are called 'events' (or earthquake), then the cumulative overlap $Q_i(t) = \int_{t_{i-1}}^{t} m dt$, $t \leq t_i$, (where two successive events of $m \geq M$ occur at times t_{i-1} and t_i) grows linearly with time up to some discrete quanta $Q_i(t_i) \cong l Q_0$, where Q_0 is the minimal overlap quantum, dependent on M and n (the generation number). Here l is an integer (see Figs. 10, 11) [14]. Although our results here are for regular fractals of finite generation n, the observed discretisation of the overlap cumulant Q_i with the time limit set by n, is a robust feature and can be seen for larger time series for larger generation number n. This part of the model study therefore indicates that one can note the growth of the cumulant seismic response $Q_i(t)$, rather than the seismic event strength $m(t)$, and anticipate some big events as the response reaches the discrete levels lQ_0, specific to the series of events.

Some prior knowledge of the precursors and their precise behavior (power laws etc.), as discussed here for three different kinds of failure models of cooperatively interacting dynamical systems which are prone to major failures, are therefore plausible. These precursor responses should help estimating the location of the global failure or critical point using proper extrapolation of the above quantities, which are available long before the failure occurs. The usefulness of such precursors can hardly be overemphasized.

Acknowledgments

We are grateful to our collaborators P. Bhattacharyya, P. Choudhuri and P. Ray for useful discussions.

References

[1] B. K. Chakrabarti and L. G. Benguigui, *Statistical Physics of Fracture and Breakdown in Disorder Systems*, Oxford Univ. Press, Oxford (1997); H. J. Herrmann and S. Roux (Eds), *Statistical Models for the Fracture of Disordered Media*, North Holland, Amsterdam (1990); P. Bak, *How Nature Works,* Oxford Univ. Press, Oxford (1997).

[2] F. T. Peires, J. Textile Inst. **17**, T355 (1926); H. E. Daniels, Proc. R. Soc. London A **183** 405 (1945); S. L. Phoenix and R. L. Smith, Int. J. Solid Struct. **19**, 479 (1983); R. da Silveira, Am. J. Phys. **67** 1177 (1999);

E. Altus, Mech. Mater. **34** 257 (2002); S. Pradhan and B. K. Chakrabarti, Proc. DMTAS (Chennai, March 2003), Int. J. Mod. Phys. B (in press), cond-mat/0307734.

[3] B. K. Chakrabarti, R. B. Stinchcombe, Physica A, **270** 27 (1999).

[4] P. Bak, C. Tang and K. Wiesenfeld, Phys. Rev. Lett. **59** 381 (1987); D, Dhar, Phys. Rev. Lett. **64** 1613 (1990).

[5] S. S. Manna, J. Phys. A: Math. Gen. **24** L363 (1991); D. Dhar, Physica A **270** 69 (1999).

[6] M. Acharyya and B. K. Chakrabarti, Physica A **224** 254 (1996); Phys. Rev. E **53** 140 (1996).

[7] S. Pradhan and B. K. Chakrabarti, Phys. Rev. E **65**, 016113 (2001).

[8] S. Ortolani and D. D. Schnack, *Magnetohydrodynamics of Plasma Relaxation, World Scientific Publ.*, Singapore (1993).

[9] S. Pradhan, P. Bhattacharyya and B. K. Chakrabarti, Phys. Rev. E **66**, 016116 (2002); P. Bhattacharyya, S. Pradhan and B. K. Chakrabarti, Phys. Rev. E **6**7, 046122 (2003).

[10] B. B. Mandelbrot, *The Fractal Geometry of Nature* Freeman, San Francisco (1982); B. B. Mandelbrot, D. E. Passoja, A. J. Pullay, Nature **308** 721 (1984); A. Hansen and J. Schmittbuhl, Phys. Rev. Lett. **90**, 045504 (2003); J. O. H. Bakke, J. Bjelland, T. Ramstad, T. Stranden, A. Hansen and J. Schmittbuhl, Proc. UASP03 (Kolkata, March 2003), Physica Scripta **T106** 65 (2003).

[11] S. Pradhan, B. K. Chakrabarti, P. Ray and M. K. Dey, Proc. UASP03 (Kolkata, March 2003), Physica Scripta **T106** 77 (2003).

[12] J. M. Carlson, J. S. Langer and Shaw, Rev. Mod. Phys. **62** 2632 (1989).

[13] See e.g., D. Stauffer and A. Aharony, *Introduction to Percolation Theory*, Taylor and Francis, London (1994).

[14] S. Pradhan, P. Choudhuri and B. K. Chakrabarti, in *Proc. NATO conf.* (CMDS-10, Soresh, Israel, July 2003), *Continuum Models of Discrete Systems*, Eds. D. J. Bergman and E. Inan, Kluwer Acad. Pub., New York, cond-mat/0307735.

Chapter 15

MULTI-SCALE INTERACTIONS AND PREDICTABILITY OF THE INDIAN SUMMER MONSOON

B. N. Goswami
Centre for Atmospheric and Oceanic Sciences
Indian Institute of Science
Bangalore 560 012, India

R. S. Ajaya Mohan
Centre for Ocean-Atmospheric Prediction Studies
Florida State University
Tallahassee, Florida, U.S.A

Abstract: Following the seminal work of Charney and Shukla (1981), the tropical climate is recognised to be more predictable than extra tropical climate as it is largely forced by 'external' slowly varying forcing and less sensitive to initial conditions. However, the Indian summer monsoon is an exception within the tropics where 'internal' low frequency (LF) oscillations seem to make significant contribution to its interannual variability (IAV) and makes it sensitive to initial conditions. Quantitative estimate of contribution of 'internal' dynamics to IAV of Indian monsoon is made using long experiments with an atmospheric general circulation model (AGCM) and through analysis of long daily observations. Both AGCM experiments and observations indicate that more than 50% of IAV of the monsoon is contributed by 'internal' dynamics making the predictable signal (external component) burried in unpredictable noise (internal component) of comparable amplitude. Better understanding of the nature of the 'internal' LF variability is crucial for any improvement in predicition of seasonal mean monsoon.

Nature of 'internal' LF variability of the monsoon and mechanism responsible for it are investigated and shown that vigorous monsoon intraseasonal oscillations (ISO's) with time scale between 10–70 days are primarily responsible for generating the 'internal' IAV. The monsoon ISO's do this through scale interactions with synoptic disturbances (1–7 day time scale) on one hand and the annual cycle on the other. The spatial structure of the monsoon ISO's is similar to that

A.S. Sharma and P.K. Kaw (eds.), Nonequilibrium Phenomena in Plasmas, 311–340.
© 2005 *Springer. Printed in the Netherlands.*

of the seasonal mean. It is shown that frequency of occurance of strong (weak) phases of the ISO is different in different seasons giving rise to stronger (weaker) than normal monsoon. Change in the large scale circulation during strong (weak) phases of the ISO make it favourable (inhibiting) for cyclogenesis and gives rise to space time clustering of synoptic activity. This process leads to enhanced (reduced) rainfall in seasons of higher frequency of occurence strong (weak) phases of monsoon ISO.

Key words:

1. Introduction

The Indian summer monsoon rainfall shapes the life, economy and culture of a large fraction of world's population. The wet summer and dry winter represent a large annual cycle characteristic of the Indian monsoon precipitation. The large annual cycle can be seen in other circulation parameters as well. The standard deviation (s.d.) of interannual variations of seasonal mean rainfall during June–September over Indian continent is not very large, approximately 10% of the long term mean ($\bar{P} = 86$ cm). The rainfall anomalies (deperture from long term mean) during drought years ($p' < -1.0$ s.d) or flood years ($p' > +1.0$ s.d.) tend to have large spatial scale covering most of the continent (Shukla, 1987). The monsoon rainfall variations, therefore, have a strong influence on the agricultural productivity of the country (Gadgil, 2003; Webster et al., 1998). With the general decrease in the growth rate of agricultural productivity associated with the fatigue of the green revolution during the past decade, the rainfall variations may have even a larger impact on agricultural productivity in the coming years. As a result, prediction of summer monsoon rainfall at least one season in advance assumes great importance. For over a century, attempts have been made to predict monsoon rainfall using statistical methods involving local and global antecedent parameters that correlate with the monsoon rainfall (Blandford, 1884; Walker, 1923, 1924; Gowarikar et al., 1989; Sahai et al., 2003). The linear or nonlinear regression models as well as neural network based models (Goswami and Srividya, 1996) perform reasonably well when the monsoon is close to normal (about 70% of the past 130 year period) but fails to predict the extremes with useful skill. Thus, the usefulness of the statistical models is limited.

Dynamical prediction of seasonal mean monsoon using state-of-the art climate models offers the logical alternative to statistical forecasting of the monsoon. Unfortunately, the alternative approach has not shown better skill than the statistical models so far. Over the years the climate models have generally improved in simulating the mean climate and a series of sensitivity studies (Charney and Shukla, 1981; Shukla, 1981; Lau, 1985; Shukla, 1998) have

shown that the tropical climate is, in general, much less sensitive to initial conditions and hence more predictable than the extra-tropical climate. This progress notwithstanding, almost all present day climate models have serious difficulty in simulating the seasonal mean monsoon climate and its interannual variations (Sperber and Palmer, 1996; Saji and Goswami, 1997; Gadgil and Sajani, 1998). Even though climate of certain tropical region show very little sensitivity to initial conditions (e.g. Shukla, 1998), the Indian summer monsoon appears to be quite sensitive to initial conditions (Sperber and Palmer, 1996; Sperber et al., 2001; Krishnamurthy and Shukla, 2001), making it the most difficult climate system to simulate and predict.

The factors that determine the interannual variability and hence the predictability of the seasonal mean Indian monsoon are schematically illustrated in Fig. 1. Two major components are LF 'external' variability and LF 'internal' variability that influence interannual variability of the monsoon. The contributions from 'external' variability such as solar forcing or slow coupled ocean-atmosphere oscillations (e.g. El Nino and Southern Oscillation (ENSO))

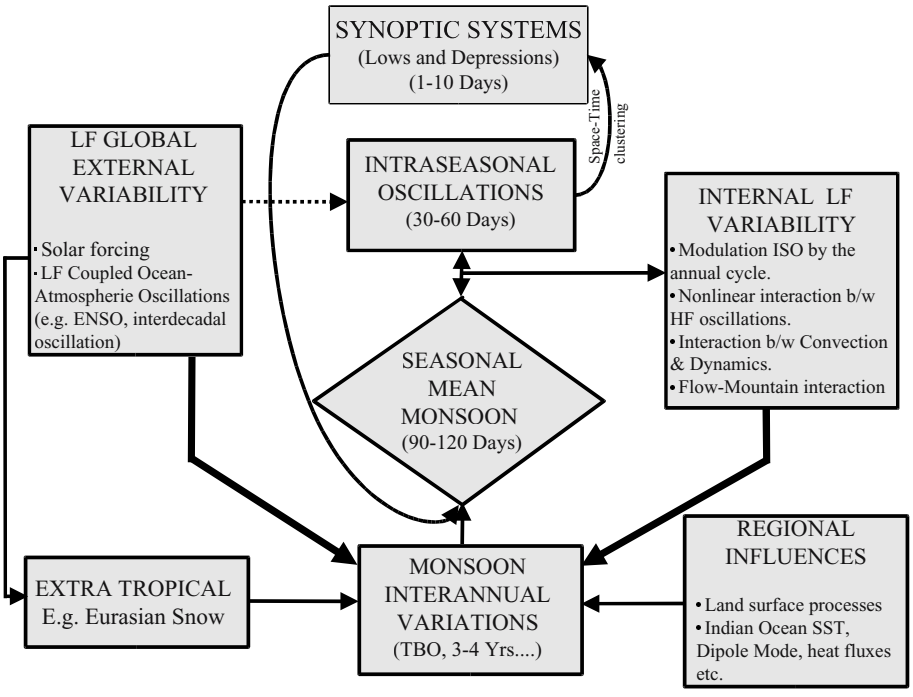


Figure 1. A schematic diagram indicating how monsoon ISO's influence the seasonal mean monsoon and its interannual variability by producing LF 'internal' variability through multi-scale interactions. Other 'external' forcing influencing the interannual variability of the monsoon are also indiacted.

are less sensitive to initial conditions and hence more predictable. The contributions from LF 'internal' variability are sensitive to initial conditions and hence are unpredictable. Extra-tropical influence such as those associated with Eurasian snow cover (Hahn and Shukla, 1976; Kripalani et al., 1996) can also be considered 'external' as the snow variability in the extra-tropics may be governed by the sea surface temperature (SST) variability in the tropics (Meehl and Arblaster, 2002). In addition to these processes, there are some regional influences to interannual variability of the monsoon such as soil moisture-radiation feedback (Meehl, 1994) and Indian Ocean SST variability like the dipole mode (Saji et al., 1999). These could also be considered as 'external' forcing for monsoon variations. LF 'internal' variability of the monsoon can arise from a number of processes such as, nonlinear interaction between high frequency (HF) oscillations, interaction between organized convection and dynamics and interaction between flow and orography. In addition, northward propagating intraseasonal oscillations (ISO's) of monsoon (Yasunari,1979; Sikka and Gadgil, 1980; Goswami and Ajayamohan, 2001b) play an important role in generating LF 'internal' oscillations. Higher frequency of occurrence active (break) condition in a season can influence the seasonal mean monsoon rainfall as the monsoon ISO's cause space time clustering of rain producing synoptic disturbances. Further, modulation of the monsoon ISO by the annual cycle could also give rise to biennial type internal variability. The monsoon ISO's arise from internal processes in the atmosphere (Goswami and Shukla, 1984; Webster, 1983; Nanjundiah et al., 1992) through interaction between organized convection and dynamics. Thus, the LF variability generated by the ISO's is also of 'internal' origin with low predictability.

What makes the Indian monsoon such a difficult system to simulate and predict? The sensitivity of monsoon climate to initial conditions indicate existence significant 'internal' low frequency (LF) variability in the monsoon region. What is responsible for such 'internal' LF variability in the monsoon region? The predictability of the monsoon is going to be determined by the extent to which 'internal' LF variability govern interannual variability of the monsoon. To what extent is the monsoon predictable? Objective of the present article is to provide some answer to these questions. Quantitative estimate of contribution of 'internal' LF variability to interannual variability of monsoon will be made and mechanisms responsible for the 'internal' LF variability will be unraveled. Evidence will be presented to support a hypothesis that multiscale interactions between synoptic variability (lows, depressions, time scale 1–10 days), intraseaonal oscillations (quasi-biwekly mode, 30–60 day mode) and the annual cycle largely results in the observed LF 'internal' variability.

If one could separate the 'internal' contribution to interannual variance, an estimate of predictability could be constructed as a ratio between the total

interannual variance (the signal) and 'internal' variance (the noise). In this paper, we present such an estimate of predictability of the monsoon using a general circulation model (GCM) (Section 3) as well from from about 40 years of daily observations (Section 4). The nature of LF 'internal' variability simulated by the GCM is investigated in Section 5 and using a nonlinear dynamical model it is indicated that a modulation of ISO's by the annual cycle could be responsible for the internal LF variability simulated by the GCM. The multi-scale interactions through which the vigorous monsoon ISO's result in LF variability of the observed seasonal mean monsoon is also illustrated in this section. The results are summerized in Section 6.

2. Model and Data Used

For the purpose of estimating predictability of the monsoon, we have used a three dimensional model of the atmosphere, an atmospheric general circulation model (AGCM) developed at the Geophysical Fluid Dynamics Laboratory (GFDL). The basic fluid dynamical equations of the model are solved using spectral element method (Gordon and Stern 1982). We carried out two long integrations with a version of the model that has rhomboidal 30 horizontal resolution (30 waves in the east-west direction and 30 associated Legendre functions in the north-south direction) and 14 unevenly spaced vertical levels. The horizontal resolution amounts to approximately 3.73 longitude by 2.25 latitude. The physical processes such as radiation (incoming short wave solar and outgoing long wave terrestrial radiation), dry and moist convection, boundary layer processes and ground hydrology are all parameterized (Gordon and Stern, 1982; Broccoli and Manabe, 1992; Goswami, 1998). At the lower boundary, surface temperature is prescribed over the ocean while it is determined from the prognostic hydrology model over land. A control integration (CTL-run) was carried out with the model in which monthly mean SST was prescribed from observations (Reynolds and Smith, 1994) for a period of 15 years (1979–1993). The observed SST has slow variations associated with the El Nino and Southern Oscillations (ENSO). These slowly varying boundary forcing induce slow 'external' variations of the model climate. Thus, simulations from this integration contains 'internal' as well as 'external' variability. A second sensitivity experiment, called FXSST-run, was carried out for 20 years in which prescribed SST had no interannual variations. In this run, long term mean SST annual cycle was prescribed at each grid point and was repeated every year. Since solar forcing is also fixed (i.e. no interannual variations), this run does not have any external interannual forcing. Therefore, any interannual variations simulated by the model in this experiment must arise from internal dynamics of the atmosphere and would give us an estimate of 'internal' interannual variance.

In order to make an estimate of predictability from observations, we use daily 850 hPa winds from NCEP/NCAR reanalysis for 33 years (1965–1997). The NCEP/NCAR reanalysis is a research quality product that uses an analysis system that is kept fixed throughout the reanalysis period and utilizes all available data. The data assimilation and forecast model used in the analysis system has horizontal resolution of T62 and 28 vertical levels. Details about the NCEP/NCAR reanalysis is available in Kalnay et al.(1996) and Kistler et al. (2001). In addition to the circulation data just mentioned, we also use satellite derived daily outgoing long wave radiation (OLR) data (Liebmann and Smith, 1996) for 23 years (1979–2001). The OLR data is a proxy for moist convection in the tropical regions. Rainfall estimate from CMAP (Climate Prediction Center's Merged Precipitation Analysis) is also used to study the clustering of synoptic systems by the monsoon ISO's. The CMAP produces pentad and monthly global analysis of precipitation in which observations from rain gauge are merged with precipitation estimates from several satellite based algorithms (Xie and Arkin, 1996). The random errors associated with different satellite products are minimized by using a linear combination of the satellite estimates with weights that are inversely proportional to known errors associated with each product.

3. Estimate of Predictability from an AGCM

Estimate of predictability of the Indian summer monsoon by an AGCM depends on estimates of total interannual variance and internal interannual variance of the Indian monsoon by the AGCM. For these estimates of variance to be reliable, the seasonal mean monsoon climate simulated by the AGCM should be realistic. The fidelity of the AGCM in simulation of the observed monsoon climate is shown in Fig. 2 where observed climatological mean 850 hPa winds (from NCEP/NCAR reanalysis) and precipitation (Xie and Arkin, 1996) averaged during June to September (JJAS) are compared with those simulated by the AGCM in the CTL-run as well as in the FXSST-run. As may be expected, the climatological mean climate in the CTL-run and in the FXSST-run are almost identical. The simulation of precipitation over the Indian continent, south China Sea and western Pacific are quite reasonable. However, the model is deficient in simulating the secondary maximum in precipitation over the equatorial Indian Ocean. Most AGCM's have difficulty in simulating the observed precipitation over the continent correctly (Gadgil and Sajani, 1998). This AGCM is one of the few AGCM's that simulates the continental precipitation reasonably well. Thus, the estimate of interannual variance of precipitation over the Indian monsoon region may be considered reasonable. Monthly mean anomalies are constructed as deviation of simulated monthly means from long term annual cycle of simulations at each grid point for both CTL-run as well as FXSST-run.

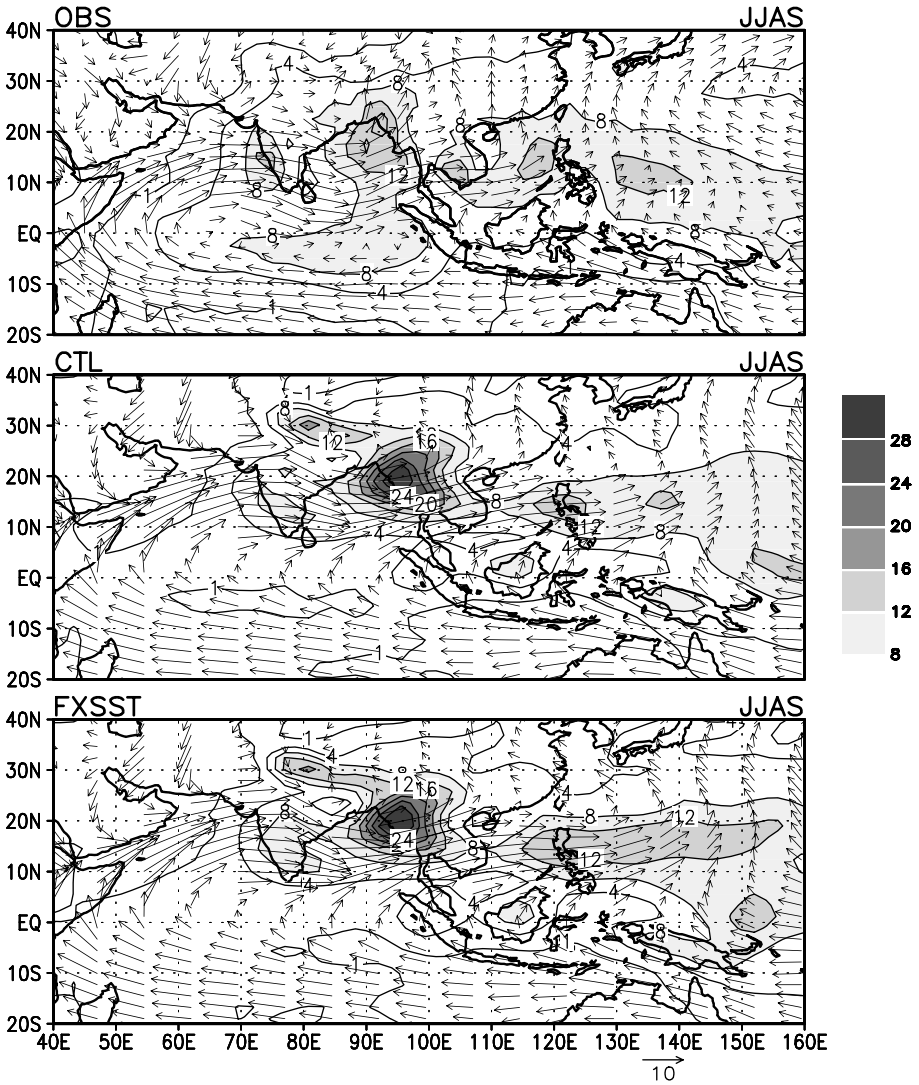


Figure 2. Long term mean wind vectors at 850 hPa and precipitation (shaded) averaged over June-September from observations (OBS), from the control run (CTL) and from fixed SST run (FXSST). Unit of precipitation is $mm\ day^{-1}$ and that for winds is $m\ s^{-1}$. Unit vector for winds is shown at the bottom.

Monthly anomalies of June, July, August and September (JJAS) for all years are collected. Interannual variance of precipitation anomalies from the CTL-run for the summer monsoon season (JJAS) is shown in Fig. 3a while ratio between the variance from CTL-run and FXSST-run is shown in Fig. 3b. Since the variance of the CTL-run is a combination of boundary forced 'external'

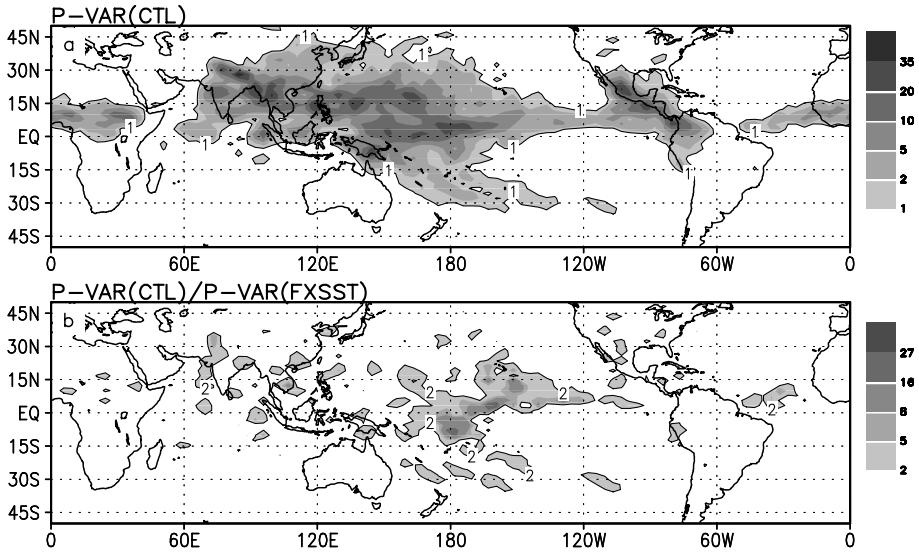


Figure 3. (Top) Variance of monthly mean precipitation anomaly ($(mm\ day^{-1})^2$) during northern summer (June-September) from 15 year simulation of the CTL-run. (Bottom) Ratio of variance between monthly mean precipitation anomaly during northern summer from the CTL-run and that from the FXSST run.

and 'internal' variances, while that from the FXSST-run is a measure of 'internal' variance, regions with a ratio of less than 2 indicates regions where the 'internal' variance is comparable or larger than the 'external' variance. The predictability is high over the equatorial central and eastern Pacific where the ratio is large and significant. The predictability is poor over the Asian monsoon regions where the ratio is barely two or less than two. In fact, with the degrees of freedom involved, the ratio of variance should be greater than 2.5 to be statistically significant. Thus, monthly mean precipitation over the Asian monsoon region during northern summer seems unpredictable. The distribution of ratio of variance of the seasonal mean precipitation during the northern summer was also calculated and was found to be very similar to Fig. 3b.

To supplement the predictability estimate for precipitation, similar estimate was made for for east-west component of wind (zonal wind) at a lower atmospheric level (860 hPa level of the model atmosphere) and is shown in Fig. 4. Consistent with the ratio of variance for precipitation, the ratio of variance for zonal winds at 860 hPa is also less than 2 over the Asian monsoon region. The distribution of ratio of variance of the seasonal mean zonal winds at 860 hPa during the northern summer was also calculated and was found to be very similar to Fig. 4b. Therefore, the monthly mean and seasonal mean circulation as

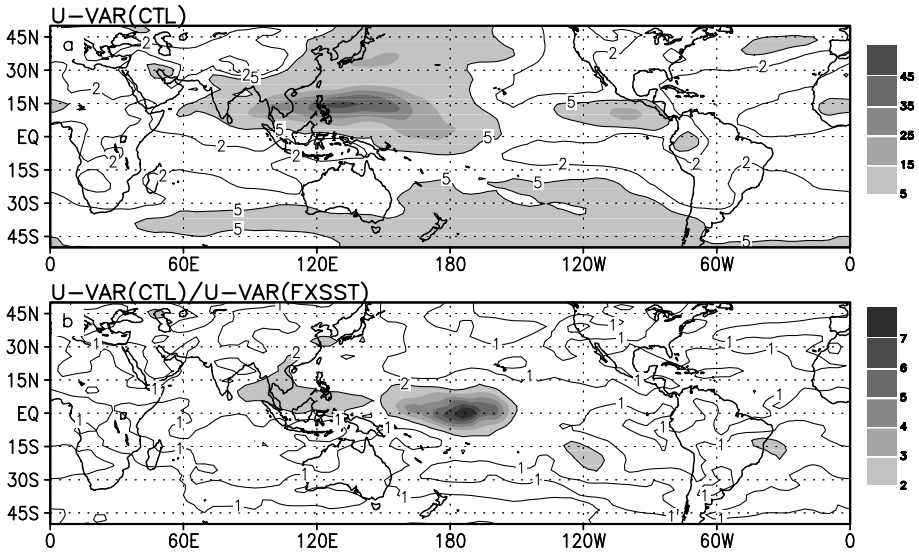


Figure 4. Same as (3) but for zonal winds at 860 hPa model level. Unit of variance of wind is $(mm\ day^{-1})^2$.

well as precipitation anomalies seem to have poor predictability over the Asian monsoon region.

4. Estimate of Predictability from Observations

While it is relatively easy to estimate the 'internal' variability in an AGCM by artificially suppressing all external interannual forcing, it is not so simple to separate the internal component of variability from only one ensemble of observed data. Some assumptions invariably need to be made. We separate the 'internal' and 'external' component of interannual variance using the following hypothesis. The main interannual external forcing is the slowly varying boundary forcing associated with the ENSO SST variations. Since the time scale of ENSO SST variability is much longer (3–4 years to decadal) than the annual cycle, this forcing essentially results in a modulation of the annual cycle. The annual cycle of each field at each grid point for each year of observations is constructed as sum of the annual mean and the first three harmonics. An example of daily zonal winds at 850 hPa over the Bay of Bengal together with its annual cycle (thick line) for the year 1995 is shown (thin line) in Fig. 5a. The variation of the annual cycle at the same point for five years is shown in Fig. 5b. Significant interannual variation of the annual cycle is evident.

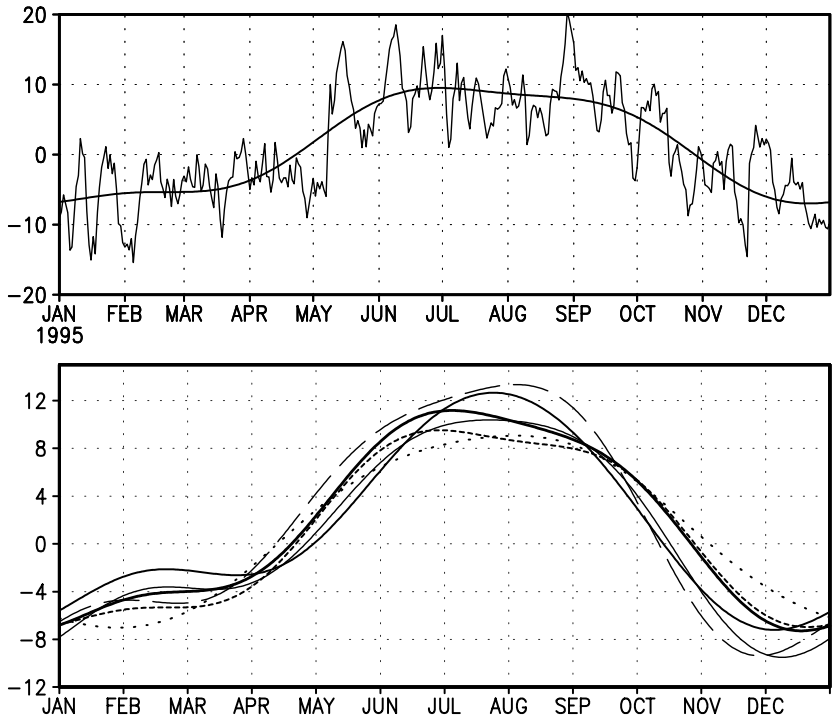


Figure 5. (Top) Daily 850 hPa zonal winds ($m\ s^{-1}$) at 90E, 15N for the year 1995 (thin line). The annual cycle is also shown (thick line). (Bottom) The annual cycles for five years are plotted illustrating the interannual variability.

A long term mean (climatological mean) annual cycle is constructed as average of annual cycles of all available years. Deviation of individual years annual cycle from the climatological annual cycle represents 'external' anomalies. Monthly mean of the 'external' anomalies for all years are created. The deviation of daily observations from the annual cycle of individual year represents 'internal' anomalies. Monthly means of the 'internal' anomalies for all years are also created.

The variance of 'external' and 'internal' anomalies of zonal winds at 850 hPa for the JJAS months are calculated based on 33 years of observations and shown in Fig. 6b and Fig. 6c and the ratio between the total variance and 'internal' variance is shown in Fig. 6a. It may be noted that the external influence is weak and 'internal' variance largest over the Asian monsoon region leading to a ratio that is less than 2. Similar 'external' and 'internal' variances for OLR are shown in Fig. 7b and Fig. 7c while the ratio of the total and internal variances is shown in Fig. 7a. Again we note that the ratio is less than 2 over the Asian monsoon region.

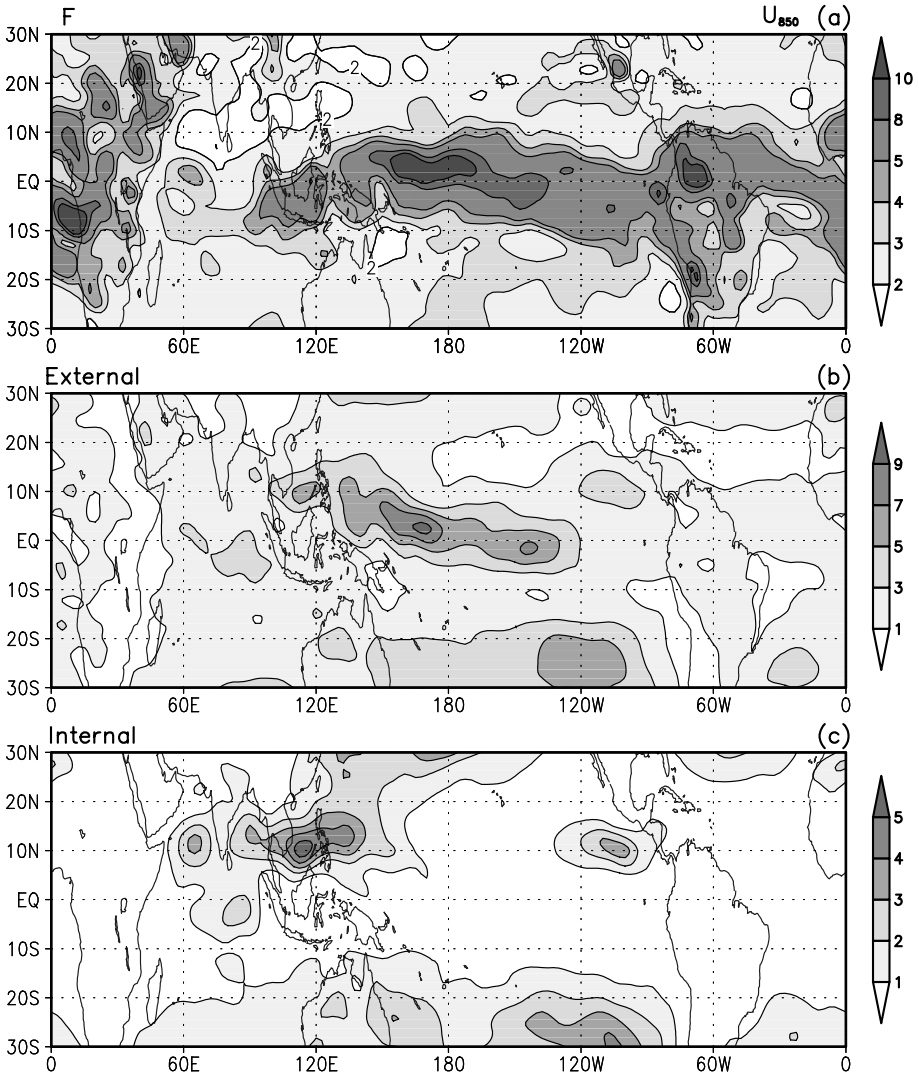


Figure 6. (a) Ratio between total variance ('external' + 'internal') and 'internal' variance during northern summer (June-August) for zonal winds at 850 hPa. Spatial distribution of (b) 'external' and 'internal' components of the variance $(m\ s^{-1})^2$.

Thus, the estimates of predictability of the Asian monsoon from an AGCM are consistent with those obtained from observations. Both the estimates indicate that the 'internal' variability in this region is comparable to or larger than the 'external' variability (the signal being comparable to the 'noise'), seriously limiting the predictability of the Asian monsoon. At the same time it is also noted that both circulation and precipitation have high degree of

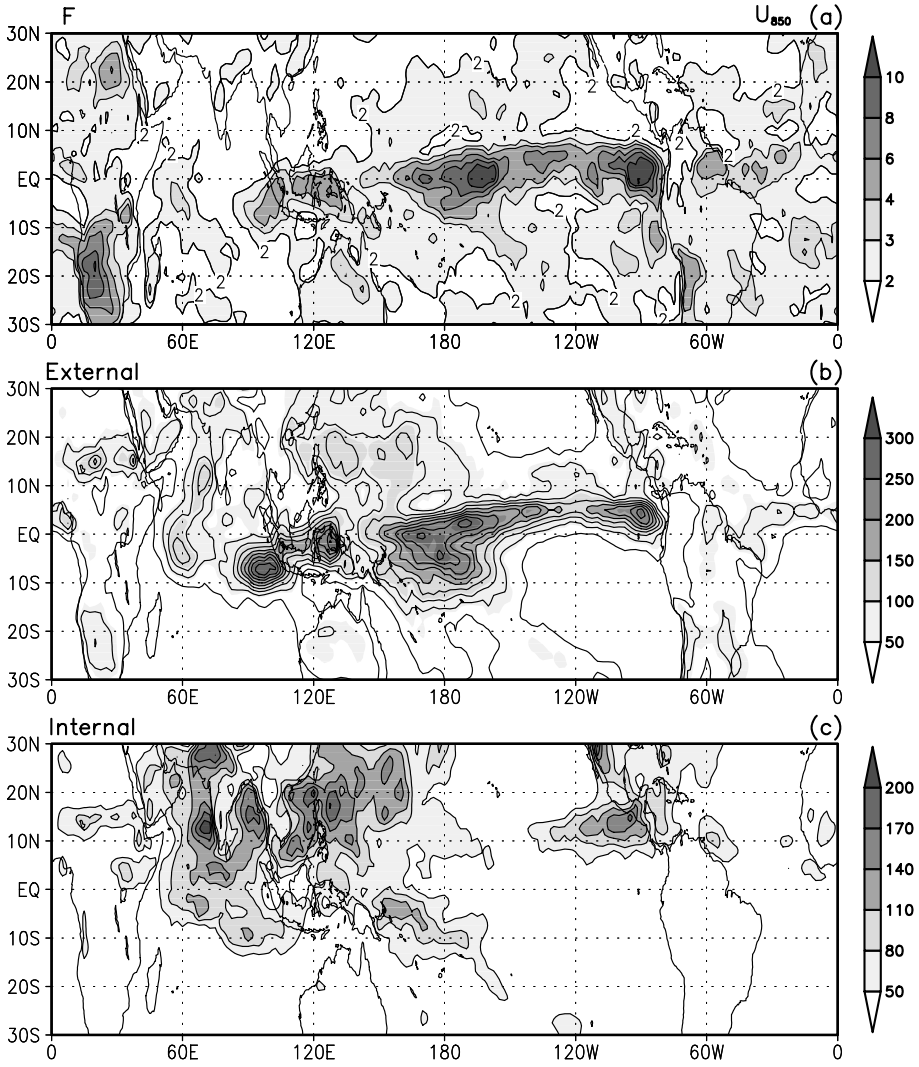


Figure 7. Same as Fig. 6 but for OLR. Unit of variance for OLR is $(W\,m^{-2})^2$.

predictability over the equatorial Pacific consistent with many other previous modelling studies.

The results of estimating predictability of monthly mean summer climate was extended to seasonal mean summer climate (Ajaya Mohan and Goswami, 2003) and it was shown that the main conclusion remains the same with seasonal climate as well. It may be noted that the 'internal' variance associated with interannual variability of the seasonal climate could not be estimated

by the method described above and a slightly different approach need to be adopted.

5. Scale Interactions and 'Internal' LF Variability

What is responsible for generating significant interannual variability in the absence of any interannually varying external forcing over the Asian monsoon region? In this section, we attempt to gain insight towards the origin of 'internal' LF variability in this region. We note that Asian monsoon region is rather unique in the tropics for several reasons. This is a region where the amplitude of the annual cycle is the largest. The existence of the Himalayan mountains and the Indian land mass to the north of warm waters of the Indian Ocean is also unique resulting in the largest northward migration of the rain band (inter tropical convergence zone, ITCZ). This unique geophysical situation is also responsible for spawning vigorous northward propagating monsoon ISO's (Sikka and Gadgil, 1980; Yasunari, 1979, 1981). We propose that the monsoon ISO's play a key role in producing the 'internal' LF variability in this region through multi-scale interactions involving synoptic activity (lows and depressions) on one hand and the annual cycle on the other hand. The temporal and spatial characteristics of the monsoon ISO's have been studied extensively over the last three decades. The westward propagating 10–20 day mode (Krishnamurti and Bhalme, 1976; Krishnamurti and Ardunay, 1980) and the northward propagating 30–60 day mode (Yasunari, 1979; Sikka and Gadgil, 1980; Goswami and Ajayamohan, 2001a) are convectively coupled and could be seen in most circulation parameters as well as in precipitation. Proper phase relationship between the two modes manifest in the active (rainy spells) and break (dry spells) phases within the monsoon season(Goswami et al., 1998, 2003).

The seminal role of the monsoon ISO in producing the observed 'internal' variability could be seen from the fact that almost all the internal variance shown in Fig. 6c and Fig. 7c is due to the monsoon ISO's. To show this, the 'internal' variance was calculated after removing the high frequency component with period less than 10 days from the daily anomalies. The daily anomalies after removing the annual cycle was passed through a 10–90 day band pass Lanczos filter. Monthly mean 'internal' anomalies were calculated from the filtered data and 'internal' variance for JJAS was recalculated with the filtered monthly mean anomalies. The variance calculated in this manner represents the 'internal' variance arising from the ISO's. This is shown for zonal winds at 850 hPa in Fig. 8b together with that from the full anomalies in Fig. 8a. It is seen that almost all the 'internal' variance comes from the ISO's. This was tested with OLR and other circulation parameters and found to be true in all cases.

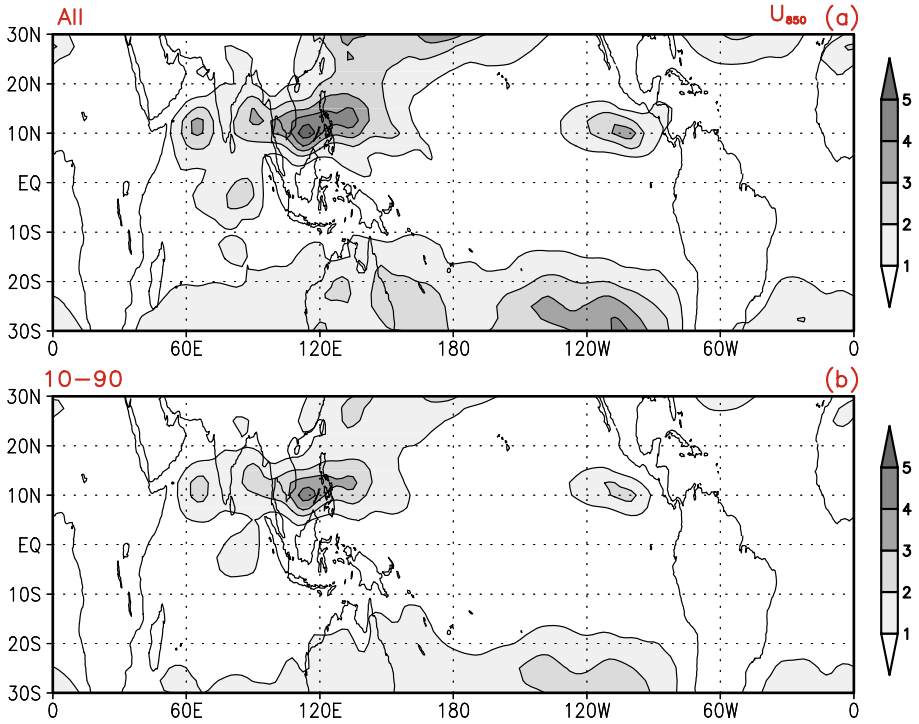


Figure 8. (a) Internal component of variance of zonal winds $(m\,s^{-1})^2$ at 850 hPa during June-July-August calculated from daily anomalies without filtering the synoptic events. (b) same as in (a) but based on 10–90 day filtered anomalies namely, after removing the synoptic events.

5.1 Nature of LF internal variability of the AGCM simulated monsoon

To gain some insight regarding the physical processes that lead to the internal LF variability, let us examine the nature of the LF variability simulated by the AGCM in the FXSST-run. To obtain a rough idea about the temporal scale of the LF internal variability, 5-month running mean of precipitation anomaly averaged between 140E-160E and 5S-5N, zonal winds at 860 hPa averaged between 50E-70E and 5S-5N and zonal winds at 170 hPa averaged between 140E-180E and 5S and 5N are plotted in Fig. 9. A visual examination shows that an approximate quasi-biennial period is present in all three time series. The power spectra of the unfiltered time series (plotted on the right hand side of the figure) also confirm the observation that the statistically significant dominant LF mode has time scale between 20–30 months. It is found that the variations of precipitation, low level and upper level winds are strongly coupled for the

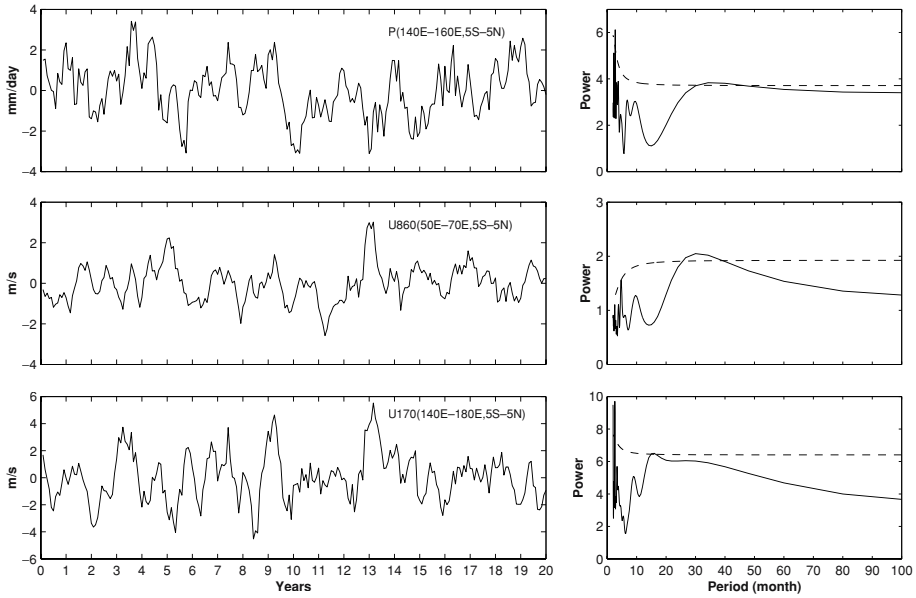


Figure 9. Evidence of existence of quasi-biennial mode of 'internal' variability in the AGCM simulated tropical climate. Five month running mean of precipitation anomalies averaged over (140E-160E, 5S-5N), zonal wind anomalies at 860hPa averaged over (50E-70E, 5S-5N) and zonal winds at 170hPa averaged over (140E-180E, 5S-5N) are shown on the left. The power spectra of unfiltered raw monthly anomalies of corresponding time series are shown on the right. 95% confidence limit for the spectra derived from theoretical red noise spectra based on lag-1 autocorrelation are also shown by dashed line.

'internal' quasi-biennial mode and that the vertical structure is that of a first baroclinic mode (not shown).

How does the model atmosphere internally produces quasi-biennial oscillation? The model atmosphere has vigorous northward propagating ISO's with time scale of 30–50 days, like in observations. Nonlinear interaction between these ISO's and the annual cycle could give rise to some LF oscillations. The annually varying mean conditions act like a annually varying forcing for the ISO's. Could such nonlinear interactions give rise to a quasi biennial mode? To investigate this possibility, a simple nonlinear dynamical system model originally constructed by (Lorenz, 1984) to describe the general circulation of the atmosphere is used. The model is described by,

$$\begin{aligned} \dot{X} &= -Y^2 - Z^2 - aX + aF \\ \dot{Y} &= XY - bXZ - Y + G \\ \dot{Z} &= bXY + XZ - Z \end{aligned} \tag{1}$$

where X may be interpreted as the zonal mean component while Y and Z may be considered as two wave components. The terms XY and XZ represent amplification of the waves through interaction with the mean flow and happens at the expense of the mean flow represented by the terms $-Y^2$ and $-Z^2$ in Eq. 1. The terms $-$bXZ and bXY represent displacement of the waves by the mean flow. The linear terms represent mechanical and thermal damping. F is forcing for the zonally symmetric component like the solar forcing while G is forcing for the wave component like the land-ocean contrast. For fixed values of a, b and G, different values of the solar forcing F leads to solutions of the Eq.1 that varies from periodic solutions with different periods to chaotic or aperiodic solutions for some values of F. Our intention is that the temporal characteristics of fluctuations in the chaotic regime should be representative of that of the monsoon ISO. It is found that this could be achieved by scaling the time in Eq.(1) by a factor C($= 0.57$). The variables X, Y and Z, the parameter a and forcings F and G are also scaled appropriately. Using unscaled parameters, a $= 0.25$, b $= 4.0$,G $= 1.18$, for F $= 7.99$, the solution is quite aperiodic Fig. 10a,b with dominant periods between 30–70 days (Fig. 10c) in X and 10–20 days in Y (Fig. 10d). The spectrum of oscillations represented by the model is characteristic of that of the monsoon ISO. The forcing F is then made to have an annual cycle like the solar forcing namely, $F = F_0 + F_1 Cos(2\pi t/T)$, with period T as one year. Taking $F_0 = 5.7$ and $F_1 = 2.6$, the equations were integrated for more than 250 years. Time series for X and Y for a typical 10 year period and the corresponding spectra are shown in Fig. 11. It is seen that modulation of the intraseasonal oscillations by the annual cycle has resulted in a strong quasi-biennial oscillation in both X and Y. The system seems to go to one attractor in one year characterized by a low mean X and high mean Y, both with very low amplitude of fluctuations while it goes to another attractor

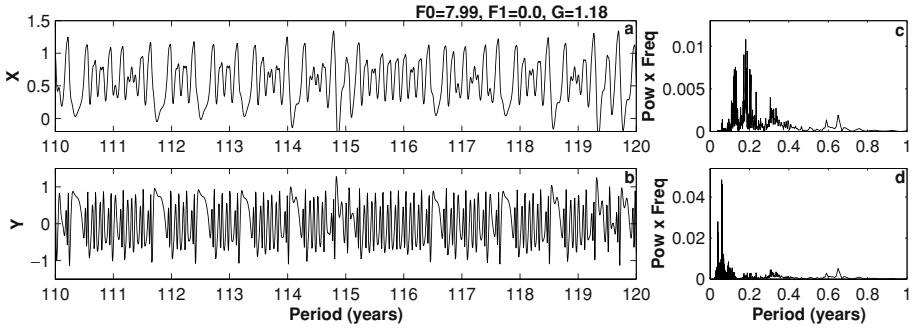


Figure 10. Time series of X and Y for constant forcing $F_0 = 7.99$, $F_1 = 0.0$ and G= 1.18 (left) for a typical 10 year period from a 200 year simulation with corresponding spectra (right). Power spectrum is plotted as power multiplied by frequency versus period.

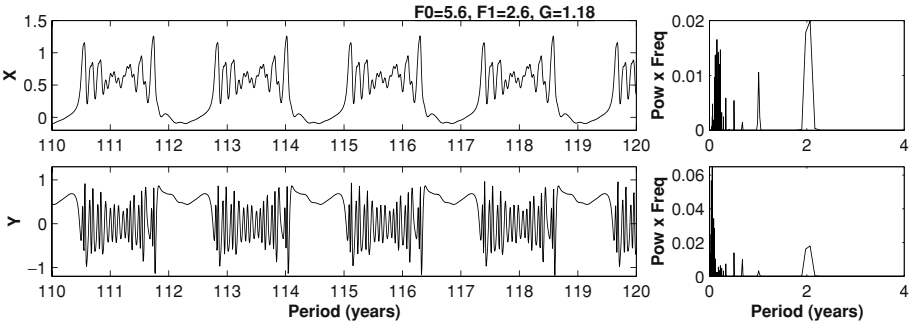


Figure 11. Same as Fig. 10 but for an annually varying forcing, $F_0 = 5.6$, $F_1 = 2.6$ and G = 1.18 that includes the chaotic regime shown in Fig. 10.

in the next year with high mean X and low mean Y, both with high amplitude oscillations. Thus, if the intraseasonal oscillations are vigorous and nonlinear and the annual cycle of the mean flow is strong, interaction between the ISO's and the annual cycle could result in an 'internal' quasi-biennial oscillation. The observed 'internal' quasi-biennial oscillation in the AGCM simulated climate may be due to such a mechanism.

5.2 Origin of 'internal' LF variability in observations

The mechanism proposed above for generating LF internal variability assumes that the nonlinear interactions amongst the ISO's is strong. Is it really strong for the tropical ISO's? The characteristic length scale associated with monsoon ISO's is approximately 10,000 km and typical velocity scale is $5 - 10$ m/s. For such systems, the non-dimensional equatorial Rossby number $R_0 = U/\beta L^2$, (with β being the meridional gradient of the Coriolis parameter) is much less than one indicating that advective nonlinearity for these systems is rather weak. Therefore, we have to look for other linear mechanisms through which the ISO's could give rise to interannual variability of the monsoon.

How could the monsoon ISO's give rise to interannual variability of the seasonal mean monsoon? We recall that the seasonal mean monsoon precipitation is characterized by a strong band of precipitation over the monsoon trough region and a secondary precipitation band in the equatorial eastern IO Fig. 2a. The mean flow at low level is characterized by the cross equatorial flow, the low-level jet and the large scale low level cyclonic vorticity or the monsoon trough Fig. 2a. The upper level mean flow also has similar large spatial scale characterized by the monsoon easterly jet (not shown). The ISO's have characteristic time scale of 10–20 days and 30–60 days. For the ISO's to influence the mean monsoon in a linear sense, the collective effect of the ISO fluctuations

within the season should be either to enhance or to weaken the large scale monsoon flow shown in Fig. 2a. The ISO's could do this *only if* the spatial scale of the ISO's has large scale structure similar to that of the seasonal mean flow. If the spatial scale of the ISO's is much smaller than that of the mean monsoon flow, the strengthening and weakening in different parts of the mean flow would result in no net strengthening or weakening of the mean flow. Even if the spatial structure of the ISO's is similar to that of the seasonal mean, they would not result in any net strengthening or weakening if the frequency of occurrence of the positive and negative phases of the ISO are the same. Thus, if the spatial scale of the ISO's is similar to that of the seasonal mean and if the frequency of occurrence of positive (active) and negative (break) phases are different in different years, the ISO's could result in an interannual variability of the monsoon.

To test this hypothesis, we first examine the spatial structure of the monsoon ISO. For this purpose a compositing technique is used. A reference time series is constructed with the 30–60 day filtered zonal wind anomalies at 850 hPa at 90E and 15N from June 1 to September 30 of each year for 20 years. The time series is normalized by its own standard deviation. Normalized index greater (lesser) than $+1$ (-1) represents strong (weak) ISO conditions. The strong and weak ISO conditions are also known as active and break phases of the monsoon. A composite (average) of all active and break days over the 20 summer seasons (1979–1998) for zonal and meridional wind anomalies is created. The composited vector wind anomalies for active and break conditions are shown in Fig. 12a,b together with associated relative vorticity anomalies. For the same dates, composites of OLR anomalies corresponding to active and break conditions are constructed based on the same period and plotted in Fig. 12c,d. It may be recalled that low OLR represents deep clouds. Thus, negative (positive) OLR anomaly represents increase (decrease) in convection. We note Fig. 12a,b that the spatial structure of the ISO wind anomalies has a large scale similar to that of the seasonal mean Fig. 2a and strengthens (weakens) the seasonal mean during active (break) phases. It may also be noted that circulation anomalies associated with active (break) condition strengthens (weakens) the cyclonic vorticity in the monsoon trough region and weakens (strengthens) the vorticity between 10S and 10N. Note that positive (negative) relative vorticity in the southern hemisphere represents anticyclonic (cyclonic) vorticity. The OLR anomalies Fig. 12c,d show a bimodal meridional structure with active (break) conditions characterized by enhancement of convection (precipitation) in the monsoon trough region and decrease (increase) in convection (precipitation) over the equatorial precipitation zone.

The similarity in spatial structure of the intraseasonal and interannual variability is further illustrated in Fig. 13 where we plot the dominant empirical orthogonal function (EOF) of intraseasonal wind anomalies at 850 hPa from

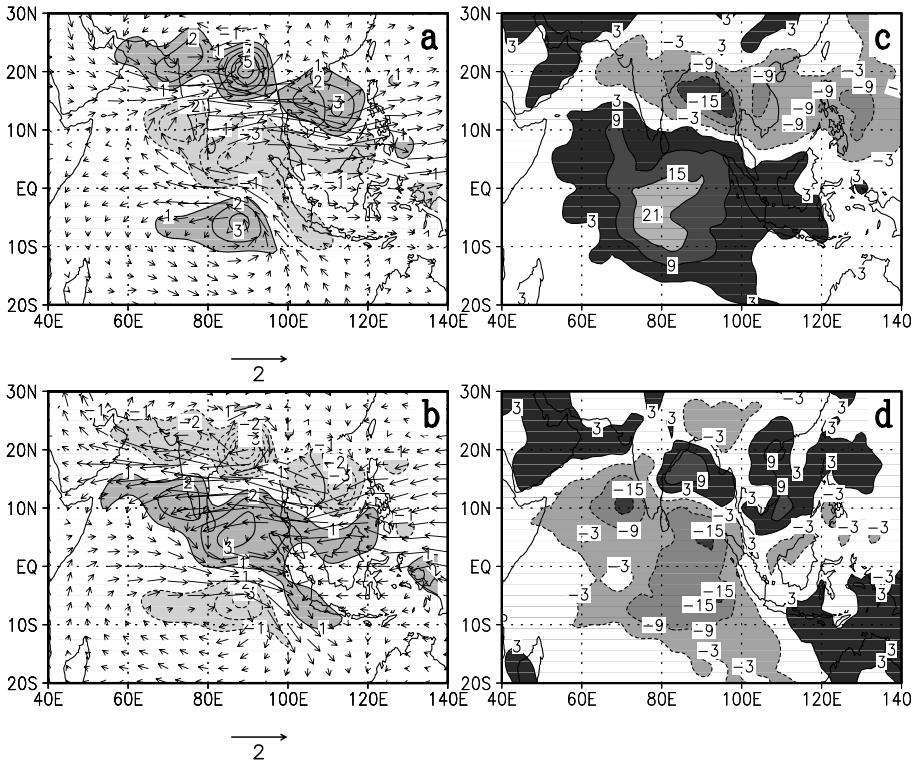


Figure 12. Mean structure of extreme phases of monsoon ISO. (a) Composite of all active phases in 20 summer seasons of winds at 850 hPa ($m\,s^{-1}$). Corresponding relative vorticity ($10^{-6}s^{-1}$) are shaded. (b) same as (a) but for all break cases. Corresponding composite of OLR anomalies ($W\,m^{-2}$) are shown in (c) and (d).

daily data for 20 summer seasons (1979–1998) together with the first EOF of seasonal mean winds (JJAS) for a period of 40 years (1959–1998). The dominant pattern of intraseasonal variability of wind anomalies at low level show high degree of similarity with the dominant pattern of interannual variability of winds at the same level.

Having established that the spatial pattern of intraseasonal oscillations is similar to that of the seasonal mean and its interannual variability, the difference in frequency of occurrence of active and break phases of the monsoon intraseasonal oscillations in different years is investigated. If the integrated influence of active conditions is larger than that of break conditions in a given season, the monsoon in that year would be stronger than normal and vice versa. Therefore, in a strong (weak) monsoon year, we expect probability density of occurrence of active (break) condition to be higher than its counterpart. Using OLR and circulation data between 1974 and 1997, the ISO's are described by

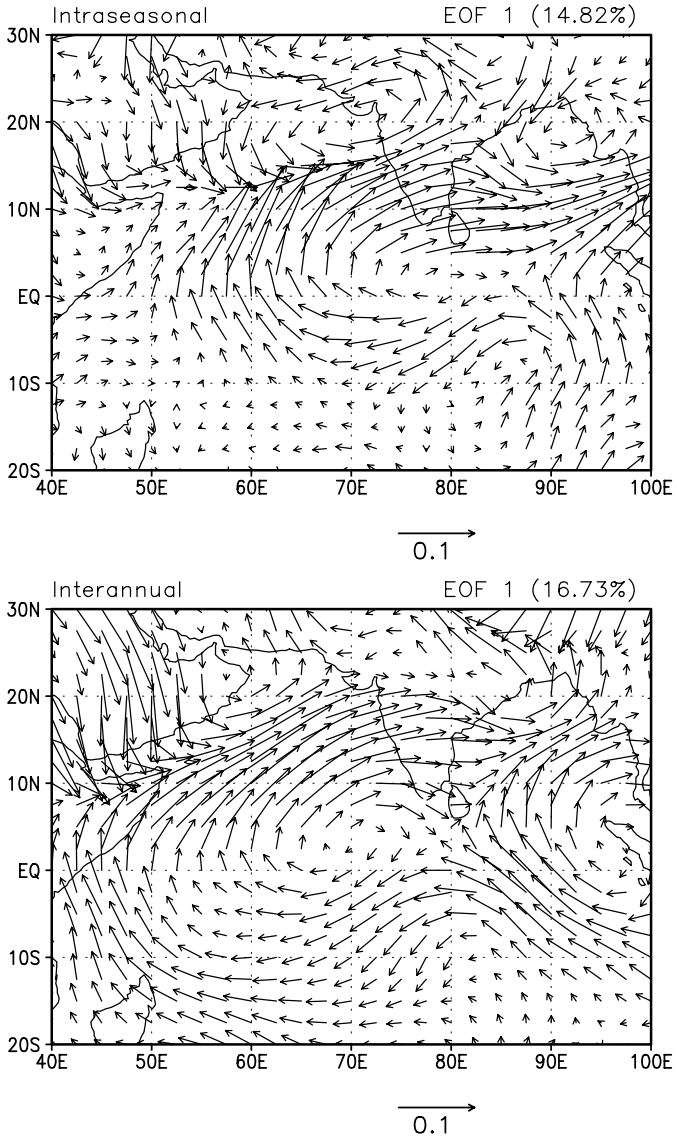


Figure 13. Similarity between the dominant mode of intraseasonal variability and interannual variability of seasonal mean. (Top) The dominant empirical orthogonal function (EOF) of 10–90 day filtered daily 850 hPa winds for 20 summer seasons (June 1 to September 30). (Bottom) The dominant EOF of interannual variability of the seasonal mean winds at 850 hPa based on 40 summer seasons. Unit of the EOF's is arbitrary.

the phase space mapped by the first two combined EOF's of 850 hPa winds and OLR. Six strong monsoon years (1975, 1978, 1983, 1988, 1990, 1994) and six weak monsoon years (1974, 1979, 1982, 1985, 1986, 1987) are selected based on rainfall over the Indian continent being more than 0.5 s.d above normal or below normal. The two dimensional probability density function (pdf) in the phase space described by the first two principal components (PC's) is estimated using a Gaussian kernel estimator (Kimoto and Ghil, 1993) and shown in Fig. 14 for the strong monsoon years, the weak monsoon years and all the years taken together. When all the years are taken together, the pdf seems to be nearly a Gaussian. However, for both strong and weak monsoon years, the pdf is non-Gaussian. To test the statistical significance of the maxima of the calculated pdf's, 1000 random sets of PC1 and PC2 time series were created having the same variance and lag–1 autocorrelation and pdf's were again created. The shading in Fig. 14a,b indicate regions where the observed pdf is significantly larger than the random ones with 90% confidence level. Thus, the maxima in Fig. 14a,b appear to be statistically significant. The spatial pattern for the most probable state is reconstructed by noting the values of PC1 and PC2 from Fig. 14 and using the corresponding EOF patterns and is shown in Fig. 15 for all the three cases. The most probable vorticity and OLR patterns in strong monsoon years are that of an active condition Fig. 12a,c while that during weak monsoon years corresponds to that of a break condition (Fig. 12b,d). However, if all years are combined, transition from active to break (or break to active) seems to be the dominant pattern (Fig. 15c). Thus, frequency of occurrence of active (break) phases in a particular monsoon season seems to modulate the intensity of seasonal mean monsoon rainfall.

How do the changes in the frequency of occurrence of phases of monsoon ISO's modulate the seasonal mean rainfall? The primary rain producing synoptic systems during the monsoon season are the lows and depressions. The lows and depressions are essentially shear instability energized by latent heat released due to convection. As we have noted in Fig. 12a,b, the monsoon ISO's intensifies (weakens) the mean monsoon flow during active (break) phase and strengthens (weakens) the cyclonic vorticity in the monsoon trough. The enhancement of meridional shear during active condition enhances the potential for instability and enhancement of low level cyclonic vorticity enhances frictional convergence of moisture and facilitates organized convection. Both these processes increases the potential for cyclogenesis. Similarly, modulation of the large scale flow by the ISO's during break conditions inhibits cyclogenesis. Thus, the ISO's could cluster the synoptic disturbances in space and time.

To investigate whether the ISO's indeed result in clustering of the synoptic disturbances, genesis dates and tracks of lows and depressions during June-September during a period of 40 years (1954–1993) over the Indian monsoon region were collected. Lows and depressions are collectively called low pressure

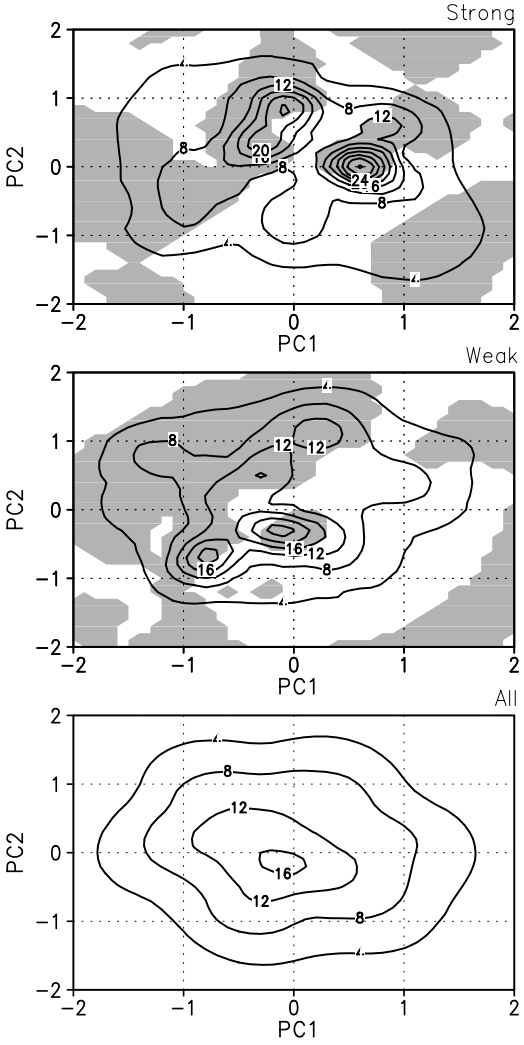


Figure 14. Two dimensional pdf's of ISO state vector represented by the two dominant combined EOF's of relative vorticity at 850 hPa and OLR. The EOFs are calculated with 10–90 filtered fields between June 1 and September 30 for 6 strong monsoon years, 6 weak monsoon years and all 23 years (1974–1997) and pdf's are calculated from the two principal component (PC) time series. The pdf estimates are multiplied by a factor of 100. The shading represents regions where the pdf estimates are statistically significant with 95% confidence level. The origin of the plots represent a very weak state representing transition from active to break condition or vice versa.

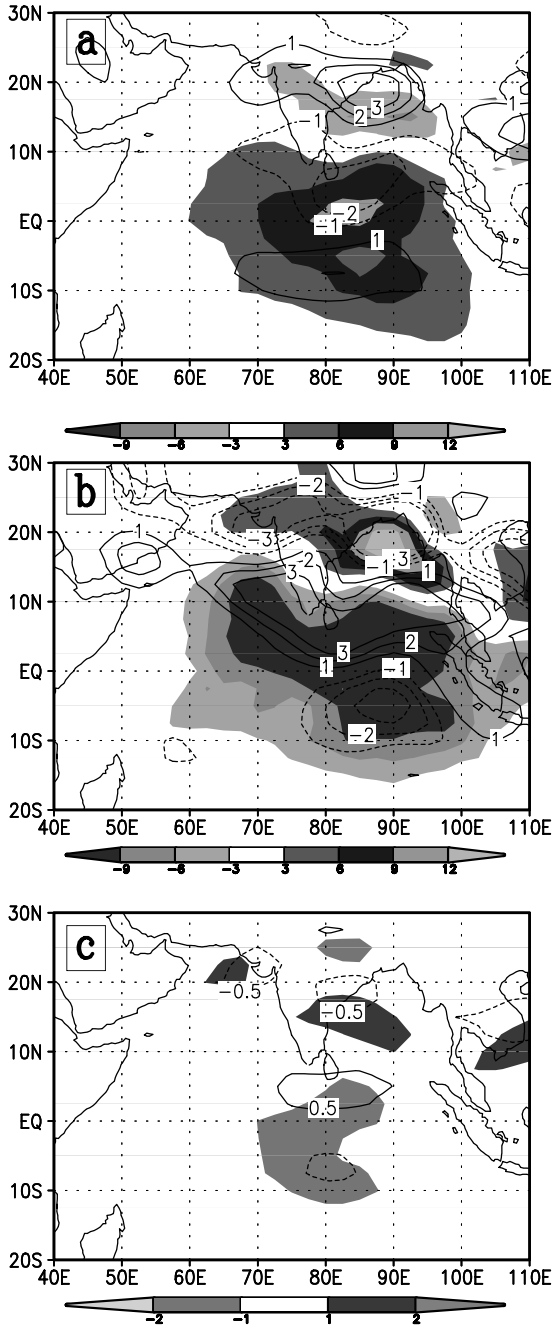


Figure 15. Spatial structure associated with the most probable patterns of intraseasonal variability during (a) strong monsoon years, (b) weak monsoon years and (c) all years combined. The vorticity pattern is shown in contours ($10^{-6}s^{-1}$) while the OLR pattern is shown in shading ($W\,m^{-2}$) .

systems (LPS). The data for the first 30 years (1954–1983) were carefully collected by Mooley and Shukla (1989) from Daily Weather Reports and annual summary of tracks of storms and depressions published by Indian Meteorology Department (IMD). The data for the last 10 years were collected by us from the summary of tracks of storms and depressions published every year by the India Meteorological Department. In order to examine the clustering of the synoptic disturbances by the ISO's, we need to characterize the ISO quantitatively. We noted earlier that the the monsoon ISO's are closely associated with fluctuations of relative vorticity at 850 hPa (Fig. 12a,b). Therefore, we define an index of monsoon ISO activity (MISI) as 10–90 day filtered relative vorticity at 850 hPa averaged over 80E-95E and 12N-22N (Goswami et al., 2003). The index is normalized by its own s.d. Normalized MISI $> +1$ represents active condition while MISI < -1 represents break conditions. The frequency distribution of LPS as a function of the phase of the ISO is obtained by putting the genesis dates of all the LPS during the 40 year period into bins of MISI of size 0.25 (Fig. 16, top). The frequency distribution is clearly skewed towards the positive MISI side with more than twice as many genesis occurring for MISI > 0 compared to those occurring for MISI < 0. In particular, birth of a LPS is 3.5 time more likely in the active phase of the ISO (MISI $> +1$) than in a break phase (MISI < -1). The tracks of LPS occurring during active and break phases are plotted in the middle and bottom panel of Fig. 16. It is clear that the LPS is not only clustered in in time (Fig. 16, top), they are highly clustered in space as well. Therefore, increased frequency of occurrence of active condition in a particular year results in significantly enhanced number of LPS formed in that year that are spatially largely confined to the monsoon trough area. The collective result of this is enhanced seasonal mean rainfall over Indian continent and a stronger than normal monsoon.

6. Conclusions

The physical basis for predictability of climate beyond the limit on deterministic predictability of weather (approximately two weeks) has been well established (Charney and Shukla, 1981; Shukla, 1981) based on realization that the climate is governed by slowly varying forcing either external or arising from slow coupled ocean-atmosphere interactions. However, the atmosphere can generate certain amount of internal LF variability through a number of internal feedbacks that would remain unpredictable. The predictability of climate would depend on relative contribution of internal and external LF variability to the total interannual variability. Advances in climate modeling has demonstrated that tropical climate has much higher predictability compared to extra-tropical climate. However, the Indian summer monsoon within the tropics remains to be the most difficult system to simulate and predict. In this study,

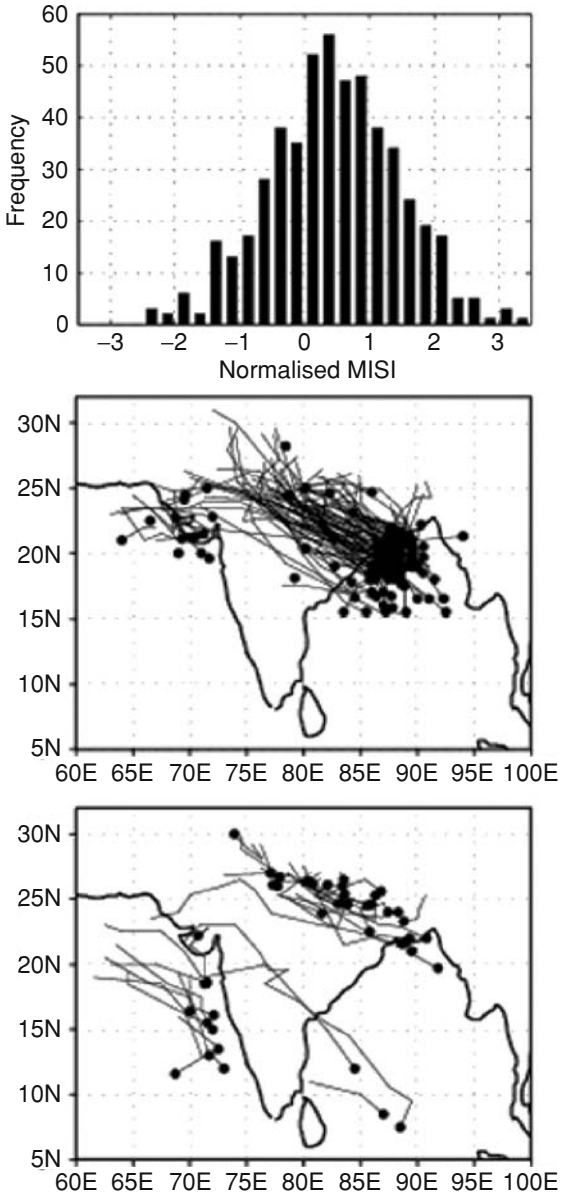


Figure 16. Clustering of synoptic activity by the monsoon ISO. (Top) Frequency distribution of low pressure systems (LPS, lows and depressions) as a function of the normalized monsoon intraseasonal index (MISI) based on 40 years of data on LPS genesis and corresponding MISI time series. (Middle) Tracks of LPS during active phases (MISI $> +1$) and (bottom) tracks of LPS during break phases (MISI < -1).

an attempt has been made to unravel the underlying reasons responsible for limited predictability of Indian summer monsoon climate.

In order to quantify the problem, an estimate of predictability of Indian summer monsoon is made using an atmospheric general circulation model (AGCM) as well as from about 40 years of daily circulation data. Having devised methods to estimate the 'internal' interannual variability in the AGCM as well as from observations, the ratio between total and 'internal' interannual variability is found to be less than 2 over the Indian monsoon region in the AGCM simulations as well as in observations. This indicates that more than 50% of interannual variability of the Indian summer monsoon is governed by 'internal' dynamics and hence are unpredictable.

The origin of the 'internal' variability in the AGCM and in observations is then investigated. It is shown that the monsoon ISO's with time scales between 10–70 days play a seminal role in generating the observed LF 'internal' variability through multi—scale interactions with synoptic disturbances on one hand and the annual cycle on the other. The nature of these scale interactions leading to LF 'internal' variability is illustrated. It is shown that a modulation of nonlinearly interacting ISO's by the annual cycle of forcing can give rise to a significant quasi-biennial 'internal' oscillation. The possibility of such a mechanism to be responsible for the quasi-biennial oscillation simulated the AGCM is indicated. However, it is pointed out that nonlinearity associated with the observed monsoon ISO's may be rather weak. Therefore, a linear mechanism through which ISO's could influence the seasonal mean and its interannual variability is sought and identified. The mechanism works as follows. Based on an analysis of more than 20 years of daily data, it is first established that the spatial structure of two extreme phases of the monsoon ISO, namely the active and break phases, is similar to that of the seasonal mean, strengthening the mean in one phase while weakening it in the other. It is further shown that the spatial structures of the dominant intraseasonal mode and interannual mode of monsoon variability are very similar. Hence, a higher than normal frequency of occurrence of active (break) phases in a season could lead to a stronger (weaker) than normal monsoon. This is then shown that strong (weak) Indian monsoons are indeed associated with higher probability density of occurrence of active (break) condition, establishing that to a large extent the interannual variability of Indian monsoon is controlled by frequency of occurrence of active/break cycles. It is further shown that the monsoon ISO's also cause strong spatial and temporal clustering of the synoptic disturbances. Monsoon ISO's influence the seasonal mean rainfall through changes in frequency distribution active or break conditions and by producing space-time clustering of lows and depressions.

The monsoon ISO's owe their origin to feedbacks between organized convection and large scale dynamics (Webster, 1983; Goswami and Shukla, 1984;

Nanjundiah et al., 1992; Chatterjee and Goswami, 2004). Thus, they are essentially of 'internal' atmospheric origin. The fraction of interannual variability of the Indian monsoon accounted for by this process is therefore, sensitive to initial condition and hence unpredictable. The amplitude of 'externally' forced variability being rather weak over Indian monsoon region while that of the 'internal' variability generated by the ISO's is relatively large limits the predictability of the Indian summer monsoon. This fundamental reason will continue to make the long range prediction of seasonal mean monsoon a difficult and challenging problem. The challenge will be to find innovative method of bringing out the small predictable signal from the background of unpredictable noise of comparable amplitude.

Part of the work presented here was done when one of the authors (BNG) was a visitor at the Geophysical Fluid Dynamics Laboratory, Princeton University. BNG is greatful to Department of Ocean Development, New Delhi for financial support. Thanks are due to R Vinay and Prince K Xavier for technical help.

References

Ajaya Mohan, R. S., and B. N. Goswami, 2003: Potential predictability of the Asian summer monsoon on monthly and seasonal time scales. *Met. Atmos. Phys.*, DOI10.1007/s00703-002-0576-4.

Blanford, H. F., 1884: On the connection of the Himalaya snowfall with dry winds and seasons of drought in India. *Proc. Roy. Soc. London*, **37**, 3–22.

Broccoli, A. J., and S. Manabe, 1992: The effects of orography on midlatitude northern hemisphere dry climates. *J. Climate*, **5**, 1181–1201.

Charney, J. G., and J. Shukla, 1981: Predictability of monsoons. Monsoon Dynamics, J. Lighthill and R. P. Pearce, Eds., Cambridge University Press, pp. 99–108.

Chatterjee, P., and B. N. Goswami, 2004: Sturcture, Genesis and Scale selection of the tropical quasi-biweekly mode. *Q. J. R. Meteorol. Soc.*, (in press).

Gadgil, S., 2003: The Indian monsoon and its variability. *Ann. Rev. Earth Planet. Sci*, **31**, 429–467.

Gadgil, S., and S. Sajani, 1998: Monsoon precipitation in the AMIP runs. *Climate Dyn.*, **14**, 659–689.

Gordon, C. T., and W. Stern, 1982: A description of the GFDL global spec-tral model. *Mon. Wea. Rev.*, **110**, 625–644.

Goswami, B. N., 1998: Interannual variations of Indian summer monsoon in a GCM: External conditions versus internal feedbacks. *J. Climate*, **11**, 501–522.

Goswami, B. N., and R. S. Ajayamohan, 2001a: Intraseasonal oscillations and interannual variability of the Indian summer monsoon. *J. Climate*, **14**, 1180–1198.

Goswami, B. N., and R. S. Ajayamohan, 2001b: Intra-seasonal oscillations and predictability of the Indian summer monsoon. *Proc. Ind. Nat. Acad. Sci.*, **67**, 369–384.

Goswami, B. N., and J. Shukla, 1984: Quasi-periodic oscillations in a symmetric general circulation model. *J. Atmos. Sci.*, **41**, 20–37.

Goswami, B. N., D. Sengupta, and G. Sureshkumar, 1998: Intraseasonal oscillations and interannual variability of surface winds over the Indian monsoon region. *Proc. Ind. Acad. Sci. (Earth & Planetary Sciences)*, **107**, 45–64.

Goswami, B. N., R. S. Ajaya Mohan, P. K. Xavier, and D. Sengupta, 2003: Clustering of low pressure systems during the Indian summer monsoon by intraseasonal oscillations. *Geophys. Res. Lett.*, **30**, 8, doi:10.1029/2002GL016,734.

Goswami, P., and Srividya, 1996: A novel neural network design for long-range prediction of rainfall pattern. *Curr. Sci.*, **70**, 447–457.

Gowarikar, V., V. Thapliyal, R. P. Sarker, G. S. Mandel, and D. R. Sikka, 1989: Parametric and power regression models: new approach to long range forecasting of monsoon rain in India. *Mausam*, **40**, 125–130.

Hahn, D., and J. Shukla, 1976: An apparent relationship between eurasian snow cover and Indian monsoon rainfall. *J. Atmos. Sci.*, **33**, 2461–2462.

Kalnay, E., et al., 1996: The NCEP/NCAR 40-year reanalysis project. *Bull. Amer. Meteor. Soc.*, **77**, 437–471.

Kimoto, M., and M. Ghil, 1993: Multiple flow regimes in the northern hemisphere winter. Part I: Methodology and hemispheric regimes. *J. Atmos. Sci.*, **50**, 2625–2643.

Kistler, R., et al., 2001: The NCEP/NCAR 50-year reanalysis: Monthly means CD-ROM and documentation. *Bull. Amer. Meteor. Soc.*, **82**, 247–267.

Kripalani, R. H., S. V. Singh, B. N. Mandal, and V. Thapliyal, 1996: Empirical study on NIMBUS-7 snow mass and Indian summer monsoon rainfall. *Int. J. Climatol.*, **16**, 23–34.

Krishnamurthy, V., and J. Shukla, 2001: Observed and model simulated interannual variability of the Indian monsoon. *Mausam*, **52**, 133–150.

Krishnamurti, T. N., and P. Ardunay, 1980: The 10 to 20 day westward propagating mode and breaks in the monsoons. *Tellus*, **32**, 15–26.

Krishnamurti, T. N., and H. N. Bhalme, 1976: Oscillations of monsoon system. Part I: Observational aspects. *J. Atmos. Sci.*, **45**, 1937–1954.

Lau, N. C., 1985: Modelling the seasonal dependence of atmospheric response to observed elnino in 1962–76. *Mon. Wea. Rev.*, **113**, 1970–1996.

Liebmann, B., and C. A. Smith, 1996: Description of a complete (interpolated) outgoing longwave radiation dataset. *Bull. Amer. Meteor. Soc*., **77**, 1275–1277.

Lorenz, E. N., 1984: Irregularity: a fundamental property of the atmosphere. *Tellus*, **36A**, 98–110.

Meehl, G. A., 1994: Coupled land-ocean-atmosphere processes and the biennial mechanism in the south Asian monsoon region. *Proc. Int. Conf. on Monsoon Variability and Prediction, Trieste, Italy, WMO*, pp. 637–644.

Meehl, G. A., and J. M. Arblaster, 2002: The tropospheric biennial oscillation and Asian-Australian monsoon rainfall. *J. Climate*, **15**, 722–744.

Mooley, D. A., and J. Shukla, 1989: Main features of the westward-moving low pressure systems which form over the Indian region during the summer monsoon season and their relation to the monsoon rainfall. *Mausam*, **40**, 137–152.

Nanjundiah, R. S., J. Srinivasan, and S. Gadgil, 1992: Intraseasonal variation of the Indian summer monsoon. Part II: Theoretical aspects. *J. Meteor. Soc. Japan*, **70**, 529–550.

Reynolds, R. W., and T. M. Smith, 1994: Improved global sea surface temperature analyses using optimum interpolation. *J. Climate*, **7**, 929–948.

Sahai, A. K., A. M. Grimm, V. Satyan, and G. B. Pant, 2003: Long-lead prediction of Indian summer monsoon rainfall from global sst evolution. *Climate Dyn.*, **20**, 855–863.

Saji, N. H., and B. N. Goswami, 1997: An intercomparison of seasonal cycle of tropical surface stress simulated by 17 AMIP GCMs. *Climate Dyn.*, **13**, 561–585.

Saji, N. H., B. N. Goswami, P. Vinayachandran, and T. Yamagata, 1999: A dipole mode in the tropical Indian ocean. *Nature*, **401**, 360–363.

Shukla, J., 1981: Dynamical predictability of monthly means. *J. Atmos. Sci.*, **38**, 2547–2572.

Shukla, J., 1987: Interannual variability of monsoon. Monsoons, J. S. Fein and P. L. Stephens, Eds., Wiley and Sons, pp. 399–464.

Shukla, J., 1998: Predictability in the midst of chaos: a scientific basis for climate forecasting. *Science*, **282**, 728–731.

Sikka, D. R., and S. Gadgil, 1980: On the maximum cloud zone and the itcz over Indian longitude during southwest monsoon. *Mon. Wea. Rev.*, **108**, 1840–1853.

Sperber, K. R., and T. N. Palmer, 1996: Interannual tropical rainfall variability in general circulation model simulations associated with atmospheric model intercomparison project. *J. Climate*, **9**, 2727–2750.

Sperber, K. R., et al., 2001: Dynamical seasonal predictability of the Asian summer monsoon. *Mon. Wea. Rev.*, **129**, 2226–2248.

Walker, G. T., 1923: Correlation in seasonal variations of weather, viii, a preliminary study of world weather. *Mem. Indian Meteorol. Dept*, **24**, 75–131.

Walker, G. T., 1924: Correlation in seasonal variations of weather, iv, a further study of world weather. *Mem. Indian Meteorol. Dept*, **24**, 275–332.

Webster, P. J., 1983: Mechanism of monsoon low-frequency variability: surface hydrological effects. *J. Atmos. Sci.*, **40**, 2110–2124.

Webster, P. J., V. O. Magana, T. N. Palmer, J. Shuka, R. T. Tomas, M. Yanai, and T. Yasunari, 1998: Monsoons: Processes, predictability and the prospects of prediction. *J. Geophys. Res.*, **103(C7)**, 14,451–14,510.

Xie, P., and P. A. Arkin, 1996: Analyses of global monthly precipitation using guage observations, satellite estimates and numerical predictions. *J. Climate*, **9**, 840–858.

Yasunari, T., 1979: Cloudiness fluctuation associated with the northern hemisphere summer monsoon. *J. Meteor. Soc. Japan*, **57**, 227–242.

Yasunari, T., 1981: Structure of an Indian summer monsoon system with around 40-day period. *J. Meteor. Soc. Japan*, **59**, 336–354.

Astrophysics and Space Science Library

Volume 324: ***Kristian Birkeland – The First Space Scientist***, by A. Egeland, W.J. Burke.
Hardbound ISBN 1-4020-3293-5, April 2005

Volume 323: ***Recollections of Tucson Operations***, by M.A. Gordon.
Hardbound ISBN 1-4020-3235-8, December 2004

Volume 322: ***Light Pollution Handbook***, by K. Narisada, D. Schreuder
Hardbound ISBN 1-4020-2665-X, November 2004

Volume 321: ***Nonequilibrium Phenomena in Plasmas***, edited by A.S. Shrama, P.K. Kaw.
Hardbound ISBN 1-4020-3108-4, December 2004

Volume 320: ***Solar Magnetic Phenomena***, edited by A. Hanslmeier, A. Veronig, M. Messerotti.
Hardbound ISBN 1-4020-2961-6, December 2004

Volume 319: ***Penetrating Bars through Masks of Cosmic Dust***, edited by D.L. Block, I. Puerari, K.C. Freeman, R. Groess, E.K. Block.
Hardbound ISBN 1-4020-2861-X, December 2004

Volume 318: ***Transfer of Polarized light in Planetary Atmospheres***, by J.W. Hovenier, J.W. Domke, C. van der Mee.
Hardbound ISBN 1-4020-2855-5. Softcover ISBN 1-4020-2889-X, November 2004

Volume 317: ***The Sun and the Heliosphere as an Integrated System***,
edited by G. Poletto, S.T. Suess.
Hardbound ISBN 1-4020-2830-X, November 2004

Volume 316: ***Civic Astronomy – Albany's Dudley Observatory***, *1852–2002*, by G. Wise
Hardbound ISBN 1-4020-2677-3, October 2004

Volume 315: ***How does the Galaxy Work – A Galactic Tertulia with Don Cox and Ron Reynolds***, edited by E. J. Alfaro, E. Pérez, J. Franco
Hardbound ISBN 1-4020-2619-6, September 2004

Volume 314: ***Solar and Space Weather Radiophysics – Current Status and Future Developments***, edited by D.E. Gary and C.U. Keller
Hardbound ISBN 1-4020-2813-X, August 2004

Volume 313: ***Adventures in Order and Chaos***, by G. Contopoulos.
Hardbound ISBN 1-4020-3039-8, January 2005

Volume 312: ***High-Velocity Clouds***, edited by H. van Woerden, U. Schwarz, B. Wakker
Hardbound ISBN 1-4020-2813-X, September 2004

Volume 311: ***The New ROSETTA Targets – Observations, Simulations and Instrument Performances***, edited by L. Colangeli, E. Mazzotta Epifani, P. Palumbo
Hardbound ISBN 1-4020-2572-6, September 2004

Volume 310: ***Organizations and Strategies in Astronomy 5***, edited by A. Heck
Hardbound ISBN 1-4020-2570-X, September 2004

Volume 309: ***Soft X-ray Emission from Clusters of Galaxies and Related Phenomena***, edited by R. Lieu and J. Mittaz
Hardbound ISBN 1-4020-2563-7, September 2004

Volume 308: ***Supermassive Black Holes in the Distant Universe***, edited by A.J. Barger
Hardbound ISBN 1-4020-2470-3, August 2004

Volume 307: ***Polarization in Spectral Lines***, by E. Landi Degl'Innocenti and M. Landolfi
Hardbound ISBN 1-4020-2414-2, August 2004

Volume 306: ***Polytropes – Applications in Astrophysics and Related Fields***, by G.P. Horedt
Hardbound ISBN 1-4020-2350-2, September 2004

Volume 305: ***Astrobiology: Future Perspectives***, edited by P. Ehrenfreund, W.M. Irvine, T. Owen, L. Becker, J. Blank, J.R. Brucato, L. Colangeli, S. Derenne, A. Dutrey, D. Despois, A. Lazcano, F. Robert
Hardbound ISBN 1-4020-2304-9, July 2004
Paperback ISBN 1-4020-2587-4, July 2004

Volume 304: ***Cosmic Gammy-ray Sources***, edited by K.S. Cheng and G.E. Romero
Hardbound ISBN 1-4020-2255-7, September 2004

Volume 303: ***Cosmic rays in the Earth's Atmosphere and Underground***, by L.I, Dorman
Hardbound ISBN 1-4020-2071-6, August 2004

Volume 302: ***Stellar Collapse***, edited by Chris L. Fryer
Hardbound, ISBN 1-4020-1992-0, April 2004

Volume 301: ***Multiwavelength Cosmology***, edited by Manolis Plionis
Hardbound, ISBN 1-4020-1971-8, March 2004

Volume 300: ***Scientific Detectors for Astronomy***, edited by Paola Amico, James W. Beletic, Jenna E. Beletic
Hardbound, ISBN 1-4020-1788-X, February 2004

Volume 299: ***Open Issues in Local Star Fomation***, edited by Jacques Lépine, Jane Gregorio-Hetem
Hardbound, ISBN 1-4020-1755-3, December 2003

Volume 298: ***Stellar Astrophysics – A Tribute to Helmut A. Abt***, edited by K.S. Cheng, Kam Ching Leung, T.P. Li
Hardbound, ISBN 1-4020-1683-2, November 2003

Volume 297: ***Radiation Hazard in Space***, by Leonty I. Miroshnichenko
Hardbound, ISBN 1-4020-1538-0, September 2003

Volume 296: ***Organizations and Strategies in Astronomy, volume 4***, edited by André Heck
Hardbound, ISBN 1-4020-1526-7, October 2003

Volume 295: ***Integrable Problems of Celestial Mechanics in Spaces of Constant Curvature***, by T.G. Vozmischeva
Hardbound, ISBN 1-4020-1521-6, October 2003

Volume 294: ***An Introduction to Plasma Astrophysics and Magnetohydrodynamics***, by Marcel Goossens
Hardbound, ISBN 1-4020-1429-5, August 2003
Paperback, ISBN 1-4020-1433-3, August 2003

Volume 293: ***Physics of the Solar System***, by Bruno Bertotti, Paolo Farinella, David Vokrouhlický
Hardbound, ISBN 1-4020-1428-7, August 2003
Paperback, ISBN 1-4020-1509-7, August 2003

Volume 292: ***Whatever Shines Should Be Observed***, by Susan M.P. McKenna-Lawlor
Hardbound, ISBN 1-4020-1424-4, September 2003

Volume 291: ***Dynamical Systems and Cosmology***, by Alan Coley
Hardbound, ISBN 1-4020-1403-1, November 2003

Volume 290: ***Astronomy Communication***, edited by André Heck, Claus Madsen
Hardbound, ISBN 1-4020-1345-0, July 2003

Volume 287/8/9: ***The Future of Small Telescopes in the New Millennium***, edited by Terry D. Oswalt
Hardbound Set only of 3 volumes, ISBN 1-4020-0951-8, July 2003

Volume 286: ***Searching the Heavens and the Earth: The History of Jesuit Observatories***, by Agustín Udías
Hardbound, ISBN 1-4020-1189-X, October 2003

Volume 285: ***Information Handling in Astronomy – Historical Vistas***, edited by André Heck
Hardbound, ISBN 1-4020-1178-4, March 2003

Volume 284: ***Light Pollution: The Global View***, edited by Hugo E. Schwarz
Hardbound, ISBN 1-4020-1174-1, April 2003

Volume 283: ***Mass-Losing Pulsating Stars and Their Circumstellar Matter***, edited by Y. Nakada, M. Honma, M. Seki
Hardbound, ISBN 1-4020-1162-8, March 2003

Volume 282: ***Radio Recombination Lines***, by M.A. Gordon, R.L. Sorochenko
Hardbound, ISBN 1-4020-1016-8, November 2002

Volume 281: ***The IGM/Galaxy Connection***, edited by Jessica L. Rosenberg, Mary E. Putman
Hardbound, ISBN 1-4020-1289-6, April 2003

Volume 280: ***Organizations and Strategies in Astronomy III***, edited by André Heck
Hardbound, ISBN 1-4020-0812-0, September 2002

Volume 279: ***Plasma Astrophysics, Second Edition***, by Arnold O. Benz
Hardbound, ISBN 1-4020-0695-0, July 2002

Volume 278: ***Exploring the Secrets of the Aurora***, by Syun-Ichi Akasofu
Hardbound, ISBN 1-4020-0685-3, August 2002

Volume 277: ***The Sun and Space Weather***, by Arnold Hanslmeier
Hardbound, ISBN 1-4020-0684-5, July 2002

Volume 276: ***Modern Theoretical and Observational Cosmology***, edited by Manolis Plionis, Spiros Cotsakis
Hardbound, ISBN 1-4020-0808-2, September 2002

Volume 275: ***History of Oriental Astronomy***, edited by S.M. Razaullah Ansari
Hardbound, ISBN 1-4020-0657-8, December 2002

Volume 274: ***New Quests in Stellar Astrophysics: The Link Between Stars and Cosmology***, edited by Miguel Chávez, Alessandro Bressan, Alberto Buzzoni, Divakara Mayya
Hardbound, ISBN 1-4020-0644-6, June 2002

Volume 273: ***Lunar Gravimetry***, by Rune Floberghagen
Hardbound, ISBN 1-4020-0544-X, May 2002

Volume 272: ***Merging Processes in Galaxy Clusters***, edited by L. Feretti, I.M. Gioia, G. Giovannini
Hardbound, ISBN 1-4020-0531-8, May 2002

Volume 271: ***Astronomy-inspired Atomic and Molecular Physics***, by A.R.P. Rau
Hardbound, ISBN 1-4020-0467-2, March 2002

Volume 270: ***Dayside and Polar Cap Aurora***, by Per Even Sandholt, Herbert C. Carlson, Alv Egeland
Hardbound, ISBN 1-4020-0447-8, July 2002

Volume 269: ***Mechanics of Turbulence of Multicomponent Gases***, by Mikhail Ya. Marov, Aleksander V. Kolesnichenko
Hardbound, ISBN 1-4020-0103-7, December 2001

Volume 268: ***Multielement System Design in Astronomy and Radio Science***,
by Lazarus E. Kopilovich, Leonid G. Sodin
Hardbound, ISBN 1-4020-0069-3, November 2001

Volume 267: ***The Nature of Unidentified Galactic High-Energy Gamma-Ray Sources***,
edited by Alberto Carramiñana, Olaf Reimer, David J. Thompson
Hardbound, ISBN 1-4020-0010-3, October 2001

Volume 266: ***Organizations and Strategies in Astronomy II***, edited by André Heck
Hardbound, ISBN 0-7923-7172-0, October 2001

Volume 265: ***Post-AGB Objects as a Phase of Stellar Evolution***,
edited by R. Szczerba, S.K. Górny
Hardbound, ISBN 0-7923-7145-3, July 2001

Volume 264: ***The Influence of Binaries on Stellar Population Studies***,
edited by Dany Vanbeveren
Hardbound, ISBN 0-7923-7104-6, July 2001

Volume 262: ***Whistler Phenomena – Short Impulse Propagation***, by Csaba Ferencz,
Orsolya E. Ferencz, Dániel Hamar, János Lichtenberger
Hardbound, ISBN 0-7923-6995-5, June 2001

Volume 261: ***Collisional Processes in the Solar System***,
edited by Mikhail Ya. Marov, Hans Rickman
Hardbound, ISBN 0-7923-6946-7, May 2001

Volume 260: ***Solar Cosmic Rays***, by Leonty I. Miroshnichenko
Hardbound, ISBN 0-7923-6928-9, May 2001

Volume 259: ***The Dynamic Sun***, edited by Arnold Hanslmeier, Mauro Messerotti,
Astrid Veronig
Hardbound, ISBN 0-7923-6915-7, May 2001

Volume 258: ***Electrohydrodynamics in Dusty and Dirty Plasmas-Gravito-Electrodynamics and EHD***, by Hiroshi Kikuchi
Hardbound, ISBN 0-7923-6822-3, June 2001

Volume 257: ***Stellar Pulsation – Nonlinear Studies***, edited by Mine Takeuti, Dimitar D.
Sasselov
Hardbound, ISBN 0-7923-6818-5, March 2001

Volume 256: ***Organizations and Strategies in Astronomy***, edited by André Heck
Hardbound, ISBN 0-7923-6671-9, November 2000

Volume 255: ***The Evolution of the Milky Way-Stars versus Clusters***, edited by Francesca
Matteucci, Franco Giovannelli
Hardbound, ISBN 0-7923-6679-4, January 2001

Volume 254: ***Stellar Astrophysics***, edited by K.S. Cheng, Hoi Fung Chau, Kwing Lam Chan, Kam Ching Leung
Hardbound, ISBN 0-7923-6659-X, November 2000

Volume 253: ***The Chemical Evolution of the Galaxy***, by Francesca Matteucci
Paperback, ISBN 1-4020-1652-2, October 2003
Hardbound, ISBN 0-7923-6552-6, June 2001

Volume 252: ***Optical Detectors for Astronomy II***, edited by Paola Amico, James W. Beletic
Hardbound, ISBN 0-7923-6536-4, December 2000

Volume 251: ***Cosmic Plasma Physics***, by Boris V. Somov
Hardbound, ISBN 0-7923-6512-7, September 2000

Volume 250: ***Information Handling in Astronomy***, edited by André Heck
Hardbound, ISBN 0-7923-6494-5, October 2000

Volume 249: ***The Neutral Upper Atmosphere***, by S.N. Ghosh
Hardbound, ISBN 0-7923-6434-1, July 2002

Volume 247: ***Large Scale Structure Formation***, edited by Reza Mansouri, Robert Brandenberger
Hardbound, ISBN 0-7923-6411-2, August 2000

Volume 246: ***The Legacy of J.C. Kapteyn***, edited by Piet C. van der Kruit, Klaas van Berkel
Paperback, ISBN 1-4020-0374-9, November 2001
Hardbound, ISBN 0-7923-6393-0, August 2000

Volume 245: ***Waves in Dusty Space Plasmas***, by Frank Verheest
Paperback, ISBN 1-4020-0373-0, November 2001
Hardbound, ISBN 0-7923-6232-2, April 2000

Volume 244: ***The Universe***, edited by Naresh Dadhich, Ajit Kembhavi
Hardbound, ISBN 0-7923-6210-1, August 2000

Volume 243: ***Solar Polarization***, edited by K.N. Nagendra, Jan Olof Stenflo
Hardbound, ISBN 0-7923-5814-7, July 1999

Volume 242: ***Cosmic Perspectives in Space Physics***, by Sukumar Biswas
Hardbound, ISBN 0-7923-5813-9, June 2000

Volume 241: ***Millimeter-Wave Astronomy: Molecular Chemistry & Physics in Space***, edited by W.F. Wall, Alberto Carramiñana, Luis Carrasco, P.F. Goldsmith
Hardbound, ISBN 0-7923-5581-4, May 1999

Volume 240: ***Numerical Astrophysics***, edited by Shoken M. Miyama, Kohji Tomisaka,Tomoyuki Hanawa
Hardbound, ISBN 0-7923-5566-0, March 1999

Volume 239: ***Motions in the Solar Atmosphere***, edited by Arnold Hanslmeier, Mauro Messerotti
Hardbound, ISBN 0-7923-5507-5, February 1999

Volume 238: ***Substorms-4***, edited by S. Kokubun, Y. Kamide
Hardbound, ISBN 0-7923-5465-6, March 1999

For further information about this book series we refer you to the following web site:
www.springeronline.com

To contact the Publishing Editor for new book proposals:
Dr. Harry (J.J.) Blom: harry.blom@springer-sbm.com